Silesian University of Technology

PH.D. THESIS

Numerical and experimental research on the influence of air on the cavitation dynamics

Author:
Emad Hasani Malekshah

Supervisor:
Prof. dr hab. inż. Włodzimierz Wróblewski

Scientific discipline: Environmental Engineering, Mining and Power Engineering

Gliwice, Poland, 2024

Acknowledgements

I extend my sincere appreciation to Professor Włodzimierz Wróblewski for his continuous support, invaluable guidance, patience, and profound insights throughout my doctoral journey. My research and academic endeavors have been greatly influenced by his mentoring.

I am deeply thankful to Professor Mirosław Majkut and Dr. Michael Strozik, as well as Dr. Krzysztof Bochon, for their invaluable assistance in conducting experiments, setting up experimental apparatus, and offering invaluable insights that significantly enriched the outcome of this thesis. I express my sincere gratitude to Professor Sławomir Dykas, the Head of the Department, for his support of doctoral students. A special thanks is extended to Dr. Krzysztof Rusin, who is more of a friend than a colleague, for his fantastic academic and administrative assistance, which has wonderfully helped in the progress of my research. Furthermore, I extend my appreciation to Grażyna Roskosz, the administrative specialist of the department, for her continuous, swift, and precise assistance.

I am extremely thankful to my family, whose everlasting love, support, and understanding have been my pillars of strength.

I dedicate my doctoral thesis to:

To my lovely mother, whose existence defines mine.

To my late brother, whose memory never fades from my thoughts.

Table of Contents

List of Publications

The thesis consists of 9 papers listed below, categorized into four chapters. The full texts of these papers can be found in the Appendices chapter. The papers are referred to by the Roman numerals throughout the thesis.

Chapter 2: Studying Dissolved Air Effects on Cavitating Flow Around Hydrofoil and Within Venturi Nozzle (Natural Cavitation)

Paper I: Wróblewski, W., Bochon, K., Majkut, M., **Malekshah, E. H.**, Rusin, K., & Strozik, M. (2021). An experimental/numerical assessment over the influence of the dissolved air on the instantaneous characteristics/shedding frequency of cavitating flow. Ocean Engineering, 240, 109960.
DOI: 10.1016/j.oceaneng.2021.109960
IF: 4.372 (2021)

Paper II: Wróblewski, W., Bochon, K., Majkut, M., Rusin, K., & **Hasani Malekshah, E.** (2022). Numerical study of cavitating flow over hydrofoil in the presence of air. International Journal of Numerical Methods for Heat & Fluid Flow, 32(5), 1440-1462.
DOI: 10.1108/HFF-03-2021-0204
IF: 5.181 (2021)

Paper III: **Malekshah, E. H.**, Wróblewski, W., & Majkut, M. (2022). Dissolved air effects on three-phase hydrodynamic cavitation in large scale Venturi-Experimental/numerical analysis. Ultrasonics Sonochemistry, 90, 106199.
DOI: 10.1016/j.ultsonch.2022.106199
IF: 8.4 (2022)

Paper IV: **Malekshah, E. H.**, Wróblewski, W., Bochon, K., Majkut, M., & Rusin, K. (2022). Experimental analysis on unsteady characteristics of sheet/cloud cavitating Venturi flow under the effect of dissolved air. Archives of Thermodynamics, 63-84.
DOI: 10.24425/ather.2022.143172
IF: 0.284 (2022)

Chapter 3: Modification of Turbulence Modelling for Three-Phase Cavitating Flow

Paper V: **Malekshah, E. H.**, & Wróblewski, W. (2022). Effect of turbulence modelling and non-condensable gas on cloud cavity dynamics. International Journal of Heat and Fluid Flow, 98, 109070.
DOI: 10.1016/j.ijheatfluidflow.2022.109070
IF: 2.6 (2022)

Paper VI: **Hasani Malekshah, E.**, Wróblewski, W., Bochon, K., & Majkut, M. (2022). Evaluation of modified turbulent viscosity on shedding dynamic of three-phase cloud cavitation around

hydrofoil–numerical/experimental analysis. International Journal of Numerical Methods for Heat & Fluid Flow, 32(12), 3863-3880.
DOI: 10.1108/HFF-03-2022-0188
IF: 4.2 (2022)

Chapter 4: Developing Merging Theory-Based Cavitation Model

Paper VII: **Malekshah, E. H.**, & Wróblewski, W. (2022). Merging theory-based cavitation model adaptable with non-condensable gas effects in prediction of compressible three-phase cavitating flow. International Journal of Heat and Mass Transfer, 196, 123279.
DOI: 10.1016/j.ijheatmasstransfer.2022.123279
IF: 5.2 (2022)

Chapter 5: Studying Air Injection Effects on Cavitating Flow Around Hydrofoil (Ventilated Cavitation)

Paper VIII: **H Malekshah, E.**, Wróblewski, W., Bochon, K., & Majkut, M. (2023). Experimental analysis on dynamic/morphological quality of cavitation induced by different air injection rates and sites. Physics of Fluids, 35(1).
DOI: 10.1063/5.0136521
IF: 4.6 (2022)

Paper IX: **Malekshah, E. H.**, Wróblewski, W., & Majkut, M. (2024). Investigation on natural to ventilated cavitation considering the air-vapor interactions by Merging theory with insight on air jet location/rate effect. International Journal of Heat and Mass Transfer, 220, 124968.
DOI:
IF: 5.2 (2022)

Chapter 6: Experimental Setup and Facilities

The above-listed papers involve describing the experimental setup and facilities.

CRediT Authorship Contribution Statement

The author and co-authors contribution to each paper was provided in the section of "CRediT authorship contribution statement" in each corresponding paper in the Appendices. The author's contribution is as follows:

Paper I: **Emad Hasani Malekshah:** Formal analysis, Writing – original draft, Writing – review & editing (Emad Hasani Malekshah's contribution was equal to 35%.).

Paper II: **Emad Hasani Malekshah:** Conceptualization, Methodology, Software, Investigation, Validation, Formal analysis, Writing – original draft, Writing – review & editing (Emad Hasani Malekshah's contribution was equal to 25%.).

Paper III: **Emad Hasani Malekshah:** Conceptualization, Methodology, Software, Investigation, Validation, Formal analysis, Writing – original draft, Writing – review & editing (Emad Hasani Malekshah's contribution was equal to 65%.).

Paper IV: **Emad Hasani Malekshah:** Conceptualization; Data curation; Formal analysis; Investigation; Validation; Visualization; Writing – original draft (Emad Hasani Malekshah's contribution was equal to 55%.).

Paper V: **Emad Hasani Malekshah:** Conceptualization, Methodology, Software, Investigation, Validation, Formal analysis, Writing – original draft, Writing – review & editing (Emad Hasani Malekshah's contribution was equal to 70%.).

Paper VI: **Emad Hasani Malekshah:** Conceptualization, Methodology, Software, Investigation, Validation, Formal analysis, Data curation, Writing – original draft, Writing – review & editing (Emad Hasani Malekshah's contribution was equal to 60%.).

Paper VII: **Emad Hasani Malekshah:** Conceptualization, Methodology, Software, Investigation, Validation, Formal analysis, Data curation, Writing – original draft, Writing – review & editing (Emad Hasani Malekshah's contribution was equal to 70%.).

Paper VIII: **Emad Hasani Malekshah:** Conceptualization; Data curation; Formal analysis; Investigation; Methodology; Software; Validation; Visualization; Writing – original draft (Emad Hasani Malekshah's contribution was equal to 55%.).

Paper IX: **Emad Hasani Malekshah:** Conceptualization, Methodology, Software, Investigation, Validation, Formal analysis, Writing – original draft, Writing – review & editing (Emad Hasani Malekshah's contribution was equal to 65%.).

Nomenclature

Abbreviations

RANS	Reynolds-averaged Navier-Stokes	-
uRANS	unsteady Reynolds-averaged Navier-Stokes	-
FVM	Finite Volume Method	-
RNG	Renormalization Group	-
SEM	State Equation Model	-
TEM	Transport Equation Model	-
ZGB	Zwart- Gerber-Belamri	-
DCM	Density Correction Model	-
FBM	Filter-Based Model	-
FBDCM	Filter-Based Density Correction Model	-

Symbols

$\dot{m}$	mass transfer rate	kg s^{-1}
ρ	density	kg m^{-3}
α	volume fraction	-
$\boldsymbol{u}$	velocity	m s^{-1}
R	source term	kg m^{-3} s^{-1}
μ	effective viscosity	Pa s
μ_t	turbulent viscosity	Pa s
μ_l	laminar viscosity	Pa s
n	normal vector	-
t	time	s
V	velocity	m s^{-1}
p_i	partial pressure of the gas	Pa
C_{si}	gas concentration at saturation in the liquid	kg m^{-3}
H_i	Henry's constant	m^{-2} s^{2}
D_i	diffusivity coefficient	m^{2} s^{-1}
σ	surface tension	N m^{-1}
ε	turbulent Dissipation Rate	m^{2} s^{-3}
Δ	local grid size	m^{3}
τ	period of cavity evolution	s
R_B	bubble radius	m
k	turbulent kinetic energy	m^{2} s^{-2}
f	mass fraction	-

Subscriptions

l	liquid	-
v	vapor	-
∞	far field	-
e	evaporation	-
c	condensation	-
ng	non-condensable gas	-

Chapter 1

Introduction

1.1 Cavitation

Cavitation, traced back to Newton (1704) and Euler (1754) [1], was first observed by Reynolds in 1873 during investigations of high-speed ship propellers [2]. The inception of cavitation tunnels dates to Parsons' construction in 1895 at Newcastle [3], where he highlighted cavitation's detrimental effects on ship propeller performance. The foundational concept of cavitation numbers was introduced by Thoma and Leroux in the years 1923–1925 [4].

Cavitation is formed when the local pressure falls below the saturated vapor pressure within a liquid. The term for this phenomenon is cavitation [1]. Cavitation flow, which includes phase transitions, unsteady characteristics, and turbulence, is a complicated multiscale cavity flow that occurs in a variety of fluidic devices, including water turbines, marine propellers, hydrofoils, and underwater vehicles [2, 3]. Franc and Michel's categorization [4] classifies cavitation structures into three primary groups:

- Transient, isolated vapor bubbles that appear within low-pressure zones.
- Periodical cavitation structures, including vapor and vapor-air formations primarily on blade suction sides (attached, partial cavities, supercavitation).
- Cavitation vortices, prevalent at the tips of ship propeller or pump/turbine blades (tip vortex cavitation).

In fluid machinery, cavitation can lead to significant challenges, such as significant reduction in efficiency, vibration, noise, and even erosion. Since cavitation is quite hard to eliminate, research on understanding this phenomenon is still ongoing. Therefore, looking for efficient strategies for better control of cavitation remains a critical scientific problem [5]. To effectively control the dynamics of cavitation, especially its unsteady flow characteristics, we must first gain a deep understanding of this phenomenon and then implement strategies and methods [6]. Knapp [7] identified and examined the mechanics of cavitation, pointing out that the cavity broke off when the re-entrant flow started to move toward it in a reverse direction than the main flow. Also, it should be noted that breaking-off may be affected by other factors such as operating fluid quality and ventilation of non-condensable gas.

1.2 Parameters Shaping Cavitation Dynamics in Fluid Systems

Understanding the complex phenomenon of cavitation requires an examination of various influential parameters that intricately impact its initiation, intensity, and behavior in fluid systems. The emergence of cavitation is contingent upon several parameters:

- Pressure: Variations in pressure levels significantly influence the onset and intensity. Low-pressure conditions facilitate bubble formation, whereas high pressure can induce bubble collapse.
- Fluid Velocity: Fluid acceleration triggers cavitation by creating low-pressure zones, fostering bubble nucleation and growth.
- Fluid Characteristics: Cavitation behavior varies among fluids due to differences in viscosity, density, and compressibility.
- Surface Geometry: Surface irregularities or specific shapes alter the flow dynamics, creating pressure differentials that induce cavitation.
- Temperature: It plays a role in cavitation by modifying liquid properties and vapor pressure, impacting both the bubble formation and collapse dynamics.
- Presence of Nuclei: Pre-existing gas pockets or particulate matter act as nucleation sites, facilitating bubble inception.
- Flow Regime: Changes in flow conditions, transition from laminar to turbulent flow, influence the onset and intensity of cavitation.
- Mechanical Vibrations: External mechanical forces or induced vibrations contribute to cavitation by promoting bubble growth or collapse.
- Chemical Additives: Introducing specific additives or impurities modifies fluid properties, consequently affecting cavitation behavior.
- System Design and Operation: Factors such as pump design, impeller speed, and fluid flow patterns within a system significantly influence the occurrence and intensity of cavitation.

Further to many above-mentioned effective parameters on the cavitating flow, the dissolved air can be known as an influential factor, which has not been fully analyzed by the researchers. Kawakami et al. [8] provided the pressure spectrum on the suction side of the NACA 0015 hydrofoil considering two amounts of dissolved air of 6 ppm and 13 ppm. They proved that the effect of dissolved air on the trend of the pressure spectrum is remarkable. Mäkiharju et al. [9] investigated the dynamics and inception of partial cavitating flows considering the dissolved air. However, the results proved that the developed partial cavity, which is accompanied by a strongly enforced separation line, would not be significantly affected by the dissolved gas mass transfer within the freestream.

1.3 Cavitation Regimes

It is helpful to think about two different phases in the formation of cavitation for practical purposes:

- Cavitation Inception: This is the phase that occurs when a flow regime changes from non-cavitating to cavitating.
- Developed Cavitation: Here, there is either periodic or permanent cavitation, which causes the performance of the machinery to significantly diminish.

This distinction is crucial for deciding whether to tolerate or mitigate cavitation in industrial applications. It becomes critical to comprehend inception or cessation levels when working with developing cavitation. However, in the case of established cavitation, manufacturers need to give priority to determining the influence of cavitation on hydraulic system operations.

Additionally, within attached cavities, a finer classification arises:

- Partial Cavities: These cavities are close to the wall.

- Supercavities: They close away from the boundary, typically observed with foils.

Understanding these differences contributes to a more sophisticated comprehension of cavitation behavior.

1.4 Typical Situations Favorable to Cavitation

Typical conditions where cavitation can form inside a flow are briefly discussed in this section:

- Wall geometry may cause abrupt local velocity increases and pressure decreases in a globally steady flow. This happens when the upper surfaces of propeller and pump blades, bends in pipe flow, or restrictions in the cross-sectional area of liquid ducts (Venturi nozzles) impose curvature on flow streamlines.
- Large turbulent pressure fluctuations can also cause cavitation in shear flows (see jets, wakes, etc.).
- Certain flows, such as fuel feed lines in diesel engines and ducts in hydraulic power plants, are inherently unstable and can quickly produce low pressures at specific points in the flow that lead to cavitation.
- Local wakes are generated by the walls' roughness (such as the concrete spillways of dams), which may lead to the development of small attached cavities.
- A.S.T.M.E. erosion device, liquid cooling of diesel engines, and other vibratory motion of the walls cause oscillating pressure fields to be generated and overlaid on an otherwise uniform pressure field. When negative oscillation happens, cavitation may arise if the oscillation amplitude is sufficiently big.

1.5 Cavitating Flows [4]

Similar to other two-phase liquid-gas flows, cavitating flows are characterized by a large number of interfaces. However, in contrast to liquid-gas flows, their reaction to external perturbations, such as a rise in pressure, can be substantially different.

Apart from shock waves, two-phase flows with gas bubbles typically do not experience sudden fluctuations in mean density. This is because the flow is given a certain level of global stability by the gas's non-condensable nature.

On the other hand, in cavitating flows, the interfaces experience a continuous pressure on one side that is almost identical to the vapor pressure. As a result, they cannot withstand changes in external pressure without quickly changing in size and shape.

Measurements within a cavitating flow are particularly challenging to acquire since intrusive probes generate their own cavitation. However, transparent liquids make surfaces simple to view because of the way they reflect light. An understanding of the flow dynamics can be obtained by observing interfaces with single-shot pictures (with short flash durations of the order of microseconds) or high-speed photography or video (at a typical rate of ten thousand frames per second).

The mass flowrate (per unit surface area) across an interface related to the exchange of liquid and vapor is proportionate to the normal velocities of the liquid or the vapor with respect to the interface. Across the interface, mass conservation results in (see Figure 1.1[4]):

$$\dot{m} = \rho_l \left[V_{ln} - \frac{dn}{dt} \right] = \rho_v \left[V_{vn} - \frac{dn}{dt} \right] \tag{1.1}$$

The normal component of the velocities is denoted by the number n in this equation, while the indices l and v stand for the liquid and vapor phases, respectively. The interface's normal velocity is represented by the notation dn/dt.

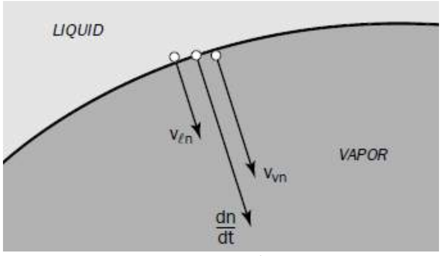

Figure 1.1. The liquid/vapor interface.

Assuming that the flowrate across the interface is low, which is typically the case, the interface is a material surface, meaning that the fluid particles on it are the same at various instants, and the three normal velocities are equal.

1.6 Typical Orders of Magnitude

Large fluctuations in size and velocity over short periods of time can result in the explosion or collapse of cavities caused by interfacial instabilities. This makes their scaling challenging, as does any experimental or numerical examination. Below are some common values found in the field of cavitation.

- A spherical vapor bubble with a radius of 1 cm collapses in about one millisecond in water when exposed to an external pressure of one bar.
- The last phase of the erosion process, known as the cavitating vortex collapse or bubble collapse, lasts about a microsecond.
- An interface's usual velocity typically ranges from a few meters per second to a few hundred meters per second.
- The implosion of vapor structures, such as bubbles and vortices, can result in overpressures that can surpass several thousand bars.

1.7 Gas Diffusion and Nucleus Stability

There are two ways that gas may exist in a liquid: it can be dissolved or trapped in free nuclei. The subject of any exchange between the forms is examined here, based on the fundamental principles guiding the liquid's saturation and the gas's transfer under non-equilibrium conditions. The nucleus and dissolved gas in a static liquid are shown in Figure 1.2.

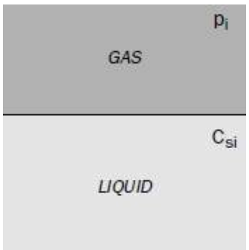

Figure 1.2. A liquid's diffusion equilibrium with its surroundings above it.

Henry's law describes the diffusion equilibrium between a liquid and the atmosphere above it:

$$C_{si} = H_i(T)p_i \tag{1.2}$$

where C_{si} is the concentration of gas I at saturation in the liquid, H_i is the appropriate HENRY's constant, and p_i is the partial pressure of gas I in the atmosphere (Figure 1.2). H_i is represented as $(m/s)^{-2}$, and C_{si} in kg/m^3.

A concentration gradient C occurs if diffusion equilibrium is not reached, and this leads to a mass flux determined by FICK's law.

$$\vec{q}_i = -D_i grad C_i \tag{1.3}$$

D_i is the diffusivity coefficient of element i in equation (1.3). The classical diffusion equation may be determined by the balance of mass transfer for a limited region.

$$\frac{\partial C_i}{\partial t} = D_i \Delta C_i \tag{1.4}$$

Concentrations of air dissolved in water are commonly given in parts per million (ppm), where 1 ppm is equal to 10^{-3} kg/m^3. Under one bar of external pressure, the concentrations of pure nitrogen and pure oxygen at saturation in water are 19 ppm and 43 ppm, respectively. When one takes into account the partial pressures of nitrogen and oxygen in the atmosphere, which are 0.79 bar and 0.21 bar, respectively, one gets 15 ppm of nitrogen and 9 ppm of oxygen, or a total of 24 ppm at atmospheric pressure. In such case, for air in water, the diffusivity coefficient is D = 2×10^{-9} m^2/s, and the HENRY constant is 0.24×10^{-6} $(s/m)^2$.

Let us examine the equilibrium of a static liquid with a spherical nucleus (Figure 1.3). The following equation must be fulfilled for mechanical equilibrium to exist.

$$P_\infty = P_g + P_v - \frac{2\sigma}{R} \tag{1.5}$$

Its diffusive equilibrium is expressed as:

$$C_s = H_{P_g} \tag{1.6}$$

Two cases must be considered:

- The gas tends to migrate from the nucleus to the liquid if the concentration, C_∞, distant from the nucleus, is lower than C_s. The surface tension term rises as the radius falls. The term p_g rises and the diffusive imbalance increases with a constant pressure p_∞ distance from the nucleus, leading to the nucleus' tendency to be resorbed.
- The reverse phenomena happens if C_∞ is greater than C_s: the diffusive imbalance keeps growing as the nucleus volume grows, just like in the preceding example.

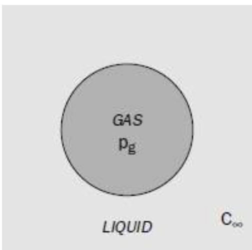

Figure 1.3. Nucleus in a static liquid.

In summary, the nucleus's twofold mechanical and diffusive equilibrium is inherently unstable. If surface tension is disregarded, the result is still the same, but the instability is less and the difference between the concentrations stays constant.

1.8 Literature Review

1.8.1 Numerical Modeling

A variety of methods of numerical modeling of cavitation flow has been proposed for several decades which differ in their complexity, solution schemes, and assumptions [10, 11]. Liu et al. [12] used a hybrid RANS and LES turbulence model to simulate the dynamic of transient cavitating flow around a Clark-Y hydrofoil. They found that the Large Eddy Simulation can capture the interactions between cavitation structures and turbulence. Mathew et al. [13] proposed a new approach for studying the phenomenon of travelling bubble cavitation. The Rayleigh–Plesset equation is numerically integrated to simulate the growth and collapse of a cavitation bubble moving in a varying pressure field over a 2D hydrofoil (NACA-0012). It is concluded that the maximum local pressure goes up to 104 bar during the bubble collapse. Kubota et al. (1992) [14] proposed the first homogeneous model based on the transport equation. They took account of cavitation through the presence of a bubble cluster. Cluster growth and decay are described by employing a modified version of the Rayleigh equation. The model was applied in the two-dimensional steady-state analysis of the flow around a hydrofoil NACA 0015.

One of the first concepts of two-phase flow analysis is the use of a homogeneous model and the assumption that a mixture of a liquid and its vapor is treated as one fluid. In this case, the main difficulty is to determine the parameters of the mixture, mainly the density. This approach was successfully applied by Coutier-Delgosha et al. (2003) [15], which solved the Reynolds-averaged Navier–Stokes equations for the mixture considered as a single fluid with variable density.

The role of turbulence closure models is substantial in the prediction of cavitating flow and its corresponding characteristics. It is associated with high Reynolds numbers and mass transfer between phases, especially when dissolved air is considered. The Reynolds-averaged Navier-Stokes (RANS) turbulence models: the original $k - \varepsilon$ and $k - \omega$ models, were developed to deal with the incompressible flows. Thus, using these turbulence models will result in unsatisfactory results in the prediction of compressible vaporous cavity closure. The existence and unstable nature of the re-entrant jet are usually attributed to the destabilization of the cavity and the transition of the attached sheet cavity to the detached cloud cavity. Based on the experimental observations, it is well demonstrated that the re-entrant jet is the main responsible mechanism for triggering the breaking up of the sheet cavity and shedding of the following unsteady cloud cavity [16, 17]. Turbulence models needed modifications to account for the significant density jump due to the cavitation and re-entrant jet adjacent to the cavity front. For this purpose, the turbulent viscosity in the mentioned regions had to be modified. Coutier-Delghosa et al. [15] showed that the standard RNG $k - \varepsilon$ turbulence model poorly reflects the experimental observations of the vapor cloud shedding when the compressibility effect is not considered. When considering the compressibility effect, the RNG $k - \varepsilon$ turbulence model presents a reliable prediction over the unsteady behavior of the cavitation process. In addition, the modified model gives satisfactory results in different geometries such as hydrofoil [18], foil cascade [19], and Venturi nozzles [15]. Wang et al. [20] analyzed the dynamics of cloud cavitating flow over a hydrofoil. They used Density Correction Model (DCM) to modify the standard RNG $k - \varepsilon$ turbulence model with a special focus on the behavior of the re-entrant jet. They reported that the standard turbulence model predicts shorter cavity lengths than those observed in the experiment. Reversely, by employing the DCM modification, a close agreement is observed between the numerical simulations and experimental observations regarding the cavity closure, re-entrant jet and dominant frequency of lift force. Johansen et al. [21] used the FBM for the modification of the turbulence model based on RANS to simulate the cavitating flow around a square obstacle. They concluded that significant improvement occurred by employing FBM for all grid resolutions: fine grid, intermediate grid, and coarse grid, but the filter-based model becomes smoothly identical to the standard $k-\varepsilon$ turbulence model as the filter size increases.

Since the turbulence and cavitation models are the key factors in the prediction of the cavitating flow, their modifications are highly demanded and necessary to obtain more reasonable results. The two cavitation models often used are the State Equation Model (SEM) [22, 23] and the Transport Equation Model (TEM) such as the Kunz Model [16], Schnerr-Sauer Model [24], Zwart-Gerber-Belamri Model [25] and Singhal Model [26]. Based on the recent experimental observations carried out by Gopalan and Katz [27] and Laberteaux and Ceccio [28], it is reported that vorticity production has a crucial impact on the cavity structure and breaking up the process due to the term of baroclinic torque. However, SEM is not capable of capturing this effect since the gradients of pressure and density are always parallel leading to zero baroclinic torque. Thus, TEM is more compatible with dealing with this phenomenon as it introduces an additional term to calculate the volume fraction of vapor considering the source term for evaporation and condensation processes. Cheng et al. [29] modified the Schnerr and Sauer cavitation model to make it more adapted to the presence of non-condensable gas. In this regard, they connected this cavitation model with the local gas concentration and derived a new mass transfer source term. It was confirmed that the gas content plays an inevitable role in the formation of the cavitation structure downstream of the hydrofoil.

1.8.2 Experimental Investigation

The experimental investigation of cavitating flows plays a pivotal role in the validation of models and numerical simulations used in industrial settings. While simulations offer insights, experiments provide crucial real-world data necessary for validating these models. Such experiments act as a crucial benchmark for refining and improving these models, enabling more effective designs and safer operational practices in various industries reliant on machinery susceptible to cavitation effects.

On the other hand, to make an efficient design of the hydraulic machines and control the cavitation, it is required to understand the unsteady characteristics of this phenomenon [30]. Knapp [7] pointed out that the re-entrant jet initiates the breaking up and alternation of sheet cavity to cloud cavity based on experimental observation. Furthermore, Ganesh et al. [31] conducted an experimental investigation to identify the influential parameters that initiate the breaking up and cloud cavity using a wedge-shaped geometric model. They reported two main cavity-shedding mechanisms, which are the re-entrant jet and the shock wave. The re-entrant jet and the shock wave initiate the cloud cavity and also generate high pulsating pressure at the surface of the object, causing its destruction [32, 33]. Although the unsteady characteristics of the cavitating flow such as force components and vibration are crucial in designing a hydraulic machine, the structure of the cavity can be vital in evaluating the details of the unsteady process. In this context, Reisman et al. [34] reported experimental observations on cloud cavitation around an oscillating hydrofoil captured by the high-speed camera. It was declared that the shape of the cavity affects the pressure pulse acting on the surface of the hydrofoil. Callenaere et al. [17] carried out an experimental analysis to study the instability of the partial cavitation caused by the re-entrant jet. They pointed out that the adverse pressure and ratio of re-entrant jet to sheet cavity thicknesses are the main parameters that determine the intensity of the breaking up process.

1.9 Motivation and Scope of The Thesis

Cavitating flow requires extensive investigation and research due to its significant impact on various industrial applications, especially in turbomachinery devices such as pumps, propellers, and turbines. Cavitation can result in erosion, vibration, noise generation, and reduced efficiency.

Although considerable research has been conducted to understand this phenomenon, the effect of a third phase (i.e. dissolved air in water) is often overlooked as a result of the complexity it introduces in both numerical simulations and experimental analysis. This doctoral thesis aims to comprehensively understand the impact of dissolved air on cavitating flow. This objective will be pursued through the following steps:

- Investigating natural and ventilated cavitating flow in the presence of dissolved air (i.e., three-phase cavitating flow) to explore its effects on the flow's characteristics. This investigation mainly relies on numerical simulations and experimental analysis.
- Modifying numerical methods, focusing on turbulence and cavitation models, to ensure adaptability to three-phase cavitation.
- Examining the modified models using experimental data.
- Implementing modified models to predict the characteristics of both natural and ventilated cavitating flow.

The methodologies and results are organized into five chapters as follows:

Chapter 2, titled "Studying Dissolved Air Effects on Cavitating Flow Around Hydrofoil and Within Venturi Nozzle (Natural Cavitation)", describes the initial phase of this Ph.D. research, involving preliminary numerical and experimental analyses to determine the potential impact of dissolved air on the dynamic and averaged characteristics of cavitating flow. Further detailed discussions about the methodology and results can be found in papers I, II, III and IV in the Appendix.

Chapter 3, titled "Modification of Turbulence Modelling for Three-Phase Cavitating Flow", aims to adapt the RNG k-ε turbulence model to accommodate cases with significant density differences. The modification seeks to mitigate the overestimation of turbulent viscosity in these scenarios. Extended discussions about the methodology and results can be found in papers V and VI in the Appendix.

Chapter 4, titled "Developing Merging Theory-Based Cavitation Model", presents the development of a modified cavitation model based on merging theory, considering the presence of dissolved air using an Eulerian approach. The validity of the developed model is tested in different flow conditions. Furthermore, results are compared with experimental measurements and visualizations. Detailed discussions about the methodology and results can be found in paper VII in the Appendix.

Chapter 5, titled "Studying Air Injection Effects on Cavitating Flow Around Hydrofoil (Ventilated Cavitation)", aims to examine ventilated cavitation, while still taking into consideration the presence of dissolved air. Further discussions about the methodology and results can be found in papers VIII, and IX in the Appendix.

Chapter 6, titled "Experimental Setup and Facilities", extensively discusses experiments conducted at the cavitation tunnel at the Silesian University of Technology. These experiments focused on cavitating flow around the Clark Y hydrofoil and Venturi Nozzle, meticulously measuring key parameters such as pressure, vibration, dissolved air quantity, flow rate, and temperature. High-speed cameras were used for visualization purposes. The experimental results play a crucial role in every stage of the research. Consequently, experimental investigations and corresponding findings are present in all the papers.

Chapter 2

Studying Dissolved Air Effects on Cavitating Flow (Natural Cavitation) – Papers I, II, III and IV

2.1 The Scope of the Investigation

The initial phase of this Ph.D. research involves conducting preliminary numerical and experimental analyses to determine the potential impact of dissolved air on the dynamic and averaged characteristics of cavitating flow. Specifically, this phase focuses on investigating the presence of dissolved air in the water flow over the hydrofoil and within the Venturi Nozzle. The examined hydrofoil is ClarkY 11.7% with an angle of attack of 8 deg. Hence, the ratio of throat height H_{th} to a height of Venturi H is defined as $AR = H_{th}/H \simeq 0.6$. Also, the throat length (i.e. the distance of throat from the inlet) is 196 mm. The flow simulations are performed under the assumption of different models. Thus, 2phases and 3phases approaches are applied to resolve the presence of dissolved non-condensable gas in combination with the full cavitation model and the Zwart-Gerber-Belamri (ZGB) cavitation model. The calculations were performed with the uRANS model with the assumption of the constant temperature of the mixture. The mixture model is used to treat the multiphase flow. The dynamics and structures of cavities are compared with literature data and experimental results.

Challenges: The primary challenge addressed in this chapter revolves around effectively and uniformly introducing dissolved air into the computational domain. To tackle this issue, the approach to introducing air is inspired by real processes observed in experiments. Consequently, it is concluded that the optimal method involves injecting dissolved air as a component of the mixture (i.e., water and air) from the inlet. 2phases and 3phases models were suggested in this regard. Furthermore, due to the inherently chaotic nature of cavitating flow, the simulations encountered divergence. To overcome this, specific settings were identified, requiring a systematic step-by-step application throughout the simulations to achieve a fully converged simulation. The resolution of both these challenges demanded significant efforts and time, involving the development, execution, and validation of the proposed solutions.

2.2 Presence of Dissolved Air through Mathematical Modeling

The mixture model for simulation of the liquid-vapor-gas flow which assumes the same velocity flow field for each phase is used. The governing conservation equations of momentum in the form of Reynolds averaged Navier-Stokes (RANS) equations and of mass were formulated for the mixture as:

$$\frac{\partial \rho}{\partial t} + \nabla \cdot (\rho \boldsymbol{u}) = 0 \tag{2.1}$$

$$\frac{\partial}{\partial t}(\rho \boldsymbol{u}) + \nabla \cdot (\rho \boldsymbol{u}\boldsymbol{u}) = -\nabla p + \nabla \cdot [\mu(\nabla \boldsymbol{u} + \nabla \boldsymbol{u}^T)] + \rho \boldsymbol{g} \tag{2.2}$$

where ρ represents the density of the mixture.

2.2.1 Full Cavitation Model (Singhal et al. [26] Model)

Singhal et al. [26] proposed a cavitation model called "the full cavitation model". This model solves the continuity equation for the liquid and vapor phases; however, the presence of dissolved non-condensable gas is only considered in a phase change process. As such, the mixture density is defined as follows:

$$\begin{cases} \rho = \rho_l \alpha_l + \rho_v \alpha_v \\ \alpha_l + \alpha_v = 1 \end{cases} \tag{2.3}$$

which is followed by two-phase continuity equations:

vapor phase:

$$\frac{\partial \rho_v \alpha_v}{\partial t} + \nabla \cdot (\rho_v \alpha_v \boldsymbol{u}) = R \tag{2.4}$$

liquid phase:

$$\frac{\partial \rho_l \alpha_l}{\partial t} + \nabla \cdot (\rho_l \alpha_l \boldsymbol{u}) = -R \tag{2.5}$$

where R is the net phase change rate $R = R_e - R_c$.

In the Singhal et al. [26] model the following expressions for vaporization and condensation rates are obtained:

$$R_c = C_c \frac{k}{\sigma} \rho_l \rho_l \sqrt{\frac{2}{3} \frac{(p - p_v)}{\rho_l}} f_v\,, \quad p > p_v \tag{2.6}$$

$$R_e = C_v \frac{k}{\sigma} \rho_l \rho_v \sqrt{\frac{2}{3} \frac{(p_v - p)}{\rho_l}} \left(1 - f_v - f_{ng}\right), \;\; p < p_v \tag{2.7}$$

$$p_v = p_{sat} + \frac{1}{2}(0.39 \rho k) \tag{2.8}$$

where the coefficients of evaporation and condensation C_v and C_c equal to 0.02 and 0.01 respectively. Also, f_v shows vapor mass fraction and f_{ng} denotes dissolved non-condensable gases mass fraction.

2.2.2 2phase and 3phase Models

The 2phase model solves the continuity equation for the liquid and mixture of vapor and air. So, the mixture density is defined as follows:

$$\begin{cases} \rho = \rho_l \alpha_l + \rho_g \alpha_g \\ \alpha_l + \alpha_g = 1 \\ \alpha_g = \alpha_v + \alpha_{ng} \end{cases} \tag{2.9}$$

which is followed by two-phase continuity equations:

vapor phase:

$$\frac{\partial \rho_g \alpha_g}{\partial t} + \nabla \cdot \left(\rho_g \alpha_g \boldsymbol{u}\right) = R \tag{2.10}$$

liquid phase:

$$\frac{\partial \rho_l \alpha_l}{\partial t} + \nabla \cdot \left(\rho_l \alpha_l \boldsymbol{u}\right) = -R \tag{2.11}$$

The cavitation model proposed by Zwart et al. [25] is used to model the process of phase change. In this model, the values of condensation and evaporation rates are calculated from the relations:

$$R_c = C_c \frac{3\rho_v \alpha_v}{R_B} \sqrt{\frac{2}{3} \frac{(p - p_v)}{\rho_l}}, \qquad p > p_v \tag{2.12}$$

$$R_e = -C_v \frac{3\rho_v (1 - \alpha_v) \alpha_{nuc}}{R_B} \sqrt{\frac{2}{3} \frac{(p_v - p)}{\rho_l}}, \qquad p < p_v \tag{2.13}$$

$$p_v = p_{sat} + \frac{1}{2}(0.39 \rho k) \tag{2.14}$$

where the value of the nucleation site volume fraction equals $\alpha_{nuc} = 0.0005$, coefficients of condensation and evaporation are $C_c = 0.01$ and $C_v = 50$. The value of the nuclei radius is assumed to be $R_B = 1$ µm.

The 3phase model solves the continuity equations for the liquid, vapor and air phases, separately. So, the mixture density is defined as follows:

$$\begin{cases} \rho = \rho_l \alpha_l + \rho_v \alpha_v + \rho_{ng} \alpha_{ng} \\ \alpha_l + \alpha_v + \alpha_{ng} = 1 \end{cases} \tag{2.15}$$

which is followed by three-phase continuity equations:

vapor phase:

$$\frac{\partial \rho_g \alpha_g}{\partial t} + \nabla \cdot \left(\rho_g \alpha_g \boldsymbol{u}\right) = R \tag{2.16}$$

liquid phase:

$$\frac{\partial \rho_l \alpha_l}{\partial t} + \nabla \cdot \left(\rho_l \alpha_l \boldsymbol{u}\right) = -R \tag{2.17}$$

Non-condensable gas phase: (2.18)

$$\frac{\partial \rho_{ng}\alpha_{ng}}{\partial t} + \nabla \cdot (\rho_{ng}\alpha_{ng}\boldsymbol{u}) = 0$$

As in 2phase model, the cavitation model proposed by Zwart et al. [25] is used to model the phase change.

In the performed work, the RNG $k - \varepsilon$ turbulence model was used to calculate the mixture turbulence viscosity.

2.3 Efficiency Analysis of Full Cavitation, 2phase and 3phase Models

This section aims to apply different numerical models for simulating unsteady three-phase cavitating flow around a hydrofoil, emphasizing their strengths and weaknesses. The objective is to provide different investigations that have been conducted to understand which model is more suitable for simulation of three-phase cavitating flow and best aligns with experimental data to be used for subsequent investigations. It is emphasized that these investigations have been done for cavitating flow around the hydrofoil. The investigations and key findings are listed and summarized below:

The numerical pressure coefficient distribution around the hydrofoil was compared with the experimental measurement over the same type of hydrofoil. The cavitation number of experimental and numerical cases are about σ = 0.8 and the amount of dissolved air is VF=0.012. By comparing the numerical and experimental results, it is concluded that:

- There is a close agreement between the numerical and experimental pressure coefficient.

In addition, the history of lift forces in a selected range of iterations, which are predicted numerically by all three models, and the corresponding main frequency have been studied. The simulations have been conducted for three levels of dissolved air including VF=0.004, 0.016 and 0.042. The results show that:

- The full cavitation model results indicate that as the air fraction increases, flow dynamics weaken, leading to the disappearance of the phenomenon, and the frequency approaches 0 Hz. This contradicts reality, suggesting incorrect predictions from the model.
- By performing simulation using 2phase model, highly unsteady behavior was observed in the case with a low level of dissolved air. However, for higher air volume fractions, the lift coefficient's amplitude and frequency were reduced compared to cases with lower air content. This aligns with both reality and expectations.
- The 3phase model produces a lift force history and frequency trend that closely resembles the 2phase model.

The average pressure distribution around a hydrofoil is investigated using various numerical methods (2-phase, 3-phase, and full cavitation) and three air contents (VF=0.004, 0.016, and 0.042). It is revealed that:

- At VF=0.004 (lowest air content), the 2-phase and 3-phase models predicted a wavy pressure distribution, indicating the complex cavitating flow. In contrast, the Singhal method yielded a smooth pressure distribution. The Singhal method missed some vortex details, although its overall trend matched the other cases. This observation indicates that the Singhal model is less accurate in predicting the highly unstable vortex flow compared to stable cavitating flow.

To demonstrate the models' ability to predict cavity structure, contours of vapor volume fraction in one period are provided and analyzed. The analysis yields the following key findings:

- While the full cavitation model demonstrates periodicity in cavitating flow for low air content, it remains fully stable in high air content with no changes in the cavity region. This does not align with experimental observations.
- The 2phase and 3phase models predict almost similar cavity structures. However, the prediction done by 3phase model fits better to the experimental observations.

In comparing the results obtained from the full cavitation, 2phase, and 3phase models, it is concluded that the 3phase model provides more accurate predictions. Therefore, the 3phase model will be utilized for subsequent simulations.

2.4 Effect of Dissolved Air on Cavitating Flow Around Clark Y Hydrofoil

The 3phase model will be employed to analyze the impact of dissolved air on cavitating flow around the hydrofoil. Also, the experimental data will complementarily validate the numerical results. To assess the impact of dissolved air on cavitating flow, several parameters were examined, including the history of vapor volume fraction, lift and drag coefficients, shedding frequency, and cavity structure. The examinations are conducted for cavitation numbers in the range of $\sigma = 0.75$ to $\sigma = 2$. Additionally, dissolved air levels of 0, 0.012, 0.022, and 0.042 are considered. The investigations and key findings are listed and summarized below:

2.4.1 Study on Shedding Frequency

The value of static pressure has been experimentally recorded by the fast pressure sensor located at the chamber outlet during the time span of 1s for three different cavitation numbers (σ=0.96, 1.48 and 2.00) and two levels of dissolved air (VF=0.012 and 0.022). Additionally, the corresponding Fast Fourier Transform (FFT) analysis was implemented to calculate the shedding frequency. Based on the measurements, it can be observed that:

- As the cavitation number increases, the amplitude of pressure fluctuations decreases regardless of the dissolved air level. It is noteworthy that a stronger cavitating flow leads to higher amplitudes in pressure fluctuations.
- The FFT analysis proves that the shedding frequency decreases when the dissolved air increases.

The output results of the vibration sensor were measured and analyzed using FFT as a function of the cavitation number and dissolved air volume fractions. The vibration spectrum is compared with the spectrum of pressure fluctuations for the same cases to illustrate the correspondence between both methods, as presented in Table 2.1. it is concluded that:

- The main frequencies of pressure fluctuations in all cases are very close to those extracted from vibrations. It declares that the chamber vibration originates from the shedding vortex of cavitating flow.

Table 2.1 Experimentally detected main frequencies of the pressure fluctuations and chamber vibration.

Dissolved air volume fraction, VF=0.012				
Cavitation number (σ)	0.79	1.08	1.48	1.85
Frequency [Hz], pressure-based	9.5	13	15	16.5
Frequency [Hz], vibration-based	9.5	13	14.5	16.5
Dissolved air volume fraction, VF= 0.022				
Cavitation number σ	0.90	1.16	1.49	1.82
Frequency [Hz], pressure-based	10	12	14.5	15
Frequency [Hz], vibration-based	10.5	11.5	14.5	-

2.4.2 Study on Pressure Distribution

So far, it has become clear that the dynamic characteristics, such as shedding frequency, of cavitating flow are highly affected by the presence of dissolved air. Moreover, it is necessary to comprehend the influence of dissolved air on the averaged features of cavitating flow. To address this, the effect of dissolved air volume fraction is considered in relation to pressure distributions on the suction side of the hydrofoil, measured by high-frequency pressure sensors. It is concluded that:

- The differences in the averaged pressure values in the sheet cavity region among different volume fractions were small and could not be attributed to variations in air content.
- The difference is more visible in the region close to the cavity end.

2.4.3 Study on Flow Structure

Given the highly dynamic and fast nature of cavitating flow, visualization is conducted using a high-speed camera. This technique enables tracking the cavity evolution from inception to detaching and shedding. Flow visualization is performed for various cavitation numbers and dissolved air contents. In addition, the flow structure has been predicted by numerical simulations. Comparison between numerical simulations and experimental observations is an effective way to approve the validity of results. The findings are listed as follows:

- Adding the dissolved air leads to increasing the size of cavity which is obvious in both inception and shedding steps. This is concluded by both numerical simulations, as shown in Figure 2.1, and the experimental observations, as shown in Figure 2.2.

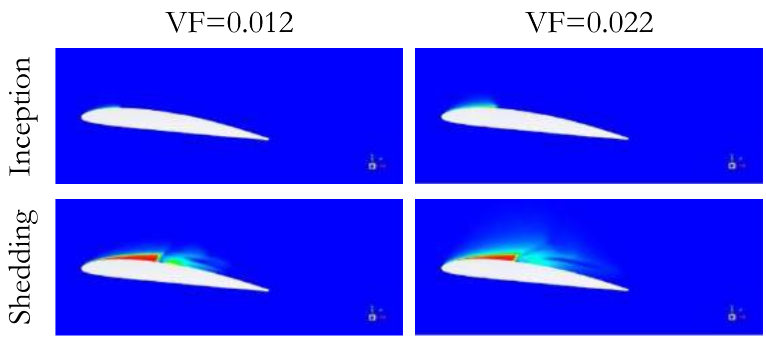

Figure 2.1. Contours of vapor volume fraction for two different air contents at σ = 1.48 (Further details can be explored in paper I).

- Detachment and shedding of the cavity are relatively faster than its generation. Consequently, the majority of the time in the cavity evolution process is devoted to the cavity generation step.

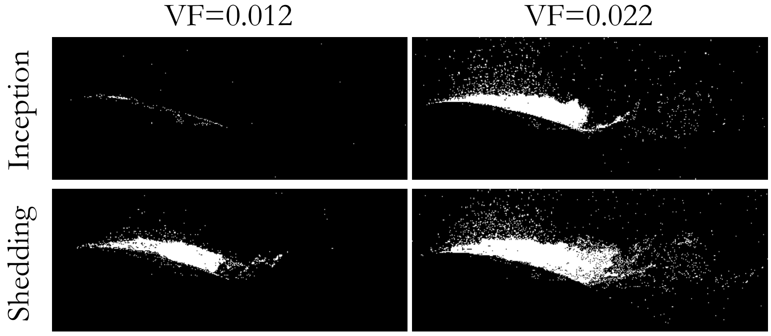

Figure 2.2. Flow visualization for two different air contents at σ = 0.77 (Further details can be explored in paper I).

- The numerical methods fairly accurately predict the characteristics of a sheet cavity, as shown in Figure 2.3.
- However, the numerical model did not satisfactorily capture the evolution of cloud structures. This suggests that tracking the formation of the cloud cavity is challenging with CFD methods.
- The numerical method needs further modification to accurately capture the details of the cloud cavity and its corresponding characteristics.

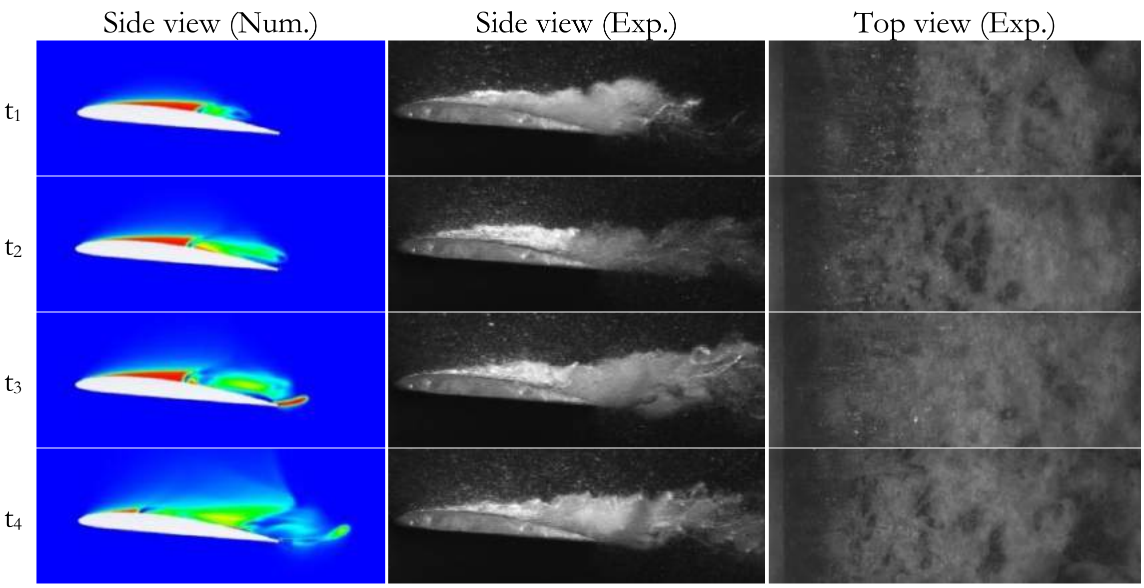

Figure 2.3. Numerical and experimental visualization of cavity at σ=0.77 and VF=0.022 (Further details can be explored in paper I).

2.4.4 Study on Re-entrant Jet

The detachment process of sheet cavitation and the evolution of the detached cloud cavity, influenced by the presence of a re-entrant jet, are studied. The analysis involves examining the three-dimensional contour of water vapor volume fraction, streamlines vectors, velocity field, and a side-view of the captured picture during experimental observation. It is noted that the case with conditions of σ = 0.77 and VF = 0.022 is selected to demonstrate the effect of a re-entrant jet. It is observed that:

- The re-entrant jet is a narrow reverse flow traveling from the trailing edge to the leading edge, primarily consisting of water.

- Following the collision of the re-entrant jet front with the tail of the sheet cavity, the cloud cavity is triggered for shedding.

2.5 Effect of Dissolved Air on Cavitating Flow in Venturi Nozzle

This section aims to investigate cavitating Venturi flow, emphasizing the impact of dissolved air through experimental and numerical methods. The dissolved air levels (6.13, 10.25, 14.83 and 17.03 mg/l) and cavitation numbers ($2.01 \leq \sigma \leq 2.33$) are the main governing parameters. Transient pressure fluctuations are recorded with surface pressure transducers, and cavity evolution is visualized with a high-speed camera. Numerical simulations predict cavitation features, and post-processing involves FFT, PSD, and temporal/spatial grey level distribution analysis. The investigations and key findings are listed and summarized below:

2.5.1 Study on Pressure Distribution

Given the significance of pressure distribution along the flow channel in illustrating the cavitation collapse process, particular emphasis was placed on examining pressure variations at different flow conditions. The study focuses on pressure distributions near the wall of the Venturi nozzle for various cavitation numbers and air contents. Also, the numerical and experimental pressure distributions are compared as shown in Figure 2.4. It is concluded that:

- The averaged pressure remains constant, approaching the saturated vapor pressure within the sheet cavity during cavitation inception and development.
- At high cavitation numbers, the unfavorable pressure gradient region is greater than at low cavitation numbers, leading to rapid collapse and severe shock.
- While the general trend of the averaged pressure distribution is similar in experimental measurements and numerical calculations, it is noted that the collapse process occurs further from the throat in numerical simulations.
- Although the influence of dissolved air on the averaged pressure distribution is negligible in the inception and development regions, it becomes more detectable in the cloud cavity region.

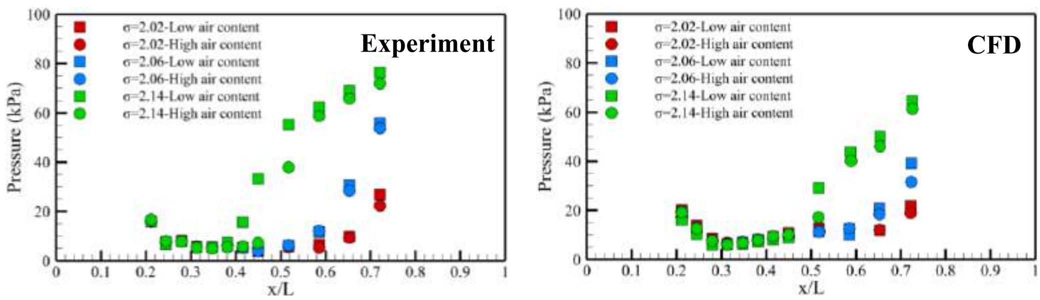

Figure 2.4. Averaged pressure distribution as a function of cavitation number and air content based on experimental measurements and numerical simulations (Further details can be explored in paper III).

2.5.2 Study on Shedding Frequency

The distributions of vapor and air volume fractions over the flow time, along with corresponding Continuous Wavelet Transform (CWT) analyses, are provided and studied. The time-dependent distributions of volume fractions are presented in two stages, illustrating cases with low and high air contents. CWT is employed to calculate the shedding frequency during various simulation stages.

- The averaged vapor volume fraction remains at the same level when the air content enhances; however, its amplitude considerably rises.
- Regardless of the cavitation number, the shedding frequency is reduced when the level of dissolved air enhances.
- The shedding frequency decreases more in the cases with a higher cavitation number.

2.5.3 Study on Flow Structure

The cavity evolution is depicted through numerical simulation for σ = 2.02 with air content of 10.25 mg/l. Snapshots of predicted cavities in Figure 2.5 provide examples. Notably, half of the computational domain is considered due to symmetric geometry. Additionally, the interference effect between the bottom and upper parts of cavitation inside the Venturi is neglected. It is observed that:

- The adverse pressure adjacent to the Venturi surface leads to the separation of the cavity from the surface.
- The re-entrant jet significantly influences cavity separation.

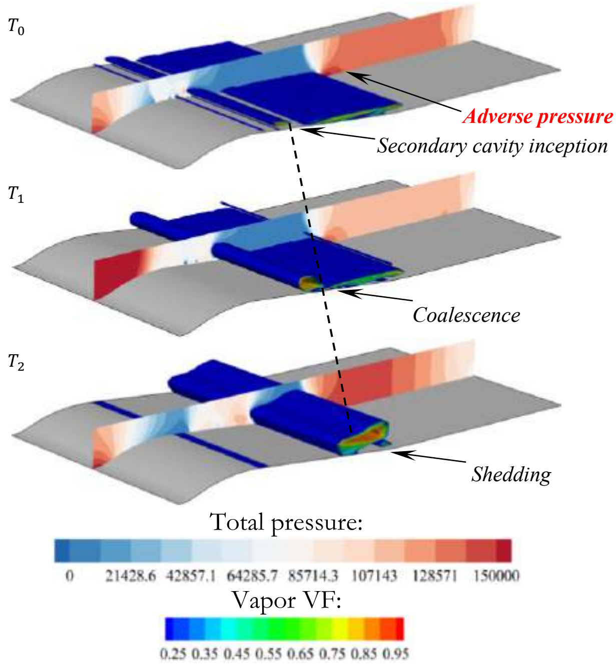

Figure 2.5. Simulated cavity evolution in Venturi Nozzle (σ=2.02 with air content of 10.25 mg/l) represented by vapor volume fraction iso-surfaces and total pressure contours (Further details can be explored in paper III).

The flow visualization is conducted for different cavitation numbers and dissolved air levels. Additionally, for all cases, one period of cavity evolution is extracted using developed in-built LabView software. Furthermore, the post-processing techniques, including mean grey level distribution and temporal/spatial grey level distribution, are applied to better and deeper interpretation of visualized pictures. The following key results are concluded:

- In the case of Venturi Nozzle and based on the presented visualizations, significant influence on the cavitation size, configuration and periodicity is observed with increasing dissolved air. It is more obvious in the case of lower cavitation number. In Figure 2.6, a single snapshot serves as a sample illustrating the impact of dissolved air and cavitation number.

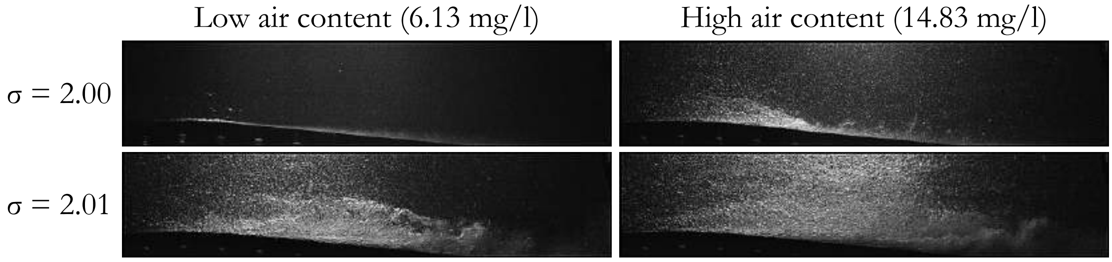

Figure 2.6. The impact of dissolved air and cavitation number on the cavity structure (Further details can be explored in paper IV).

2.5.4 Study on Re-entrant Jet

The structure, location, and strength of the re-entrant jet front between specific time span are studied based on experimental visualization. For this purpose, the images show the cavity evolution within half of the test section along with the Venturi nozzle for the case with $\sigma = 2.06$ and low air content 10.25 mg/l. Using the visualization, the main conclusions are as follows:

- The shedding vortex is repeatedly generated in the cloud cavity region. The shedding vortex inflates, detaches, and sheds downstream.
- The re-entrant jet does not move steadily forward or backward; it is temporarily pushed forth and back. The forward motion is faster than the backward movement.

2.5.5 Temporal-Spatial Grey Level Distribution (Image Processing)

Given the highly dynamic nature of cavitating flow, a tool facilitating a deeper understanding of its dynamic features is crucial. The temporal-spatial grey level distribution is proposed to analyze the structure of cavitating flow at specific times and locations, developed using LabView. Temporal-spatial grey level distributions at various cross-sections for cases with $\sigma = 2.14$, both low and high air contents, are examined. The results of this analysis show that:

- The strongest cavity region is generated near the throat and inside the sheet cavity.
- A significant increase in cavity length is observed as the level of air content increases, clearly evident across all cross-sections.
- In the case with a higher amount of dissolved air, the grey level distributions indicate the presence of numerous scattered bubbles in the chamber, particularly around the throat where the pressure level is lower than in other regions.

Furthermore, morphological analysis is performed using the temporal-spatial grey level distribution to explore the influence of cavitation number and air content level on cavity structure. Figure 2.7 illustrates this analysis for a specific cavitation number (σ=2.02) as an example. The analysis reveals that:

- When comparing the length of the sheet cavity with the full cavity zone, it is evident that in the case of a higher cavitation number, the cavity is predominantly composed of the sheet cavity, irrespective of the level of air content.
- The addition of dissolved air results in a higher increment rate of (L_{sheet}/L_{cavity}) compared to (L_{cloud}/L_{cavity}). This observation indicates a greater impact of dissolved air on the sheet cavity than on the cloud cavity.

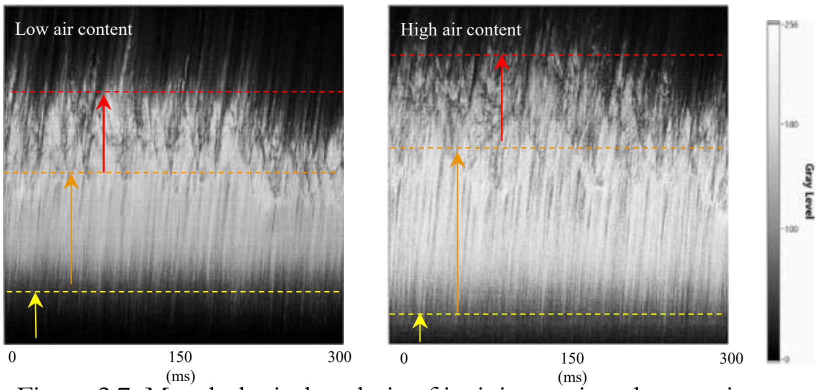

Figure 2.7. Morphological analysis of incipient point, sheet cavity and cloud cavity for σ=2.02 low (10.25 mg/l) and high (17.03 mg/l) air contents (Further details can be explored in paper III).

2.5.6 Mean Grey Level Distribution (Image Processing)

The mean grey level distribution is a technique which shows the general shape of cavitation with dynamic features eliminated. By averaging the gray level of each pixel of the captured image over a specific period, the mean value of the gray level is a sort of image processing that shows the mean cavity length and depicts clearer boundaries of cavity region. The mean value of the grey level and schematic of the cavity boundary to indicate the impact of cavitation number (σ=2.02, 2.06, 2.14 and 2.16) and the dissolved air content (10.25 and 17.03 mg/l) on the structure of the cavity are calculated and studied. The mean value is taken over 300ms of the captured movie covering five periods. The Mean grey level distribution for one cavitation number (σ=2.02) is shown in Figure 2.8. The analysis leads to following conclusions:

- It is confirmed that a larger cavity is generated at lower cavitation numbers.
- Larger cavities observed in cases with a higher amount of dissolved air.

Figure 2.8. Mean value of grey level for cavitation number σ=2.02 and air contents 10.25 and 17.03 mg/l (Further details can be explored in paper III).

These assessments confirm the effect of dissolved air. However, the extent of impact varied depending on the quantity of dissolved air, the specific parameter studied, and the numerical simulation method employed. Also, it underscores computational challenges in simulating dynamic cavitation flow and calls for refined numerical models, particularly in turbulence modeling, to enhance accuracy and align with experimental quantifications.

Chapter 3

Modification of Turbulence Modeling for Three-Phase Cavitating Flow – Papers V and VI

3.1 The Scope of the Investigation

In Chapter 2, the crucial role of dissolved air in the dynamics of cavitating flow is understood. Additionally, the superiority of the 3-phase model in handling three-phase cavitating flow is emphasized. This chapter aims to modify the RNG $k-\varepsilon$ turbulence model to ensure compatibility with the present problem since the RNG $k-\varepsilon$ model yields an overestimation of the turbulent viscosity; it leads to damping the dynamics of the cavitating flow. To solve this problem, the Density-Corrected Method (DCM), Filter-Based Model (FBM) and Filter-based density correction model (FBDCM) are used to modify the turbulent viscosity. The simulations are carried out for different cavitation numbers with and without dissolved air based on standard and modified turbulence models. Furthermore, the numerical results are compared with the experimental data.

Challenges: To prevent cavitation damping, modifications are made to the turbulent viscosity in the RNG $k-\varepsilon$ turbulence model. The primary challenge lies in choosing the optimal modification model to achieve accurate and desirable results. Consequently, numerous simulation cases must be conducted, and the results must be validated against experiments. This process involves extensive efforts and time for simulations, post-processing, and data interpretation. It is important to note that Ansys Fluent employs the standard form of the turbulence model. The second significant challenge involves the need to develop User-Defined Functions for modification models and integrate them into Ansys Fluent.

3.2 Turbulence Model and Modification Methods

The RNG $k-\varepsilon$ turbulence model is defined by the following equations:

$$\frac{\partial(\rho k)}{\partial t} + \nabla \cdot (\rho \boldsymbol{u} k) = \nabla \cdot \left[\left(\mu + \frac{\mu_t}{\sigma_k}\right)\nabla k\right] + G_k - \rho\varepsilon \tag{3.1}$$

$$\frac{\partial(\rho \varepsilon)}{\partial t} + \nabla \cdot (\rho \boldsymbol{u} \varepsilon) = \nabla \cdot \left[\left(\mu + \frac{\mu_t}{\sigma_\varepsilon}\right)\nabla \varepsilon\right] + \frac{c_1\varepsilon}{k}G_k - c_2\rho\frac{\varepsilon^2}{k} \tag{3.2}$$

where the effective viscosity is defined as $\mu = \mu_t + \mu_l$ and $\mu_t = \rho C_\mu k^2/\varepsilon$ denotes the turbulent viscosity and the constant is assumed as $C_\mu = 0.084$.

3.2.1 Density Corrected Model (DCM)

The modified turbulent viscosity is given as follows [15]:

$$\mu_t = f(\rho) C_\mu k^2 / \varepsilon \tag{3.3}$$

$$f(\rho) = \rho_v + \left(\frac{\rho_v - \rho}{\rho_v - \rho_l}\right)^n (\rho_l - \rho_v) \tag{3.4}$$

with such a treatment, the eddy viscosity is locally adjusted based on the DCM factor $f(\rho)$.

3.2.2 Filter-Based Model (FBM)

Modified turbulent viscosity based on FBM is defined as follows [21, 35]:

$$\mu_{t-FBM} = C_\mu \rho_m f_{FBM} \frac{k^2}{\varepsilon} \tag{3.5}$$

$$f_{FBM} = min\left[1.0, C_3 \frac{\Delta}{l_{RANS}}\right], l_{RANS} = \frac{k^{3/2}}{\varepsilon} \tag{3.6}$$

$$C_3 \approx \frac{\gamma}{4C_\mu\sqrt{3/2}} \tag{3.7}$$

where the filter size is calculated based on the local grid size as $\Delta = \left(\Delta_x \Delta_y \Delta_z\right)^{1/3}$.

3.2.3 Filter-Based Density Correction Model (FBDCM)

This model combines the merits of both DCM and FBM and is defined as follows:

$$\mu_{T-FBDCM} = \frac{C_\mu \rho_m k^2}{\varepsilon} f_{hybrid} \tag{3.8}$$

$$f_{hybrid} = \xi(\rho/\rho_l) f_{FBM} + [1 - \xi(\rho/\rho_l)] f_{DCM} \tag{3.9}$$

$$\xi(\rho/\rho_l) = 0.5 + \tanh\left(\frac{\frac{C_1(0.6(\rho/\rho_l) - C_2)}{0.2(1 - 2C_2) + C_2}}{2tanh(C_1)}\right) \tag{3.10}$$

where C_1, C_2 and C_μ are model constants and set as 4, 0.2 and 0.09, respectively.

3.3 Effects of Turbulence Model's Modifications

The present paper aims to modify the turbulence models based on DCM, FBM and FBDCM approaches to provide a better numerical prediction of the cavitating flow around the hydrofoil when the dissolved air is taken into consideration as the third phase. Moreover, the numerical simulations are supplemented by experimental observation and measurements. Two amounts of dissolved oxygen of 0 and 2.1 ppm were taken into consideration in a range of cavitation numbers between 0.91 and 2.04. The investigations and key findings are listed and summarized below:

3.3.1 Study on Shedding Frequency

Based on the literature survey, one can notice that different frequency has been reported for a case with similar operating and boundary conditions. The shedding frequencies determined by the present numerical simulations with different viscosity modifications were compared with some other numerical and experimental references, as presented in Table 3.1. The case study is cavitating flow around a ClarkY hydrofoil, for σ=0.8, Re=7×10^5, without consideration of dissolved air. The following key results are revealed:

- It is declared that there are different modes of frequency, however, the one with the highest amplitude is known as the shedding frequency.
- It can be concluded that predictions made by DCM align more closely with those reported by other researchers by comparing the results.

Table 3.1. Shedding frequency at σ=0.8, Re=7×10^5 (Further details can be explored in paper V and VI).

Source	Shedding frequency	
	$f_1(Hz)$	$f_2(Hz)$
Present study [Standard $k-\varepsilon$]	25.2	65.1
Present study [DCM]	29.4	69.9
Present study [FBM]	20.0	42.8
Present study [FBDCM]	18.32	38.3
Wei et al. [34] [Standard $k-\varepsilon$]	27.3	50.8
Wei et al. [34] [DCM]	35.1	70.3
Liu et al. [20] [FBM]	29.3	72.4
Huang Biao et al. [35] [FBM]	25.2	-
Wei et al. [34] [FBDCM]	27.3	43.0

During experimental measurements, the shedding frequency is determined from pressure fluctuations recorded by a fast sensor on the hydrofoil surface. Sensors are placed at x/c=0.12, 0.46, and 0.79. Prior to using recorded fluctuations, a location sensitivity analysis is performed to assess the impact of sensor placement on shedding frequency. Shedding frequencies from pressure and vibration sensors are compared for three cavitation numbers. It is concluded that:

- The data from the last pressure sensor, closer to the trailing edge, is more suitable for calculating the main shedding frequency and aligns with the vibration frequency.

The primary purpose of employing viscosity modification models is to prevent over-prediction of viscosity. Also, applying the viscosity modification models is expected to result in a more dynamic and realistic cavitation flow. To demonstrate these effects, the distribution of vapor volume over time for different models (standard, DCM, and FBM), along with their corresponding dominant frequencies are thoroughly analyzed. The results revealed that:

- The standard model predicts harmonic behavior in vapor volume, while modification models induce a more chaotic fluctuation in cavitating flow.
- DCM predicts a higher shedding frequency, while FBM and FBDCM forecast a lower frequency compared to the standard model.

This section aims to analyze the impact of adding dissolved air on shedding frequency through numerical simulations. The fluctuation of vapor volume before and after adding dissolved air is examined for cavitation numbers σ=1.01 and σ=1.18 based on DCM and FBM models. The continuous wavelet transform (CWT) is used as a supplementary tool to extract frequency continuously over time. After adding dissolved air, it is observed that:

- The main frequency decreases regardless of cavitation number and modification model.
- The cloud cavity exhibits stronger local dynamic behavior leading to micro-instability and more stable global characteristics as shown in Figure 3.1, resulting in a lower shedding frequency.

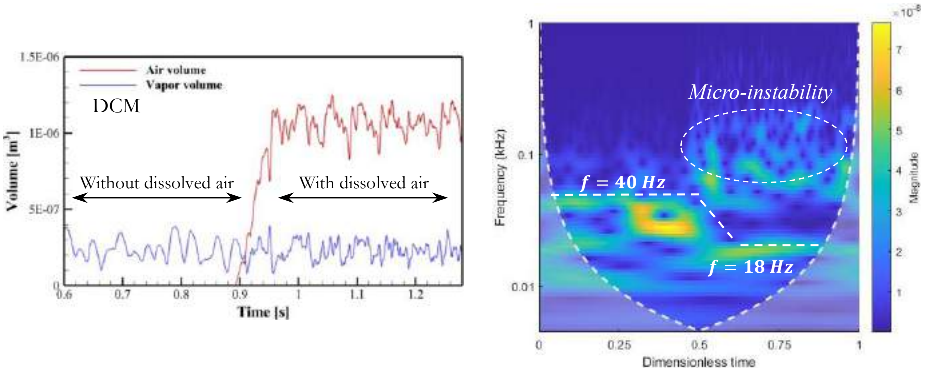

Figure 3.1. Effect of dissolved air on the dynamic of cavitating flow and shedding frequency based on the numerical prediction (Further details can be explored in paper V).

3.3.2 Study on Lift and Drag Forces

The study on lift and drag coefficients as a function of cavitation number, viscosity modification models, and dissolved air levels concludes:

- Reducing the cavitation number results in an enhanced drag coefficient and reduced lift coefficient.
- Different viscosity modification models exhibit a more significant impact on the drag coefficient distribution than on the lift coefficient.
- Predicted values for both lift and drag coefficients by DCM and FBM surpass those calculated using the standard model.
- Dissolved air has a negligible effect on the lift coefficient, but it leads to a consistent rise in the drag coefficient across various cavitation numbers.

3.3.3 Study on Flow Structure under Effect of Viscosity Modification

To assess the predictive capability of standard, DCM, FBM and FBDCM models for flow structure, the evolution of cavitation at σ=1.18 with dissolved air is characterized through numerical simulation and compared with experimental observations. Three snapshots of cavitating flow are shown in Figure 3.2 as a sample. This comparison with experimental observations aids in understanding local parameters like velocity vector and vorticity magnitude, which can be challenging or impossible to obtain solely through experimental techniques. The comparison revels that:

- The standard model predicts smaller cavities with respect to experimental ones.
- The modified models generate larger cavity closures which fits better with the experimental observation.
- Comparing the volume of the cavity, we can conclude that the DCM model releases the best prediction of cavity structure.

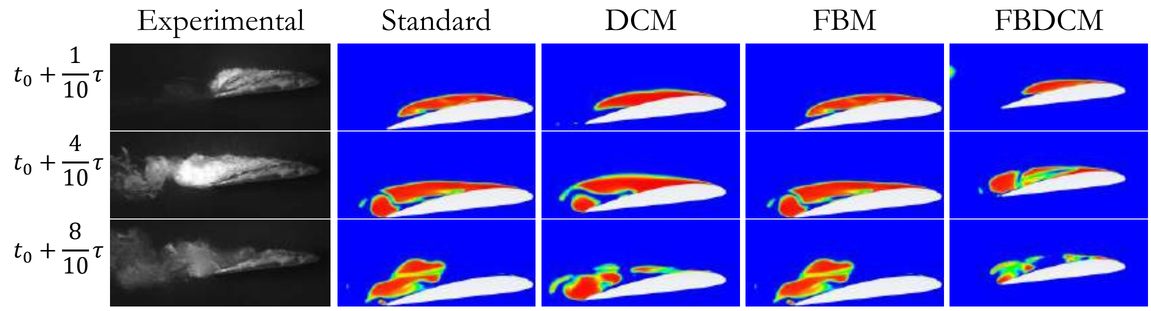

Figure 3.2. Cavity structure as function of viscosity modification methods, σ=1.18, with dissolved air - 2.1ppm (Further details can be explored in paper V and VI).

These findings collectively emphasize the nuanced impact of turbulence model modifications on cavity behavior and shed light on the diverse predictive capacities of these adjustments in different aspects of flow dynamics. Considering these outcomes, the DCM method emerges as particularly advantageous for portraying cavity structure dynamics amidst turbulence model modifications. Consequently, for future investigations, the DCM method will be prioritized to delve deeper into the intricacies of cavitating flow dynamics.

Chapter 4

Developing Merging Theory-Based Cavitation Model – Paper VII

4.1 The Scope of the Investigation

In Chapters 2 and 3, it was declared that a three-phase model for solving the governing equations is more suitable for handling three-phase cavitating flow. Furthermore, the turbulence model has been modified to adapt to the significant density differences and prevent the overestimation of turbulent viscosity. This chapter is devoted to developing a modified cavitation model based on the merging theory, considering the dissolved air in an Eulerian approach. The diffusion process is modeled to constitute the new bubble of the mixture; as a result, the bubble pressure is corrected based on the local air level. Also, the pressure fluctuation effect is applied in the calculation of the pressure of the mixture bubble. After introducing the developed cavitation model, its validity is tested via both natural and ventilated cavitation. Additionally, the obtained results are compared with experimental measurements and visualizations.

Challenges: The standard cavitation models employed in Ansys Fluent do not account for the impact of a third phase, as they are specifically designed for two-phase cavitation scenarios involving mass transfer between water and vapor. Developing a concept for a new cavitation model presents a formidable challenge, as it necessitates alignment with the physics of cavitation while achieving convergence in simulations. Furthermore, to validate the accuracy of the model, multiple case studies are essential.

4.2 Merging Process of Vapor and Gas Phases

The current approach suggests including the dissolved non-condensable gas, in this example air, into the cavitation model. This method contributes to the formation, expansion, and collapse of a mixture bubble, which can help the prediction to get closer to experimental data. Although some variables, such as α_{nuc} and R_B, are affected due to the presence of dissolved non-condensable gas, the current method solely facilitates estimating changes in the pressure of cavity bubble p_B.

Under the assumption of the polytropic behavior of a bubble and using merging theory, the mixture pressure p_m is computed as the sum of partial pressures of gas and vapor. Also, the merging process concept is used for this purpose relying upon the Eulerian point of view, and Figure 4.1 illustrates the process, helping to schematically explain the concept. Furthermore, the concept of merging theory is thoroughly discussed in paper VII.

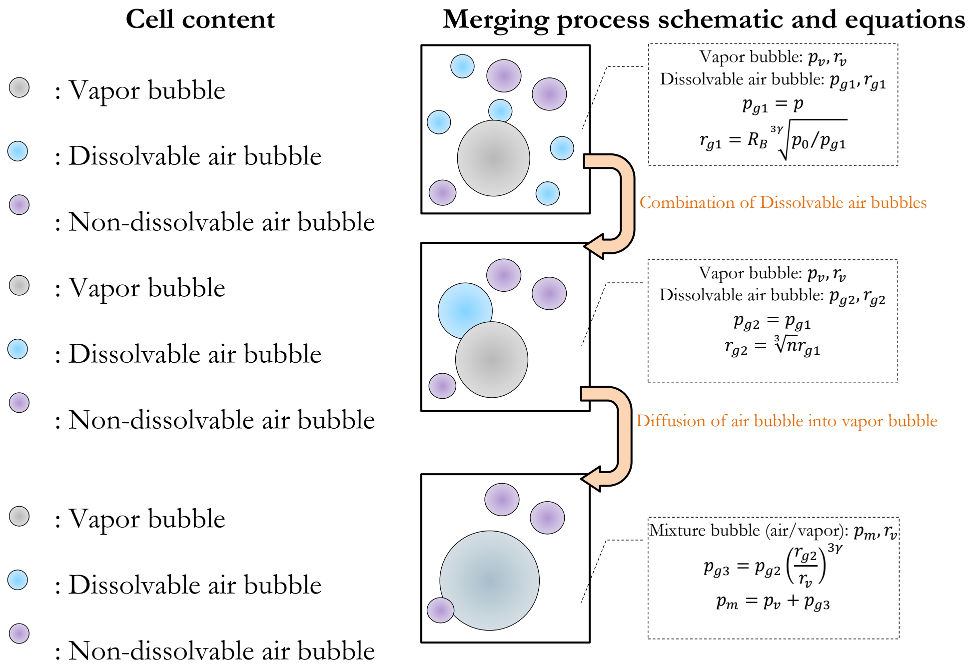

Figure 4.1. Merging process of vapor and gas bubbles (if $r_v > r_{g2}$).

Employing the merging theory, the Rayleigh-Plesset equation can be rewritten as follows:

$$R_B \frac{d^2 R_B}{dt^2} + \frac{3}{2}\left(\frac{dR_B}{dt}\right)^2 + \frac{4\mu_l}{\rho_l R_B}\left(\frac{dR_B}{dt}\right) + \frac{2S}{\rho_l R_B} = \frac{\left(p_v + p_{g2}\left(R_{g2}/R_v\right)^{3\gamma}\right) - p}{\rho_l}, \quad (4.1)$$

Using the developed Rayleigh-Plesset equation, the modified cavitation source terms are obtained using the same method as for the original ZGB cavitation source term, by ignoring the impacts of the second-order terms and surface tension:

$$\begin{cases} R_e = F_{vap} \dfrac{3\alpha_{nuc}(1-\alpha_v)\rho_v}{R_B} \sqrt{\dfrac{2}{3} \dfrac{p_v + p_{g2}\left(R_{g2}/R_v\right)^{3\gamma} - p}{\rho_l}}, & p_m > p \\ R_c = -F_{cond} \dfrac{3\alpha_v \rho_v}{R_B} \sqrt{\dfrac{2}{3} \dfrac{p - p_v + p_{g2}\left(R_{g2}/R_v\right)^{3\gamma}}{\rho_l}}, & p_m < p \end{cases}. \quad (4.2)$$

4.3 Effects of Cavitation Model Modifications

In the present chapter, an attempt has been made to develop a cavitation model based on a merging theory that is compatible with the effects of dissolved non-condensable gas. According to this theory, the pressure inside the vapor bubble is influenced by the surrounding dissolved air bubbles. To assess the efficiency and accuracy of the new cavitation model, the analysis of three-phase cavitating flow is conducted at two cavitation numbers (σ=0.9 and 1.75) and two levels of dissolved air (VF=0.009 and 0.013). It is important to note that the current simulations were performed using a modified and developed numerical method presented in the preceding and current chapters. The investigations and key findings are listed and summarized below:

4.3.1 Function analysis of modified Rayleigh-Plesset equation

To show the influence of the merging process on the behavior of a single bubble, it is applied to the Rayleigh-Plesset equation (Equation 4.1), and the radius of the bubble is calculated and compared with the corresponding radius given by the standard RP equation. Figure 4.2 depicts the comparison of the bubble radius evolutions for different local driving pressures. The conclusion drawn is that incipient cavitation occurs earlier in all cases when considering the merging process. This results in a larger cavity region when applying the merging process compared to the standard model under the same farfield conditions.

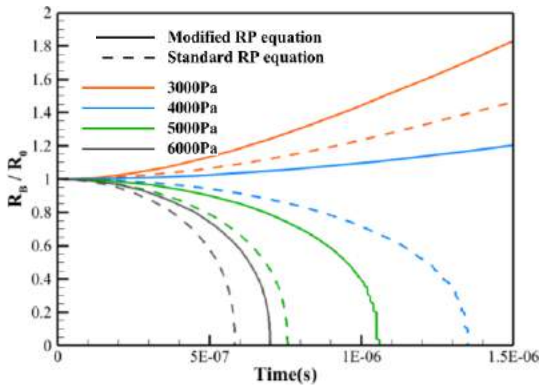

Figure 4.2. Effect of local pressure (p) on the temporal evolution of a single bubble.

4.3.2 Study on Unsteady Characteristics of Cavitating Flow

Unsteady and highly dynamic characteristics of cavitating flow considerably requires to be analyzed since it is the main source of vibration. As such, the unsteady characteristic of cavitating flow is investigated in terms of shedding frequency. For this purpose, the Continuous Wavelet Transform (CWT) is used to calculate the corresponding shedding frequency during various stages of the simulation. When the merging theory-based cavitation model is applied, the following key results are revealed:

- The amplitudes of fluctuations considerably rose which shows the stronger and larger cavity around the hydrofoil.
- The reduction in shedding frequency is detected regardless of the amount of dissolved air.

Determination of the shedding frequency using experimental and numerical methods is a challenging task since not only different operating parameters can be highly influential on it but also the used approach to extract the frequency plays a vital role. Two numerical methods, including volume fraction-based and force-based and two experimental approaches, pressure-based and vibration-based, are used as the sources for calculation of the shedding frequency. The Power Spectral Density (PSD) technique is used for this calculation. Based on the numerical volume fraction-based frequency analysis, it is concluded:

- By applying merging theory-based cavitation model, a much stronger and larger cavity is generated around the hydrofoil which can be concluded by a larger amplitude of vapor volume fraction.
- It is concluded that adding the dissolved air causes a lower shedding frequency which means that the cavitating flow is stabilized.

Based on the numerical force-based frequency analysis, it is concluded:

- The average value of the lift and drag coefficients are influenced by employing the merging theory; however, the percentage of differences vary depending on the case.

Based on the experimental pressure-based vibration-based frequency analysis, it is concluded:

- The main frequency of pressure fluctuations (i.e. shedding frequency) is well matched with the main frequency of vibration. It means the vibration of the test section is mainly due to the cavitating flow.

4.3.3 Study on Morphological Characteristics of Cavity

One of the crucial characteristics of cavitating flow, significantly influenced by numerical methods, is the structure of the cavity during different periods. Given that the merging theory-based cavitation model alters the onset of cavitation when dissolved air is considered, it is anticipated that the cavity structure will be affected. One snapshot of cavitating flow at σ=0.9, VF=0.009 and 0.013 based on the experimental observation, semi-modified and modified numerical approaches, are illustrated in Figure 4.3. It is important to note that the term "semi-modified numerical approach" refers to the numerical model that incorporates all modifications outlined in the previous chapter, in addition to accounting for the compressibility effect. The observations confirm the following results:

- It is obvious that the semi-modified model predicted a smaller cavity. The modified model predicted a more extended cavity that is closer to the experimental observations.
- The procedure of cavity evolution is similar in low and high amount of dissolved air.
- The lower amount of dissolved air content leads to smaller cavities.

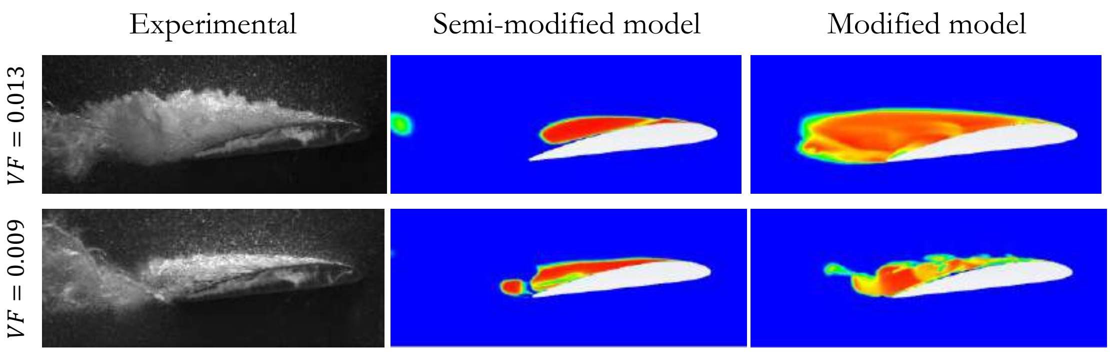

Figure 4.3. The cavitating structure in a period at σ=0.9, VF=0.009 and 0.013 (Further details can be explored in paper VII).

The utilized visualization system is equipped with a trigger which makes it possible to match the captured frames with other measured unsteady parameters such as pressure and vibration. Using this technique one can make a relationship between the structure of the cavity and other characteristics. Figure 4.4 shows the matched pressure fluctuations with flow structure in one period at σ= 0 .9 and VF = 0.009. It is concluded that:

- There is a reverse relationship between the pressure level and volume of the cavity.
- The flow structures in the middle of the half-cycle differ, indicating distinct generation and collapsing processes.

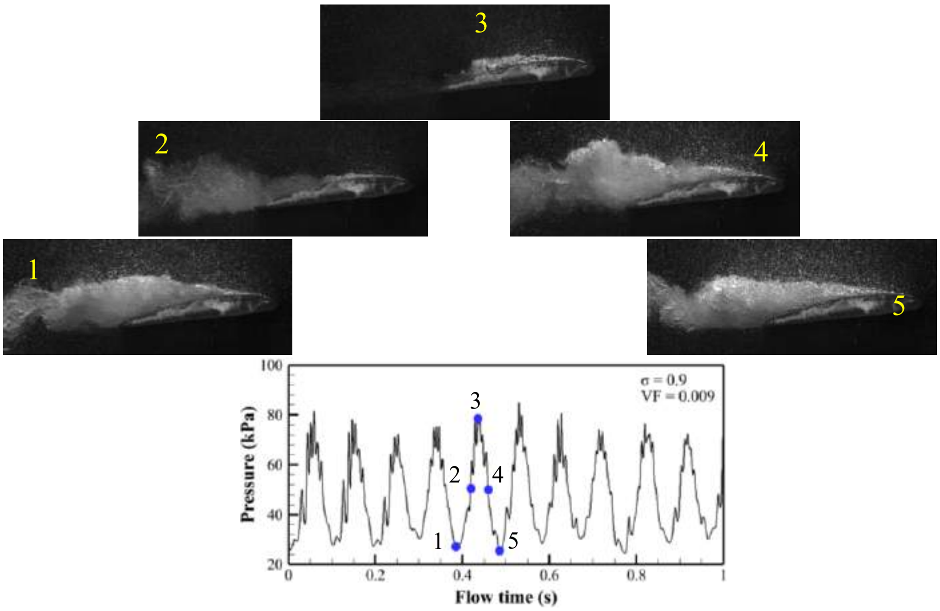

Figure 4.4. Pressure fluctuation with corresponding selected cavity structure during one cycle at σ=0.9 and VF=0.009 (Further details can be explored in paper VII).

4.3.4 Study on Re-entrant Jet

One of the most important factors that initiate the collapsing process is the re-entrant jet. The re-entrant jet is known as a liquid sublayer adjacent to the suction side of the hydrofoil passing from the rear upwards to the leading edge. Despite the remarkable importance of the re-entrant jet, the mechanism by which it alters and converts sheet cavity to detached cloud cavity is not well understood. In addition, which parameters are effective on it, and how much the re-entrant jet is influential on the collapsing process need to be thoroughly analyzed. For this purpose, the quasi-3D cavity structure and the corresponding velocity vector are thoroughly analyzed. It is concluded that:

- The effect of the re-entrant jet is more dominant in case of lower cavitation number.
- The re-entrant jet configuration varies throughout a period based on the velocity vector. Initially, no re-entrant jet is detected, but it emerges in the next phase, moving in the opposite direction to the main flow.
- No significant difference is observed in the re-entrant jet configuration when comparing cases with different cavitation numbers.

4.3.5 Temporal-Spatial Grey Level Distribution (Image Processing)

Due to the highly dynamic nature of the cavitating flow, the analysis of experimental observation is a challenging task. The temporal-spatial grey level distribution, which is an image processing technique, is employed to explore the experimentally visualized cavitating in detail. To have a comprehensive overview of the periodic characteristics of cavitating flow, cavity length, and spatial analysis of the re-entrant jet, the temporal-spatial gray level distribution of cavitating flow during three selected cycles at σ=0.9, 1.75 and VF=0.009, 0.013, are provided. A sample of temporal-spatial gray level distribution is illustrated in Figure 4.5. It is concluded that:

- By adding the dissolved air, the cavity is remarkably elongated, which is more obvious in the case with a higher cavitation number.
- The spatial analysis of the re-entrant jet declares that the effective re-entrant jet is penetrated toward the leading edge more in the case with lower dissolved air.

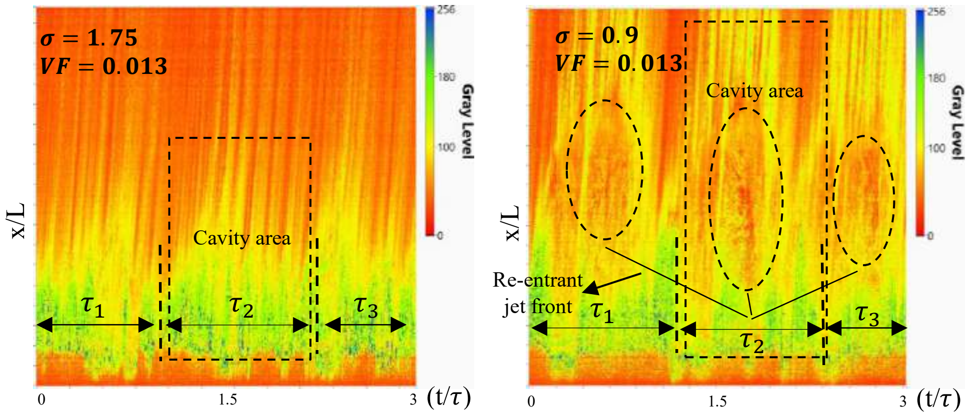

Figure 4.5. Comparison of cavity length using a temporal-spatial distribution of grey level on the selected reference line at the suction side (Further details can be explored in paper VII).

Overall, the remarkable contribution of the modified cavitation model in the correction of shedding frequency is approved. Furthermore, the utilization of the modified cavitation model results in larger cavitation that is well-matched with the observations from experiments. As such, the efficiency of merging theory-based cavitation model in prediction of dynamic and average characteristics of cavitating flow is admitted.

Chapter 5

Studying Air Injection Effects on Cavitating Flow Around Hydrofoil (Ventilated Cavitation) – Papers VIII and IX

5.1 The Scope of the Investigation

Thus far, the crucial role of dissolved air in changing the features of cavitating flow has been thoroughly investigated and confirmed in the previous chapters. The primary objective of the current chapter is to examine ventilated cavitation, while still taking into consideration the presence of dissolved air. It is important to note that ventilated cavitation refers to a type of cavitation in which gas is injected into the cavity region from an external source. It should be kept in mind that the nature of dissolved air and injected air differs: the former is present in the working fluid as dissolved gas throughout the domain, whereas the latter is introduced locally into the domain and is initially non-dissolved.

The proposed numerical approaches, including the 3-phases method, modified turbulence model, and the developed merging theory-based cavitation model (all of which have been discussed in previous sections), are employed to analyze and simulate three-phase ventilated cavitation in the present chapter. Additionally, extensive experimental work has been carried out using a newly designed hydrofoil capable of introducing an air jet into the suction side of the hydrofoil within the cavity region. The experimental data have been utilized to gain a deeper understanding of ventilated cavities and to validate the numerical results.

Challenges: The study of ventilated cavitation presented several formidable challenges in both numerical and experimental analyses. In the numerical part, a particularly demanding issue surfaced during simulations, where extensive modifications to the numerical method were implemented to account for dissolved air and the introduction of an air jet. This introduced a high degree of complexity and dynamism, resulting in divergence challenges. This combined with the task of creating a well-structured mesh distribution proved to be exceptionally time and energy-consuming, demanding an innovative approach, especially given the narrow injection hole. These intricate challenges collectively make the numerical modeling of ventilated cavitation a hard task, underscoring the intricacies faced in unraveling the complexities of this phenomenon. On the other hand, the experimental work demands meticulous attention to detail to enable the setup to introduce air jets into the test section. Firstly, the design and manufacture of half-millimeter internal channels within the hydrofoil were imperative for guiding the air to the suction side. This involved a highly precise design and manufacturing process to prevent channel choking. Secondly, the injection of air necessitates exact and specific flow rates, for which a specialized high-precision

Mass Flow Controller is essential. Working with such a high-precision device demands meticulous precision, careful calibration procedures and continuous monitoring of the injection process.

5.2 Numerical and Experimental Setups

As stated in section 5.1, this chapter focuses on investigating ventilated cavitation using both numerical modeling and experimental analysis. The numerical methods used for modeling have been extensively covered in previous chapters, and to avoid redundancy, a detailed repetition is deliberately omitted. However, it is essential to provide insight into the computational domain, dimensions, and the type of boundary conditions.

In this study, a Clark Y hydrofoil is used that has a chord length of c = 0.07m. The span is also 0.07m, and the angle of attack is 8º. The computational domain, boundaries, and dimensions, which are similar to the experimental setup, are depicted in Figure 5.1; the inlet is 3.2c from the hydrofoil's leading edge, the outlet is located 5.8c from the hydrofoil's trailing edge, and the top wall extends 2.5c above the lower wall. A small hole with a diameter of 0.5 mm is made at locations P1 to P11 to deal with ventilation and pressure measurement. The locations of taps from the leading edge are summarized in Figure 5.1. The inlet velocity, with a constant velocity of vin = 10.45m/s, defines the inlet boundary. The pressure is set at the outlet boundary, allowing regulation of the flow-field cavitation. The upper and lower walls; as well as, the hydrofoil surface, are addressed as non-slip walls. To simplify the simulation, the side walls are set as symmetrical. Air is injected through the first or fifth holes, called Tap1-injection and Tap5-injection, respectively, to examine the effect of the injection location. The injection rates are at controlled levels of Q=0, 0.25, 0.5, 0.75 and 1 l/min. In addition, all of these test cases are conducted in three cavitation numbers of σ=1.1, 1.25 and 1.6.

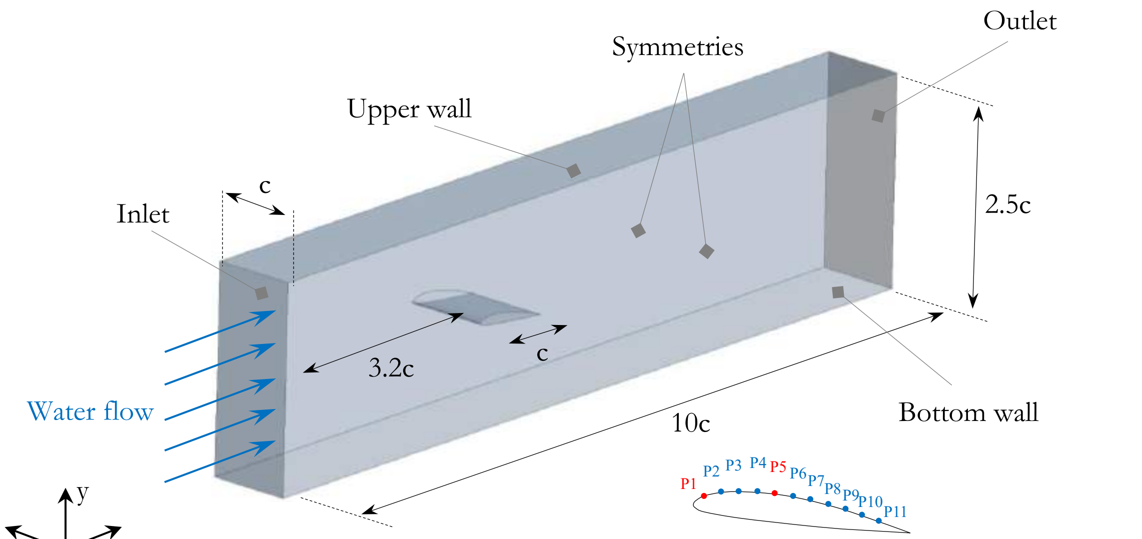

Tap No.	P1	P2	P3	P4	P5	P6	P7	P8	P9	P10	P11
Location (mm)	2.8	8.4	14.1	19.8	25.4	31.1	36.8	42.4	48.1	53.8	59.5

Figure 5.1. The surface meshing of the 3-D hydrofoil domain.

Three grid layouts with total nodes number of 1.28, 1.59 and 1.84 million are provided and examined to find the best possible balance between computation accuracy and efficiency. At the adjacent foil surface, the computational domain utilizing a C-Grid is refined to be sufficiently precise. Figure 5.2 depicts a typical three-dimensional hydrofoil surface mesh that includes 80 nodes along the spanwise axis. Finally, the second layout is selected to use for performing further simulations.

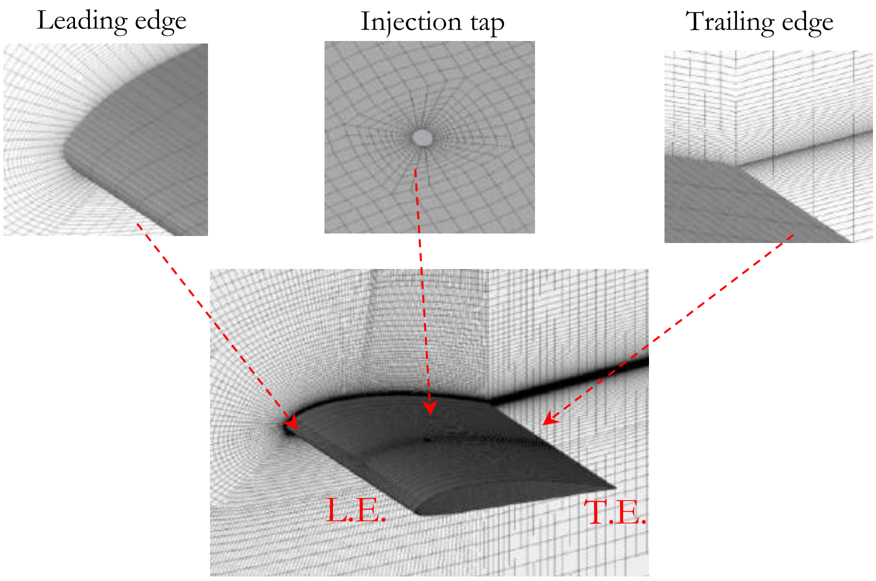

Figure 5.2. The surface meshing of the 3-D hydrofoil domain.

The schematic of the test chamber along with the hydrofoil, measuring and visualization systems are presented in Figure 5.3. The measuring unit consists of sensors, regulator, transducers, data acquisition and computer. In addition, the visualization unit consists of a high-speed camera, MultiLED lighters and a computer. The hydrofoil includes 10 holes which are connected to the root of the fixing disk via channels created inside the hydrofoil. These holes may be used either for pressure measurement or air injection.

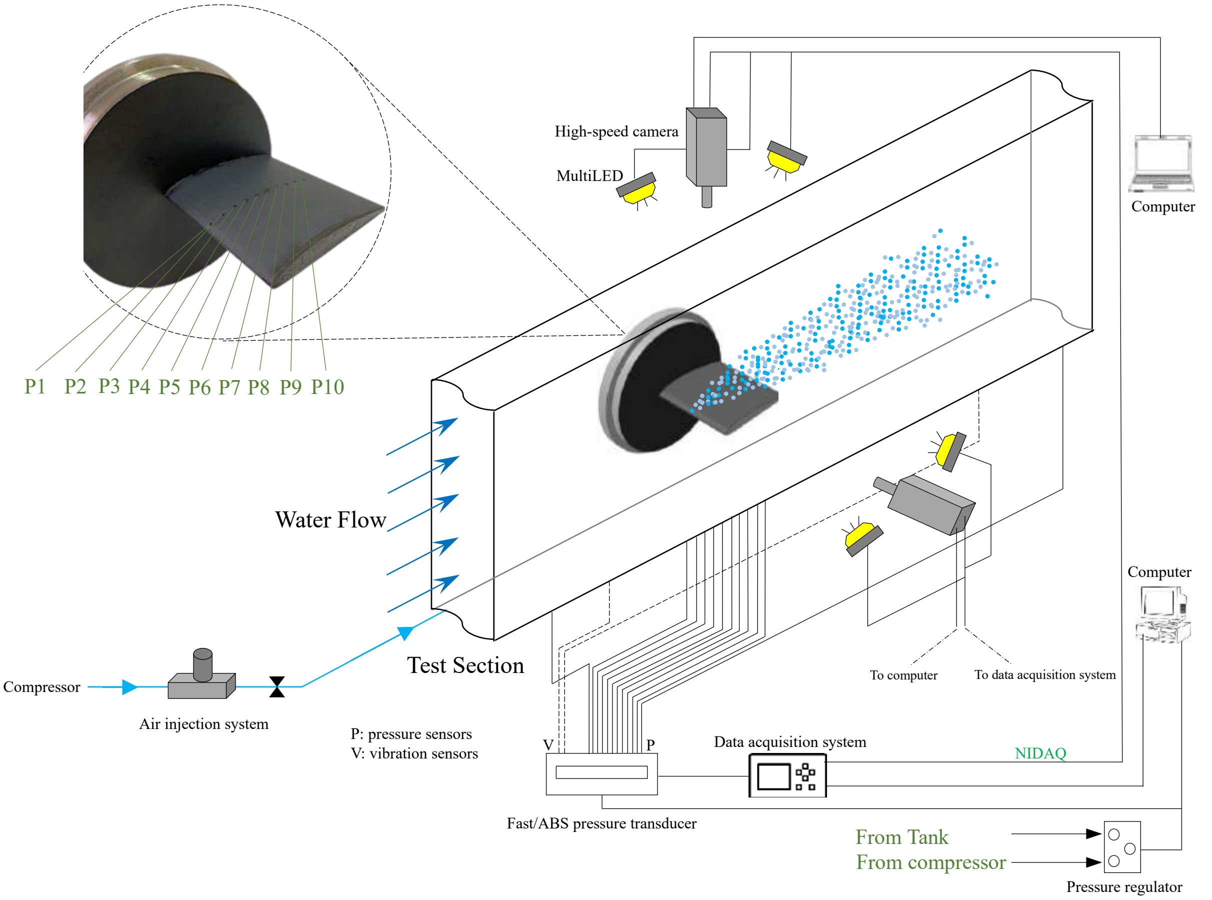

Figure 5.3. Schematic of experimental setup including measuring and visualization systems.

The controlled concentration of dissolved oxygen used for the experimental testing is 4.6 mg/l. According to Henry's law, it corresponds to an air content of 11.7 mg/l at atmospheric pressure. Before and after each experimental campaign, the dissolved air is measured, and the mean amount is presented. The CF-401 multifunction meter is used to monitor the dissolved air.

5.3 Effect of Air Injection on Cavitation

Despite the considerable impact of dissolved air on cavitation, the air injection technique may potentially be recognized as a controlling mechanism capable of altering the characteristics of cavitation. The superiority of this method lies in its ability to introduce air locally to the cavity region, efficiently influencing cavitation. This hypothesis holds true when the effectiveness of this method is confirmed. To this end, the ventilated cavitating flow around a hydrofoil is characterized numerically and experimentally. The governing parameters are the air injection site (i.e. location of the injector) on the surface of the hydrofoil (Tap1-Injection and Tap5-Injection), the air injection rate (Q=0, 0.25, 0.5, 0.75 and 1 l/min) and cavitation number (σ=1.1, 1.25 and 1.6). In addition, the numerical simulations are performed using modified and developed numerical methods, which are already discussed in the previous chapter. The investigations and key findings are listed and summarized below:

5.3.1 Study on Pressure Distribution

The pressure coefficient distribution can perfectly illustrate how the injection rate and injection site (i.e. the location where air jet is injected) affects the behavior of a mean characteristic. The estimated and measured pressure coefficients based on numerical simulation and experimental data, respectively; are studied. Based on the results, the following main observations are reported:

- In all cases and with changing the injection rate, the changes that occur in the sheet cavity, that is, the area before a sharp drop in the pressure coefficient, are more apparent than those in other areas.
- According to a prolonged flat region of Cp, the sheet cavity is lengthened by increasing the air injection rate.
- Injection from Tap1, so-called Tap1-injection, is more effective in the sense of changing the pressure distribution around the hydrofoil.

5.3.2 Study on Shedding Frequency

The shedding frequency is one of the essential parameters which needs to be analyzed in the cavitation phenomenon since it plays an important role in some physical disadvantages such as vibrations and noise. The shedding frequency is calculated based on the fast Fourier transform (FFT) analysis of pressure fluctuation at Tap8. It is concluded that:

- The shedding frequency reduces when the air injection rate increases.
- For higher cavitation numbers, the air injection leads to a more reduction of shedding frequency.
- It is noticed that the shedding frequency tends to reduce more in Tap1-injection than Tap5-injection.

5.3.3 Study on Vibration

Vibrations usually appear during the cavitating flow which results from the induced periodic force imposed on the object. The vibration of the test chamber and the corresponding power spectra density (PSD) for different injection sites/rates in specific cavitation numbers, is investigated. It is revealed that:

- The main frequency of vibration slightly reduces with increasing of injection rate.
- Despite slight changes in the main frequency, the amplitude of the vibration decreases significantly.

5.3.4 Flow Visualization and Study on Morphological Effect of Air Injection

The cavitating flow visualization is carried out using a high-speed camera. This technique makes it possible to track the cavity evolution from inception to detaching and shedding. The cavity evolution of the Tap1-injection case is visualized during a period for different cavitation numbers and injection rates. One snapshot of cavitating flow is shown in Figure 5.4 as a sample to show the effect of air injection on the cavity length. It is observed that:

- The cavity's length is extended when the air is injected.
- Although the cavity shrinks and disappears in the last steps of a period in the non-injection case, the air injection causes continuous cavitation during a period.

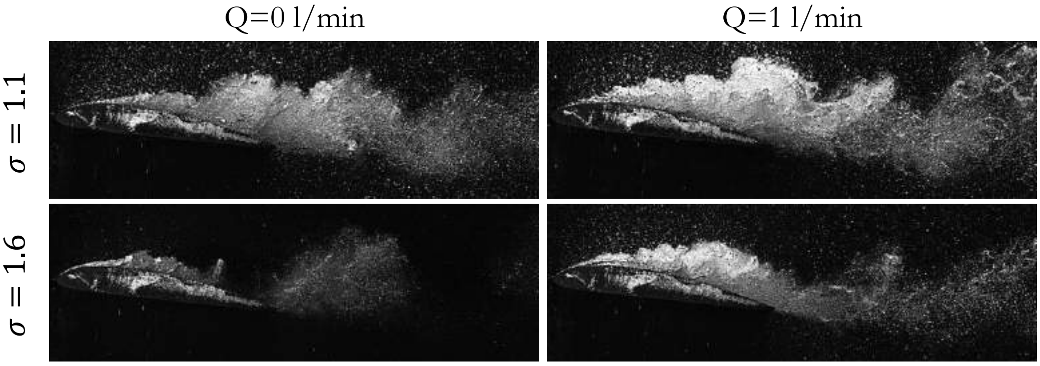

Figure 5.4. The impact of injection rate and cavitation number on the cavity structure (Further details can be explored in paper VIII).

- The comparison between numerical simulations of cavity structure and experimental visualizations confirms a good agreement in terms of the general structure of the cavity. However, it is noted that the numerical approach tends to estimate the cavity to be slightly smaller than observed in experiments.

The mean grey level distribution is a technique that reveals the general shape of cavitation with dynamic features eliminated. By averaging the grey level of each pixel in the captured image over a specific period, this image processing method depicts the mean cavity length and illustrates clearer boundaries of the cavity region. To this end, the mean value of the gray level is calculated based on five periods of cavity evolution for different cavitation numbers and injection rates/sites. Figure 5.5 shows an example of the mean grey level distribution at different cavitation numbers and injection rates around hydrofoil. The results draw the following conclusions:

- Increasing the injection rate leads to elongation of cavity, as illustrated in Figure 5.5.
- Not only the cavity is expanded because of air injection, but the intensity of the cloud cavity also rises which is exposed by brighter cavity regions in the cases with higher injection rates.

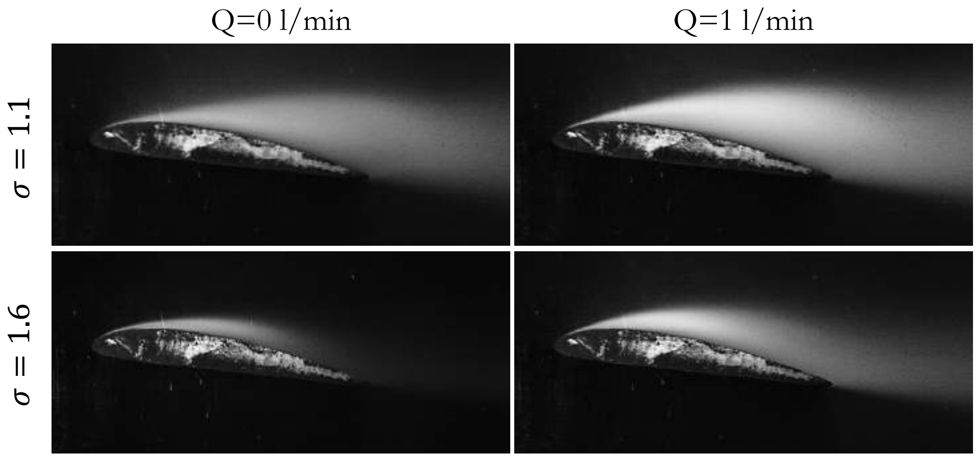

Figure 5.5. Cavity structure for cavitation numbers σ=1.1, 1.25, 1.6 and injection rates Q=0 and 1 l/min (Further details can be explored in paper VIII).

The Q distribution for natural and ventilated cavitation, which is colored by vorticity magnitude, is provided to helps highlight regions of high vorticity, providing a way to identify and analyze the structure and behavior of vortices in a fluid. It is concluded that:

- The development of vortices during ventilated cavitation and natural cavitation are comparable, however, more complications in ventilated cavitation are seen, as depicted in Figure 5.6.
- From the top, it can be identified that the injection squeezes the cavity, forming an M-shape. Therefore, the same effect is happening from the front, where the cavity's mid-section has been dragged inward.

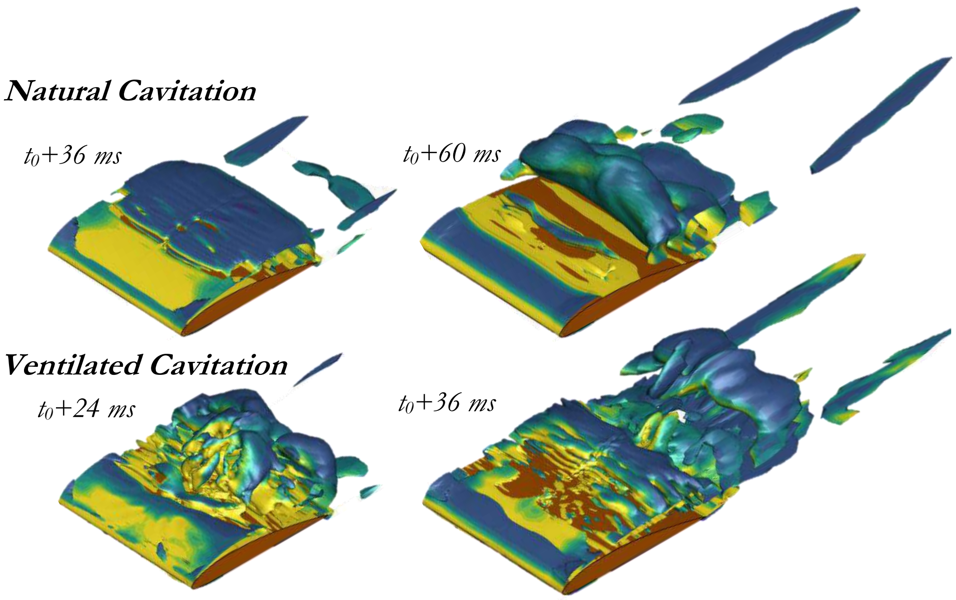

Figure 5.6. The structures of the vortex based on the Q-criterion (Q-criterion = 40000 s^{-2}) colored by the vorticity magnitude for natural and ventilated cavitation (Q = 0, 1 l/min, σ = 1.1, Tap5-injection) (Further details can be explored in paper IX).

The temporal-spatial grayscale distribution is used for further post-processing of visualized cavitation. This technique suggests an examination of how grayscale values change not only in different regions of an image but also over time. The temporal-spatial gray scale distributions at various cavitation numbers and air injection rate are performed. This technique helped us to understand:

- The periodicity of the cavitating flow is more obvious for higher cavitation numbers where the length of the cavity fluctuates strongly.
- The cavity significantly grows when the air is injected through the hole. Also, air injection results in continuity of cavitation during the time.

Chapter 6

Experimental Setup and Facilities

6.1 The Scope of the Investigation

Thus far, the investigation has progressed through four steps in exploring numerical methods and their modifications to accommodate the presence of dissolved non-condensable gas during natural and ventilated cavitating flow. Our efforts aimed to ensure compatibility of the numerical methods with the presence of dissolved gas, specifically air in this study. Numerical simulations have effectively revealed the role of dissolved gas, contributing to a robust prediction of the dynamic characteristics of cavitating flow. The primary goal of experimental investigations is to validate numerical results. In this regard, throughout the preceding stages, the numerical results were consistently compared against the original experimental measurements and observations to make a reliable validation. However, they have also significantly contributed to deepening our understanding of three-phase cavitating flow. For this purpose, certain experimental results are separately post-processed and analyzed, addressing aspects where numerical simulations may lack in-depth predictions.

The current chapter is dedicated to discussing the experimental setup, measurement and visualization techniques, devices, and post-processing methods. It is acknowledged that the findings from experimental investigations were previously discussed in the preceding chapters, along with numerical results. This approach is taken because, in many instances, numerical and experimental results complement each other. Consequently, there is no repetition of the findings in this chapter.

The experiments were conducted within the cavitation tunnel at the Silesian University of Technology, focusing on the cavitating flow around the Clarck Y hydrofoil and within Venturi Nozzle. Key parameters, including pressure, vibration, dissolved air quantity, flow rate, and temperature, were meticulously measured. Additionally, high-speed cameras were employed for visualization purposes.

Gathering experimental data constitutes the most crucial step in an experimental study. However, postprocessing, often regarded as the final step, is essential for interpreting this data. Post-processing techniques such as Fast Fourier Transform (FFT), Power Spectral Density (PSD), temporal/spatial Grey Level distribution and mean value grey level distribution are employed to analyze the experimental observations and measurement.

In the following sections, the details of experimental setup, techniques and approaches will be discussed.

Challenges: The exploration of cavitating flows in experimental studies faces crucial challenges due to the intricate nature of these phenomena, characterized by transient and dynamic features. Achieving precision in capturing the inception, growth, and collapse of cavitation bubbles and understanding their impact on surrounding structures demands sophisticated measurement techniques and instrumentation. To ensure the accuracy and reliability of data, it is imperative to calibrate all pressure and vibration sensors before conducting experiments. Calibration involves meticulous adjustments and verifications against known standards, addressing any potential drift or inaccuracies that may arise during prolonged use. Furthermore, the necessity to replace the working fluid, which is water in this research, after each experimental campaign is driven by the need for consistent and unobstructed visualization. Cavitating flows can introduce impurities and microscopic debris into the fluid, potentially affecting the clarity of observations. By replenishing the working fluid, it is possible to maintain optimal experimental conditions, minimizing the risk of contamination and ensuring that subsequent experiments provide clear and reliable visual data. The extreme conditions associated with cavitation, such as high-speed flows and rapid pressure changes, pose significant hurdles in obtaining reliable and repeatable experimental data. Overcoming the latest challenge necessitates the execution of multiple rounds of experiments and a meticulous diagnosis of errors to refine experimental setups and enhance the overall accuracy of the collected data.

6.2 Experimental Setup

The experiments were carried out at the laboratory of the Department of Power Engineering and Turbomachinery, The Silesian University of Technology, using a hydraulic setup, as shown in Figure 6.1. Water, as the working fluid, circulated through 200 mm diameter pipes driven by a 30kW electric motor-powered pump, ensuring consistent water flow up to 490 m^3/h. A manual valve and an electromagnetic flowmeter were included for emergency flow stop and continuous flow rate measurement, respectively. Components such as a honeycomb and cross section inverter ensured uniform water flow entering the test chamber. The test chamber is replaceable which is an adaptable feature of the setup, enabling the study of various objects. A shaped diffuser altered the cross section from rectangular to circular before the water returned to a 1.5 m^3 tank, maintaining the required water volume. An elastic airbag in the tank regulated the closed-loop circuit’s pressure level, adjusting it as needed in a range between 105–180 kPa. A Pt100 thermocouple monitored the working fluid’s temperature, while three elastic compensators mitigated vibrations caused by the pump and cavitation. A monitoring unit facilitated circuit control, measurement, and visualization during experimentation.

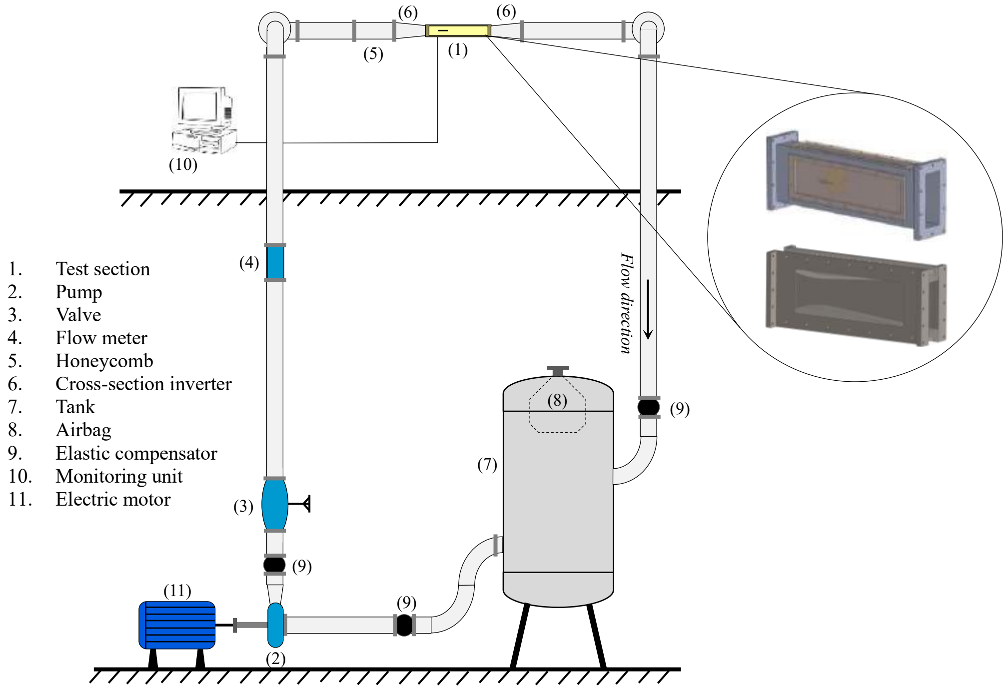

Figure 6.1. Schematic of water tunnel along with the main components.

The test chamber, designed horizontally with a rectangular cross-section. The length (L), height (H) and width (W) of the chamber are equal to 700 mm, 189 mm and 70 mm, respectively. For optimal observation, three sides, including the front, top, and bottom sides, are built from transparent polycarbonate, allowing visual tracking of cavitation. The backside, made of metal, supports both the hydrofoil and vibration sensors. Based on the requirement of research, the test chamber can be equipped by Clark Y 11.7% and Venturi Nozzle, as shown in Figure 6.2. The Clark Y hydrofoil features a chord length (c) of 70 mm, while the test chamber maintains a fixed height of 2.7c and width of 1c. This configuration ensures a height-to-chord ratio of 2.7, effectively minimizing the confinement effect on hydrodynamic cavitation performance. Furthermore, the length of Venturi throat (L_{th}) is equal to 113.5 mm, hence the ratio of throat length to height of the chamber is defined as $L_{th}/H \simeq 0.6$. Also, the ratio of chamber height to width was fixed as $H/W = 2.7$.

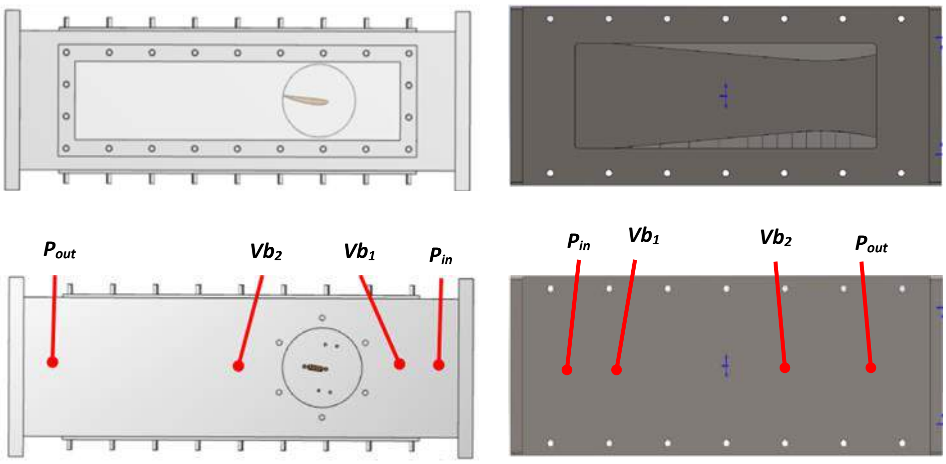

Figure 6.2. Test chamber equipped with hydrofoil (Left) and Venturi Nozzle (Right) with the location of inlet/outlet pressure sensors and vibration sensors.

The experimental tests are conducted with controlled levels of dissolved oxygen. The multifunction meter CF-401 is used to monitor the dissolved air level. This device can measure the dissolved air in liquid; as a result, the non-dissolved air bubbles were not considered. The measurements are carried out before and after each experimental campaign, and the average value is reported. In addition, the accumulated air within the tank due to the air injection is deployed after each experiment using exhaust valve installed at the top of the tank. Also, enough time internal, which is about 3 – 4 min, is given to make the quasi-steady state condition before starting a new round of the experiment.

The schematic of measuring and visualization units are shown in Figure 6.3. The measuring unit consists of high- and low-frequency pressure sensors, pressure regulator, fast/ABS pressure transducers, vibration sensors, data acquisition, and computer. In addition, the visualization unit consists of a high-speed camera, MultiLED lighters, and a computer. The models of high-frequency and low-frequency sensors are XP5 type with amplifier type ARD154 and APLISENS PC-28, respectively. The accuracy of the fast-frequency pressure sensor is 0.25% in 500 kPa full-scale. Moreover, the accuracy of the low-frequency sensor is 0.16% in 160 kPa full-scale. The temperature of the working fluid is monitored using resistance thermocouple type APLISENS CT-GN1 Pt100. The accuracy of the thermocouple in full-scale 0 –100 °C is $\pm(0.15K+0.002|T|)$. The model of the employed electromagnetic flowmeter is UniEMP-05 DN200, which can measure the flow rate up to 1080 m^3/h with an accuracy of ±0.25%. Two piezoelectric accelerometers are mounted on the backside of the test chamber. These accelerometers measure the vibration caused by the cavitating flow. The accelerometers are connected with the 0028 (RFT) type charge amplifier connected with the fast analogue-to-digital converter AC 16 bit, 250 kS/s. The system is calibrated before the experiments using the electrodynamic vibration calibrator EET101 (RFT) type. The maximum error of this type of accelerometer is less than 5%. The measurement system was set based on the National Instruments module NI USB 6216. Furthermore, the pressure measuring cluster cooperates with the NI/PXI-6255 module. The data acquisition process and the executive elements are controlled using a LabView program. The high-speed video camera Phantom Miro C110 with a recording speed of 3200 f/s and spatial resolution of 960×280 pixels, is used. The MULTILED L48-XF is used for lightening.

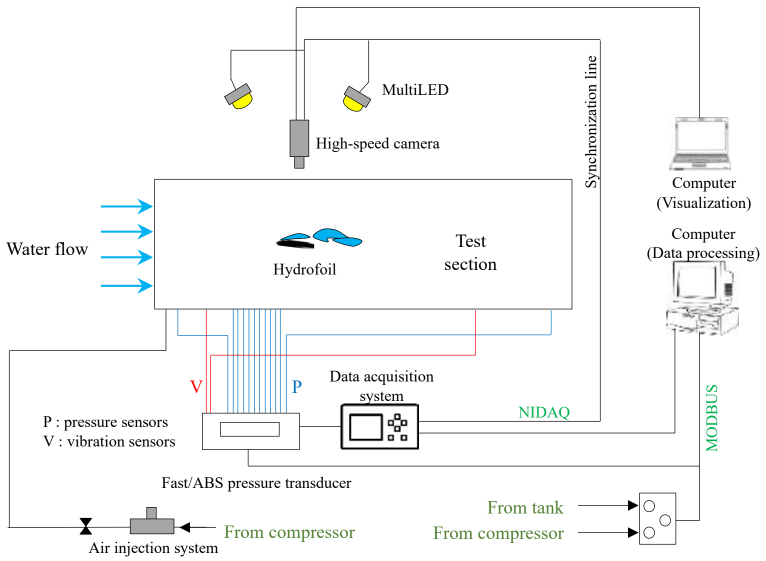

6.3. Schematic of the test section including measurement and visualization systems.

In experimental assessment, accounting for uncertainty analysis stands as a critical factor. Alongside defining the cavitation number in Eq. (6.1), the relative uncertainty is computed through the formula provided below [36]:

$$\sigma = \frac{p_{in} - p_v}{\frac{1}{2}\rho {v_{in}}^2} \tag{6.1}$$

$$\frac{U_\sigma}{\sigma} = \sqrt{\left(\frac{p_{in}}{p_{in} - p_v}\right)^2 \left(\frac{U_{P_{in}}}{p_{in}}\right)^2 + \left(\frac{p_v}{p_{in} - p_v}\right)^2 \left(\frac{U_{P_v}}{p_v}\right)^2 + \left(\frac{U_\rho}{\rho}\right)^2 + 4\left(\frac{U_{v_{in}}}{v_{in}}\right)^2} \tag{6.2}$$

Based on the experimental condition during the present sets of the experiment, the relative uncertainties of inlet pressure, vapor saturation pressure, density and mean inlet velocity are 0.0016, 0.0117, 4×10^{-5} and 0.0026, respectively. Then the impact of each physical value on the uncertainty of the cavitation number (σ) can be given in Table 6.1. Therefore, the uncertainty U_σ/σ of cavitation number amounts to 0.54%.

Table 6.1. The effect of every single parameter on the uncertainty of σ.

X_i	Range of X_i	$U(X_i)/X_i$	Maximum contribution to $(U_\sigma/\sigma)^2$
P_{in}	60-90 kPa	0.0016	2.7×10^{-6}
P_v	2.728 kPa	0.0117	1.3×10^{-7}
ρ	997.65 kg.m^{-3}	4×10^{-5}	8×10^{-10}
v	10.4 m.s^{-1}	0.0026	2.7×10^{-5}
Total	-	-	2.9×10^{-5}

The pictures captured with a high-speed camera are in their raw form, making interpretation challenging. Consequently, post-processing is essential, and LabVIEW is employed for this purpose. Three distinct in-built software applications using LabVIEW were created for specific functionalities. The first in-built software is designed to extract snapshots at specific time intervals during a single period of cavity evolution. The second in-built software focuses on generating the mean gray level distribution, illustrating the average cavity area within a desired time range. Finally, the third in-built software is developed to provide temporal-spatial gray level distribution, enabling the determination of cavity intensity at specific times and locations within the test section.

To ensure experiment repeatability, each case has undergone multiple tests. Typically occurring within a single working day, each experimental campaign comprises several trials to cover the desired cavitation number range. Additionally, each experimental trial takes an average of 3 minutes. It is noteworthy that efforts have been made to minimize the duration of each trial to prevent a temperature rise in the working fluid. Detailed information on the number of experiments is available in Table 6.2.

Table 6.2. Detailed information on the number of experiments.

Case of study	Number of campaigns	Number of trials	Total time (min)
Natural cavitating flow around hydrofoil	33	292	876
Natural cavitating flow around Venturi	6	36	108
Ventilated cavitating flow around hydrofoil	8	194	582
Ventilated cavitating flow around Venturi	2	24	72

6.3 Measurements

The experimental data, comprising measurements and visualizations, are extensively captured, and utilized to validate the numerical results; as well as enhance our understanding of the physics underlying cavitating flow. In this regard, the following measurements have been done:

- Pressure: The pressure distribution for different cavitation numbers is investigated to understand the impact of dissolved air and air injection on the pressure near to surface. In addition, the calculation of shedding frequency is done by using pressure fluctuations recorded by high-frequency pressure sensors. Also, the shedding frequency is calculated using two methods including Fast Fourier Transform (FFT), Power Spectral Density (PSD).
- Vibration: The vibration of the test section is measured using two sensors mounted at the backside of it. Also, the frequency is calculated using FFT and PSD.
- Temperature: The temperature of the working fluid is continuously measured using a temperature sensor. It is observed that the temperature of the working fluid slightly rises during the experiments. The effect of this temperature difference is considered in calculating the density of the working fluid.
- Flow Rate: The flow rate of the working fluid inside the water tunnel is continuously measured. This flow rate information is then utilized to calculate the flow velocity within the test section.
- Dissolved Air: The quantity of dissolved air is measured using an oxygen sensor. Samples of the working fluid, which is water in this research, are taken both before and after each experimental campaign.
- Air Injection: In the case of ventilated cavitation, air injection is controlled by a Mass Flow Controller, which has the capability to inject air at any specific rate.

6.4 Flow visualization

Considering the fact that the cavitating flow is highly dynamic and fast phenomenon, the cavitating flow visualization is carried out using a high-speed camera. This technique makes it possible to track the cavity evolution from inception to detaching and shedding. The flow visualization is conducted for different cavitation numbers, dissolved air contents and injection rates/sites. Additionally, for all cases, one period of cavity evolution is extracted using developed in-built LabView software. Furthermore, the post-processing techniques, including mean grey level distribution and temporal/spatial grey level distribution, are applied to better and deeper interpretation of visualized pictures.

Chapter 7

Summary and Conclusions

In this doctoral thesis, we aim to comprehend the impact of dissolved air on cavitating flow, a factor often overlooked due to its complexity in numerical simulations and experiments. Our focus lies in assessing its influence and devising approaches to incorporate dissolved air in both simulation and experimentation. The research unfolds in two parts: first, through CFD modeling of three-phase cavitating flow, and second, via experimental investigations. Here's a summary of the design and methodology for each section:

7.1 Numerical modelling

The CFD modeling employs Ansys Fluent software, utilizing the Finite Volume Method (FVM) to discretize the transient three-dimensional Navier-Stokes equations. A pressure-based method is employed, incorporating pressure-velocity coupling through the SIMPLEC algorithm. The simulation utilizes a mixture model for liquid-vapor-gas flow, assuming uniform velocity across phases. Turbulent flow is handled using the $k - \varepsilon$ RNG and $k - \omega$ SST turbulence models. The liquid phase represents water with constant thermophysical properties, while the vapor phase maintains constant properties except for specific heat capacity (C_p), modeled via a piecewise-polynomial function dependent on temperature. Air is treated as an ideal gas. Computational domain dimensions mirror those of the experimental setup.

Since we have an additional phase (i.e. gas phase as dissolved air) in the cavitating flow, the numerical method needs to be modified to be adapted to the presence of dissolved air. Initially, numerical modelling aims to determine the potential impact of dissolved air on the dynamic and averaged characteristics of cavitating flow. Different models, including 2phases and 3phases approaches, are used to address the presence of dissolved non-condensable gas in conjunction with full cavitation and Zwart-Gerber-Belamri (ZGB) models. The second modification focuses on adapting the RNG $k - \varepsilon$ turbulence model to suit this problem. The overestimated turbulent viscosity in the RNG k-ε model dampens cavitating flow dynamics, prompting the use of the Density-Corrected Method (DCM), Filter-Based Model (FBM), and Filter-based density correction model (FBDCM) to rectify this issue. The final adjustment centers on creating a modified cavitation model based on merging theory, incorporating dissolved air through a Eulerian approach. This revised model accounts for the diffusion process shaping new mixture bubbles and adjusts bubble pressure based on local air levels, while also considering pressure fluctuation effects in the mixture bubble calculations. Subsequently, the developed cavitation model is implemented and evaluated within the simulations.

7.2 Experiments

The experiments were conducted in the laboratory of the Department of Power Engineering and Turbomachinery at the Silesian University of Technology, utilizing hydraulic equipment. The primary components of the water tunnels include the test section, tank, pump, valve, flowmeter, membrane, and pipes. Operational control of the water tunnel is facilitated by an electric pump capable of sustaining a constant flow rate of up to 490 m^3/h, while pressure regulation within the tank is managed by the membrane, maintaining a range between 105–180 kPa.

Pressure measurements employ both high-frequency and low-frequency sensors, while vibration resulting from cavitating flow is assessed using vibration sensors. Furthermore, the dynamics of cavitation flow are captured by a high-speed camera. Also, experimental tests are conducted with controlled levels of dissolved oxygen. In addition, in the case of ventilated cavitation, the air injection is controlled using Mass Flow Controller.

7.3 Findings

The conducted experiments confirmed that changes in dissolved oxygen levels in water had a detectable impact on cavitation frequencies. Specifically, as the volume fraction of air increased from 0.012 to 0.022, there was an observed shift in cavitation frequencies, ranging from 0.5 to 1 Hz, depending on the cavitation number. Additionally, notable alterations in cloud structures were identified. On the other hand, as the cavitation number increased, there was a noticeable upward trend in the primary frequencies of the shedding frequency. In the case of Clark Y hydrofoil, a clear increment of approximately 79% was observed when the cavitation number changed from 0.79 to 2 for VF=0.012. Similarly, a significant increment of about 65% was recorded when the cavitation number changed from 0.9 to 1.94 for VF=0.022. This tendency persisted across different air volume fractions, albeit with slightly lower frequencies observed in cases with higher air content.

Numerical simulations further highlighted the substantial impact of air content on shedding frequency, particularly evident at lower cavitation numbers. Elevated air content correlated with significant reductions in pressure pulsation amplitudes at higher cavitation numbers, signaling a stabilizing effect on cavitating flow dynamics.

Increasing dissolved air content led to an enlarged volume of cavity closure during evolution, resulting in both a larger cloud cavity and a notable stabilization of the cavitating flow. While quantifying the exact enlargement value of the cavity proves challenging, as a demonstration, we can assert that the averaged cavity area is enhanced by approximately 30%. This enhancement is observed when the volume fraction of dissolved air increases from 0.012 to 0.022. However, this augmentation introduced smaller-scale instabilities, manifesting in dynamic and unstable cavity closures. The addition of dissolved air not only influenced cavity morphology but also altered the inception points of both sheet and cloud cavities. The most important point is that the employed modifications over the turbulence and cavitation models lead to great agreement between numerical predictions and experimental observations.

Furthermore, introducing dissolved air into water resulted in enhanced lift and drag coefficients, with various models predicting substantial increments across different coefficients. For instance, demonstrating this effect, the lift coefficients increased by 17% at σ=0.9 and 2% at σ=1.75. Simultaneously, the drag coefficients experienced a 9% increase at σ=0.9 and a notable 40% increase at σ=1.75, both observed when the volume fraction of air increased from 0.009 to 0.013. The role of the re-entrant jet in generating cloud cavities was emphasized, especially at lower dissolved air contents, where it played a more significant role. Additionally, dissolved air affected the behavior of the re-entrant jet, shifting its front towards the trailing edge and consequently reducing the travelling velocity of the cloud cavity.

Measurement of shedding frequency via pressure fluctuation necessitated precautions against external sources, such as shock waves, and optimal sensor placement to ensure accurate frequency capture. The impact of air injection on pressure coefficient distribution in both sheet and cloud cavity regions was evident, with variations depending on cavitation number and injection specifics.

Increased air injection led to notable changes in pressure coefficients, particularly pronounced in specific injection scenarios. Additionally, higher injection rates correlated with reduced shedding frequencies and mitigated vibration frequencies in the test chamber. The effectiveness of air injection in altering cavitation characteristics was contingent on injection site proximity to the inception point and flow conditions, demonstrating varied impacts on unsteady cavitation features.

Bibliography

1. Arndt, R.E. *Cavitation research from an international perspective*. in *IOP Conference Series: Earth and Environmental Science*. 2012. IOP Publishing.
2. Breslin, J.P. and P. Andersen, *Hydrodynamics of ship propellers*. 1994: Cambridge university press.
3. Atlar, M. *A history of the Emerson cavitation tunnel*. in *International Conference on Propeller Cavitation,(NCT'50)*. 2000.
4. Franc, J.-P. and J.-M. Michel, *Fundamentals of Cavitation*. Vol. 76. 2006: Springer Science & Business Media.
5. Hasani Malekshah, E., et al., *Evaluation of modified turbulent viscosity on shedding dynamic of three-phase cloud cavitation around hydrofoil–numerical/experimental analysis.* International Journal of Numerical Methods for Heat & Fluid Flow, 2022. **32**(12): p. 3863-3880.
6. Sun, T., et al., *Computational modeling of cavitating flows in liquid nitrogen by an extended transport-based cavitation model.* Science China Technological Sciences, 2016. **59**: p. 337-346.
7. Knapp, R.T., *Recent investigations of the mechanics of cavitation and cavitation damage.* Transactions of the American Society of Mechanical Engineers, 1955. **77**(7): p. 1045-1054.
8. Kawakami, D.T., Q. Qin, and R. Arndt. *Water quality and the periodicity of sheet/cloud cavitation*. in *Fluids Engineering Division Summer Meeting*. 2005.
9. Mäkiharju, S.A., H. Ganesh, and S.L. Ceccio, *The dynamics of partial cavity formation, shedding and the influence of dissolved and injected non-condensable gas.* Journal of Fluid Mechanics, 2017. **829**: p. 420-458.
10. Nguyen, V.L., et al., *Numerical simulation of bubbly flow around a cylinder by semi-Lagrangian–Lagrangian method.* International Journal of Numerical Methods for Heat & Fluid Flow, 2019. **29**(12): p. 4660-4683.
11. Liu, C., et al., *On the application of passive flow control for cavitation suppression in torque converter stator.* International Journal of Numerical Methods for Heat & Fluid Flow, 2019. **29**(1): p. 204-222.
12. Liu, C., Q. Yan, and H.G. Wood, *Numerical investigation of passive cavitation control using a slot on a three-dimensional hydrofoil.* International Journal of Numerical Methods for Heat & Fluid Flow, 2020. **30**(7): p. 3585-3605.
13. Mathew, S., T.G. Keith Jr, and E. Nikolaidis, *Numerical simulation of traveling bubble cavitation.* International Journal of Numerical Methods for Heat & Fluid Flow, 2006. **16**(4): p. 393-416.
14. Kubota, A., H. Kato, and H. Yamaguchi, *A new modelling of cavitating flows: a numerical study of unsteady cavitation on a hydrofoil section.* Journal of Fluid Mechanics, 1992. **240**: p. 59-96.
15. Coutier-Delgosha, O., R. Fortes-Patella, and J.-L. Reboud, *Evaluation of the turbulence model influence on the numerical simulations of unsteady cavitation.* J. Fluids Eng., 2003. **125**(1): p. 38-45.
16. Kunz, R.F., et al., *A preconditioned Navier–Stokes method for two-phase flows with application to cavitation prediction.* Computers & Fluids, 2000. **29**(8): p. 849-875.
17. Callenaere, M., et al., *The cavitation instability induced by the development of a re-entrant jet.* Journal of Fluid Mechanics, 2001. **444**: p. 223-256.

18. Hofmann, M., et al. *Numerical and experimental investigations on the self-oscillating behaviour of cloud cavitation: part I: visualisation*. in *ASME, FEDSM99-6755*. 1999.
19. Lohrberg, H., et al., *Numerical and experimental investigations on the cavitating flow in a cascade of hydrofoils.* Experiments in Fluids, 2002. **33**(4): p. 578-586.
20. Wang, G., et al., *Unsteady dynamics of cloud cavitating flows around a hydrofoil.* 2009.
21. Johansen, S.T., J. Wu, and W. Shyy, *Filter-based unsteady RANS computations.* International Journal of Heat and Fluid Flow, 2004. **25**(1): p. 10-21.
22. Coutier-Delgosha, O., J. Reboud, and Y. Delannoy, *Numerical simulation of the unsteady behaviour of cavitating flows.* International Journal for Numerical Methods in Fluids, 2003. **42**(5): p. 527-548.
23. Goncalves, E. and R.F. Patella, *Numerical simulation of cavitating flows with homogeneous models.* Computers & Fluids, 2009. **38**(9): p. 1682-1696.
24. Schnerr, G.H. and J. Sauer. *Physical and numerical modeling of unsteady cavitation dynamics*. in *Fourth international conference on multiphase flow*. 2001. ICMF New Orleans New Orleans, LO, USA.
25. Zwart, P.J., A.G. Gerber, and T. Belamri. *A two-phase flow model for predicting cavitation dynamics*. in *Fifth international conference on multiphase flow, Yokohama, Japan*. 2004.
26. Singhal, A.K., et al., *Mathematical basis and validation of the full cavitation model.* J. Fluids Eng., 2002. **124**(3): p. 617-624.
27. Gopalan, S. and J. Katz, *Flow structure and modeling issues in the closure region of attached cavitation.* Physics of Fluids, 2000. **12**(4): p. 895-911.
28. Laberteaux, K. and S. Ceccio, *Partial cavity flows. Part 1. Cavities forming on models without spanwise variation.* Journal of Fluid Mechanics, 2001. **431**: p. 1-41.
29. Cheng, H., et al., *A new Euler-Lagrangian cavitation model for tip-vortex cavitation with the effect of non-condensable gas.* International Journal of Multiphase Flow, 2021. **134**: p. 103441.
30. Chen, G., et al., *Combined experimental and computational investigation of cavitation evolution and excited pressure fluctuation in a convergent–divergent channel.* International Journal of Multiphase Flow, 2015. **72**: p. 133-140.
31. Ganesh, H., S.A. Mäkiharju, and S.L. Ceccio, *Bubbly shock propagation as a mechanism for sheet-to-cloud transition of partial cavities.* Journal of Fluid Mechanics, 2016. **802**: p. 37-78.
32. Yuan, C., et al., *Numerical investigation on cavitating jet inside a poppet valve with special emphasis on cavitation-vortex interaction.* International Journal of Heat and Mass Transfer, 2019. **141**: p. 1009-1024.
33. Sedlar, M., et al., *Numerical and experimental investigation of three-dimensional cavitating flow around the straight NACA2412 hydrofoil.* Ocean Engineering, 2016. **123**: p. 357-382.
34. Reisman, G., Y.-C. Wang, and C.E. Brennen, *Observations of shock waves in cloud cavitation.* Journal of Fluid Mechanics, 1998. **355**: p. 255-283.
35. Liu, J., et al., *Numerical investigation of shedding dynamics of cloud cavitation around 3D hydrofoil using different turbulence models.* European Journal of Mechanics-B/Fluids, 2021. **85**: p. 232-244.
36. Malekshah, E.H., W. Wróblewski, and M. Majkut, *Dissolved air effects on three-phase hydrodynamic cavitation in large scale Venturi-Experimental/numerical analysis.* Ultrasonics Sonochemistry, 2022. **90**: p. 106199.

Abstract

Cavitating Flow refers to a complex hydrodynamic phenomenon occurring when the local static pressure in a fluid drops below its vapor pressure, causing vapor bubbles to form and collapse rapidly. This process generates intense shockwaves, leading to significant mechanical stresses on nearby surfaces. In turbomachinery, such as pumps, propellers, and turbines, cavitation can lead to erosion, vibration, noise generation, and reduced efficiency. As such, understanding and mitigating cavitation effects are crucial for maintaining the reliability and efficiency of turbomachinery devices.

In this doctoral thesis, the primary aim is to comprehensively understand the often-overlooked impact of dissolved air on cavitating flow. Acknowledging the inherent complexity in both numerical simulations and experimental setups, our research focuses on evaluating and elucidating the influence of dissolved air. We strive to develop methodologies that effectively integrate dissolved air considerations into both simulation and experimental analysis, aiming for a deep understanding of its effects.

The research unfolds in two distinct yet interrelated parts. Firstly, employing Computational Fluid Dynamics (CFD) modeling techniques, we delve into the intricate dynamics of three-phase cavitating flow. The CFD modeling phase utilizes Finite Volume Methodology (FVM) to discretize the transient three-dimensional Navier-Stokes equations. The emphasis here is on modification and development of turbulence models, cavitation models, and incorporation of dissolved air through a mixture model to account for the presence of dissolved air. Various models and approaches are explored, seeking to accurately simulate the behavior of cavitating flows in the presence of dissolved air. Secondly, experimental investigations are conducted to validate and augment the insights gained from numerical simulations. The experimental tests are conducted in a hydraulic setup, carefully designed to measure and observe the cavitation behaviors in water with controlled dissolved air levels. The test chamber, hydrofoil, and monitoring systems are configured to facilitate detailed observations and data collection.

The culmination of experiments and numerical simulations revealed a profound correlation between dissolved air levels and cavitating flow dynamics. Variations in dissolved oxygen levels distinctly influenced cavitation frequencies and cloud structures, notably amplifying shedding vortex frequencies with increasing cavitation numbers. Both experimental validations and numerical simulations underscored the pivotal role of dissolved air, showcasing significant reductions in pressure pulsation amplitudes at higher cavitation numbers, indicating a stabilizing effect on cavitating flow dynamics. Augmented dissolved air content not only expanded cavity closure volumes, leading to larger cloud cavities and stabilized cavitating flow, but also introduced smaller-scale instabilities in cavity closures. The introduction of dissolved air showcased enhancements in lift and drag coefficients, prominently altering the behavior of the re-entrant jet, and influencing pressure coefficient distributions in sheet and cloud cavity regions. Additionally, the injection of air demonstrated vital impacts on shedding frequencies and vibration frequencies in the test chamber, highlighting its effectiveness in altering cavitation characteristics, contingent upon injection specifics and flow conditions. These findings collectively emphasize the intricate relationship between dissolved air and cavitating flow, elucidating its multifaceted impacts on cavitation phenomena.

Streszczenie

Przepływ kawitacyjny jest złożonym zjawiskiem hydrodynamicznym, które występuje, gdy lokalne ciśnienie statyczne w przepływie cieczy spada poniżej ciśnienia nasycenia, powodując szybkie powstawanie i rozpad pęcherzy parowych. Ten proces generuje intensywne fale uderzeniowe, powodując znaczące naprężenia na sąsiednich powierzchniach. W maszynach przepływowych, takich jak pompy, śruby napędowe i turbiny, kawitacja może prowadzić do erozji, drgań, generacji hałasu i obniżenia sprawności. Dlatego zrozumienie procesu kawitacji i łagodzenie jej efektów są kluczowe dla utrzymania niezawodności i sprawności maszyn przepływowych.

Głównym celem niniejszej pracy doktorskiej jest kompleksowe rozpoznanie wpływu rozpuszczonego powietrza na przepływ kawitacyjny, co często jest pomijane. Mając na uwadze kompleksowość badań ocenę i wyjaśnienie wpływu rozpuszczonego powietrza przeprowadzono przy zastosowaniu zarówno symulacji numerycznych, jak i eksperymentalnych,. Opracowano metodologia uwzględniającą obecność rozpuszczonego powietrza zarówno w symulacjach numerycznych, jak i w czasie badań eksperymentalnych pozwoliła na zrozumienie jego wpływu na dynamikę kawitacji.

Zakres badań składał się z dwóch odrębnych, lecz powiązanych części. W pierwszej, stosując techniki modelowania numerycznego CFD, badano złożoną dynamikę przepływu kawitacyjnego w obecności powietrza. W modelach numerycznych wykorzystano metodę objętości skończonych Objętości (FVM) do dyskretyzacji niestacjonarnych trójwymiarowych równań Naviera-Stokesa. Na podkreślenie zasługuje zastosowanie modyfikacji w modelach turbulencji, modeli kawitacji oraz uwzględnienie rozpuszczonego powietrza w modelu mieszaniny w celu uwzględnienia obecności rozpuszczonego powietrza. Badano różne modele i podejścia w modelowaniu przepływu kawitacyjnego, dążąc do możliwie dokładnej symulacji dynamiki przepływu w obecności rozpuszczonego powietrza. W drugiej części przeprowadzono badania eksperymentalne w celu walidacji i uwiarygodnienia wniosków uzyskanych z symulacji numerycznych. Testy eksperymentalne były przeprowadzane na stanowisku laboratoryjnym zaprojektowanym do pomiaru i obserwacji przepływów kawitacyjnych w wodzie o kontrolowanych poziomach rozpuszczonego powietrza. Komora testowa, konstrukcja profilu i dyszy oraz systemy pomiarowe oraz regulacyjne były przystosowane do przeprowadzenia szczegółowych obserwacji i zbierania danych.

Zebrane dane z eksperymentów i symulacji numerycznych wskazały na zależność między poziomami rozpuszczonego powietrza a dynamiką przepływu kawitacyjnego. Zmiany poziomów tlenu w wodzie wyraźnie wpłynęły na częstotliwości kawitacji i struktury chmur kawitacyjnych, znacząco wzmacniając częstotliwości powstawania kawern wraz z wzrastającymi liczbami kawitacji. Zarówno badania eksperymentalne, jak i symulacje numeryczne podkreśliły kluczową rolę rozpuszczonego powietrza, wykazując znaczne zmniejszenia amplitud pulsacji ciśnienia przy wyższych liczbach kawitacyjnych, co wskazuje na stabilizujący wpływ na dynamikę przepływu. Zwiększona zawartość rozpuszczonego powietrza nie tylko powiększa objętość kawerny, prowadząc do większych rozmiarów chmur kawitacyjnych i stabilizacji przepływu kawitacyjnego, ale również wprowadza niestabilności o mniejszej skali w objętości kawern. Wprowadzenie rozpuszczonego powietrza powoduje wzrost współczynników zarówno siły nośnej i siły oporu. Wyraźnie zmienia się zachowanie strumienia wstecznego przy profilu, co wpływa na rozkład

współczynnika ciśnienia w zakresie kawitacji warstwowej i chmurowej. Dodatkowo badano przepływ z wentylacją wymuszoną w którym strumień powietrza był wprowadzany do przepływu i wykazano, że w wpływ dodatkowego powietrza na częstotliwości odrywania i częstotliwości drgań w komorze testowej był istotny. Wskazano skuteczność strumienia powietrza w zmianie cech kawitacji, w zależności od lokalizacji strumienia i parametrów przepływu. Otrzymane wyniki wskazują na złożony związek między obecnością powietrza a parametrami przepływowymi i stanowią krok na drodze do wyjaśnienia szczegółów zjawiska kawitacji i możliwości jego kontroli.

Appendices

In this Chapter, the full-text papers, that were briefly described in Chapters 2 – 6, are presented. The papers are listed in the following order:

Paper I: Wróblewski, W., Bochon, K., Majkut, M., **Malekshah, E. H.**, Rusin, K., & Strozik, M. (2021). An experimental/numerical assessment over the influence of the dissolved air on the instantaneous characteristics/shedding frequency of cavitating flow. Ocean Engineering, 240, 109960.

Paper II: Wróblewski, W., Bochon, K., Majkut, M., Rusin, K., & **Hasani Malekshah, E.** (2022). Numerical study of cavitating flow over hydrofoil in the presence of air. International Journal of Numerical Methods for Heat & Fluid Flow, 32(5), 1440-1462.

Paper III: **Malekshah, E. H.**, Wróblewski, W., & Majkut, M. (2022). Dissolved air effects on three-phase hydrodynamic cavitation in large scale Venturi-Experimental/numerical analysis. Ultrasonics Sonochemistry, 90, 106199.

Paper IV: **Malekshah, E. H.**, Wróblewski, W., Bochon, K., Majkut, M., & Rusin, K. (2022). Experimental analysis on unsteady characteristics of sheet/cloud cavitating Venturi flow under the effect of dissolved air. Archives of Thermodynamics, 63-84.

Paper V: **Malekshah, E. H.**, & Wróblewski, W. (2022). Effect of turbulence modelling and non-condensable gas on cloud cavity dynamics. International Journal of Heat and Fluid Flow, 98, 109070.

Paper VI: **Hasani Malekshah, E.**, Wróblewski, W., Bochon, K., & Majkut, M. (2022). Evaluation of modified turbulent viscosity on shedding dynamic of three-phase cloud cavitation around hydrofoil–numerical/experimental analysis. International Journal of Numerical Methods for Heat & Fluid Flow, 32(12), 3863-3880.

Paper VII: **Malekshah, E. H.**, & Wróblewski, W. (2022). Merging theory-based cavitation model adaptable with non-condensable gas effects in prediction of compressible three-phase cavitating flow. International Journal of Heat and Mass Transfer, 196, 123279.

Paper VIII: **Malekshah, E. H.**, Wróblewski, W., Bochon, K., & Majkut, M. (2023). Experimental analysis on dynamic/morphological quality of cavitation induced by different air injection rates and sites. Physics of Fluids, 35(1).

Paper IX: **Malekshah, E. H.**, Wróblewski, W., & Majkut, M. (2024). Investigation on natural to ventilated cavitation considering the air-vapor interactions by Merging theory with insight on air jet location/rate effect. International Journal of Heat and Mass Transfer, 220, 124968.

Paper I:

An experimental/numerical assessment over the influence of the dissolved air on the instantaneous characteristics/shedding frequency of cavitating flow

Ocean Engineering 240 (2021) 109960

Contents lists available at ScienceDirect

Ocean Engineering

journal homepage: www.elsevier.com/locate/oceaneng

An experimental/numerical assessment over the influence of the dissolved air on the instantaneous characteristics/shedding frequency of cavitating flow

Włodzimierz Wróblewski, Krzysztof Bochon, Mirosław Majkut, Emad Hasani Malekshah *, Krzysztof Rusin, Michał Strozik

Silesian University of Technology, Department of Power Engineering and Turbomachinery, 44-100, Gliwice, Poland

ARTICLE INFO

Keywords:
Cavitation
Clark Y 11.7% hydrofoil
Dissolved gas content
Dynamical behaviors
Shedding frequency

ABSTRACT

The paper reports the numerical/experimental investigations of the cavitation phenomenon in the water flow in the presence of dissolved air. The dissolved air in the water was taken into account in the flow over a Clark Y 11.7% hydrofoil, one of the most common research objects of cavitating flow. The different cavitating flow regimes including the incipient, sheet/cloud and supercavitation were analyzed both numerically and experimentally with different amounts of air dissolved in the water. The dynamics of the cavitating flow, as well as; the main flow parameters, were compared and validated against the experimental data obtained from the closed-loop cavitation tunnel located at the Silesian University of Technology and the literature reports. The FFT analysis of outlet pressure fluctuation and vibration signals were applied to extract the main frequencies of the cavitating flows. The spectrum of vibrations and spectrum of pressure signals at the chamber outlet were in good agreement. The frequency of the main cavitating flow structures increased when the cavitation number increases. It was confirmed that for the tested values of dissolved oxygen in water (2.6 ppm and 5.5 ppm), it was possible to observe a detectable influence of air on cavitation frequencies and noticeable influence on cloud structures.

1. Introduction

Cavitation is known as a multi-phase phenomenon that occurs as the local pressure of the operating liquid drops below its saturation vapor pressure. The cavitation has different types including incipient, sheet, cloud and supercavitation. The emergence of each of these stages depends on different geometrical and non-geometrical parameters. The cavitation, due to its extremely unsteady and complex nature, has a considerable impact on hydrodynamic performance (Wang et al., 2015, 2018a, 2020; Usta and Korkut, 2018; Wu et al., 2017; Wróblewski et al., 2021). Its impact may manifest as a reduction of force coefficients, noise, vibration and erosion (Ji et al., 2015; Long et al., 2018). The complex mechanism of cavity cloud formation, which sequentially consists of detachment, condensation, collapse and shedding, has not been fully explored. Many experimental and numerical investigations have been conducted to understand this process, especially shedding, due to its significant influence on hydrodynamic performance (Astolfi et al., 2000; Wang et al., 2001; Huang et al., 2014a; Zhu et al., 2016). As a result, the recognition and control of cavitation are required to improve the reliability, performance and prolong the life cycle of hydrodynamic machinery.

Partial cavitation has inherently unstable nature and causes considerable oscillations in the force coefficients and length of the cavity. A comprehensive review of the studies related to sheet/cloud cavitation shedding in the past ten years has been reported by Arndt (2012). The outlook provided by this review paper indicates that the re-entrant jet and bubbly flow shock wave are the two competing factors for the induction of cloud cavitation shedding. In a general view, the re-entrant jet can be recognized as a thin layer of liquid induced by the adverse pressure gradient and forced into the cavity closure at its rear region. Then, the re-entrant jet is able to move along the suction side of the foil underneath sheet cavitation in the upstream direction. This process occurs as the re-entrant jet has sufficiently high momentum. Finally, the re-entrant jet collides with the cavity interface and makes it to be separated or shed and transported downstream by its large portion. The sheet cavity is transformed into a frothy cavity structure, which forms

* Corresponding author.
E-mail addresses: wlodzimierz.wroblewski@polsl.pl (W. Wróblewski), Krzysztof.Bochon@polsl.pl (K. Bochon), Miroslaw.Majkut@polsl.pl (M. Majkut), Emad.Hasani@polsl.pl (E.H. Malekshah), Krzysztof.Rusin@polsl.pl (K. Rusin), Michal.Strozik@polsl.pl (M. Strozik).

https://doi.org/10.1016/j.oceaneng.2021.109960
Received 26 May 2021; Received in revised form 12 August 2021; Accepted 1 October 2021
Available online 20 October 2021

the cloud cavitation (Chen et al., 2015; Wu et al., 2015; Gnanaskandan and Mahesh, 2015; Gavaises et al., 2015).

In recent years, many investigations have been conducted to describe the nature and process of transient sheet/cloud cavitation over different types of hydrofoils (Roohi et al., 2013; Ausoni et al., 2007; Huang et al., 2013; Morgut et al., 2011), which prove that unsteady cloud cavity would be created and moved downstream even under stationary conditions on the hydrofoil and steady inlet flow. The experimental results demonstrated that the cloud cavitation has a central core with a maximum value of vorticity and a surrounding cluster containing numerous small cavitation bubbles. It was indicated by Kawanami et al. (1997) that the shedding of the cloud cavity is triggered by the re-entrant jet that existed after the closure regions. The re-entrant jet is moved from the trailing edge to the leading edge of the sheet cavity through the gap that existed between the foil and the downside of the sheet cavity due to an adverse pressure gradient. Additionally, the impact of foil configuration on the re-entrant jet structure was analyzed. It was declared that an obstacle that has enough height and is located after the closure region, can prevent the collision of the re-entrant jet with the sheet cavity interface together with drag and noise reduction. Gopalan and Katz (2000) indicated that the main reason for vorticity generation is the vapor bubble collapsing in the sheet cavity closure. Furthermore, both the momentum thickness of the downstream boundary layer and the level of turbulence are significantly influenced by the cavity size. In experimental work, Callenaere et al. (2001) observed the instability of the cavitation process induced by the propagation of a re-entrant jet for a water flow over a type of back step channel. It was claimed that the existence of a large adverse pressure gradient is required to push the re-entrant jet to the upstream direction. Also, they developed a simplified analytical solution relating the thickness of the re-entrant jet with the length of the cavity. Dular et al. (2012) conducted experiments to show the scale effects on the dynamics and the structure of developed cavitation which has periodical cloud shedding. The results proved the considerable impact of small scale on the dynamics of cavitation. When the scale of the test chamber, especially the height of the test section, becomes smaller, the re-entrant jet is not fully developed. As a result, the sheet cavity has a more stable behavior without dense cloud cavity shedding on a small scale due to the absence of a high impact re-entrant jet. Finally, it is recommended to keep such an optimal threshold to avoid scale effect on the dynamics of the cavitating flow.

Although the influence of configuration, scale, movement of foil and other geometrical parameters on the dynamics of cavitating flow is undeniable, the impact of air dissolved in the water or injected superficially by an air injector cannot be underestimated. The presence of air in the water has some considerable impacts on the dynamics and the structure of cavitating flow such as significant enhancement of void ratio of a cavity, reduction of cavitation collapse rate (i.e. collapse frequency) and increment of cavity length which makes a remarkable difference in the pressure distribution through the development of cavitation (Brennen, 2014; Germano et al., 1991). Tsuru et al. (2018) observed the cavitation appearance and measured forces on the Clark Y 11.7% hydrofoil for various dissolved air conditions. Three categories of the conditions: low, medium and high, were taken into account based on the measured oxygen content. They concluded that the influence of the dissolved gas content on the averaged values of the lift and drag coefficients were observed in the selected cases only, but the influence on the appearance of cavitation was noticed in all cases. Kawakami et al. (2005) calculated the pressure spectrum at the suction side for the NACA 0015 hydrofoil by considering two amounts of dissolved air including 6 ppm and 13 ppm. Based on the results, the considerable effect of dissolved air on the pressure spectrum trends was proved. Numerous peaks were observed for the case with high gas content regardless of the cavitation number located between $\sigma/2\alpha = 2$ to 4. Contrarily, a steady behavior is seen for $\sigma/2\alpha$ less than 4 when the gas content is low. Mäkiharju (Mäkiharju et al., 2017a) also found some influences on the dynamics and inception of a partial cavity by taking the gas content into account. However, the results proved that the developed partial cavity accompanied by a strongly enforced separation line would not be significantly affected by the dissolved gas mass transfer within the freestream. The impact of cavitation on the erosion of surface under influence of air-injection was experimentally evaluated by Arndt et al. (1995) by means of erosion detection techniques. All three employed methods confirmed that air injection has a positive effect on minimizing erosion. Reisman et al. (1997) described a series of experiments in which the influence of continuous and pulsed air injections in the cloud cavitation over an oscillating hydrofoil was studied. The acoustic pressure measurements were done both on the surface of the hydrofoil and downstream on the test section bottom side. The results confirmed the positive effect of air injection on the noise reduction of cloud cavitation. Pham et al. (1999) studied the sheet cavitation over a hydrofoil and its unsteady characteristics which leads to forming cloud cavitation based on experimental observations using high-speed visualization technique and pressure sensors. They used air injection as one of the controlling methods of the cloud cavitating flow and found it applicable. The observations have shown that the cavitation process was significantly suppressed on the specific amount of ventilated gas flow rate. Karn et al. (2015) studied the configuration of turbulent bubbly wake based on the experimental observations around a ventilated hydrofoil. They observed that the larger bubbles were located adjacently to the injection slot due to their stronger inertia, and the smaller ones were transported in the wake. Liu et al. (Liu et al., 2017/01) reported the results of an experimental investigation aiming to investigate the pattern of ventilated partial cavitating flow using a closed-loop cavitation tunnel. They considered the influences of different governing parameters including ventilation flow rate, water velocity and gas entrainment coefficient. The results showed the significant impact of Froude number and gas entrainment coefficient on the structures of multi-phase ventilated flow. Also, the observations proved the remarkable impact of flow pattern on the unsteady characteristics of cavity shedding. Makiharju et al. (Mäkiharju et al., 2017b) conducted experimental work to evaluate the vapor production rate of natural cavitating process and examined how the non-condensable gas injection could affect the rate of vapor production, cavity flow and shedding step. The gas injection near the apex resulted in pressure enhancement close to suction peak, thereby the vapor formation was considerably suppressed. Hence, it was declared that the effect of dissolved gas without injection process on the cavity dynamics is minor.

The turbulence model in the numerical calculations plays a major role in the cavitation process with unstable behavior. The validity and accuracy of the results depend on the turbulence model used in simulations (Wang et al., 2018b; Chen et al., 2019). Moreover, the cavitating flow inherently influences the shaping of the large-scale eddies in the flow, which include the complex and unstable structure of the cavity. So far, most of the numerical simulations have been conducted using Reynolds-averaged Navier-Stokes (RANS) method for the prediction of cavitating flow and its characteristics. It is due to reasonable computational cost, acceptable stability and reasonable accuracy (Sun et al., 2016). Li et al. (2014) analyzed the large scale cavity structure in a three-dimensional case and its unsteady characteristics over two types of hydrofoils using modified shear stress transport (SST) model. Also, they proposed an erosion intensity function to evaluate the cavitation erosion on the surface of the investigated hydrofoil. For this purpose, the results of RANS-based simulations were used, and the mean value of the time derivative of the local pressure which exceeds an assumed threshold was selected. Zhang et al. (2020) used the numerical approach to find the relationship between the transient cavitating flow and hydrodynamic performance of a pitching Clark Y 11.7% hydrofoil. They solved the incompressible UNRANS equations using CFX commercial code. For this purpose, $k-\omega$ SST turbulence model coupled with $\gamma - Re_\theta$ transition model was used to predict the turbulent cavitation process and its transient characteristics. The predicted pattern of the cavity was in good agreement with the experimental observations. Senocak and Shyy (2002) utilized a pressure-based algorithm for the simulation of turbulent cavitating flow over a corner. For this purpose, they developed a pressure-velocity-density coupling scheme to overcome the large density ratio resulting from the cavitation process. Also, the original $k-\varepsilon$ turbulence model with wall function was employed to predict the unsteady, turbulent cavitating flow. Zhou and Wang (2008) simulated the cavitating flow over a hydrofoil utilizing RANS-based approach by taking the effect of non-condensable gas into account. Their results indicated that the pressure distribution on the suction side can be predicted properly when the standard renormalization-group (RNG) $k-\varepsilon$ turbulence was used as the turbulence model.

Several methods involving the introduction of an additional transport equation have been proposed in recent years to improve the robustness and flexibility of cavitating flow modelling. In this type of numerical approach, the volume or mass fraction of phases (liquid, vapor and gas in three-phase cases) is converted. The concept of cavitation models proposed by Kubota et al. (1992), Singhal et al. (Singhal, 1997), Merkle et al. (Merkle, 1998), and Kunz et al. (Kunz et al., 1999; Kunzet al., 2000) are similar, and the differences arise from the source terms. One of the most important advantages of this sort of modelling results from the convective character of the equation, making it possible to deal with existed inertial forces, including bubbles elongation, detachment and drift. Kubota et al. (1992) firstly developed a transport equation-based homogeneous model. The cavitation process is taken into account through the existence of a bubble cluster, as well. The proposed model was employed for two-dimensional cavitating flow over NACA 0015 hydrofoil. Kunz et al. (Kunz et al., 1999; Kunzet al., 2000) declared that the further development of the model involving the improvement of cavitation dynamics would require the solution of the continuity equations for both continuous and dispersed phases. The presence of dissolved air or superficially added air (i.e. injected air) as the third phase besides liquid and vapor is often an important factor influencing the cavitation, so it cannot be omitted. To conduct a precise prediction, the previous innovative concept was further developed by Merkle et al. (Merkle, 1998) whose model can take a third phase account in the form of non-condensable gas. Also, another cavitation model which is commonly used was proposed by Singhal et al. (Singhal, 1997). The elaborated model is compatible with the iso-thermal flow in the presence of non-condensable gas with a constant rate of concentration.

This paper presents the numerical and experimental investigations of cavitation in the water flow with the presence of air. The flow over a Clark Y 11.7% hydrofoil was selected as it is one of the most common examples of cavitating flow, which has been extensively studied for many years. The different flow regimes with the incipient, sheet/cloud and supercavitation with different amounts of air dissolved in the water were analyzed. The mixture model in the variant with three phases liquid-vapor-air (3phases model) was implemented for the numerical analysis. The Zwart-Gerber-Belamri cavitation model was employed in the calculations and non-condensable gas was considered as the third phase. The dynamics of the cavitating flow, as well as the main flow parameters, were compared and validated against the experimental data obtained from the closed-loop cavitation tunnel located at the Department of Power Engineering and Turbomachinery of The Silesian University of Technology.

2. Experimental setup

2.1. Test rig

The experiments were performed using a hydraulic installation with a cavitation test chamber built in the laboratory of the Department of

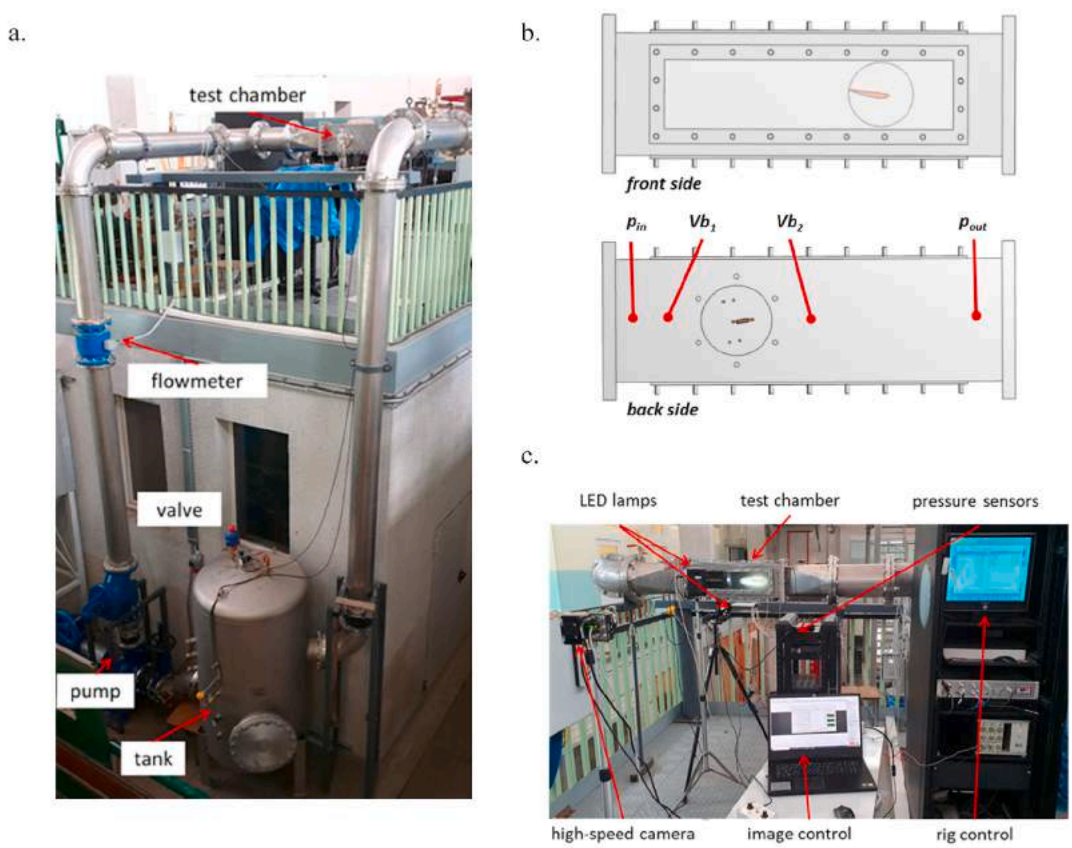

Fig. 1. Closed-loop installation with cavitation test chamber, a. location of main devices, b. Test chamber with the location of inlet and outlet pressure taps, c. Test chamber with main instruments.

Power Engineering and Turbomachinery at the Silesian University of Technology. The main elements of the closed-loop installation were presented in Fig. 1. The pump of 30 kW power drives a water flow in the 200 mm-pipe installation. After the pump, the manual valve and electromagnetic flowmeter were installed. The elevation difference between the pump level and the test chamber is about 5m. Then the water passes through two 90-degree elbows. The flow straightener was mounted before the inlet nozzle where a pipe changes shape from circular to rectangular. The diffusor mounted right after a test chamber changes back the pipe shape into the circular one. Next, the pipe is heading to the tank, which is located on the ground level. The tank of about 1.5 m^3 was designed with the internal air-bag located in the top section of the tank. The air-bag is an elastic membrane connected with the compressed air system. It made it possible to regulate and control the pressure in the installation. The test rig in this configuration can operate with the constant volume flow rate and with the different pressure levels at the inlet to the test chamber. To reduce forces and vibration propagation, three elastic couplings, one before the tank, one after the pump and one between the tank, and the pump were inserted.

The test chamber has a rectangular cross-section of height $h = 189$ mm, span $c = 70$ mm and length 700 mm. The chamber height to chord ratio equals $h/c = 2.7$. The hydrofoil was fixed to the wall on one side at half of the chamber's height, 210 mm downstream from the chamber inlet. The transparent windows, which are made of polycarbonate, were placed at the top, bottom and one sidewall of the test chamber to enable optical access and observations.

A hydrofoil of the constant profile Clark Y 11.7% was investigated in the present study. The hydrofoil had a chord length of $c = 70$ mm and a span of 70 mm (Fig. 2). It can be adjusted to the specific angle of attack. The trailing edge was manufactured with a radius of 0.5 mm. The mounting foot located at one side of the hydrofoil was fixed with the round disk. The internal channels in the foil connect the taps with the pressure impulse tubes fixed to the mounting foot. The hydrofoil was printed from titanium using SLM manufacturing technology. Also, 10 taps are located in the mid-span of the suction side to detect the static pressure signals (Fig. 2). The high-frequency pressure sensor was connected with the tap P6 and the low-frequency pressure sensors were connected to the remaining taps.

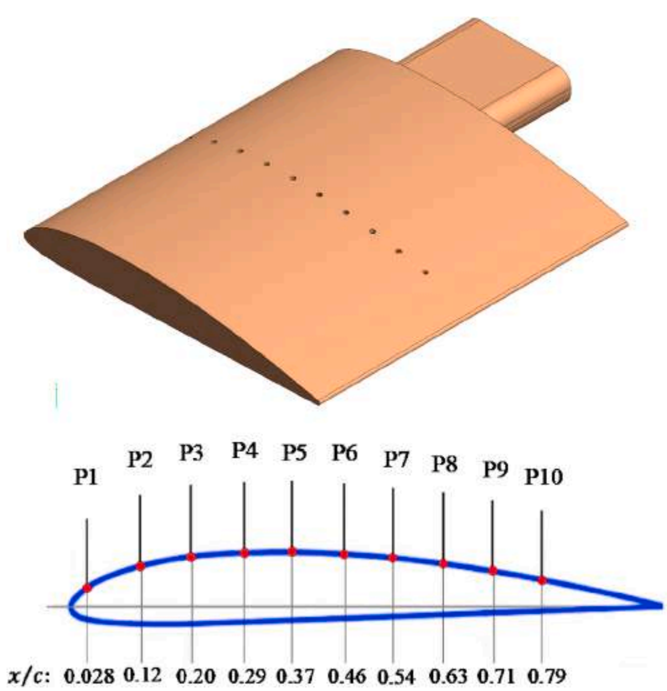

Fig. 2. Clark Y 11.7% hydrofoil with the location of pressure taps.

The air content was measured using measurement of oxygen level of operating water in the closed-loop test rig using oxygen sensor (multi-function device CF-401). The oxygen level was measured before and after experiment in the steady conditions and the ambient pressure. The measurements were done immediately after sampling, as a result; the effect of ambient condition was negligible.

The air content was increased by the injection of air and mixing air and water, when the facility was running, till the desired level of air in the water was reached. The non-dissolved air was removed from the installation.

On the other hand, the present closed-loop test rig is insulated which results in keeping the air content constant. Also, the values before and after experiment are close to each other with the discrepancy of less than 10%. The assumed value was an averaged one.

2.2. Measurement system

The pressure at the chamber inlet and the suction side of the hydrofoil (Fig. 2) was measured with the low-frequency sampling rate by pressure transducers APLISENS PC-28, with the full scale (FS) of 160 kPa and an accuracy of 0.16%. Pressure signals were sent to the measuring clusters via impulse tubes. The pressure at the chamber outlet (Fig. 1) was detected by high-frequency miniature pressure sensor XP5 with amplifier ARD154. The upper threshold of the sensor was 5 bar and its accuracy equaled 0.25%. The temperature of the water was measured by the resistance thermometer APLISENS CT-GN1 Pt100 with a full scale of 0–100 °C and accuracy of ±(0.15K + 0.002 |T|). The flow rate was measured by electromagnetic flowmeter UniEMP-05 DN200 with a measuring range up to 1080 m^3/h and accuracy of ± 0.25%.

The vibroacoustic signals were at the outer walls of the chamber by two piezoelectric transducers. The two stiff piezoelectric accelerometers KD35 (RTF) were located externally on the sidewall of the test chamber. The Vb_1 was located about one profile chord length before the leading edge and the second Vb_2 about one and a half chord behind the trailing edge (Fig. 1b). The accelerometers were connected with the 0028 (RFT) type charge amplifier connected with the fast response converter AC 16 bit, 250 kS/s. The system was calibrated before the experiments using electrodynamic vibration calibrator EET101 (RFT) type. The upper value of the error was less than 5%.

The measurement system used in the research was based on a National Instruments module NI USB 6216. The NI/PXI-6255 module co-operates with measuring clusters, which include sets of sensors, and measuring transducers. The executive elements and the data acquisition process were managed by a system programmed in the LabView environment.

An important part of the data acquisition system was image recording and processing. The structures of cavitation were recorded by high-speed video camera Phantom Miro C110. The recording speed was set to 3200 frames per second with a spatial resolution of 960 × 280 pixels. The settings of the camera resolution and speed were selected as a compromise between image quality and picture size.

2.3. Flow conditions

The flow rate was set constant in all experiments which results in constant velocity at the inlet to the test chamber of $u_{in} = 10.63\ m/s$. The corresponding Reynolds number defined by the hydrofoil chord is about 7.3e5. The temperature of the water was about t = 24 °C. The temperature discrepancies between experiments were observed due to the losses and differences in the ambient conditions but did not exceed 2K. The hydrofoil in all experiments was positioned with an angle of attack of 8°.

Each case with different inlet pressure, saturation pressure, density and inlet velocity, is defined with a single cavitation number calculated as follows:

$$\sigma = (p_{in} - p_{sat}) \Big/ \left(0.5\rho_l u_{in}^2\right) \tag{10}$$

where p_{in} and p_{sat} denote the static pressure at inlet and water saturation pressure, respectively. The value of the static pressure at the inlet is calculated based on the time-averaged value in the experiment. The saturation pressure was determined for the temperature of 24 °C, ρ_l denotes the density of water calculated at corresponding temperature and pressure for each measurement series and u_{in} represents the velocity at the inlet. The experiment was performed for the cavitation numbers presented in Table 1.

In the experiment, two levels of dissolved oxygen were investigated, $2.6 mgO_2/l$ and $5.5 mgO_2/l$. The level of dissolved oxygen was estimated by the multifunction device CF-401 before and after the experiment. It corresponds to the air content of 6.7 mg_air/l and 14.0 mg_air/l, respectively and the volume fraction of air about 1.2% and 2.2% for the gauge pressure of about −0.5 bar. Also, the corresponding Reynolds number for the present case is $Re = \rho_l uc/\mu_l = 825770$, where c is the hydrofoil chord. Thus, the fluid flow over the hydrofoil is fully turbulent.

3. Numerical method

3.1. Mathematical model

In the present study, the homogeneous mixture model was used for the simulation of the liquid-vapor-gas flow. The homogeneous flow idea assumes that the flow of a single-fluid mixture was considered with the same velocity flow field for each phase. The consequence of the assumption, which causes the negligence of slip condition between phases, is the reduction in the number of the governing equations. The governing equations are mass and momentum conservation laws:

$$\frac{\partial \rho}{\partial t} + \nabla \cdot (\rho \boldsymbol{u}) = 0 \tag{1}$$

$$\frac{\partial}{\partial t}(\rho \boldsymbol{u}) + \nabla \cdot (\rho \boldsymbol{u}\boldsymbol{u}) = -\nabla p + \nabla \cdot \left[\mu\left(\nabla \boldsymbol{u} + \nabla \boldsymbol{u}^T\right)\right] + \rho \boldsymbol{g} \tag{2}$$

$$\rho = \rho_l \alpha_l + \rho_v \alpha_v + \rho_{ng} \alpha_{ng} \tag{3}$$

The last term in equation (2), which represents the body force, was neglected in the numerical scheme due to the little effect on the modelled phenomenon. The numerical model takes the presence of air into account, and therefore in equation (3), the third term representing the fraction of non-condensing gases (air) was added to the terms of the liquid and vapor phases of the water. The mixture model with three phases: liquid-vapor-air (3phases model) solves the continuity equations for the vapor volume fraction and the air volume fraction. The mass transfer between a liquid and a mixture of gaseous phases was modelled between species:

$$\frac{\partial \rho_v \alpha_v}{\partial t} + \nabla \cdot (\rho_v \alpha_v \boldsymbol{u}) = -\Gamma \tag{4}$$

$$\frac{\partial \rho_{ng} \alpha_{ng}}{\partial t} + \nabla \cdot \left(\rho_{ng} \alpha_{ng} \boldsymbol{u}\right) = 0 \tag{5}$$

$$\alpha_l + \alpha_v + \alpha_{ng} = 1 \tag{6}$$

The phase change in the flow was governed by the source term Γ in equation (4) which represents the mass transfer between the liquid phase and vapor phase in both evaporation and condensation processes.

Table 1
Cavitation numbers for the experimental cases.

Air volume fraction (VF)	Cavitation number (σ)							
0.012	0.79	0.96	1.08	1.28	1.48	1.68	1.85	2.00
0.022	0.90	1.03	1.16	1.34	1.49	1.62	1.82	1.94

The model of the mass transfer between phases, the cavitation model, used in this study, was proposed by Zwart et al. (Long et al., 2018). Like other commonly used cavitation models, it is based on the simplified form of the Rayleigh-Plesset equation for vapor bubble growth in the fluid. In this cavitation model, the values of condensation and evaporation rates were calculated by the following equations:

$$\Gamma = C_c \frac{3\rho_v \alpha_v}{R} \sqrt{\frac{2}{3}\frac{(p - p_s)}{\rho_l}}, p > p_s \tag{7}$$

$$\Gamma = -C_v \frac{3\rho_v (1 - \alpha_v)\alpha_{nuc}}{R} \sqrt{\frac{2}{3}\frac{(p_s - p)}{\rho_l}}, p < p_s \tag{8}$$

$$p_s = p_{sat} + \frac{1}{2}(0.39\rho k) \tag{9}$$

where the value of nucleation site volume fraction equals $\alpha_{nuc} = 0.0005$, coefficients of condensation and evaporation are $C_c = 0.01$ and $C_v = 50$. The value of the nuclei radius is assumed to be R = 1 μm. The above values are the standard for the model proposed by Zwart et al. (Long et al., 2018). It should be noted that the number of nucleation sites is assumed to be constant at different levels of dissolved air contents.

The two-equation RNG k-ε turbulence model was used to calculate the mixture turbulence viscosity. Both RNG k-ε and SST k-ω models has been reported as the best for the prediction of the cavitating flow and used in most simulations of the flow around the hydrofoil (Yin et al., 2021/02).

Numerical modelling of cavitating flows is a challenging task since they are characterized by highly dynamic phenomena due to phase change and turbulence. During the phase change, there are rapid changes in the mixture density and pressure.

3.2. Numerical model

The calculations were performed on the hexahedra-type mesh. The length and height of the calculation domain presented in Fig. 3 corresponded to the dimensions of the test chamber. The domain has 8 main blocks with the O-grid around the hydrofoil. The overall number of grid nodes on the hydrofoil amounted to 368 and the edge normal to the foil had 101 nodes. The domain had an overall width of 0.09 mm discretized by 3 layers of 0.03 mm in thickness. The thin domain was selected to reduce the aspect ratio in the domain close to the hydrofoil in the O-grid region. The whole mesh consisted of 220k hexahedra elements and the value y^+ on the hydrofoil was less than 1. The overview of the mesh with the zoomed O-grid region is depicted in Fig. 3.

Validation of the numerical grid performed in (Homa et al., 2019; Homa, 2018) showed that the numerical grid with a total number of nodes equal to 160k and 270 nodes around the hydrofoil was sufficient for the prediction of the pressure distribution on the hydrofoil. The mesh applied in the present study was finer in the O-grid region to preserve better uniformity of the grid where cavitation is present.

The constant velocity $u_{in} = 10.63\, m/s$ was set at the inlet as a boundary condition along with the volume fractions of water vapor and air and the turbulence level. The boundary condition at the outlet was the static pressure. The free-slip conditions were assumed at the top and bottom boundaries of the calculation domain instead of the actual chamber walls to eliminate a boundary layer and reduce the grid size. The symmetry was set at both lateral sides of the computational domain.

In the numerical calculations, the cavitation number was calculated using the same procedure as in the experiment. However, the value of the static pressure at the inlet was evaluated based on the average value in the numerical simulation. The saturation pressure was determined for the temperature of 22 °C which was assumed in the computations.

The ANSYS Fluent was utilized as the 3-D RANS solver. The coupled pressure-based solver with mixture model was selected with the PRESTO scheme for the pressure-velocity coupling. The second-order implicit

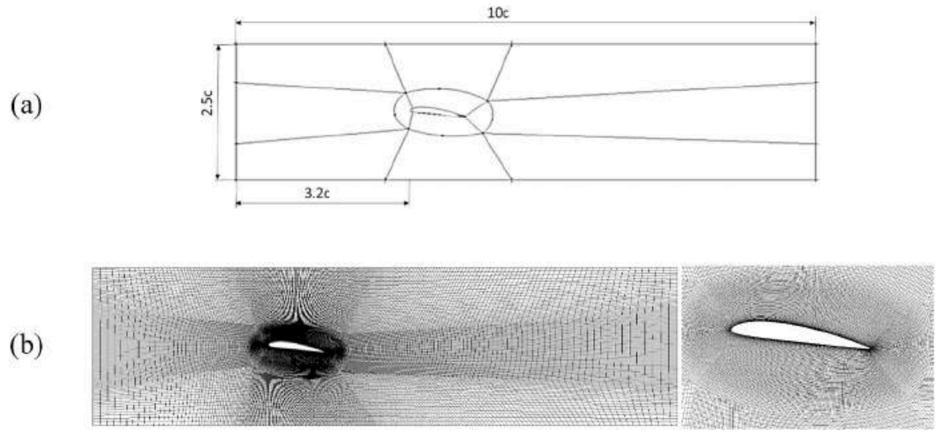

Fig. 3. (a) The calculation domain with the block structure of the mesh, (b) an overview of the numerical mesh and zoomed mesh close to the hydrofoil.

time scheme was applied to account for the transient multiphase phenomena. The second-order spatial discretisation was used for the mixture and turbulence variables. However, the first-order discretisation was set for the volume fraction.

3.3. Validation

The experimental results were validated as a comparison between the distributions of averaged pressure coefficient (C_p) measured for various cavitation numbers in the present work and those reported by Matsunari et al. (2012), as shown in Fig. 4. It is worth mentioning that Matsunari et al. (2012) presented the experimental results obtained in the Laboratory of Kyushu University. They measured the averaged pressure distribution in the mid-span of the two-dimensional Clark Y 11.7% hydrofoil with a chord length of $c = 100\ mm$ and the span of $b = 81\ mm$. The pressure taps were located on both the suction and pressure sides. The height to chord ratio of the chamber which is defined based on the dimension of the chamber is equal to 2. This quantity is different from the ratio of the chamber presented in this paper which is constant and equal to 2.7. The span to chord ratio for the reference and present chambers are $b/c = 0.81$ and $b/c = 1$, respectively. Those differences

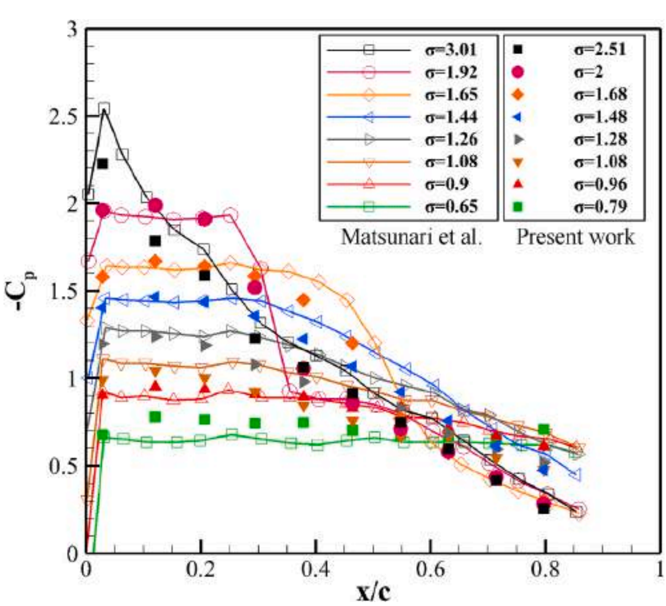

Fig. 4. Comparison of experimental pressure coefficient around hydrofoil measured by the present work and those reported by Matsunari et al. (Matsunari et al., 2012) for various cavitation numbers (dissolved oxygen in the present work 2.6 ppm and Matsunari et al. 2 ppm).

show the higher blockage effect of the water tunnel. In this work, the mean velocity $u_{in} = 10.63\ m/s$ and reference inlet pressure measured at the chamber inlet 120 mm upstream from the leading edge were used to calculate the cavitation number. In contrast to the reference work, where the pressure distribution was detected with 25 pressure sensors located at suction and pressure sides, but in the present work, 10 pressure sensors were mounted at the suction side of the hydrofoil. The amounts of dissolved oxygen were considered constant in both experiments, which were less than 2 ppm in the reference case and about 2.6 ppm in the present work. In this study, it was difficult to keep the cavitation numbers the same as those reported in Matsunari et al. (2012) since there were some slight differences between the operating and boundary conditions and configuration. In addition, the amounts of dissolved air between these two experiments are slightly different which is inevitable since it is hard to reach a certain amount of oxygen content during the experiment. On the other hand, the difference between geometrical parameters such as chord and span must be taken into consideration when the results are being compared. Overall, it should be noted that the reason for using the work done by Matsunari et al. (2012). for validation, is its similarity to the present case and indicated amount of air content which is not common in other works. The inlet pressures were highly unsteady in most of the cases so the averaged values had to be applied in the cavitation number definition. As can be observed in Fig. 4, most of the compared cases have very similar cavitation numbers except the cases with the highest values. The highest cavitation numbers refer to the cases with the non-cavitating flow and are equal to $\sigma = 2.5$ for the present experiment and $\sigma = 3.01$ for the reference experiment. As expected, in the reference experiment, the C_p distribution had higher values, but the tendencies were similar. Comparing the pattern of pressure coefficient distribution of the non-cavitating flow with others, substantial differences can be seen, especially around the leading edge. Since there was no cavity closure around the leading edge in this case, the value of the pressure coefficient reached a peak and then falls rapidly. At $\sigma = 2$, the flat distribution of pressure was observed confirming the existence of the cavity around the leading edge. With a reduction of the cavitation number, the flat distribution of pressure coefficient was extended through the suction side indicating the development of cavity closure along the surface of the hydrofoil. For the minimum values of the cavitation numbers, the distributions for $\sigma = 0.65$ and $\sigma = 0.79$ are depicted. The visible discrepancy was observed but the shape and location of the points corresponded to the cavitation number difference. For the low values of the cavitation numbers, the pressure coefficient distribution was almost flat, declaring the fully-developed cavitation. Finally, the pressure coefficient distributions were in good agreement, which proves the accuracy of the present experimental data.

So far, the accuracy of experimental data of the present work has been verified by making a comparison for the pressure coefficient distribution, but it is required to validate the numerical simulations. For this purpose, the pressure distributions around the hydrofoil as a function of cavitation number for two air volume fractions predicted by numerical simulation were compared with the experimental data, as shown in Fig. 5. Four cavitation numbers are selected for making a comparison to cover the conditions of fully-developed cavitation to partial cavitation. As can be seen in Fig. 5, there are slight differences between the value of the cavitation number in the numerical and experimental cases. These differences originated from the employed reference pressure at the inlet. It was not possible to retain the same value of pressure at the inlet; so there were minor differences between the calculation of cavitation number for the numerical and experimental cases. At high cavitation number $(\sigma = 1.76)$, the pressure distribution was almost flat between $x/c = 0$ to 0.2, which showed the short region near the leading edge with cavity closure. As the cavitation number decreased, the flat pattern of pressure distribution extended until the cavitation phenomenon was fully developed at $\sigma = 0.77$. Based on the comparison between values and tendency of the pressure distribution, it was proved that there was qualitative consistency between numerical and experimental results in all cases.

Fig. 6 presents the time-averaged lift and drag coefficients, which are plotted against the cavitation number. Additionally, a comparison between the numerical result with numerical (Matsunari et al. (2012)) and experimental (Numachi (1938)) data was carried out. The lift $C_L = F_L/(\rho_l u_{in}^2 A/2)$ and drag $C_D = F_D/(\rho_l u_{in}^2 A/2)$ coefficients were calculated, where F_L, F_D, ρ_l, u_{in} denote lift force, drag force, density and velocity, respectively. An effective area, $A = bc$, was calculated using the values of span b and chord c. The cavitation phenomenon has an unstable nature, which is highly affected by the flow condition. For different flow conditions, various regimes of cavitation occur, including incipient cavitation, partial cavitation, sheet cavitation and supercavitation, each with a specific range of forces resulting in different tendencies of force coefficient distribution. For the cavitation number $\sigma > 2$, the lift coefficient predicted by the numerical method was slightly lower than the one obtained at Tohoku University but fitted well with the experimental results from Kyushu University (Senocak and Shyy, 2002). The differences between the experimental results were explained in (Senocak and Shyy, 2002) by the discrepancies in the test chamber dimensions. The domain in the calculations was the same as in the chamber dimensions of Tohoku University and therefore reference to those results is preferred.

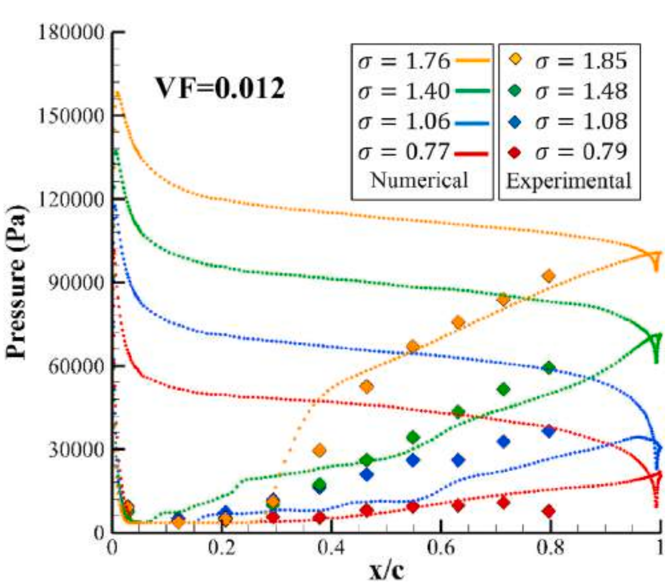

Fig. 5. Comparison between numerical and experimental averaged pressure distributions along the hydrofoil surface.

The calculated lift coefficients were generally lower than the experimental ones. The shape of the distribution was similar except for the range from $\sigma = 1.2$ to 2. In this range, the cavitation was characterized by high dynamics of the cloud structures when most turbulence models suffer from inaccuracy. In Fig. 6, the results from (Senocak and Shyy, 2002) were plotted to show the same tendency in the calculated distribution of the lift coefficient in the discussed range. Surprisingly, the drag coefficient distribution agreed relatively well with the experimental results obtained at Tohoku University.

Overall, no numerical approach is able to predict the cavitation process and its dynamic characteristics perfectly. In addition, many assumptions are usually adopted to simplify the numerical simulation. As such, one can expect slight discrepancy between numerical and experimental data. Based on the comparison provided in Fig. 6, we can conclude that the present numerical results are aligned with experimental data performed at Tohoku University regarding almost the same trend and magnitude of lift and drag coefficient during most parts of the cavitation number range.

4. Results and discussion

The influence of the air in the water was investigated both experimentally and numerically. Two amounts of air contents in the water in different conditions were analyzed in the flow around the hydrofoil in the cavitation tunnel (Table 1). The numerical simulations were performed for four amounts of air content in the water including, apart from the experimentally analyzed cases, the case with VF = 0 which means that air was not taken into account, and the case with the volume fraction of air of VF = 0.042 which corresponds to the value which is close to that in ambient conditions.

4.1. Measured pressures and vibrations

Fig. 7 indicates the value of static pressure recorded by the fast pressure sensor located at the chamber outlet (Fig. 1b) during the time span of 1s for three different cavitation numbers and two air volume fractions. Additionally, the corresponding Fast Fourier Transform (FFT) analysis was provided. Based on the measurements, it can be observed that, depending on the case; the patterns of pressure fluctuations were generally irregular, which proved the complexity of the cavitation phenomenon. It is also visible in the FFT analysis, that the more complex cases, the more frequencies detected. Higher amplitude was observed for the cases with the medium cavitation numbers. The frequency of maximum pressure pulses, which can be detected by the dominant frequency in FFT analysis, depends on the cavitation number. They are easier to recognize if the harmonic frequencies are visible. When comparing the lowest cavitation numbers, it can be seen that the harmonic frequency appeared for the lowest air content. For the higher cavitation numbers, the peaks appeared for two frequencies that were very close to each other. In this case, two values were indicated.

The main frequencies obtained in the experiment from the pressure signals are summarized in Table 2 based on the Strouhal number, which is defined as follows:

$$St = \frac{f.C}{u_{ref}} \tag{11}$$

where f, C and u_{in} represent the shedding frequency, chord of the hydrofoil and velocity at the inlet, respectively.

For the values of low air content, the frequencies increased from 9.5Hz (St = 0.062) for the low cavitation number to the value of about 17Hz (St = 0.111) for the cavitation numbers higher than 1.68. The frequencies, obtained for the higher value of the air content, were generally similar. In most of the cases, slightly lower values were detected, but the difference was too small to provide unambiguous information to conclude the trend. Both methods of high-frequency signals

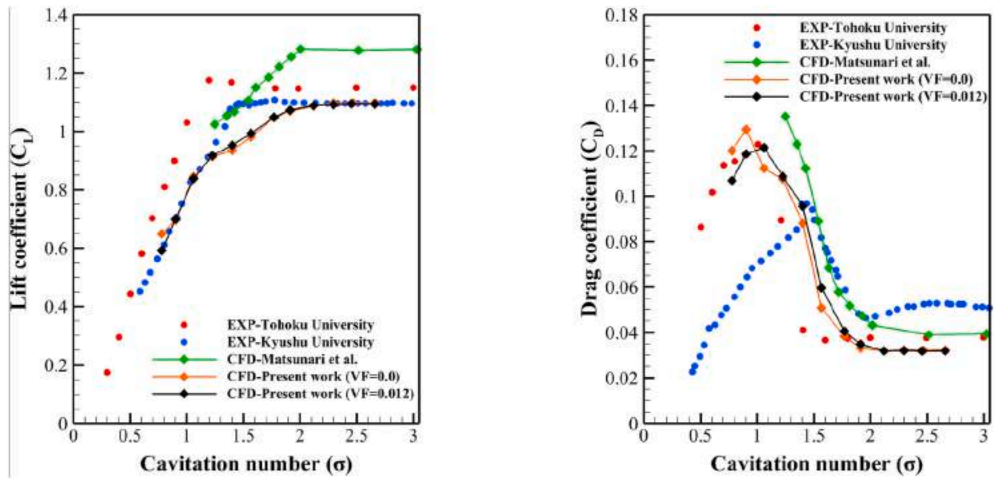

Fig. 6. Time-averaged lift and drag coefficients versus cavitation number for different air volume fractions.

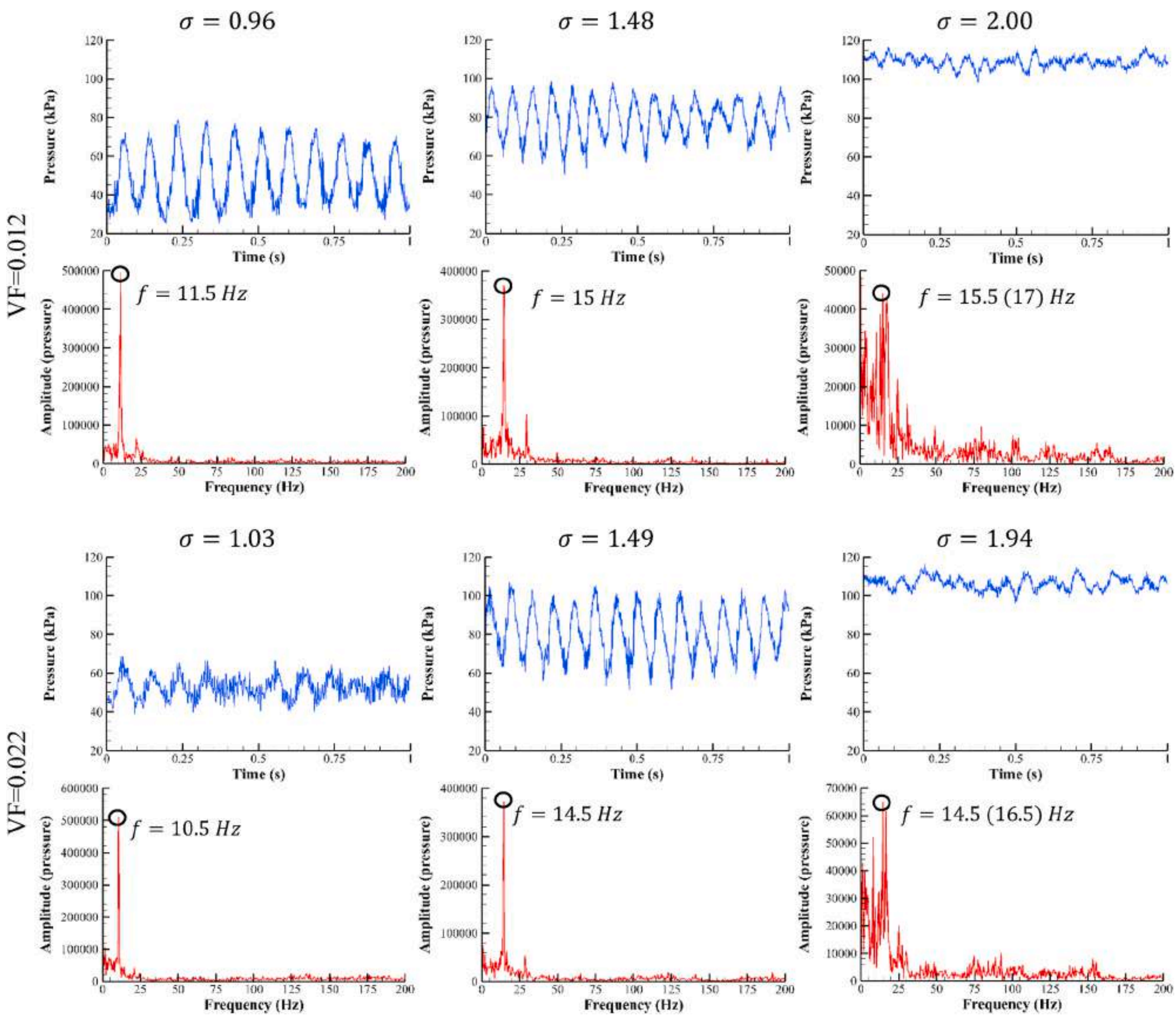

Fig. 7. Samples of pressure fluctuation at the outlet (blue line) and corresponding FFT analysis (red line) for different cavitation numbers and air volume fractions.

Table 2
Experimentally detected main frequencies (Strouhal number) of the pressure fluctuations at the chamber outlet.

Air volume fraction, VF = 0.012								
Cavitation number σ	0.79	0.96	1.08	1.28	1.48	1.68	1.85	2.00
Frequency [Hz] (Strouhal number), pressure-based	9.5 (0.062)	11.5 (0.075)	13 (0.085)	13 (0.085)	15 (0.098)	15 (0.098)	16.5 (0.108)	17 (0.111)
Frequency [Hz] (Strouhal number), vibration-based	9.5 (0.062)	11 (0.075)	13 (0.085)	14 (0.092)	14.5 (0.095)	15 (0.098)	16.5 (0.108)	17.5 (0.115)
Air volume fraction, VF = 0.022								
Cavitation number σ	0.90	1.03	1.16	1.34	1.49	1.62	1.82	1.94
Frequency [Hz] (Strouhal number), pressure-based	10 (0.065)	10.5 (0.069)	12 (0.079)	13.5 (0.088)	14.5 (0.095)	15 (0.098)	15 (0.098)	16.5 (0.108)
Frequency [Hz] (Strouhal number), vibration-based	10.5 ()	10.5 (0.069)	11.5 (0.075)	13.5 (0.088)	14.5 (0.095)	–	–	–

detection, pressure probe and vibration sensor, gave very similar results. The signals from the vibration sensor Vb2 (Fig. 1b) were analyzed due to the lack of any substantial difference with the signals from the sensor Vb1. In the cases with high air content and with high cavitation numbers, the signals from vibration sensors did not allow to extract the cavitation cloud frequencies due to small amplitudes. They were on the level of the detected background amplitudes, which occurred in the chamber surroundings.

The output results of the vibration sensor Vb2 (Fig. 1b) were presented in Fig. 8 as a function of cavitation number for two analyzed air volume fractions. The spectrum of vibrations is presented with the spectrum of pressure fluctuations for the same cases to show the correspondence between both methods. The two other flow conditions with the cavitation numbers of $\sigma = 0.79,\ 1.28$ for the low air content and $\sigma = 0.9,\ 1.34$ for the high air content were selected to supplement the visualization showed in Fig. 7. The value of dominant frequency, which is likely to be in correspondence with shedding frequency, are noted in the figures. It can be concluded that the first mode of chamber vibration originated from the shedding vortex what indicates the major impact of the shedding vortex on the vibration.

The spectrums of vibration are more complex and reveal many signals of higher frequency, especially in the range of 40–70Hz. The origin of these frequencies is difficult to determine but has to be related to the operational conditions.

Frequencies reported in the literature used for the comparison for the cavitation number of σ = 0.8 are as follows: 8.3Hz (Watanabe et al. (2014)), 20Hz (Wang et al. (2001)), 22 Hz (Wang et al. (2009)) and 24.1Hz (Huang et al. (2014a)). For the cavitation number of 1.45, Watanabe et al. (2014) reported a frequency of 8 Hz. In the above reports, the frequencies were estimated based mainly on the lift coefficient evolutions. Watanabe et al. (2014), during their analyses, confirmed the correspondence between the lift coefficient fluctuations and pressure fluctuations at the chamber outlet.

Additionally, the effect of air volume fraction is taken into account in Fig. 9 where pressure distributions at the suction side of the hydrofoil measured by transducers, are presented. As it can be observed for all presented flow conditions, the differences in the averaged values of pressure for both volume fractions were small and could not be attributed to the differences in air content. It can be noticed that the difference was visible in the region close to the cavity end.

4.2. Simulation of unsteady pressures

Fig. 10 depicts the averaged pressure distributions over the hydrofoil computed for different volume fractions of air in water for four selected cavitation numbers. The pressure distributions on the pressure side were almost the same for all air volume fractions and the subsequent cavitation numbers. On the suction side, the differences were much more distinctive. For the air volume fractions of VF = 0, the shape of the distribution was irregular except for the case with the cavitation number

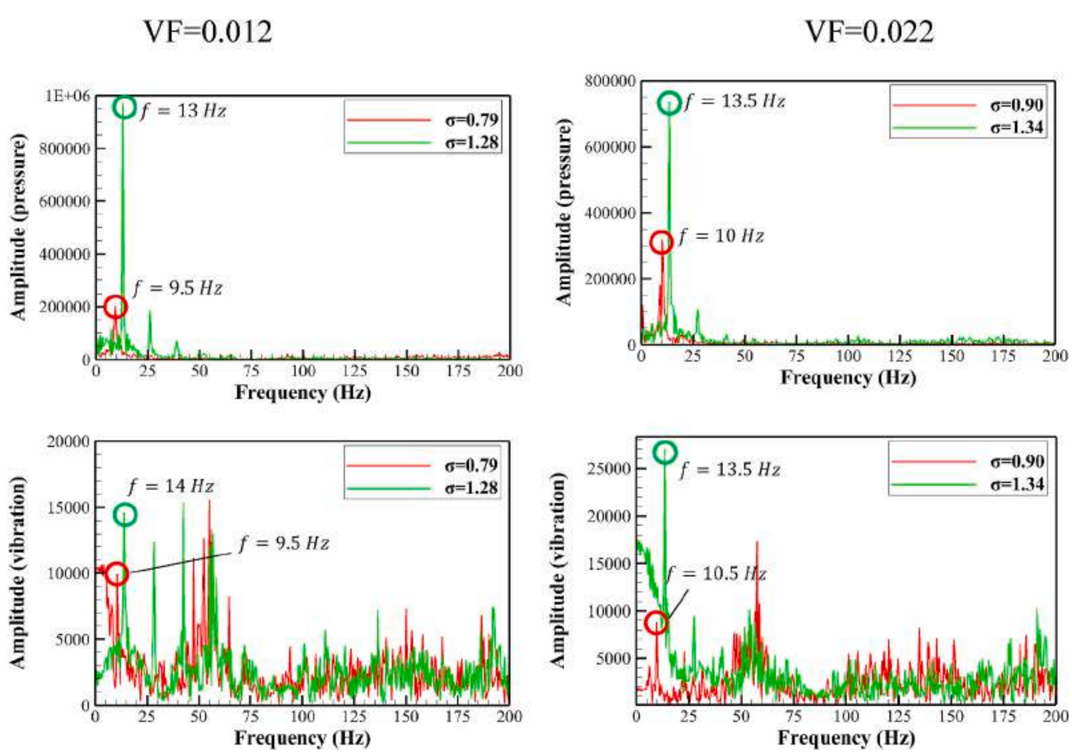

Fig. 8. Comparison between frequencies of pressure fluctuation (outlet) and induced vibration (Vb_2) during cavitating flow.

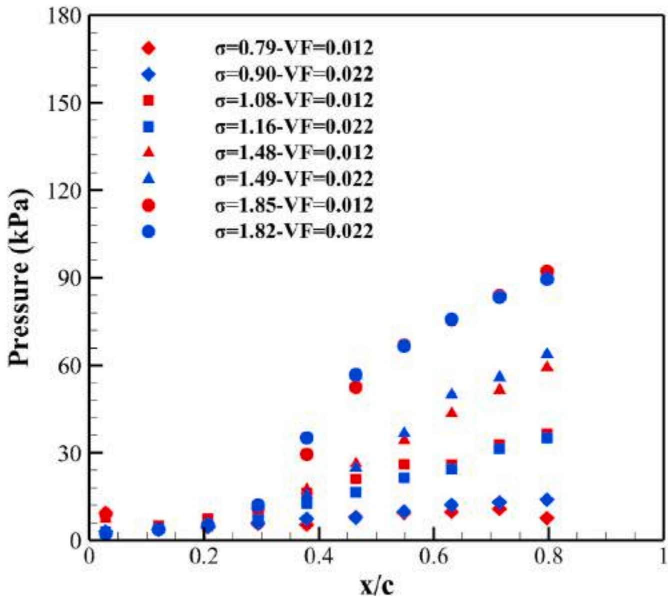

Fig. 9. Averaged pressure distribution measured by transducers at the suction side as a function of two air volume fractions and different cavitation numbers.

of 1.76. In those cases, the unsteady character of the flow was dominant. With the increase of the air volume fraction, the pressure was closer to the saturation pressure starting from the leading edge zone. For the cavitation number of 0.77 and values of air volume fraction of 0.022 and 0.042, the cavitation was detected almost over the whole surface. For the higher cavitation numbers, the distance occupied by the saturation pressure was shorter until about $x/c = 0.25$. It means that downstream of this point, the higher fluctuations were present and influenced the average value significantly. The pressure distributions for the $\sigma = 1.76$ were very similar for all the volume fractions. The cavity was shifted slightly upstream with the increase of air content.

Fig. 11 shows the averaged (red lines) and instantaneous (blue lines) pressure distributions on the hydrofoil for different air contents and one value of cavitation number of $\sigma = 1.4$. The high dynamics in the pressure fluctuations could be observed in all cases. The closer the average pressure distribution to the saturation pressure in the first part of the hydrofoil up to the $x/c = 0.5$, the smaller pressure fluctuations in this part were observed. With an increase of air content, the length of the cavity became more stable and the pressure changes were smaller in the larger region of the rear part of the hydrofoil.

The numerically detected frequencies of the cloud shedding for the case $\sigma = 0.77$ decreased from 200Hz for the air volume fraction of VF = 0 to the value of 8Hz for the VF = 0.042 and reached about 38Hz for the medium values of air volume fractions. For the cases with the cavitation numbers in the range of $\sigma = 0.89 - 1.4$, the values of the frequency were within 17–35 Hz but with the majority in the threshold 22–26Hz and dependence of the air volume fraction was not observed. For the cases with cavitation numbers of $\sigma = 1.76$ and 1.91, the stable cavity structures for all volume fractions of air were present.

For comparison, the value of the frequency of the cavitating structure reported in the literature was 25Hz (Wang et al. (2001), Ji et al. (2017), Long et al. (2017)). This value was calculated for the similar hydrofoil and cavitation number of $\sigma = 0.8$. Huang et al. (2014b) reported a

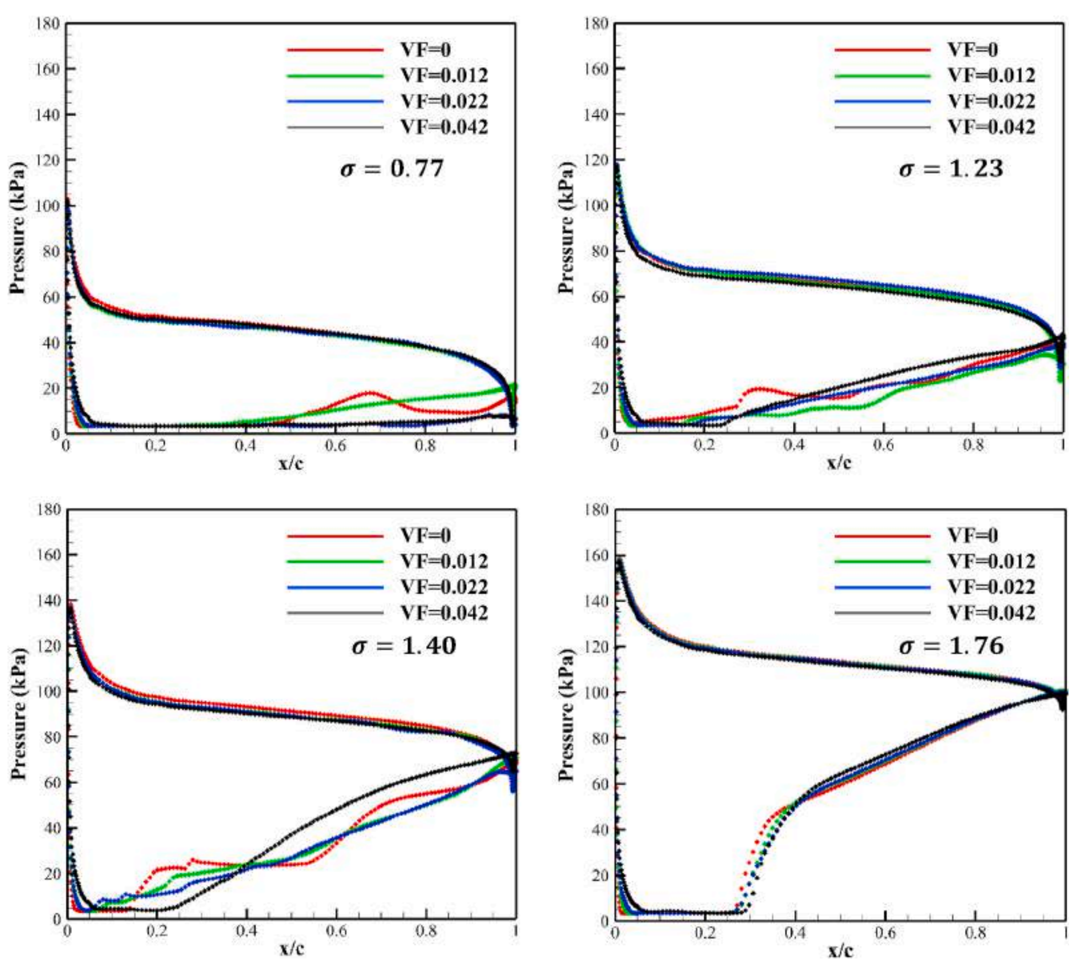

Fig. 10. Averaged pressure distributions around the hydrofoil for the different air volume fractions and four cavitation numbers.

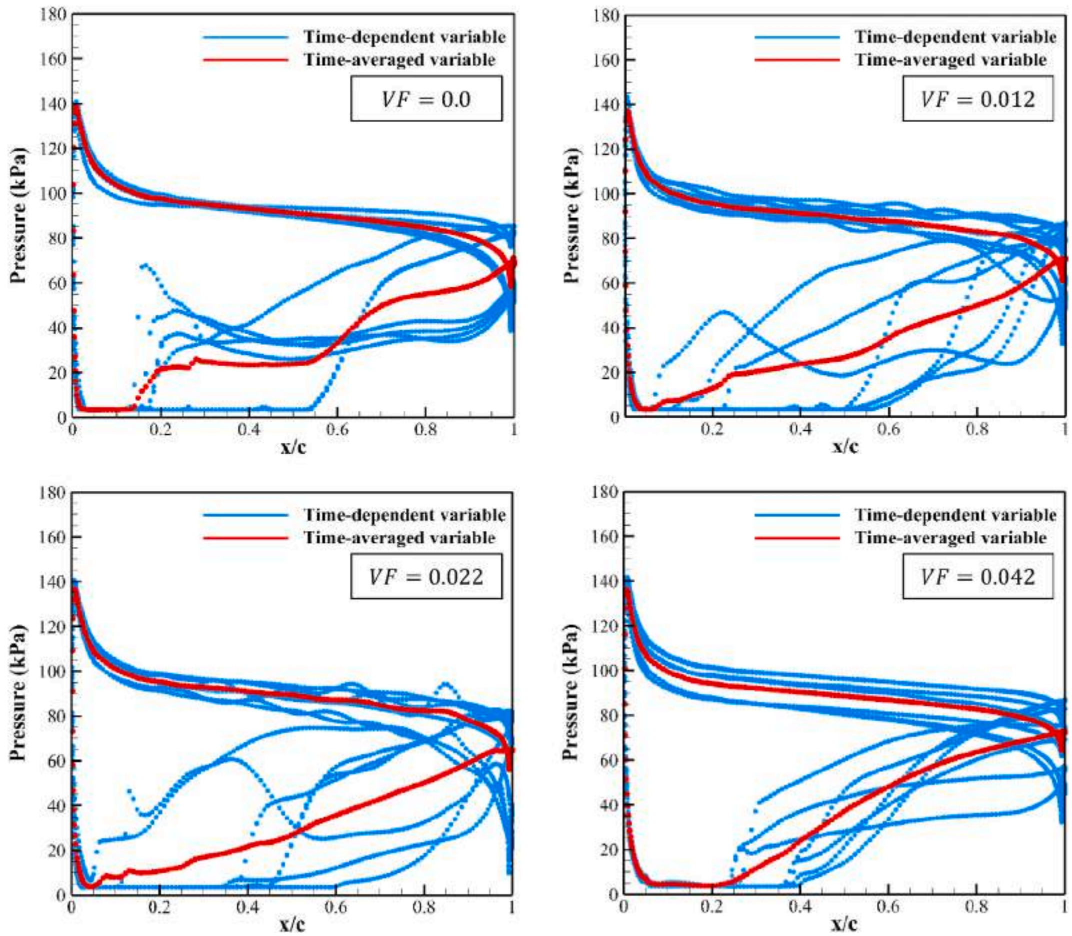

Fig. 11. Selected time-dependent vs. time-averaged pressure distribution around hydrofoil in one period (σ = 1.40).

frequency of 20.1Hz for a standard k-ε model and frequencies from 24.8 to 28.5Hz for the different variants of density and filter-based turbulence closure models. Huang et al. (2017) 2017 reported frequencies of 27.7Hz–41.5Hz for the Partially Averaged Navier-Stokes (PANS) turbulence model, depending on the variant and value of 26.6Hz for the standard k-ε model.

4.3. Comparison of the unsteady cavitation structures

Fig. 12 depicts time variations of the predicted lift coefficient for two nominal flow conditions, the first one with the cavitation number of σ = 1.48 and air volume fraction of $VF = 0.012$ and the second one with σ = 1.49 and $VF = 0.022$, respectively. Both charts showed very similar unsteady behavior of the lift coefficient, nevertheless, the lower amplitude for the higher air content was noticeable. Both curves were characterized by the periodicity of oscillations, so only one cycle sampled by 10 points was subjected to extensive analysis irrespective on the period length. . The contour map of the vapor void fraction is presented in Fig. 13. It is worth noting that the computed void fraction contours are synchronized with the contours of vapor volume fraction. Additional smaller fluctuations were accompanying the main cycle trend, which was a result of the unstable nature of the cavitating flow. Ascending to the peak values was in both cases slower than descending to the initial value of the cycle. The explanation of these phenomena requires referring to the evolution of cavity closure, shown in Fig. 13. Comparing the surging of lift coefficient and the cavity evolution at the corresponding time (i.e. t_1 to t_7), it can be seen that the sheet cavity was mainly created in this time span. Thus, it can be concluded that the sheet

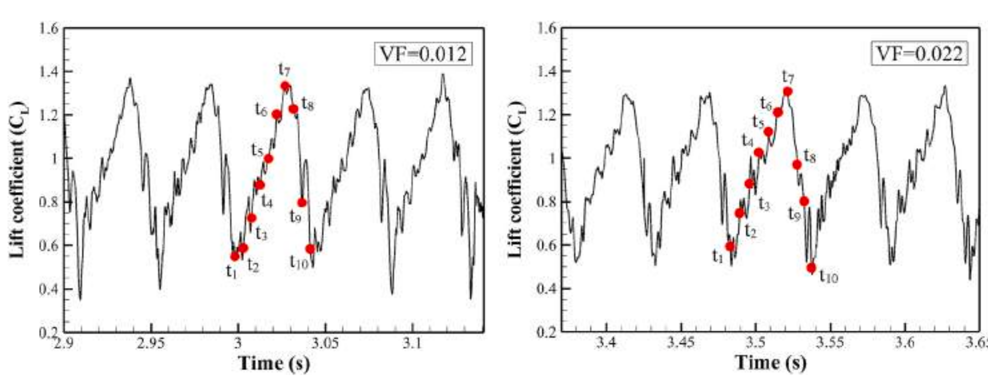

Fig. 12. Time-dependent lift coefficients at $VF = 0.012$ (σ = 1.48) and $VF = 0.022$ (σ = 1.49) along with time selection in a period (coupled with Fig. 13).

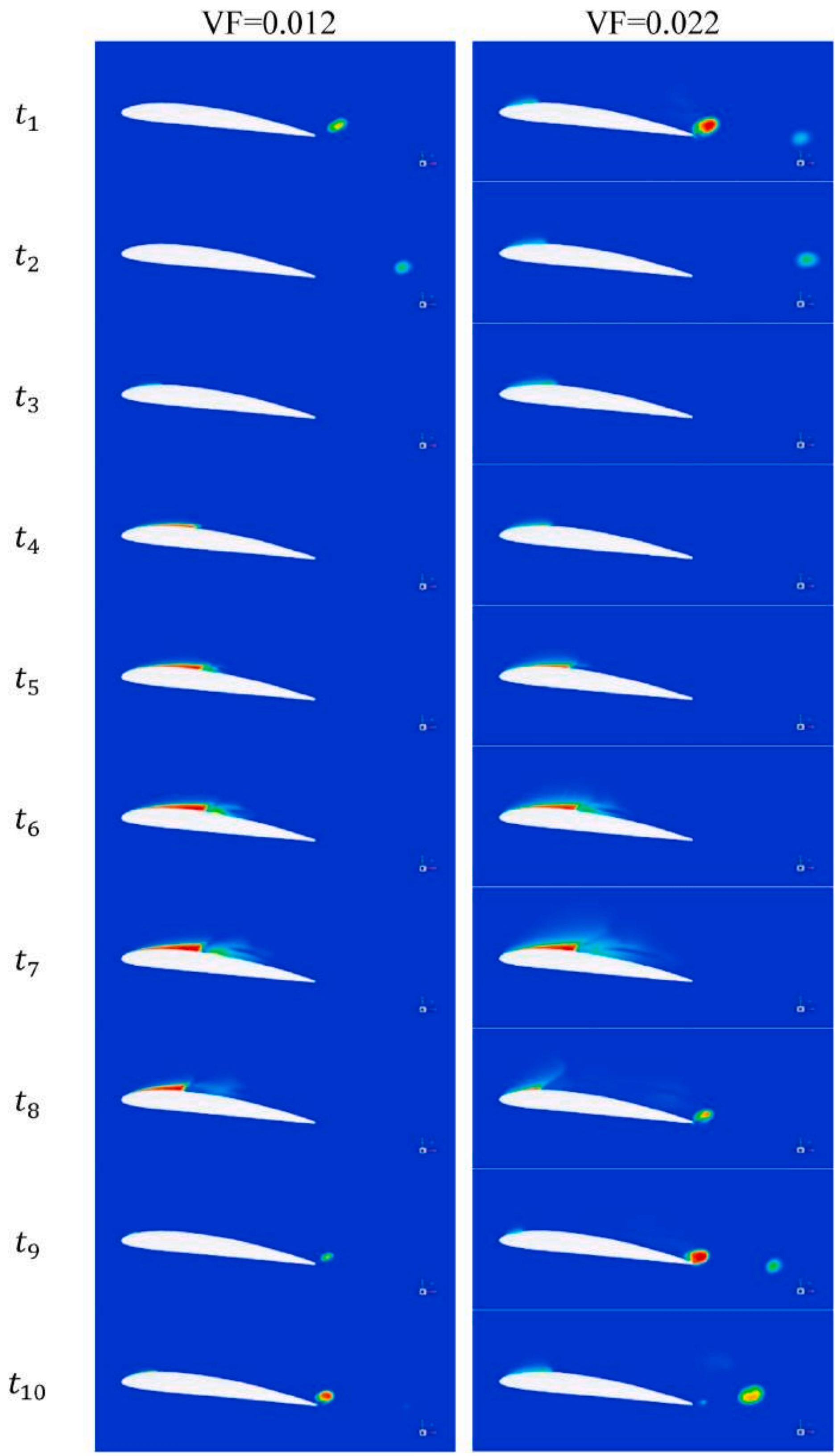

Fig. 13. Contours of vapor volume fraction for two different air contents during one period at the selected points (coupled with Fig. 12).

cavity was the main source of force imposed on the hydrofoil. Although a gradual increment of lift coefficients was observed, reduction of these parameters took less time since the evolution of cloud cavity, including detachment and shedding, was relatively faster than that for the creation of sheet cavity.

Numerical and experimental visualizations of cavity evolution in one period at $\sigma = 0.77$ and $VF = 0.022$ are presented in Fig. 14. Despite remarkable oscillations within the length of the cavity and the existence of cloud cavitation in most of the time span, the numerical model did not reflect the evolution of the cloud structures satisfactory. It means that

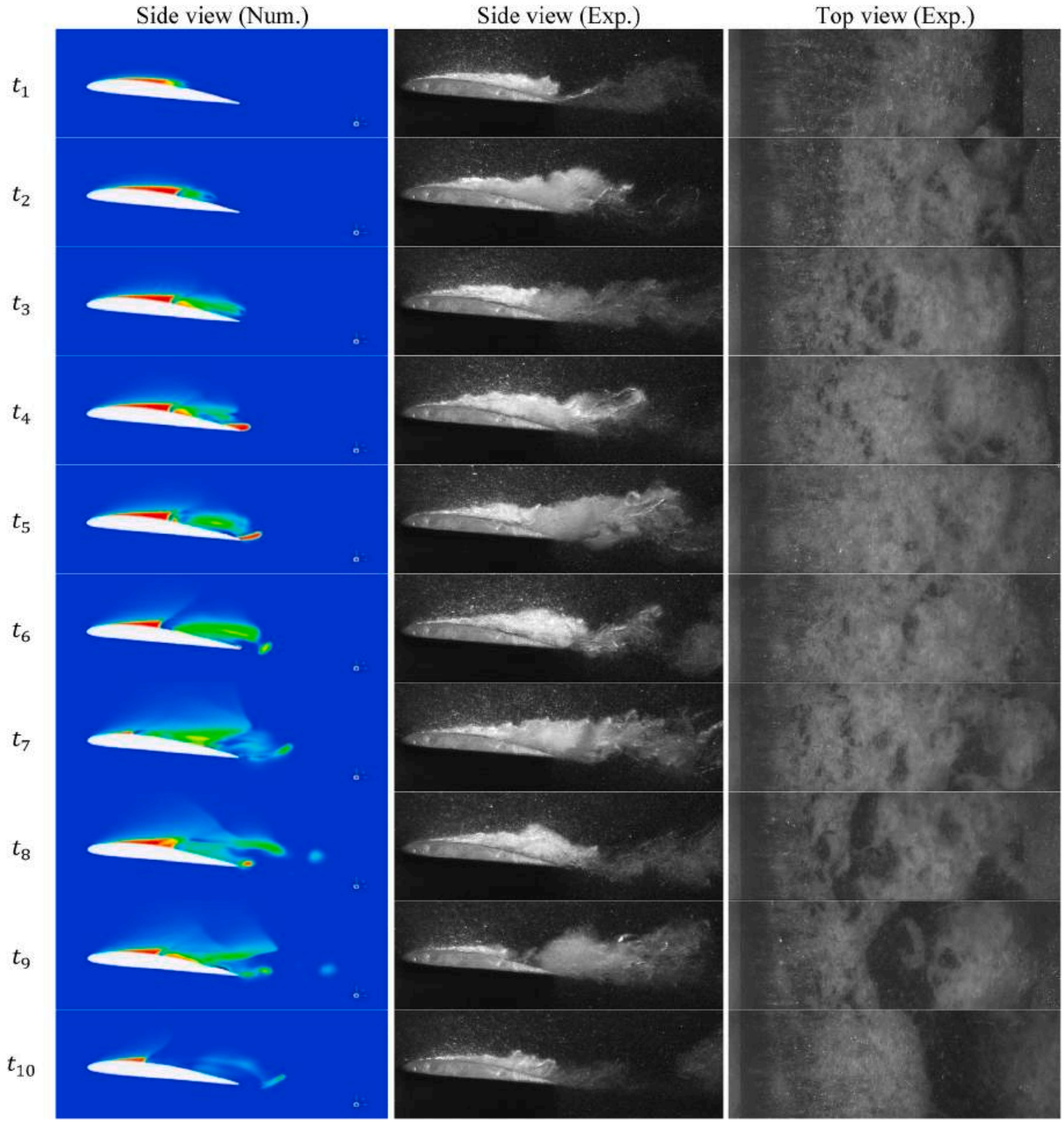

Fig. 14. Numerical and experimental visualization of cavity evolution in one period at $\sigma = 0.77$ and $VF = 0.022$.

the formation of the cloud cavity is hard to track using CFD methods. A different pattern compared to the experiment was observed, especially downstream hydrofoil. However, the prediction of the numerical methods for the characteristics of a sheet cavity was fairly acceptable. This seems to be a source of discrepancy for other numerical results such as pressure distribution and force coefficients in comparison with the experiment. The attached cavity develops in the time span t_1 to t_3, where the sheet cavitation was enlarging from the leading edge to mid-chord of the hydrofoil, which leads to the expansion of the local boundary layer thickness along the surface of the hydrofoil. Within the time span between t_4 to t_8, some relatively stabilized partial cavities were observed with a series of vortices and bubbly flow at the cloud borders. However, a massive cloud shedding, which seems to be the final step of each cycle, did not occur yet. The cloud cavity was finally fully detached and convected downstream.

Fig. 15 depicts the detachment process of sheet cavitation and evolution of detached cloud cavity due to the presence of re-entrant jet. For this purpose, the three-dimensional contour of water vapor volume fraction, side-view of the captured picture during experimental observation and streamlines vector with velocity field at the background are shown. It should be noted that the same case with nominal conditions of $\sigma = 0.77$ and $VF = 0.022$ is selected to show the effect of a re-entrant jet. Furthermore, three different time points are chosen to show the cavity structure before introducing a re-entrant jet and after that. It is worth mentioning that the re-entrant jet is necessary to sufficiently increase momentum to impact the sheet cavity during the collision. This condition was established in the existence of a large adverse pressure gradient pushing the re-entrant jet upstream. At t_6, an attached vortex was detected at the rear of the hydrofoil. However, there is no re-entrant jet colliding the interface of the sheet cavity. Observing the streamline at the narrow region between hydrofoil and beneath of the attached vortex, one can detect evidence of a strong backflow from the trailing edge to the leading edge. So far, a backflow known as the re-entrant jet was introduced along the hydrofoil. After the collision of the re-entrant jet

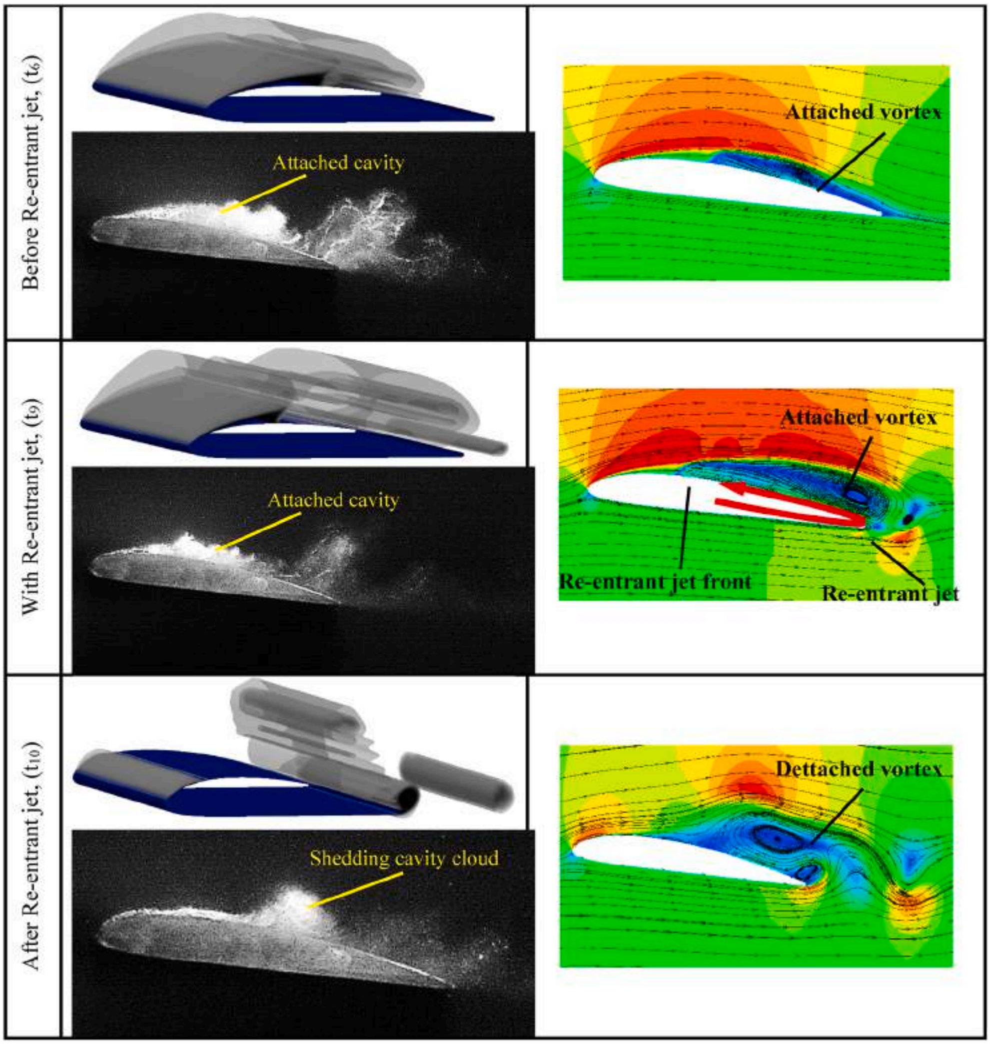

Fig. 15. Effect of re-entrant jet in the formation of shedding cavity cloud (σ = 0.77 and VF = 0.022).

front with the tail of the sheet cavity, the cloud cavity was triggered by detaching the vortex from the surface of the hydrofoil.

To analyze the influence of air content dissolved in the water, two different cycles of the cavitation process for cavitation number of $\sigma =$ 0.77 and two air volume fractions of VF = 0.012 and VF = 0.022 are shown in Fig. 16. To recognize the cavity closure effectively, color filtering is employed on the captured pictures. Within the filtering process, all unnecessary components like the side surface of the hydrofoil and other light bubbles are faded. Thus, the figures consist of only dense cavity and bubbles. When the volume fraction of dissolved air rose, the clouds of the gaseous phase were enlarged in both length and width. On the other hand, it can be seen that the clouds in the case of higher air content seemed to have scattered boundary, and many small bubbles were convected from the cloud. The reason for this phenomenon was the existence of more dissolved air inside the water which facilitated the bubble formation. Comparing the cavity at the first and last steps, one can conclude that there was no incipient cavitation stage at VF = 0.022. It means that the sheet cavity was observed continuously along the hydrofoil even at the transition moment between two cycles. The last point made the cavity lasted longer.

To evaluate the influence of cavitation number and air volume fraction on the cavity area, the normalized cavity area (NCA) for cavitation number in the range of 0.79–2 and air volume fraction of VF = 0.012 and VF = 0.022 during a cycle was compared and shown in Fig. 17a and Fig. 17b, respectively. Calculation of the normalized cavity area was performed based on the color-filtering technique. Figures like Fig. 16 were used to analyze the total share of black, white and grey pixels in the image. Thus, the normalized cavity area was calculated as $NCA = 1 - (Black\% / 100)$. When employing this parameter, it was possible to make a relative comparison between the cavity areas. The cavity area was being gradually enhanced in time. In most cases except the two first lowest cavitation numbers, the maximum cavity area took place between t_5 to t_8. The increase of cavitation number was causing the decrease of the cavity area, although this relationship did not apply for the case with the lowest cavitation number ($\sigma = 0.79$). To clarify the effect of air volume fraction, the average value of the cavity area at each time step was calculated and compared for two air volume fractions, as shown in Fig. 17c. It can be observed that the cavity area was extending through all time steps when the air volume fraction rose.

5. Conclusions

In the present study, the results of the examination of the cavitating flow around the Clark Y 11.7% hydrofoil at 8° were presented. The water tunnel located at the Department of Turbomachinery and Power Engineering at the Silesian University of Technology was used for the experimental part of the research. The implemented measurement systems included high-speed video recording, static pressure measurements with high and low-frequency sensors and recording of cavitation-induced vibration signals. The flow structures and dynamics of the

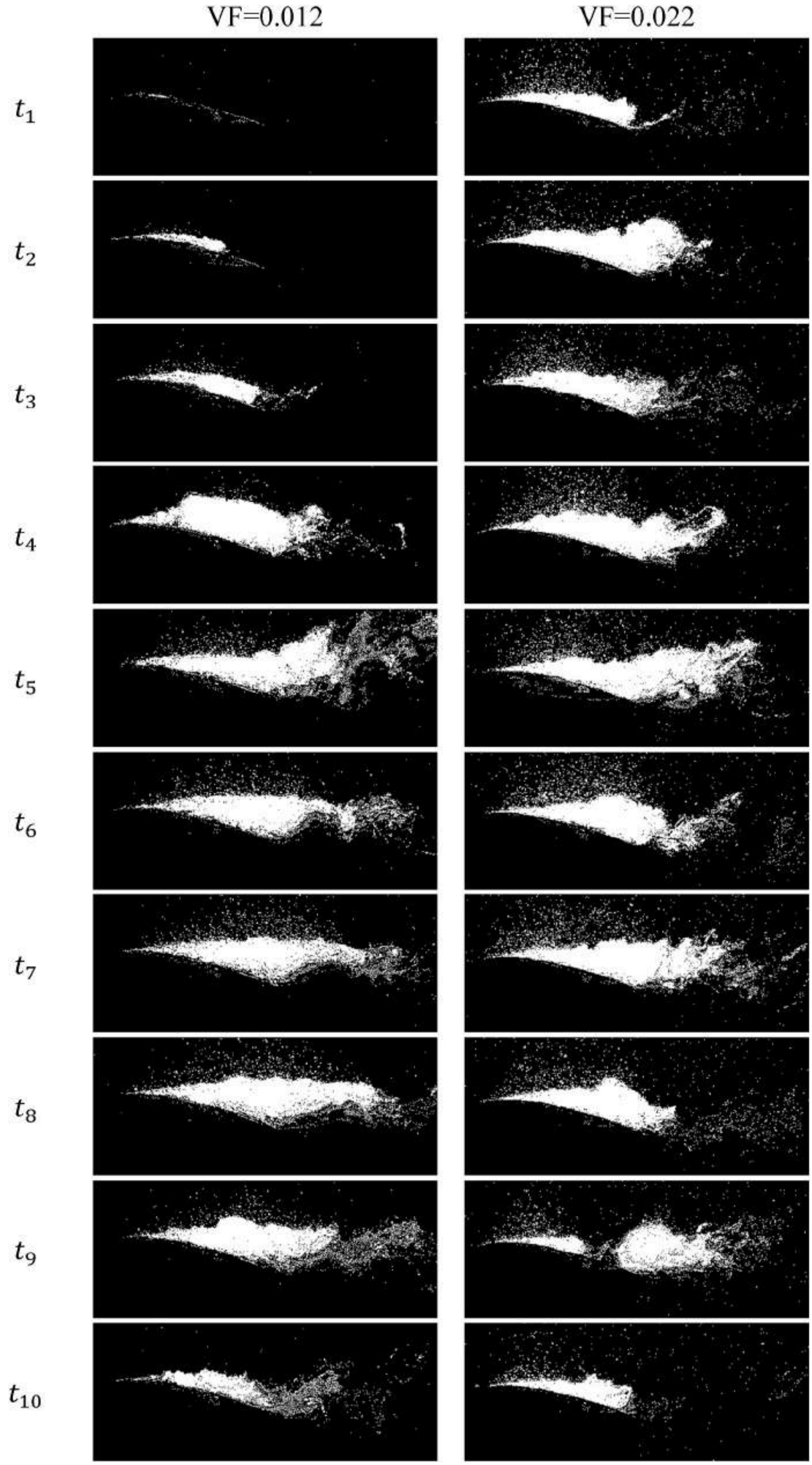

Fig. 16. Cavity area detection over a period for different air volume fractions at $\sigma = 0.77$ based on color filtering process.

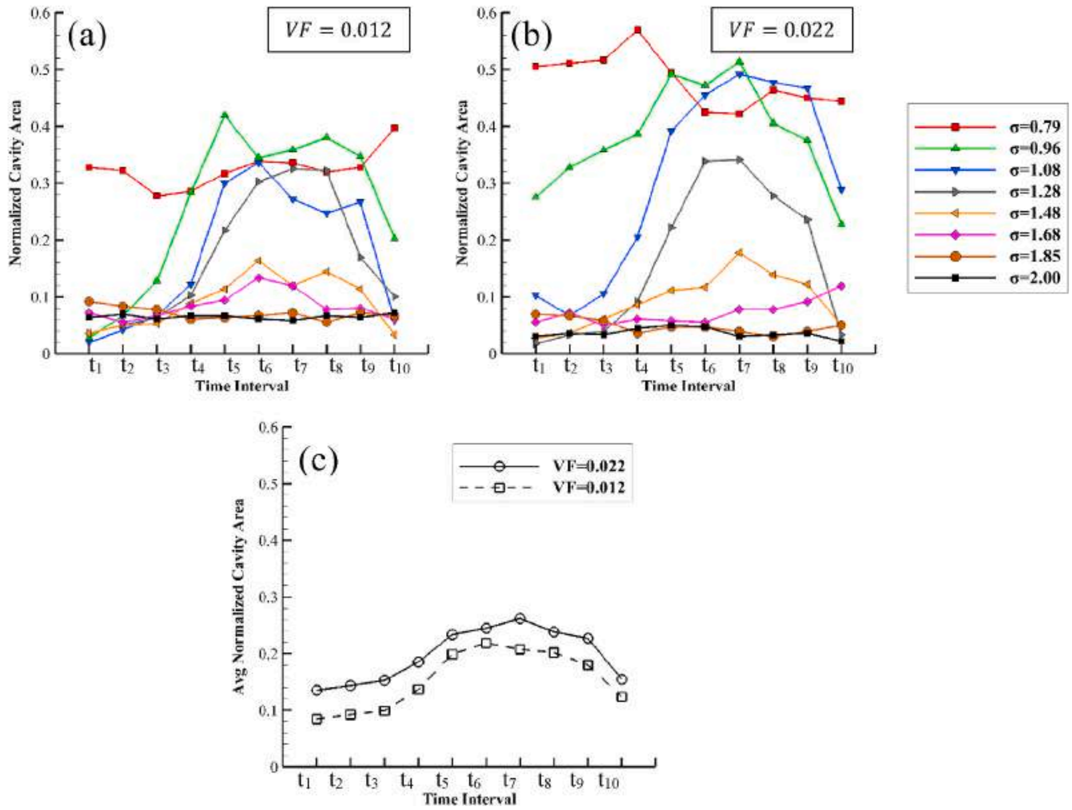

Fig. 17. Normalized cavity area at time interval over a period a) for different cavitation numbers and VF = 0.012, b) for different cavitation numbers and VF = 0.022 and c) averaged normalized cavity area at time interval for different air volume fractions.

unsteady cavitation phenomena for different flow conditions were analyzed. The influence of the dissolved air in the water on the instability of the cavitating structures was examined.

The experiments performed for eight cavitation numbers showed good agreement in the averaged pressure distribution along the hydrofoil surface with the results reported in the literature. The unsteady behavior was examined using the high-frequency pressure sensors at the chamber outlet and vibration sensors. The FFT analysis of the pressure and vibration signals was applied to extract the main frequencies in the cavitating flows. Both spectra of vibration and outlet pressure signals were in good agreement. For higher cavitation numbers and higher air content, the extraction of frequencies of cavitation origin was not possible. The main frequencies of the shedding vortex increased from the value of 9.5Hz–17Hz when the cavitation number increased. The same tendency was observed for both values of the air volume fractions, which corresponded to the values of oxygen dissolved in water equal to 2.6 ppm and 5.5 ppm, although the frequencies in the cases with the higher air content were mostly slightly lower. The difference in the range of 0.5–1Hz, was too small to confirm the trend. When the air content was higher, the amplitudes of the pressure pulsations started to decrease significantly for higher cavitation numbers.

The high-speed camera images enabled the analysis of the cavitation clouds and shedding vortices. The image analysis revealed that the cavity area was extended through all time steps when the air volume fraction enhances.

It was confirmed that for the tested values of dissolved oxygen in water (2.6 ppm and 5.5 ppm), it was possible to observe a slight but detectable influence of air on cavitation frequencies and a noticeable influence on cloud structures.

Overall, the main impacts of dissolved air content on the cavitating flow are as follows:

- The experimental study showed that increasing air content from 2.6 ppm to 5.5 ppm has no considerable effect on the shedding frequency.
- The numerical simulations showed the substantial influence of air content on the frequency of the shedding for the smaller cavitation numbers. When the cavitation number increases the front part of the cavity is being stabilized and the shedding frequencies present smaller dependence on the air content. For the cases with the highest analyzed cavitation numbers, the stable cavity structures for all volume fractions of air were present
- It is hard to specify the shedding frequency using FFT analysis due to the highly dynamic characteristics of the cavitation process in higher value of air content.
- The volume of cavity closure is enlarged during the cavity evolution with increasing dissolved air content.
- The impact of dissolved air on the frequency and cloud structure is minor and major, respectively.

The numerical model was used to resolve the flow conditions of the cavitating flow. The 3phases model which takes into account the presence of air in the water was implemented to analyze the influence of the non-condensing gas on the flow dynamics. The averaged pressure distributions on the hydrofoil surface were validated with the experimental data. The frequencies predicted by the numerical model were generally higher than those detected experimentally and in the range of reported data in the literature. The accuracy of the numerical model needs improvement in turbulence modelling which will be the aim of future research.

CRediT authorship contribution statement

Włodzimierz Wróblewski: Conceptualization, Methodology, Writing – review & editing, Supervision. **Krzysztof Bochon:**

Investigation, Validation. **Mirosław Majkut:** Investigation. **Emad Hasani Malekshah:** Formal analysis, Writing – original draft, Writing – review & editing. **Krzysztof Rusin:** Investigation. **Michał Strozik:** Investigation.

Declaration of competing interest

The authors declare that they have no known competing financial interests or personal relationships that could have appeared to influence the work reported in this paper.

Acknowledgement

The presented work was supported by the Polish National Science Centre funds within the project UMO-2016/21/B/ST8/01164.

Nomenclature

C	coefficient
f	mass fraction
u	velocity (m/s)
p	static pressure (Pa)
t	time (s)
ρ	mixture density (kg/m^3)
μ	effective viscosity of mixture (Pa.s)
α	volume fraction
σ	cavitation number
Γ	mass transfer source term (kg/m^3.s)
k	turbulence kinetic energy (m^2/s^2)

Indices

c	condensation
g	gas (vapor and non-condensable gas)
l	liquid
ng	non-condensable gas (air)
sat	saturation conditions
s	corrected saturation
v	vapor, evaporation
∞	free stream

References

Arndt, R.E., 2012. Some remarks on hydrofoil cavitation. J. Hydrodyn. 24 (3), 305–314.
Arndt, R.E., Ellis, C., Paul, S., 1995. Preliminary Investigation of the Use of Air Injection to Mitigate Cavitation Erosion.
Astolfi, J.-A., Dorange, P., Billard, J.-Y., Tomas, I.C., 2000. An experimental investigation of cavitation inception and development on a two-dimensional Eppler hydrofoil. J. Fluid Eng. 122 (1), 164–173.
Ausoni, P., Farhat, M., Escaler, X., Egusquiza, E., Avellan, F., 2007. Cavitation influence on von Kármán vortex shedding and induced hydrofoil vibrations.
Brennen, C.E., 2014. Cavitation and Bubble Dynamics. Cambridge University Press.
Callenaere, M., Franc, J.-P., Michel, J.-M., Riondet, M., 2001. The cavitation instability induced by the development of a re-entrant jet. J. Fluid Mech. 444, 223.
Chen, G., Wang, G., Hu, C., Huang, B., Gao, Y., Zhang, M., 2015. Combined experimental and computational investigation of cavitation evolution and excited pressure fluctuation in a convergent–divergent channel. Int. J. Multiphas. Flow 72, 133–140.
Chen, Y., Li, J., Gong, Z., Chen, X., Lu, C., 2019. Large eddy simulation and investigation on the laminar-turbulent transition and turbulence-cavitation interaction in the cavitating flow around hydrofoil. Int. J. Multiphas. Flow 112, 300–322.
Dular, M., Khlifa, I., Fuzier, S., Maiga, M.A., Coutier-Delgosha, O., 2012. Scale effect on unsteady cloud cavitation. Exp. Fluid 53 (5), 1233–1250.
Gavaises, M., Villa, F., Koukouvinis, P., Marengo, M., Franc, J.-P., 2015. Visualisation and les simulation of cavitation cloud formation and collapse in an axisymmetric geometry. Int. J. Multiphas. Flow 68, 14–26.
Germano, M., Piomelli, U., Moin, P., Cabot, W.H., 1991. A dynamic subgrid-scale eddy viscosity model. Phys. Fluid. Fluid Dynam. 3 (7), 1760–1765.
Gnanaskandan, A., Mahesh, K., 2015. A numerical method to simulate turbulent cavitating flows. Int. J. Multiphas. Flow 70, 22–34.
Gopalan, S., Katz, J., 2000. Flow structure and modeling issues in the closure region of attached cavitation. Phys. Fluids 12 (4), 895–911.
Homa, D., 2018. Eksperymentalne I Numeryczne Badanie Zjawiska Kawitacji Dla Różnych Warunków Przepływu. Polish. Silesian University of Technology, Gliwice. PhD Thesis.
Homa, D., Wróblewski, W., Majkut, M., Strozik, M., 2019. Research on unsteady cavitating flow around a Clark-Y 11.7% hydrofoil. J. Theor. Appl. Mech. 57.
Huang, B., Young, Y.L., Wang, G., Shyy, W., 2013. Combined experimental and computational investigation of unsteady structure of sheet/cloud cavitation. J. Fluid Eng. 135 (7).
Huang, B., Zhao, Y., Wang, G., 2014a. Large eddy simulation of turbulent vortex-cavitation interactions in transient sheet/cloud cavitating flows. Comput. Fluid 92, 113–124.
Huang, B., Wang, G.-y., Zhao, Y., 2014b. Numerical simulation unsteady cloud cavitating flow with a filter-based density correction model. J. Hydrodyn. 26 (1), 26–36.
Huang, R., Luo, X., Ji, B., 2017. Numerical simulation of the transient cavitating turbulent flows around the Clark-Y hydrofoil using modified partially averaged Navier-Stokes method. J. Mech. Sci. Technol. 31 (6), 2849–2859.
Ji, B., Luo, X., Arndt, R.E., Peng, X., Wu, Y., 2015. Large eddy simulation and theoretical investigations of the transient cavitating vortical flow structure around a NACA66 hydrofoil. Int. J. Multiphas. Flow 68, 121–134.
Ji, B., Long, Y., Long, X.-p., Qian, Z.-d., Zhou, J.-j., 2017. Large eddy simulation of turbulent attached cavitating flow with special emphasis on large scale structures of the hydrofoil wake and turbulence-cavitation interactions. J. Hydrodyn. B 29 (1), 27–39.
Karn, A., Ellis, C., Hong, J., Arndt, R.E., 2015. Investigations into the turbulent bubbly wake of a ventilated hydrofoil: moving toward improved turbine aeration techniques. Exp. Therm. Fluid Sci. 64, 186–195.
Kawakami, D.T., Qin, Q., Arndt, R., 2005. Water quality and the periodicity of sheet/cloud cavitation. Fluids Eng. Div. Summer Meeting 41995, 513–517.
Kawanami, Y., Kato, H., Yamaguchi, H., Tanimura, M., Tagaya, Y., 1997. Mechanism and Control of Cloud Cavitation.
Kubota, A., Kato, H., Yamaguchi, H., 1992. A new modelling of cavitating flows: a numerical study of unsteady cavitation on a hydrofoil section. J. Fluid Mech. 240, 59–96.
Kunz, R.F., Boger, D.A., Chyczewski, T.S., Stinebring, D., Gibeling, H., Govindan, T., 1999. Multi-phase CFD analysis of natural and ventilated cavitation about submerged bodies. In: Proceedings of the 3rd ASME-JSME Joint Fluids Engineering Conference.
Kunz, R.F., et al., 2000. A preconditioned Navier–Stokes method for two-phase flows with application to cavitation prediction. Comput. Fluid 29 (8), 849–875.
Li, Z.-r., Pourquie, M., van Terwisga, T., 2014. Assessment of cavitation erosion with a URANS method. J. Fluid Eng. 136 (4).
Liu, T., Huang, B., Wang, G., Zhang, M., Gao, D., 2017/01/01/2017. Experimental investigation of the flow pattern for ventilated partial cavitating flows with effect of Froude number and gas entrainment. Ocean. Eng. 129, 343–351. https://doi.org/10.1016/j.oceaneng.2016.11.026.

Long, X., Cheng, H., Ji, B., Arndt, R.E., 2017. Numerical investigation of attached cavitation shedding dynamics around the Clark-Y hydrofoil with the FBDCM and an integral method. Ocean. Eng. 137, 247–261.
Long, X., Cheng, H., Ji, B., Arndt, R.E., Peng, X., 2018. Large eddy simulation and Euler–Lagrangian coupling investigation of the transient cavitating turbulent flow around a twisted hydrofoil. Int. J. Multiphas. Flow 100, 41–56.
Mäkiharju, S.A., Ganesh, H., Ceccio, S.L., 2017a. The dynamics of partial cavity formation, shedding and the influence of dissolved and injected non-condensable gas. J. Fluid Mech. 829, 420.
Mäkiharju, S.A., Ganesh, H., Ceccio, S.L., 2017b. The dynamics of partial cavity formation, shedding and the influence of dissolved and injected non-condensable gas. J. Fluid Mech. 829, 420–458.
Matsunari, H., Watanabe, S., Konishi, Y., Suefuji, N., Furukawa, A., 2012. Experimental/numerical study on cavitating flow around Clark Y11. 7% hydrofoil. In: Proceedings of Eighth International Symposium on Cavitation, pp. 358–363.
Merkle, C.L., 1998. Computational modelling of the dynamics of sheet cavitation. In: Proc. Of the 3rd Int. Symp. on Cavitation, p. 1998. Grenoble, France.
Morgut, M., Nobile, E., Biluš, I., 2011. Comparison of mass transfer models for the numerical prediction of sheet cavitation around a hydrofoil. Int. J. Multiphas. Flow 37 (6), 620–626.
Numachi, F., 1938. Cavitation performance of 4 types of hydrofoil. Trans. JSME 7 (28), 1–9.
Pham, T., Larrarte, F., Fruman, D.H., 1999. Investigation of Unsteady Sheet Cavitation and Cloud Cavitation Mechanisms.
Reisman, G., Duttweiler, M., Brennen, C., 1997. Effect of Air Injection on the Cloud Cavitation of a Hydrofoil.
Roohi, E., Zahiri, A.P., Passandideh-Fard, M., 2013. Numerical simulation of cavitation around a two-dimensional hydrofoil using VOF method and LES turbulence model. Appl. Math. Model. 37 (9), 6469–6488.
Senocak, I., Shyy, W., 2002. A pressure-based method for turbulent cavitating flow computations. J. Comput. Phys. 176 (2), 363–383.
Singhal, A., 1997. Multi-dimensional simulation of cavitating flows using a PDF model of phase change. In: Proc. ASME FED Meeting. Canada, Vancouver, p. 1997.
Sun, T., Ma, X., Wei, Y., Wang, C., 2016. Computational modeling of cavitating flows in liquid nitrogen by an extended transport-based cavitation model. Sci. China Technol. Sci. 59 (2), 337–346.
Tsuru, W., Yushin Ehara, Y., Kitamura, S.S., Watanabe, S., Shin-ichi, T., 2018. Mechanism of lift increase of cavitating Clark Y-11.7% hydrofoil. In: 10th International Symposium on Cavitation. CAV2018, pp. 706–709.
Usta, O., Korkut, E., 2018. A study for cavitating flow analysis using DES model. Ocean. Eng. 160, 397–411.
Wang, G., Senocak, I., Shyy, W., Ikohagi, T., Cao, S., 2001. Dynamics of attached turbulent cavitating flows. Prog. Aero. Sci. 37 (6), 551–581.
Wang, G., Zhang, B., Huang, B., Zhang, M., 2009. Unsteady Dynamics of Cloud Cavitating Flows Around a Hydrofoil.
Wang, Z., Huang, B., Wang, G., Zhang, M., Wang, F., 2015. Experimental and numerical investigation of ventilated cavitating flow with special emphasis on gas leakage behavior and re-entrant jet dynamics. Ocean. Eng. 108, 191–201.
Wang, C., Wu, Q., Huang, B., Wang, G., 2018a. Numerical investigation of cavitation vortex dynamics in unsteady cavitating flow with shock wave propagation. Ocean. Eng. 156, 424–434.
Wang, Z., Huang, B., Zhang, M., Wang, G., 2018b. Experimental and numerical investigation of ventilated cavitating flow structures with special emphasis on vortex shedding dynamics. Int. J. Multiphas. Flow 98, 79–95.
Wang, Z., Li, L., Cheng, H., Ji, B., 2020. Numerical investigation of unsteady cloud cavitating flow around the Clark-Y hydrofoil with adaptive mesh refinement using OpenFOAM. Ocean. Eng. 206, 107349.
Watanabe, S., Yamaoka, W., Furukawa, A., 2014. Unsteady lift and drag characteristics of cavitating Clark Y-11.7% hydrofoil. In: IOP Conference Series: Earth and Environmental Science, vol. 22. IOP Publishing, 52009, 5.
Wróblewski, W., Bochon, K., Majkut, M., Rusin, K., Hasani Malekshah, E., 2021. Numerical study of cavitating flow over hydrofoil in the presence of air. Int. J. Numer. Methods Heat Fluid Flow. https://doi.org/10.1108/HFF-03-2021-0204 ahead-of-print, no. ahead-of-print.
Wu, Q., Huang, B., Wang, G., Gao, Y., 2015. Experimental and numerical investigation of hydroelastic response of a flexible hydrofoil in cavitating flow. Int. J. Multiphas. Flow 74, 19–33.
Wu, Q., Wang, Y., Wang, G., 2017. Experimental investigation of cavitating flow-induced vibration of hydrofoils. Ocean. Eng. 144, 50–60.
Yin, T., Pavesi, G., Pei, J., Yuan, S., 2021/02/01/2021. Numerical investigation of unsteady cavitation around a twisted hydrofoil. Int. J. Multiphas. Flow 135, 103506. https://doi.org/10.1016/j.ijmultiphaseflow.2020.103506.
Zhang, M., Huang, B., Wu, Q., Zhang, M., Wang, G., 2020. The interaction between the transient cavitating flow and hydrodynamic performance around a pitching hydrofoil. Renew. Energy 161, 1276–1291.
Zhou, L., Wang, Z., 2008. Numerical simulation of cavitation around a hydrofoil and evaluation of a RNG κ-ε model. J. Fluid Eng. 130 (1).
Zhu, J., Zhao, D., Xu, L., Zhang, X., 2016. Interactions of vortices, thermal effects and cavitation in liquid hydrogen cavitating flows. Int. J. Hydrogen Energy 41 (1), 614–631.

Paper II:

Numerical study of cavitating flow over hydrofoil in the presence of air

The current issue and full text archive of this journal is available on Emerald Insight at:
https://www.emerald.com/insight/0961-5539.htm

Numerical study of cavitating flow over hydrofoil in the presence of air

Włodzimierz Wróblewski, Krzysztof Bochon, Mirosław Majkut, Krzysztof Rusin and Emad Hasani Malekshah
Department of Turbomachinery and Power Engineering, Silesian University of Technology, Gliwice, Poland

Received 17 March 2021
Revised 4 May 2021
Accepted 12 May 2021

Abstract

Purpose – The presence of air in the water flow over the hydrofoil is investigated. The examined hydrofoil is ClarkY 11.7% with an angle of attack of 8 deg. The flow simulations are performed with the assumption of different models. The Singhal cavitation model and the models which resolve the non-condensable gas including 2phases and 3phases are implemented in the numerical model. The calculations are performed with the uRANS model with assumption of the constant temperature of the mixture. The two-phase flow is simulated with a mixture model. The dynamics and structures of cavities are compared with literature data and experimental results.

Design/methodology/approach – The cavitation regime can be observed in some working conditions of turbomachines. The phase transition, which appears on the blades, is the source of high dynamic forces, noise and also can lead to the intensive erosion of the blade surfaces. The need to control this process and to prevent or reduce the undesirable effects can be fulfilled by the application of non-condensable gases to the liquid.

Findings – The results show that the Singhal cavitation model predicts the cavity structure and related characteristics differently with 2phases and 3phases models at low cavitation number where the cavitating flow is highly dynamic. On the other hand, the impact of dissolved air on the cloud structure and dynamic characteristic of cavitating flow is gently observable.

Originality/value – The originality of this paper is the evaluation of different numerical cavitation models for the prediction of dynamic characteristics of cavitating flow in the presence of air.

Keywords Cavitation, Cavitation shedding dynamics, Clark Y 11.77% hydrofoil, Non-condensing gases, Two-phase models

Paper type Research paper

Nomenclature

C = coefficient, [–];
f = mass fraction, [–];
u = velocity, [m/s];
p = static pressure, [Pa];
t = time, [s];
ρ = mixture density, [kg/m^3];
μ = effective viscosity of the mixture, [Pa.s];
α = volume fraction, [–];
σ = cavitation number $\sigma = \frac{p_\infty - p_{sat}}{0.5\rho_l u_\infty^2}$, [–];

The presented work was supported by the Polish National Science Centre funds within the project UMO-2016/21/B/ST8/01164.

International Journal of Numerical Methods for Heat & Fluid Flow

0961-5539
DOI 10.1108/HFF-03-2021-0204

Γ = mass transfer source term, [kg/(m^3·s)];
k = turbulence kinetic energy, [m^2/s^2]; and
ε = energy dissipation rate, [m^2/s^3].

Indices
c = condensation;
g = gas (vapour and non-condensable gas), -;
l = liquid;
ng = non-condensable gas (air), -;
sat = saturation conditions;
s = corrected saturation;
v = vapour, evaporation;
∞ = free stream; and
t = turbulent.

1. Introduction

The cavitating flows are present in many industrial devices, machines and engines. The cavitation phenomenon occurs in the regions where the high speed of the liquid is reached and the local pressure falls below the value of saturation pressure. As a result, highly unsteady cavities are formed which can produce harmful effects like erosion, vibration and in fluid machines a reduction of efficiency. Therefore, an important issue from the technical point of view is to control the dynamics of the cavitating flow.

Modelling of cavitation flows is a complex task, as it concerns two-phase flows with high dynamics of parameter changes. It is becoming more complicated when flows with complex geometry are considered.

A variety of methods of numerical modelling of cavitation flow has been proposed for several decades which differ in their complexity, solution schemes and assumptions (Nguyen *et al.*, 2019; Liu *et al.*, 2019; Kinnas and Young, 2003). Liu *et al.* (2020) used a hybrid RANS and LES turbulence model to simulate the dynamic of transient cavitating flow around a Clark-Y hydrofoil. They found that the Large Eddy Simulation can capture the interactions between cavitation structures and turbulence. Mathew *et al.* (2006) proposed a new approach for studying the phenomenon of travelling bubble cavitation. The Rayleigh-Plesset equation is numerically integrated to simulate the growth and collapse of a cavitation bubble moving in a varying pressure field over a 2 D hydrofoil (NACA-0012). It is concluded that the maximum local pressure goes up to an order of 10^4 bar during the bubble collapse. Kubota *et al.* (1992) proposed the first homogeneous model based on the transport equation. They took account of cavitation through the presence of a bubble cluster. The cluster growth and decay are described by employing a modified version of the Rayleigh equation. The model was applied in the two-dimensional steady-state analysis of the flow around a hydrofoil NACA 0015.

One of the first concepts of two-phase flow analysis is the use of a homogeneous model and the assumption that a mixture of a liquid and its vapour is treated as one fluid. In this case, the main difficulty is to determine the parameters of the mixture, mainly density. This approach was successfully applied by Coutier-Delgosha *et al.* (2003), which solved the Reynolds-averaged Navier–Stokes equations for the mixture considered as a single fluid with variable density.

In the case of cavitation, the phenomena accompanying the phase transition process leads to a special way in changing the properties of the system, from the incompressible to the compressible one. Due to that, the application of appropriate descriptions of the two-phase system properties plays an essential role in the correct modelling of the flow field structure and; consequently, of the inter-phase interactions. It should also be kept in mind that in such flows different factors have to be dealt with, such as different time scales of the course of individual phenomena of nuclei formation, of the flow average time and of the time of evolution of turbulent structures.

Despite the differences that the studies and modelling of cavitating flows involve, some progress can be noticed in this field. The proposed cavitation models and the conducted experimental testing try to explain the course of the phenomenon as much as possible. The simplest models are based on the description of the bubble dynamics using empirical equations defining different kinds of forces. Integration of these equations makes it possible to track the two-phase system evolution. In the case of sheet cavitation, a model can be applied in which two phases separated by an inter-phase layer are considered. Methods, where the approach used for the dispersed phase is the same as the one for the continuous phase, have found a much wider application in the two-phase flow analysis. In them, transport equations for the dispersed phase are formulated assuming a different level of simplification, depending on the method.

The first models took account of only one continuity equation (Chen and Heister, 1995). Kunz *et al.* (Kunz *et al.*, 1999; Kunz, 2000) proved that the models which solve continuity equations both for the continuous and dispersed phases can reflect the tendencies in dynamics of the cavitating process. That approach drew on the method proposed by Merkle (1998), which introduced an additional possibility of considering a third component of the mixture in the form of a non-condensing gas. The changes in the density of individual phases were ignored, using parameters for the mixture and introducing separated local time and pseudo-time derivatives. The numerical scheme required using a series of empirical coefficients. The turbulence model was applied for a single-phase, using the wall function. The results obtained employing this model were satisfactory only in the case of selected geometrical configurations.

The model still employed in some commercial codes is the one proposed by Sinhal *et al.* (2002). The model utilized a simplified form of the Rayleigh-Plesset bubble dynamics equation, featured better stability compared to previous models and made use of coefficients with a more universal scope of application. The model assumed an isothermal flow and a constant concentration of the non-condensing gas in the mixture. There was a relatively good agreement between the obtained results and the experimental data for various characteristic geometrical configurations.

Senocak and Shyy (2002) proposed another model from this group which took into account the effects of a high-velocity flow using a pressure-correcting equation. Turbulence was modelled utilizing a k-ε model whose constants were modified by replacing them with quantities depending on turbulence parameters. The applied solution algorithm reflected the stationary phenomena in the cavitating flow very well.

Another group of methods used in the cavitating flow computations includes those based on equations formulated for the compressible fluid. In this case, the hyperbolic nature of differential equations can be retained, and the computations can be performed using the time-stepping method. Kubota *et al.* (1992) solved the Navier-Stokes equations for the mixture, assuming the incompressibility of the continuous phase. In this model, they took account of cavitation through the presence of a bubble cluster. The cluster growth and decay are described by employing a modified version of the Rayleigh equation. An extension of this model was the concept introduced by Schmidt *et al.* (1999), which allowed modelling high-velocity flows with large ratios of the density of the two phases.

Schnerr and Sauer (2001) used a model describing the bubble growth and decay process. The model concept assumes that nucleation occurs on a set number of nuclei, and the dynamics of the bubble growth process is described utilizing the Rayleigh-Plesset equation. By applying this concept, it was possible to simulate the physics of the cavitating flow satisfactorily.

Chen and Heister (1995) proposed the other version of the source terms in the continuity equations. By introducing the volume fraction of nuclei into the source term, which models the evaporation process, they took into account the phenomenon of mutual influence of expanding steam bubbles. This model allowed good compliance of the hydrofoil flow with the experiment (Kunz *et al.*, 1999).

Developing the code written for the two-phase flow by Kunz *et al.* (1999), Venkateswaran *et al.* (2002) solved the system of equations in a form taking account of compressibility. This novel approach introduced finite sound velocities into both phases, allowed the identification of supersonic flow phenomena and the process of shock wave propagation in the mixture. The comparison of the incompressible and compressible versions of the computational algorithm makes it possible to state that the compressible model reflects the dispersed phase dynamics more accurately.

Saurel and Lemetayer (2001) proposed a model based on the formulation of conservation equations for the compressible flow. In it, the hyperbolic-type equations are solved with a scheme that ensures unconditioned stability. This method can also be used in a wide range of cases of the two-phase flow. The model can also be applied to describe the dynamics of the inter-phase layer formation in the case of flows with cavitation.

Murrone and Guillard (2005) used the Eulerian approach to simulate the compressible two-phase flow, taking account of the difference in velocities and pressures between the phases. The computation stability was ensured using relaxation. The algorithm for solving the Riemann linearized problem was used in the procedure leading to the solution to the equations. Romenski and Toro (2004) proposed an algorithm for solving the problem of the compressible two-phase flow using a system of conservation equations of the hyperbolic type. Most of the models mentioned above were developed with consideration of two phases: water and vapour. In reality and normal conditions, non-condensable gases are present in the water what would make the solution more complex.

Air is dissolved in water or can be added into the stream either upstream of the element being tested (e.g. hydrofoil, nozzle) (Kozubkova *et al.*, 2016) or at a certain location on the hydrofoil surface (Sun *et al.*, 2020). Presence of air influences the dynamics of cavitation and air injection can be used to control cavitation (Sun *et al.*, 2020; Bin *et al.*, 2010).

Unless the water is deaerated, there is dissolved air in the liquid phase which is released due to the lowering pressure during acceleration of water and cavitation. Tsuru *et al.* (2018) observed cavitation on the Clark Y 11.7% hydrofoil for various dissolved air conditions. They analysed images and measured forces for three oxygen content levels: low, medium and high. The conclusion was that the influence of the dissolved gas content on the averaged values of the lift and drag coefficients can be observed in the selected cases only, but the influence on the appearance of cavitation was noticed in all cases. Kawakami *et al.* (2005) calculated the pressure spectrum at the suction side for the NACA 0015 hydrofoil by considering two amounts of dissolved air including 6 ppm and 13 ppm. Based on the results, the considerable effect of dissolved air on the pressure spectrum trends was proved. Mäkiharju *et al.* (2017) also found some influences on the dynamics and inception of a partial cavity by taking the gas content into account. However, the results declared that the developed partial cavity accompanied by a strongly enforced separation line would not be significantly affected by the dissolved gas mass transfer within the freestream.

In many applications, the air is injected into the water to get artificial cavities and to improve the hydrofoil performance (Sun *et al.*, 2020; Kopriva *et al.*, 2008), to obtain supercavitation in the development of high-speed vehicles (Ahn *et al.*, 2017) and to reduce drag. Air injection is one of the factors which reduces the effects of cavitation noise and erosion.

The different numerical models are employed to take air presence into account. In Iannetti *et al.* (2016), the full cavitation model was implemented to simulate the cavitating flow in a positive displacement pump. The discrepancies in the prediction of flow dynamics were reported. Compliance of CFD calculations with the experiment deteriorates as the air content increases. It has been suggested that to explain in detail the reason for these discrepancies, it is necessary both to increase the accuracy of experimental data and to apply a more advanced calculation model.

The three-component model for liquid, vapour and air were proposed by Bin *et al.* (2010). They analysed the natural and ventilated cavitation around an under-water vehicle. The proposed model gave satisfactory agreement with experimental data and with the increase of the gas ventilation, the vapour cavity is suppressed by the gas cavity remarkably.

The comprehensive numerical study of the influence of the air injection on the dynamics of the cavitating flow around NACA66 hydrofoil was performed by Sun *et al.* (2020). The vortex structure modelled by the LES technique changed significantly with the increase of air injection. Ventilation transforms large-scale eddies into small-scale vortices and affects hydrodynamic performance.

This paper reports the investigation of the numerical models of cavitating flow with air presence. The flow over a hydrofoil Clark Y 11.7% was selected as one of the most common examples of cavitating flow which has been studied both experimentally and numerically for many years. The flow regime with the cloud cavitation was analysed with different amounts of air present in the water. The dynamics of the cavitating flow as the main parameters simulated by the different methods were compared and validated against the experimental data. Overall, the main purpose of the present work is the evaluation of different cavitation-numerical models on the dynamic of unsteady three-phase cavitating flow and show their advantages and disadvantages under the effect of different amounts of dissolved air. Finally, the cavitation model which predicts the cavitation evolution in better agreement with the experimental data will be adopted for future research.

2. Mathematical model

The mixture model for simulation of the liquid-vapour-gas flow which assumes the same velocity flow field for each phase is used. The governing conservation equations of momentum in the form of Reynolds averaged Navier-Stokes (RANS) equations and of mass were formulated for the mixture as:

$$\frac{\partial \rho}{\partial t} + \nabla \cdot (\rho \boldsymbol{u}) = 0 \tag{1}$$

$$\frac{\partial}{\partial t}(\rho \boldsymbol{u}) + \nabla \cdot (\rho \boldsymbol{u}\boldsymbol{u}) = -\nabla p + \nabla \cdot \left[\mu\left(\nabla \boldsymbol{u} + \nabla \boldsymbol{u}^T\right)\right] + \rho \boldsymbol{g} \tag{2}$$

$$\rho = \rho_l \alpha_l + \rho_v \alpha_v \tag{3}$$

Eddy-viscosity turbulence model is assumed able to be extended to multiphase applications without discussion. It has been a regular way in most of the cavitation simulations in the literature. The $k-\varepsilon$ and $k-\omega$ turbulence models are the most commonly used of all two-equation turbulence models. The primary disadvantage of the $k-\omega$ model, in its original form, is that boundary layer computations are very sensitive to the values of the vorticity ω in the free stream. In the case of unsteady cavitating flows, this sensitivity might cause inaccurate predictions of fluid physics. The original $k-\varepsilon$ turbulence model falls within this class of turbulence models and has been the workhorse of practical engineering flow calculations since it was proposed by Jones and Launder (1972). The benefit of the $k-\varepsilon$ model is that it is not as sensitive to the free stream compare with in the $k-\omega$ model. The original $k-\varepsilon$ model was originally developed for fully incompressible single phase flows and was not intended for flow problems involving highly compressible multiphase mixtures.

In the present work, the RNG $k-\varepsilon$ turbulence model was used to calculate the mixture turbulence viscosity. This model employs some corrections in the coefficient of models for the ε equation of the standard form of $k-\varepsilon$ turbulence model. In this turbulence model, the k and ε equations are given as follows:

$$\frac{\partial}{\partial t}(\rho k) + \nabla \cdot (\rho k \boldsymbol{u}) = G_k + \rho\varepsilon + \nabla \cdot \left[\alpha_k(\mu_m + \mu_t)\nabla k\right], \tag{4}$$

$$\frac{\partial}{\partial t}(\rho\varepsilon) + \nabla \cdot (\rho\varepsilon \boldsymbol{u}) = C_{1\varepsilon}\frac{\varepsilon}{k}G_k - C_{2\varepsilon}\rho_m\frac{\varepsilon^2}{k} + \nabla \cdot \left[\alpha_\varepsilon(\mu_m + \mu_t)\nabla k\right], \tag{5}$$

$$\mu = \rho c_\mu \frac{k^2}{\varepsilon}, \tag{6}$$

where the dissipation rate of turbulent kinetic energy and generation term of turbulent kinetic energy are represented by ε and G_k, respectively. Also, the applied empirical constant in these equations as $\alpha_k = 1.39$ and $\alpha_\varepsilon = 1.39$ and $c_\mu = 0.09$.

Numerical modelling of cavitating flows is a challenge because they are characterised by highly dynamic phenomena due to phase change and turbulence. During the phase change, there are rapid changes in the density of the mixture and changes in pressure. The process of evaporation and condensation is described by the equation of bubble dynamics. For flow simulation, the two variants of cavitation models Sinhal *et al.* (2002) model and Zwart-Gerber-Belamri model (Zwart *et al.*, 2004) are selected.

The numerical models take into account the presence of air. The three variants of numerical models are considered to simulate the presence of non-condensable gas (air) in the water flow. In the full cavitation model (Sinhal *et al.*, 2002, model), the air mass fraction is implemented in the cavitation model and corrects the evaporation mass transfer rate. The Zwart-Gerber-Belamri (Zwart *et al.*, 2004) cavitation model is used in the models where non-condensable gas is considered as the third phase. The mixture model in two variants is investigated: with three phases liquid-vapour-air (3phases model) and with the two phases liquid-gas mixture (2phases model), where the gas mixture is handled as a species of vapour and air.

2.1 Singhal et al. model- full cavitation model

Sinhal *et al.* (2002) proposed a cavitation model called "the full cavitation model". The name "full" results from the fact that the model includes the presence of non-condensing gases, phase change, bubble dynamics and turbulent pressure fluctuations. The continuity equation for the vapour phase has to be coupled with the continuity and momentum conservation equations (1) and (2):

$$\frac{\partial \rho_v \alpha_v}{\partial t} + \nabla \cdot (\rho_v \alpha_v \boldsymbol{u}) = -\Gamma \tag{7}$$

Generally, the cavitation models differ from each other by the way the source term Γ is determined. In the Singhal *et al.* model the following expressions for vaporization and condensation rates are obtained:

$$\Gamma = C_c \frac{k}{\sigma} \rho_l \rho_l \sqrt{\frac{2}{3} \frac{(p - p_s)}{\rho_l}} f_v, \qquad p > p_s \tag{8}$$

$$\Gamma = -C_v \frac{k}{\sigma} \rho_l \rho_v \sqrt{\frac{2}{3} \frac{(p_s - p)}{\rho_l}} (1 - f_v - f_{ng}), \qquad p < p_s \tag{9}$$

$$p_s = p_{sat} + \frac{1}{2}(0.39 \rho k) \tag{10}$$

where the coefficients of evaporation and condensation C_v and C_c equal to 0.02 and 0.01 respectively.

2.2 2phases model

The 2phases model solves the continuity equation for the mixture of vapour and air. The mass transfer between a liquid phase and a mixture of gaseous phase is modelled between species of vapour and liquid by the cavitation model. The continuity equation for the mixture of the gaseous phase is in the form:

$$\frac{\partial \rho_g \alpha_g}{\partial t} + \nabla \cdot (\rho_g \alpha_g \boldsymbol{u}) = -\Gamma \tag{11}$$

$$\alpha_g = \alpha_v + \alpha_{ng} \tag{12}$$

where the mixture density is

$$\rho = \rho_l \alpha_l + \rho_g \alpha_g \tag{13}$$

The cavitation model proposed by Zwart *et al.* (2004) is used to model the process of phase change. In this model the values of condensation and evaporation rates are calculated from the relations:

$$\Gamma = C_c \frac{3 \rho_v \alpha_v}{R} \sqrt{\frac{2}{3} \frac{(p - p_s)}{\rho_l}}, \qquad p > p_s \tag{14}$$

$$\Gamma = -C_v \frac{3 \rho_v (1 - \alpha_v) \alpha_{nuc}}{R} \sqrt{\frac{2}{3} \frac{(p_s - p)}{\rho_l}}, \qquad p < p_s \tag{15}$$

where the value of nucleation site volume fraction equals $\alpha_{nuc} = 0.0005$, coefficients of condensation and evaporation are $C_c = 0.01$ and $C_v = 50$. The value of the nuclei radius is assumed to be $R = 1\ \mu m$.

2.3 phases model

The 3phases model solves the continuity equations for the vapour volume fraction and the air volume fraction. The mass transfer between a liquid phase and a mixture of gaseous phase is modelled between species:

$$\frac{\partial \rho_v \alpha_v}{\partial t} + \nabla \cdot (\rho_v \alpha_v \boldsymbol{u}) = -\Gamma \tag{16}$$

$$\frac{\partial \rho_{ng} \alpha_{ng}}{\partial t} + \nabla \cdot (\rho_{ng} \alpha_{ng} \boldsymbol{u}) = 0 \tag{17}$$

$$\alpha_l + \alpha_v + \alpha_{ng} = 1 \tag{18}$$

The same Zwart-Gerber-Belamri (Zwart *et al.*, 2004) model is used to model the mass transfer between vapour and liquid.

3. Numerical model

The calculations were performed on the mesh composed of hexahedra-type elements and generated in ICEM-CFD. The dimensions of the calculation domain corresponded to the length and height of the experimental chamber. In the first step, the flat structural grid was generated and then extruded in the perpendicular direction. The geometry has been divided into 8 blocks and the O-grid was generated around the blade. The blade profile was split into 4 edges: leading, upper side, lower side and trailing edge. On both lower and upper side edges 129 grid nodes were set, on both the leading and trailing edges 55 nodes. On the edge normal to the foil 101 elements were used. The domain has an overall width of 0.09 mm discretized by 3 layers of 0.03 mm thickness each. The thin domain was selected to reduce the aspect ratio in the domain close to the hydrofoil in the O-grid region. The whole mesh consisted of 220k hexahedra elements. The overview of the mesh with the zoomed O-grid region is depicted in Figure 1.

Validation of the numerical grid performed in (Homa *et al.*, 2019; Homa, 2018) shows that the numerical grid with total nodes above 160k and 270 nodes around the hydrofoil is satisfactory for the hydrofoil computations. The mesh applied in the present study is about 35% finer in the O-grid region to preserve better uniformity of the grid in places where high unsteady effects are present and to achieve the y^+ on the hydrofoil less than 1.

The boundary conditions at the inlet are the inlet velocity, the volume fractions of water vapour and air and the turbulence level. The boundary condition at the outlet was the static pressure. The slip walls were assumed at the top and bottom walls and symmetry boundary conditions were set at both lateral sides of the computational domain.

The ANSYS Fluent was used as the 3-D RANS solver. The coupled pressure-based solver with mixture model was selected with the PRESTO scheme for the pressure-velocity coupling. The second-order implicit time scheme was applied to account for the transient multiphase phenomena. The second-order spatial discretisation for the mixture and turbulence variables was used but for the volume fraction, the first-order discretisation was set.

4. Results

The numerical simulations of the multiphase cavitating flow over the Clark Y 11.7% hydrofoil with an angle of attack of 8° were performed. The static pressure at the outlet was $p_{out} = 51400$Pa. At the inlet, the velocity of $u = 11.84$m/s was set. The temperature of 293 K was assumed constant. The flow conditions corresponded to the cavitation number of $\sigma = 0.75$ and natural, cloud cavitation type. Cavitation number σ is defined as follows:

$$\sigma = \frac{p_\infty - p_{sat}}{0.5\rho_l u_\infty^2} \tag{19}$$

The volume fraction of air was set to the values of 0.004, 0.016 and 0.042, respectively. It corresponds to the low amount of air around 3 ppm (e.g. after partial deaeration process), close to a value of 12 ppm, and aerated water with the air in an amount of 32 ppm. The corresponding Reynolds number for the present case is $Re = \rho_l uc/\mu_l = 825770$, where c is the hydrofoil chord. Thus, the fluid flow over the hydrofoil is fully turbulent.

The time step of the simulation was $\Delta t = 4{\cdot}10^{-6}$ s and remained constant during computations. This made it possible to perform computations with the Courant number less than 1. A maximum of 10 internal iterations per time step was assumed. Depending on the case and initial conditions, it was necessary to perform 100k-200k time steps to reach the solution or even more in some cases with the worse stability of the solution.

The solutions with less amount of air were highly unsteady and the flow parameters varied widely. The solution might become unstable due to the unphysical jump of the variables. In such cases, the different solution strategies were implemented to lead the solution through the difficult point such as temporally increasing the number of internal iterations per time step or temporally decreasing the under-relaxation factors of the changes of variables.

The most important for the stability of the solution were initial conditions. For every single model variants, a simulation was started as a steady-state without cavitation to get a steady-state solution for the liquid phase only. In the next step, the steady-state solution with cavitation was switched on and after a certain number of iterations, depending on the residual course, the correct parameters for the transient

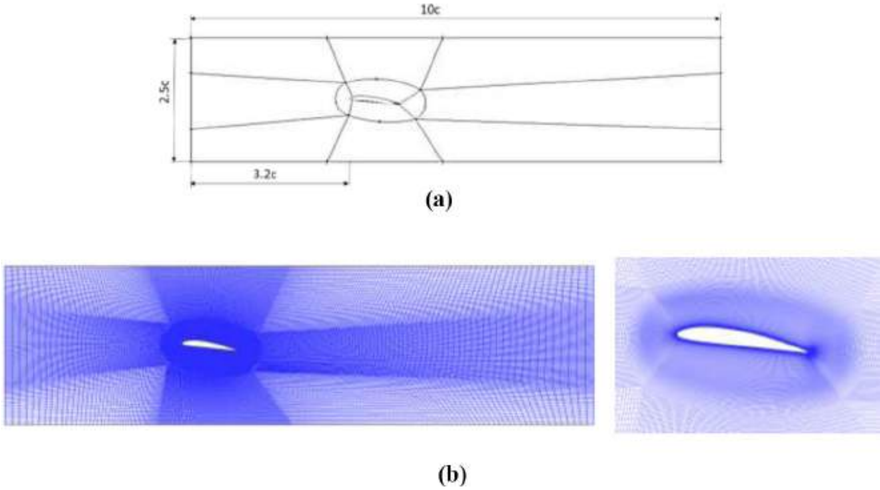

Figure 1. The calculation domain with the block structure of the mesh (above), an overview of the numerical mesh (left) and zoomed mesh close to the hydrofoil (right)

simulation were set. The simulations conducted for individual models were initialised with the solutions obtained for the previous air content.

The numerical results showed that all models were able to predict qualitatively the influence of the air content on the dynamics of the cavitation. The differences in flow quantities in some cases could be vital. The amplitude of the lift coefficients decreases with the increase of the air volume fraction at the inlet to the domain. The Sinhal *et al.* (2002) model had more problems with stability and in some cases, the second-order accuracy scheme of time had to be changed to the bounded second-order accuracy scheme.

The numerical pressure coefficient distribution around the hydrofoil was compared with the experimental measurement over the same type of hydrofoil, as shown in Figure 2. It is worth mentioning that there was a small difference between the air content in numerical and experimental cases which were about VF = 0.016 and VF = 0.012, respectively. The cavitation number of experimental and numerical cases were σ = 0.79 and σ = 0.8, respectively. The disparity was a consequence of differences between the operating conditions of numerical and experimental cases. Also, the experimental data concerned the suction side of the foil and were collected by pressure transducers at ten points with equal distances between each other. The pressure coefficient is calculated based on the following definition:

$$C_p = \frac{p - p_{ref}}{0.5\rho_l u_\infty^2} \tag{20}$$

Where p denotes the local pressure, p_{ref} is set to pressure at the outlet, ρ_l shows the density of the operating fluid and the velocity of freestream is presented by u_∞. These values for numerical results were defined in the description of the boundary conditions. In the experiment, the pressure at the outlet was p_{out}= 42 kPa and the velocity was u_∞=10.6m/s.

Comparing the results, it was observed that despite the difference between the dissolved air volume fractions, there was a quantitative agreement between the numerical and experimental pressure coefficient.

The lift coefficient changes in the selected range of iterations obtained for the three models are presented in Figure 3. The results for the Sinhal *et al.* (2002) model [Figure 3(a)] show that with an increase of the air fraction, the dynamics of flow becomes weaker and the phenomenon was disappearing. The highly unsteady flow for the air volume fraction of 0.004 was observed and the lift coefficient changed in a range of 0.1–1.1. The amplitude was

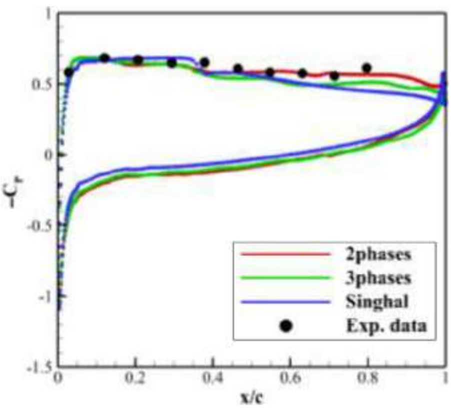

Figure 2.
Comparison of distributions of time-averaged pressure coefficient. Experimental data (VF = 0.012) and different cavitation models (VF = 0.016)

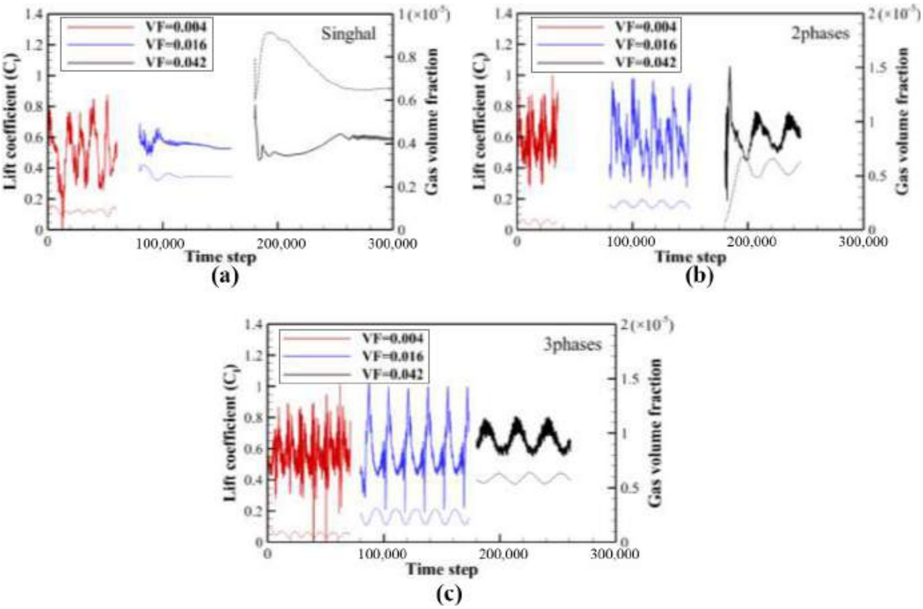

Figure 3.
The lift coefficient (solid line) and gas volume fraction (dash line) evolutions in time predicted by (a) Singhal model; (b) 2phases model and (c) 3phases model for air volume fractions of 0.004, 0.016 and 0.042

changing but the stabilisation of the period was observed. The frequency of the lift coefficient changed by about 27 Hz. The behaviour of the flow structures was highly unstable. When air content was higher, the flow was becoming steady and the lift coefficient stabilized. The detected frequency (with very small amplitude) in the case with the air volume fraction of 0.042 was 195 Hz. The tendency that with increasing air content, the average lift coefficient is higher was observed. The values of the average lift and drag coefficients are given in Table 2.

The calculated lift coefficient changes during the computations for the 2phases model are presented in Figure 3(b). The highly unsteady character was observed and the two tendencies were visible. The higher the air content, the higher the average value of the lift coefficient and the longer the period of the main changes. The frequencies of the lift coefficient for all air volume fractions are presented in Table 2. The amplitude of the lift coefficient for the air volume fraction of 0.042 was reduced in comparison with the cases with lower values of air content.

The lift coefficient changes during the computations for the 3phases model are presented in Figure 3(c). A very similar picture of the lift coefficient changes was visible. For the case with the air volume fraction of 0.004, the spikes with close to zero values were present which might cause a solver crash. For the higher values of the air content, the course of the lift coefficient was more regular. The higher the air content, the higher the average value of the lift coefficient was and the longer the period of its main changes, similar to the 2phases model. The frequencies of the lift coefficient are summarised in Table 2.

Figure 3 presents, apart from the lift coefficient, also the course of changes in gas volume fraction. In all cases, these two parameters influenced each other: the peaks were in the counter phase since the length of the cavity and value of the lift coefficient had a reverse relationship. Notably, the plots of vapour volume fraction were remarkably smoother than those for lift coefficients.

Figure 4 depicts the average pressure distribution around a hydrofoil under the effect of different numerical methods (i.e. 2phases, 3phases and Singhal) and three air contents of

VF = 0.004, 0.016 and 0.042. In a general view, it was obvious that both the numerical method and air content affected the pressure distribution. At the lowest amount of dissolved air (VF = 0.004), the pressure distribution was predicted as wavy by 2phases and 3phases models, which proves the highly dynamic and complex behaviour of cavitating flow around the hydrofoil. On the contrary, the Singhal method gave smooth pressure distribution at both pressure and suction sides. Comparing the pressure distribution using these three methods at VF = 0.004, one can realize that the Singhal method left out the detailed vortex flow at the surface of the hydrofoil, but the predicted trend was quite similar to the other cases. It is worth mentioning that the cavitating flow stabilizes and lasts longer as the air volume fraction enhances. By adding the dissolved air, the close agreement and similarity between the pressure distributions predicted by different models were observed and no significant differences were detected between the Singhal model and the other ones. This observation proved that the Singhal model is less capable to predict accurately the highly unstable vortex flow than stable cavitating flow.

Figure 5 shows the selected instant pressure distribution for one period of cavitating flow computed using 3phases and Singhal models and the assumption of air volume fractions on the level of VF = 0.004 and 0.042. As it can be observed, at low air content 3phases model yielded chaotic instant pressure distributions, but no remarkable deviations occurred in the case modelled by the Singhal model. It means that the 3phases model is more sensitive to vortex flow characteristics and capable to predict the process in details. When the air

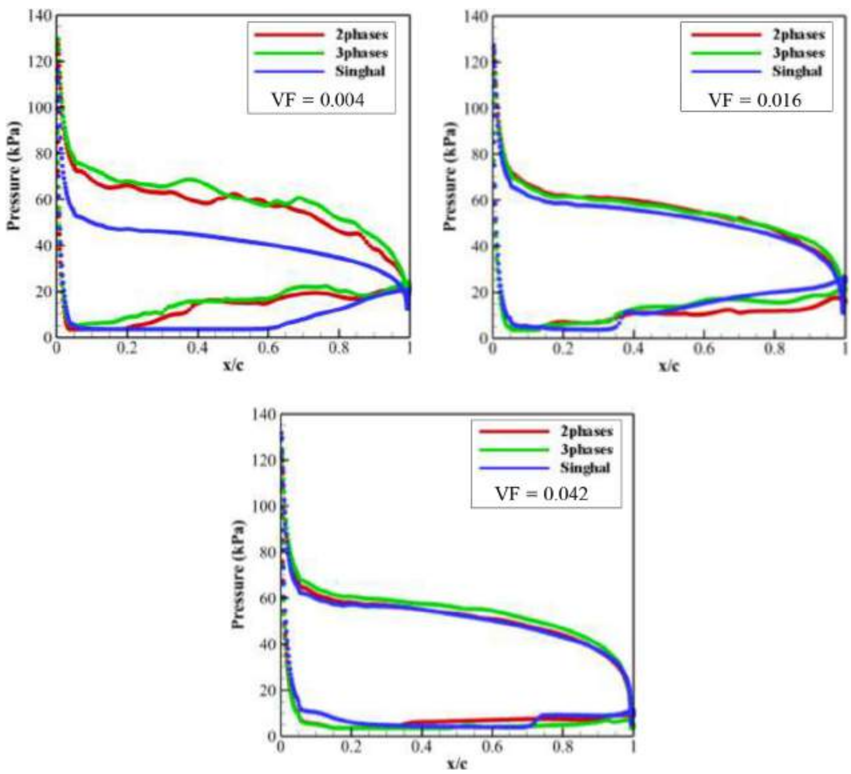

Figure 4.
Time-averaged pressure distributions around the hydrofoil for the different air volume fractions and cavitation models

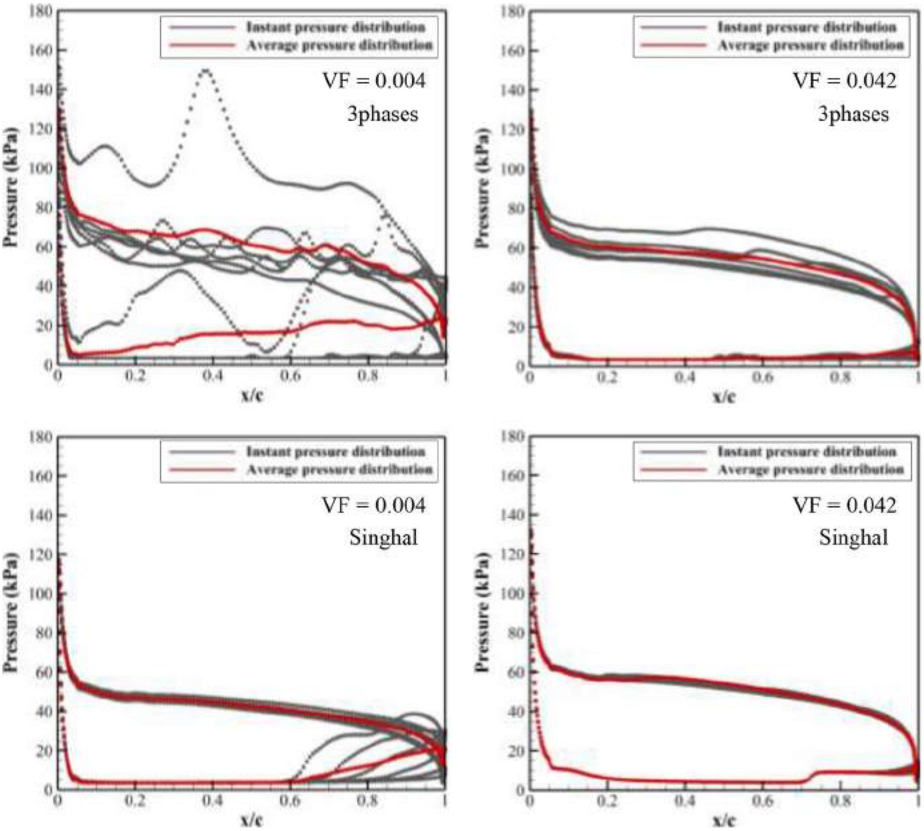

Figure 5.
Selected time-dependent vs. time-averaged pressure distribution around hydrofoil in one period

volume fraction increased, the instant pressure distributions were mainly smooth which proves the stability of the cavitating flow.

The flow structures observed in one period of changes for the Singhal *et al.* model are presented in Figure 6. The high dynamics of the gas volume fraction was visible for the case with the air volume fraction of 0.004. [Figure 6(a)]. The formation of the gas clouds started developing on the profile in the region with the high velocity. The relatively small cavity was observed in Figure 6(b) which is stable in the whole computations. The very different picture of the gas content was visible in Figure 3(c) for the case with the air volume fraction of 0.042. The gas cavity was relatively large and stable except for the trailing edge region where some unsteady structures were present.

Figure 7 presents the structures of gas volume fraction for the 2phases model. For the air volume fraction of 0.004, the size of the formed clouds was comparable with the chord of the hydrofoil and the instant without clouds was present. The thickness of the cavitating structures was of the same size as for the Singhal *et al.* model. The instants are present when the gaseous phase almost disappears, and the process of cloud creation starts close to the leading edge. The detected frequency of the lift coefficient fluctuations totalled 22 Hz and was noticeably lower than in the Singhal et al. model.

As the air content increased, the clouds of the gaseous phase were getting larger. The clouds in the case with the air volume fraction of 0.016 seemed to have external boundaries blurred out

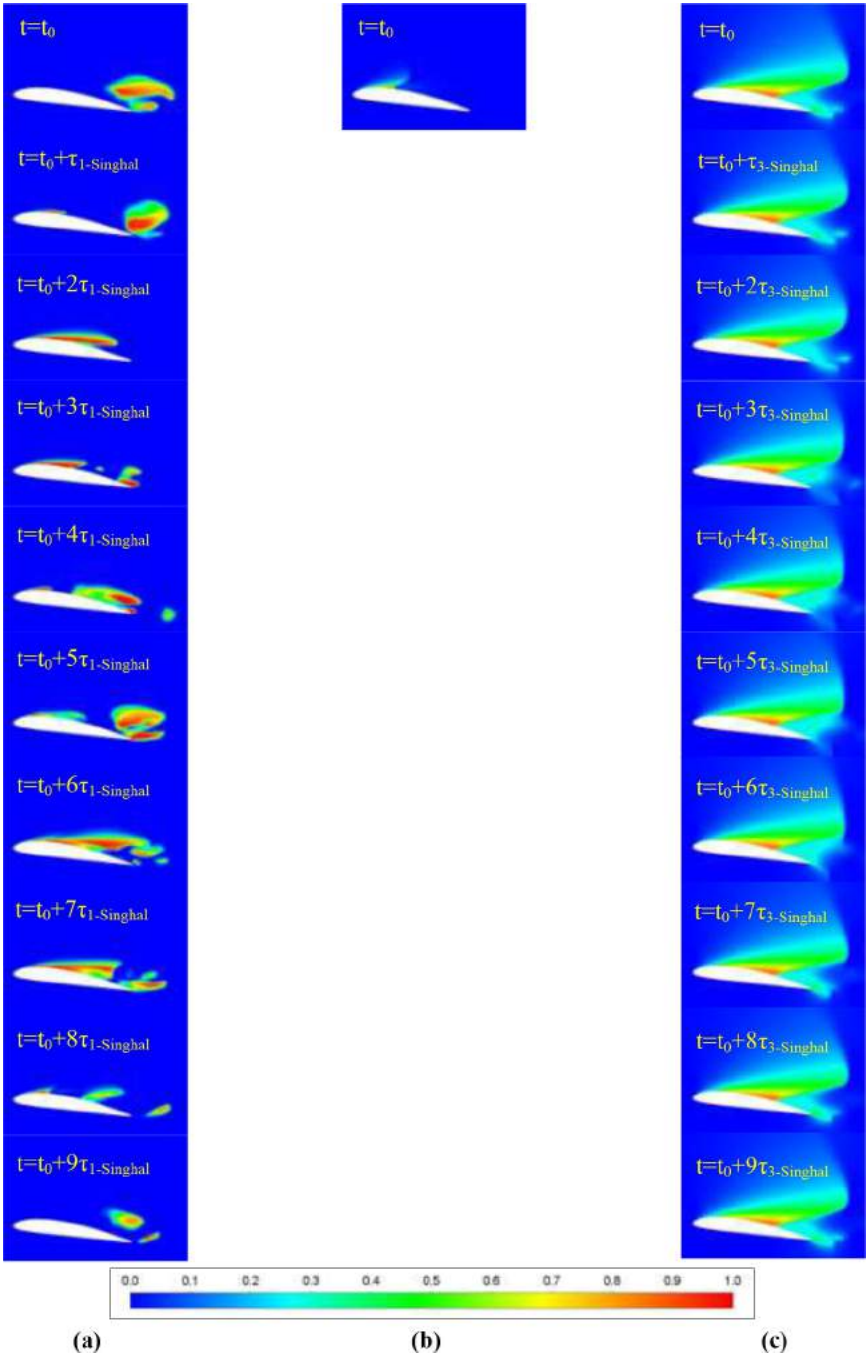

Figure 6.
The contours of gas volume fraction in one period for different air volume fraction (Singhal model, $\sigma = 0.75$, $\alpha = 8^{\circ}$)

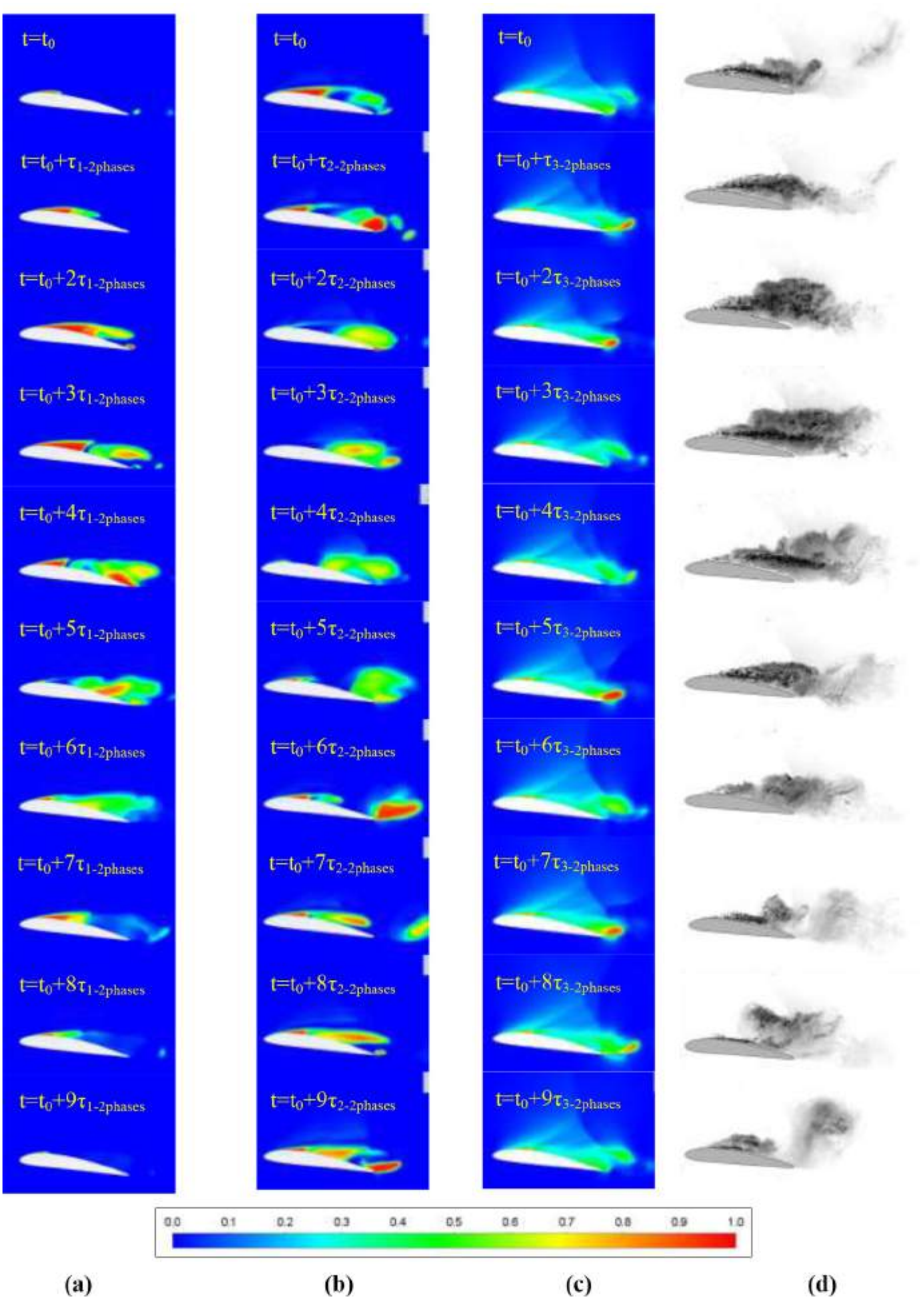

Figure 7.
The contours of gas volume fraction in one period for different air volume fractions (2phases model, $\sigma = 0.75$, $\alpha = 8^{\circ}$) and experiment for air volume fraction 0.014

but its structures close to the hydrofoil wall were similar to the case with the air volume fraction of 0.004 (Figure 7b). In contrast to the case with lower air content, in this case, the clouds close to the hydrofoil wall were present in all depicted moments. The frequency of the lift coefficient was lower and amounted 14.7 Hz. For the air content of 0.042, the regions with the value of gas volume fraction close to 1 were reduced and the region with moderate gas volume fraction was larger. The shape of the clouds was more stable. The changes were observed in the trailing edge region. The frequency was reduced to the value of 9 Hz.

One period of cloud changes recorded at the test rig is depicted in Figure 7(d). Details of the experimental test stand and the measuring procedure can be found in the works (Homa *et al.*, 2019; Homa, 2018). The colour inverse is applied to better visualise the cloud structures. The air content in the air in the open-loop installation was estimated at 0.014. The recorded structures were larger and much finer. The pictures revealed the moment when the cloud close to the hydrofoil wall was significantly reduced which was similar to the numerical computations with the air volume fraction of VF = 0.016 or less.

When comparing the results, it should be borne in mind that the simulations concerned flow in the thin layer so cavitation structures were quasi-2D. In the pictures from the experiment, multiple layers in the spanwise direction were visible simultaneously (the length of the hydrofoil was 70 mm), and it was not possible to extract only one from them. The frequency of cloud formation observed in the experiment was 16.7 Hz which corresponded to the values obtained in computations for both 2phases and 3phases models with the air volume fraction of 0.016.

It is worthy to mention that the numerical method is fairly able to predict the dominant frequency of the shedding cavity. The predicted results are highly dependent on the adopted approaches such as turbulence models, cavitation models, turbulent viscosity modification models, etc. For instance, the value of the frequency of the cavitating structure, quoted in the literature, is 25 Hz (Wang *et al.*, 2001; Ji *et al.*, 2017; Long *et al.*, 2017), calculated for the similar hydrofoil and cavitation number of $\sigma = 0.8$. Huang *et al.* (2014) reported a frequency of 20.1 Hz for a standard k-ε model and frequencies from 24.8 to 28.5 Hz for the different variants of density based and filter based turbulence closure models, Huang *et al.* (2017) 2017 reported frequencies of 27.7 Hz to 41.5 Hz for Partially Averaged Navier-Stokes (PANS) turbulence model, depending on the variant, and value of 26.6 Hz for the standard k-ε model.

Figure 8 presents results for the 3phases model in the same way as it was for the 2phases model. Generally, the shapes of the clouds of the gaseous phase in all cases were similar to the shapes depicted for the 2phases model. The frequencies of lift coefficient fluctuations summarized in Table 1 were very close to the 2phases model except for the case with the low air content. In this case, the frequency is lower by 15% and amounts to 18.6 Hz.

The values of time-averaged lift and drag coefficients obtained from analysed models are summarised in Table 2. The same tendency that with an increase of air content the lift coefficient also increased was observed for all models. The value of the lift coefficients for the Singhal *et al.* model was lower than compared to values obtained from the other models. The drag coefficient was similar in all cases. The values of lift coefficients obtained with the 2phases model and the 3phases model were close to each other.

Table 3 summarised results presented in the literature and obtained experimentally for the Clark Y 11.7% hydrofoil. The values of lift coefficient were in the range of 0.55–0.70 but the value close to 0.70 occurred more often. The amount of air in the water is unknown. Assuming that the air content was close to the content in natural conditions, the computed results for the case with the air volume fraction can be compared with those experimental results. The results for the 2phases and 3phases models were in the range of experimental data. The results of the drag coefficient were at the end of the range registered in experiments.

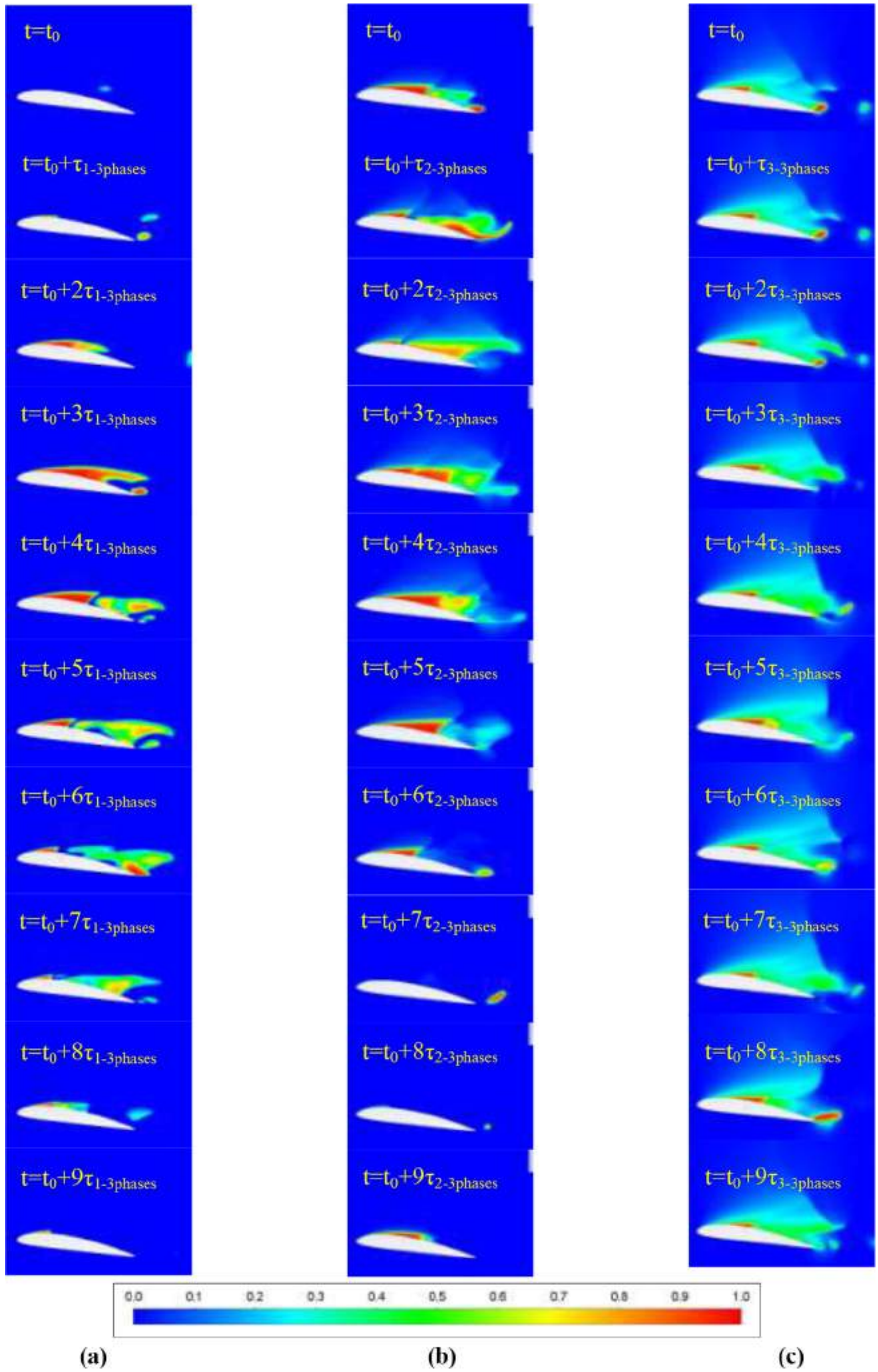

Figure 8: The contours of gas volume fraction in one period for different air volume fraction (3phases model, $\sigma = 0.75$, $\alpha = 8^{\circ}$)

The experimentally determined values of the drag and lift coefficients, presented in Table 3, relate to cases for which the cavitation number σ was in the range of 0.76–0.80.

Based on the numerical results, a clear cyclic behaviour with different periods could be perceived in the flow field. To show the evolution of the cavity closure, the contours of vapour volume fraction in a series of time points in one period are shown in Figure 9, where the effect of the numerical method and volume fraction of dissolved air were taken into account. It should be noted that the behaviour of the cavitation process is periodic, and the process will be repeated after the last step. So, it is neglected to show the last picture of the process which is identical to the first one. The regions covered by the cavity closure indicated the area where the local pressure was lower than the vapour pressure (p_v). In the early stages of cavity evolution, a sheet cavity appeared in the leading edge region. Although some attached vortices could be observed downstream, they belonged to the previous period. The cloud cavitation started its development when the sheet cavity reached about the middle of the hydrofoil. When the sheet cavity reached a certain point on the hydrofoil surface, which location varies with the cavitation number and air volume fraction, the re-entrant jet was established and directed to the rear side of cavity closure due to increasing pressure within the sheet cavity. Due to the collision between the re-entrant jet and the sheet cavity, the complex vortex flow appeared. The development of the cloud cavity continued when the created vortex shredded downstream. Although the remnant part of the sheet cavity was still attached to the leading edge, it was significantly shrunk due to the lost amount of vapour and push-back effect of increasing pressure in the closure.

The numerical method had a considerable impact on determining the shape of cavity closure and its evolution. The 2phases and 3phases methods predict almost the same cavity

Table 1.
The frequencies of lift coefficient for different volume fraction of air calculated with different models

Air volume fraction	2phases model	3phases model	Singhal et al. model
0.004	$f_{1\text{-}2phases} = 22$ Hz	$f_{1\text{-}3phases} = 18.6$ Hz	$f_{1\text{-}Singhal} = 27$ Hz
0.016	$f_{2\text{-}2phases} = 14.7$ Hz	$f_{2\text{-}3phases} = 14.4$ Hz	$f_{2\text{-}Singhal} = 0$ Hz
0.042	$f_{3\text{-}2phases} = 9$ Hz	$f_{3\text{-}3phases} = 8.9$ Hz	$f_{3\text{-}Singhal} = 0$ Hz (195 Hz)

Table 2.
The Time-averaged values of lift and drag coefficient for the different volume fraction of air calculated with different models

	2phases model		3phases model		Singhal *et al.* model	
Air volume fraction	Lift coef.	Drag coef.	Lift coef.	Drag coef.	Lift coef.	Drag coef.
0.004	0.58	0.11	0.56	0.11	0.52	0.11
0.016	0.59	0.12	0.59	0.11	0.53	0.10
0.042	0.63	0.13	0.66	0.14	0.59	0.14

Table 3.
The experimental, time-averaged values of lift and drag coefficients (natural cavitation)

Source	Lift coefficient	Drag coefficient
Kyushu University Watanabe *et al.* (2015)	0.55	0.05 (± 0.02)
Tohoku University Watanabe *et al.* (2015)	0.7	0.11
Watanabe *et al.* (2014)	0.6	0.055
Wang *et al.* (2001)	0.69	0.11
Tsuru et al. (2018)	0.7	0.09

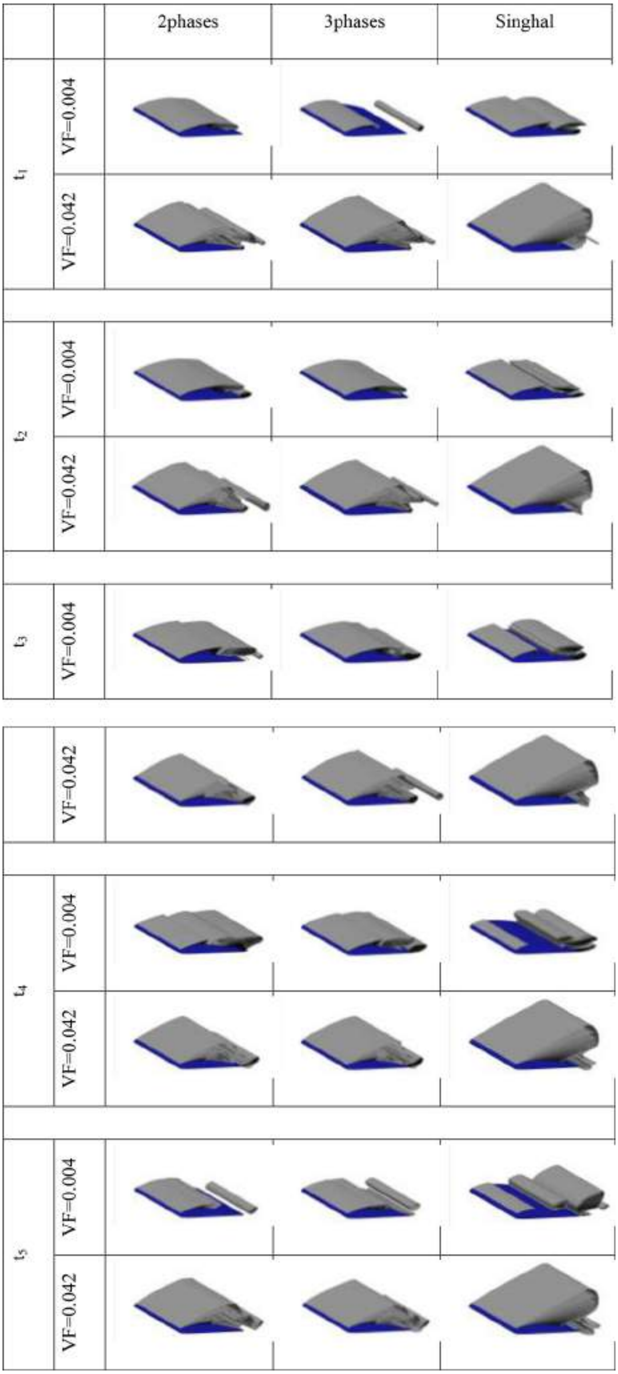

Figure 9. Evolution of the cavitation process over a period for different cavitation models and two air volume fractions (VF = 0.004 and 0.042)

configuration during one period, but the simulated cavity configuration using the Singhal method was different. The main difference between the configurations was the length of the sheet cavity which was substantially smaller than those predicted by the other methods. Besides, the length and volume of both sheet and cloud cavity were intensified by adding air content. Also, it was obvious that the surface of the hydrofoil was fully covered by the cavity at all time points during a period causing smooth pressure distribution around the hydrofoil when the air content increased.

To show the effect of re-entrant jet flow on the detachment process, Figure 10 shows this phenomenon obtained from the 3phases model at three points of time and for two cases; with VF = 0.004 and 0.042. In this regard, the contour of the vapour volume fraction and the velocity vector are presented to investigate the detachment process in details. It is worth mentioning that the main requirement for a re-entrant jet flow, which makes it capable of having an impact on the sheet cavity and detaching a part of it, is sufficiently high momentum. It is clear that not every reverse flow at the surface of a hydrofoil is an impactful re-entrant jet. Also, the large adverse pressure gradient is the main parameter in the establishment of an impactful re-entrant jet. At t_1, it can be observed that the re-entrant jet flow pushed the sheet cavity upstream. In the next time point t_2, the re-entrant jet became stronger using an adverse pressure gradient and pushed the sheet cavity further upstream and upward. Also, the re-entrant jet penetrated to sheet cavity more than in the previous time step. Finally, at t_3, a portion of the sheet cavity was detached through a strong collision between jet front and sheet cavity, and the created vortex was shed downstream by the main flow. The main process of the detachment of the vortex is

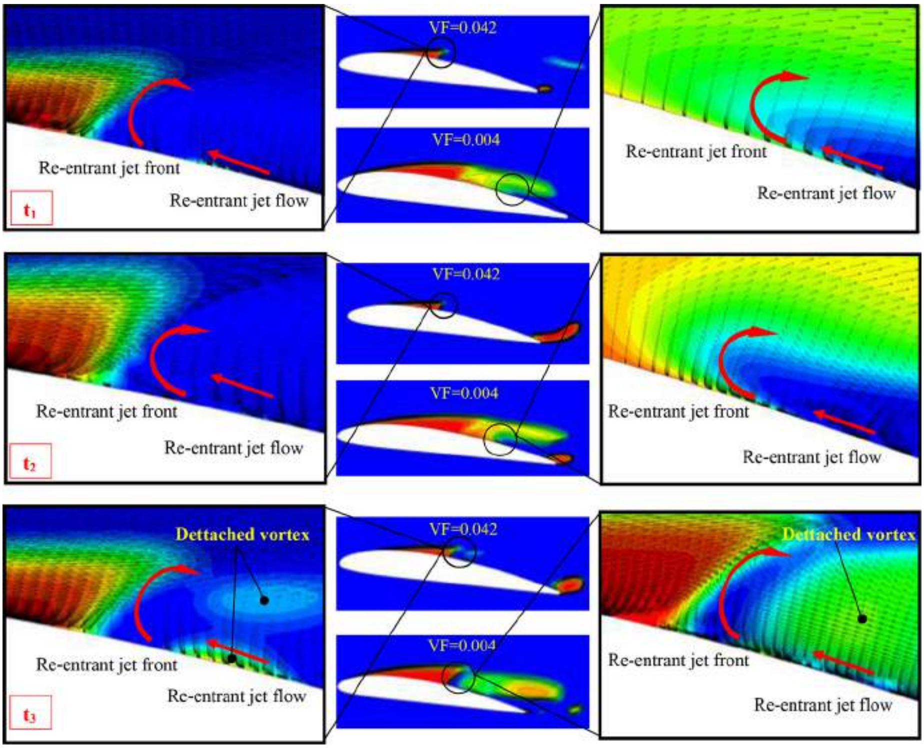

Figure 10.
Effect of the re-entrant jet in the formation of shedding cavity cloud based on 3phases model

the same, although some minor differences can be detected due to the addition of the dissolved air. At high air volume fraction VF = 0.004, it was obvious that the re-entrant jet penetrated to the sheet cavity and pulled the sheet cavity up at the first two steps (t_1 and t_2). Also, a large portion of the sheet cavity was lifted close to the trailing edge, unlike the case with a lower volume fraction. At VF = 0.042, the detached cavity was not lifted up, however, it departed from the main sheet cavity and still stuck to the surface.

4. Conclusions

Cavitating flow around a Clark Y 11.7% hydrofoil was analysed numerically to study the ability of the numerical models to include the presence of air in the water flow and to understand the influence of air on the cavitation performance of hydrofoil.

The structures of cavitating flow obtained from uRANS calculations were less extensive and, when compared with structures recorded with a camera, strongly averaged. The application of the uRANS model for calculations with a two-equation turbulence model did not provide the possibility of obtaining an image of small vertices structures. Also, the mixture model for two-phase flow did not allow determining the image of real, fine dispersion structures. Nevertheless, several global parameters of the phenomenon of cavitation can be tracked and analysed using such models. It should be emphasized that due to the significant dynamics of flow parameters, simulations of cavitation flow are a computational challenge. The simulation process and its control have to be adapted to each calculation case. The simulation results obtained using various models allow stating that Singhal *et al.* model did not reflect the dynamics of cavitation flow in all range of air contents. Contrarily, the 2phases and 3phases models were more suitable for simulations of multiphase flow with additional air in water. By adding the air, the structure of the cloud cavity was highly extended. Although a larger cloud cavity was formed at a higher air volume fraction, the cavitating flow was significantly stabilized and its dynamic behaviour was damped which can be proved by the analysis of the pressure distribution. The dynamics of the calculated cloud structures for both models (i.e. 2phases and 3phases) were similar and close to the value obtained from the image analysis recorded in the experiment. The time-averaged values of both the lift coefficient and drag coefficient were similar to the corresponding values obtained in the experiments. The addition of dissolved air to the water causes enhancement of both lift and drag coefficients. The 2phase, 3phase and Singhal models predict 8.6%, 17.8% and 13.4% enchantment for lift coefficient, respectively; and 18.1%, 27.2% and 27.2% increment for drag coefficient, respectively. The more detailed validation of the models with data collected on the test rig is planned as the next step of the research.

References

Ahn, B.-K., Jeong, S.-W., Kim, J.-H., Shao, S., Hong, J. and Arndt, R.E. (2017), "An experimental investigation of artificial supercavitation generated by air injection behind disk-shaped cavitators", *International Journal of Naval Architecture and Ocean Engineering*, Vol. 9 No. 2, pp. 227-237.

Bin, J., Luo, X-W., Peng, X-X., Zhang, Y., Wu, Y-L. and Xu, H-Y. (2010), "Numerical investigation of the ventilated cavitating flow around an under-water vehicle based on a three-component cavitation model", *Journal of Hydrodynamics*, Vol. 22 No. 6, pp. 753-759.

Chen, Y. and Heister, S.D. (1995), "Two-phase modeling of cavitated flows", *Computers and Fluids*, Vol. 24 No. 7, pp. 799-809.

Coutier-Delgosha, O., Fortes-Patella, R. and Reboud, J.-L. (2003), "Evaluation of the turbulence model influence on the numerical simulations of unsteady cavitation", *Journal of Fluids Engineering*, Vol. 125 No. 1, pp. 38-45.

Homa, D. (2018), "Eksperymentalne i numeryczne badanie zjawiska kawitacji dla różnych warunków przepływu", (in Polish), PhD Thesis, Silesian University of Technology, Gliwice,

Homa, D., Wróblewski, W., Majkut, M. and Strozik, M. (2019), "Research on unsteady cavitating flow around a Clark-Y 11.7% hydrofoil", *Journal of Theoretical and Applied Mechanics*, Vol. 57 No. 3.

Huang, B., Wang, G-y. and Zhao, Y. (2014), "Numerical simulation unsteady cloud cavitating flow with a filter-based density correction model", *Journal of Hydrodynamics*, Vol. 26 No. 1, pp. 26-36.

Huang, R., Luo, X. and Ji, B. (2017), "Numerical simulation of the transient cavitating turbulent flows around the Clark-Y hydrofoil using modified partially averaged Navier-Stokes method", *Journal of Mechanical Science and Technology*, Vol. 31 No. 6, pp. 2849-2859.

Iannetti, A., Stickland, M.T. and Dempster, W.M. (2016), "A CFD and experimental study on cavitation in positive displacement pumps: Benefits and drawbacks of the 'full' cavitation model", *Engineering Applications of Computational Fluid Mechanics*, Vol. 10 No. 1, pp. 57-71.

Ji, B., Long, Y., Long, X-P., Qian, Z-D. and Zhou, J-J. (2017), "Large eddy simulation of turbulent attached cavitating flow with special emphasis on large scale structures of the hydrofoil wake and turbulence-cavitation interactions", *Journal of Hydrodynamics*, Vol. 29 No. 1, pp. 27-39.

Jones, W. and Launder, B.E. (1972), "The prediction of laminarization with a two-equation model of turbulence", *International Journal of Heat and Mass Transfer*, Vol. 15 No. 2, pp. 301-314.

Kawakami, D.T., Qin, Q. and Arndt, R. (2005), "Water quality and the periodicity of sheet/cloud cavitation", *Fluids Engineering Division Summer Meeting*, Vol. 41995, pp. 513-517.

Kinnas, S.A. and Young, Y.L. (2003), "Modeling of cavitating or ventilated flows using BEM", *International Journal of Numerical Methods for Heat and Fluid Flow*, Vol. 13 No. 6, pp. 672-697, doi: 10.1108/09615530310498376.

Kopriva, J., Arndt, R.E. and Amromin, E.L. (2008), "Improvement of hydrofoil performance by partial ventilated cavitation in steady flow and periodic gusts", *Journal of Fluids Engineering*, Vol. 130 No. 3.

Kozubkova, M., Bojko, M., Jablonska, J., Homa, D. and Tůma, J. (2016), "Experimental research of multiphase flow with cavitation in the nozzle", *in EPJ Web of Conferences, vol. 114: EDP Sciences*, p. 2058.

Kubota, A., Kato, H. and Yamaguchi, H. (1992), "A new modelling of cavitating flows: a numerical study of unsteady cavitation on a hydrofoil section", *Journal of Fluid Mechanics*, Vol. 240 No. 1, pp. 59-96.

Kunz, R.F., et al. (2000), "A preconditioned navier–stokes method for two-phase flows with application to cavitation prediction", *Computers and Fluids*, Vol. 29 No. 8, pp. 849-875.

Kunz, R.F., Boger, D.A., Chyczewski, T.S., Stinebring, D., Gibeling, H., and Govindan, T. (1999), "Multi-phase CFD analysis of natural and ventilated cavitation about submerged bodies", in *Proceedings of the 3rd ASME-JSME Joint Fluids Engineering Conference*.

Liu, C., Yan, Q. and Wood, H.G. (2020), "Numerical investigation of passive cavitation control using a slot on a three-dimensional hydrofoil", *International Journal of Numerical Methods for Heat and Fluid Flow*, Vol. 30 No. 7, pp. 3585-3605, doi: 10.1108/HFF-05-2019-0395.

Liu, C., Wei, W., Yan, Q., Weaver, B.K. and Wood, H.G. (2019), "On the application of passive flow control for cavitation suppression in torque converter stator", *International Journal of Numerical Methods for Heat and Fluid Flow*, Vol. 29 No. 1, pp. 204-222, doi: 10.1108/hff-11-2017-0473.

Long, X., Cheng, H., Ji, B. and Arndt, R.E. (2017), "Numerical investigation of attached cavitation shedding dynamics around the Clark-Y hydrofoil with the FBDCM and an integral method", *Ocean Engineering*, Vol. 137, pp. 247-261.

Mäkiharju, S.A., Ganesh, H. and Ceccio, S.L. (2017), "The dynamics of partial cavity formation, shedding and the influence of dissolved and injected non-condensable gas", *Journal of Fluid Mechanics*, Vol. 829, p. 420.

Mathew, S., Theo G. Keith, T.G.K., Jr,. and Nikolaidis, E. (2006), "Numerical simulation of traveling bubble cavitation", *International Journal of Numerical Methods for Heat and Fluid Flow*, Vol. 16 No. 4, pp. 393-416. doi: 10.1108/09615530610653055.

Merkle, C.L. (1998), "Computational modelling of the dynamics of sheet cavitation", *in Proc. of the 3rd Int. Symp. on Cavitation, Grenoble, France, 1998*.

Murrone, A. and Guillard, H. (2005), "A five equation reduced model for compressible two phase flow problems", *Journal of Computational Physics*, Vol. 202 No. 2, pp. 664-698.

Nguyen, V.L., Degawa, T., Uchiyama, T. and Takamure, K. (2019), "Numerical simulation of bubbly flow around a cylinder by semi-Lagrangian–lagrangian method", *International Journal of Numerical Methods for Heat and Fluid Flow*, Vol. 29 No. 12, pp. 4660-4683, doi: 10.1108/HFF-03-2019-0227.

Romenski, E. and Toro, E. (2004), "Compressible two-phase flows: two-pressure models and numerical methods", *Computational Fluid Dynamics Journal*, Vol. 13, pp. 403-416.

Saurel, R. and Lemetayer, O. (2001), "A multiphase model for compressible flows with interfaces, shocks, detonation waves and cavitation", *Journal of Fluid Mechanics*, Vol. 431, p. 239.

Schmidt, D.P., Rutland, C.J. and Corradini, M.L. (1999), "A fully compressible, two-dimensional model of small, high-speed, cavitating nozzles", *Atomization and Sprays*, Vol. 9 No. 3,

Schnerr, G.H. and Sauer, J. (2001), "Physical and numerical modeling of unsteady cavitation dynamics", *in Fourth international conference on multiphase flow, vol. 1*, ICMF New Orleans.

Senocak, I. and Shyy, W. (2002), "A pressure-based method for turbulent cavitating flow computations", *Journal of Computational Physics*, Vol. 176 No. 2, pp. 363-383.

Sinhal, A., Athavale, M. and Li, H. (2002), "Mathematical basis and validation of the full cavitation model", *Journal of Fluids Engineering*, Vol. 124 No. 3, pp. 617-624.

Sun, T., Wang, Z., Zou, L. and Wang, H. (2020), "Numerical investigation of positive effects of ventilated cavitation around a NACA66 hydrofoil", *Ocean Engineering*, Vol. 197, p. 106831.

Tsuru, W.Y., Ehara, S., Kitamura, S., Watanabe, and Tsuda, S.-I. (2018), "Mechanism of lift increase of cavitating clark Y-11.7% hydrofoil", in Katz, J. (Ed.), *in Proceedings of the 10th International Symposium on Cavitation (CAV2018)*, ASME Press.

Venkateswaran, S., Lindau, J.W., Kunz, R.F. and Merkle, C.L. (2002), "Computation of multiphase mixture flows with compressibility effects", *Journal of Computational Physics*, Vol. 180 No. 1, pp. 54-77.

Wang, G., Senocak, I., Shyy, W., Ikohagi, T. and Cao, S. (2001), "Dynamics of attached turbulent cavitating flows", *Progress in Aerospace Sciences*, Vol. 37 No. 6, pp. 551-581.

Watanabe, S., Yamaoka, W. and Furukawa, A. (2014), "Unsteady lift and drag characteristics of cavitating clark Y-11.7% hydrofoil", *in IOP Conference Series: Earth and Environmental Science, 2014, vol. 22, no. 5*, IOP Publishing, p. 52009.

Watanabe, S., Suefuji, N., Yamaoka, W. and Furukawa, A. (2015), "Lift and drag characteristics of a cavitating Clark-Y 11.7% hydrofoil", *Turbomachinery*, Vol. 41 No. 7, pp. 440-446, doi: 10.11458/tsj.41.440.

Zwart, P.J., Gerber, A.G. and Belamri, T. (2004), "A two-phase flow model for predicting cavitation dynamics", in *Fifth International Conference on Multiphase Flow*, Vol. 152, Yokohama.

Corresponding author
Emad Hasani Malekshah can be contacted at: emadhasani1993@gmail.com

Paper III:

Dissolved air effects on three-phase hydrodynamic cavitation in large scale Venturi-Experimental/numerical analysis

Ultrasonics Sonochemistry 90 (2022) 106199

Contents lists available at ScienceDirect

Ultrasonics Sonochemistry

journal homepage: www.elsevier.com/locate/ultson

Dissolved air effects on three-phase hydrodynamic cavitation in large scale Venturi- Experimental/numerical analysis

Emad Hasani Malekshah *, Włodzimierz Wróblewski, Mirosław Majkut

Department of Power Engineering and Turbomachinery, Silesian University of Technology, 44-100 Gliwice, Poland

A R T I C L E I N F O

Keywords:
Cavitation
Venturi flow
Dissolved air
Shedding mechanism
Density correction

A B S T R A C T

Hydrodynamic cavitation (HC) in the Venturi nozzle, apart from the harmful influence on the devices, can be used to improve a range of industrial processes, such as biofuel generation, emulsion preparation, and wastewater treatment. The present investigation deals with the influence of dissolved air in Venturi cavitating flow based on numerical and experimental approaches. The experimental campaigns have been done in a closed-loop water tunnel equipped with a Venturi test section. The post-processing techniques such as Fast Fourier Transform (FFT), Power Spectral Density (PSD), temporal/spatial Grey Level distribution and mean value grey level distribution are employed to analyse the experimental observations and measurement. The URANS numerical method is modified based on the Density Corrected-Based Model (DCM) to be more adaptable for flows with high differences in density. The results approve the remarkable effect of dissolved air on the configuration of the cavity, its evolution process, and transient/averaged characteristics. It is observed that the incipient point and ratio of sheet cavity length to cloud cavity length are changed. Furthermore, the flow velocity inside of the sheet and cloud cavities is different; as well as, the higher content of dissolved air leads to slower flow velocity inside the cloud cavity. In addition, the shedding frequency is significantly reduced in case of higher level of air content.

1. Introduction

Cavitation is known as a dynamic phase-change process characterized by an alternation of water and vapour phases [1]. The cavitation phenomenon is started by nucleation and followed by the enlargement of cavity bubbles. Considering the operating parameters like pressure and stream velocity, different types of cavitation including sheet cavity, cloud cavity and supercavitation, may occur. Those phenomena can be observed on blades of water turbines, high-speed propellers, and pumps. Furthermore, due to the high impact of the cavitation on the noise, vibration, erosion, performance alternation and structural damage, it is important to analyse this phenomenon and find out the controlling approaches. Although there are several applications in the turbomachinery, the sludge stabilization which increases removal efficiency of dyes or other emerging contaminants in wastewater, is a promising environmental application of hydrodynamic cavitation [2].

Among the main types of cavitation, partial cavitation, which consists of sheet cavity and cloud cavity, is often detected around the hydraulic components and is known to be highly responsible for negative effects. Such cavitation has a more complex behaviour than other types since the cavitating flow is characterized by strong unsteadiness, major shedding cloud cavity and fully 3D flow. The cavity configuration and corresponding average/instantaneous characteristics of the partial cavitating flow are highly interesting areas of investigation. The detachment region of the cavity where the type of cavity is altered from sheet to cloud cavity is the first interesting region which is generally followed by the re-entrant jet. Furthermore, another critical part is the region where the sheet cavity is formed due to the low-pressure zone. Afterwards, the sheet cavity is shed downstream and violently collapses when it reaches a high-pressure zone. In the present case, the clouds are generated in the vortex shedding which is filled by the numerous vapour bubbles. The re-entrant jet is one of the principal sources producing the shedding cavity. It mainly consists of liquid and penetrates upstream and hit the sheet cavity border. The existence of a re-entrant jet is already observed and approved by numerical and experimental investigations carried out by Malekshah and Wróblewski [3]. The main structures of the partial cavitation in the flow through a Venturi nozzle are characterized in Fig. 1. The air content is also considered which may exist in the form of dissolved air and dispersed bubbles. It is worth mentioning that different parts of cavities from inception to bubbly clouds are shown

* Corresponding author.
E-mail address: emad.hasani@polsl.pl (E. Hasani Malekshah).

https://doi.org/10.1016/j.ultsonch.2022.106199
Received 8 July 2022; Received in revised form 6 October 2022; Accepted 10 October 2022
Available online 11 October 2022

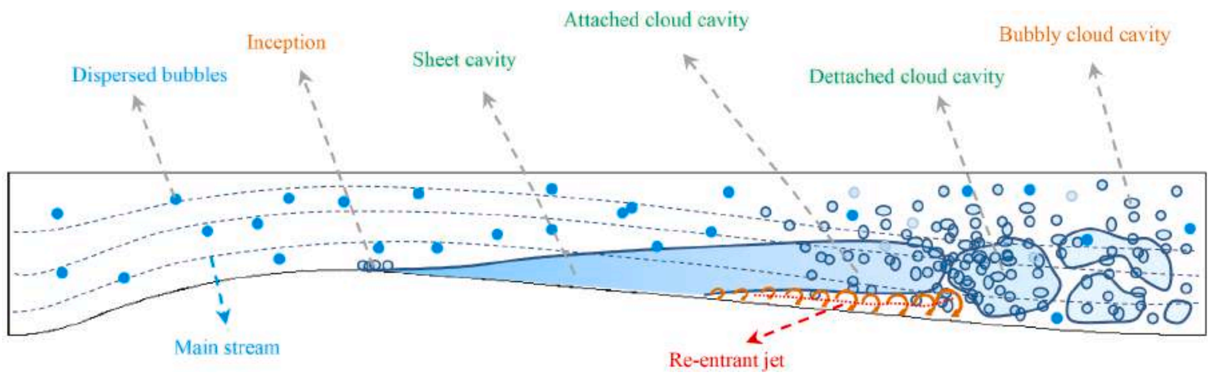

Fig. 1. Schematic of cavitating flow in Venturi Nozzle.

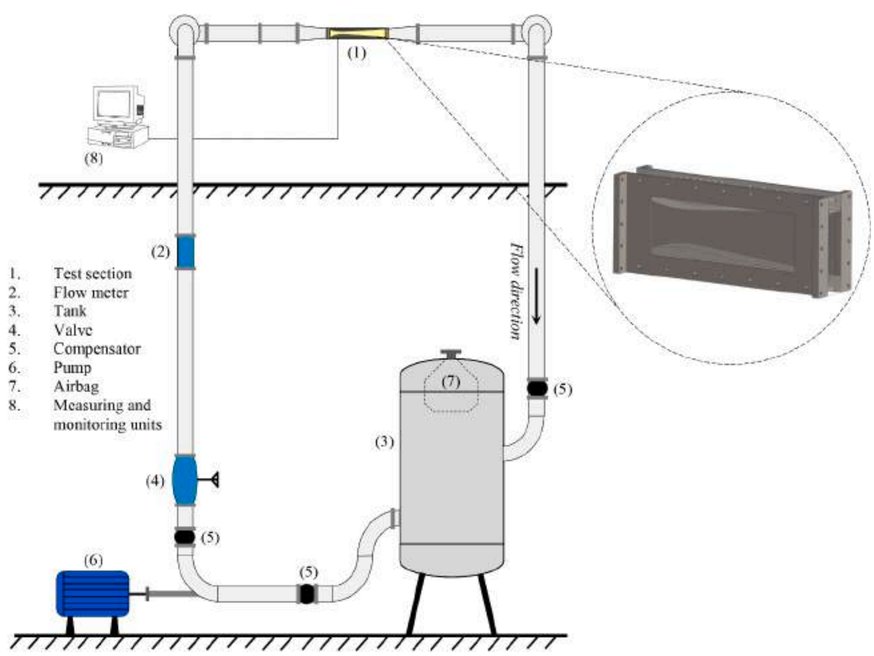

Fig. 2. Hydraulic installation along with main components.

by different scales. The incipient vapour bubbles and bubbly cloud cavity are microscale structures. However, the sheet cavity and attached–detached cavity are categorized as macro-scale. It is to note that the macroscale zones are the regions of interest.

The breakup and shedding process of partial cavitating flow has been studied around the symmetric and asymmetric objects and nozzles using experimental and numerical approaches [4–6]. As already discussed, the re-entrant jet is known as a principal reason for shedding which was firstly observed by Knapp [7] using a visualization technique and a high-speed camera. In an experimental/theoretical investigation, the attached cavities within a two-dimensional convergent-divergent nozzle have been investigated by Furness and Hutton [8]. They conducted many experiments to detect the behaviour of the partial cavity to the re-entrant jet reaction and approved that the re-entrant jet is mainly responsible for the instabilities at the rear part of the cavity. Kawanami et al. [9] studied the generation of cloud cavitation by implanting an obstacle on the foil surface to ban the re-entrant jet toward the leading edge. They declared that the shedding and breaking up rates have been significantly damped when the re-entrant jet hardly reaches the sheet cavity. Stutz and Reboud [10,11] used a double optical probe to evaluate the sheet cavity structure inside a Venturi nozzle. They quantitatively declared the existence of a re-entrant jet at the adjacent foil surface which flows upstream toward the sheet cavity and causes the periodical breaking off. Huang et al. [4,12] and Ji et al. [13–15] formulated the relationship between the re-entrant jet and the large-scale vortex generated at the rear zone of the sheet cavity. They figured out that the reverse pressure gradient and reverse flow close to the wall are the products of a large-scale vortex. On the other hand, it was declared by Kubota et al. [16] that the cloud cavity is convected downstream with a lower velocity than the bulk flows. However, in the experiment conducted by Pham et al. [17], the velocity of the jet stream was found to be in the same order as the main flow.

To simulate the turbulent cavitating flows, it is often assumed that the mixture of liquid–vapour in the two-phase cavitation model and liquid–vapour-air in the three-phase cavitation model, are homogenous phases. Also, the variation of mixture density is calculated based on either a barotropic equation of state (EOS) [18,19] or a transport equation [20,21] during the cavitating flow. The cavitating flows are usually categorized among high-Reynolds number flows where the turbulence also plays an inevitable role in the prediction of its unsteady characteristics. The URANS approaches are used in many works because they can predict averaged flow characteristics with low computational cost compared to other numerical models. The disadvantage of the URANS approach is the poor capability of resolving details of flow structures. It is mostly devoted to the prediction of averaged flow structures [22–25]. Wróblewski et al. [26] carried out a numerical

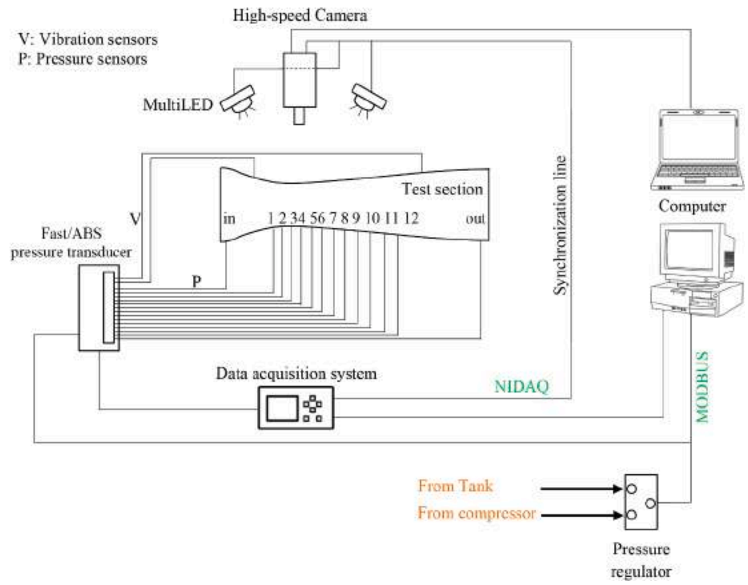

Fig. 3. Schematic of measuring and visualization systems.

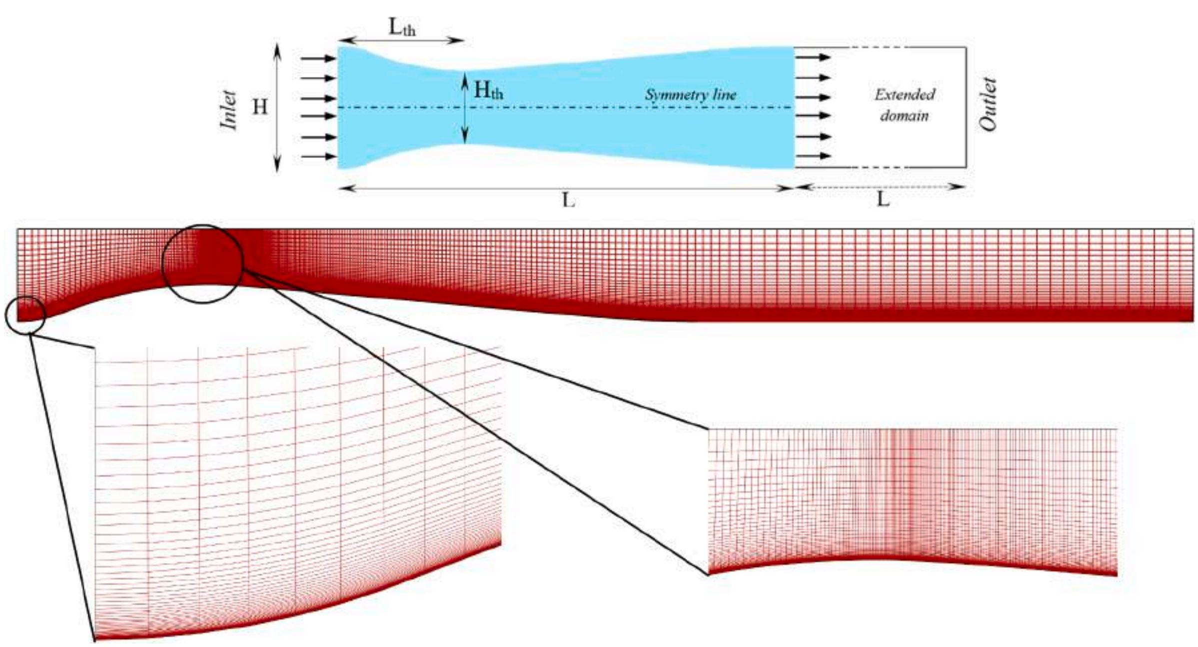

Fig. 4. Computational domain, dimensions, and grid distribution.

Table 1
Characteristics of mesh distributions.

Mesh Symbol	Number of elements	Number of nodes on Venturi surface
M1	51,000	230
M2	57,300	260
M3	59,500	290
M4	61,500	300
M5	63,500	310

investigation of the cavitating flow when the air is taken into consideration. They used URANS numerical approach with RNG $k-\varepsilon$ turbulence model. To deal with the presence of air as the third phase, they adopted two approaches of 2phase and 3phase in which the phases are assumed as water/vapour-air and water/vapour/air, respectively. In both approaches, the mixture model was employed. Based on the comparison of numerical results with conducted experiments, it was declared that the 3phase approach, which considers water, vapour and air as three separated phases, gives better prediction over the cavity structure and unsteady characteristics. Furthermore, the influence of air on the dynamic characteristics and cavity configuration was demonstrated. The larger cavity with more steady behaviour was the outcome of adding dissolved air. In another work, the three-phase cavitating flow was addressed based on numerical/experimental investigation by Wróblewski et al. [27]. The cavitating flow in presence of air was visualized and corresponding unsteady characteristics were measured using a high-speed camera and pressure transducers. The global and local features of the cavitation in the flow around the ClarkY hydrofoil were exported. The numerical simulations were carried out based on the URANS model considering three phases water, vapour and air. Also, two levels of oxygen contents including 2.6 ppm and 5.5 ppm are measured during the test, and the same conditions were adopted for numerical

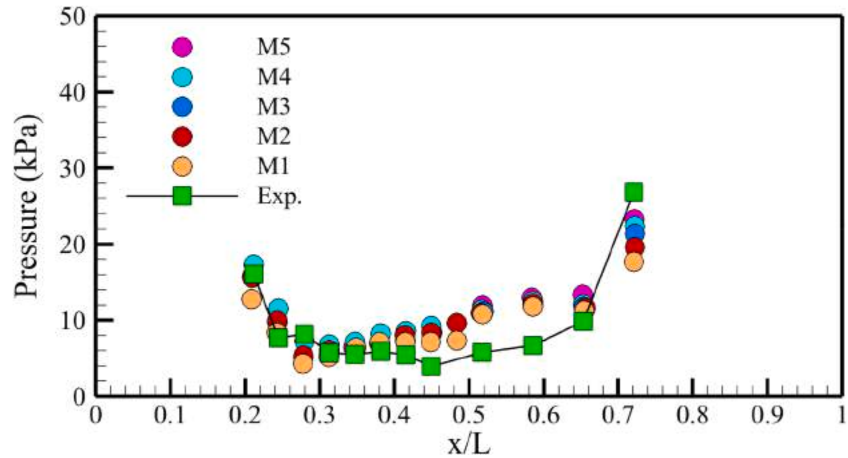

Fig. 5. Comparison of pressure distributions in different grid sizes ($\sigma = 2.02$ with low air content).

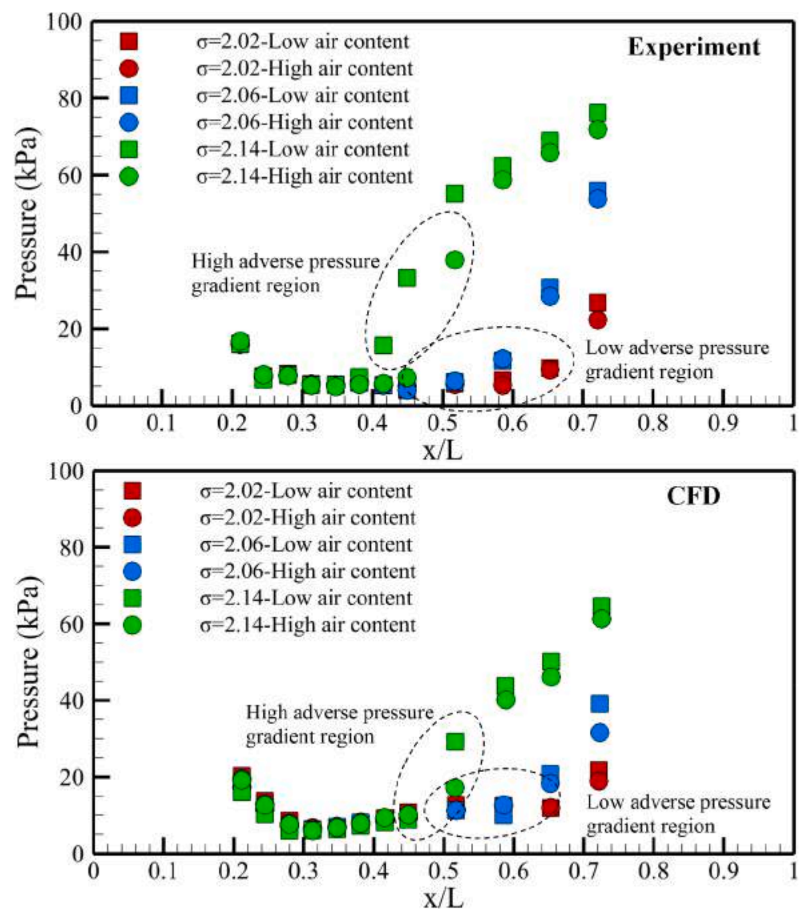

Fig. 6. Averaged pressure distribution as a function of cavitation number and air content based on experimental measurements (above) and numerical calculations (bottom).

simulations. The results confirmed the noticeable impact of dissolved air on the enlargement of the cavity and reduction in shedding frequency. To overcome the incapability of the standard turbulence models in perfect prediction of instability of cavitating flow, Coutier-Delgosha et al. [28] proposed a modification over the dynamic viscosity which avoids its overestimation. They proved the positive effect of modifications on the simulation of cavity evolution and corresponding unsteady characteristics. To simulate the cavitation inside a Venturi channel, Chen et al. [23] adopted a modified density corrected model coupled with an energy equation. Also, the heat transfer effect is taken into consideration. Their simulations were in good agreement with the experimental data in the same geometry and operating conditions. Malekshah et al. [29] concentrated on the cavitating flow around the Clark-Y hydrofoil with dissolved air as the third phase. Because the RNG k-epsilon model overestimates viscosity and yields poor predictions, the turbulence model is changed using the density corrected model (DCM) and filter-based density correction model (FBM). The numerical results and the experimental data are also compared. It is determined that when the improved turbulence models are used, the numerical prediction will be more accurate.

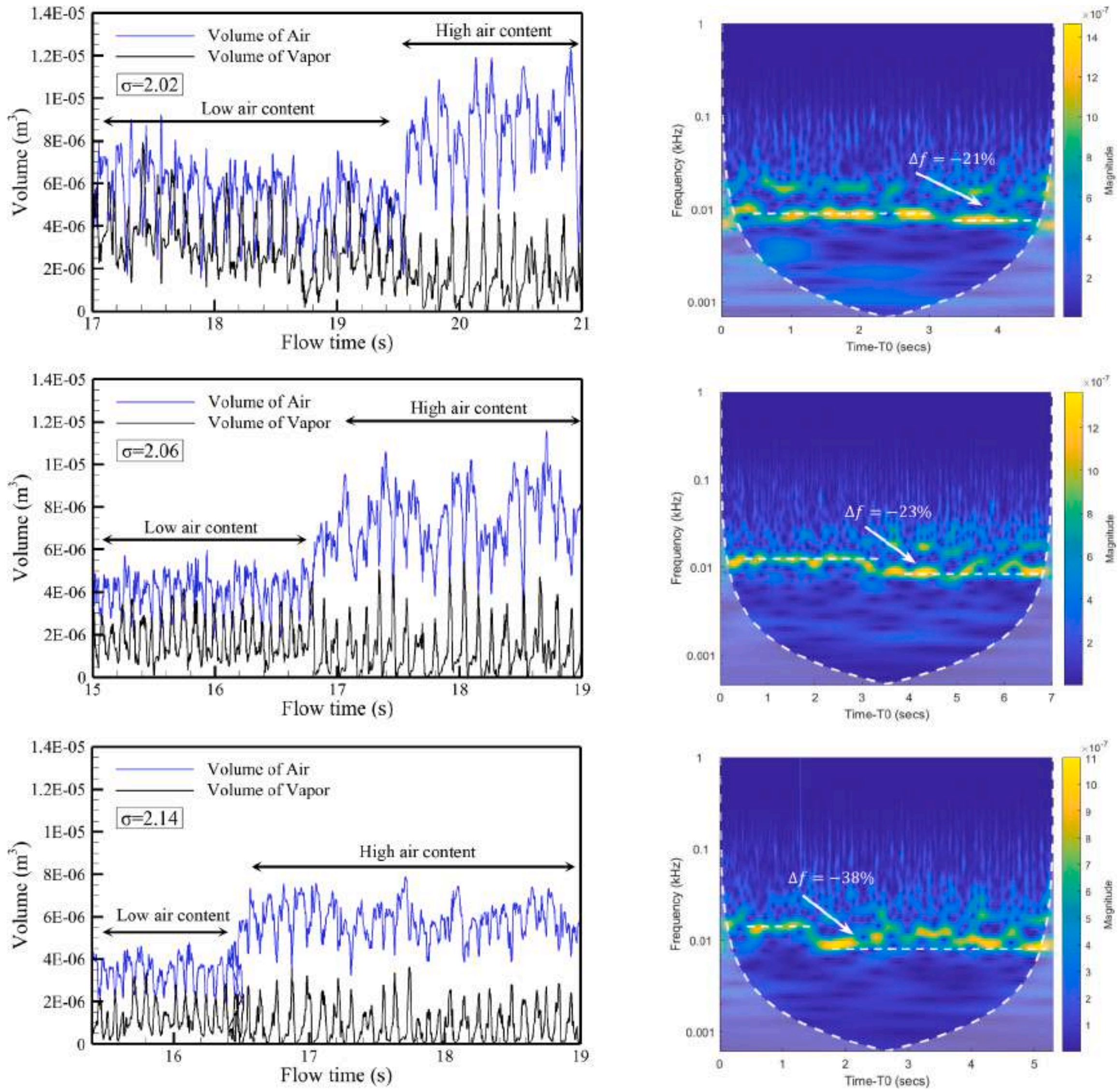

Fig. 7. Numerical-predicted time-dependent distributions of vapour and volume fractions and corresponding Continuous Wavelet Transform (CWT) for different cavitation numbers.

The present work aims to analyse the impact of dissolved air on the cavitating Venturi flow using experimental observations and numerical simulations. Experiments are conducted at three cavitation numbers and two dissolved air levels. The URANS simulations are carried out to predict the transient and average features of the cavitation process.

2. Experimental facilities and procedure

The experiments were conducted using hydraulic installation built and mounted at the laboratory of the Department of Power Engineering and Turbomachinery, The Silesian University of Technology. The schematic of the installation along with the main components is illustrated in Fig. 2. The installation is a closed-loop circuit equipped with a replaceable test section. The operation fluid inside the circuit is water which flows through the 200 mm pipes using an electric pump with a power of 30 kW. The manual valve and the electromagnetic flowmeter are installed after the pump. The water stream flows through the pipe upward around 5 m to reach the section. Before the test section, the straightener is installed to reduce the vorticity of the water stream. In addition, the pipe is connected to the test section using a cross-section inverter. The water stream passes the test section and Venturi nozzle which is the region of interest. Then, the cross-section is changed from rectangular to circular using a shaped diffuser. Afterwards, the pipe heads to the tank which is located on the ground floor. The tank of 1.5 m^3 volume is designed to keep the required water for the experiment; as well, as to adjust the pressure level inside the circuit. For this purpose, an internal elastic airbag is mounted inside of the tank which may be inflated using the controlled compressed air system. This enables the test rig is capable to be operated with the same flow rate and different pressure levels in order to set up different operating conditions. To reduce forces and vibration propagation, three elastic compensators, one before the tank, one after the pump and one between the tank, and the pump were inserted.

The cavitation test chamber has a rectangular cross-section and includes a Venturi nozzle. The transparent window, which was made of polycarbonate, was placed at the one sidewall of the test chamber to enable optical access and observations. The length L, height H and width W of the chamber are equal to 700 mm, 189 mm and 70 mm, respectively. The ratio of chamber height to width was fixed as $H/W = 2.7$. Hence, the ratio of throat height H_{th} to a height of chamber H is defined as $AR = H_{th}/H \simeq 0.6$. Also, the throat length (i.e. the distance of throat from the inlet) is 196 mm.

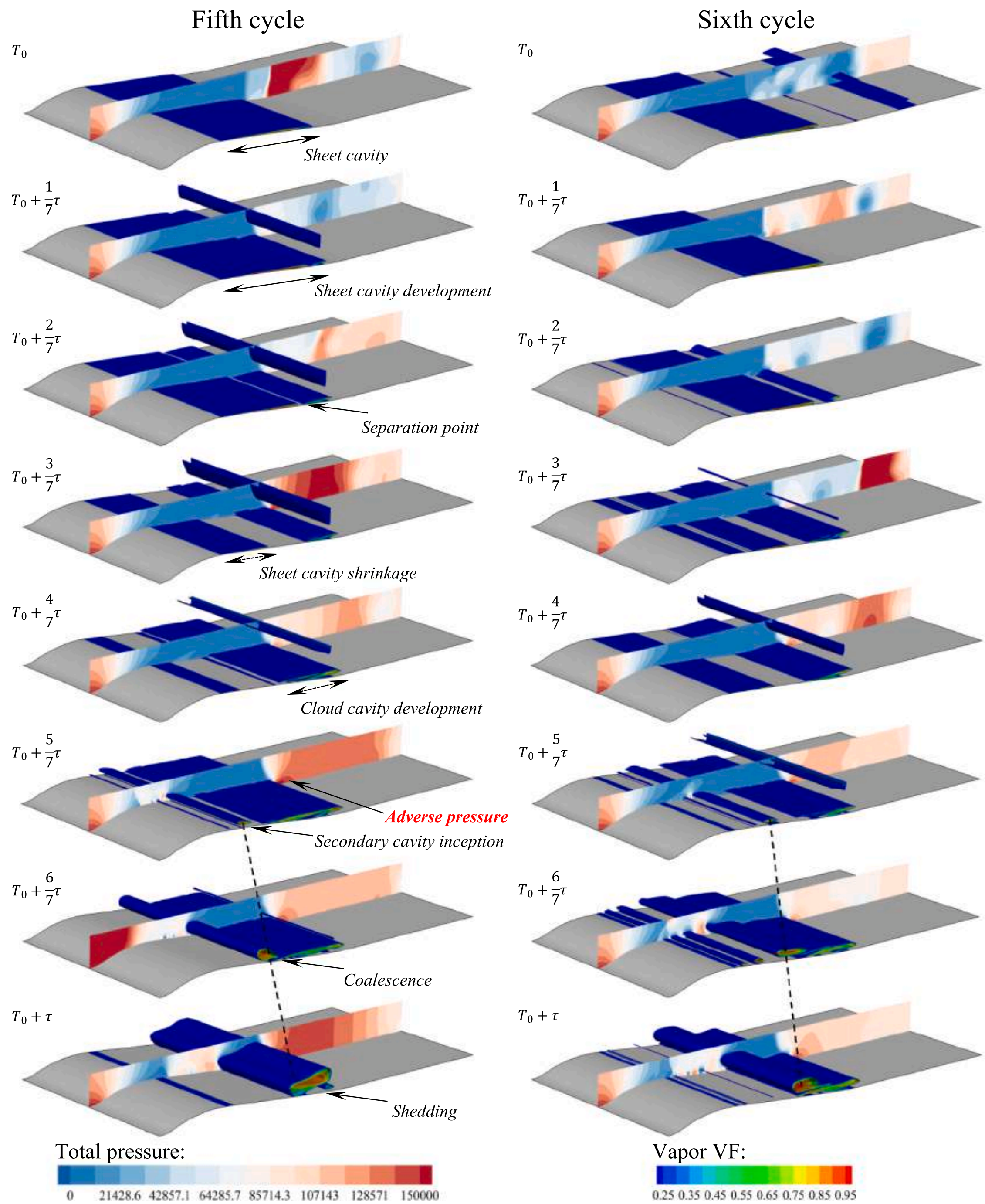

Fig. 8. Simulated cavity evolution in two sequential cycles ($\sigma = 2.02$ with low air content) represented by vapor volume fraction isosurfaces and total pressure contours.

The experimental tests were conducted based on two specific levels of dissolved oxygen of 4.01 mg/l and 6.66 mg/l. Based on Henry's law, it corresponds to the air content of 10.25 mg/l and 17.03 mg/l, respectively. The current levels of air only include the dissolved air; as a result, the amount and effect of non-dissolved air bubbles are not taken into account. The multifunction meter CF-401 was employed to measure the oxygen levels before and after the experimental campaign in steady conditions. The average value of the oxygen is reported in this work. The ranges of oxygen levels for the first and second experimental campaigns were 4.32 – 3.71 mg/l and 7.22–6.15 mg/l, respectively.

It is worth mentioning that two aeration process was performed to increase the level of air content. For this purpose, the air was injected into the water channel when the facility is running. Then, the injection was stopped; however, the facility was still running for 1–2 min. So, it could be assured that the injected air was perfectly dissolved into water. In the next step, the water sample was taken from the water channel, and the level of dissolved air was measured. Also, the sampling and measuring were repeated after each experimental campaign. The average value of dissolved air is reported in the present work. The amount of dissolved air is calculated during the tests; however, the cavitating flow is characterized using the visualization and frequency measuring over the shedding process. Therefore, other approaches exist to analyze the feature of cavitating flow such as vibration noise measurement [30].

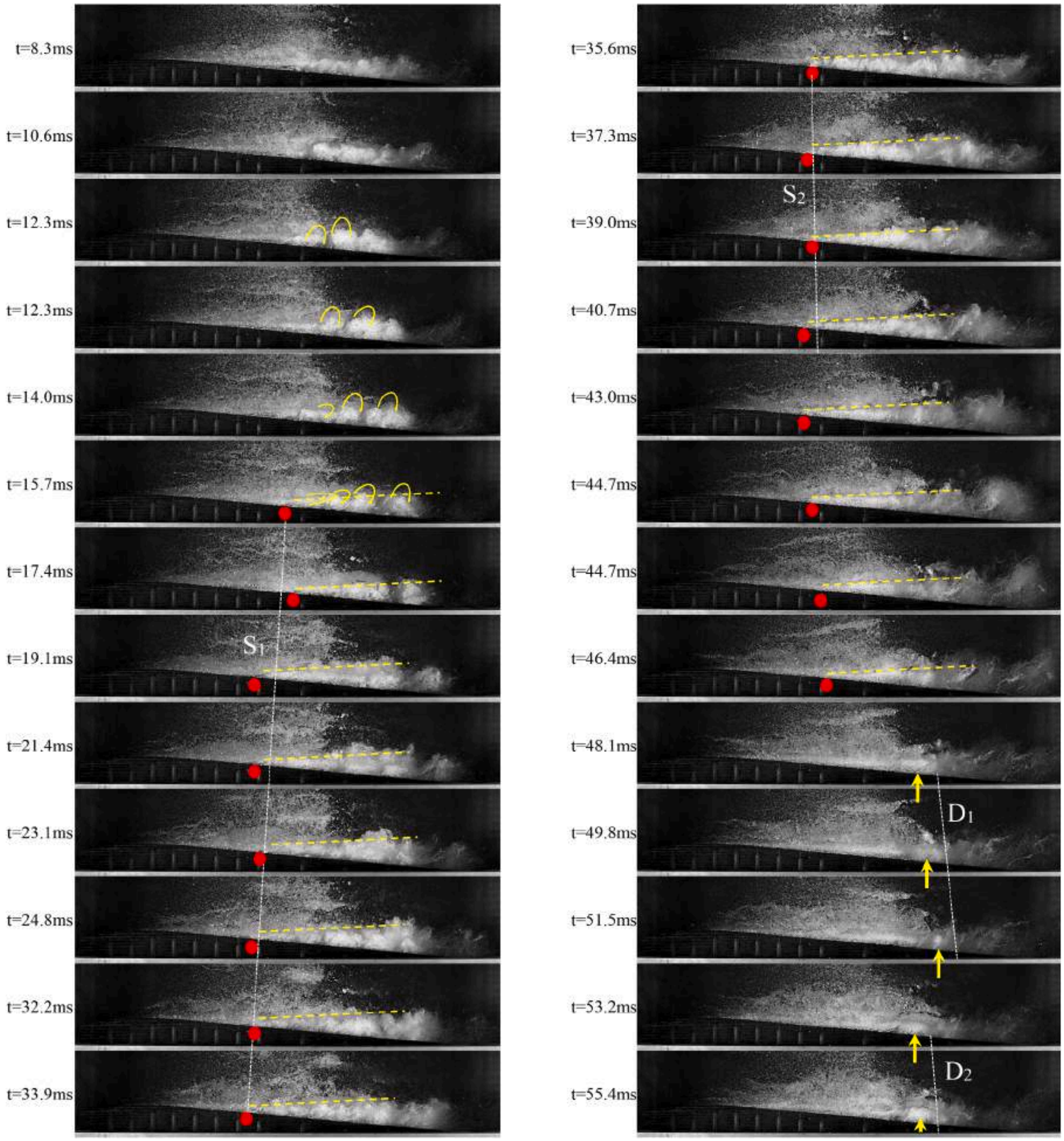

Fig. 9. Visualization of cavity evolution ($\sigma = 2.06$ with low air content, t = 8.3 ms to t = 55.4 ms).

The schematic of the measuring and visualization systems is demonstrated in Fig. 3. The unit consists of a pressure regulator, low/high-frequency pressure sensors, vibration sensors, fast/ABS pressure transducers, data acquisition system, multiLED lighting, high-speed camera, and computer. Twelve pressure sensors are installed at the surface of the Venturi profile, and two sensors at the inlet and outlet of the chamber. Among the sensors, three are fast-frequency and the rest are low-frequency sensors. The model of low-frequency sensors is APLISENS PC-28 with a full-scale (FS) of 160 kPa and an accuracy of 0.16 %. The pressure waves were transmitted to the measuring cluster using impulse tubes. The pressure fluctuations of P_{inlet}, P_3 and P_8 were detected using high-frequency miniature pressure sensors of XP5 type with amplifier ARD154. The maximum detectable pressure for XP5 is 500 kPa with an accuracy of 0.25 %. The temperature of the water was measured by the resistance thermometer APLISENS CT-GN1 Pt100 with a full scale of 0–100 °C and accuracy of $\pm(0.15\ K + 0.002\ |T|)$. The electromagnetic flowmeter UniEMP-05 DN200 was used to measure the flow rate up to 1080 m^3/h with an accuracy of $\pm$ 0.25 %. To measure the vibration generated by the cavitating flow, the vibroacoustic signal at the outer wall of the chamber was measured using two piezoelectric sensors. The stiff piezoelectric accelerometers KD35 (RTF) were installed at the external wall of the chamber and located before and after the throat. The accelerometers were connected with the 0028 (RFT) type charge amplifier connected with the fast analog-to-digital converter AC 16 bit, 250 kS/s. The system was calibrated before the experiments using the electrodynamic vibration calibrator EET101 (RFT) type. The upper value of the error was less than 5 %. The measurement system was set based on the National Instruments module NI USB 6216. In addition, the NI/PXI-6255 module cooperated with the pressure measuring cluster consisting of sets of pressure sensors and measuring transducers. The executive elements and the data acquisition process were managed by a system programmed in the LabView environment. The visualization unit

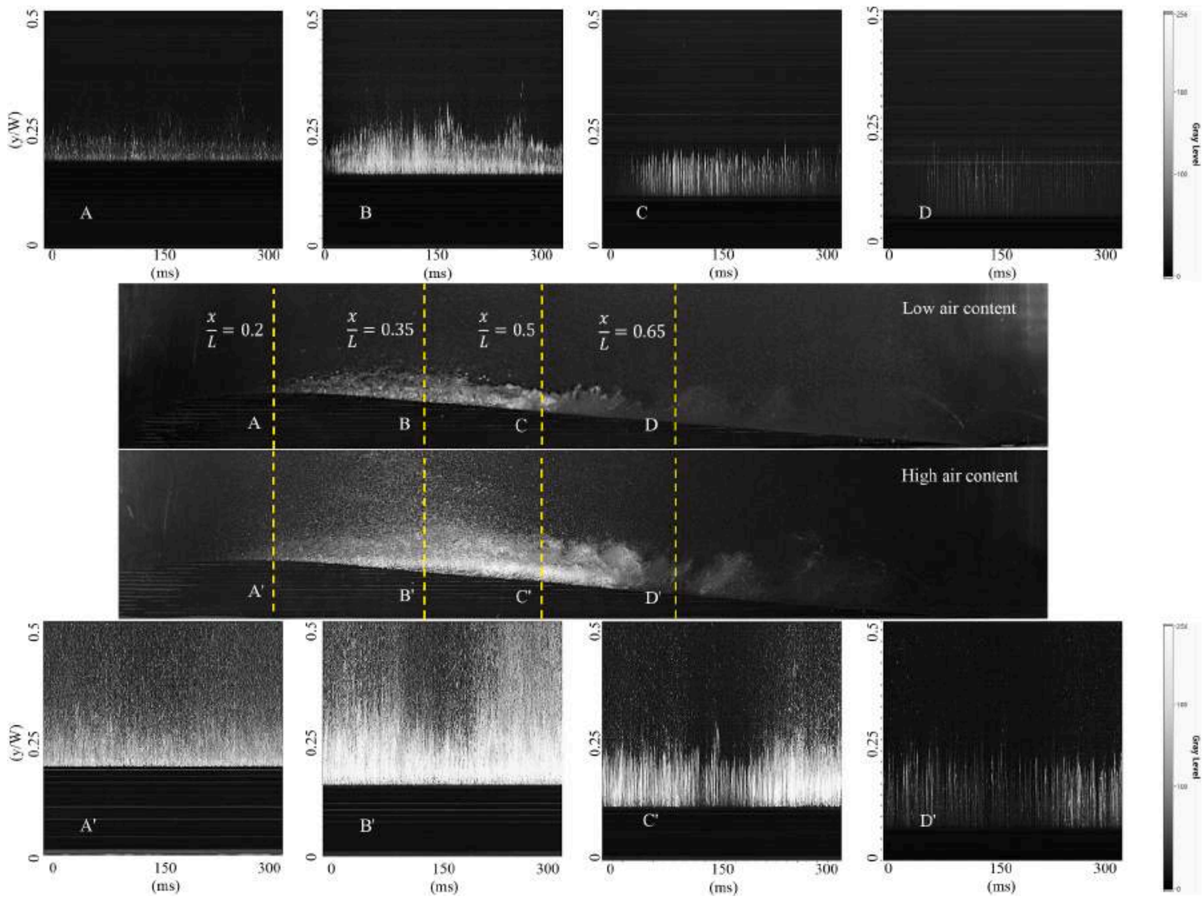

Fig. 10. Temporal-spatial grey scale distributions ($\sigma = 2.14$, low and high air contents).

consisted high-speed camera, lighting and monitor. The high-speed video camera Phantom VEO 710 is used to record the cavitating flow. The recording speed was set to 7000 fps with a resolution of 1280×800 pixels. The MULTILED L48-XF was utilized for lighting purposes.

3. Numerical approach

3.1. Multiphase numerical model

The homogeneous mixture model is employed to perform the numerical simulation of multiphase flow. Based on the mixture model, the three phases of water, vapour and air are assumed as a single homogeneous fluid with the same velocity field and negligible slip velocity between the continuous and dispersed phases. Based on the above-mentioned assumptions the governing equations read:

$$\frac{\partial \rho}{\partial t} + \nabla \bullet (\rho \boldsymbol{u}) = 0 \tag{1}$$

$$\frac{\partial}{\partial t}(\rho \boldsymbol{u}) + \nabla \bullet (\rho \boldsymbol{u}\boldsymbol{u}) = -\nabla p + \nabla \bullet \left[\mu\left(\nabla \boldsymbol{u} + \nabla \boldsymbol{u}^T\right)\right] + \rho \boldsymbol{g} \tag{2}$$

$$\begin{cases} \rho = \rho_v \alpha_v + \rho_l \alpha_l + \rho_{ng}\alpha_{ng} \\ \mu = \mu_v \alpha_v + \mu_l \alpha_l + \mu_{ng}\alpha_{ng} \end{cases} \tag{3}$$

In the present simulations, the body force is neglected due to the minor effect of the body force on the cavitation. As a result, the last term on the right-hand side of equation (2) is not taken into account. Since it is intended to take the air into consideration, the third term with subscript *ng* which denotes the non-condensable gas is added to equation (3). As such, the mixture consists of three phases (i.e., water, vapour, and air), and the mixture model solves the continuity equation for the vapour volume fraction and air volume fraction. In addition, the mass transfer between the liquid and vapour phases is modelled. The equations are as follows:

$$\frac{\partial \rho_v \alpha_v}{\partial t} + \nabla \bullet (\rho_v \alpha_v \boldsymbol{u}) = R \tag{4}$$

$$\frac{\partial \rho_{ng}\alpha_{ng}}{\partial t} + \nabla \bullet \left(\rho_{ng}\alpha_{ng}\boldsymbol{u}\right) = 0 \tag{5}$$

$$\alpha_l + \alpha_v + \alpha_{ng} = 1 \tag{6}$$

The mass transfer between the liquid and vapour phases is governed by the source term R denoting the mass transfer per volume unit in both evaporation and condensation processes. It is worth mentioning that there is no mass transfer between the air phase with other phases. In this regard, the source term in Eq.5 is zero.

The Zwart-Gerber-Belamri (ZGB) cavitation model is employed to calculate the source term in the mass transfer equation (eq.4). In this respect, the source term R to describe evaporation ($R = R_e$) and condensation ($R = R_c$) is expressed by the following equations [31]:

$$\begin{cases} R_e = F_{vap}\dfrac{3\alpha_{nuc}(1-\alpha_v)\rho_v}{R_B}\sqrt{\dfrac{2}{3}\dfrac{p_v - p}{\rho_l}} p_v > p \\[2ex] R_c = -F_{cond}\dfrac{3\alpha_v\rho_v}{R_B}\sqrt{\dfrac{2}{3}\dfrac{p - p_v}{\rho_l}} p_v < p \end{cases} \tag{7}$$

where the empirical coefficients $F_{vap} = 50$ and $F_{cond} = 0.1$ are adopted for the water cavitating flow at ambient temperature. Also, the nucleation site volume fraction (α_{nuc}) is assigned to 5×10^{-4}, the fixed spherical bubble radius is equal to 1×10^{-6} m.

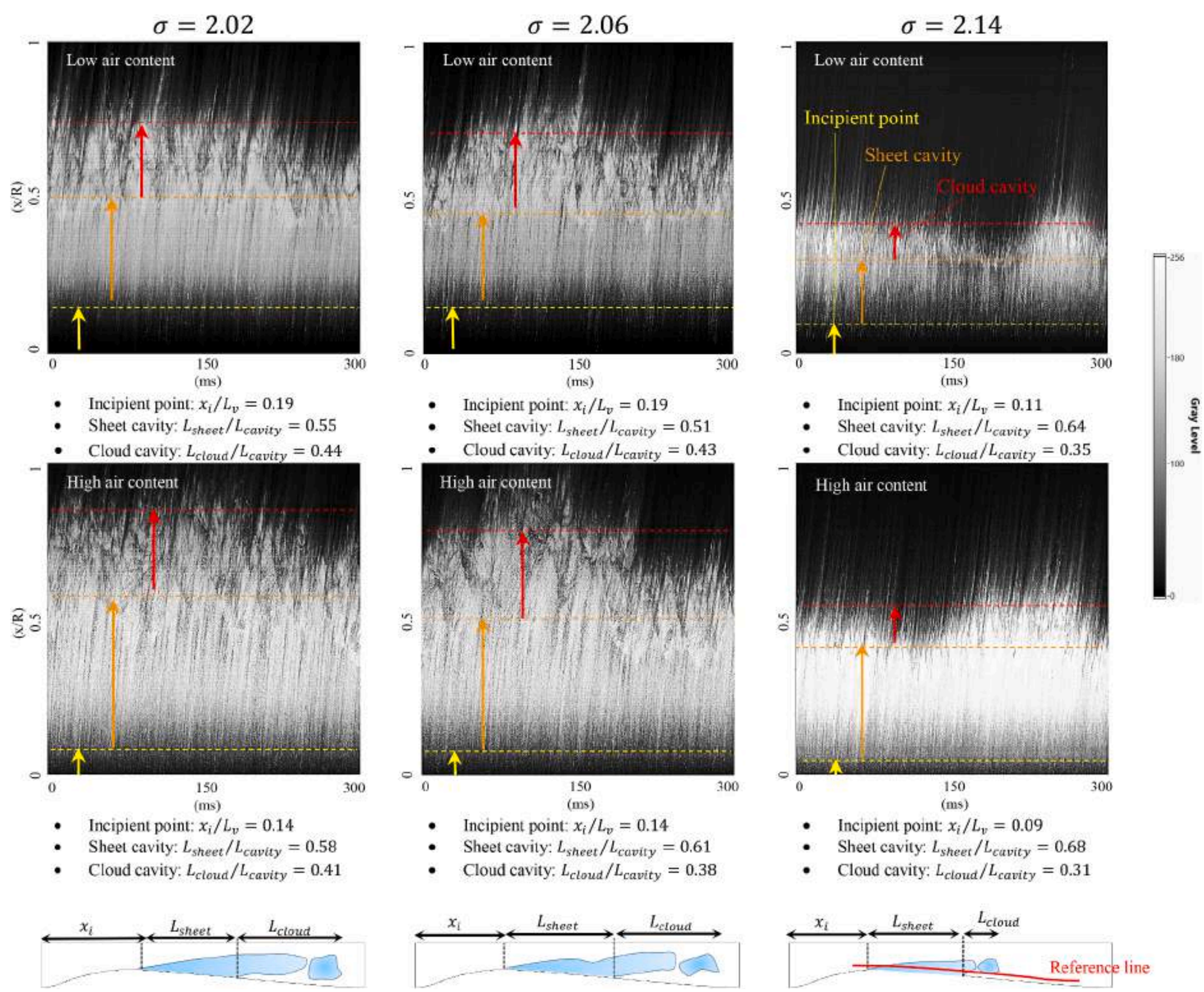

Fig. 11. Morphological analysis of incipient point, sheet cavity and cloud cavity ($\sigma = 2.02, 2.06, 2.14$, low and high air contents).

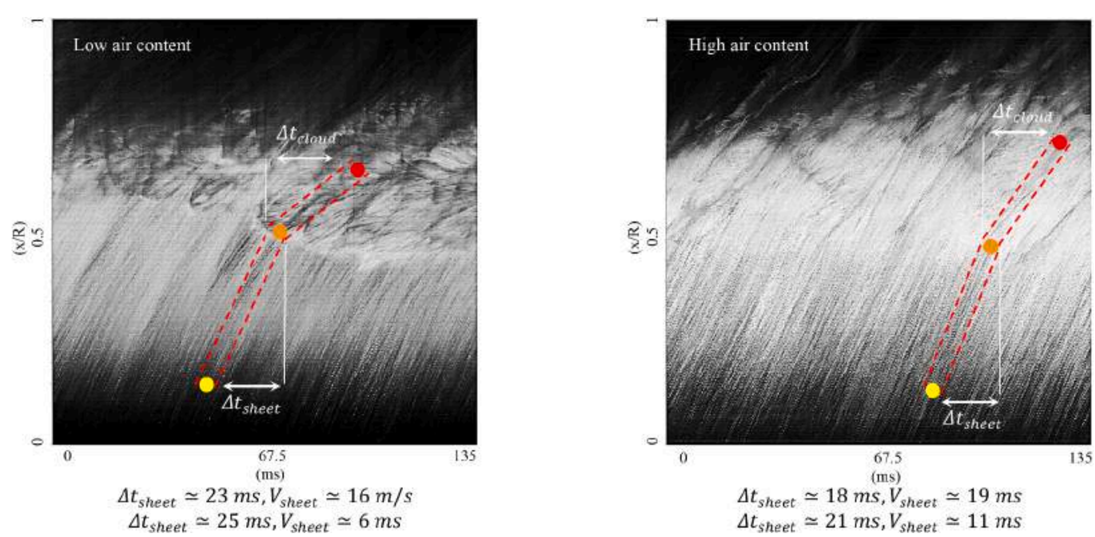

Fig. 12. Velocity analysis of sheet cavity and cloud cavity ($\sigma = 2.06$, low and high air contents).

3.2. Turbulence model

The RNG $k - \varepsilon$ is employed to model the turbulent cavitating flow and is defined as follows:

$$\frac{\partial(\rho k)}{\partial t} + \nabla \bullet (\rho \boldsymbol{u} k) = \nabla \bullet \left[\left(\mu + \frac{\mu_t}{\sigma_k} \right) \nabla k \right] + G_k - \rho\varepsilon, \tag{8}$$

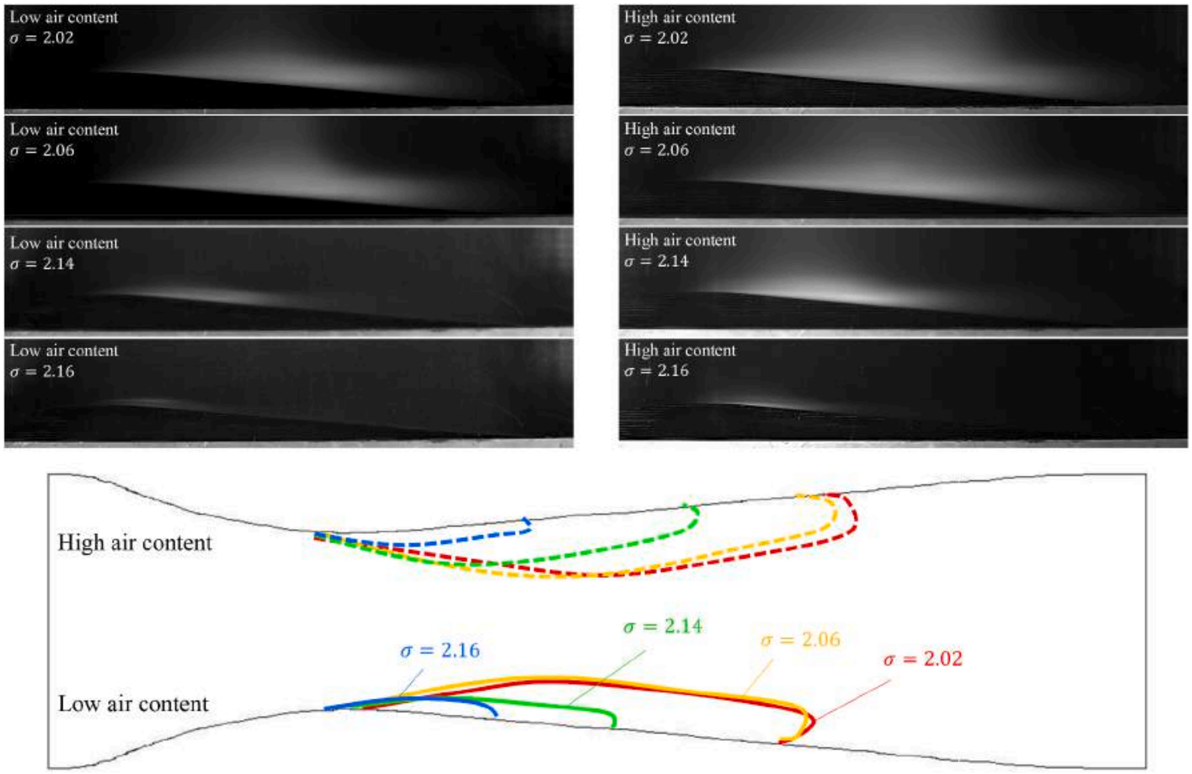

Fig. 13. Mean value of greyscale (above) and schematic drawing of cavity growth (bottom) over different cavitation numbers and air contents.

$$\frac{\partial(\rho\varepsilon)}{\partial t}+\nabla\bullet(\rho\boldsymbol{u}\varepsilon)=\nabla\bullet\left[\left(\mu+\frac{\mu_t}{\sigma_\varepsilon}\right)\nabla\varepsilon\right]+\frac{c_1\varepsilon}{k}G_k-c_2\rho\frac{\varepsilon^2}{k}. \tag{9}$$

where $\mu_t=\rho C_\mu k^2/\varepsilon$ defines the turbulent viscosity with $C_\mu=0.084$ [32]. Furthermore, k, ε and G_k show the turbulent kinetic energy, turbulent energy dissipation rate and production of turbulent energy term, respectively.

The standard form of the turbulence model usually overestimates the turbulent viscosity. Also, no treatment over the standard turbulence model is applied to deal with the high jump in density of the mixture. To overcome the damping effect, the standard turbulent viscosity is modified based on the Density Correction based Model (DCM) which was first proposed by Coutier-Delgosha et al. [28]. Using this correction, the turbulent viscosity is simply reduced in the region with a mixture of vapour and liquid. As a result, the damping effect of the standard turbulence model will be compensated. The modified turbulent viscosity is given as follows:

$$\mu_t=f(\rho)C_\mu k^2/\varepsilon, \tag{10}$$

where,

$$f(\rho)=\rho_v+\left(\frac{\rho_v-\rho}{\rho_v-\rho_l}\right)^n(\rho_l-\rho_v). \tag{11}$$

where the constant n is set to 10.

4. Computational domain, meshing and grid independence analysis

The computational domain's length and height, as well as the boundary conditions shown in Fig. 4, match the real physical dimensions of the test chamber. However, due to the symmetrical geometry of the Venturi nozzle, half of the domain is used for numerical simulation to reduce the computational cost. In addition, the calculation domain is extended at the outlet side to avoid backflow. The extended section is of the same length as the Venturi nozzle. The velocity inlet and pressure outlet boundary conditions are set on the left and right walls, respectively. Furthermore, the bottom wall, which is the surface of the Venturi nozzle, is assumed to be a non-slip, stationary surface; as well as the top wall is set as symmetry. Fig. 4 shows an overview of the grid. The domain is divided into three primary blocks. The gird is considered finer near the throat; as well as, adjacent to the wall. Based on the selected mesh distribution according to grid independence analysis, the computational domain has 70 and 260 nodes along the edge normal and along the Venturi surface, respectively. The domain had an overall width of 1.0 mm discretized by 3 layers. The whole mesh consisted of 61 k hexahedra elements and the value of y^+ on the wall was less than 1.

The grid was generated in ICEM CFD software. It was a 2D structured grid extruded to the overall width by 3 layers of 0.333 mm thickness each. Five different meshes were examined. Their parameters are summarized in Table 1.

The pressure distributions along the Venturi surface obtained for five various grid sizes are compared with the present experimental results for one case ($\sigma=2.02$ with low air content). Based on the comparison (see Fig. 5), it is determined that mesh distribution M4 is the best match for the experimental data and should be used for further investigations.

5. Results and discussion

The cavitating Venturi flow is studied based on experimental and numerical methods with special emphasis on the effect of dissolved air. Two levels of dissolved air and three cavitation numbers are taken into consideration. The transient pressure fluctuations are recorded using pressure transducers on the surface of Venturi, and the cavity evolution is visualized using the high-speed camera. Hence, the cavitation features are predicted using numerical simulations. The FFT, PSD and temporal/spatial grey level distribution are employed for the post-processing.

The averaged pressure distributions at the wall of the Venturi nozzle for various cavitation numbers and air contents are shown in Fig. 6. Considering the fact that the pressure distribution along the flow

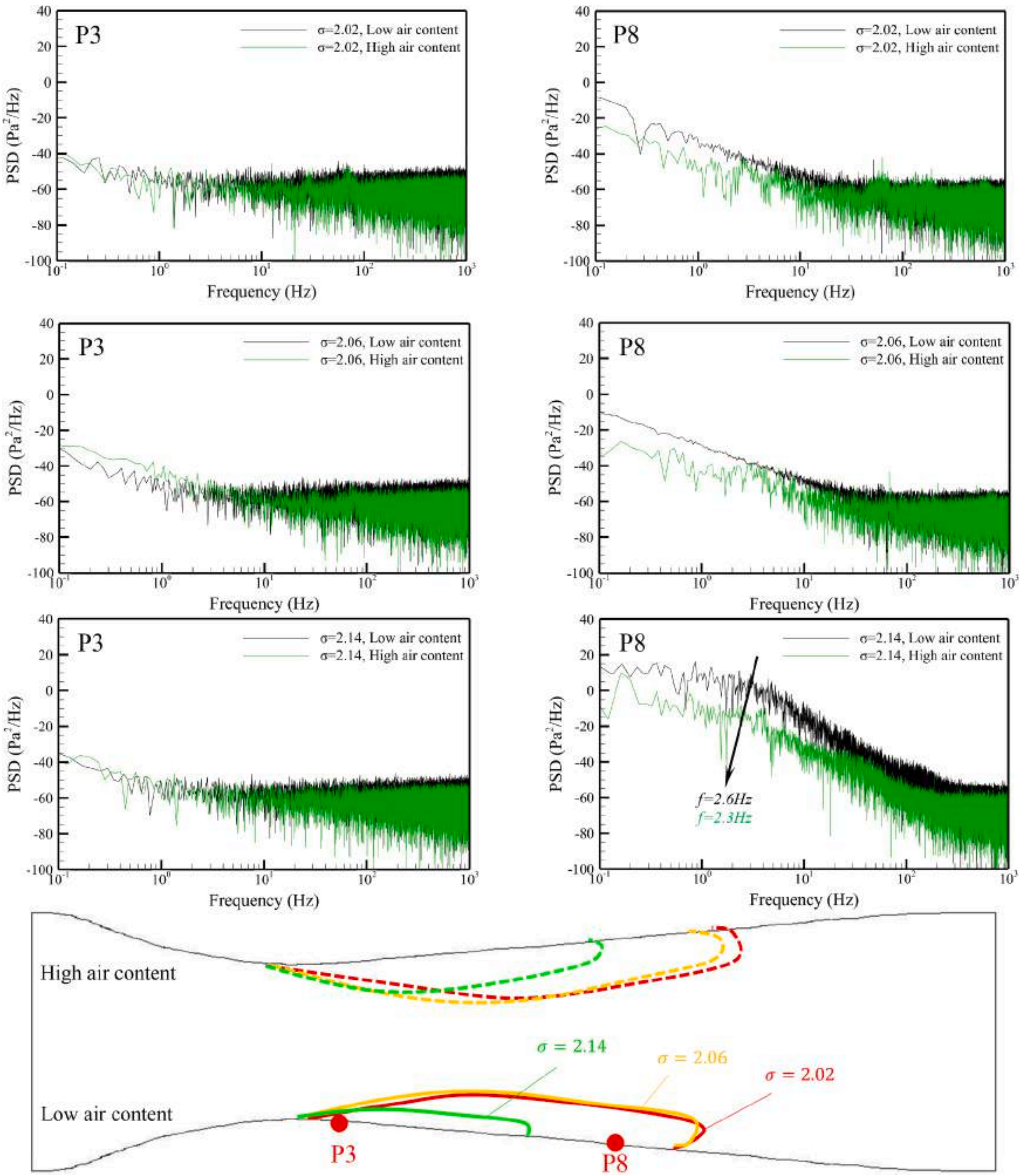

Fig. 14. Power spectral density (PSD) based on measured pressure fluctuation of *P*3 (left) and P8 (right) experimentally.

channel is crucial in showing the cavitation collapse process, special attention was paid to the pressure variation in various locations at different flow conditions. The averaged pressure stays constant and closes to the saturated vapour pressure during cavitation inception and development regions. It experiences a significant increase in the collapse region. The averaged pressure increases slowly along the flow channel in the downstream region where no cavitation exists. At high cavitation numbers, the unfavourable pressure gradient region is higher than at low cavitation numbers, resulting in rapid collapse and severe shock. However, it is observed that the general trend of the averaged pressure distribution is similar in experimental measurements and numerical calculations, it is understood that the collapse process happens further from the throat in numerical simulations. Although the impact of dissolved air on the averaged pressure distribution is negligible in inception and development regions, the pressure magnitude slightly drops when the amount of dissolved air is higher, regardless of the cavitation number.

The distributions of vapour and air volume fractions over the flow time and corresponding Continuous Wavelet Transform (CWT) are presented in Fig. 7. The following time-dependent distribution is predicted using numerical simulation. The Continuous Wavelet Transform (CWT) is employed to calculate the corresponding shedding frequency during various stages of the simulation. The continuous wavelet transform (CWT) is a formal (i.e., non-numerical) tool that provides an overcomplete representation of a signal by letting the translation and scale parameter of the wavelets vary continuously. The time-dependent distributions of volume fractions include two parts demonstrating the cases with low air and high air contents. It is concluded that the averaged vapour volume fraction remains at the same level when the air content enhances; however, its amplitude considerably rises. The latest observation declares that a larger cloud cavity emerges inside of the Venturi nozzle when the dissolved air increases. The level of dissolved air influences not only the structure of the cavity but also considerable impacts its dynamics. Regardless of the cavitation number, the shedding frequency is reduced when the level of dissolved air enhances. The shedding frequency decreases more in the cases with a higher cavitation number. As a result, the influence of dissolved air on the dynamic of the cavity is more considerable at the higher cavitation number.

The cavity evolution based on the numerical simulation for two cycles (i.e., fifth and sixth cycles) for $\sigma = 2.02$ with low air content is represented in Fig. 8. It should be noted that half of the computational domain is taken into consideration due to the symmetric geometry. Also, the interference effect between the bottom and upper parts of the cavitation inside the Venturi is neglected since those cavity closures are not merged in the considered operating conditions of this study. Two sequential cycles are presented to declare the possible similarity and differences in the cavity structure and evolution. It is observed that structures of sheet and cloud cavities are almost similar however, the separation point happens slightly earlier in the fifth cycle. The cycle starts with the inception of the sheet cavity. The incipient cavity is extended gradually. Then, the extended sheet cavity is torn from the separation point. As a result, two regions of the cavity appear. The torn part of the cavity enlarges and changes to a cloud cavity and the remained sheet cavity is shrunk till disappears. Afterwards, limited numbers of small cavities emerge at the throat of the Venturi nozzle which are shed significantly fast to reach the cloud cavity. The small cavities are merged into a cloud cavity making it larger. The adverse pressure that occurs adjacent to the Venturi surface causes separation of the cavity from the surface. The influence of the re-entrant jet on cavity separation is considerable and will be discussed in the following section. Finally, the separated cloud cavity sheds downstream.

The cavity evolution and the location of the re-entrant jet front between t = 8.3 ms to t = 55.4 ms are depicted in Fig. 9 based on experimental visualization. The images show the cavity evolution within half of the test section along with the Venturi nozzle for the case with $\sigma = 2.06$ and low air content. It should be noted that the average form of the cavity structure at the bottom and upper parts inside the Venturi is almost similar; however, the instantaneous parameters such as the location of the re-entrant jet and shed cloud cavity may have differences. The time range is selected to declare the behaviour of the re-entrant jet in a cycle. In some of the first images between t = 12.3 ms to t = 15.7 ms, the generated vortex is depicted by drawing the schematic arrows. It is observed that the shedding vortex is generated repeatedly in the cloud cavity region. The shedding vortex is inflated, detached and excessively shed to downstream. Going further downstream, the shedding vortices collapse when they reach the high-pressure zone outside of the cloud cavity region. Using images between t = 15.7 ms to t = 46.4 ms, it is focused on the location of the re-entrant jet. The red spots and the white dash line demonstrate the front of the re-entrant jet and its average movement, respectively. It is revealed that the re-entrant jet penetrates toward the throat being close to the wall. The re-entrant jet is not steadily moved forward or backward as it's pushed forth and back temporarily. Moving forward (S_1) and backward (S_2) took 16.5 ms and 10.8 ms respectively, which means that the penetration process needs to overcome the main flow.

The temporal-spatial grey level distributions at four different cross-sections ($x/L = 0.2, 0.35, 0.5, 0.65$) for the cases with $\sigma = 2.14$, low and high air contents are represented in Fig. 10. The cross-sections are specifically selected to show the behaviour of different regions like incipient zone, sheet cavity, cloud cavity and bubbly cloud cavity. First, it is observed that the strongest cavity region is generated in sections B and B', which are located near the throat and inside of the sheet cavity. Moreover, remarkable intensification of the cavity length has happened when the level of air content enhances which is obviously detectable at all cross-sections. In the case with a higher amount of dissolved air, the grey level distributions declare that many scattered bubbles existed in the chamber, especially around the throat where the pressure level is lower than in other regions.

To investigate the impact of cavitation number and level of air content on the structure of the cavity, morphological analysis is provided, as shown in Fig. 11, using the temporal-spatial grey level distribution. The ratio of inception point x_i and length of Venturi nozzle L_v is defined by x_i/L_v. At a higher cavitation number, it is concluded that the inception point is closer to the throat edge meaning that the cavitation is generated earlier locally. Similarly, the inception point gets closer to the leading edge by increasing air content. In addition, to compare the length of sheet cavity and cloud cavity with the length of full cavity zone, the ratios of L_{sheet}/L_{cavity} and L_{cloud}/L_{cavity} are defined, respectively. Comparing the length of the sheet cavity with the full cavity zone, it is clear that, in the case with a higher cavitation number, the cavity mainly consists of the sheet cavity regardless of the level of air content. The ratio L_{cloud}/L_{cavity} is inversely related to the cavitation number for both levels of air content. By adding dissolved air, the increment rate of L_{sheet}/L_{cavity} is higher than L_{cloud}/L_{cavity}. The latest observation demonstrates the higher effect of dissolved air on the sheet cavity than on the cloud cavity.

To analyse the velocity of flow inside of the sheet cavity and cloud cavity, the velocity analysis is carried out using temporal-spatial grey distribution level for the case with $\sigma = 2.06$, low and high air contents. For this purpose, the average angle of the grey level distribution in combination with a specified point, which shows the borders of the sheet cavity and cloud cavity, can be used, as shown in Fig. 12. It is worth mentioning that yellow, orange and red spots point out the start of sheet cavity, end of sheet cavity and end of cloud cavity, respectively. In the case with lower air content, the flow velocity inside the sheet cavity is around 16 m/s which is greater than the main flow velocity. However, the flow velocity in the cloud cavity is almost 6 m/s. As such, not only the flow velocity inside the sheet cavity is higher than the main flow velocity, but also it is higher than the velocity of the cloud cavity more than two times. By adding the dissolved air, flow velocities inside the sheet cavity and cloud cavity are almost equal to 19 m/s and 11 m/s, respectively, which are higher than flow velocity. It is concluded that adding the dissolved air results in an increase in flow velocity in the cavity zone.

Fig. 13 shows the mean value of the grey scale (above) and schematic of the cavity boundary to indicate the impact of cavitation number and the dissolved air content on the structure of the cavity. The mean value is taken over 300 ms of the captured movie covering five periods. Comparing the mean value over different cavitation numbers, it is confirmed that the bigger cavity is generated in the lower cavitation number. In addition, the remarkable influence of the dissolved air on the length of the cavity is visible where the bigger cavity appears in the cases with a higher amount of dissolved air. The boundary of cavities on different cavitation numbers and air contents are sketched schematically using the mean values.

The power spectral density (PSD) based on the pressure distribution recorded by pressure transducers $P3$ and P8 is presented in Fig. 14. The locations of pressure transducers $P3$ and P8 are shown on the wall of the Venturi nozzle. It can be seen that $P3$ is always located inside of the sheet cavity and P8 is also located inside, except case with $\sigma = 2.14$. It should be noted that three fast pressure sensors were used in the present experiments, installed at the inlet and in points $P3$ and P8. Since the shedding frequency must reflect the frequency of cloud cavity detachment, the pressure distribution which is going to be used to extract the shedding frequency needs to be located outside of the sheet cavity, where there exists a steady cavity region. As such, the pressure distribution inside the sheet cavity may not be desirable for measuring the shedding frequency. As can be seen in Fig. 14, no dominant peaks on the PSD plots can be detected till 1000 Hz for all cases except for P8 in the case with $\sigma = 2.14$. The frequency of 2.3 Hz and 2.6 Hz are measured. Overall, it can be concluded that not only the pressure distribution is not a reliable parameter to measure the shedding frequency since it is usually influenced by induced pressure shock wave inside of the Venturi nozzle, but also the location of the pressure transducer is so effective in determining the pressure fluctuation.

6. Conclusion

The main purpose of the present experimental/numerical research is to study the effect of dissolved air on the cavitating flow in the Venturi nozzle. For this purpose, experimental tests have been conducted in the closed-loop water tunnel. The water tunnel is equipped with a Venturi test section; as well as the measurement devices such as pressure transducers, vibration transducers and a high-speed camera. The experiential campaigns have been done in two levels of dissolved air and three cavitation numbers. Furthermore, the numerical simulation is carried out and the transient/averaged features of the cavitation process are predicted. Also, the post-processing techniques such as Fast Fourier Transform (FFT), Power Spectral Density (PSD), temporal/spatial Grey Level distribution and mean value grey level distribution are used. The following key results may be drawn:

- Addition of dissolved air reduces the shedding frequency in the range of 21 % to 38 % depending on the cavitation number.
- Not only the addition of dissolved air is influential on the morphology of the cavity, but also it changes the inception point of the sheet and cloud cavity.
- The travelling velocity of the cloud cavity reduces when the level of dissolved air enhances.
- The mean value of the grey scale declares that the cavity enlarges and shrinks by enhancing the level of dissolved air and cavitation number, respectively.
- When pressure fluctuation is used to measure the shedding frequency, it is necessary to avoid the side effects of external sources such as shock waves. In addition, the best location of the pressure sensor must be determined based on the location sensitivity analysis to be sure that the captured frequency demonstrates the shedding frequency.

Funding

The presented work was supported by the Polish National Science Centre funds within the project UMO-2016/21/B/ST8/01164. Moreover, the project was additionally supported by the Department of Power Engineering and Turbomachinery, The Silesian University of Technology within the grant BKM-586/RIE5/2022 (08/050/BKM_22/274). Also, the authors certify that they have NO conflict of interest.

CRediT authorship contribution statement

Emad Hasani Malekshah: Conceptualization, Methodology, Software, Investigation, Validation, Formal analysis, Writing – original draft, Writing – review & editing. **Włodzimierz Wróblewski:** Conceptualization, Investigation, Writing – review & editing, Supervision, Funding acquisition. **Mirosław Majkut:** Software, Investigation.

Declaration of Competing Interest

The authors declare that they have no known competing financial interests or personal relationships that could have appeared to influence the work reported in this paper.

Data availability

The authors do not have permission to share data.

References:

[1] C.E. Brennen, Cavitation and bubble dynamics, Cambridge University Press, 2014.
[2] G. Mancuso, M. Langone, G. Andreottola, A critical review of the current technologies in wastewater treatment plants by using hydrodynamic cavitation process: principles and applications, J. Environ. Health Science and Eng. 18 (1) (2020) 311–333.
[3] E. Hasani Malekshah, W. Wróblewski, Merging theory-based cavitation model adaptable with non-condensable gas effects in prediction of compressible three-phase cavitating flow, Int. J. Heat Mass Transf. 196 (2022/11/01/ 2022,), 123279, https://doi.org/10.1016/j.ijheatmasstransfer.2022.123279.
[4] B. Huang, Y.L. Young, G. Wang, W. Shyy, Combined experimental and computational investigation of unsteady structure of sheet/cloud cavitation, J. Fluids Eng. 135 (7) (2013) pp.
[5] Z. Wang, B. Huang, G. Wang, M. Zhang, F. Wang, Experimental and numerical investigation of ventilated cavitating flow with special emphasis on gas leakage behavior and re-entrant jet dynamics, Ocean Eng. 108 (2015) 191–201.
[6] T. Liu, B. Huang, G. Wang, M. Zhang, D. Gao, Experimental investigation of the flow pattern for ventilated partial cavitating flows with effect of Froude number and gas entrainment, Ocean Eng. 129 (2017) 343–351.
[7] R.T. Knapp, Recent investigations of the mechanics of cavitation and cavitation damage, Transactions of the ASME 77 (1955) 1045–1054.
[8] R. Furness and S. Hutton, "Experimental and theoretical studies of two-dimensional fixed-type cavities," 1975.
[9] Y. Kawanami, H. Kato, H. Yamaguchi, M. Tanimura, and Y. Tagaya, "Mechanism and control of cloud cavitation," 1997.
[10] B. Stutz, J. Reboud, Experiments on unsteady cavitation, Exp. Fluids 22 (3) (1997) 191–198.
[11] B. Stutz, J.-L. Reboud, Two-phase flow structure of sheet cavitation, Phys. Fluids 9 (12) (1997) 3678–3686.
[12] B. Huang, Y. Zhao, G. Wang, Large eddy simulation of turbulent vortex-cavitation interactions in transient sheet/cloud cavitating flows, Comput. Fluids 92 (2014) 113–124.
[13] B. Ji, X. Luo, R.E. Arndt, Y. Wu, Numerical simulation of three dimensional cavitation shedding dynamics with special emphasis on cavitation–vortex interaction, Ocean Eng. 87 (2014) 64–77.
[14] B. Ji, X. Luo, R.E. Arndt, X. Peng, Y. Wu, Large eddy simulation and theoretical investigations of the transient cavitating vortical flow structure around a NACA66 hydrofoil, Int. J. Multiph. Flow 68 (2015) 121–134.
[15] B. Ji, Y. Long, X.-P. Long, Z.-D. Qian, J.-J. Zhou, "Large eddy simulation of turbulent attached cavitating flow with special emphasis on large scale structures of the hydrofoil wake and turbulence-cavitation interactions," *Journal of Hydrodynamics*, Ser. B 29 (1) (2017) 27–39.
[16] A. Kubota, H. Kato, H. Yamaguchi, and M. Maeda, "Unsteady structure measurement of cloud cavitation on a foil section using conditional sampling technique," 1989.
[17] T. Pham, F. Larrarte, and D. H. Fruman, "Investigation of unsteady sheet cavitation and cloud cavitation mechanisms," 1999.
[18] B. Charrière, J. Decaix, E. Goncalvès, A comparative study of cavitation models in a Venturi flow, European Journal of Mechanics-B/Fluids 49 (2015) 287–297.
[19] T. Liu, B. Khoo, W. Xie, Isentropic one-fluid modelling of unsteady cavitating flow, J. Comput. Phys. 201 (1) (2004) 80–108.
[20] I. Senocak, W. Shyy, Interfacial dynamics-based modelling of turbulent cavitating flows, Part-1: Model development and steady-state computations, Int. J. Numer. Meth. Fluids 44 (9) (2004) 975–995.
[21] A.K. Singhal, M.M. Athavale, H. Li, Y. Jiang, Mathematical basis and validation of the full cavitation model, J. Fluids Eng. 124 (3) (2002) 617–624.
[22] X. Peng, et al., Combined experimental observation and numerical simulation of the cloud cavitation with U-type flow structures on hydrofoils, Int. J. Multiph. Flow 79 (2016) 10–22.
[23] T. Chen, B. Huang, G. Wang, Numerical study of cavitating flows in a wide range of water temperatures with special emphasis on two typical cavitation dynamics, Int. J. Heat Mass Transf. 101 (2016) 886–900.
[24] B. Ji, X. Luo, Y. Wu, X. Peng, H. Xu, Partially-Averaged Navier-Stokes method with modified k–ε model for cavitating flow around a marine propeller in a non-uniform wake, Int. J. Heat Mass Transf. 55 (23–24) (2012) 6582–6588.
[25] Q. Wu, B. Huang, G. Wang, Lagrangian-based investigation of the transient flow structures around a pitching hydrofoil, Acta Mech. Sin. 32 (1) (2016) 64–74.
[26] W. Wróblewski, K. Bochon, M. Majkut, K. Rusin, E.H. Malekshah, Numerical study of cavitating flow over hydrofoil in the presence of air, Int. J. Numer. Meth. Heat Fluid Flow (2021).
[27] W. Wróblewski, K. Bochon, M. Majkut, E.H. Malekshah, K. Rusin, M. Strozik, An experimental/numerical assessment over the influence of the dissolved air on the instantaneous characteristics/shedding frequency of cavitating flow, Ocean Eng. 240 (2021/11/15/ 2021,), 109960, https://doi.org/10.1016/j.oceaneng.2021.109960.
[28] O. Coutier-Delgosha, R. Fortes-Patella, J.-L. Reboud, Evaluation of the turbulence model influence on the numerical simulations of unsteady cavitation, J. Fluids Eng. 125 (1) (2003) 38–45.
[29] E. Hasani Malekshah, W. Wróblewski, K. Bochon, M. Majkut, Evaluation of modified turbulent viscosity on shedding dynamic of three-phase cloud cavitation around hydrofoil – numerical/experimental analysis, Int. J. Numer. Meth. Heat Fluid Flow vol. ahead-of-print, no (2022), https://doi.org/10.1108/HFF-03-2022-0188 ahead-of-print,.

[30] G. Mancuso, Experimental and numerical investigation on performance of a swirling jet reactor, Ultrason. Sonochem. 49 (2018/12/01/ 2018,) 241–248, https://doi.org/10.1016/j.ultsonch.2018.08.011.
[31] A. Kubota, H. Kato, H. Yamaguchi, A new modelling of cavitating flows: a numerical study of unsteady cavitation on a hydrofoil section, J. Fluid Mech. 240 (1992) 59–96.
[32] V. Yakhot, S. Orszag, S. Thangam, T. Gatski, C. Speziale, Development of turbulence models for shear flows by a double expansion technique, Phys. Fluids A 4 (7) (1992) 1510–1520.

Paper IV:

Experimental analysis on unsteady characteristics of sheet/cloud cavitating Venturi flow under the effect of dissolved air

archives
of thermodynamics
Vol. **43**(2022), No. 3, 63–84
DOI: 10.24425/ather.2022.143172

Experimental analysis on unsteady characteristics of sheet/cloud cavitating Venturi flow under the effect of dissolved air

EMAD HASANI MALEKSHAH*
WŁODZIMIERZ WRÓBLEWSKI
KRZYSZTOF BOCHON
MIROSŁAW MAJKUT
KRZYSZTOF RUSIN

Silesian University of Technology, Department of Power Engineering and Turbomachinery, Konarskiego 18, 44-100 Gliwice, Poland

Abstract The highly dynamic and unsteady characteristics of the cavitating flow cause many negative effects such as erosion, noise and vibration. Also, in the real application, it is inevitable to neglect the dissolved air in the water, although it is usually neglected in the previous works to reduce the complexity. The novelty of the present work is analysing the impact of dissolved air on the average/unsteady characteristics of Venturi flow by conducting sets of experimental tests. For this purpose, two different amounts of dissolved air at five pressure levels (i.e. five different sets of cavitation numbers) were considered in the study of cavitating flow inside a Venturi nozzle. The fast Fourier transform analysis of pressure fluctuations proved that the shedding frequency reduces almost by 50% to 66%, depending on the case, with adding the amount of dissolved air. However, the reduction of 14% to 25% is achieved by the vibration transducers. On the other hand, the cavity enlarges as well as bubbly flow is observed in the test chamber at a higher level of dissolved air. Furthermore, it is observed that the re-entrant jet, as the main reason for the cavity detachment, is more effective for the detachment process in cases with a lower level of dissolved air, where the re-entrant jet front penetrates more toward the leading edge.

Keywords: Cavitating flow; Venturi nozzle; Dissolved air; Unsteady characteristic; Experimental observation

*Corresponding Author. Email: emad.hasani@polsl.pl

Nomenclature

A	–	area
C_p	–	pressure coefficient
H	–	height
L	–	length
p	–	pressure
q	–	flow rate
t	–	evolution time
t_0	–	onset time of cavitation
Re	–	Reynolds number
u	–	velocity
W	–	width
x	–	coordinate along the cavitation chamber axis

Greek symbols

μ	–	dynamic viscosity
σ	–	cavitation number
τ	–	one ninth of a period

Subscripts

in	–	inlet
l	–	liquid
th	–	throat
sat	–	saturation

1 Introduction

Cavitation is known as a sudden phase change phenomenon, which usually can be observed in high-speed flow and is due to low-pressure regions falling below the local saturation pressure of the operating fluid. This phenomenon exists in many applications such as hydro-power turbines, high-speed propellers, pumps and rockets [1–4]. The existence of highly dynamic cavitating flow, in particular with intensive cavity breakup, may lead to severe destructive effects such as erosion on the surface of the object, vibration, noise and high-frequency pressure fluctuations [5–10].

The Venturi-type sections and foils have been usually employed to study the unsteady cavitating flow and measure the corresponding parameters. These investigations help the researchers to improve their understanding of this phenomenon. Chen *et al.* [8] investigated the cavitation evolution based on experimental and numerical tests to evaluate the influence of exciting pressure fluctuations within a convergent-divergent Venturi nozzle.

They used a modified RNG k-ε turbulence model to predict the dynamics of cavitating flow. It is confirmed by both numerical and experimental results that the quasi-periodic sheet-cloud cavitating flow has three main stages, which are: 1) attached cavity growth, 2) attached cavity shedding, 3) detached cavity growth and collapse. Also, it is reported that the main source of the pressure fluctuation is the acceleration originating from changes in cavity volume. In experimental work, Stutz and Reboud [11] analysed the cavitating flow structure as two-phase flow. They considered both types of quasi-steady sheet cavitation and unsteady cloud cavitating flow within a convergent-divergent nozzle. They measured the mean volume fraction of the cavity and the velocity distribution inside the cavity closure. In another work, Stutz and Reboud [12] demonstrated that the break-off of sheet cavity is due to the re-entrant jet which flows periodically upstream. Shi *et al.* [13] studied the cavitating flow inside a Venturi tube based on experimental and numerical approaches. They have considered two geometries with convergent angles of 19° and 45° to evaluate the influence of configuration on the local and global characteristics of Venturi flow. It is proved that the changing of convergent angle has a considerable impact on the generation of cavitation at the throat and the related local characteristics. The influence of several geometrical parameters on cavitation initiation detected by a hydrophone and microbubble formation monitored by a high-speed camera was explored mathematically and experimentally by Li *et al.* [14]. Regardless of the design of the Venturi tube, the flow resistance generated by cavitation increases linearly with the decreasing downstream cavitation number while the upstream cavitation number remains constant in the cavitation regime. Low cavitation inception and strong microbubble production come from a small outlet angle. Furthermore, the increased flow resistance and dissolved gas concentration were observed to increase the degree of microbubble generation. Niedźwiedzka *et al.* [15] carried out an analytical investigation on cavitating flow inside the Venturi tube. The purpose of this paper is to verify the similarity of the characteristics obtained and those described in the literature, as well as to verify the range of the obtained characteristics in relation to parallel diagrams. Both objectives were met, indicating that the quality of the previous experimental data is at least adequate for achieving the project's major goal: the development of numerical models of cavitating flow in a Venturi tube. Charrière and Goncalves [16] performed a numerical study on periodic cavitation shedding inside a Venturi tube. One-fluid compressible simulations of a self-sustained oscillating cavitation region forming along a Venturi geometry are shown in this study.

A void ratio transport equation model drives mass transfer between the phases. Travelling pressure waves' importance in the physical mechanism is demonstrated. The significance of considering a non-equilibrium condition for the vapour phase is also highlighted. Fang *et al.* [17] studied the cavity shedding mechanism in a Venturi tube based on the numerical analysis. A numerical investigation of a Venturi reactor is undertaken in this paper, based on experimental research, using a self-developed compressible cavitation phase-change solution to discover the shedding mechanism. The key characteristics and physical indicators of the re-entrant jet and bubbly shock mechanisms are explored using the quasi-periodic evolution of the cavity combined with the contour of stream velocity and pressure. The evolution of cavitation in a Venturi reactor with a long throat was discovered to be split into four stages: conception, development, two shedding stages and collapse. The separation between the cavity and the wall is the most prominent feature of the shedding mechanism caused by the re-entrant jet. Reisman *et al.* [18] studied the short period and significantly large amplitude during cloud cavitation collapse. They have detected several types of propagating structures, so-called bubbly shock waves. In addition, Leroux *et al.* [19] studied the pressure fluctuation originated from the unsteady cavitating flow. It is interestingly declared that the shock wave created by the collapse of the cloud cavity has probably contributed to the occurrence of the re-entrant jet. Wu *et al.* [20] conducted a couple of experiments to analyse the sheet cavity structure followed by bubbly flow within a convergent-divergent test section. They used fast pressure transducers to collect the pressure distribution and a high-speed camera to record the flow structures. It is indicated that the frequency of recurring sheet cavity has a reverse relationship with the velocity of inlet flow. Also, it is observed that the flow structure changes from vortex shedding included with entrapped thin cavities to sheet cavity producing cloud cavity by re-entrant jet. Barre *et al.* [21] carried out a combined numerical and experimental work in order to study the attached sheet cavity structure in Venturi geometries. They employed a new double optical probe and a novel data processing approach for the evaluation of the velocity distribution and void ratio of the cavity. When the experimental and numerical results are compared, it is interestingly indicated that the applied barotropic model predicts the local characteristics of the sheet cavity well. On the contrary, some discrepancies can be detected between numerical predictions and experimental measurements. Dular *et al.* [22] conducted some experiments to visualize the cavitating flow and the related characteristics that deal with its unsteady behaviour influenced by the different scale ratios. This work was motivated by the vague data provided by experimental measurement inside a Venturi-type section which was scaled down 10 times [23]. A significant influence on the cavitation process is found on a small scale. Especially the height of the test section plays a major role in the dynamics of the re-entrant jet that drives the periodical shedding observed at a large scale.

The researchers have introduced many types of approaches to control the unsteady dynamic behaviour of the cavitating flow, like geometrical parameters, the flexibility of foil, and scale factor [24–27]. However, it is worth mentioning that the impact of dissolved air in the water and ventilation is not negligible. In some cases, they have a considerable effect on the structure of the cavity and unsteady characteristics. Kawakami *et al.* [28] calculated the pressure spectrum at the suction side for the NACA 0015 hydrofoil by considering two amounts of dissolved air including 6 ppm and 13 ppm. Based on the results, the considerable effect of dissolved air on the pressure spectrum trends is proved. Numerous peaks are observed for the case with high gas content regardless of cavitation number located between $\sigma/2\alpha = 2$ to 4, where σ and α show the cavitation number and angle of attack, respectively. Reversely, a steady behaviour is seen for $\sigma/2\alpha$ less than 4 when the gas content is low. Pham *et al.* [29] used pressure transducers and a high-speed camera to study the unsteady behaviour of the sheet/cloud cavity and the mechanism which can be employed to control its instability using obstacles and air injection. The results showed that applying an obstacle has a remarkable effect on reducing the amplitude of the pressure flections. Also, the structure of the cavity closure is changed by employing air injection as well as; the positive effect of air injection on suppressing the cloud cavitation is approved. Wang *et al.* [30] evaluated the characteristics of the unsteady sheet/cloud cavity in a convergent-divergent channel under the effect of air injection. They conducted a series of experiments in the $10°$ divergent section equipped with a ventilation slot located near the throat. They observed that the air injection from the throat into the sheet cavity causes suppression in the cavitating flow and pressure fluctuations. Also, the fast Fourier transform (FFT) analysis showed that the period of cavitation cycle and shedding frequency enhances and reduces, respectively, due to the air injection.

This experimental work aims to investigate the cavitating flow in a Venturi nozzle. The cavitation process is visualized using a high-speed video camera, and the unsteady characteristics of the cavitation phenomenon are measured employing the pressure and vibration transducers. The main purpose of the present work is to investigate what is usually neglected in the research on cavitating flow that is the dissolved air influence on the local and global characteristics of the cavitation process.

2 Experimental installation

2.1 Test rig

The experimental tests were carried out using a hydraulic test setup equipped with a cavitation chamber fabricated at the laboratory of the Department of Power Engineering and Turbomachinery at the Silesian University of Technology. Figure 1 presents the main components used in the close-loop installation. The water flow is streamed by a pump with 30 kW power output in the pipe installation with 200 mm diameter. A manual valve and electromagnetic flowmeter are installed in the circuit after the pump to control the flow rate. It is to note that the cavitation test chamber is located about 5000 mm above the pump level. Then, the water passes through two 90° elbows. The honeycomb is installed before the inlet nozzle where the shape of the pipe alters from circular to rectangular. In addition, the dif-

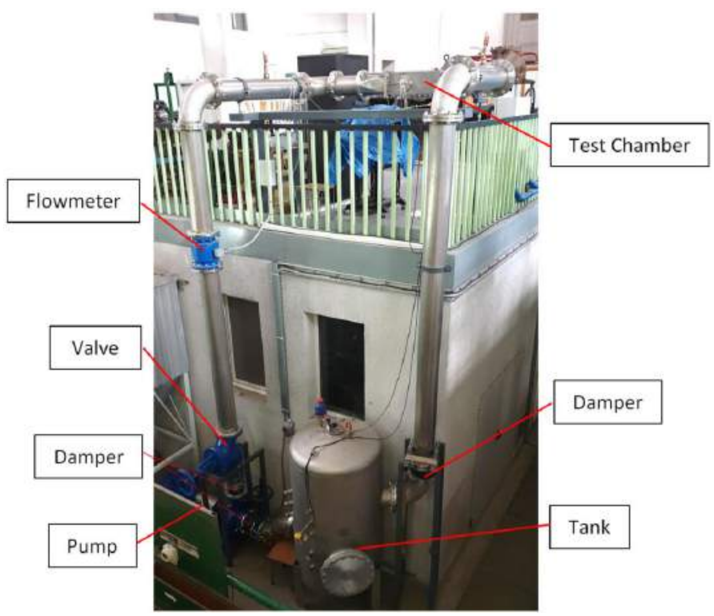

Figure 1: Closed-loop installation with the main components.

fuser is employed after the test chamber to change the pipe shape back to circular. Afterwards, the water flow passes two elbows and is headed to the tank fixed at the ground level. The capacity of the tank is about 1.5 m^3, which is designed to be able to control the pressure value. For this purpose, an internal elastic airbag is mounted at the top section inside of the tank. The airbag is connected with the compressed air system making it possible to be enlarged and with a release valve creating the control system to regulate the pressure level of the circuit. Based on the design of the present closed-loop circuit, the test can be run with a constant flow rate and different pressure values at the inlet to the test chamber. Three elastic couplings (damper) are used to damp the induced forces and vibration during the test campaign which are located before the tank, after the pump and one between the tank and pump.

The cavitation test chamber had a rectangular cross-section, as shown in Fig. 2. The transparent window, which was made of polycarbonate, was placed at the one sidewall of the test chamber to enable optical access and observations. The length (L), height (H) and width (W) of the chamber are equal to 700 mm, 189 mm and 70 mm, respectively. The length of Venturi throat (L_{th}) is equal to 113.5 mm, hence the ratio of throat length to height of the chamber is defined as $L_{th}/H \simeq 0.6$. The ratio of chamber height to width was fixed as $H/W = 2.7$.

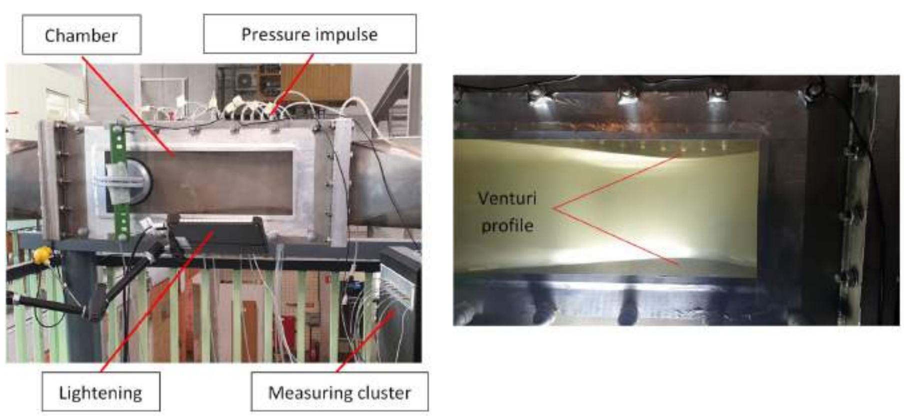

Figure 2: A view of cavitation test chamber including related components (left) and Venturi nozzle (right).

The schematic configuration of the Venturi nozzle included with internal channels and the location of pressure taps are represented in Fig. 3. The Venturi profile is equipped with 10 internal channels connecting the pressure taps (*P1*$-$*P10*) at the surface of the Venturi nozzle to the pressure transducers. The diameter of pressure taps is equal to 1 mm. Moreover, two more pressure taps are installed at the inlet ($P_{\rm in}$) and outlet ($P_{\rm out}$). In addition, the vibration due to cavitating flow is measured using two vibration sensors installed at the back-side wall. As shown in Fig. 3 (right), the Venturi profiles at the bottom and top of the channel are the same. To show more details during the visualization process, only half of the Venturi nozzle is captured considering the fact that the cavitating flow is symmetric.

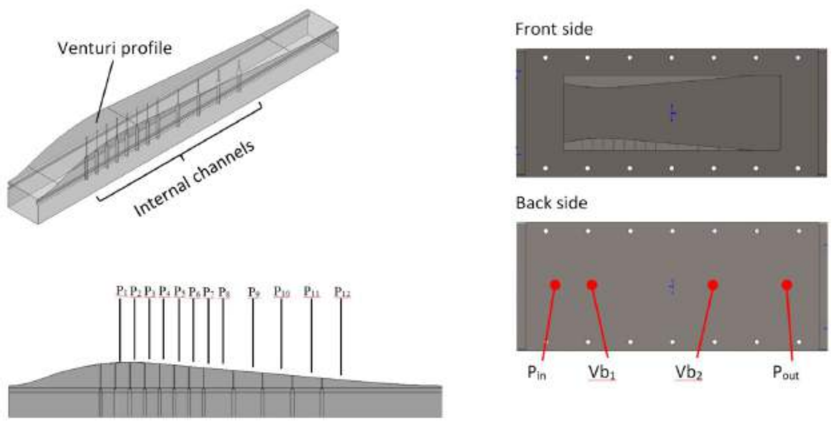

Figure 3: 3D view of Venturi profile (left) and the location of pressure taps (P) and piezoelectric transducers – accelerometers (Vb) (right).

2.2 Measurement system

The measuring system including a high-speed camera, image control, rig control, lightening and test chamber is shown in Fig. 4. The instantaneous pressure values at the surface of the top Venturi profile are measured with the low-frequency sampling rate by pressure transducers Aplisens PC-28. The accuracy of 0.16% is approved for the full scale amounting to 160 kPa. The pressure sensor type XP5 with amplifier ARD154 is used as a fast pressure sensor at pressure tap *P8*. The full scale of this type of sensor is given by 500 kPa with an accuracy of 0.25%. The pressure impulse tubes are used to send the pressure signal to the measuring cluster. Furthermore, the same low-frequency pressure sensors are used to measure the pressure level at the outlet. The temperature of the water is measured by the resistance thermometer Aplisens CT-GN1 Pt100, having a full scale of 0$-$100°C and accuracy of $\pm(0.15\,\mathrm{K} + 0.002|\mathrm{T}|)$. The flow rate is measured by electromagnetic flowmeter UniEMP-05 DN200 with a measuring range up to 1080 m^3/h and accuracy of $\pm 0.25\%$ of the measured value.

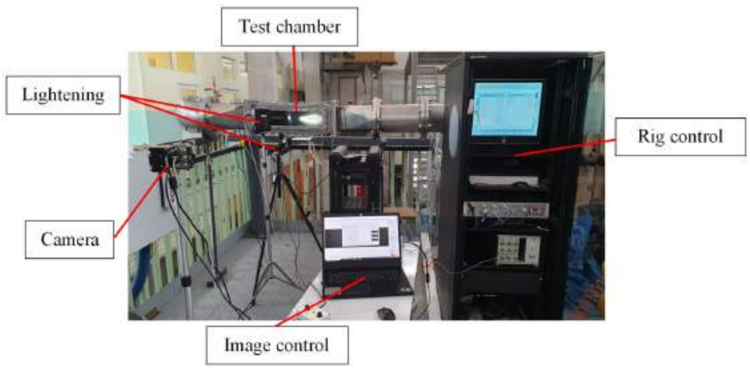

Figure 4: The measuring system including a high-speed camera, image control, rig control, lightening and test chamber.

The vibroacoustic signals were recorded from outside the chamber by two piezoelectric transducers. The two stiff piezoelectric accelerometers KD35 (RTF) are located externally on the sidewall of the test chamber. The Vb_1 is located about one profile chord before the leading edge and the second Vb_2 about one and a half chord behind the trailing edge, Fig. 3 (right). The accelerometers are connected with the 0028 (RFT) type charge amplifier connected with the fast response converter AC 16 bit, 250 kS/s. The system was calibrated before experiments using the electrodynamic vibration calibrator EET101 (RFT) type. The value of achieved limiting error was less than 5%.

The measurement system used in the research is based on a National Instruments module NI USB 6216. The NI/PXI-6255 module co-operates with measuring clusters which include sets of sensors and measuring transducers. The executive elements and the data acquisition process are managed by a system programmed in the LabView environment.

An important part of the data acquisition system is image recording and processing. The structures of cavitation were recorded by a high-speed video camera Phantom Miro C110. The recording speed was set to 3200 frames per second with a spatial resolution of 960×280 pixels. The settings of the camera resolution and speed were selected as a compromise between image quality and picture size.

2.3 Flow conditions

The volume flow rate of the circuit was kept constant in all rounds of experiments. So, the velocity of the stream is constant at the inlet, throat and outlet during the time, when the inlet velocity is calculated as $u_{\text{in}} = q/\rho_l A_{\text{in}}$ $= 10.4$ m/s, where q, A_{in} represent the volume flow rate and area of inlet section, respectively. The Reynolds number is calculated as $\text{Re} = \dfrac{\rho_l u_{\text{in}} L_{th}}{\mu_l}$ $\simeq 1.15 \times 10^6$, where ρ_l, u_{in}, L_{th}, and μ_l represent the density of water, velocity of flow at the inlet, length of Venturi throat, and dynamic viscosity of water, respectively.

The temperature of the water was between 27°C to 31°C at two successive rounds of the test campaign dealing with 4 different cavitation numbers (i.e. two contents of dissolved air and two pressure levels). The detected temperature differences were due to the friction between the stream and the pipe as well as differences in the ambient conditions, but not exceeded 2°C at each test campaign.

Each case with different inlet pressure, saturation pressure, density and inlet velocity, is defined with a single cavitation number calculated as follows:

$$\sigma = \frac{p_{\text{in}} - p_{\text{sat}}}{0.5 \rho_l u_{\text{in}}^2}\,, \tag{1}$$

where p_{in} and p_{sat} denote the static pressure at the inlet and water saturation pressure, respectively. Also, the value of inlet pressure is based on the average pressure calculated from instantaneous pressure fluctuations during the round of the related experiment. Furthermore, the saturation pressure is calculated based on the average temperature calculated over the related experiment. Also, ρ_l shows the density of water calculated at the corresponding temperature and pressure at each case with the nominal cavitation number. Finally, u_{in} represents the velocity at the inlet, which is also based on the average value.

In the present work, five levels of rig pressure (150, 155, 160, 165, and 170 kPa), which are categorized with different names as PT150, PT155, PT160, PT165, and PT170 and represented by cavitation number, and two air contents (i.e high and low) are studied. It should be noted that two first letters is abbreviation of pressure transducer (PT), and the number denotes the pressure level. The corresponding cavitation number for each case is presented in Table 1.

Table 1: Cavitation numbers for the experimental cases.

	Case name				
	PT150	PT155	PT160	PT165	PT170
Air content	Cavitation number				
Low: 6.13 mg/l	2.01	2.04	2.10	2.20	2.33
High: 14.83 mg/l	2.04	2.07	2.08	2.18	2.35

The experimental tests are conducted based on two levels of dissolved oxygen of 2.4 mg_O_2/l and 5.8 mg_O_2/l. The multifunction meter CF-401 is employed to measure the oxygen levels before and after each experimental campaign. The average value of the oxygen is reported in this work. Based on Henry's law, it corresponds to the air content of 6.13 mg_air/l and 14.83 mg_air/l, respectively.

3 Results and discussion

The main aim of the present experimental work is to investigate the effect of dissolved air on the cavitating flow inside a Venturi nozzle. Two amounts of air content, so-called high and low levels, with 6.13 mg_air/l and 14.83 mg_air/l, respectively; and five levels of rig pressure were taken into consideration. Thus, five sets of cavitation numbers, as presented in Table 1, are taken into consideration. The evolution of the cavitation process was visualized using a high-speed camera and image processing. In addition, the unsteady characteristics of cavitating flow such as pressure fluctuation and vibration were recorded using pressure and vibration transducers. The FFT analysis was employed to detect the main frequency of shedding.

3.1 Pressure coefficient distribution

The pressure coefficient distributions for different cavitation numbers are presented in Fig. 5. The presented pressure coefficient distribution is based on the measured pressure values at the surface of the Venturi profile and calculated as follows:

$$C_p = \frac{p - p_{\text{in}}}{0.5\rho_l u_{\text{in}}^2} \,. \tag{2}$$

It is observed that there is a strong pick near the throat in all cases. In the cases with a higher air content, the difference of the pressure coefficient correspondence to different cavitation numbers is more significant. In the

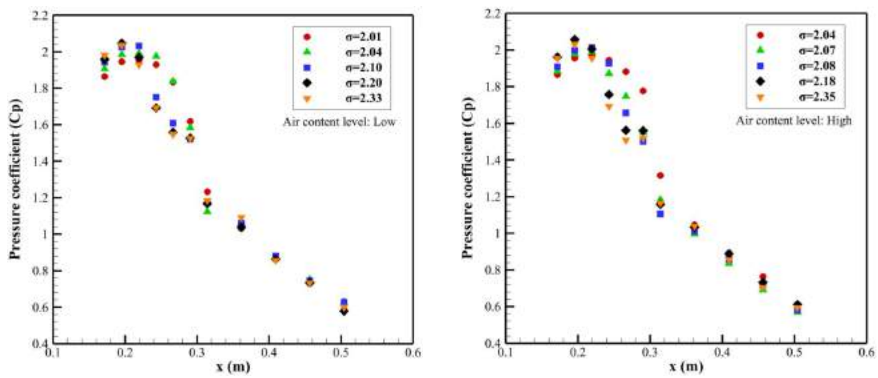

(a) (b)

Figure 5: Pressure distribution coefficient at the surface of Venturi nozzle along the cavitation test chamber axis as a function of cavitation number at two air contents.

case with lower air content, the flat distribution of pressure coefficient is observed in a very small region close to the throat. By increasing the amount of dissolved air, the flat distribution extended for all cases, especially the one with a lower cavitation number. It means that the cavity closure elongated through the channel. In addition, the sudden pressure drop is due to the transition from sheet cavity to cloud cavity since there is a considerable pressure difference between inside and outside of the cavity closure.

3.2 Fast Fourier transform analysis

In Fig. 6, the fast Fourier transform (FFT) analysis is employed to extract the frequency associated with the unsteady behaviour of the cavitating flow over different cavitation numbers. The FFT analysis is based on the pressure fluctuation measured by the fast pressure sensor located at P_8 and vibration fluctuations collected by the sensor Vb_2. Using the provided FFT analysis, it is possible to detect the influence of air content and cavitation number on the rate of cavity evolution. It is expected that the frequency of shedding would enhance with the cavitation number since smaller cavities oscillate faster than larger ones. This is what is concluded by the present FFT analysis for lower air content, but is not applied to the higher one. In addition, the FFT analysis of vibration approves the reverse relationship of the cavitation number and frequency. In low air content, the frequency provided by vibration FFT analysis reduces from 8 Hz to 6 Hz as the cavitation number enhances. No difference is detected in the vibration frequency at the higher air content. On the other hand, the changes in the frequency of cavitation cloud shedding, dealing with different air contents, are more observable in the lower cavitation number. The shedding frequency reduces when the air content rises. Thus, one can conclude that increasing air content results in stabilization of the cavitation flow as the cavity evolution lasts longer.

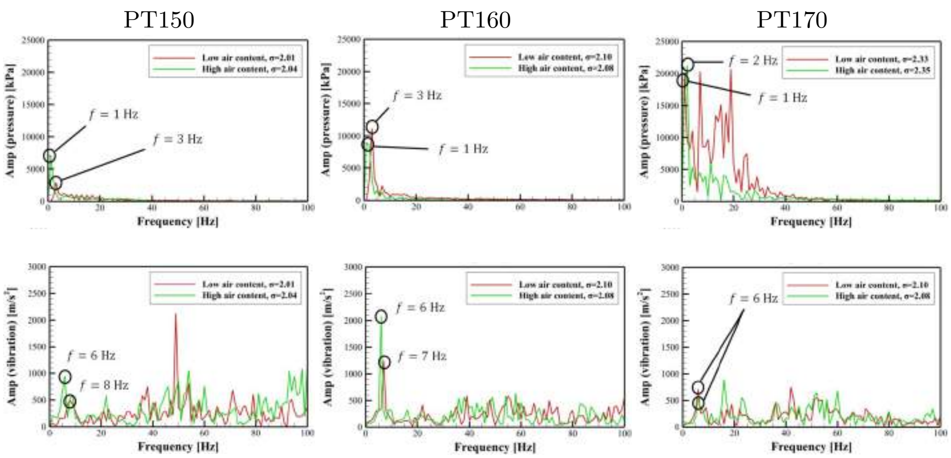

Figure 6: FFT analysis based on pressure fluctuation collected by fast pressure sensor *P8* and vibration transducer Vb_2.

3.3 Pressure and vibration fluctuations

Figure 7 shows the instantaneous pressure fluctuation collected by the fast pressure sensor (P_8) and vibration sensor (Vb_2). Firstly, the collected data show the high dynamic behaviour and unsteady characteristic of the cavitating flow. Based on the fluctuation plots, it can be concluded that the unsteadiness and the cavitation number have a reverse relationship since the pressure difference between the minimum and maximum peaks is higher in the cases with lower cavitation number. Furthermore, the stronger unsteadiness of the cavitating flow at a lower cavitation number can be concluded by the vibration fluctuation, where the average difference between the minimum and maximum points is higher than in other cases. On the other hand, the higher level of dissolved air in water results in a stable cavitation process, which is proved by comparing the pressure and vibration ranges.

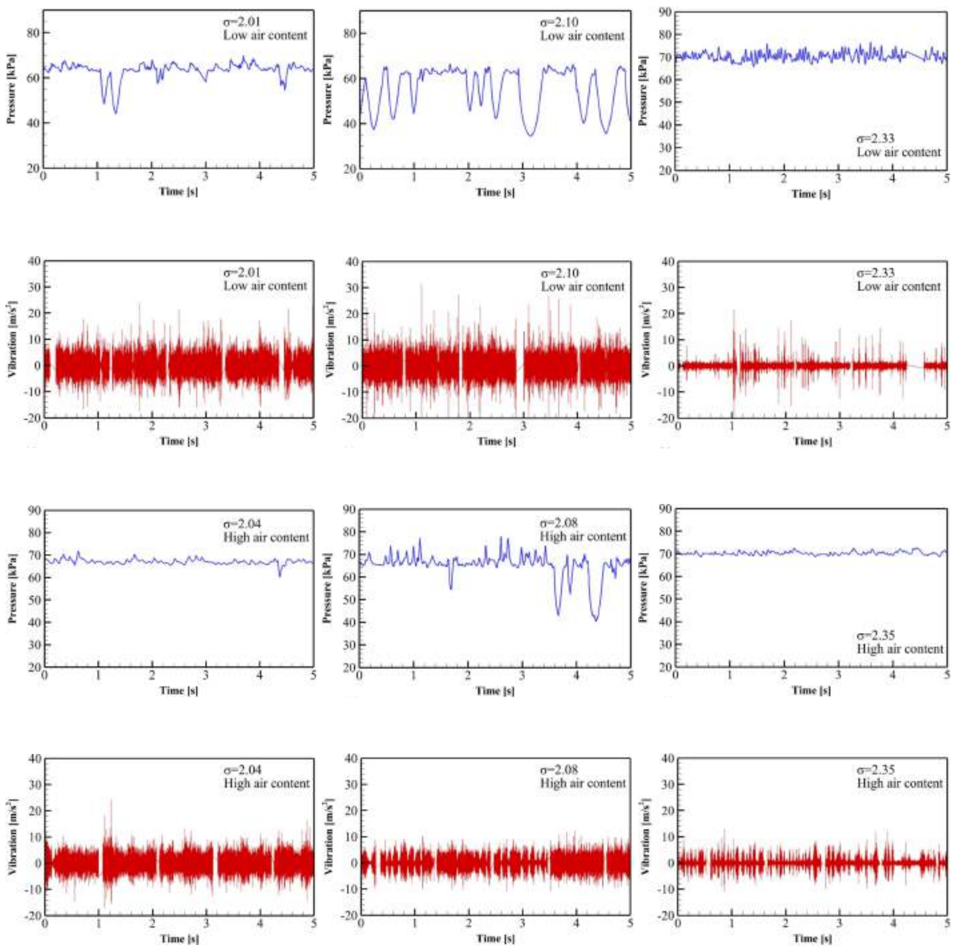

Figure 7: Pressure and vibration fluctuations for different air volume fractions and cavitation numbers.

3.4 Cavity evolution visualization

The evolutions of cavitating flow over one period are presented in Figs. 8–9, where t, t_0, and τ present the evolution time, onset time of cavitation and one ninth of a period, respectively. Based on the presented visualizations, significant influence on the cavitation flow is observed considering various air contents and pressure levels. Thus, the cavity evolution is required to be studied from both points of view, separately. Comparing the cases at lower and higher pressure levels, it may be understood that the area of cavity closure is elongated and covers a larger area of the channel when the pressure level is lower.

Low air content ($\sigma = 2.01$) High air content ($\sigma = 2.04$)

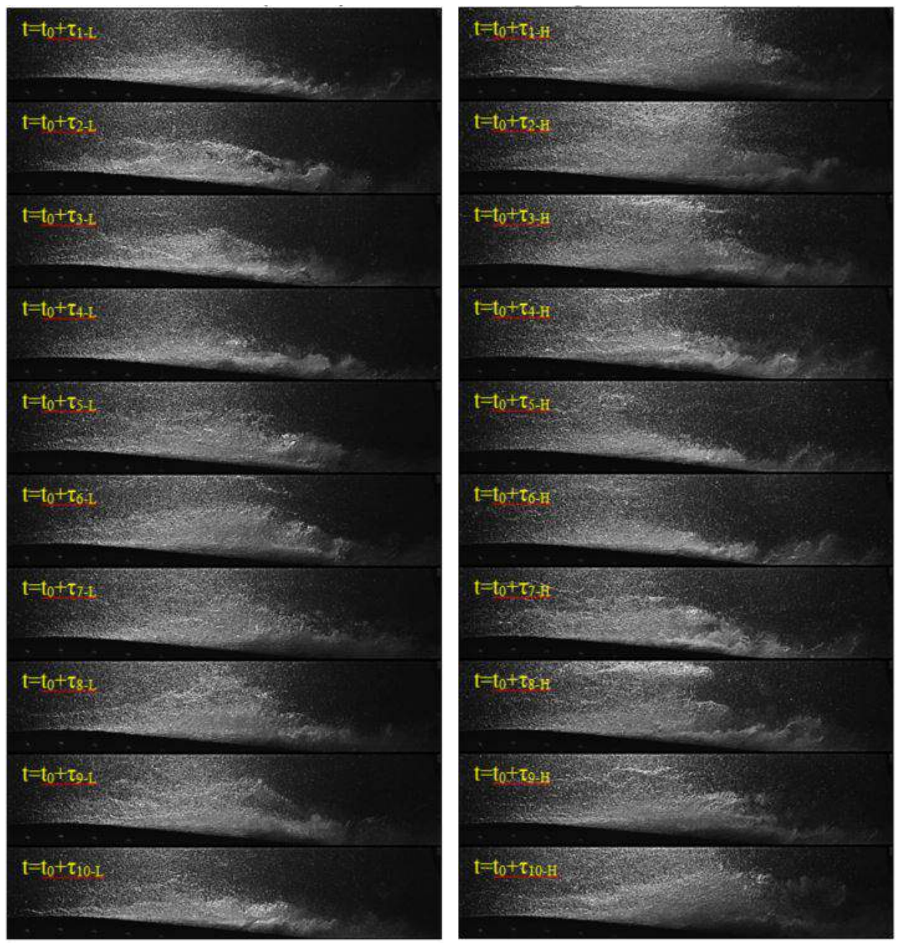

Figure 8: Experimental visualization of cavity evolution in one period for PT150.

At the low pressure level, it is observed that the steady cloud cavity exists during the period. On the contrary, when the pressure level increases, no cloud cavity can be found in some time intervals. Furthermore, it is hard to recognize the detachment and shedding process in the case with the high pressure level. Hence, the air content in the water has a remarkable influence on the size, frequency and configuration of the cloud cavity. Liquids

Low air content ($\sigma = 2.10$) High air content ($\sigma = 2.08$)

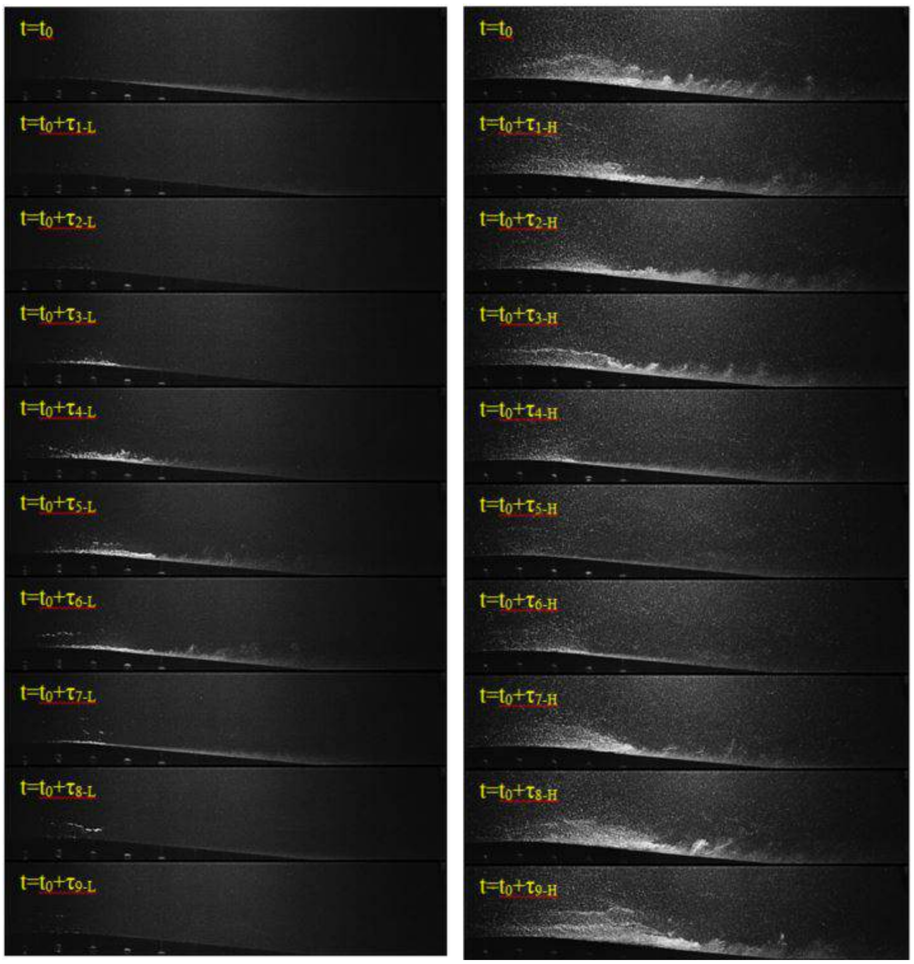

Figure 9: Experimental visualization of cavity evolution in one period for PT160.

and solids exhibit practically no change in solubility with changes in pressure. Gases as might be expected, increase in solubility with an increase in pressure. Henry's law states that the solubility of a gas in a liquid is directly proportional to the pressure of that gas above the surface of the solution. If the pressure is increased, the gas molecules are "forced" into the solution since this will best relieve the pressure that has been applied. The relationship between pressure and the solubility of a gas as described quantitatively by Henry's law can be defined as $C = kP$, where C denotes the concentration of dissolved gas at equilibrium, P shows the partial pressure of the gas and k is Henry's law constant. Thus, it is expected that the dissolved air releases from the water partially in the regions with low pressure. It is known that the local pressure inside the cavity is lower than in other regions, which results in decreasing the solubility. The released dissolved air causes the creation of a larger sheet cavity. In addition, a larger sheet cavity can be easier detached by the re-entrant jet. Overall, it is likely to have a larger cloud cavity with a faster shedding process. This can be observed in the visualized cavity evolution, as the larger cavity exists during the period for all cavitation numbers.

3.5 Influence of dissolved air on re-entrant jet

Figure 10 shows the evolution of the re-entrant jet based on the dissolved air content for PT150. In the present figure, the cavity region, including the

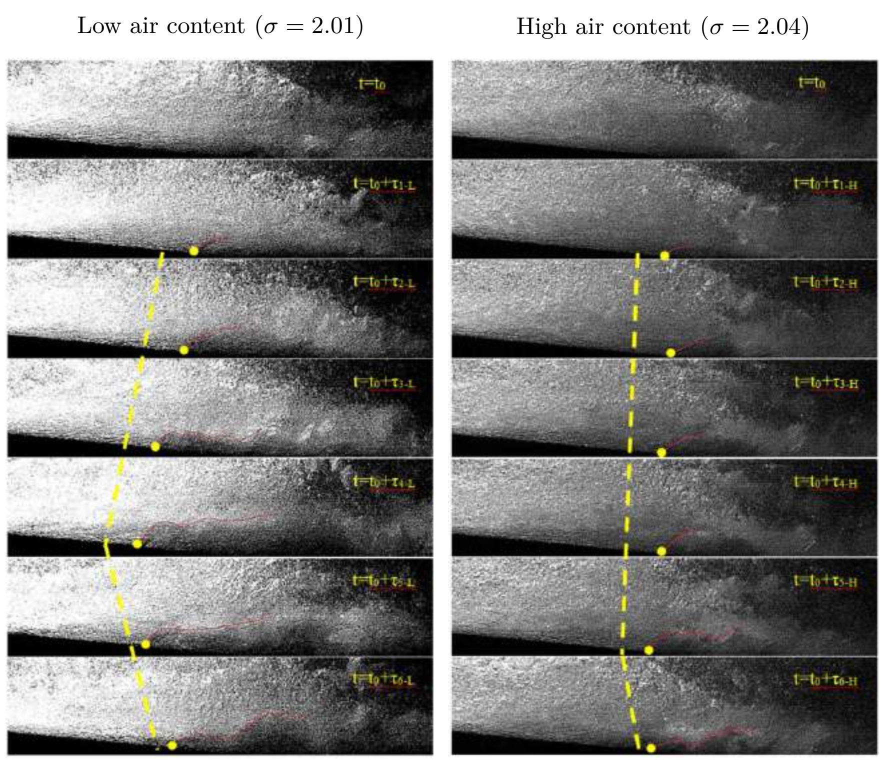

Figure 10: Influence of dissolved air volume fraction on the re-entrant jet for PT150.

sheet and cloud cavity, are shown with white and grey colours depending on the density of the bubble, and the pure water can be detected in black colour. The periodic shedding of cavitation cloud is one form of cavitation instability common to both external bodies and internal cavitating flows. The transient nature of the instability is known to be dependent upon a liquid sublayer referred to as a re-entrant jet. Despite the importance of the re-entrant jet, the mechanism by which it controls the periodic motion is not entirely understood. As a result, it is worth keeping this phenomenon under investigation dealing with different influential parameters. The re-entrant jet establishes when the vapour vortex inside the cavity becomes strong. Then, the re-entrant jet flows upstream along the nozzle wall toward the throat. In the present figure, one can characterize the re-entrant jet when the grey level of pixels slightly reduces to the black level. Hence, it is to note that the re-entrant jet mainly consists of pure liquid. On the other hand, not all of the re-entrant jets can change the type of cavity from sheet to cloud, but just the ones with strong momentum. It is required for the re-entrant jet to penetrate enough beneath the sheet cavity to be able to detach it. Overall, when the re-entrant jet arrives at the rear front of the sheet cavity and penetrates enough on it, it will cut off the sheet cavity and detach the whole or part of it. The detached portion of the sheet cavity moves downstream and collapses in the high-pressure region. As shown in Fig. 10, the re-entrant jet moves upstream and detaches parts of the sheet cavity, and then it deteriorates and moves back when its momentum gets low. With increasing the dissolved air content, the penetration level of the re-entrant jet reduces compared to the case with lower air content. This causes less cloud cavity and collapse and more sheet cavity, which improves the stability of the cavitating flow.

Figure 11 represents the result of image processing to show the effect of dissolved air content on the cavity length. This analysis is performed for three cases of PT140, PT150 and PT160 for both levels of air contents (i.e. low and high air contents). Calculation of the normalized cavity area was performed based on the colour-filtering technique. Figures like Fig. 11 were used to analyze the total share of black, white and grey pixels in the image. Thus, the normalized cavity (NCA) area was calculated as NCA $= 1 - (\text{black area }\%/100)$. When employing this parameter, it was possible to make a relative comparison between the cavity areas. It is declared that the length of the cavity has a direct relationship with the level of dissolved air. As the level of dissolved air increases, the cavity length enlarges in all cases.

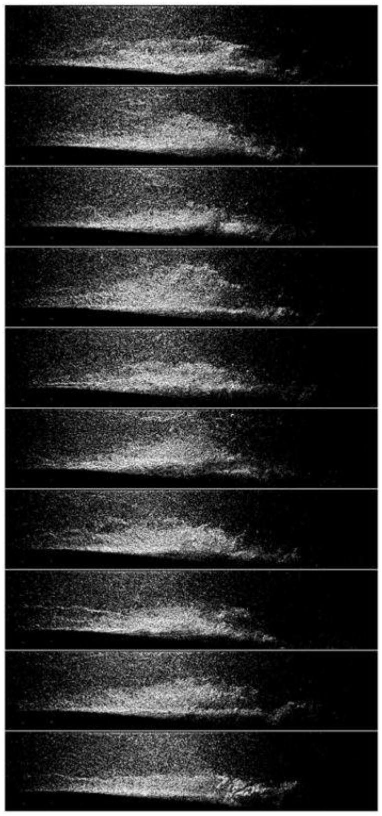

(a)

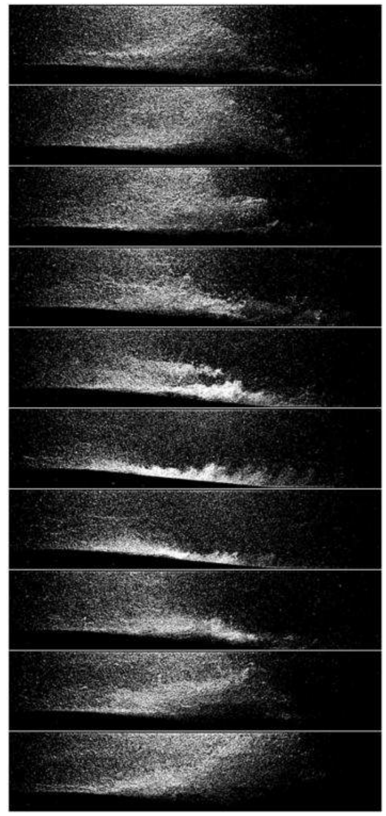

(b)

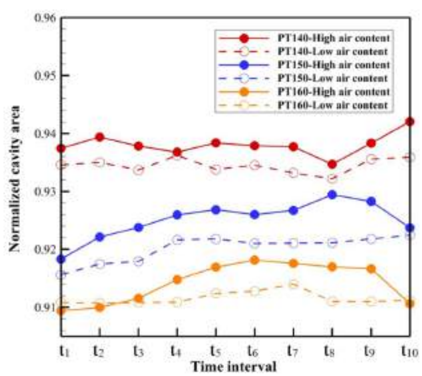

(c)

Figure 11: Sample of cavity area detection over a period based on colour-filtering process: (a) PT140 – low air content, (b) PT140 – high air content; (c) a quantitative result of normalized cavity area over a time period.

4 Conclusion

The present work aims to investigate the cavitating flow inside a Venturi nozzle. The influence of the dissolved air in the water and two pressure levels (i.e four different cavitation numbers) is taken into consideration. The experimental observations are carried out in the closed-loop cavitation tunnel located at the Department of Power Engineering and Turbomachinery of the Silesian University of Technology. Also, the high-speed camera and image processing are used to visualize the cavity structure and evolution. In addition, the pressure and vibration transducers are employed to collect the local instantaneous characteristics of the cavitation process. The following key results have been concluded:

1. The periodical behaviour of internal cavitating flow around the Venturi nozzle is proved using pressure and vibration fluctuations.

2. The shedding frequency is in the range of 2–3 Hz and 1–2 Hz in the cases with low and high air contents.

3. Based on the fast Fourier transform analysis of pressure fluctuation, the shedding frequency reduces between 50% to 60%, depending on the case, when the air content increases.

4. The reduction of 14% to 25% is observed for shedding frequency recorded in the FFT of vibration plots.

5. The cavity closure is elongated with the increasing content of dissolved air.

6. The re-entrant jet plays a more important role to generate the cloud cavity at low dissolved air content.

7. A larger sheet attached cavity is found in cases with a high dissolved air content.

Acknowledgement The presented work was supported by the Polish National Science Centre within the project UMO-2016/21/B/ST8/01164.

Received 24 February 2022

References

[1] Brennen C.E.: *Cavitation and Bubble Dynamics*. Cambridge Univ. Press, 2014.

[2] Malekshah E.H., Wróblewski W., Bochon K., Majkut M.: *Evaluation of modified turbulent viscosity on shedding dynamic of three-phase cloud cavitation around hydrofoil–numerical/experimental analysis*. Int. J. Numer. Method. H. (in press).

[3] Wróblewski W., Bochon K., Majkut M., Malekshah E.H., Rusin K., Strozik M.: *An experimental/numerical assessment over the influence of the dissolved air on the instantaneous characteristics/shedding frequency of cavitating flow. Ocean Eng.* **240**(2021), 109960.

[4] Niedźwiedzka A., Schnerr G.H., Sobieski W.: *Review of numerical models of cavitating flows with the use of the homogeneous approach*. Arch. Thermodyn. **37**(2016), 2, 71–88.

[5] Joseph D.D.: *Cavitation in a flowing liquid. Phys. Rev. E,* **51**(1995), 3, R1649-R1650. https://doi.org/10.1103/PhysRevE.51.R1649.

[6] Paik B.-G., Kim K.-S., Kim K.-Y., Ahn J.-W., Kim T.-G., Kim K.-R., Jang Y.-H., Lee S.-U.: *Test method of cavitation erosion for marine coatings with low hardness*. Ocean Eng. **38**(2011), 13, 1495–1502.

[7] Chen G., Wang G., Hu C., Huang B., Zhang M.: *Observations and measurements on unsteady cavitating flows using a simultaneous sampling approach*. Exp. Fluids **56**(2015), 2, 1–11.

[8] Chen G., Wang G., Hu C., Huang B., Gao Y., Zhang M.: *Combined experimental and computational investigation of cavitation evolution and excited pressure fluctuation in a convergent–divergent channel*. Int. J. Multiphas. Flow **72**(2015), 133–140.

[9] Simpson A., Ranade V.V.: *Modeling hydrodynamic cavitation in venturi: Influence of venturi configuration on inception and extent of cavitation*. AIChE J. **65**(2019), 1, 421–433.

[10] Wróblewski W., Bochon K., Majkut M., Rusin K., Malekshah E.H.: *Numerical study of cavitating flow over hydrofoil in the presence of air*. Int. J. Numer. Method. H. **32**(2021) 5, 1440–1462.

[11] Stutz B., Reboud J.: *Experiments on unsteady cavitation*. Exp. Fluids **22**(1997), 3, 191–198.

[12] Stutz B., Reboud J.L.: *Two-phase flow structure of sheet cavitation*. Phys. Fluids. **9**(1997), 12, 3678–3686.

[13] Shi H., Li M., Nikrityuk P., Liu Q.: *Experimental and numerical study of cavitation flows in venturi tubes: From CFD to an empirical model*. Chem. Eng. Sci. **207**(2019), 672–687.

[14] Li M., Bussonničre A., Bronson M., Xu Z., Liu Q.: *Study of Venturi tube geometry on the hydrodynamic cavitation for the generation of microbubbles*. Miner. Eng. **132**(2019), 268–274.

[15] Niedźwiedzka A., Sobieski W.: *Analytical analysis of cavitating flow in Venturi tube on the basis of experimental data*. Tech. Sci. **19**(2016), 3, 215–229.

[16] Charričre B., Goncalves E.: *Numerical investigation of periodic cavitation shedding in a Venturi*. Int. J. Heat Fluid Fl. **64**(2017), 41–54.

[17] Fang L., Li W., Li Q., Wang Z.: *Numerical investigation of the cavity shedding mechanism in a Venturi reactor*. Int. J. Heat Mass Tran. **156**(2020), 119835.

[18] Reisman G., Wang Y.-C., Brennen C.E.: *Observations of shock waves in cloud cavitation*. J. Fluid Mech. **355**(1998), 255–283.

[19] Leroux J.-B., Astolfi J. A., Billard J.Y.: *An experimental study of unsteady partial cavitation*. J. Fluids Eng. **126**(2004), 1, 94–101.

[20] Wu X., Maheux E., Chahine G.L.: *An experimental study of sheet to cloud cavitation*. Exp. Therm. Fluid Sci. **83**(2017), 129–140.

[21] Barre S., Rolland J., Boitel G., Goncalves E., Patella R.F.: *Experiments and modeling of cavitating flows in Venturi: attached sheet cavitation*. Eur. J. Mech. B-Fluid. **28**(2009), 3, 444–464.

[22] Dular M., Khlifa I., Fuzier S., Maiga M.A., Coutier-Delgosha O.: *Scale effect on unsteady cloud cavitation*. Exp. Fluids **53**(2012), 5, 1233–1250.

[23] Coutier-Delgosha O., *et al.*: *Local measurements in cavitating flow by ultra-fast X-ray imaging*. In: Proc. Fluids Engineering Division Summer Meet. **43734**(2009), 371–379.

[24] Xu S., Wang J., Cheng H., Ji B., Long X.: *Experimental study of the cavitation noise and vibration induced by the choked flow in a Venturi reactor*. Ultrason. Sonochem. **67**(2020), 105183.

[25] Long X., Zhang J., Wang J., Xu M., Lyu Q., Ji B.: *Experimental investigation of the global cavitation dynamic behavior in a venturi tube with special emphasis on the cavity length variation*. Int. J. Multiphas. Flow **89**(2017), 290–298.

[26] Tomov P., Khelladi S., Ravelet F., Sarraf C., Bakir F., Vertenoeuil P.: *Experimental study of aerated cavitation in a horizontal Venturi nozzle*. Exp. Therm. Fluid Sci. **70**(2016), 85–95.

[27] Kozák J., Rudolf P., Hudec M., Urban O., Štefan D., Huzlík R., Čala M.: *Investigation of the cavitation within venturi tube: influence of the generated vortex*, In: Advances in Hydroinformatics. Springer, 2018, 1049–1067.

[28] Kawakami D.T., Qin Q., Arndt R.: *Water quality and the periodicity of sheet/cloud cavitation*. In: Proc. Fluids Engineering Division Summer Meet. **41995**(2005), 513–517.

[29] Pham T., Larrarte F., Fruman D.H.: *Investigation of unsteady sheet cavitation and cloud cavitation mechanisms*. J. Fluids Eng. **121**(1999), 2, 289–296.

[30] Wang C., Huang B., Zhang M., Wang G., Wu Q., Kong D.: *Effects of air injection on the characteristics of unsteady sheet/cloud cavitation shedding in the convergent-divergent channel*. Int. J. Multiphas. Flow **106**(2018), 1–20.

Paper V:

Effect of turbulence modelling and non-condensable gas on cloud cavity dynamics

International Journal of Heat and Fluid Flow 98 (2022) 109070

Contents lists available at ScienceDirect

International Journal of Heat and Fluid Flow

journal homepage: www.elsevier.com/locate/ijhff

Effect of turbulence modelling and non-condensable gas on cloud cavity dynamics

Emad Hasani Malekshah *, Włodzimierz Wróblewski

Department of Power Engineering and Turbomachinery, Silesian University of Technology, 44-100 Gliwice, Poland

ARTICLE INFO

Keywords:
Cavitating flow
Viscosity modification
Density corrected method (DCM)
Filter-based model (FBM)
Dissolved air

ABSTRACT

Turbulence modelling plays an important role in the prediction of unsteady and highly dynamic characteristics of cavitating flows. The models with turbulent viscosity modification as Density-Corrected Method (DCM) and Filter-Based Model (FBM), can deal with the dynamics of cavitating flows. Taking it into account, the application of these models to the cavitating flows of water with dissolved air (i.e. third phase) to predict the unsteady phenomena are worth to be analysed and compared. Due to poor self-oscillation characteristics of RNG k-epsilon model in modelling of the cavitating flow, in the present study, the DCM and FBM are implemented to perform the simulation of cavitating flow with consideration of dissolved air. Also, the numerical results are compared with the experimental data. The experiments are conducted in a rectangular test section equipped with Clark Y hydrofoil providing cavity visualisation, instantaneous pressure and vibration fluctuations. The simulations are carried out for different cavitation numbers with and without dissolved air. The Fast Fourier Transform and Continues Wavelet Transform are implemented to extract and compare the shedding frequency of experiments and numerical predictions. In addition, the influence of modification models on the cloud cavitation shedding evolution, dominant shedding frequency, vorticity, pressure, velocity profile, lift/drag coefficient is evaluated.

1. Introduction

The cavitation process typically initiates once the local fluid pressure becomes lower than the vapor pressure at the local thermodynamic state (Brennen, 1995; Joseph, 1995; Joseph, 1998). When the cavitation appears, it is often followed by undesired phenomena such as vibration, erosion, noise and power loss (Sun et al., 2019; Wang et al., 2017; Ahn et al., 2018; Long et al., 2018). It can occur in all types of turbomachinery components, where the flow accelerates and pressure drops reaching the cavitation conditions, like a high-speed propeller, underwater bodies, hydrofoil, nozzle and injector. In addition, depending on the cavitation number, the type of cavitation varies between incipient cavitation, sheet cavitation, cloud cavitation and supercavitation (Chen et al., 2016). It is essential to understand the behaviour and characteristics of this phenomenon to control the impact of cavitation on turbomachines. Although many investigations have been carried out based on numerical and experimental approaches, many unknown questions remain on this topic.

The role of turbulence closure models is substantial in the prediction of cavitating flow and its corresponding characteristics. It is associated with high Reynolds numbers and mass transfer between phases, especially when the dissolved air is considered. The Reynolds-averaged Navier-Stokes (RANS) turbulence models: the original $k-\varepsilon$ and $k-\omega$ models, were developed to deal with the incompressible flows. Thus, using of these turbulence models will result in unsatisfactory results in the prediction of compressible vaporous cavity closure. The existence and unstable nature of the re-entrant jet is usually attributed to the destabilization of the cavity and transition of the attached sheet cavity to the detached cloud cavity. Based on the experimental observations, it is well demonstrated that the re-entrant jet is the main responsible mechanism to trigger the breaking up of the sheet cavity and shedding of the following unsteady cloud cavity (Kunz, 2000; Callenaere et al., 2001). Turbulence models needed modifications to account for the significant density jump due to the cavitation and re-entrant jet adjacent to cavity front. For this purpose, the turbulent viscosity in the mentioned regions had to be modified. Coutier-Delghosa et al. (Coutier-Delgosha et al., 2003) showed that the standard $k-\varepsilon$ RNG turbulence model poorly reflects the experimental observations of the vapor cloud shedding when the compressibility effect is not taken into account. By considering the compressibility effect, the $k-\varepsilon$ RNG turbulence model

* Corresponding author.
E-mail address: emad.hasani@polsl.pl (E. Hasani Malekshah).

https://doi.org/10.1016/j.ijheatfluidflow.2022.109070
Received 6 July 2022; Received in revised form 4 September 2022; Accepted 14 October 2022
Available online 22 October 2022

presents a reliable prediction over the unsteady behaviour of the cavitation process. Also, the modified model gives satisfactory results over different geometries such as hydrofoil (Hofmann et al., 1999), foil cascade (Lohrberg et al., 2002) and Venturi nozzles (Coutier-Delgosha et al., 2003). Wang et al. (Wang et al., 2009) analyzed the dynamics of cloud cavitating flow over a hydrofoil. They used Density Correction Model (DCM) to modify the standard $k-\varepsilon$ RNG turbulence model with a special focus on the behaviour of re-entrant jet. They reported that the standard turbulence model predicts shorter cavity lengths than those observed in the experiment. Reversely, by employing the DCM modification, a close agreement is observed between the numerical simulations and experimental observations regarding the cavity closure, re-entrant jet and dominant frequency of lift force. Wei et al. (Yin et al., 2021) compared different modifications of the turbulence model to simulate the time-dependent cavitating flows around the hydrofoil. The turbulence model modified by DCM predicted the mean lift distribution far from the experimental data. Also, the estimated dominant frequency of lift force is higher than the experimental measurements. In addition, a significant overestimation of the structure of the detached cavity is observed. Also, they claimed that no single modification model could predict all aspects of a cavitating flow well. Thus, it was recommended to use the combination of different modification models to overcome the disability of each model. Yin et al. (Yin et al., 2021) employed the density correction method (DCM) in the Shear Stress Transport (SST) $k-\omega$ turbulence model for simulation of unsteady cloud cavitating flow over a three-dimensional Clark-Y hydrofoil under the effect of end-wall. They reported that the modified SST $k-\omega$ model shows a better ability to predict both types of unsteady cavitation: cloud (Li et al., 2009) and tip leakage vortex (Zhang et al., 2015). Reboud et al. recommended the exponent n in the formula of the DCM model between 1 and 10. Besides, both Chen et al. (Chen et al., 2016) and Ducoin et al. (Ducoin et al., 2012) found the most satisfactory results compared with the experimental data when n is equal to 3. In this regard, Zhan et al. applied n equal to 3 and used the DCM with the $k-\varepsilon$ RNG turbulence model. The modified turbulence model demonstrated great capability in reproducing the cavitation process with cloud cavity and re-entrant jet regions. Li et al. (Li et al., 2009) observed that the SST $k-\omega$ gives unrealistic behavior of the cavitating flow due to overestimated level of turbulent viscosity. So, the standard model failed to capture the dynamic nature of unsteady sheet/cloud cavitating flow around the hydrofoil. Reversely, by improving the turbulence model with DCM, the cavity formation was captured well, and the lift/drag forces were in close agreement with the measured data. For turbulence, the ensemble-averaged modelling with a two-equation closure along with a filter-based model (FBM) is another viscosity modification approach. The dynamics of cloud cavity in the flow around a Clark-Y at a constant angle of attack of 8° was analyzed by Liu et al. (Liu, 2021). They used the $k-\varepsilon$ RNG turbulence model modified by the FBM. They concluded comparing the numerical results with the experimental data that even though the overestimation of turbulent viscosity, the standard turbulence model fails to predict the dynamics of cloud shedding, the structure of clouds, oscillation of lift coefficient and time-averaged velocity distributions were well recognized. In a similar work, Johansen et al. (Johansen et al., 2004) used the FBM for modification of turbulence model based on RANS to simulate the cavitating flow around a square obstacle. They concluded that significant improvement occurred by employing FBM for all grid resolutions: fine grid, intermediate grid and coarse grid, but the filter-based model becomes smoothly identical to the standard $k-\varepsilon$ turbulence model as the filter size increases. The results of a work carried out by Biao et al. (Huang et al., 2014) showed that the FBM, which causes a reduction in turbulent viscosity in the whole cavity closure, can reduce the eddy viscosity at the rear region of a hydrofoil. On the other hand, the FBM causes a stronger re-entrant jet that will be extended to upstream while it has a minor influence on the region far from the near-wall area. Thus, the combination of the two models can be used to obtain a comprehensive simulation of cavitating flow. Also, Biao et al. (Biao and Guo-Yu, 2011) reported that using of FBM leads to a larger recirculating zone and significant stronger time-dependency with respect to the original turbulence model.

Many factors analysed by the researchers, such as the configuration of foil, angle of attack, scale factor, flow condition and other geometrical parameters, have an influence the structure and dynamics of the cavitating flow. One of the factors considered to a limited extent is dissolved air. The presence of dissolved air in the water causes enhancement on the void ratio of cavity closure, increment of cavity length, reduction of shedding frequency and differences in pressure and force distributions around the hydrofoil (Brennen, 2014; Germano et al., 1991). Recently, Wróblewski et al. (Wróblewski et al., 2021) analysed the effects of dissolved air on the cavitating flow around the Clark Y hydrofoil and the corresponding unsteady characteristics and shedding frequencies based on numerical simulations and experimental observations. They used the 3phases model to consider liquid, vapor and air as three governing phases. Two different amounts of dissolved air (i.e. 2.6 ppm and 5.5 ppm oxygen) were taken into account. In addition, the numerical results were compared with the experimental observations. The results of the numerical simulation and image processing of experimental data declared that the addition of dissolved air is associated with enlarged cavity closure during the evolution of the cavity. In addition, based on the FFT evaluation of pressure fluctuations, the authors reported that the shedding frequency decreases in the case of a higher volume fraction of dissolved air. In another work, Wróblewski et al. (Wróblewski et al., 2021) examined the cavitating flow in the presence of dissolved air at three different levels (i.e. VF = 0.004, 0,016 and 0.042). They considered the cavitating flow around a Clark Y hydrofoil with a fixed angle of attack of 8 deg. They evaluated the Singhal model and Zwart-Gerber-Belamri (ZGB) model, using the 2phase and 3phase approaches. Numerical calculations were carried out using the uRANS model with the assumption of the constant temperature of the mixture. In addition, the numerical results are compared with the original experimental data. They concluded that the Singhal model gives a high unstable solution; as well as, the predicted cavity structures were not satisfactory, especially for low cavitation numbers. However, a convincible cavity structure is detected when the 2phase and 3phase approaches are employed. Hence, On the other hand, the impact of dissolved air on the cloud structure and dynamic characteristics of cavitating flow is gently observable. Tsuru et al. (Tsuru et al., 2018) studied the effect of gas content on the force characteristics under the impact of three angles of attacks of 2.0, 8.0 and 20.0 degrees. At the angle of attack of 2.0 degrees, the effect of dissolved air was observable in both force characteristics and initiation of cavitation. At the angle of attack of 8.0 degrees, the influence of dissolved air on the cavitation and force was hard to detect. At the angle of attack of 20.0 degrees, the cavitation process and corresponding characteristics were similar regardless of gas content. Kawakami et al. (Kawakami et al., 2005) provided the pressure spectrum at the suction side of the NACA 0015 hydrofoil considering two amounts of dissolved air of 6 ppm and 13 ppm. They proved that the effect of dissolved air on the trend of pressure spectrum is remarkable. For cases with high air content, many peaks in the pressure spectrum were detected, which means that the cavitating flow with air is highly unsteady regardless of the value of cavitation number ($\sigma/2\alpha$) in the range of 2 to 4. Reversely, when the gas content is low, the cavitating flow is steady. Mäkiharju et al. (Mäkiharju et al., 2017) investigated the dynamics and inception of the partial cavitating flows considering the dissolved air. However, the results proved that the developed partial cavity, which is accompanied by a strongly enforced separation line, would not be significantly affected by the dissolved gas mass transfer within the freestream.

The present work aims to investigate the cavitating flow around the hydrofoil in presence of dissolved air. For this purpose, numerical and experimental investigations are employed. The experimental tests allow us to visualize the cavitating flow and measure the dynamic characteristics. To obtain accurate numerical predictions, the k-ε RNG turbulence model has been modified using DCM and FBM. The numerical simulations are carried out for the cavitating flow for the cases with and without dissolved air (i.e. air content of 0 and 2.1 ppm) and selected cavitation numbers in the range of 0.9 to 2.5.

2. Mathematical formulations

Fig. 1 represents an overview regarding the scales involved in the cavitation flow. The capability of different numerical approaches in taking into account the scale is different. Those numerical methods, which can consider micro to macro scale, can predict the phenomenon in detail. The existed scales in the cavitating flow can be explained as follows:

- Microscale: it is related to pre-existed non-dissolved bubbles in the flow, nucleation from a solid surface at the leading edge and dispersed bubble generated after breaking up from vaporous/gaseous cavity.
- Mesoscale: it appears during bubble growth and bubble shrinking at generation and breaking up of cavity, respectively.
- Macroscale: it deals with the large sheet and cloud cavity known as the most effective part which characterizes the cavitating flow.

In the present work, the numerical simulations deal with the macroscale based on a three-phase continuum-based flow on an Eulerian grid.

2.1. Multi-phase model

In the present study, the homogeneous mixture model was used for the simulation of the liquid–vapour-gas flow. The homogeneous flow idea assumes that the flow of a single-fluid mixture was considered with the same velocity flow field for each phase. The consequence of the assumption, which causes the negligence of slip condition between phases, is the reduction in the number of the governing equations. The governing equations are mass and momentum conservation laws:

$$\frac{\partial \rho}{\partial t} + \nabla \bullet (\rho \boldsymbol{u}) = 0, \tag{1}$$

$$\frac{\partial}{\partial t}(\rho \boldsymbol{u}) + \nabla \bullet (\rho \boldsymbol{u}\boldsymbol{u}) = -\nabla p + \nabla \bullet \left[\mu\left(\nabla \boldsymbol{u} + \nabla \boldsymbol{u}^T\right)\right] + \rho \boldsymbol{g}, \tag{2}$$

$$\rho = \rho_l \alpha_l + \rho_v \alpha_v + \rho_{ng} \alpha_{ng}, \tag{3}$$

The last term in Eq. (2), which represents the body force, was neglected in the numerical scheme due to the minor effect on the modelled phenomenon. The numerical model takes the presence of air into account, and therefore in Eq. (3), the third term representing the fraction of non-condensing gases (air) was added to the terms of the liquid and vapour phases of the water. The mixture model with three phases: liquid–vapour-air (3phases model) solves the continuity equations for the vapour volume fraction and the air volume fraction. The mass transfer between a liquid and a mixture of gaseous phases was modelled between species:

$$\frac{\partial \rho_v \alpha_v}{\partial t} + \nabla \bullet (\rho_v \alpha_v \boldsymbol{u}) = \dot{m} = \dot{m}^+ - \dot{m}^-, \tag{4}$$

$$\frac{\partial \rho_{ng} \alpha_{ng}}{\partial t} + \nabla \bullet \left(\rho_{ng} \alpha_{ng} \boldsymbol{u}\right) = 0, \tag{5}$$

$$\alpha_l + \alpha_v + \alpha_{ng} = 1. \tag{6}$$

The phase change in the flow was governed by the source term $\dot{m}$ in Eq. (4) which represents the mass transfer per volume unit between the liquid phase and vapour phase in both evaporation and condensation processes. The phase change between the non-condensable gas and other phases is neglected to keep the simplification since the gas diffusion is considered as a slow process, comparing to the cavitating flow, which may have minor impact on cavitation.

2.2. Zwart-Gerber-Belamri (ZGB) model

The present cavitation model is inspired by the mass transfer equation of vapor volume fraction, which is originated from the Rayleigh-Plesset (RP) equation (Brennen, 2014). The RP equations are given as follows:

$$R_B \frac{d^2 R_B}{dt^2} + \frac{3}{2}\left(\frac{dR_B}{dt}\right)^2 + \frac{4\mu_l}{\rho_l R_B}\left(\frac{dR_B}{dt}\right) + \frac{2S}{\rho_l R_B} = \frac{p_v(T_\infty) - p}{\rho_l}, \tag{7}$$

where R_B denotes the spherical bubble radius, p represents the local fluid pressure, $p_v(T_\infty)$ shows the saturation vapor pressure, and S shows the surface tension. To simplify the RP equation, the second derivative of bubble radius and the effect of surface tension are ignored. As a result, the simplified RP equation is derived as follows:

$$\frac{dR_B}{dt} = \sqrt{\frac{2}{3}\frac{p_v(T_\infty) - p_\infty}{\rho_l}}, \tag{8}$$

The phase change source term $\dot{m}$ is given as follows:

$$\frac{dm_B}{dt} = \rho_v \frac{dV_B}{dt} = \rho_v \frac{d}{dt}\left(\frac{4}{3}\pi R_B^3\right) = 4\pi R_B^2 \rho_v \sqrt{\frac{2}{3}\frac{p_v(T_\infty) - p_\infty}{\rho_l}}, \tag{9}$$

Assuming N_B represents the number of bubbles in the unit volume,

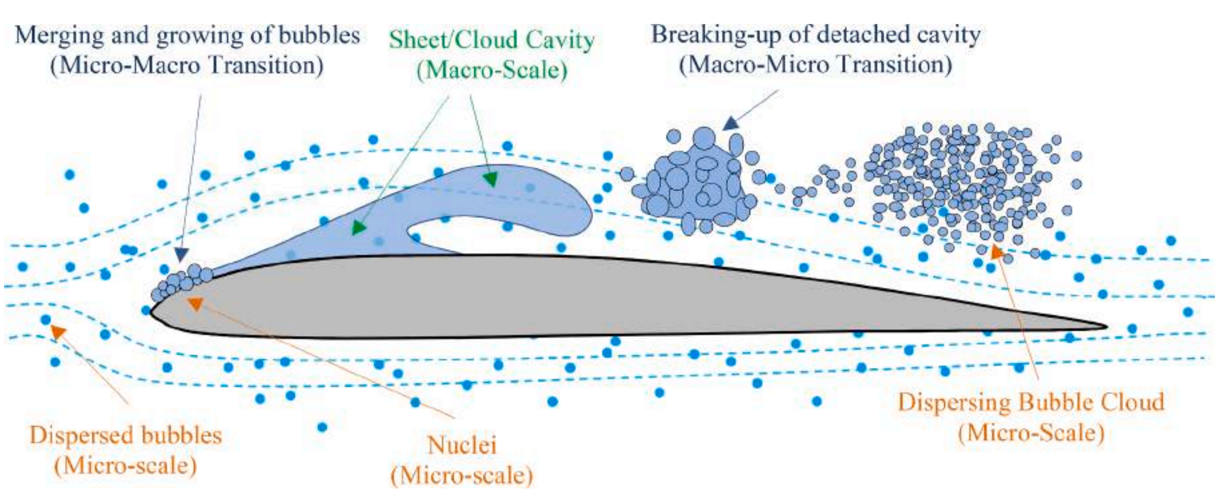

Fig. 1. Overview of the involved scales in the cavitating flow.

the vapor volume fraction is given as follows;

$$\alpha_v = V_B N_B = \frac{4}{3}\pi R_B^3 N_B, \tag{10}$$

As a result, the source terms describing evaporation ($\dot{m}^+$) and condensation ($\dot{m}^-$) are expressed by the following equations (Kubota et al., 1992):

$$\dot{m}^+ = F_{vap}\frac{3\alpha_{nuc}(1-\alpha_v)\rho_v}{R_B}\sqrt{\frac{2}{3}\frac{max(p_v(T_\infty)-p,0)}{\rho_l}}, \tag{11}$$

$$\dot{m}^- = -F_{cond}\frac{3\alpha_v\rho_v}{R_B}\sqrt{\frac{2}{3}\frac{max(p-p_v(T_\infty),0)}{\rho_l}}. \tag{12}$$

where the empirical coefficient $F_{vap} = 50$ and $F_{cond} = 0.1$ are adopted for the water cavitating flow at ambient temperature. Also, the nucleation site volume fraction (α_{nuc}) is assigned to 5×10^{-4}, the fixed spherical bubble radius is equal to 1×10^{-6} m.

2.3. Turbulence model and modifications

2.3.1. Standard $k-\varepsilon$ RNG

The standard $k-\varepsilon$ RNG turbulence model is defined by the following equations:

$$\frac{\partial(\rho k)}{\partial t} + \nabla \bullet (\rho \boldsymbol{u} k) = \nabla \bullet \left[\left(\mu + \frac{\mu_t}{\sigma_k}\right)\nabla k\right] + G_k - \rho\varepsilon, \tag{13}$$

$$\frac{\partial(\rho \varepsilon)}{\partial t} + \nabla \bullet (\rho \boldsymbol{u} \varepsilon) = \nabla \bullet \left[\left(\mu + \frac{\mu_t}{\sigma_\varepsilon}\right)\nabla \varepsilon\right] + \frac{c_1\varepsilon}{k}G_k - c_2\rho\frac{\varepsilon^2}{k}. \tag{14}$$

In this turbulence model, the effective viscosity which is applied to Reynolds equations is defined as $\mu = \mu_t + \mu_l$ where $\mu_t = \rho C_\mu k^2/\varepsilon$ denotes the turbulent viscosity and the constant is assumed as $C_\mu = 0.084$ (Yakhot et al., 1992). Also, k and ε represent the turbulent kinetic energy and turbulent energy dissipation rate, respectively. Furthermore, G_k shows the production of turbulent energy term.

2.3.2. Density corrected model (DCM)

It is worthy to mention that no particular correction is applied to $k-\varepsilon$ RNG turbulence model dealing with the two-phase flow with significant compressible behaviour. In this case, the changes of mean density ρ is the only factor applying the compressibility effect into turbulence equations.

To overcome the discrepancies due to high-density jump which occur in the cavity closure and re-entrant jet at the adjacent of hydrofoil surface, the $k-\varepsilon$ RNG turbulence model is modified based on a density correction based model (DCM) proposed by Coutier-Delgosha et al. (Coutier-Delgosha et al., 2003), which simply reduces the mixture turbulent viscosity in the mentioned regions and avoid over-estimated turbulent viscosity. Using this modification, the behaviors of the re-entrant jet and the vapor cloud shedding will be better simulated. The modified turbulent viscosity is given as follows:

$$\mu_t = f(\rho)C_\mu k^2/\varepsilon, \tag{15}$$

$$f(\rho) = \rho_v + \left(\frac{\rho_v - \rho}{\rho_v - \rho_l}\right)^n(\rho_l - \rho_v). \tag{16}$$

With such a treatment, the eddy viscosity is decreased based on the DCM factor $f(\rho)$. The distribution of DCM factor $f(\rho)$ as a function of n is presented in Fig. 2. It is noted that $n = 10$ is considered for the present simulations. The reduction of turbulent viscosity of mixture flow leads to remarkable changes on the re-entrant jet flow behavior since it is mainly composed by pure liquid. Overall, it is expected to have a more realistic simulation after the implementation of DCM modification.

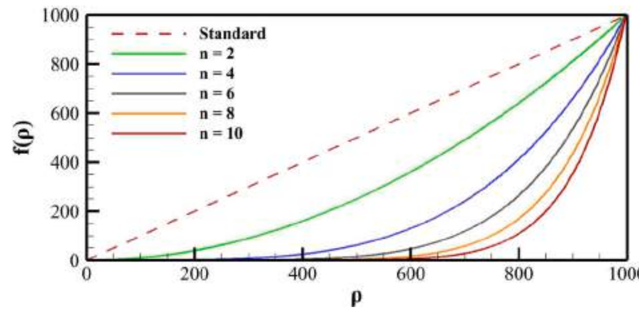

Fig. 2. Distribution of DCM factor $f(\rho)$ as a function of n.

2.3.3. Filter-based model (FBM)

In the RANS simulation, the resolution of the computational domain depends on the mesh size δ and magnitude of eddy viscosity ν_{eff}^{RANS}. Thus, the filtering process based on the Filter-based Model (FBM) is derived employing length scale l_{RANS} of corresponding RANS model and the filter scale Δ associated with mesh size.

The modified turbulent viscosity based on the FBM is defined as follows:

$$\mu_{t-FBM} = C_\mu \rho_m f_{FBM}\frac{k^2}{\varepsilon}, \tag{17}$$

$$f_{FBM} = min\left[1.0, C_3\frac{\Delta}{l_{RANS}}\right], \tag{18}$$

$$l_{RANS} = \frac{k^{3/2}}{\varepsilon}, \tag{19}$$

where the filter size is calculated based on the local grid size as $\Delta = (\Delta_x\Delta_y\Delta_z)^{1/3}$, the density of the mixture is declared by ρ_m, and $C_\mu = 0.084$ is the model constant. In addition, the new model coefficient C_3 is presented as follows:

$$C_3 \approx \frac{\gamma}{4C_\mu\sqrt{3/2}}. \tag{20}$$

where $\gamma = 1$ in the isotropic flows. Also, it is worthy to mention that C_3 is taken equal to 1 in many works (Liu, 2021; Johansen et al., 2004). Thus,

- If $\Delta \gg l_{RANS}$, $\mu_{t-FBM} = C_\mu \rho_m \frac{k^2}{\varepsilon}$

  Then, the RANS formulation is fully recovered.

- If $\Delta \ll l_{RANS}$, $\mu_{t-FBM} = C_\mu \rho_m \Delta k^{0.5}$

  Then, the model can be assumed equivalent to the LES model.

3. Description of test rig and devices

3.1. Hydraulic installation

The experiments were conducted in the hydraulic installation equipped with a test section designed to analyse the cavitating flow at the Department of Power Engineering and Turbomachinery, Silesian University of Technology. The structure of the closed-loop cavitation test setup along with the main elements is presented in Fig. 3. The operating fluid in the installation was water. The electronic pump with a power of 30 kW flows the water inside the pipe with a diameter of 200 mm. after the pump, a manual valve was installed to control the water flow, if required. In addition, to measure the flow rate, an electromagnetic flowmeter was installed as a junction between the pipes. Then, the water flow passes two elbows before reaching the chamber. Before entering the chamber, the water flow passes a honeycomb in order to

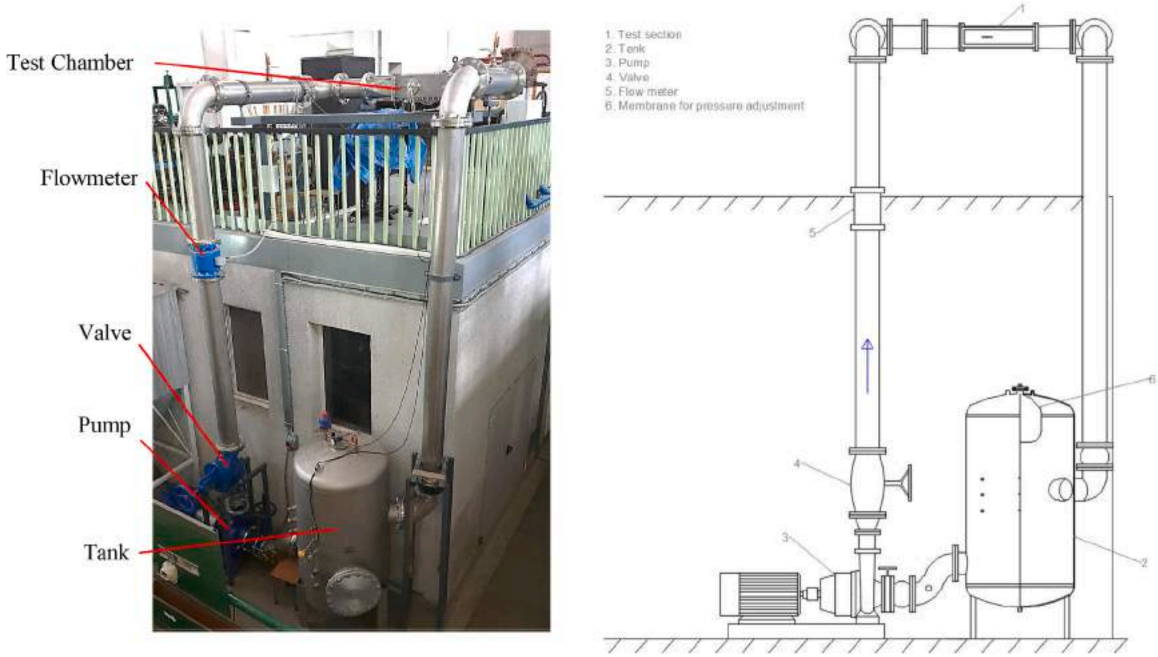

Fig. 3. The designed (right) and constructed (left) hydraulic installation with presentation of main components.

make a straightened flow. After flowing through the chamber, the water flow diffuses to the pipe, passes two elbows, and reaches the tank. The tank of about 1.5 m^3 was designed with the internal air-bag located in the top of the tank. The airbag is an elastic membrane connected with the compressed air system. It made it possible to regulate and control the pressure in the installation. Hence, three elastic junctions along the installation are mounted, one before the tank, one after the pump and one between the tank, and the pump, to reduce the vibration. The elevation difference between the pump level and the test chamber is about 5 m. The designed installation is capable to maintain a constant flow rate of 500 m^3/min and variable pressure level inside of the chamber in the range of 90 to 190 kPa.

The test chamber and the main devices for data collection and visualization are represented in Fig. 4. The test chamber has a rectangular cross-section with height (h), span (w) and length (L) of 189 mm, 70 mm and 700 mm, respectively. The chamber height to chord ratio equals $w/c = 2.7$. The tested hydrofoil was mounted on one side of the chamber at half of the chamber's height, 210 mm downstream from the chamber inlet. The transparent windows, which are made of polycarbonate, were placed at the above, bottom and one sidewall of the test chamber to enable optical access and observations. Furthermore, two pressure sensors were installed at the inlet and outlet to measure the pressure level. Furthermore, two vibration sensors before and after the mounted hydrofoil were used to evaluate the generated vibration. The measuring system including high-speed camera, image control, rig control, lightening and test chamber, is shown in Fig. 4. The instantaneous pressure magnitudes at the surface of the hydrofoil are measured with the low-frequency sampling rate by pressure transducers APLISENS PC-28. The accuracy of 0.16 % is approved for the full scale (FS) amounts 160 kPa. The pressure sensor type XP5 with amplifier ARD154 is used as fast pressure sensor at pressure tap P8. The full scale of this type of sensor is given by 5 bar with an accuracy of 0.25 %. The pressure impulse tubes were used to send the pressure signal to the measuring cluster. Furthermore, the same low-frequency pressure sensors are used

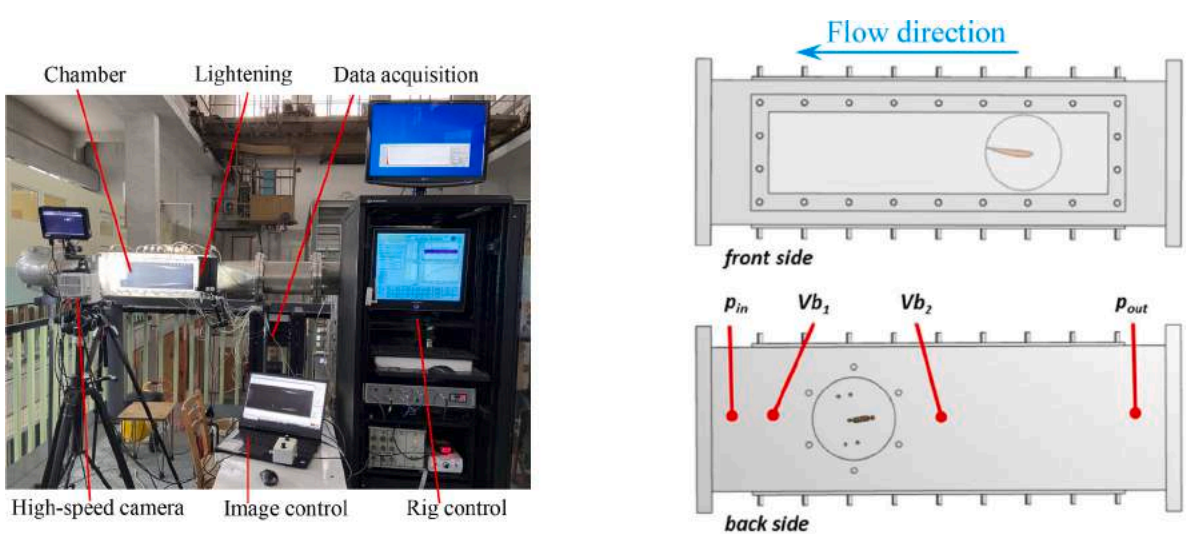

Fig. 4. Test chamber with main devices of data collection and visualization (left), and schematic of the chamber with the location of pressure and vibration sensors (right).

to measure the pressure level at the outlet. The temperature of the water is measured by the resistance thermometer APLISENS CT-GN1 Pt100, having a full scale of 0–100 °C and accuracy of ±(0.15 K + 0.002 |T|). The flow rate is measured by electromagnetic flowmeter UniEMP-05 DN200 with a measuring range up to 1080 m^3/h and accuracy of ± 0.25 % of the measured value.

The vibroacoustic signals were recorded from outside of the chamber by two piezoelectric transducers. Two stiff piezoelectric accelerometers KD35 (RTF) are located externally on the sidewall of the test chamber. The Vb_1 is located about one profile chord before the leading edge and the second Vb_2 about one and a half chord behind the trailing edge (Fig. 4). The accelerometers are connected with the 0028 (RFT) type charge amplifier connected with the fast response converter AC 16 bit, 250kS/s. The system was calibrated before experiments using electrodynamic vibration calibrator EET101 (RFT) type. The value of achieved limiting error was less than 5 %.

The measurement system used in the research is based on a National Instruments module NI USB 6216. The NI/PXI-6255 module co-operates with measuring clusters which include sets of sensors and measuring transducers. The executive elements and the data acquisition process are managed by a system programmed in the LabView environment.

An important part of the data acquisition system is image recording and processing. The structures of cavitation were recorded by high-speed video camera Phantom Miro C110. The recording speed was set to 3200 frames per second with a spatial resolution of 960 × 280 pixels. The settings of the camera resolution and speed were selected as a compromise between image quality and picture size.

The type of hydrofoil used in the present work was Clark Y 11.7 %. The designed and manufactured hydrofoil, as well as; the location of the pressure taps are shown in Fig. 5. The hydrofoil had a chord length of c = 70 mm and a span of w = 70 mm spanning the width of the measuring section. Also, the angle of attack was adjustable which was fixed to 8 degrees. The trailing edge was manufactured with a radius of 0.5 mm. The root of the hydrofoil was fixed to a round disk made with the same material. To connect the pressure taps at the surface of the hydrofoil with the pressure transducers, the internal channels inside the hydrofoil with a diameter of 2 mm were created. The hydrofoil was printed from titanium using SLM manufacturing technology. The 10 taps are located in the mid-span of the suction side to detect the static pressure signals.

3.2. Flow conditions

The flow rate of the circuit was kept constant in all rounds of experiments. So, the velocity of the stream is constant through the test chamber which is almost equal to $u_{in} = 10.4m/s$. The Reynolds number equals $Re = \frac{\rho_l u_{in} c}{\mu_l} \simeq 0.79\times 10^6$, where ρ_l, u_{in}, c and μ_l represent the density of water, velocity of flow at the inlet, hydrofoil chord and dynamic viscosity of water, respectively.

The temperature of the water was between 22 °C and 26 °C at one round of the test campaign dealing with 8 different cavitation numbers. The detected temperature differences were due to the friction in the pump and installation and differences in the ambient conditions. It should be noted that the average temperature of 24 °C was used to calculate the Reynolds and cavitation numbers.

Each case with different inlet pressure, saturation pressure, density and inlet velocity, is defined with a single cavitation number calculated as follows:

$$\sigma = (p_{in} - p_v)/\left(0.5\rho_l u_{in}^2\right) \tag{21}$$

where p_{in} and p_v denote the static pressure at inlet and water saturation pressure, respectively. Also, the value of inlet pressure is based on the average pressure calculated from instantaneous pressure fluctuations detected during the round of the related experiment. Furthermore, the saturation pressure is calculated based on the average temperature calculated over the related experiment. Also, ρ_l shows the density of water calculated at corresponding temperature and pressure at each case with nominal cavitation number. Finally, u_{in} represents the velocity at the inlet, which is also based on the average value.

In the present work, eight levels of rig pressure were considered and represented by cavitation numbers (σ) of 0.91, 1.01, 1.18, 1.37, 1.51, 1.72, 1.93 and 2.04.

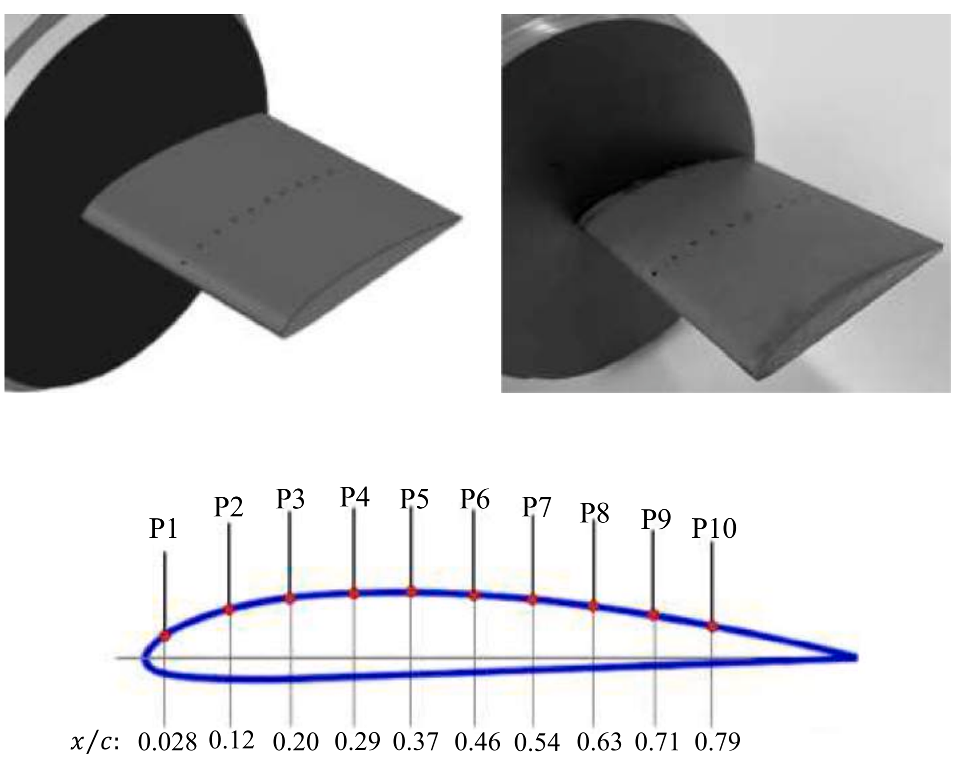

Fig. 5. The designed (top-left) and manufactured (top-right) Clark Y 11.7% hydrofoil with the location of pressure taps (bottom).

The experimental tests were conducted based on one specific level of dissolved oxygen of 2.1 ppm. The multifunction meter CF-401 was employed to measure the oxygen levels before and after the experimental campaign.

4. Numerical setup

The length and height of the computational domain presented in Fig. 6 corresponding to the dimensions of the test chamber. The left and right walls with a length of 2.5c are considered as the inlet and outlet, respectively. The top and bottom walls with a length of 10c are set as no-slip surfaces. The distance between the leading edge and the inlet is fixed to 3.2c. The mesh distribution is represented in Fig. 7.

The domain has 8 main blocks with the O-grid around the hydrofoil. The overall number of grid nodes on the hydrofoil's profile amounted to 368 and the edge normal to the foil had 101 nodes. The domain had an overall width of 0.09 mm discretized by 3 layers of 0.03 mm in thickness. The thin domain was selected to reduce the aspect ratio in the domain close to the hydrofoil in the O-grid region. The whole mesh consisted of 220 k hexahedra elements and the value y^+ on the hydrofoil was less than 1.

Validation of the numerical grid performed in (Homa et al., 2019; Homa, 2018) showed that the numerical grid with a total number of nodes equal to 160 k and 270 nodes around the hydrofoil was sufficient for the prediction of the pressure distribution on the hydrofoil. The mesh applied in the present study was finer in the O-grid region to preserve better uniformity of the grid where cavitation is present.

5. Results and discussion

The present work aims to study the capability of different viscosity modification models including a standard model, density-corrected model and filter-based model for prediction of cavitating flow around the Clark Y hydrofoil with and without dissolved air. For this purpose, the numerical simulation is combined with the experimental observations carried out at the Department of Power Engineering and Turbomachinery, the Silesian University of Technology. Two amounts of dissolved oxygen of 0 and 2.1 ppm were taken into consideration in a range of cavitation numbers between 0.91 and 2.04. The Fast Fourier Transform (FFT) and Continues Wavelet Transform (CWT) were implemented to extract and compare the shedding frequency of experiments and numerical predictions. In addition, the influence of modification models on the cloud cavitation shedding evolution, dominant shedding frequency, vorticity, pressure, velocity profile near the hydrofoil, lift/drag coefficient was evaluated.

5.1. Validation of experimental data

The present experimental results were verified based on a comparison between pressure coefficient distribution (C_p) at different cavitation numbers around the hydrofoil measured during present experimental campaigns and those reported by Matsunari et al. (Matsunari et al., 2012) which were obtained in the Laboratory of Kyushu University. The comparison is presented in Fig. 8 in the form of pressure coefficient distribution versus dimensionless location around the hydrofoil as a function of cavitation number. It is worth mentioning that Matsunari et al. (Matsunari et al., 2012) measured the averaged pressure distribution at the mid-span of the two-dimensional Clark Y 11.7 % hydrofoil with a chord length of $c = 100$ mm and the span of $b = 81$ mm. Also, 25 pressure taps were located in both suction and pressure sides at the surface of hydrofoil, and the height to chord ratio of the chamber which is defined based on the dimension of the chamber is equal to 2. While, in the present experiments, 10 pressure taps were spread along the suction side, and height to chord ratio of the chamber is constant and equal to 2.7. The span to chord ratio for the reference and present chambers are $b/c = 0.81$ and $b/c = 1$, respectively. Those differences show the higher blockage effect of the water tunnel. In addition, the mean flow velocity is constant and equal to $u_{in} = 10.4$ m/s; as well as, the inlet pressure is used as reference pressure located at 120 mm upstream from the leading edge were used to calculate the cavitation number. The amount of oxygen content in the reference work was reported as less than 2 ppm which is close to measured 2.1 ppm in the present work. As can be observed in Fig. 8, there are slight differences in the cavitation numbers which is due to different boundary conditions and configurations, which may result in a difference in the value of pressure coefficients in some cases. At the highest cavitation number $\sigma = 1.92$, it is observed that a sudden pressure coefficient drop exists which is due to the transition from cavitating flow to non-cavitating region. In addition, the flat section of the pressure coefficient distribution represents the length of the sheet cavity. By decreasing the cavitation number, the flat section elongates which means that the cavity closure is extending. The lower cavitation number like $\sigma = 1.19$ and $\sigma = 0.91$ show the stronger cavitating flow around the hydrofoil. The last conclusion can be made by the almost flat pressure coefficient distribution along the hydrofoil. The unremarkable pressure difference along the hydrofoil denotes that there is no transition from cavity closure to normal flow, which declares the fully-developed cavitation. Finally, pressure coefficient distributions were in good agreement, which proves the accuracy of the present experimental data.

5.2. Validation of numerical data

The time-averaged lift and drag coefficient versus the cavitation number as a function of different viscosity modification models (standard, DCM and FBM) are plotted in Fig. 9. The numerical prediction of lift and drag coefficients are compared with the experimental data reported by Numachi (Numachi, 1938) and numerical simulation performed by Matsunari et al. (Matsunari et al., 2012). The lift and drag coefficients are calculated by $C_L = F_L/(\rho_l u_{in}^2 A/2)$ and $C_D = F_D/(\rho_l u_{in}^2 A/2)$, where F_L, F_D, ρ_l, u_{in} denote lift force, drag force, water density and inlet velocity, respectively. The effective area, $A = bc$, was calculated using the values of span b and chord c. The unsteady nature of the cavitating flow is highly affected by the flow conditions. In this regard, different regimes of cavitating flow including incipient cavitation, sheet cavitation, cloud cavitation and supercavitation generated with

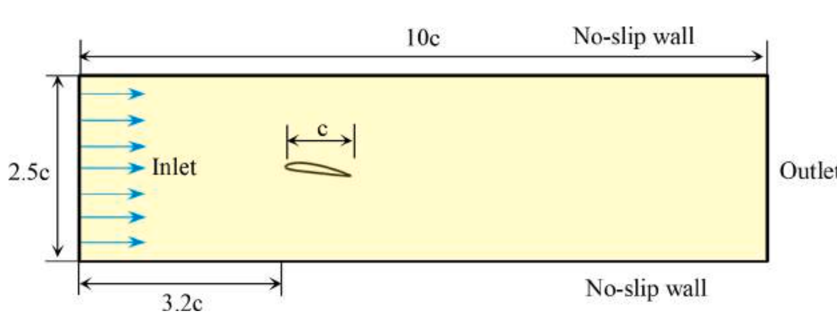

Fig. 6. The computational domain with related dimensions and boundary conditions.

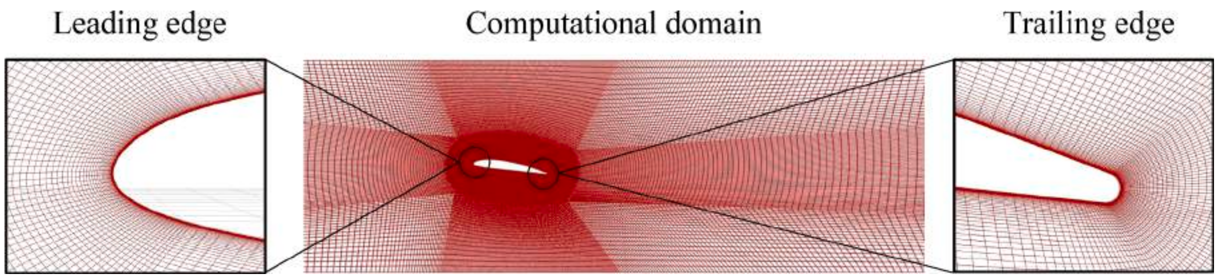

Fig. 7. Presentation of mesh distribution.

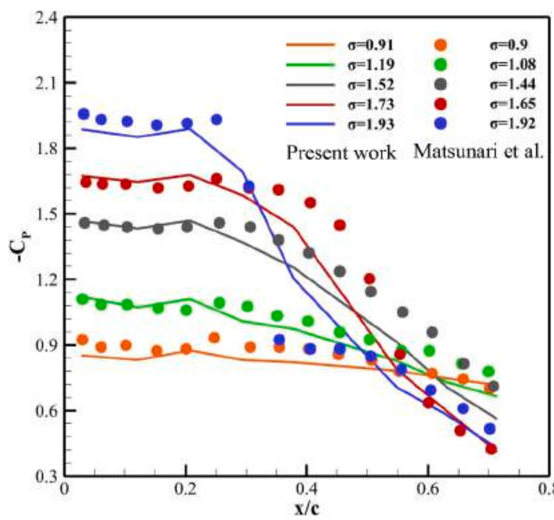

Fig. 8. Time-averaged experimental pressure coefficient around the hydrofoil for present work and those reported by Matsunari et al. (Matsunari et al., 2012) for various cavitation numbers (dissolved oxygen in the present work 2.1 ppm and Matsunari et al. 2 ppm).

changing the flow condition. It is worthy to mention that the flow condition can be changed by different parameters like stream velocity, pressure and quality of operating fluid. Therefore the flow conditions are defined by the dimensionless cavitation number. On the other hand, each type of regime influences the tendency and magnitude of lift and drag coefficient. It is visible that there is no significant difference in the lift and drag coefficients when the cavitation number is higher than 2. It is because of this range of cavitation numbers which specifies the non-cavitating region. In this range, the DCM and FBM predict the lift coefficient better than the standard model, although a slight difference is detected in the magnitude of a drag coefficient. In the range of $\sigma = 0.8$ to 1.2, the magnitude of lift coefficients predicted by different models is almost the same. On the contrary, the differences between drag coefficients corresponding to employed models are more remarkable. The distribution of the drag coefficient given by the standard model is close to the experimental data reported by Tohoku University. The distribution of the drag coefficient given by the DCM model agrees with the experimental data reported by Kyushu University and numerical data provided by Matsunari et al. (Matsunari et al., 2012). In addition, the FBM mode over-predicts the drag force. Because the DCM results agreed better with both experimental and numerical references, this model is more successful to predict the averaged forces acting on a hydrofoil.

Fig. 10 presents the comparison between the present computational predicted normalized main streamwise velocity with the experimental data provided by Huang et al. (Huang et al., 2014; Huang et al., 2013) for Standard, DCM and FBM models for the case with $\sigma = 0.8$, $\alpha = 8^{\circ}$ and $U_{\infty} = 10$ m/s. The horizontal and vertical axes denote the dimensionless average velocity (u/U_{∞}) and vertical distance from the hydrofoil surface (y/c), respectively. In addition, the comparison was made for the different sections along the chord of hydrofoil from near leading edge to near to trailing edge $(x/c = 0.2, 0.4, 0.6, 0.8)$. Firstly, it was observed that the differences between the averaged velocity profiles predicted by different modification models are not remarkable. The negative value of the velocity in the vicinity of the hydrofoil showed the re-entrant jet moving upstream toward the leading edge. Each model predicted the front of the re-entrant jet differently. The front of the re-

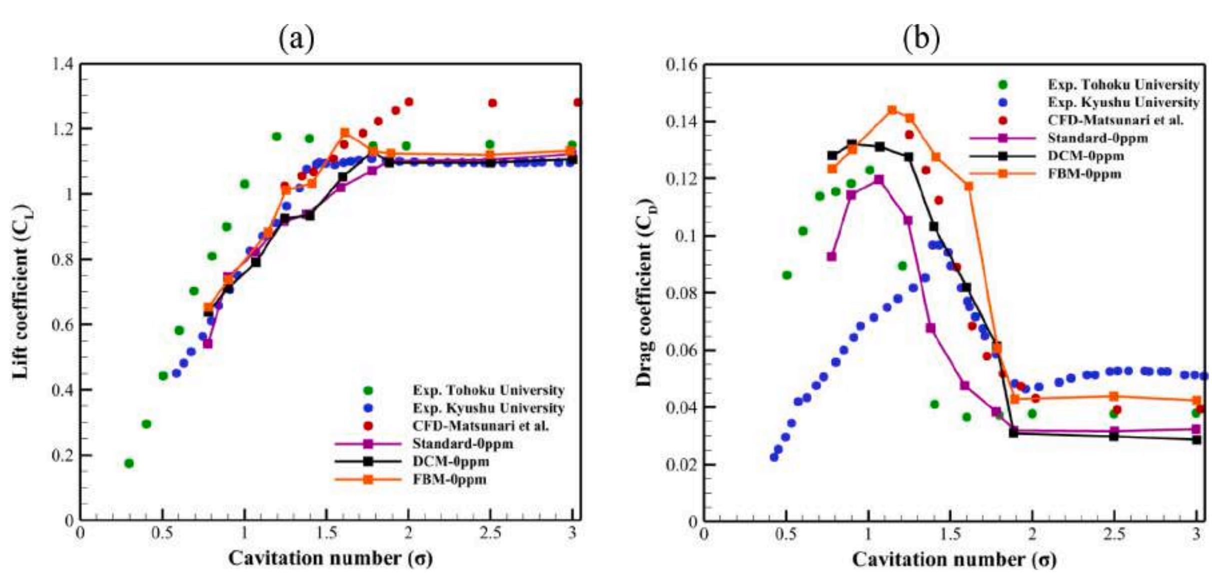

Fig. 9. (a) The time-averaged lift (C_L) and (b) drag (C_D) coefficients versus cavitation number (σ) calculated based on different viscosity modification models.

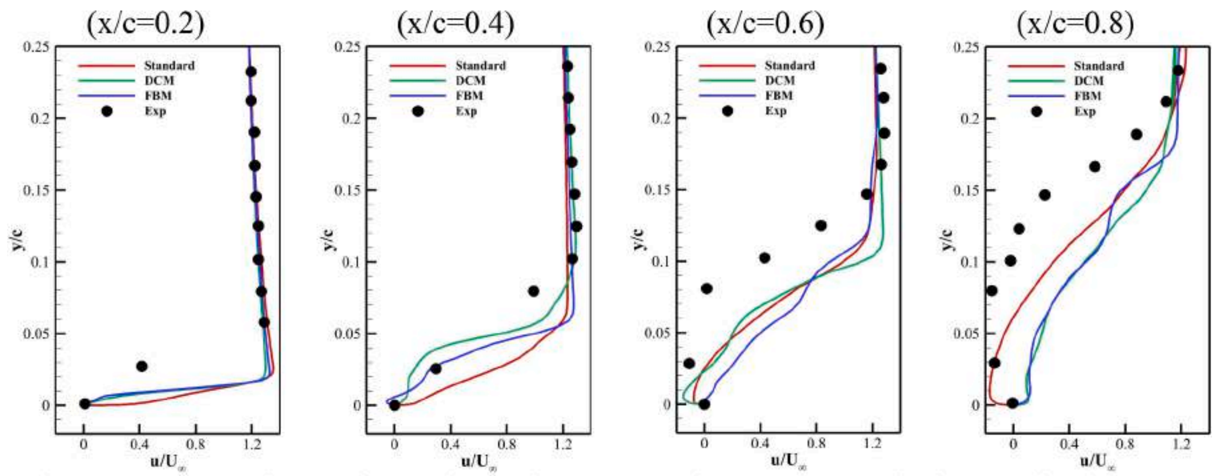

Fig. 10. Comparisons of experimental (Huang et al., 2014; Huang et al., 2013) and present numerical normalized average velocity near the suction side of the hydrofoil. Standard, DCM and FBM models, $\sigma = 0.8$, $\alpha = 8^{\circ}$ and $U_{\infty} = 10$ m/s.

entrant jet was located at $x/c = 0.4$ when predicted by FBM. Hence, the standard and DCM models gave the same location of the re-entrant jet front at $x/c = 0.6$. Besides, comparing the numerical and experimental data, approves that there was good agreement between them. It is noted that the maximum difference between them could be found near the trailing edge where the cloud cavity is dominant, and the numerical simulations over-predict the velocity magnitude. Furthermore, the thickness of the re-entrant jet was larger in the experiment compared with the numerical predictions.

5.3. Shedding frequency

The shedding frequency is one of the main parameters used to validate the numerical models. Based on the literature survey, one can notice that different frequency has been reported for a case with similar operating and boundary conditions. Moreover, in many cases, the extracted shedding frequencies from numerical and experimental data differ noticeably. As such, more investigations are required to provide precise reference works with convergent results. The shedding frequencies determined by the present numerical simulations with different viscosity modifications were compared with some other numerical and experimental references, as presented in Table 1. The shedding frequencies were detected for the ClarkY hydrofoil, for $\sigma = 0.8$, $Re = 7 \times 10^5$, without consideration of dissolved air. A different number of modes may be determined from the signals, depending on the case and the sensor location. Three modes of cavitation frequency based on three peaks were reported in some cases. It can be seen, that the

Table 1
Shedding frequency of cloud cavities around a Clark-Y hydrofoil ($\sigma = 0.8$, $Re = 7 \times 10^5$).

Source	Shedding frequency		
	f_1(Hz)	f_2(Hz)	f_3(Hz)
Present study [Standard $k-\varepsilon$]	25.2	65.1	–
Present study [DCM]	29.4	69.9	125.1
Present study [FBM]	20.0	42.8	–
Wei et al. (Wei et al., 2011) [Standard $k-\varepsilon$]	27.3	50.8	–
Liu et al. (Liu, 2021) [PANS]	26.5	68.5	105.4
Wei et al. (Wei et al., 2011) [DCM]	35.1	70.3	–
Liu et al. (Liu, 2021) [FBM]	29.3	72.4	112.8
Wei et al. (Wei et al., 2011) [FBM]	27.3	50.8	–
Huang Biao et al. (Huang et al., 2014) [FBM]	25.2	–	–
Wei et al. (Wei et al., 2011) [FBDCM]	27.3	43.0	–
Wang et al. (Wang et al., 2001) [Experimental]	20.0	–	–
Wang et al. (Wang et al., 2009) [Experimental]	22.0	–	–

shedding frequencies differ when comparing their values from different references, even for the cases with the same numerical approach. The present results of simulations showed that the DCM and standard models were the best in predicting shedding frequency compared with other experimental and numerical data.

In the present work, the shedding frequency is measured based on experimental measurements and numerical calculations. During the experimental measurements, the shedding frequency is extracted based on the recorded pressure fluctuations by a fast pressure sensor at the surface of the hydrofoil. Three fast pressure sensors were installed at different locations of $x/c = 0.12, 0.46$ and 0.79. Before using a recorded fluctuation to measure the shedding frequency, the location sensitivity analysis should be done to clarify if the location of the fast pressure sensor affects the shedding frequency. For this purpose, the shedding frequencies (i.e. first mode of frequency) extracted by pressure and vibration sensors were compared for three cavitation numbers, as shown in Fig. 11. It is concluded that the dominant frequency at the leading edge is quite different than the dominant frequency close to trailing edge since the first pressure sensor P2 is located inside the sheet cavity and doesn't record the shedding; however, the pressure sensor P10 records the shedding process as it senses the cloud cavity region. Overall, the recorded data by the last pressure sensor is more suitable to calculate the main shedding frequency as its fluctuation shows the fluctuation of the cloud cavity.

Fast Fourier Transform (FFT) is a widely used, powerful tool to understand vibrations and fluctuations better. This method converts the vibration signal from the time domain to the frequency domain. By this way, one can get an overview of the entire signal and can see how acceleration is divided across the frequency spectrum. In this respect, the FFT analysis of vibrations and corresponding pressure fluctuations are presented in Fig. 12. Firstly, the comparison of the amplitude of vibration at different cavitation numbers represents interesting results. It is visible that the amplitude of the vibration at $\sigma = 2.04$ is slightly higher than other ones. However, in the real observation of the test chamber, it was observed that the chamber was vibrating with larger movements at a low cavitation number. Thus, it is concluded that the amplitude of vibration, as shown in Fig. 12, depicts the acceleration of movement during direction changing which is larger in the smaller movements. Comparing the FFT analysis of pressure and vibration fluctuations, many micro frequencies are detected in the vibration, which cannot be observed in the pressure FFT plot. Besides, the pressure FFT analysis shows different modes of cavitating flow based on existing peaks in the FFT analysis; however, the modes are not detectable using vibration FFT analysis. Finally, in our case the inapplicability of FFT method for vibrations for high cavitation numbers is indicated. The last observation

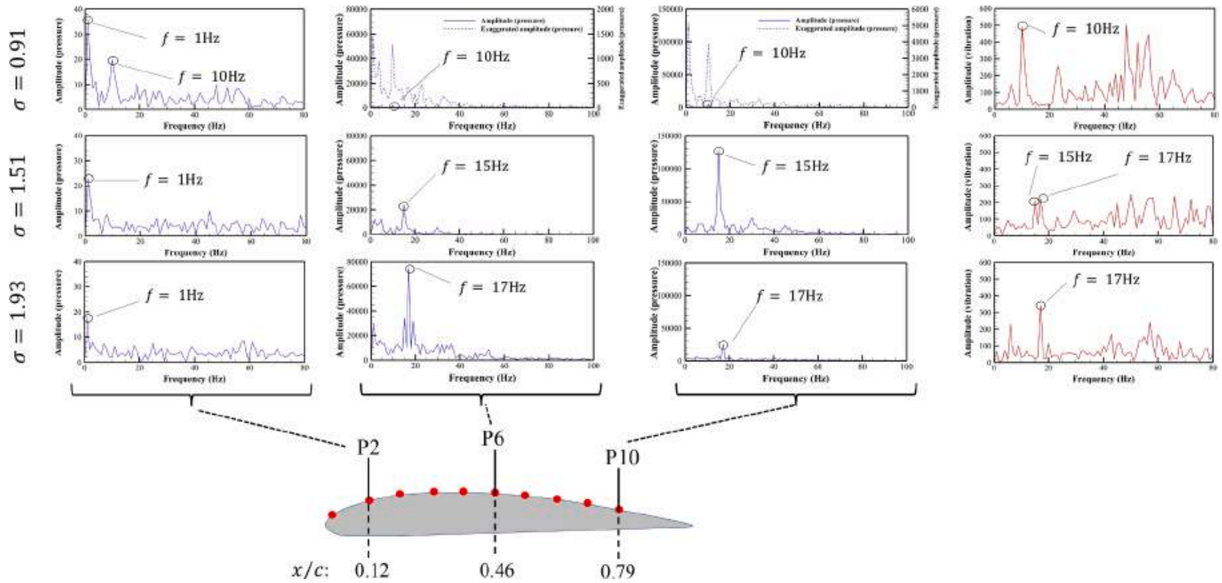

Fig. 11. Location sensitivity analysis of fast pressure sensors for the application of shedding frequency calculation.

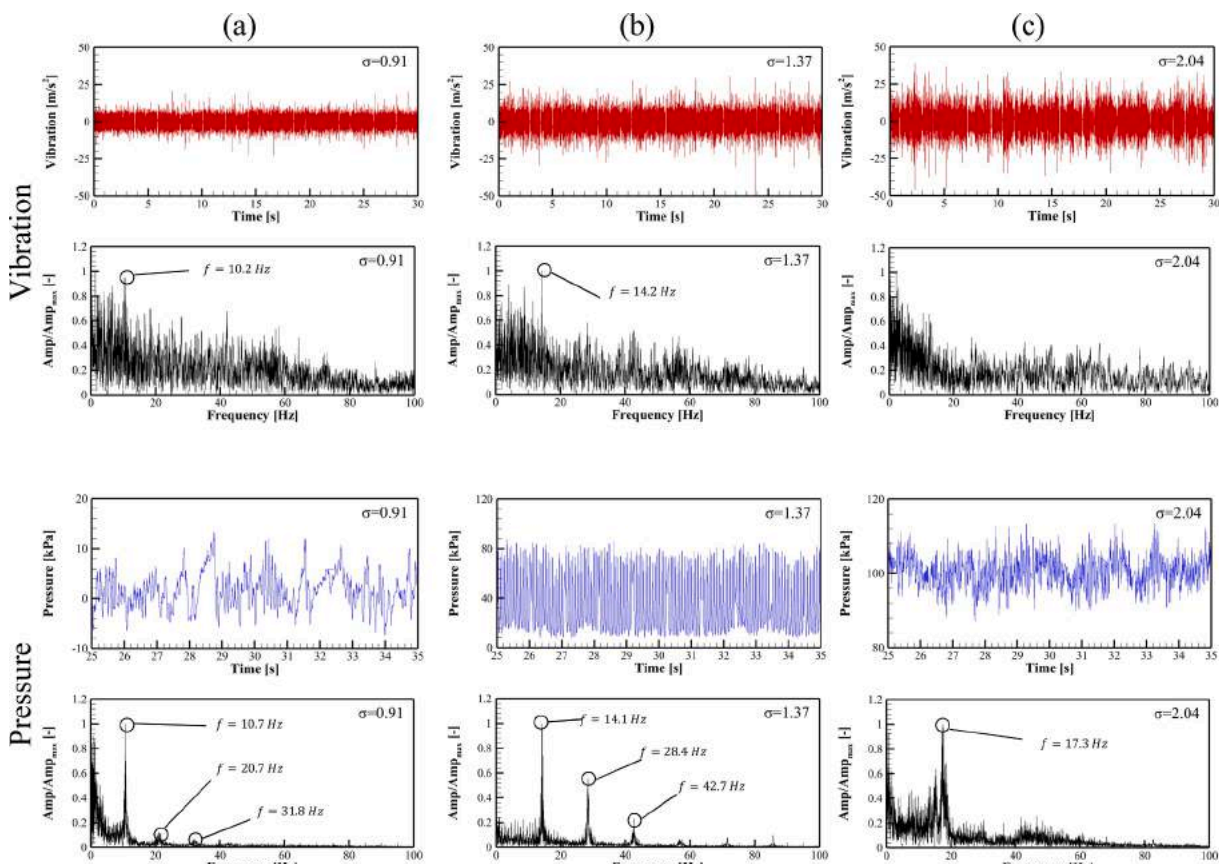

Fig. 12. Fast Fourier Transform (FFT) analysis of vibration and pressure fluctuations at different cavitation numbers of (a) $\sigma = 0.91$, (b) $\sigma = 1.37$ and (c) $\sigma = 2.04$.

emphasizes the necessity of extracting the shedding frequency with at least two parameters like pressure and vibration to be ensured about the accuracy of the result.

One of the main functions of adding dissolved air is its effect on the shedding frequency. In this section, the influence of dissolved air on the shedding frequency has been analysed based on the numerical simulations. For this purpose, the fluctuation of the volume of vapor during the time span before and after adding the dissolved air is analyzed. In addition, the continuous wavelet transform (CWT) is provided as a supplementary tool to continuously extract the frequency during the time span. The use of continuous wavelet transform (CWT) allows for more visible localization of the frequency components in the analyzed signals than commonly used Fast Fourier transform (FFT) which has one specific value for a signal during a time span. The distributions of the volume of vapor and air; as well as, the continuous wavelet transform (CWT) for two cavitation numbers $\sigma = 1.01$ and $\sigma = 1.18$ based on DCM and FBM models are provided in Fig. 13. It is worth explaining that the simulations were performed for the case without dissolved air in the first step, and after some while, the dissolved air is taken into account. It is observed that the distribution of the volume of vapor is more stable before adding the dissolved air regardless of cavitation number and modification model. Once the dissolved air is added, the volume distribution is more fluctuated declaring the more unsteady nature of cavitating flow included with dissolved air. Although the volume

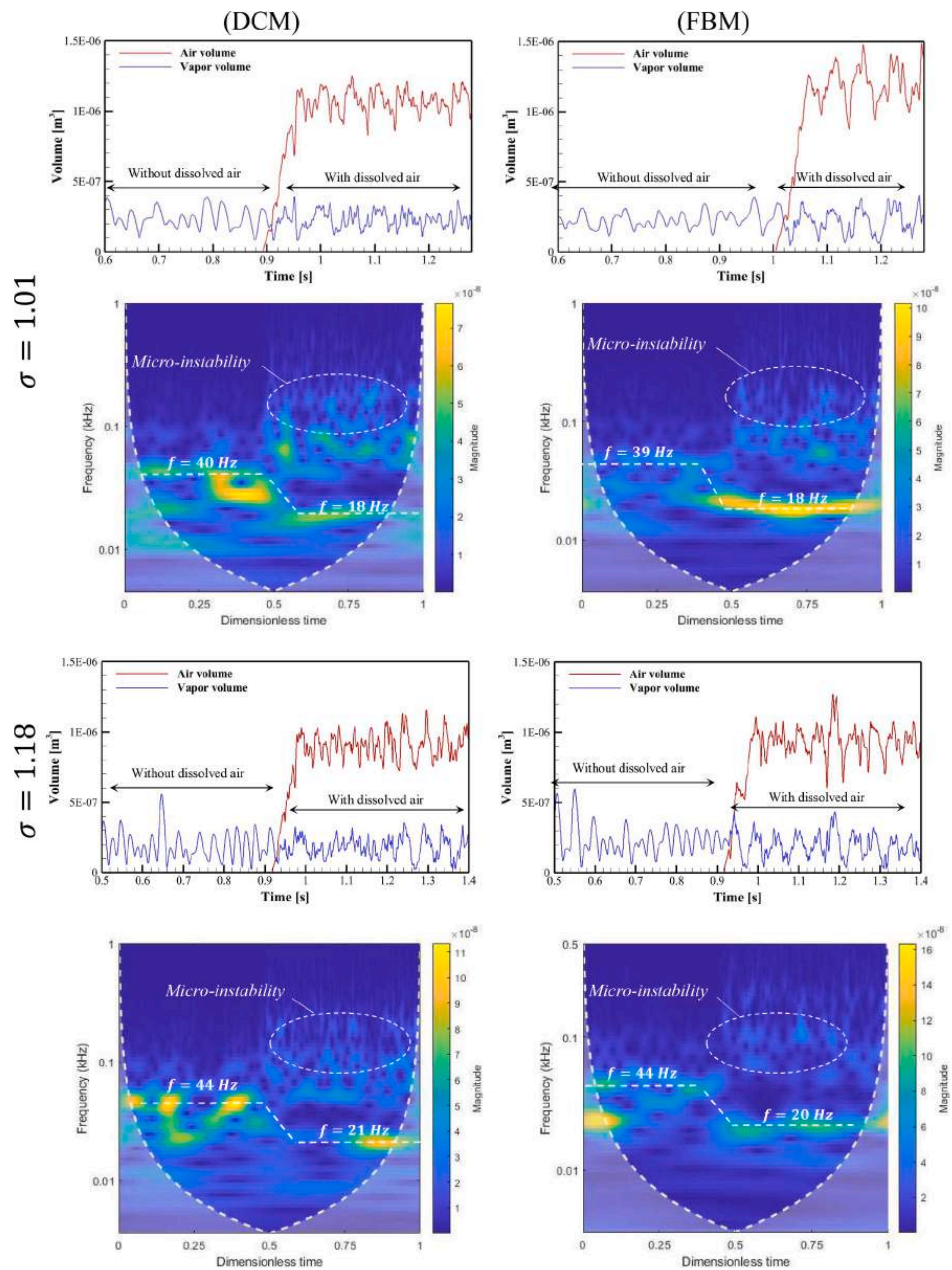

Fig. 13. Effect of dissolved air on the dynamic of cavitating flow and shedding frequency based on the numerical prediction.

distribution seems more unsteady and dynamic, the main frequency reduces. To prove the latest conclusion, one can refer to CWT analysis. The CWT analysis provided for the whole time span of vapor volume distribution. Two main conclusions can be derived using CWT analysis. Firstly, it is proved that the main frequency decreases regardless of cavitation number and modification model. Secondly, the cloud cavity has stronger local dynamic behaviour, which causes micro-instability, and more stable global characteristics generating lower shedding frequency.

The main concept of using viscosity modification models is avoiding the over-prediction of viscosity results in damping the dynamic characteristic and self-oscillation of cavitating flow. Thus, more dynamic and realistic cavitation flow is expected by using viscosity modification models. To prove the mentioned effects of viscosity modification models, the distribution of volume vapor in a time span for different models (i.e. standard, DCM and FBM) and the corresponding dominant frequency are presented in Fig. 14. It is worth explaining that the simulations were performed for the case with the standard model in the first step, and after some while, the modification models are taken into account. Based on the vapor volume distribution, a harmonic behaviour of cavitating flow is predicted by the standard model; however, the fluctuation of cavitating flow becomes more chaotic once the modification models are applied. Furthermore, the area of cavity closure is predicted to be enlarged while the modification models are applied which is expectable because of weaker viscosity, especially at the boundary of cavity closure. The dominant frequency of cavitation enhances when the DCM model was applied; reversely, the lower frequency is predicted by FBM, which was unexpected.

5.4. Averaged/instantaneous characteristics with/without air

This section discusses the influence of dissolved air on the instantaneous and averaged characteristics of cavitating flow and compares them with the cases without dissolved air. Firstly, the impact of both the viscosity modification model and dissolved air on the instantaneous behaviour of cavitating flow will be discussed. For this purpose, the history of the lift coefficient is considered representative of the instantaneous behaviour of the cavitating flow. So, the history of lift coefficient versus time for different viscosity modification models for the cases with and without dissolved air is represented in Fig. 15. Comparing the history of lift force in time, it is concluded that the unsteadiness and dynamic nature of the lift force enhanced once the modification models were applied regardless of the type of model. This observation proves the great impact of viscosity modification models in avoiding the overestimation of viscosity, especially inside of the cavity closure, resulting in damping of shedding process and self-oscillation. In the previous section, the results declared that although the dissolved air augments the micro-instability of cavitating flow, it becomes stable from a global point of view resulting in a reduced value of shedding frequency. To justify the importance of micro-instability and global shedding frequency, generated by adding dissolved air, on the hydrofoil, the lift force under influence of dissolved air is presented in Fig. 15. The lift force is assumed as one of the best choices since it shows the effect of cavitating flow from a global point of view. By increasing the dissolved air regardless of the type of viscosity modification model, the lift coefficient becomes extremely stable showing the great importance of dissolved air in damping the highly dynamic behaviour of the cavitating flow.

The lift and drag coefficients versus cavitation number as a function of viscosity modification models and levels of dissolved air are presented in Fig. 16. By reducing the cavitation number, an intensive cavitating flow is generated. This issue results in the enhancement of the drag coefficient and reduction of the lift coefficient. By employing different types of viscosity modification models, a greater influence on the drag coefficient distribution is recorded in comparison to the changes in the lift coefficient. The latest observation is also reported by Shi et al. (Shi et al., 2013) when they compared the lift and drag coefficient predicted by standard, FBDCM and PANS models. They reported a 15 % and 11 % enhancement in time-averaged drag coefficient comparing the results predicted by FBDCM and PANS models with the standard model, whilst the corresponding increments for time-averaged lift coefficient were 8 % and 5 %. On the other hand, the predicted values for both lift and drag coefficients by DCM and FBM are higher than those calculated using the standard model. Furthermore, the dissolved air does not affect the lift coefficient significantly, while the drag coefficient rises over almost all cavitation numbers in the cases with dissolved air.

5.5. Flow structure

Flow visualization based on experimental and numerical approaches is one of the interesting and demanding topics in an investigation of cavitating flow. Once the cavitating flow is visualized in detail, the influential parameter such as re-entrant jet can be studied. In addition, the experimental visualization can be utilized as a valid reference for the verification of numerical simulation. After providing the numerical simulation of flow structure verified by comparing with experimental visualization, many local parameters like velocity vector and vorticity magnitude, which are impossible or hard to obtain based on experimental techniques, may be extracted. To evaluate the capability of the standard, DCM and FBM models to predict the flow structure, the evolution of cavitation over the period $\sigma = 1.18$ with dissolved air is characterized in Fig. 17. The general view of cavitation evolution regardless of visualization technique is almost similar. At the first step, the incipient cavity has appeared close to the leading edge. It means that the local pressure is going below the vapor saturation pressure in this region. As the pressure is still lower than the saturation pressure, the cavity closure enlarged gradually in time. When the cavity closure is becoming large enough and reaches almost the last quarter of hydrofoil, the momentum of the re-entrant jet would be enough to detach the cloud cavity. This is

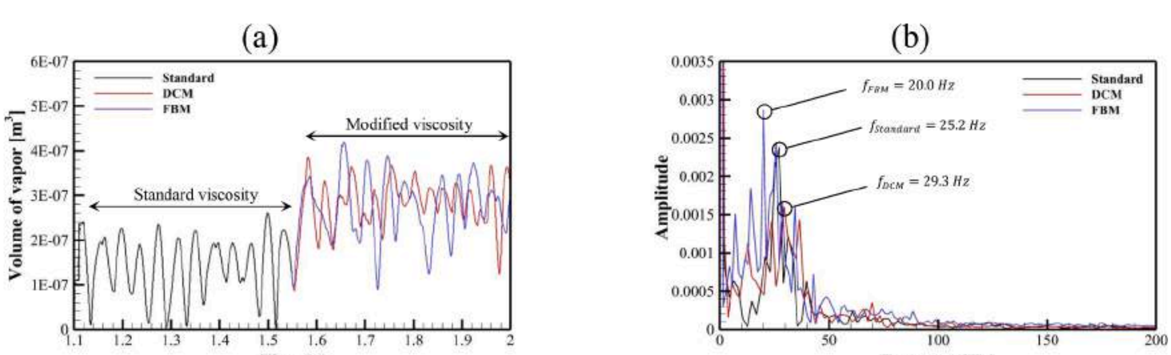

Fig. 14. Effect of viscosity modification models on the (a) dynamic of cavitating flow and (b) shedding frequency based on the numerical prediction ($\sigma = 0.91$, without dissolved air).

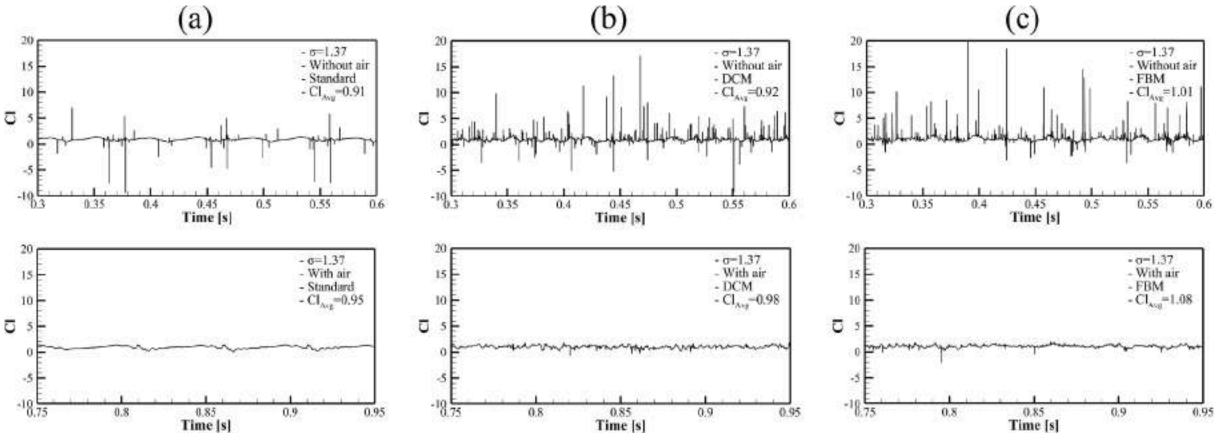

Fig. 15. Effect of viscosity modification models (a) Standard (b) DCM (c) FBM and dissolved air on the history of lift force over a specific time span and cavitation number.

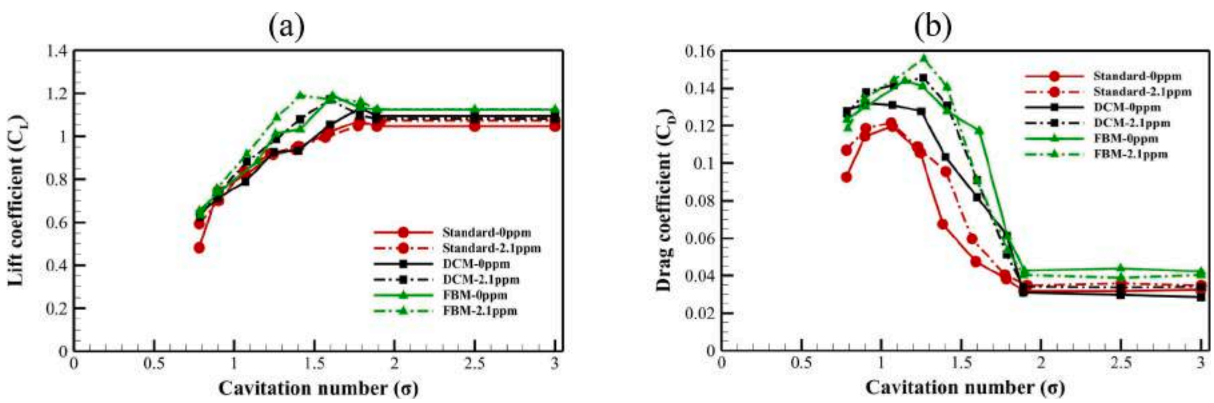

Fig. 16. Effect of viscosity modification model and dissolved air on the the time-averaged (a) lift and (b) drag coefficients versus cavitation number.

created by the re-entrant jet, which penetrates toward the leading edge through and collides with the front of cavity closure. As a result, the cloud cavity is shedding downstream. This process will continue over the next period and create a periodic cavitating flow. As is expected, the standard model predicts smaller cavity closure due to overestimated viscosity, especially in the cavitation region. By modifying the viscosity using viscosity modification models (i.e. DCM and FBM), the significantly enlarged cavity appeared during the period. The comparison between numerical and experimental observations leads us to the conclusion that the modified models are highly applicable for the numerical flow visualization. It is worth noting that the prediction performed by DCM and FBM are almost similar, and the differences are negligible.

The shedding process is the main factor, which cusses periodical features of cavitating flow like periodical pressure and force components. On the other hand, it cusses vibration and noise when the cloud cavity breaks up. Thus, having a numerical model, which is capable to capture the shedding process, would be helpful for better prediction of other periodical characteristics. To assess the ability of the standard model as well as DCM and FBM approaches for this purpose, the shedding process over a period $\sigma = 1.51$ with dissolved air is characterized in Fig. 18. The shedding process and detachment highly depends on the re-entrant jet. As shown in the three-dimensional flow structure, the detached cavity is not well simulated by the standard model compared with the experimental observation. The standard model overestimates the viscosity damping the shedding process in two ways. Viscosity is a measure of resistance to fluid flow. Thus, a higher value means it has more resistance and thus flows more slowly. As a result, the velocity of the re-entrant jet, which is the main reason for detachment, reduces. Therefore, a weaker re-entrant jet is unable to detach the cloud cavity. On the other hand, the detached cloud cavity moves harder through a viscous fluid. On the contrary, the detached cavity is captured well when the modification models are applied. No significant differences are identified in the results of the DCM and FBM models. The DCM model shows minor better capability in this purpose since the structure of the detached could cavity is in closer agreement with the experimental observations.

The effect of cavitation on the local variables such as local pressure, velocity and vorticity can be characterized based on the numerical results. In addition, by comparing them with each other, one can detect the relation between those variables. At this end, the contours of static pressure, velocity magnitude and vorticity along with experimental visualization of flow structures are presented in Fig. 19. The distributions of all variables in the standard model are more uniform than other modified models due to a damped oscillation of cavitating flow. It is declared that the magnitude of vorticity inside the cavity closure is highly considerable showing the spinning characteristic of the cavity. It is due to the existence of both the re-entrant jet from the bottom side and the main flow from above that are flowing reversely and making the circulation.

The re-entrant jet is identified as the main factor in the detachment of the cloud cavity from the surface of the hydrofoil. Therefore, the nature of the re-entrant jet and related characteristics must be clarified. The effect of the re-entrant jet on the detaching of the cloud cavity is represented in Fig. 20. At this end, two steps before detachment, which are accompanied by the three-dimensional flow structure, pressure contour and velocity vector, are shown. In the first step, the cloud cavity is fully attached to the surface, and the reverse flow is initiated from the trailing

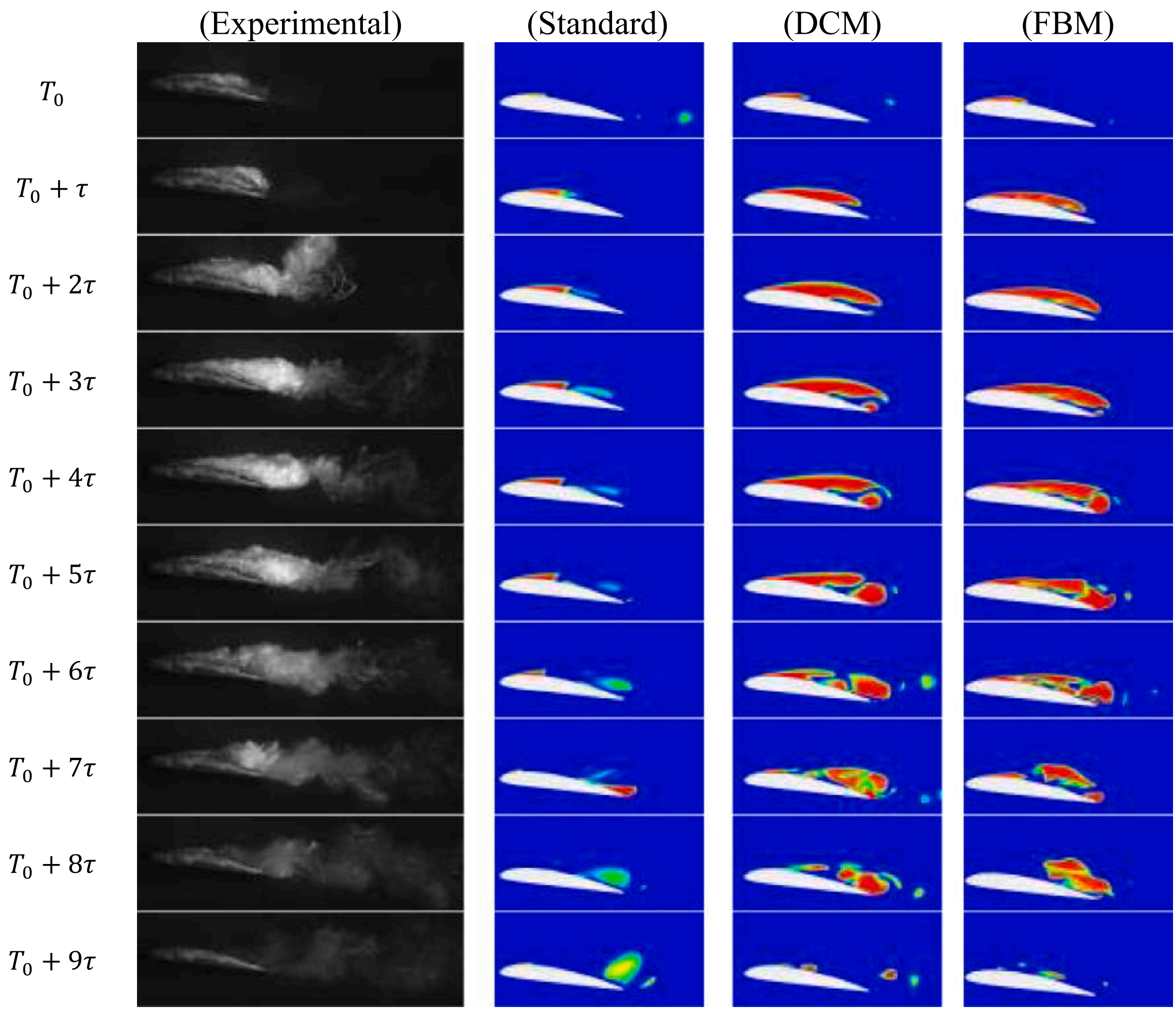

Fig. 17. Cavitation evolution over a period- Experimental observation versus numerical prediction ($\sigma = 1.18$ with dissolved air).

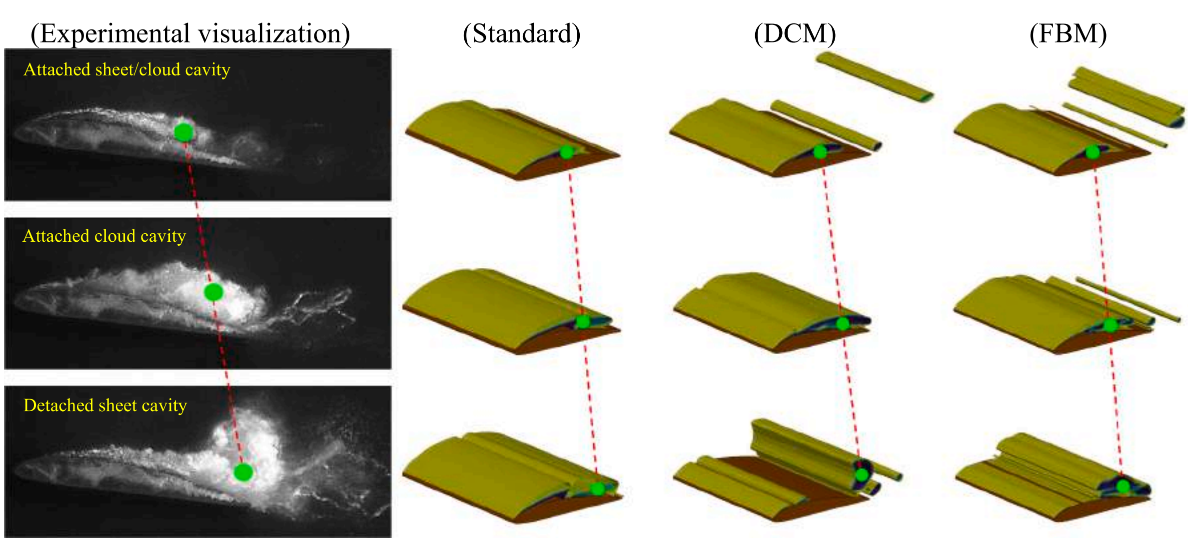

Fig. 18. Flow structure during shedding process- Experimental observation versus numerical prediction ($\sigma = 1.51$ with dissolved air).

edge. The collision of the reverse flow with the main flow creates the water vortex near the trailing edge. Hence, a narrow reverse flow penetrates beneath the cloud cavity, which can be known as the first sign of detachment. In the second step, the re-entrant jet with a considerably stronger front moved toward to leading edge. The re-entrant jet is strong enough to detach the cloud cavity from the surface, which can be concluded by the generated deformation on the cavity closure. Moreover, the front of the re-entrant jet becomes sharper than the previous

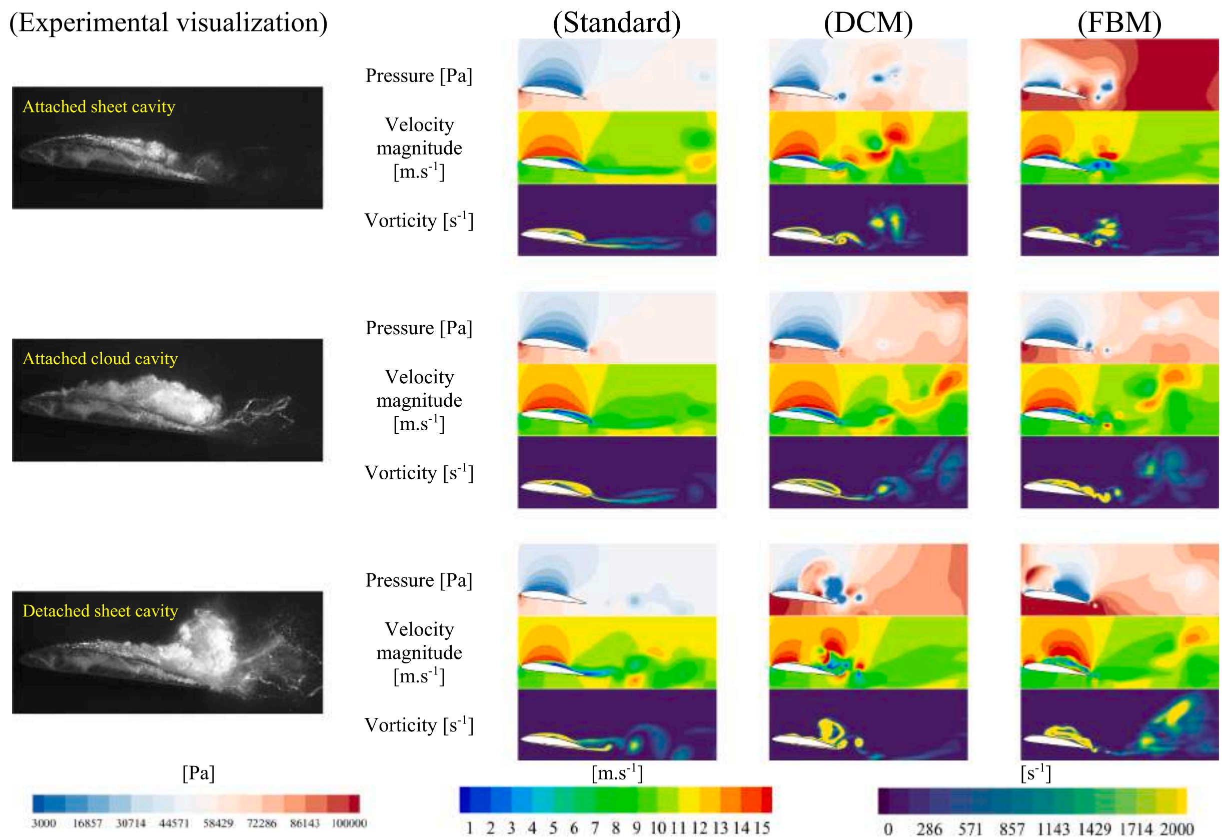

Fig. 19. Contours of pressure, velocity magnitude and vorticity predicted by different modification models ($\sigma = 1.51$ with dissolved air).

step that is more influential in detachment. In the third step, the cloud cavity is detached and shed to downstream along with the main flow. However, the re-entrant jet still moves toward the leading edge and hits the remained attached cavity.

6. Conclusion

The purpose of the present work is to analyse the cavitating flow over a Clark Y hydrofoil considering the dissolved air as the third phase. To this end, the numerical and experimental approaches are employed to provide a comprehensive investigation. To improve the capability of the mathematical modelling dealing with the dynamic behaviour of cavitating flow, the turbulence models are modified based on the Density-Corrected Model and Filter-Based Model. Furthermore, the transient characteristics of the cavitating flow like pressure and vibration are measured, and the structure of cavity closure is visualized using a high-speed camera. To evaluate the transient data, the Fast Fourier Transfer and Continuous Wavelet Transform are applied to extract and compare the shedding frequency of experiments and numerical predictions. In addition, the influence of modification models on the cloud cavitation shedding evolution, dominant shedding frequency, vorticity, pressure, velocity profile near the hydrofoil, lift/drag coefficient is evaluated. Based on the analysis conducted over the experimental observations and numerical simulations, the following conclusions may be drawn:

- The viscosity modification has larger effect on the drag coefficient than the lift coefficient. In addition, the models with a reduced eddy viscosity, predict higher values of force coefficients.
- The predicted front of the re-entrant jet is getting closer to the leading edge once the viscosity modification is applied. However, the distributions of velocity profiles are almost the same.
- Comparing the shedding frequency (i.e. first mode of frequency) predicted by the present model and those by other researchers, it is hard to conclude which model can better predict the shedding frequency since all frequencies are in the range reported in the literature.
- The frequency measured by the pressure fluctuation from the taps near to leading edge does not draw the shedding frequency since those taps are located inside of the sheet cavity. However, the taps near trailing edges can be used for measuring the shedding frequency.
- The shedding frequency and the cavitation number are in a direct relationship.
- Adding dissolved air to the water causes a reduction in shedding frequency. Furthermore, instabilities in smaller scale occur when the dissolved air is taken into account since the cavity closure becomes more dynamic and unstable.
- Although the viscosity modifications have impact on the transient behaviour of cavitating flow, the average characteristics are fairly similar.
- Adding dissolved air to the water causes enhancement of lift and drag coefficients.
- Since the modified turbulence models prevent over-estimation of viscosity and damping of self-oscillation, the larger cavity is predicted by these models.

The future plan of the present work is further modification over the viscosity modification models to make them compatible with the non-condensable gas effect.

Funding and conflicts of interests

The experimental part of this project was supported by the Polish National Science Centre, Poland funds within the project UMO-2016/21/B/ST8/01164. Moreover, the project was additionally supported by the Department of Power Engineering and Turbomachinary, The

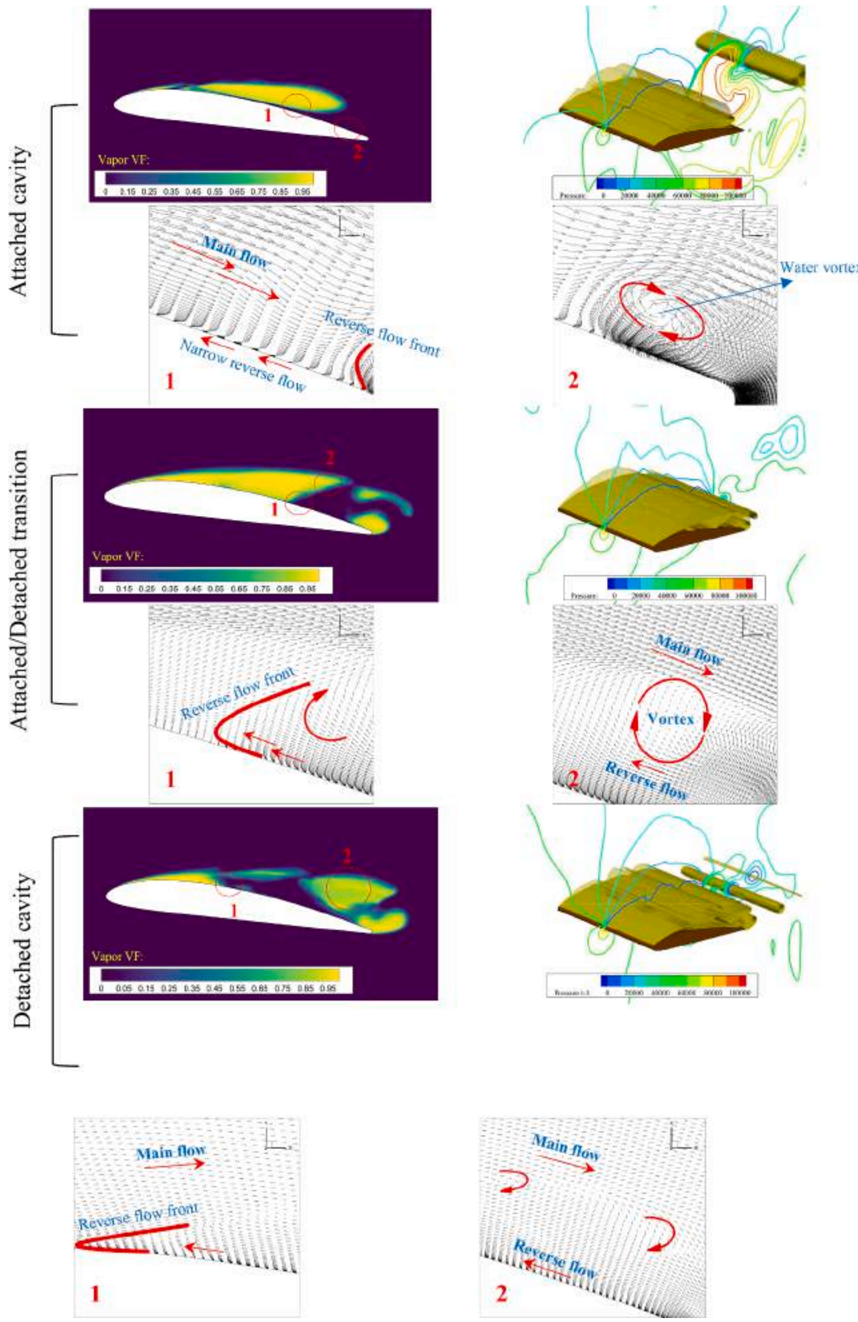

Fig. 20. Detailed observation on the re-entrant jet ($\sigma = 1.37$ with dissolved air, DCM).

Silesian University of Technology within the grant BKM-605/RIE5/2021 (08/050/BKM21/0243). Also, the authors certify that they have NO conflict of interest.

CRediT authorship contribution statement

Emad Hasani Malekshah Fazel: Conceptualization, Methodology, Software, Investigation, Validation, Formal analysis, Writing – original draft, Writing – review & editing. **Włodzimierz Wróblewski:** Conceptualization, Writing – review & editing, Supervision.

Declaration of Competing Interest

The authors declare that they have no known competing financial interests or personal relationships that could have appeared to influence the work reported in this paper.

Data availability

The authors do not have permission to share data.

References

Ahn, S.-H., Xiao, Y., Wang, Z., Luo, Y., Fan, H., 2018. Unsteady prediction of cavitating flow around a three dimensional hydrofoil by using a modified RNG k-ε model. Ocean Eng. 158, 275–285.
Biao, H., Guo-Yu, W., 2011. Evaluation of a filter-based model for computations of cavitating flows. Chin. Phys. Lett. 28 (2), 026401.
C. E. Brennen, "New York Oxford Oxford University Press," 1995.
Brennen, C.E., 2014. Cavitation and bubble dynamics. Cambridge University Press.
Callenaere, M., Franc, J.-P., Michel, J.-M., Riondet, M., 2001. The cavitation instability induced by the development of a re-entrant jet. J. Fluid Mech. 444, 223–256.

Chen, Y., Chen, X., Gong, Z., Li, J., Lu, C., 2016. Numerical investigation on the dynamic behavior of sheet/cloud cavitation regimes around hydrofoil. Appl. Math. Model. 40 (11–12), 5835–5857.
Chen, T., Huang, B., Wang, G., 2016. Numerical study of cavitating flows in a wide range of water temperatures with special emphasis on two typical cavitation dynamics. Int. J. Heat Mass Transf. 101, 886–900.
Coutier-Delgosha, O., Reboud, J., Delannoy, Y., 2003. Numerical simulation of the unsteady behaviour of cavitating flows. Int. J. Numer. Meth. Fluids 42 (5), 527–548.
Coutier-Delgosha, O., Fortes-Patella, R., Reboud, J.-L., 2003. Evaluation of the turbulence model influence on the numerical simulations of unsteady cavitation. J. Fluids Eng. 125 (1), 38–45.
Ducoin, A., Huang, B., Young, Y.L., 2012. Numerical modeling of unsteady cavitating flows around a stationary hydrofoil. Int. J. Rotating Mach. 2012.
Germano, M., Piomelli, U., Moin, P., Cabot, W.H., 1991. A dynamic subgrid-scale eddy viscosity model. Phys. Fluids A 3 (7), 1760–1765.
M. Hofmann, H. Lohrberg, G. Ludwig, B. Stoffel, J.-L. Reboud, and R. F. Patella, "Numerical and experimental investigations on the self-oscillating behaviour of cloud cavitation: part I: visualisation," in *ASME, FEDSM99-6755*, 1999.
Homa, D., Wróblewski, W., Majkut, M., Strozik, M., 2019. Research on unsteady cavitating flow around a Clark-Y 11.7% hydrofoil. J. Theor. Appl. Mech. 57.
D. Homa, "Eksperymentalne i numeryczne badanie zjawiska kawitacji dla różnych warunków przepływu," (in Polish), *PhD Thesis, Silesian University of Technology, Gliwice,* 2018.
Huang, B., Young, Y.L., Wang, G., Shyy, W., 2013. Combined experimental and computational investigation of unsteady structure of sheet/cloud cavitation. J. Fluids Eng. 135 (7), pp.
Huang, B., Wang, G.-Y., Zhao, Y., 2014. Numerical simulation unsteady cloud cavitating flow with a filter-based density correction model. J. Hydrodyn. 26 (1), 26–36.
Johansen, S.T., Wu, J., Shyy, W., 2004. Filter-based unsteady RANS computations. Int. J. Heat Fluid Flow 25 (1), 10–21.
Joseph, D.D., 1995. Cavitation in a flowing liquid. Phys. Rev. E 51 (3), R1649.
Joseph, D.D., 1998. Cavitation and the state of stress in a flowing liquid. J. Fluid Mech. 366, 367–378.
Kawakami, D.T., Qin, Q., Arndt, R., 2005. Water quality and the periodicity of sheet/cloud cavitation. Fluids Eng. Div. Summer Meet. 41995, 513–517.
Kubota, A., Kato, H., Yamaguchi, H., 1992. A new modelling of cavitating flows: a numerical study of unsteady cavitation on a hydrofoil section. J. Fluid Mech. 240, 59–96.
Kunz, R.F., et al., 2000. A preconditioned Navier-Stokes method for two-phase flows with application to cavitation prediction. Comput. Fluids 29 (8), 849–875.
D. Li, M. Grekula, and P. Lindell, "A modified SST k-? turbulence model to predict the steady and unsteady sheet cavitation on 2D and 3D hydrofoils," 2009.
Liu, J., et al., 2021. Numerical investigation of shedding dynamics of cloud cavitation around 3D hydrofoil using different turbulence models. Eur. J. Mech.-B/Fluids 85, 232–244.
Lohrberg, H., Stoffel, B., Fortes-Patella, R., Coutier-Delgosha, O., Reboud, J., 2002. Numerical and experimental investigations on the cavitating flow in a cascade of hydrofoils. Exp. Fluids 33 (4), 578–586.
Long, X., Wang, J., Zhang, J., Ji, B., 2018. Experimental investigation of the cavitation characteristics of jet pump cavitation reactors with special emphasis on negative flow ratios. Exp. Therm. Fluid Sci. 96, 33–42.
Mäkiharju, S.A., Ganesh, H., Ceccio, S.L., 2017. The dynamics of partial cavity formation, shedding and the influence of dissolved and injected non-condensable gas. J. Fluid Mech. 829, 420–458.
H. Matsunari, S. Watanabe, Y. Konishi, N. Suefuji, and A. Furukawa, "Experimental/Numerical Study on Cavitating Flow Around Clark Y11. 7% Hydrofoil," in *Proceedings of Eighth International Symposium on Cavitation*, 2012, pp. 358-363.
Numachi, F., 1938. Cavitation performance of 4 types of hydrofoil. Trans. JSME 7 (28), 1–9.
W. Shi, G. Zhang, and D. Zhang, "Evaluation of turbulence models for the numerical prediction of transient cavitation around a hydrofoil," in *IOP Conference Series: Materials Science and Engineering*, 2013, vol. 52, no. 6: IOP Publishing, p. 062013.
Sun, T., Wei, Y., Zou, L., Jiang, Y., Xu, C., Zong, Z., 2019. Numerical investigation on the unsteady cavitation shedding dynamics over a hydrofoil in thermo-sensitive fluid. Int. J. Multiph. Flow 111, 82–100.
W. Tsuru, S. Ehara, S. Kitamura, S. Watanabe, and S. Tsuda, "Mechanism of lift increase of cavitating Clark Y-11.7% hydrofoil," in *in Proceedings of the 10th International Symposium on Cavitation (CAV2018)*, 2018: ASME Press.
G. Wang, B. Zhang, B. Huang, and M. Zhang, "Unsteady dynamics of cloud cavitating flows around a hydrofoil," Proceedings of the 7th International Symposium on Cavitation CAV2009, 2009.
Wang, C., Huang, B., Wang, G., Zhang, M., Ding, N., 2017. Unsteady pressure fluctuation characteristics in the process of breakup and shedding of sheet/cloud cavitation. Int. J. Heat Mass Transf. 114, 769–785.
Wang, G., Senocak, I., Shyy, W., Ikohagi, T., Cao, S., 2001. Dynamics of attached turbulent cavitating flows. Prog. Aerosp. Sci. 37 (6), 551–581.
Wei, Y.-J., Tseng, C.-C., Wang, G.-Y., 2011. Turbulence and cavitation models for time-dependent turbulent cavitating flows. Acta Mech. Sin. 27 (4), 473–487.
Wróblewski, W., Bochon, K., Majkut, M., Malekshah, E.H., Rusin, K., Strozik, M., 2021. An experimental/numerical assessment over the influence of the dissolved air on the instantaneous characteristics/shedding frequency of cavitating flow. Ocean Eng. 240, 109960.
Wróblewski, W., Bochon, K., Majkut, M., Rusin, K., Malekshah, E.H., 2021. Numerical study of cavitating flow over hydrofoil in the presence of air. Int. J. Numer. Meth. Heat Fluid Flow.
Yakhot, V., Orszag, S., Thangam, S., Gatski, T., Speziale, C., 1992. Development of turbulence models for shear flows by a double expansion technique. Phys. Fluids A 4 (7), 1510–1520.
Yin, T., Pavesi, G., Pei, J., Yuan, S., 2021. Numerical analysis of unsteady cloud cavitating flow around a 3D Clark-Y hydrofoil considering end-wall effects. Ocean Eng. 219, 108369.
Zhang, D., Shi, L., Shi, W., Zhao, R., Wang, H., van Esch, B.B., 2015. Numerical analysis of unsteady tip leakage vortex cavitation cloud and unstable suction-side-perpendicular cavitating vortices in an axial flow pump. Int. J. Multiph. Flow 77, 244–259.

Paper VI:

Evaluation of modified turbulent viscosity on shedding dynamic of three-phase cloud cavitation around hydrofoil–numerical/experimental analysis

The current issue and full text archive of this journal is available on Emerald Insight at:
https://www.emerald.com/insight/0961-5539.htm

Evaluation of modified turbulent viscosity on shedding dynamic of three-phase cloud cavitation around hydrofoil – numerical/experimental analysis

Received 24 March 2022
Revised 2 April 2022
Accepted 8 April 2022

Emad Hasani Malekshah, Wlodzimierz Wróblewski, Krzysztof Bochon and Mirosław Majkut
Department of Power Engineering and Turbomachinery, Silesian University of Technology, Gliwice, Poland

Abstract

Purpose – This paper aims to focus on the cavitating flow around the Clark-Y hydrofoil when the dissolved air is taken into account as the third phase. As the RNG k-epsilon model yields poor prediction due to overestimation of viscosity, the modification approaches including density corrected method, filter-based model and filter-based density correction model are used, and the turbulence model is modified. Also, the numerical results are compared with the experimental data.

Design/methodology/approach – The cavitating flow is known as a complex multi-phase flow and appeared in the regions where the local pressure drops under saturation vapor pressure. Many researches have been conducted to analyze this phenomenon because of its significant impact on the erosion, vibration, noise, efficiency of turbomachines, etc.

Findings – The experiments are conducted in a rectangular test section equipped with Clark-Y hydrofoil providing cavity visualization, instantaneous pressure and vibration fluctuations. The simulations are carried out for different cavitation numbers with and without dissolved air. The Fast Fourier Transform, continues wavelet transform and temporal-spatial distribution of gray level are implemented to extract and compare the shedding frequency of experiments and numerical predictions and cavitation evolution. It is concluded that the flow structure, shedding frequency and time-averaged characteristics are highly influenced by the dissolved air. Also, the numerical prediction will be more satisfactory when the modified turbulence models are applied.

Originality/value – To the best of the authors' knowledge, the originality of this study is the modification of the turbulence model for better prediction of cavitating flow, and the validation of numerical results with corresponding experimental data.

Keywords Cavitating flow, Density corrected method (DCM), Dissolved air, Filter-based density correction model (FBDCM), Filter-based model (FBM), Viscosity modification

Paper type Research paper

1. Introduction

The cavitation process initiates in the regions where the local pressure drops below the vapor saturation pressure at the local thermodynamic state (Brennen, 2014; Wróblewski *et al.*, 2021b; Ullas *et al.*, 2022). Generally, the cloud cavity is known as a highly unsteady

The presented work was supported by the Polish National Science Centre funds within the project UMO-2016/21/B/ST8/01164. Also, the authors certify that they have NO conflict of interest.

International Journal of Numerical Methods for Heat & Fluid Flow

0961-5539
DOI 10.1108/HFF-03-2022-0188

turbulent flow which is characterized by large cavity shedding (Laberteaux and Ceccio, 2001; Reisman *et al.*, 1998), strong cavity collapse resulting in the intensive damage on the objected surface (Wróblewski *et al.*, 2021b; Li *et al.*, 2014; Schenke and van Terwisga, 2019). Thus, the cavitating flow will be followed by noise, vibration, erosion, etc. As a result, it is necessary to understand this phenomenon to adopt the best controlling approach and reduce the negative effect. Two different shedding instabilities are observed, which is mainly categorized by structure, so-called transitional cavity oscillation (TCO) (Kawanami *et al.*, 1997) and partial cavity oscillation (PCO) (Arndt, 1981). The first type TCO usually follows by attached cavity which its length exceeds 75% of the hydrofoil chord with highly unstable nature causing strong vibration. In addition, the cavity considerably alters between partial and super cavity with low frequency, large cavity shedding region and observable re-entrant jet (Sato *et al.*, 2002). However, when the cavity starts to shed around the trailing edge with small-scale shed cloud cavity with rather high frequency, its length is usually not exceed almost 75% of chord corresponding to PCO (Watanabe *et al.*, 2009).

Further to many effective parameters on the cavitating flow, the dissolved air can be known as an influential factor, which has not been fully analyzed by the researchers. Recently, Wróblewski *et al.* (2021a) analyzed the effects of dissolved air on the cavitating flow around the Clark Y hydrofoil and the corresponding unsteady characteristics and shedding frequencies based on numerical simulations and experimental observations. They used the three phases model to consider liquid, vapor and air as three governing phases. Two different amounts of dissolved air (i.e. 2.6 and 5.5 ppm oxygen) were taken into account. In addition, the numerical results were compared with the experimental observations. The results of numerical simulation and image processing of experimental data declared that the addition of dissolved air is associated with enlarged cavity closure during the evolution of the cavity. In addition, based on the FFT evaluation of pressure fluctuations, the authors reported that the shedding frequency decreases in the case of a higher volume fraction of dissolved air. Mäkiharju *et al.* (2017) conducted an experimental work to evaluate the shedding dynamic of cavity based on analysis on the vapor production rate of natural cavity. Also, they tried to investigate the impact of injection of non-condensable gas on the vapor production resulting on cavity flow and cavity shedding. They used the high-speed visualization camera and X-ray densitometry. The observations declared that the gas injection results in substantial reduction of cavity void fraction. Furthermore, changes on the cavity void fraction dramatically alter the bubbly shock formation. Moreover, it was approved that the injection is clearly more effective than gas content alone (i.e. without injection).

Furthermore, the turbulence model plays an important role in determining the characteristics of the cavitating flow since this phenomenon is a highly turbulent flow. The standard turbulence models overestimate the viscosity; as a result, the damping effect causes unrealistic simulation. For this purpose, the turbulent viscosity in the mentioned regions had to be modified. Reboud *et al.* (1998) first proposed an empirical correlation for the mixture of vapor and liquid which is validated with experimental data gathered by X-ray imaging technique. Coutier-Delgosha *et al.* (2003a) showed that the RNG $k-\varepsilon$ turbulence model poorly reflects experimental observations of the vapor cloud shedding when the compressibility effect is not taken into account. By considering the compressibility effect, the RNG $k-\varepsilon$ turbulence model presents a reliable prediction over the unsteady behavior of the cavitation process. Also, the modified model gives satisfactory results over different geometries such as hydrofoil (Hofmann *et al.*, 1999), foil cascade (Lohrberg *et al.*, 2002) and Venturi nozzles (Coutier *et al.*, 2003b). Yin *et al.* (2021) used the density correction method (DCM) in the shear stress transport (SST) $k-\omega$ turbulence model for simulation of unsteady cloud cavitating flow over a three-dimensional Clark-Y hydrofoil under the effect of end-wall. They reported that the modified SST $k-\omega$ model shows a better ability to predict both types of unsteady cavitation. The dynamics of cloud cavity in the flow around a Clark-Y at a constant angle of attack of 8° was analyzed by Liu *et al.* (2021b). They used the $k-\varepsilon$ RNG turbulence model modified by the FBM. They concluded comparing the numerical results with the experimental data that even though the overestimation of turbulent viscosity, the standard turbulence model fails to predict the dynamics of cloud shedding, the structure of clouds, oscillation of lift coefficient and time-averaged velocity distributions were well recognized. Yu *et al.* (2015) used filter-based density corrected model (FBDCM) to study the cavitation shedding dynamics around a NACA66 hydrofoil. The results revealed that the FBDCM turbulent model can efficiently predict the cavitation process including growth, break-off and collapse. In addition, this model proved its ability in simulation of strong interaction between cloud cavity and trailing edge vortex.

The present paper aims to study the cavitating flow around the hydrofoil when the dissolved air is taken into consideration as the third phase. To provide a better numerical prediction, the turbulence models are modified based on DCM, FBM and FBDCM approaches. Moreover, the numerical simulations are supplemented by experimental observation and measurements. The Fast Fourier Transfer and continuous wavelet transform are used to analyze the transient behavior of the cavitation.

2. Mathematical formulations

2.1 Multi-phase model

In the present work, the mixture model is used to treat the multiphase flow consisting of water, vapor and air. Based on this model, the mixture of the phases is considered as a single fluid sharing the same velocity field. As such, no-slip velocity between the phases exists. It is worth mentioning that the present simulation is carried out as three-dimensional; however, the span of the computational domain is considered very thin to reduce the computational cost. The continuity and momentum conservation are defined as follows:

$$\frac{\partial \rho}{\partial t} + \nabla \cdot (\rho u) = 0 \tag{1}$$

$$\frac{\partial}{\partial t}(\rho u) + \nabla \cdot (\rho u u) = -\nabla p + \nabla \cdot \left[\mu\left(\nabla u + \nabla u^T\right)\right] + \rho g \tag{2}$$

$$\begin{cases} \rho = \rho_l \alpha_l + \rho_v \alpha_v + \rho_{ng} \alpha_{ng} \\ \mu = \mu_l \alpha_l + \mu_v \alpha_v + \mu_{ng} \alpha_{ng} \end{cases} \tag{3}$$

It should be noted that the body force effect is neglected. In addition, the presence of dissolved non-condensable gas is taken into account; as a result, equation (3) consists of the properties of liquid, vapor and gas. Moreover, the mixture phase adopts the three phases model to solve the governing equations for the phases, separately. The mass transfer between a liquid and a mixture of gaseous phases was modelled between species:

$$\frac{\partial \rho_v \alpha_v}{\partial t} + \nabla \cdot (\rho_v \alpha_v u) = \dot{m} = \dot{m}^+ - \dot{m}^- \tag{4}$$

$$\frac{\partial \rho_{ng}\alpha_{ng}}{\partial t} + \nabla \cdot (\rho_{ng}\alpha_{ng}u) = 0 \tag{5}$$

$$\alpha_l + \alpha_v + \alpha_{ng} = 1 \tag{6}$$

The phase change in the flow was governed by the source term $\dot{m}$ in equation (4), which represents the mass transfer per volume unit between the liquid phase and vapor phase in both evaporation and condensation processes.

To calculate the source terms for evaporation $(\dot{m}^+)$ and condensation $(\dot{m}^-)$ processes, the Zwart–Gerber–Belamri (ZGB) model is used (Kubota *et al.*, 1992):

$$\dot{m}^+ = F_{vap}\frac{3(\alpha_{nuc} - \alpha_v)\rho_v}{R_B}\sqrt{\frac{2\max(\rho_v - \rho, 0)}{3\rho_l}} \tag{7}$$

$$\dot{m}^- = -F_{cond}\frac{3\alpha_v\rho_v}{R_B}\sqrt{\frac{2\max(\rho - \rho_v, 0)}{3\rho_l}} \tag{8}$$

where the empirical coefficient $F_{vap} = 50$ and $F_{cond} = 0.1$ are adopted for the water cavitating flow at ambient temperature. Also, the nucleation site volume fraction (α_{nuc}) is assigned to 5×10^{-4}, the fixed spherical bubble radius is equal to 1×10^{-6}m.

The Zwart–Gerber–Belamri (ZGB) model has been used to simulate the cavitation for a variety of applications like elastic hydrofoil (Zhifeng *et al.*, 2021), impeller (Liu *et al.*, 2021a) and water turbine (Semenova *et al.*, 2021).

2.2 Turbulence model and modification methods

The RNG $k - \varepsilon$ turbulence model is defined by the following equations:

$$\frac{\partial(\rho k)}{\partial t} + \nabla \cdot (\rho u k) = \nabla \cdot \left[\left(\mu + \frac{\mu_t}{\sigma_k}\right)\nabla k\right] + G_k - \rho\varepsilon, \tag{9}$$

$$\frac{\partial(\rho \varepsilon)}{\partial t} + \nabla \cdot (\rho u \varepsilon) = \nabla \cdot \left[\left(\mu + \frac{\mu_t}{\sigma_\varepsilon}\right)\nabla \varepsilon\right] + \frac{c_1\varepsilon}{k}G_k - c_2\rho\frac{\varepsilon^2}{k}, \tag{10}$$

In this turbulence model, the effective viscosity which is applied to Reynolds equations is defined as $\mu = \mu_t + \mu_l$ where $\mu_t = \rho C_\mu\, k^2/\,\varepsilon$ denotes the turbulent viscosity and the constant is assumed as $C_\mu = 0.084$ (Yakhot *et al.*, 1992). Also, k and ε represent the turbulent kinetic energy and turbulent energy dissipation rate, respectively. Furthermore, G_k shows the production of turbulent energy term.

2.2.1 Density corrected model. The modified turbulent viscosity is given as follows (Coutier-Delgosha *et al.*, 2003a):

$$\mu_t = f(\rho)C_\mu k^2/\varepsilon \tag{11}$$

$$f(\rho) = \rho_v + \left(\frac{\rho_v - \rho}{\rho_v - \rho_l}\right)^n (\rho_l - \rho_v) \tag{12}$$

With such a treatment, the eddy viscosity is decreased based on the DCM factor $f(\rho)$.Dular *et al.* (2005) and Coutier-Delgosha *et al.* (2003a) suggested $n = 10$; as well as, this value is used by Liu *et al.* (2012) to simulate the flow around pump-turbine resulted in satisfactory results. In the present work, $n = 10$ is adopted to modify the viscosity. Using DCM correction, the overestimated turbulent viscosity will be avoided in which a better prediction over the cavitating flow happens. At this end, the structure of cavity is not damped which gives a more realistic cavity evolution and sizes.

2.2.2 Filter-based model. The modified turbulent viscosity based on the FBM is defined as follows (Liu *et al.*, 2021b; Johansen *et al.*, 2004):

$$\mu_{t-FBM} = C_\mu \rho_m f_{FBM} \frac{k^2}{\varepsilon} \tag{13}$$

$$f_{FBM} = min\left[1.0, \quad C_3 \frac{\Delta}{l_{RANS}}\right] \tag{14}$$

$$l_{RANS} = \frac{k^{3/2}}{\varepsilon} \tag{15}$$

where the filter size is calculated based on the local grid size as $\Delta = (\Delta_x \Delta_y \Delta_z)^{1/3}$, the density of the mixture is declared by ρ_m, and $C_\mu = 0.084$ is the model constant. In addition, the new model coefficient C_3 is presented as follows:

$$C_3 \approx \frac{\gamma}{4C_\mu \sqrt{3/2}} \tag{16}$$

where $\gamma = 1$ in the isotropic flows. Also, it is worthy to mention that C_3 is taken equal to 1 in many works (Liu *et al.*, 2021b; Johansen *et al.*, 2004). Thus:

- If $\Delta \gg l_{RANS}, \mu_{t-FBM} = C_\mu \rho_m \frac{k^2}{\varepsilon}$

Then, the RANS formulation is fully recovered

- If Δ\ll$l_{RANS}, \mu_{t-FBM} = C_\mu \rho_m \Delta k^{0.5}$

Then, the turbulent viscosity is modified.

The proposed special filter helps to reduce μ_t, if the turbulent scales are smaller than a set filter size like the regions close to wall, they will not be resolved. In the regions where the eddy sizes are much larger than the grid size, the FBM becomes equivalent to the LES model. Thus, by adjusting the filter scale function added in the eddy viscosity, the FBM can be smoothly transformed from a RANS model to LES. Specifically, the level of the turbulent viscosity is corrected by comparing the turbulence length scale and the filter size Δ, which is selected based on the local grid spacing.

2.2.3 Filter-based density correction model. Based on this model, the modified turbulent viscosity is defined as follows (Yu *et al.*, 2015):

$$\mu_{T-FBDCM} = \frac{C_\mu \rho_m k^2}{\varepsilon} f_{hybrid} \tag{17}$$

$$f_{hybrid} = \xi(\rho/\rho_l).f_{FBM} + [1 - \xi(\rho/\rho_l)].f_{DCM} \tag{18}$$

$$\xi(\rho/\rho_1) = 0.5 + \tanh\left(\frac{\left[\frac{C_1(0.6.(\rho/\rho_l) - C_2)}{0.2(1-2C_2)+C_2}\right]}{[2tanh(C_1)]}\right) \tag{19}$$

where C_1, C_2 and C_μ are model constants. Also, k and ε are the turbulent kinetic energy and dissipation rate, respectively. In addition, ξ represents the blend function that combines DCM and FBM which is varied based on the case study. Moreover, the f_{DCM} and f_{FBM} are defined in Sections 2.2.1 and 2.2.2, respectively.

This model is named FBDCM approach, which combines the merits of both DCM and FBM. The hybrid function ξ (ρ/ρ_l) blends the FBM and DCM, and takes the values based on employed blending function. The filter size Δ is selected based on the local mesh size. This can help to limit the occurrence of the overproduction of the turbulent eddy viscosity both near the foil wall and in the wake. Huang *et al.* (2014b) and Yu *et al.* (2015) validated the FBDCM model in simulation of cavitating flow.

3. Description of test rig and devices

The installation of closed-loop is shown in Figure 1. The installation consists of some main components including a test section, tank, pump, valve, flow meter and membrane for pressure adjustment. The pump with a power of 30 kW runs the water flow within the pipeline with a diameter of 200 mm. Furthermore; the electromagnetic flowmeter measures the flow rate. The water flow is straightened before reaching the test section by means of a honeycomb. The tank of 1.5 m^3 volume is equipped with a flexible membrane that can be inflated with air which results in changing the pressure inside the installation. Hence, the temperature sensor is installed in the tank to measure water temperature. To avoid the propagation of vibration generated by the pump and cavitation, three elastic couplings are mounted along the pipeline.

The test section along with visualization and data collection systems are represented in Plate 1. The test chamber has a rectangular cross-section with height (h), span (w) and length (L) of 189, 70 and 700 mm, respectively. The chamber height to chord ratio equals $h/c = 2.7$ where c denotes the cord of hydrofoil. In addition, one pressure sensor is installed at the inlet and another at the outlet. Furthermore, two vibration sensors before and after the mounted hydrofoil were used to evaluate the generated vibration. Also, three transparent walls are used at the top, bottom and front sides to ease the visualization. The high-speed camera along with the lighting system is used to capture the cavity evolution.

The final view of the hydrofoil and disc is shown in Figure 2. The surface of the hydrofoil is polished, and then a thin layer of black acrylic paint is applied. During the experiments, the surface of the hydrofoil and disk are covered with black paint for better visualization (the disc was made of PA6 Aluminium). Also, 10 taps at the suction side are connected to the pressure transducers via internal channels inside the hydrofoil. Hence, the hydrofoil is fixed on the disk which is mounted on the test section and allows to set the angle of attack.

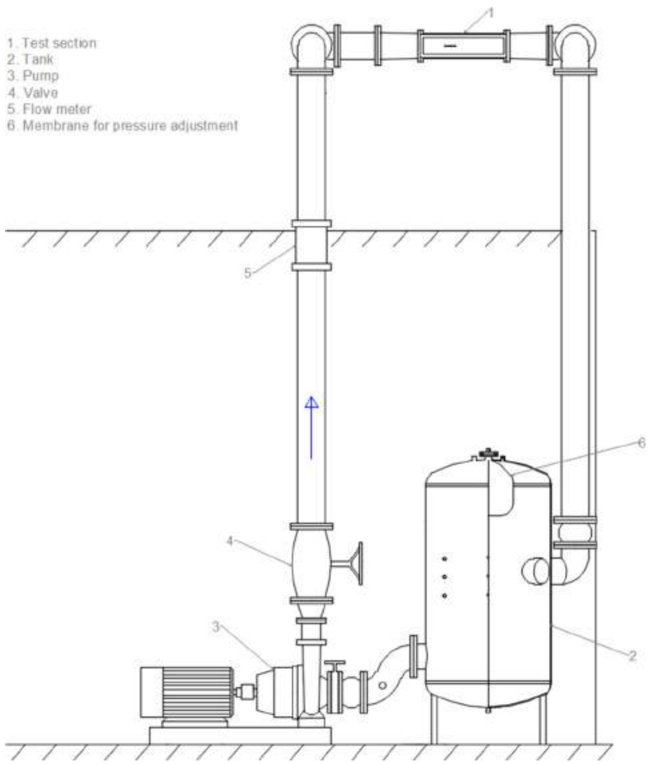

Figure 1. The designed hydraulic installation with presentation of the main components

4. Flow conditions and numerical setup

The flow rate of the circuit was kept constant in all rounds of experiments. So, the velocity of the stream is constant through the test chamber which is almost equal to $u_{in} = 10.4\,m/s$. The Reynolds number equals $Re = \frac{\rho_l u_{in} c}{\mu_l} \simeq 0.79 \times 10^6$, where ρ , u_{in}, c and μ_l represent the density of water, velocity of flow at the inlet, hydrofoil chord and dynamic viscosity of water, respectively.

Each case with different inlet pressure, saturation pressure, density and inlet velocity, is defined with a single cavitation number calculated as follows:

$$\sigma = (p_{in} - p_v)/\left(0.5\rho_l u_{in}^2\right) \tag{20}$$

where p_{in} and p_v denote the static pressure at inlet and water saturation pressure, respectively. Also, the value of inlet pressure is based on the average pressure calculated from instantaneous pressure fluctuations detected during the round of the related experiment. Furthermore, the saturation pressure is calculated based on the average temperature calculated over the related experiment. Also, ρ_l shows the density of water calculated at corresponding temperature and pressure at each case with nominal cavitation number. Finally, u_{in} represents the velocity at the inlet, which is also based on the average value. In the present work, eight levels of rig pressure were considered and represented by cavitation numbers (σ) of 0.91, 1.01, 1.18, 1.37, 1.51, 1.72, 1.93 and 2.04.

Plate 1.
Test chamber and main components

The experimental tests were conducted based on one specific level of dissolved oxygen of 2.1 mg/l. The multifunction meter CF-401 was employed to measure the oxygen levels before and after the experimental campaign. The average value of the oxygen was reported in this work. Based on Henry's law, it corresponds to the air content of 5.37 mg/l.

The length and height of the computational domain presented in Figure 3 (top) correspond to the dimensions of the test chamber. The left and right boundaries with a length of 2.5c are considered as the inlet and outlet, respectively. The top and bottom boundaries with a length of 10c are set as no-slip walls. The distance between the leading edge and the inlet is fixed to 3.2c. The mesh distribution is represented in Figure 3 (bottom).

The grid was generated in ICEM CFD software. It was a 2 D structured grid extruded to the overall width equal to 0.9 mm (three layers of 0.3 mm thickness each). O-grid was generated around the blade, and the profile edge was divided into four parts: the leading-edge part, upper side, lower side and trailing edge part. Four different meshes were examined. Their parameters are summarized in Table 1.

To performance the mesh independency analysis, the pressure distribution along the hydrofoil is compared with the experimental data reported by Matsunari *et al.* (2012) for the same hydrofoil. Based on the comparison, as shown in Figure 4, it is concluded that mesh distribution M4 is selected for further investigation as it gives the best results matching the experimental data.

5. Results and discussion

The purpose of the present work is to study the cavitating flow when the dissolved air is taken into account as the third phase. At this end, the numerical simulations along with experimental observations are employed. The numerical simulation performed by Ansys Fluent; as well as, the turbulence modifications are applied using UDF. The turbulence model is modified to make a better prediction. Thus, three different viscosity modification models such as DCM, FBM and FBDCM are used. The results of the numerical simulations are compared together and with experimental measurements.

5.1 Validation and numerical data

The time-averaged lift and drag coefficients predicted by the numerical simulation are compared, as shown in Figure 5, with the numerical and experimental results carried out by

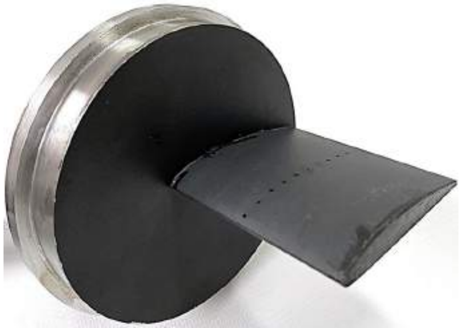

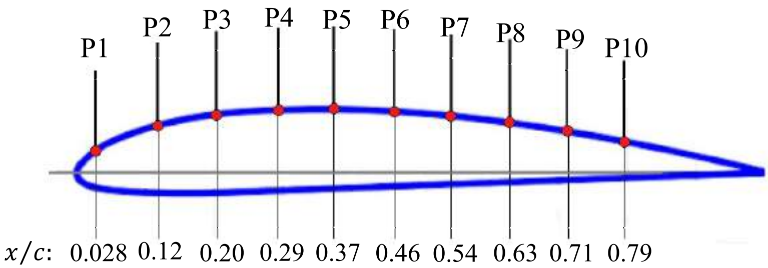

Figure 2.
The hydrofoil and disk

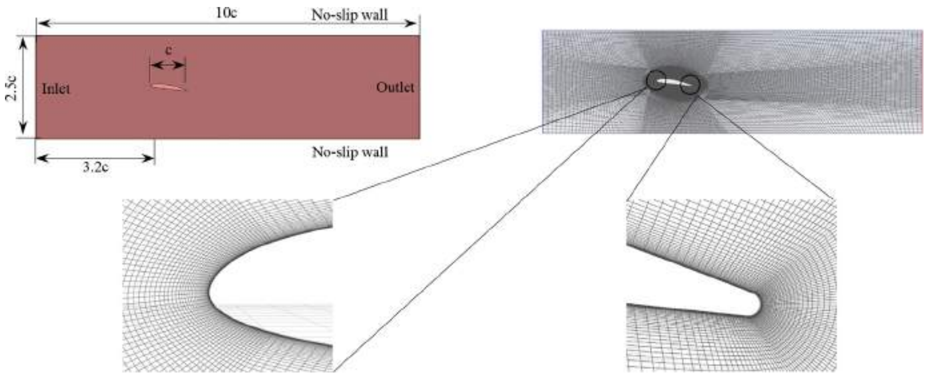

Figure 3.
Computational domain (top) and mesh distribution (bottom)

Numachi (1938) and Matsunari *et al.* (2012). The tunnel height to chord length ratio is 190 mm/70 mm = 2.71 in Numachi's experiments (i.e. Tohoku University), which is larger than 2.0 of Matsunari's experiments (i.e. Kyushu University) where the blockage effect is expected to be more significant. In the present study, the chamber height to chord ratio equals h/c = 2.7 where c denotes the cord of hydrofoil. Other parameters are kept similar to perform accurate comparison. In the comparison, the range of cavitation numbers covers all of the regimes including non-cavitation, sheet cavitation and cloud cavitation. It is observed that there is no big difference between the lift coefficients regardless of the cavitation number. Reversely, a considerable difference is detected in the drag coefficient. It is worth mentioning that the chord to length ratios are different in these two experiments; as a result, this factor can be assumed as one of the reasons for such a discrepancy.

On the other hand, the volume of cavity closure predicated by different modified turbulence models, are different, which will be discussed in the following parts. As a result, one can conclude that the structure of cavitating flow is more effective on the drag coefficient than the lift coefficient. Furthermore, the values of both coefficients become higher once the modifications are applied. Overall, the results of the DCM model fit better with the experiments.

5.2 Shedding frequency

The shedding frequency is one of the important topics, which must be measured in the cavitating flow as it can be known as a scale generation of vibration and noise. In addition, a

Table 1. Characteristics of mesh distributions

Mesh symbol	No. of elements	No. of nodes around hydrofoil
M1	93900	190
M2	116200	195
M3	155000	260
M4	160000	270

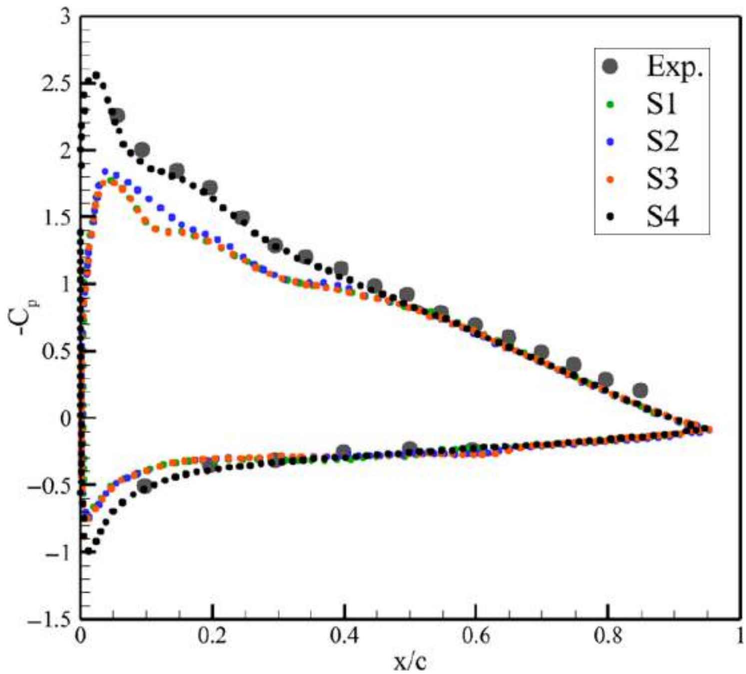

Figure 4. Pressure coefficient distributions for different grids

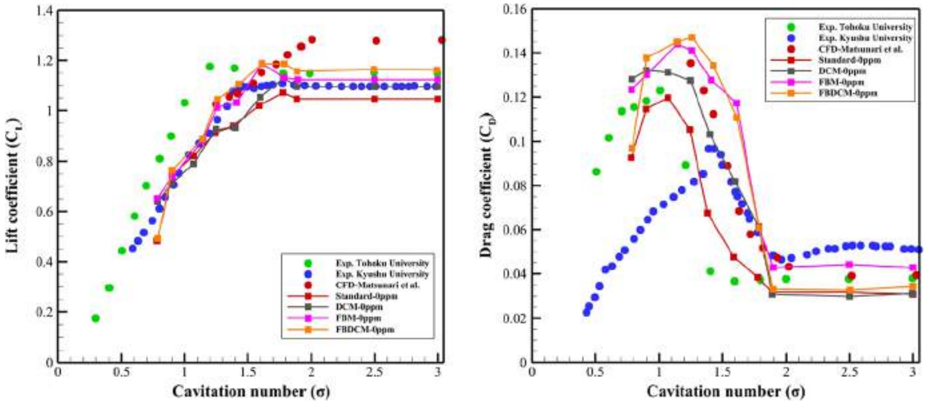

Figure 5.
Lift coefficient (top) and drag coefficient (bottom) versus cavitation number

different value for shedding frequency is reported by the researchers in the same operating condition. Thus, it needs to be analyzed precisely and in more detail. To this end, the shedding frequencies predicted by the standard, DCM, FBM and FBDCM models are presented in Table 2. It is worth mentioning that the present shedding frequency is extracted based on the evolution of cavity structure (i.e. vapor volume fraction). Also, the Fast Fourier transform is used to obtain the shedding frequency where the sampling rate is high enough ($\Delta t = 10^{-5}$) to avoid aliasing. It is declared that there are different modes of frequency, however, the one with the highest amplitude is known as the shedding frequency. In addition, it is indicated that the value of shedding frequency is different even for the same modification model. This issue proves the sensitivity of shedding frequency. It is worth mentioning that the approach of extracting shedding frequency from experimental and numerical results is also important and influential. Comparing the results, it can be concluded that prediction done by DCM fits better to ones reported by other researchers.

The dissolved air is another parameter, which is effective on the shedding frequency. In this context, the history of vapor volume fraction is presented in the conditions of with and without dissolved air, as shown in Figure 6. In addition, the continuous wavelet transform is provided to

	Shedding frequency	
Source	$f_1(Hz)$	$f_2(Hz)$
Present study [Standard $k-\varepsilon$]	25.2	65.1
Present study [DCM]	29.4	69.9
Present study [FBM]	20.0	42.8
Present study [FBDCM]	18.32	38.3
Wei *et al.* (2011) [Standard $k-\varepsilon$]	27.3	50.8
Liu *et al.* (2021b) [PANS]	26.5	68.5
Wei *et al.* (2011) [DCM]	35.1	70.3
Liu *et al.* (2021b) [FBM]	29.3	72.4
Wei *et al.* (2011) [FBM]	27.3	50.8
Huang *et al.* (2014a) [FBM]	25.2	–
Wei *et al.* (2011) [FBDCM]	27.3	43.0
Wang *et al.* (2001) [Experimental]	20.0	–
Wang *et al.* (2001) [Experimental]	22.0	–

Table 2.
Shedding frequency ($\sigma = 0.8$, $re = 7 \times 10^5$)

investigate the shedding frequency before and after adding the dissolved air. By adding the dissolved air, the shedding frequency significantly decreases which means that the cavity becomes more stable. The reason for the latest observation is not fully understood; however, it may be due to the longer time taking for the generation and collapse of the cavity which is remarkably elongated with adding the dissolved air. However, the micro-instability appears which is also detectable in the history of the volume of vapor. When the dissolved air is added to the liquid, the cavity region is significantly extended which has pulsated behavior, especially at the border of cavity and liquid. As such, this behavior may generate some secondary frequencies during the cavity evolution. The predicted shedding frequency by DCM and FBM is comparable; however, the FBDCM predicts lower frequency, especially for the case without dissolved air.

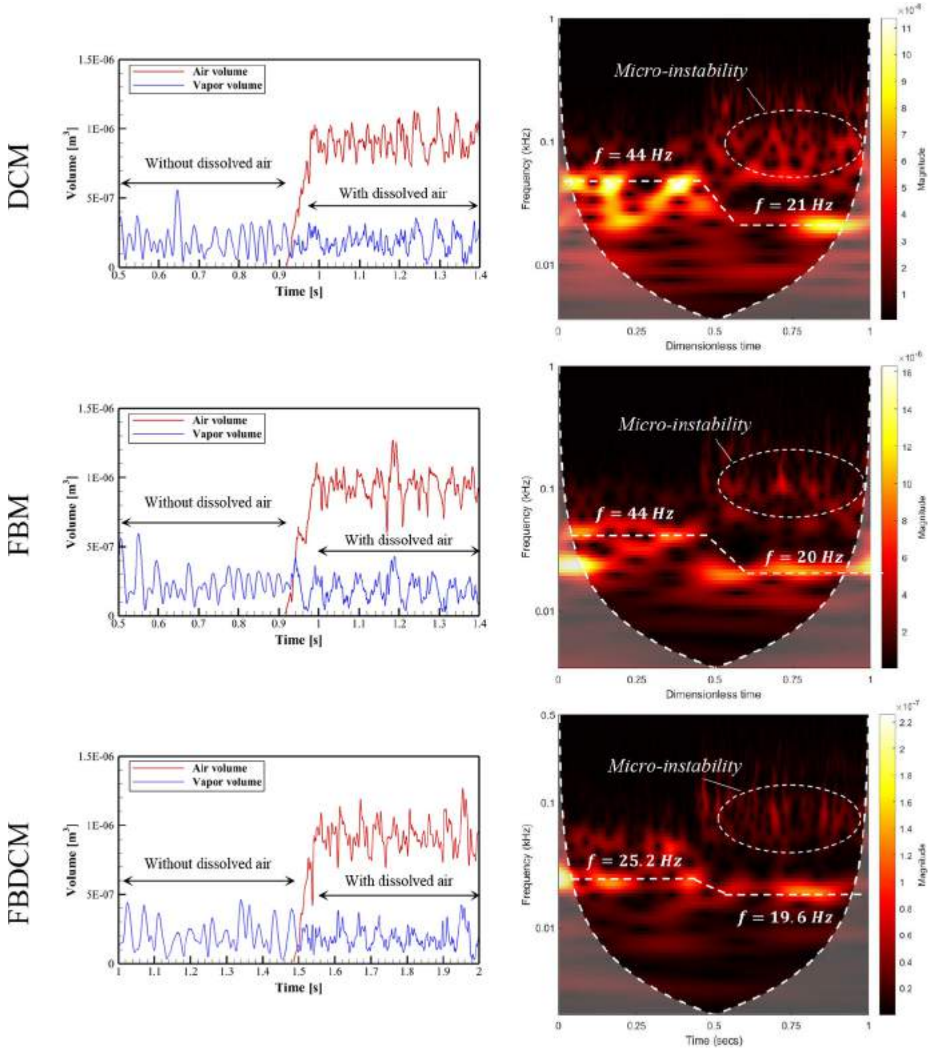

Figure 6.
CWT and history of volume of vapor (σ = 1.18)

The influences of the viscosity modification model on the distribution of vapor volume fraction and the shedding frequency are presented in Figure 7. Once the modification is applied to the turbulence model, the volume vapor is enlarged. It is due to the reduced viscosity applied by the modification models, which allows the cavity closure to grow larger. Moreover, the modification models are influential on how fast the cavity closure grows and collapses. This issue can be detected by the shedding frequency, which is predicted to be higher by the DCM and lower by FBM and FBDCM.

The lift and drag coefficients versus cavitation number as a function of viscosity modification models and levels of dissolved air are presented in Figure 8. As adding the dissolved air is influential on the structure of the cavity closure, which causes changes in the pressure distribution around the hydrofoil, it is expected that the time-averaged lift and drag forces vary at various levels of dissolved air. It is observed that by adding the current amount of air, no big difference in the lift coefficient appears. Reversely, a considerable increment in the drag coefficient occurs.

5.3 Flow structure

To evaluate the capability of the viscosity modification models on the flow structure, the cavity evolution over a period is represented in Figure 9. It is observed that the standard model predicts smaller cavities with respect to experimental ones. It is due to the overestimation of the viscosity. Besides, the modified models depict the larger cavity closures due to reduced viscosity. Obviously, the predictions done by modified models fit better with the experimental observation. Comparing the volume of the cavity, we can conclude that the DCM model releases the best prediction of cavity structure.

To figure out the process of cavity evolution captured by experimental visualization at various cavitation numbers, the temporal-spatial distribution of gray level is used, as shown in Figure 10. It should be noted that the red color, the highest level, and blue color, the lowest level are specifying the black and white pixels, respectively. Also, the contour shows the

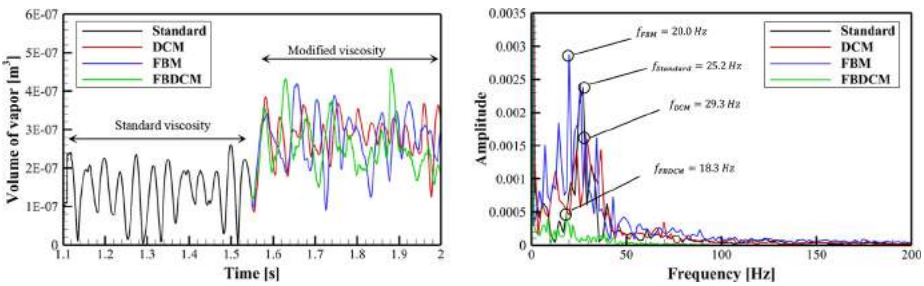

Figure 7.
Effect of modification models on the dynamic of cavitation and shedding frequency ($\sigma = 0.91$ without dissolved air)

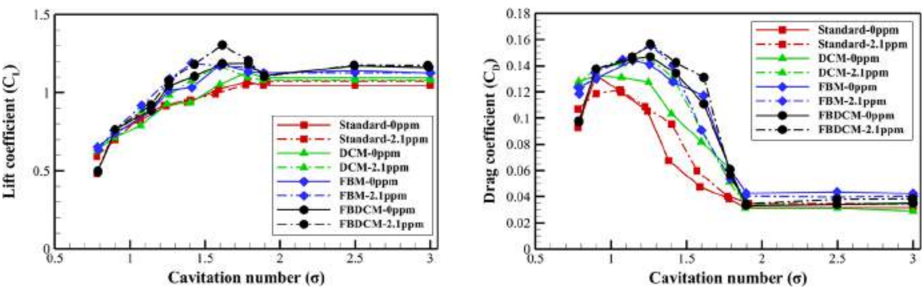

Figure 8.
Effect of dissolved air on the time-averaged lift and drag coefficients

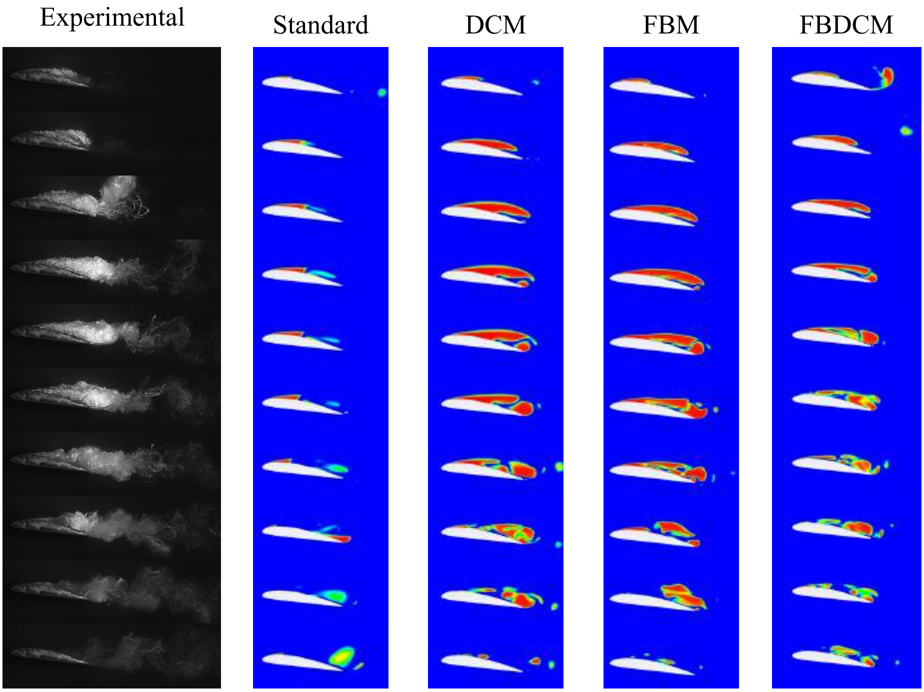

Figure 9.
Evolution of cavity in one period (σ = 1.18 with dissolved air)

temporal-spatial distribution along the reference line (L). In this figure, five cycles are illustrated to figure out the impact of cavitation number on the cavitation cycles. In the case of lower cavitation number σ = 0.91, it is observed that the new cavitation process begins immediately after shedding of previous cycle. At this end, gray level distribution shows an almost continuous cavitation. With increasing of the cavitation number, the moment exists between two interval cavitation processes when there is no cavity around the hydrofoil. Furthermore, to make a clear overview on the cavity structure, three points are selected on gray level distribution and matched with corresponding visualized structure.

To demonstrate the detail of the flow characteristics around the hydrofoil during a cavity evolution, the pressure distribution, streamline and vortex magnitude are depicted in Figure 11. The results show that the streamlines are considerably influenced by the cavity generated around the cavity. In general, the cavity contains swirling streamlines with low pressure. The swirling streamlines causes by the counter-flows at the above and bottom sides of the cavity which are main stream and re-entrant jet, respectively. On the other hand, it is understood that the vorticity magnitude at the boundary of the cavity is higher than its core. In addition, in the beginning and ending of the cavity evolution, the reversed vortex is generated by means of main stream at pressure side. As such, it can be concluded that the shape of trailing may play an important role on the latest observation.

6. Conclusion

The present work focuses on the experimental and numerical investigation of the cavitating flow around the hydrofoil when the dissolved air is taken into account as the third phase.

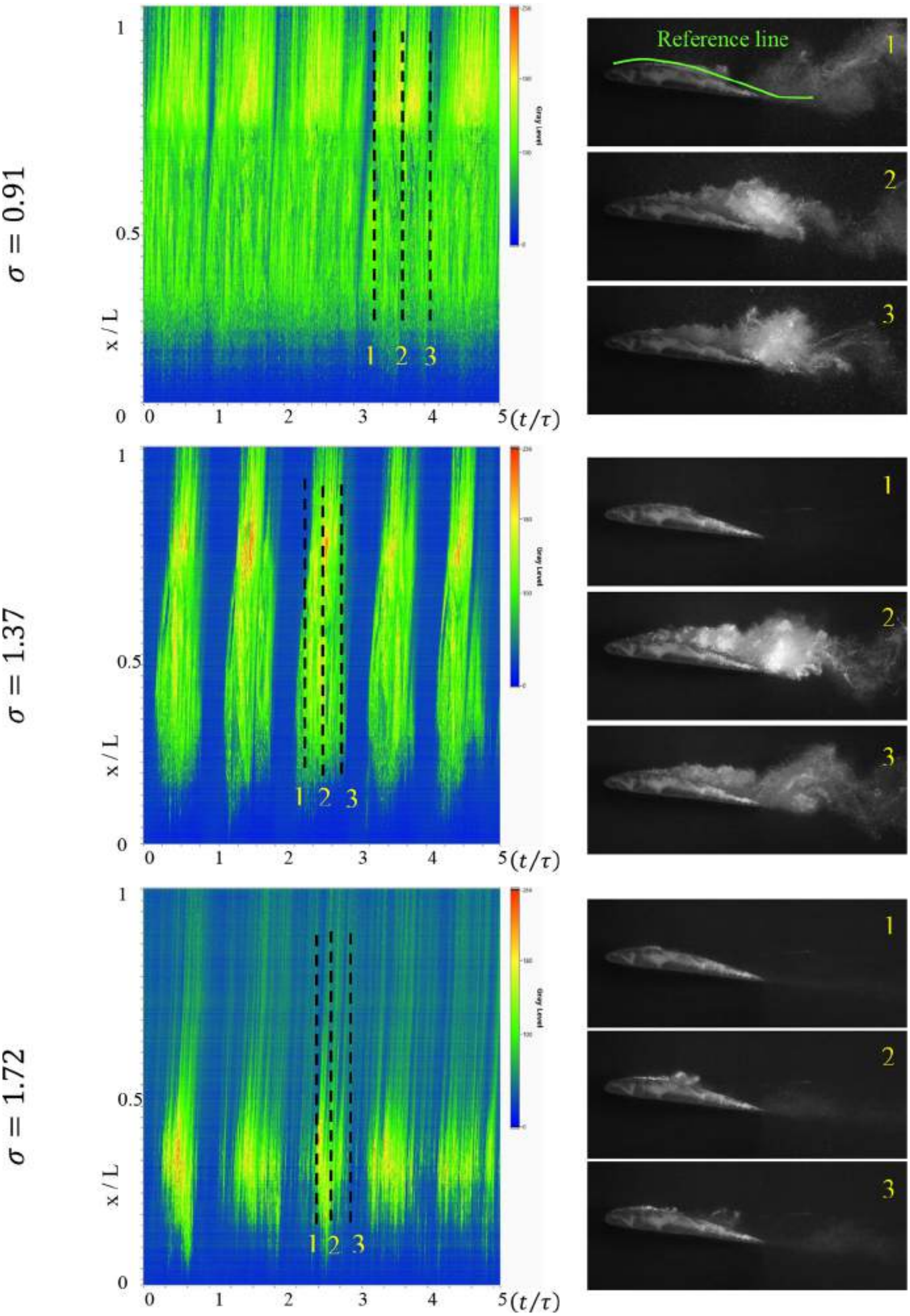

Figure 10.
Temporal-spatial distribution of gray level along the reference line (with dissolved air)

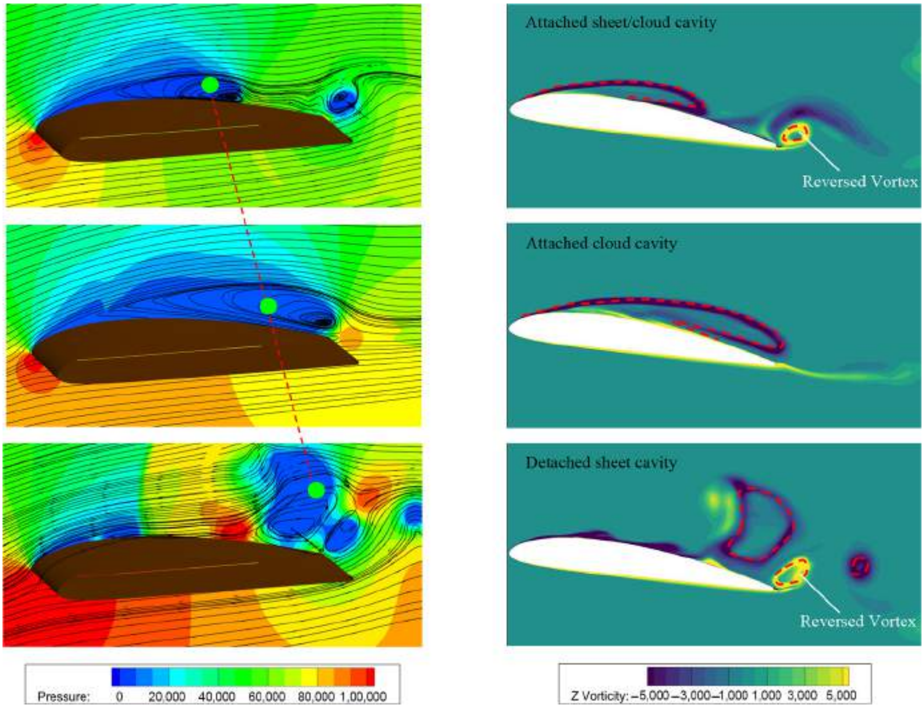

Figure 11.
Pressure field and streamline (left), vorticity distribution (right), (σ = 1.51 with dissolved air and DCM model)

The RNG k-epsilon model is modified using DCM, FBM and FBDCM. Based on the analysis, the main findings are as follows:

- The modified turbulence models yield larger cavity closure due to reduced viscosity.
- Although the lift coefficient has no significant changes in different modification models, the drag coefficient enhances.
- Adding the dissolved air causes enhancement of the drag coefficient.
- By adding the dissolved air, the cavity closure becomes stable; however, micro-instability appears.
- Comparing the shedding frequency calculated by the current simulation and those by other researchers, the FBDCM model has the best-fitted prediction; however, the DCM model leads to a better prediction of cavity structure.

References

Arndt, R.E. (1981), "Cavitation in fluid machinery and hydraulic structures", *Annual Review of Fluid Mechanics*, Vol. 13 No. 1, pp. 273-326.

Brennen, C.E. (2014), *Cavitation and Bubble Dynamics*, Cambridge University Press, Cambridge.

Coutier-Delgosha, O., Fortes-Patella, R. and Reboud, J.-L. (2003a), "Evaluation of the turbulence model influence on the numerical simulations of unsteady cavitation", *Journal of Fluids Engineering*, Vol. 125 No. 1, pp. 38-45.

Coutier, -Delgosha, O., Reboud, J. and Delannoy, Y. (2003b), "Numerical simulation of the unsteady behaviour of cavitating flows", *International Journal for Numerical Methods in Fluids*, Vol. 42 No. 5, pp. 527-548.

Dular, M., Bachert, R., Stoffel, B. and Širok, B. (2005), "Experimental evaluation of numerical simulation of cavitating flow around hydrofoil", *European Journal of Mechanics – B/Fluids*, Vol. 24 No. 4, pp. 522-538.

Hofmann, M., Lohrberg, H., Ludwig, G., Stoffel, B., Reboud, J.-L. and Patella, R.F. (1999), "Numerical and experimental investigations on the self-oscillating behaviour of cloud cavitation: part I: visualization", *ASME, FEDSM99-6755*.

Huang, B., Wang, G-y. and Zhao, Y. (2014a), "Numerical simulation unsteady cloud cavitating flow with a filter-based density correction model", *Journal of Hydrodynamics*, Vol. 26 No. 1, pp. 26-36.

Huang, B., Zhao, Y. and Wang, G. (2014b), "Large eddy simulation of turbulent vortex-cavitation interactions in transient sheet/cloud cavitating flows", *Computers and Fluids*, Vol. 92, pp. 113-124.

Johansen, S.T., Wu, J. and Shyy, W. (2004), "Filter-based unsteady RANS computations", *International Journal of Heat and Fluid Flow*, Vol. 25 No. 1, pp. 10-21.

Kawanami, Y., Kato, H., Yamaguchi, H., Tanimura, M. and Tagaya, Y. (1997), "Mechanism and control of cloud cavitation", *Journal of Fluids Engineering*, Vol. 119 No. 4, pp. 788-794.

Kubota, A., Kato, H. and Yamaguchi, H. (1992), "A new modelling of cavitating flows: a numerical study of unsteady cavitation on a hydrofoil section", *Journal of Fluid Mechanics*, Vol. 240 No. 1, pp. 59-96.

Laberteaux, K. and Ceccio, S. (2001), "Partial cavity flows. Part 1. Cavities forming on models without spanwise variation", *Journal of Fluid Mechanics*, Vol. 431, pp. 1-41.

Li, Z-R., Pourquie, M. and Van Terwisga, T. (2014), "Assessment of cavitation erosion with a URANS method", *Journal of Fluids Engineering*, Vol. 136 No. 4.

Liu, J., Lin, H., Duan, L., Sun, L., He, M. and Chen, S. (2021a), "CFD simulation of cavitation erosion behavior in an impeller of industrial lean amine liquid pump", *Pressure Vessels and Piping Conference*, Vol. 85321, American Society of Mechanical Engineers, p. V002T03A003.

Liu, J., Liu, S., Wu, Y., Jiao, L., Wang, L. and Sun, Y. (2012), "Numerical investigation of the hump characteristic of a pump–turbine based on an improved cavitation model", *Computers and Fluids*, Vol. 68, pp. 105-111.

Liu, J., Yu, J., Yang, Z., He, Z., Yuan, K., Guo, Y. and Li, Y. (2021b), "Numerical investigation of shedding dynamics of cloud cavitation around 3D hydrofoil using different turbulence models", *European Journal of Mechanics – B/Fluids*, Vol. 85, pp. 232-244.

Lohrberg, H., Stoffel, B., Fortes-Patella, R., Coutier-Delgosha, O. and Reboud, J. (2002), "Numerical and experimental investigations on the cavitating flow in a Cascade of hydrofoils", *Experiments in Fluids*, Vol. 33 No. 4, pp. 578-586.

Mäkiharju, S.A., Ganesh, H. and Ceccio, S.L. (2017), "The dynamics of partial cavity formation, shedding and the influence of dissolved and injected non-condensable gas", *Journal of Fluid Mechanics*, Vol. 829, pp. 420-458.

Matsunari, H., Watanabe, S., Konishi, Y., Suefuji, N. and Furukawa, A. (2012), "Experimental/numerical study on cavitating flow around Clark Y 11.7% hydrofoil", *Proceedings of Eighth International Symposium on Cavitation*, pp. 358-363.

Numachi, F. (1938), "Cavitation performance of 4 types of hydrofoil", *Transactions of the Japan Society of Mechanical Engineers*, Vol. 7 No. 28, pp. 1-9.

Reboud, J.-L., Stutz, B. and Coutier, O. (1998), "Two phase flow structure of cavitation: experiment and modeling of unsteady effects", *3rd international symposium on cavitation CAV1998*, *Grenoble, France*, Vol. 26.

Reisman, G., Wang, Y.-C. and Brennen, C.E. (1998), "Observations of shock waves in cloud cavitation", *Journal of Fluid Mechanics*, Vol. 355, pp. 255-283.

Sato, K., Tanada, M., Monden, S. and Tsujimoto, Y. (2002), "Observations of oscillating cavitation on a flat plate hydrofoil", *JSME International Journal Series B*, Vol. 45 No. 3, pp. 646-654.

Schenke, S. and van Terwisga, T.J. (2019), "An energy conservative method to predict the erosive aggressiveness of collapsing cavitating structures and cavitating flows from numerical simulations", *International Journal of Multiphase Flow*, Vol. 111, pp. 200-218.

Semenova, A., Chirkov, D. and Ustimenko, A. (2021), "Prediction of runaway characteristics of Kaplan turbines using CFD analysis", *E3S Web of Conferences*, Vol. 320, EDP Sciences, p. 04008.

Ullas, P., Chatterjee, D. and Vengadesan, S. (2022), "Prediction of unsteady, internal turbulent cavitating flow using dynamic cavitation model", *International Journal of Numerical Methods for Heat and Fluid Flow*.

Wang, G., Senocak, I., Shyy, W., Ikohagi, T. and Cao, S. (2001), "Dynamics of attached turbulent cavitating flows", *Progress in Aerospace Sciences*, Vol. 37 No. 6, pp. 551-581.

Watanabe, S., Yamaoka, W. and Furukawa, A. (2009), "Unsteady lift and drag characteristics of cavitating Clark Y-11.7% hydrofoil", *IOP Conference Series: Earth and Environmental Science, 2014*, Vol. 22, No. 5, IOP Publishing, p. 052009.

Wei, Y.-J., Tseng, C.-C. and Wang, G.-Y. (2011), "Turbulence and cavitation models for time-dependent turbulent cavitating flows", *Acta Mechanica Sinica*, Vol. 27 No. 4, pp. 473-487.

Wróblewski, W., Bochon, K., Majkut, M., Rusin, K. and Malekshah, E.H. (2021b), "Numerical study of cavitating flow over hydrofoil in the presence of air", *International Journal of Numerical Methods for Heat and Fluid Flow*, Vol. 32 No. 5, pp. 1440-1462.

Wróblewski, W., Bochon, K., Majkut, M., Malekshah, E.H., Rusin, K. and Strozik, M. (2021a), "An experimental/numerical assessment over the influence of the dissolved air on the instantaneous characteristics/shedding frequency of cavitating flow", *Ocean Engineering*, Vol. 240, p. 109960.

Yakhot, V., Orszag, S., Thangam, S., Gatski, T. and Speziale, C. (1992), "Development of turbulence models for shear flows by a double expansion technique", *Physics of Fluids A: Fluid Dynamics*, Vol. 4 No. 7, pp. 1510-1520.

Yin, T., Pavesi, G., Pei, J. and Yuan, S. (2021), "Numerical analysis of unsteady cloud cavitating flow around a 3D Clark-Y hydrofoil considering end-wall effects", *Ocean Engineering*, Vol. 219, p. 108369.

Yu, A., Ji, B., Huang, R., Zhang, Y., Zhang, Y. and Luo, X. (2015), "Cavitation shedding dynamics around a hydrofoil simulated using a filter-based density corrected model", *Science China Technological Sciences*, Vol. 58 No. 5, pp. 864-869.

Zhifeng, Y., Guihua, L., Jing, L. and Yongshun, Z. (2021), "Numerical simulations of the effect of leading edge cavitation on the vibration characteristics of an elastic hydrofoil", *Journal of Tsinghua University (Science and Technology)*, Vol. 61 No. 11, pp. 1325-1333.

Corresponding author
Emad Hasani Malekshah can be contacted at: emad.hasani@polsl.pl

Paper VII:

Merging theory-based cavitation model adaptable with non-condensable gas effects in prediction of compressible three-phase cavitating flow

International Journal of Heat and Mass Transfer 196 (2022) 123279

Contents lists available at ScienceDirect

International Journal of Heat and Mass Transfer

journal homepage: www.elsevier.com/locate/hmt

Merging theory-based cavitation model adaptable with non-condensable gas effects in prediction of compressible three-phase cavitating flow

Emad Hasani Malekshah*, Włodzimierz Wróblewski

Department of Power Engineering and Turbomachinery, Silesian University of Technology, Gliwice 44-100, Poland

A R T I C L E I N F O

Article history:
Received 30 May 2022
Revised 7 July 2022
Accepted 22 July 2022

Keywords:
Three-phase cavitating flow
Cavitation model
Pressure fluctuation effect
Merging theory
Non-condensable gas

A B S T R A C T

The phenomenon of turbulent multiphase flow, such as cavitating flow, with phase change, becomes more complicated taking into account the non-condensable gas as an additional phase. The water, which is the operating fluid, contains a specified amount of dissolved air; as a result, the cavitating flow needs to be considered as a three-phase (i.e. water, vapor and air) flow. Although the existence of dissolved air is well known, most numerical models neglect it; as such, its effect is usually underestimated so far. To this end, the present work is devoted to developing a modified cavitation model based on the merging theory, taking into account the dissolved air in an Eulerian approach. The diffusion process is modeled to constitute the new bubble of the mixture; as a result, the bubble pressure is corrected based on the local air level. Also, the pressure fluctuation effect is applied in the calculation of the pressure of the mixture bubble. To have a more accurate estimation of the density of phases in the situation with a high-pressure difference, the liquid and gas phases are assumed as compressible fluids and modeled by the Tait equation and ideal gas law, respectively. To avoid overestimation of the turbulent viscosity while the standard turbulence model is used, the Density Corrected-Based model is employed to modify the turbulent viscosity employed in $k-\varepsilon$ turbulence model. The dynamic characteristics of cavitating flow are analyzed using Power Spectral Density (PSD) and Continuous Wavelet Transform (CWT) techniques. In addition, the cavitating flow is visualized experimentally, and the captured frames are analyzed using image processing to provide temporal-spatial gray level distribution. The present work declares the major role of gas content on the cavitating flow and assesses the efficiency of the proposed numerical model in the prediction of three-phase cavitating flow.

1. Introduction

The cavitation phenomenon appears in the liquid flow where the local pressure drops below the saturation pressure. This phenomenon has transient nature and generates noise, vibration and erosion around the object. As a result, cavitation is known as an important flow phenomenon, which influences the design and efficiency of hydraulic machines such as propellers, impellers, pumps and hydraulic turbines [1–3]. Since the cavitating flow significantly influences the operating parameters such as pressure distribution, unwanted vibration and noise, numerical and experimental assessments of the cavitating flow are necessary. The semi-steady limited cavity is a common type of cavitation at the design condition. However, the large sheet cavity and its breaking-up and formation of a large vaporous cloud cavity can be expected at the off-design conditions (e.g. low cavitation number). The cloud cavity is known to be more destructive and noisy due to the periodic growth and collapse process [4].

To make an efficient design of the hydraulic machines and control the cavitation, it is required to understand the unsteady characteristics of this phenomenon, especially the possibility to intensify or damp it [4]. It was pointed out by Knapp [5] that the re-entrant jet initiates the breaking up and alternation of sheet cavity to cloud cavity based on experimental observation. Furthermore, Ganesh et al. [6] conducted an experimental investigation to identify the influential parameters that initiate the breaking up and cloud cavity using a wedge-shaped geometric model. They reported two main cavity-shedding mechanisms, which are the re-entrant jet and the shock wave. The re-entrant jet and the shock wave initiate the cloud cavity and also generate high pulsating pressure at the surface of the object, causing its destruction [7,8]. Although the unsteady characteristics of the cavitating flow such as force components and vibration are crucial in designing a hydraulic

* Corresponding author.
E-mail address: emad.hasani@polsl.pl (E. Hasani Malekshah).

https://doi.org/10.1016/j.ijheatmasstransfer.2022.123279

machine, the structure of the cavity can be vital in the assessment of detail of the unsteady process. In this context, Reisman et al. [9] reported the experimental observations on the cloud cavitation around an oscillating hydrofoil captured by the high-speed camera. It was declared that the shape of the cavity affects the pressure pulse acting on the surface of the hydrofoil. Le et al. [10] investigated partial cavitation and the related global characteristics such as cavitation pattern, cavity length, mean pressure distribution and periodic shedding. It has been proved that the cavitation instability is closely related to the thickness of the cavity and the re-entrant jet resulting in the vorticity production at the rear boundary of the sheet cavity. Moreover, the shedding rate of the circulation generated by the re-entrant jet can be estimated. Callenaere et al. [11] carried out an experimental analysis to study the instability of the partial cavitation caused by the re-entrant jet. They pointed out that the adverse pressure and ratio of re-entrant jet to sheet cavity thicknesses are the main parameters that determine the intensity of the breaking up process. The mass transfer cavitation model and the modified RNG k-model with a local density adjustment for turbulent eddy viscosity were used by Ji et al. [12] to numerically study the structure of the cavitating flow around a twisted hydrofoil. The projected shedding frequency and three-dimensional cavity configurations match experimental findings fairly well. A deeper examination of the flow field reveals that cavitation encourages the formation of vortices and thickens the boundary layer in conjunction with local separation and flow instability. In another work conducted by Ji et al. [13] investigates numerically the cavitating flow around a NACA66 hydrofoil with a focus on understanding the cavitation structures and the shedding dynamics. For the purpose of calculating the pressure, velocity, vapor volume percentage, and vorticity surrounding the hydrofoil, a large eddy simulation (LES) and a homogeneous cavitation model were combined. The growth, break-off, and collapse downstream of the cavities, as well as the expected cavitation shedding dynamics behavior, accord fairly well with experiment. Kolahan et al. [14] carried out the wavelet analysis on the cavitating flow around a sphere. Using this technique, they captured the transient and dynamic behavior of cavitating flow. The results showed that the fluctuation of the cavitating flow intensifies with increasing of cavitation number and the dominant frequency of the fluctuation is in the low range. Ghahramani et al. [15] carried out a numerical simulation on the multi-scale cavitating flows around a sharp-edged bluff body. Combining a mixture model with a Lagrangian bubble model leads to the formation of a hybrid cavitation model. The Lagrangian model uses a four-way coupling technique and novel sub-models to take into account a variety of small-scale cavitation dynamics events. Additionally, an enhanced approach that is in line with the flow physics is used to couple the mixture and Lagrangian models. The results demonstrate significant gains in both predicting the large cavities and capturing the small-scale features using the hybrid model when compared to experiment results. Peters et al. [16] assessed the cavitation-induced erosion based on multi-scale-Lagrange model. The developed method for converting vapor volumes between Eulerian and Lagrangian frames was verified and subjected to a sensitivity analysis. The simulations showed that the largest impact pressures and best agreement with measured erosion depths were produced by bubbles collapsing within a normalized stand-off distance of less than unity. Additionally, it is determined that the estimated collapses close to the wall contributed the most to erosion, which is consistent with experimental studies on bubble collapses close to walls.

Because of the strong coupling between the cavitation, turbulence and compressibility effect, the cavitating flow becomes a complex phenomenon. Not only the mentioned factors make this phenomenon remarkably hard to be predicted numerically, but also the highly dynamic behavior and rapid changes in the structure enhance the complexity of experimental measurements. In recent years, the numerical simulation of the cavitating flow becomes a strong and important tool due to promising improvements in the numerical approaches. However, the numerical approaches still need to be treated to be well compatible with the unsteadiness of cavitating flow. Since the turbulence and cavitation models are the key factors in the prediction of the cavitating flow, their modifications are high-demanded and necessary to obtain more reasonable results. The mixture model is used by many researchers to treat the multiphase flow which considers the cavity area as a homogenous region and assumes the mixture of water, vapor and additional dissolved gas as a single phase of the fluid. The two cavitation models often used are the State Equation Model (SEM) [17,18] and the Transport Equation Model (TEM) such as Kunz Model [19], Schnerr and Sauer Model [20], Zwart-Gerber-Belamri Model [21] and Singhal Model [22]. Based on the recent experimental observations carried out by Gopalan and Katz [23] and Laberteaux and Ceccio [24], it is reported that vorticity production has a crucial impact on the cavity structure and breaking up the process because of the baroclinic torque term. However, SEM is not capable to capture this effect since the gradients of pressure and density are always parallel leading to zero baroclinic torque. Thus, TEM is more compatible to deal with this phenomenon as it introduces an additional term to calculate the volume fraction of vapor considering the source term for evaporation and condensation processes. Cheng et al. [25] modified the Schnerr and Sauer cavitation model to make it more adapted to the presence of non-condensable gas. In this regard, they connected this cavitation model with the local gas concentration and derived a new mass transfer source term. It was confirmed that the gas content plays an inevitable role in the formation of the cavitation structure downstream of the hydrofoil. On the other hand, the turbulence model is also crucial since the cavitating flow is unsteady in essence, and a strong connection between the boundary layer and the cavity interface exists. The Reynolds Average Navier-Stokes (RANS) has been widely employed for simulations of turbulent flows, however; the capability of the RANS model is doubtful in this case due to overestimation of the turbulent eddy viscosity, which is considerably influential in the determination of cavity structure. At this end, some useful model modifications have been proposed including Density Corrected-based Model (DCM) [26], Filter-based Model (FBM) [27] and Density-Corrected Filter-Based Model (FBDCM) [28]. Wang et al. [29] analyzed the dynamics of cloud cavitating flow over a hydrofoil. They used the Density Correction Model (DCM) to modify the standard $k-\varepsilon$ RNG turbulence model with a special focus on the behavior of re-entrant jet. They reported that the standard turbulence model predicts shorter cavity comparing to those observed in the experiment. Reversely, by employing the DCM modification, a close agreement is observed between numerical simulations and experimental observations regarding the cavity closure, re-entrant jet and dominant frequency of lift force.

In the real condition, all liquids contain some amounts of dissolved gas which is inevitable to remove from any substantial volume of liquid. The nuclei are the initiation points for the cavitation phenomenon. Considering the dissolved gas, the partial pressure of the nuclei is composed of the partial pressure of the created vapor in the phase transition and the partial pressure of the non-condensable gas. Due to changes in the partial pressure of the nuclei, incipient cavitation is highly affected. Holl [30] declared that vaporous cavitation and gaseous cavitation may occur simultaneously during one campaign of an experiment. These two types of cavitation are different in essence, but it is hard to distinguish between them. However, in the cases with high content of dissolved gas, the cavitation process is remarkably impacted. Although the vaporous cavity can be illustrated in conditions with low gas content and high flow velocity, the gaseous cavitation needs a high amount of gas content [31,32]. To achieve a breakthrough in the prediction of the cavitating flow in close agreement with experimental observations, it is necessary to consider the effect of dissolved gas. A three-phase cavitation model is proposed by Mithun et al. [33] and Stavropoulos Vasilakis et al. [34], in which the influence of non-condensable gas is taken into account. In addition, Egerer et al. [35] analyzed the water quality implicitly. Although the effect of non-condensable gas was considered, it was assumed that the gas content is uniformly distributed in the whole domain, which is known as a drawback of this proposed model. Recently, Wróblewski et al. [36] analyzed the effects of dissolved air on the cavitating flow around the Clark Y hydrofoil and the corresponding unsteady characteristics and shedding frequencies based on numerical simulations and experimental observations. They used the 3phases model to consider liquid, vapor and air as three governing phases. Two different amounts of dissolved air (i.e. 2.6 ppm and 5.5 ppm oxygen) were taken into account. In addition, the numerical results were compared with the experimental observations. The results of numerical simulation and image processing of experimental data declared that the addition of dissolved air is associated with enlarged cavity closure during the evolution of the cavity. In addition, based on the FFT evaluation of pressure fluctuations, the authors reported that the shedding frequency decreases in the case of a higher volume fraction of dissolved air. In another work, Wróblewski et al. [37] examined the cavitating flow in the presence of dissolved air at three different levels (i.e. VF = 0.004, 0,016 and 0.042). They considered the cavitating flow around a Clark Y hydrofoil with a fixed angle of attack of 8 deg. They evaluated the Singhal model and Zwart-Gerber-Belamri (ZGB) model, using the 2phase and 3phase approaches. Numerical calculations were carried out using the unsteady RANS (URANS) model with the assumption of the constant temperature of the mixture. In addition, the numerical results are compared with the original experimental data. They concluded that the Singhal model gives high unstable solutions, as well as; the predicted cavity structures are not satisfactory, especially for low cavitation numbers. However, a convincible cavity structure was detected when the 2phase and 3phase approaches are employed. On the other hand, the impact of dissolved air on the cloud structure and dynamic characteristics of cavitating flow was gently observable.

The present work focuses on developing a modified cavitation model based on merging theory which is adaptable to include the effect of non-condensable dissolved gas. Moreover, all phases (i.e. water, vapor and air) are assumed as compressible fluids. The dynamic characteristics of cavitating flow are analyzed using Power Spectral Density (PSD) and Continuous Wavelet Transform (CWT). In addition, the cavitation evolution and shedding process are visualized using experimental observation and image processing.

2. Physical description and numerical modeling

Fig. 1 illustrates the cavitation around the hydrofoil consisting of the attached sheet cavity, detached sheet cavity and detached bulk/cloud cavity. Moreover, the focus of the present work, which is considering the non-condensable gas, is represented. Practically, two types of gas bubbles may exist in the operating liquid, bubbles with dissolvable gas and with non-dissolvable gas. The present model only deals with the dissolved gas bubble, which substantially influenced the mixture bubble pressure. The dissolved gas bubbles diffuse to the vapor bubble and generate the mixture bubble, whose pressure is a sum of partial pressures of vapor and gas. It should be pointed out that the non-dissolvable gas bubbles and their corresponding influences are not taken into consideration.

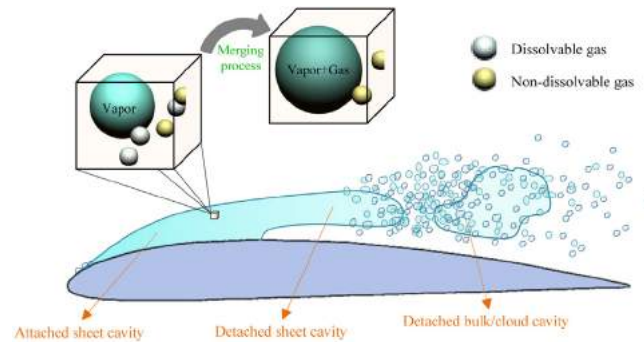

Fig. 1. Schematic of cavitation around the hydrofoil and content of cavity.

2.1. Multiphase model

To treat the multiphase flow, the homogenous mixture model is employed. Based on the mixture model, the liquid-vapor-gas (i.e. three phases) flow is considered as a single homogenous fluid with the same velocity field for each phase resulting in negligence of the slip between the phases. As such, the number of governing equations is reduced accordingly. The governing equations are mass and momentum conservation laws:

$$\frac{\partial \rho}{\partial t} + \nabla \cdot (\rho \boldsymbol{u}) = 0 \tag{1}$$

$$\frac{\partial}{\partial t}(\rho \boldsymbol{u}) + \nabla \cdot (\rho \boldsymbol{u}\boldsymbol{u}) = -\nabla p + \nabla \cdot \left[\mu\left(\nabla \boldsymbol{u} + \nabla \boldsymbol{u}^T\right)\right] + \rho \boldsymbol{g} \tag{2}$$

$$\begin{cases} \rho = \rho_v\alpha_v + \rho_l\alpha_l + \rho_{ng}\alpha_{ng} \\ \mu = \mu_v\alpha_v + \mu_l\alpha_l + \mu_{ng}\alpha_{ng} \end{cases} \tag{3}$$

The last term in Eq. (2), which represents the body force, was neglected in the numerical scheme due to a little effect on the modeled phenomenon. The numerical model takes the presence of air into account, and therefore in Eq. (3), the third term representing the fraction of non-condensing gasses (air) was added to the terms of the liquid and vapor phases of the water. The mixture model with three phases: liquid-vapor-air (3phases model) solves the continuity equations for the vapor volume fraction and the air volume fraction. The mass transfer between a liquid and a mixture of gaseous phases was modeled between species:

$$\frac{\partial \rho_v\alpha_v}{\partial t} + \nabla \cdot (\rho_v\alpha_v\boldsymbol{u}) = R \tag{4}$$

$$\frac{\partial \rho_{ng}\alpha_{ng}}{\partial t} + \nabla \cdot (\rho_{ng}\alpha_{ng}\boldsymbol{u}) = 0 \tag{5}$$

$$\alpha_l + \alpha_v + \alpha_{ng} = 1 \tag{6}$$

The phase change in the flow was governed by the source term R in Eq. (5) which represents the mass transfer per volume unit between the liquid phase and vapor phase in both evaporation and condensation processes.

2.2. Liquid and vapor compressibility models

2.2.1. Tait equation (liquid phase)

Tait equation establishes a nonlinear relationship between the density of the liquid and corresponding pressure under the isothermal conditions [38]. As a result, the Tait equation is presented in terms of density and pressure as follows:

$$p = a + b^n, \tag{7}$$

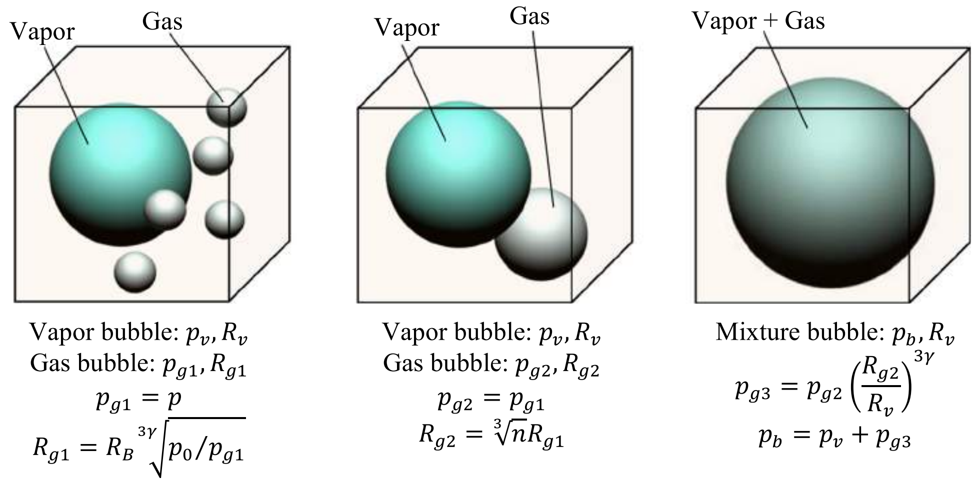

Fig. 2. Merging process of vapor and gas bubbles ($\boldsymbol{R}_v > \boldsymbol{R}_{g2}$).

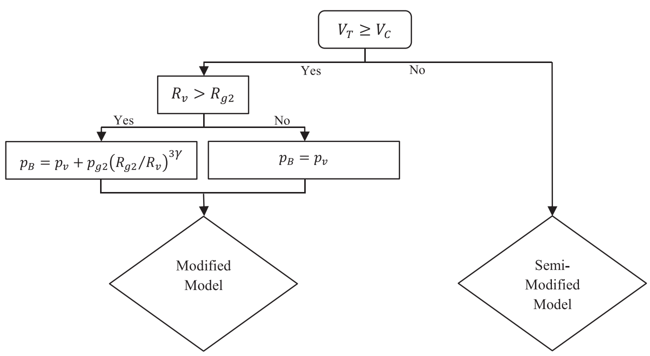

Fig. 3. Switching algorithm between semi-modified and modified cavitation models.

where a and b represent the coefficients defined by assuming that the bulk modulus is a linear function of pressure. Moreover, the values of these coefficients are determined based on the reference state of density, pressure and bulk modulus. Also, n shows the density exponent demonstrates the same role as a ratio of specific heats [39].

The simplified Tait equation is as follows:

$$\left(\frac{\rho}{\rho_0}\right)^n = \frac{K}{K_0}, \tag{8}$$

where,

$$K = K_0 + n\Delta p, \tag{9}$$

and,

$$\Delta p = p - p_0, \tag{10}$$

where p_0 is the reference liquid pressure, ρ_0 is the reference liquid density at the reference pressure p_0, n is the density exponent, for which the value 7.15 is used which corresponds to weakly compressible materials such as liquids [39], K_0 is the reference bulk modulus at the reference pressure p_0, p is the liquid pressure (absolute), ρ and K is the liquid density and bulk modulus at the pressure p, respectively.

2.2.2. Ideal gas law (vapor and air phases)

The ideal gas law is considered to model the vapor and air densities, which is defined as follows:

$$\rho_{v,\ a} = \frac{p}{RT}, \tag{11}$$

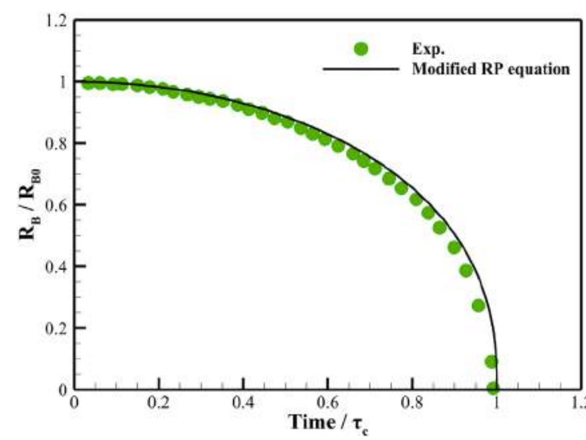

Fig. 4. Comparison of the collapsing process of a single bubble predicted by RP equation and experimental measurements.

where R represents the specific gas constant.

The speed of sound in the gas/vapor phase is calculated using the following equation:

$$a_{v,\ a} = \sqrt{\gamma RT} = \sqrt{\frac{c_p RT}{c_p - R}} = \sqrt{\frac{c_p}{c_p - R}\frac{p}{\rho_{v,\ a}}}, \tag{12}$$

where γ points out the specific heat ratio, which is defined as follows:

$$\gamma = \frac{c_p}{c_v} = \frac{c_p}{c_p - R}, \tag{13}$$

where R, c_p and c_v show the specific gas constant, the specific heat capacity at the constant pressure and the specific heat capacity at the constant volume, respectively.

2.3. Turbulence model and modifications

2.3.1. Standard $k-\varepsilon$ RNG

The standard $k-\varepsilon$ RNG turbulence model is defined by the following equations:

$$\frac{\partial(\rho k)}{\partial t} + \nabla\cdot(\rho \boldsymbol{u} k) = \nabla\cdot\left[\left(\mu + \frac{\mu_t}{\sigma_k}\right)\nabla k\right] + G_k - \rho\varepsilon, \tag{14}$$

$$\frac{\partial(\rho\varepsilon)}{\partial t} + \nabla\cdot(\rho \boldsymbol{u}\varepsilon) = \nabla\cdot\left[\left(\mu + \frac{\mu_t}{\sigma_\varepsilon}\right)\nabla \varepsilon\right] + \frac{c_1\varepsilon}{k}G_k - c_2\rho\frac{\varepsilon^2}{k}\ .$$

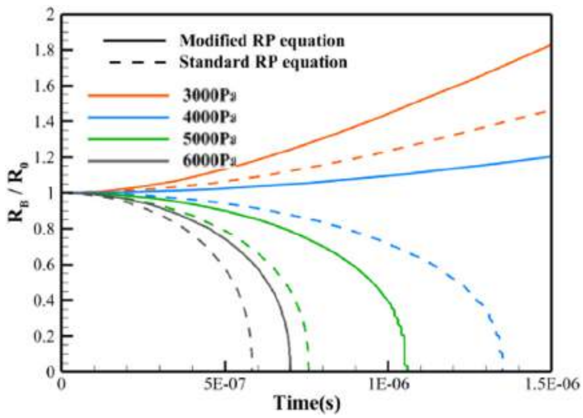

Fig. 5. Effect of local pressure (p) on the temporal evolution of a single bubble.

Table 1
Characteristics of mesh distributions.

Mesh Symbol	Number of elements	Number of nodes around hydrofoil
M1	93,900	190
M2	116,200	195
M3	155,000	260
M4	160,000	270

$$ \tag{15}$$

In this turbulence model, the effective viscosity which is applied to Reynolds equations is defined as $\mu = \mu_t + \mu_l$ where $\mu_t = \rho C_\mu k^2/\varepsilon$ denotes the turbulent viscosity and the constant is assumed as $C_\mu = 0.084$ [40]. Also, k and ε represent the turbulent kinetic energy and turbulent energy dissipation rate, respectively. Furthermore, G_k shows the production of turbulent energy term.

2.3.2. Density corrected model (DCM)

The standard $k-\varepsilon$ RNG turbulence model was originally developed to model the fully incompressible fluid flows. As a result, there is no treatment to deal with the multi-phase flow where compressibility plays an important role [26].

To overcome the discrepancies due to the high-density jump which occurs in the cavity closure and re-entrant jet at the adjacent hydrofoil surface, the $k-\varepsilon$ RNG turbulence model is modified based on a density correction model (DCM) proposed by Coutier-Delgosha et al. [26], which simply reduces the mixture turbulent viscosity in the mentioned regions and avoid over-estimated turbulent viscosity. Using this modification, the behaviors of the re-entrant jet and the vapor cloud shedding can be better resolved. The modified turbulent viscosity is given as follows:

$$\mu_t = f(\rho) C_\mu k^2/\varepsilon, \tag{16}$$

where

$$f(\rho) = \rho_v + \left(\frac{\rho_v - \rho}{\rho_v - \rho_l}\right)^n (\rho_l - \rho_v)\ . \tag{17}$$

With such a treatment, the eddy viscosity is decreased based on the DCM factor $f(\rho)$. It is noted that $n = 10$ is considered for the present simulations, as proposed by Coutier-Delgosha et al. [26]. The reduction of turbulent viscosity of mixture flow leads to remarkable changes in cavity structure where the viscosity will be highly modified. Overall, it is expected to have a more realistic simulation after the implementation of DCM modification.

2.4. Zwart-Gerber-Belamri (ZGB) cavitation model

The present cavitation model is inspired by the mass transfer equation of vapor volume fraction, which originated from the Rayleigh-Plesset (RP) equation [41]. The RP equation is given as follows:

$$R_B \frac{d^2 R_B}{dt^2} + \frac{3}{2}\left(\frac{dR_B}{dt}\right)^2 + \frac{4\mu_l}{\rho_l R_B}\left(\frac{dR_B}{dt}\right) + \frac{2S}{\rho_l R_B} = \frac{p_v - p}{\rho_l}, \tag{18}$$

where R_B denotes the spherical bubble radius, p represents the local fluid pressure, p_v shows the vapor saturation pressure, and S presents the surface tension. To simplify the RP equation, the second derivative of bubble radius, viscosity effect, and the effect of surface tension are ignored. As a result, the simplified RP equation is derived as follows:

$$\frac{dR_B}{dt} = sign(p_v - p)\sqrt{\frac{2}{3}\frac{|p_v - p|}{\rho_l}}, \tag{19}$$

The mass change rate of a single vapor bubble is given as follows:

$$\frac{dm_B}{dt} = \rho_v \frac{dV_B}{dt} = \rho_v \frac{d}{dt}\left(\frac{4}{3}\pi R_B^3\right) = 4\pi R_B^2 \rho_v \frac{dR_B}{dt}, \tag{20}$$

Assuming N_B represents the number of bubbles in the unit volume, the vapor volume fraction is given as follows;

$$\alpha_v = V_B N_B = \frac{4}{3}\pi R_B^3 N_B, \tag{21}$$

Using the bubble number density, the total interphase mass transfer rate is calculated as follows:

$$R = 4\pi R_B^2 \rho_v N_B \frac{dR_B}{dt}, \tag{22}$$

Using Eqs. (19), (21) and (22), the following equation is derived:

$$R = sign(p_v - p)\frac{3\alpha_v \rho_v}{R_B}\sqrt{\frac{2}{3}\frac{|p_v - p|}{\rho_l}}, \tag{23}$$

As a result, the source term R to describe evaporation ($R = R_e$) and condensation ($R = R_c$) is expressed by the following equations [42]:

$$\begin{cases} R_e = F_{vap}\frac{3\alpha_{nuc}(1-\alpha_v)\rho_v}{R_B}\sqrt{\frac{2}{3}\frac{p_v - p}{\rho_l}} & p_v > p \\ R_c = -F_{cond}\frac{3\alpha_v \rho_v}{R_B}\sqrt{\frac{2}{3}\frac{p - p_v}{\rho_l}} & p_v < p \end{cases} \tag{24}$$

where the empirical coefficients $F_{vap} = 50$ and $F_{cond} = 0.1$ are adopted for the water cavitating flow at ambient temperature. Also, the nucleation site volume fraction (α_{nuc}) is assigned to 5×10^{-4}, the fixed spherical bubble radius is equal to 1×10^{-6}m.

2.5. Semi-modified cavitation model

2.5.1. Pressure fluctuation effect

The concept of applying the turbulent eddy viscosity in the RANS equations is firstly introduced by Boussinesq [28]. This equation is introduced to close the Reynolds Averaged Navier-Stokes (RANS) equation and relate the turbulent stress and mean strain rate. The following equation is proposed by Boussinesq:

$$-\overline{u'_i u'_j} = 2\nu_t S_{ij}^* - \frac{2}{3}k\delta_{ij}, \tag{25}$$

where S_{ij}^* is the traceless mean rate of the strain tensor, k is the turbulence kinetic energy, and δ_{ij} is the Kronecker delta.

Using the above-mentioned concept, the pressure fluctuation and kinetic turbulent energy can be derived as follows:

$$p_t = -\frac{1}{3}\rho\left(\overline{(u')^2} + \overline{(v')^2} + \overline{(w')^2}\right), \tag{26}$$

$$k = \frac{1}{2}\left(\overline{(u')^2} + \overline{(v')^2} + \overline{(w')^2}\right), \tag{27}$$

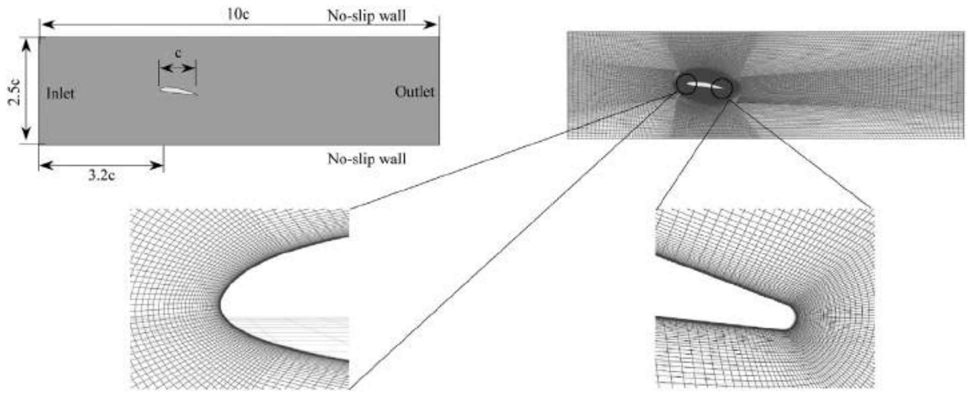

Fig. 6. Computation domain and mesh distribution.

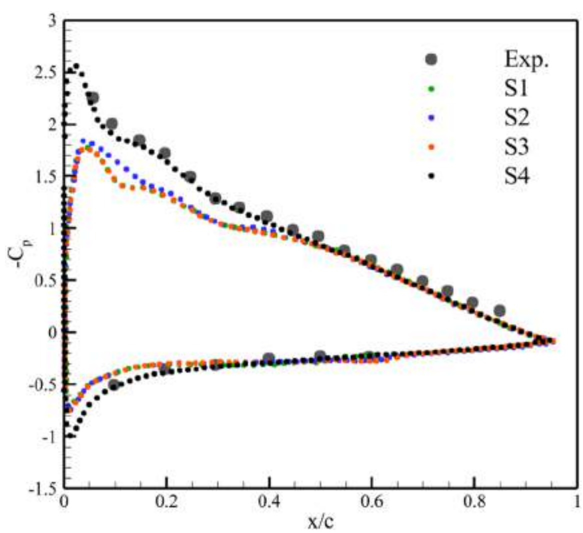

Fig. 7. Pressure coefficient distributions for different grids.

Therefore, the pressure fluctuation P_t is defined as follows:

$$p_t = -\frac{2}{3}\rho k, \tag{28}$$

A linear empirical coefficient F_t is introduced to make this equation compatible with practical applications. As such, the final form of the effective local pressure can be defined as follows:

$$p_{eff} = p_t + p = F_t\left(-\frac{2}{3}\rho k\right) + p, \tag{29}$$

where F_t denotes the Egler coefficient equal to 1.2 as suggested by Hinze [43] and Giannadakis et al. [44]. Thus, the effective pressure is calculated as a sum of averaged pressure and pressure fluctuation. Based on this model, the likelihood of cavitation inception in the pressure level higher than the saturation pressure is demonstrated.

Considering the effective pressure, the semi-modified cavitation model is derived and the source terms can be re-written as follows:

$$\begin{cases} R_e = F_{vap}\frac{3\alpha_{nuc}(1-\alpha_v)\rho_v}{R_B}\sqrt{\frac{2}{3}\frac{p_v-\left(F_t\left(-\frac{2}{3}\rho k\right)+p\right)}{\rho_l}} & p_v > F_t\left(-\frac{2}{3}\rho k\right) + p \\ R_c = -F_{cond}\frac{3\alpha_v\rho_v}{R_B}\sqrt{\frac{2}{3}\frac{\left(F_t\left(-\frac{2}{3}\rho k\right)+p\right)-p_v}{\rho_l}} & p_v < F_t\left(-\frac{2}{3}\rho k\right) + p \end{cases}. \tag{30}$$

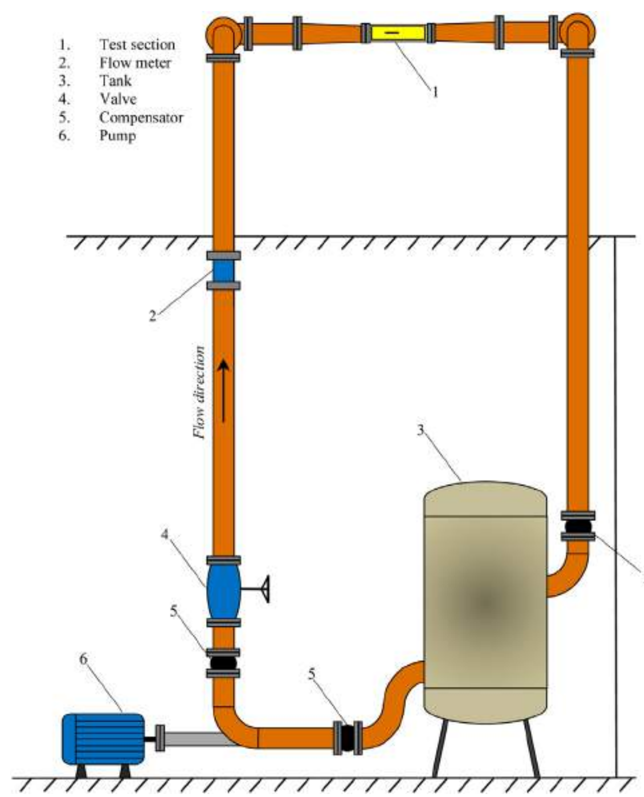

Fig. 8. Schematic of closed-loop cavitation test installation (left), test chamber and measuring devices (right).

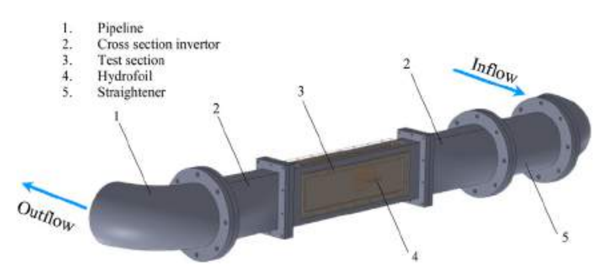

Fig. 9. Schematic of the test section and connected components.

2.6. Modified cavitation model

2.6.1. Bubble growth considering bubble contents [45]

To achieve a breakthrough in the prediction of three-phase cavitating flow, consideration of the bubble contents is crucial because

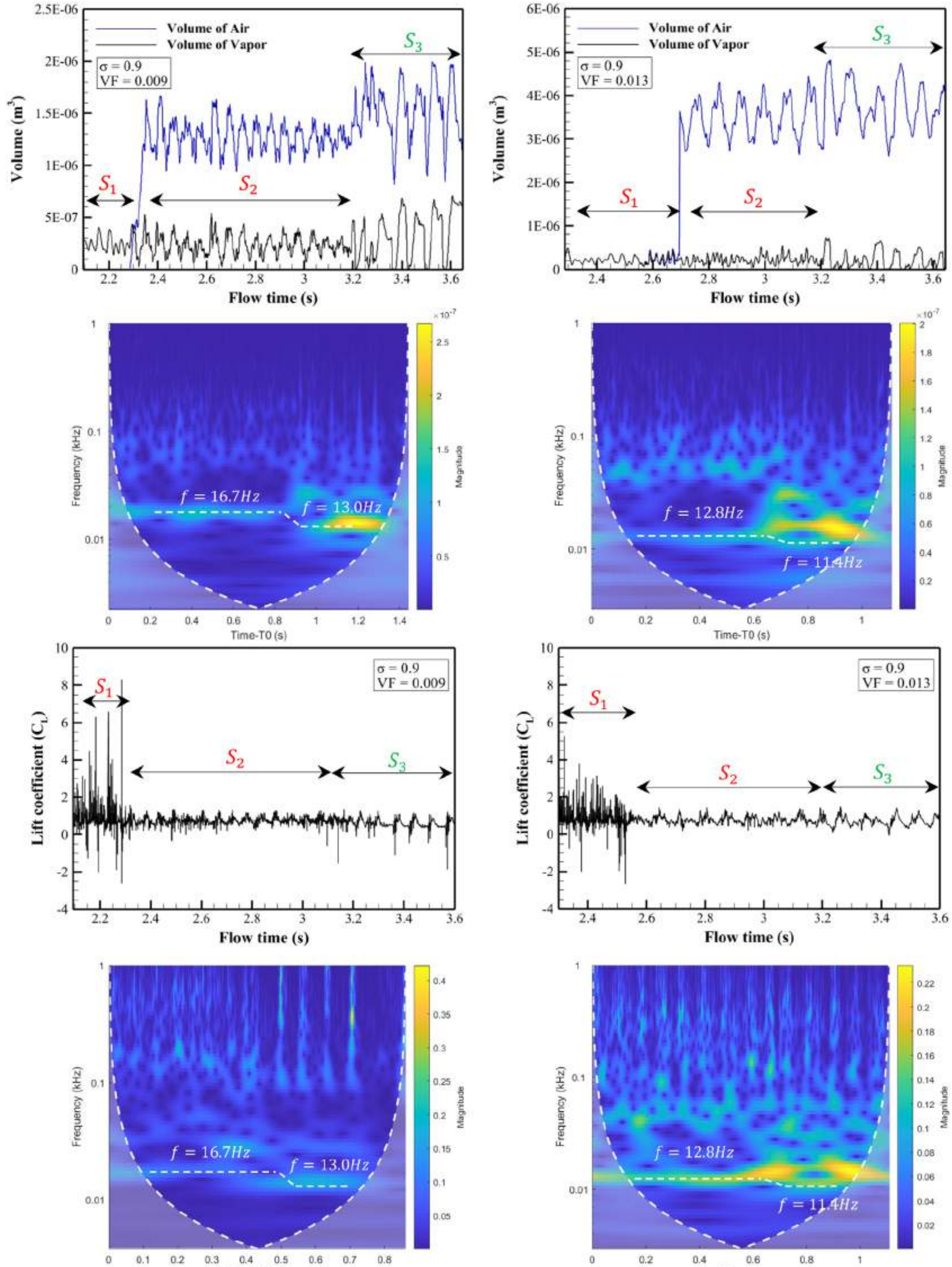

Fig. 10. Histories of vapor volume fraction and lift coefficient and corresponding shedding frequency of cavitating flow for semi-modified and modified models using Continuous Wavelet Transform (CWT).

of its remarkable impact on the inception of cavitation. To make a general overview, it is assumed that the bubble contains vapor and a specific quantity of non-condensable gas whose partial pressure equals to p_{G0} with a reference size of R_0. In addition, the thermal effect is neglected, and the non-condensable gas is air in the present work. Then, assuming the diffusive mass transfer between air and vapor phase, as well as; the inappreciable mass transfer between air and liquid phases, the general form of the pressure of mixture bubble, in the case when gas diffuses to vapor phase, is derived as follows:

$$p_B = p_V + p_{G0}\left(\frac{R_0}{R}\right)^{3\gamma}, \tag{31}$$

where γ denotes the heat capacity ratio equals 1.4 for air.

Therefore, the Rayleigh-Plesset equation in the case of non-negligible gas content is defined as follows:

$$R_B \frac{d^2R_B}{dt^2} + \frac{3}{2}\left(\frac{dR_B}{dt}\right)^2 + \frac{4\mu_l}{\rho_l R_B}\left(\frac{dR_B}{dt}\right) + \frac{2S}{\rho_l R_B} = \frac{p_v - p}{\rho_l} + \frac{p_{G0}}{\rho_l}\left(\frac{R_0}{R}\right)^{3\gamma}, \tag{32}$$

Following the same procedure for derivation of ZGB cavitation source term with the ignored second derivation of bubble radius, viscosity and surface tension effects, the modified source terms are derived as follows:

$$\begin{cases} R_e = F_{vap}\frac{3\alpha_{nuc}(1-\alpha_v)\rho_v}{R_B}\sqrt{\frac{2}{3}\frac{p_B-\left(F_t\left(-\frac{2}{3}\rho k\right)+p\right)}{\rho_l}} & p_B > F_t\left(-\frac{2}{3}\rho k\right)+p \\ R_c = -F_{cond}\frac{3\alpha_v\rho_v}{R_B}\sqrt{\frac{2}{3}\frac{\left(F_t\left(-\frac{2}{3}\rho k\right)+p\right)-p_B}{\rho_l}} & p_B < F_t\left(-\frac{2}{3}\rho k\right)+p \end{cases}. \tag{33}$$

Calculation of partial pressure of the bubble p_B depends on the content of each computational cell, which is done by the following established physical scheme.

2.6.2. Merging process of vapor and gas phases [25]

The present model proposes to take into account the non-condensable gas, which is air in this case, in the cavitation model. Using this approach, the inception, growth and collapse of the mixture bubble are influenced and can make the prediction closer to reality.

Although some terms are affected by the existence of non-condensable gas like α_{nuc} and R_B, one of the most crucial differences occurs in the prediction of pressure p_B in the mixture bubble. Pressure p_B is calculated as a sum of partial pressure of vapor (p_v) and partial pressure of the gas with an assumption of polytropic behavior in the bubble ($p_{G0}(\frac{R_0}{R})^{3\gamma}$). For this purpose, the merging process concept is employed based on the Eulerian point of view, where this process is illustrated in Fig. 2 to briefly clarify the idea.

It is assumed that the initial radius of gas bubbles in equilibrium is R_B, and as a result; the partial pressure of the bubble needs to satisfy the following equation when the surface tension and the viscosity are neglected.

$$p_\infty = p_v + p_{g0}, \tag{34}$$

where p_∞, p_V and p_{g0} represent the initial surrounding pressure, vapor pressure and initial partial pressure of non-condensable gas inside the bubble. Practically, the partial vapor pressure is much smaller than the partial pressure of non-condensable gas. In the present work, the initial surrounding pressure in equilibrium conditions is set to inlet pressure. Thus, the vapor pressure is also neglected. Then, Eq. (34) is given as follows:

$$p_{g0} = p_\infty = p|_{inlet}, \tag{35}$$

Given that the gas volume fraction is α_{ng}, the number of micro gas bubbles at each cell is calculated as follows:

$$V_{g0} = \alpha_{ng}.V_{cell}, \tag{36}$$

$$n_0 = \frac{3}{4}\frac{V_{g0}}{\pi R_B^3}, \tag{37}$$

where V_{cell} and V_{g0} represent the volume of the cell and, the volume of gas content; respectively, and n_0 is the number of micro gas bubbles of gas at each cell being in the initial equilibrium in initial conditions.

During the bubble migration from the far-field to the cavitation region, a sudden pressure drop appears which results in the radius increment. As such, the new equilibrium condition leads to the following equations:

$$p_{g1} = p, \tag{38}$$

$$R_{g1} = R_B 3\gamma\sqrt{p_{g0}/p_{g1}}, \tag{39}$$

where p shows the local pressure. In addition, R_{g1} represents the new radius.

Then, the total volume of non-condensable gas in the new equilibrium condition is calculated as follows:

$$V_{g1} = \sum_{i=1}^{n_0}\frac{4}{3}\pi R_{g1}^3, \tag{40}$$

In addition, these gas micro-bubbles are regarded to be merged, and a single gas bubble is generated, whose pressure and radius can be calculated as follows:

$$p_{g2} = p, \tag{41}$$

$$R_{g2} = 3\sqrt{n}R_{g1}, \tag{42}$$

where the pressure of a single gas bubble is equal to surrounding local pressure.

Given that the vapor volume fraction is α_v, the radius of the vapor bubble R_v is determined as follows,

$$V_v = \alpha_v V_{cell}, \tag{43}$$

$$R_v = 3\sqrt{\frac{3}{4}\frac{V_v}{\pi}}, \tag{44}$$

The merging process of the vapor and gas bubbles happens, when the total volume of vapor and gas bubbles ($V_T = V_v + V_{g1}$) is large enough. In addition, the coalescence of vapor and gas bubbles is hard to happen when the volume of air and vapor is substantially smaller than the cell volume. In this respect, it is assumed that the merging process is likely to be initiated when the sum of vapor and gas reaches 1/100 of each cell ($V_C = \frac{1}{100}V_{cell}$). As such, this volume ratio is a critical point to initiate the merging process. It should be noted that some other fractions of V_C/V_{cell} are tested, and it is concluded that 1/100 is the best value in case of agreement between the numerical predictions and experimental observations.

Under this condition, two scenarios for coalescence of vapor and gas bubbles can be considered which are defined as follows:

$$\begin{cases} p_B = p_V + p_{g2}\left(\frac{R_{g2}}{R_v}\right)^{3\gamma} & R_v > R_{g2} \\ p_B = p_V & R_v \le R_{g2} \end{cases}, \tag{45}$$

It is noted that the modified cavitation model will be activated when the critical volume ratio is satisfied, otherwise; the semi-modified cavitation model will be recalled. The switching scheme between the modified and semi-modified cavitation models is demonstrated in Fig. 3.

Employing the merging theory, Eq. (32) can be rewritten as follows:

$$R_B \frac{d^2R_B}{dt^2} + \frac{3}{2}\left(\frac{dR_B}{dt}\right)^2 + \frac{4\mu_l}{\rho_l R_B}\left(\frac{dR_B}{dt}\right) + \frac{2S}{\rho_l R_B} = \frac{\left(p_v + p_{g2}\left(R_{g2}/R_v\right)^{3\gamma}\right) - p}{\rho_l}. \tag{46}$$

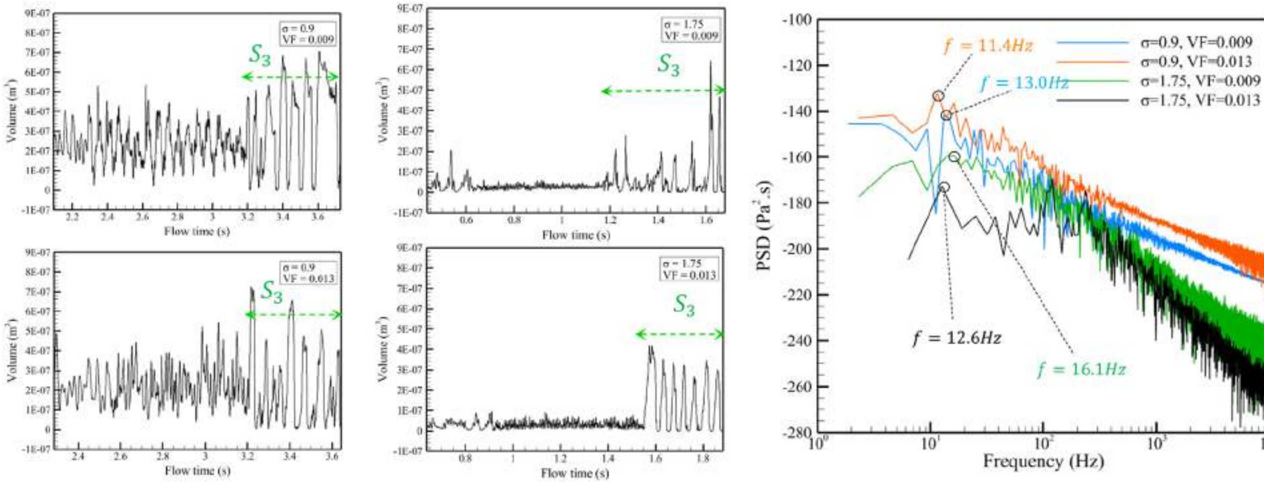

Fig. 11. The history of vapor volume fraction and corresponding Power Spectral Density (PSD) at different cavitation numbers ($\sigma = 0.9,\ 1.75$) and amounts of dissolved air (VF = 0.009, 0.013).

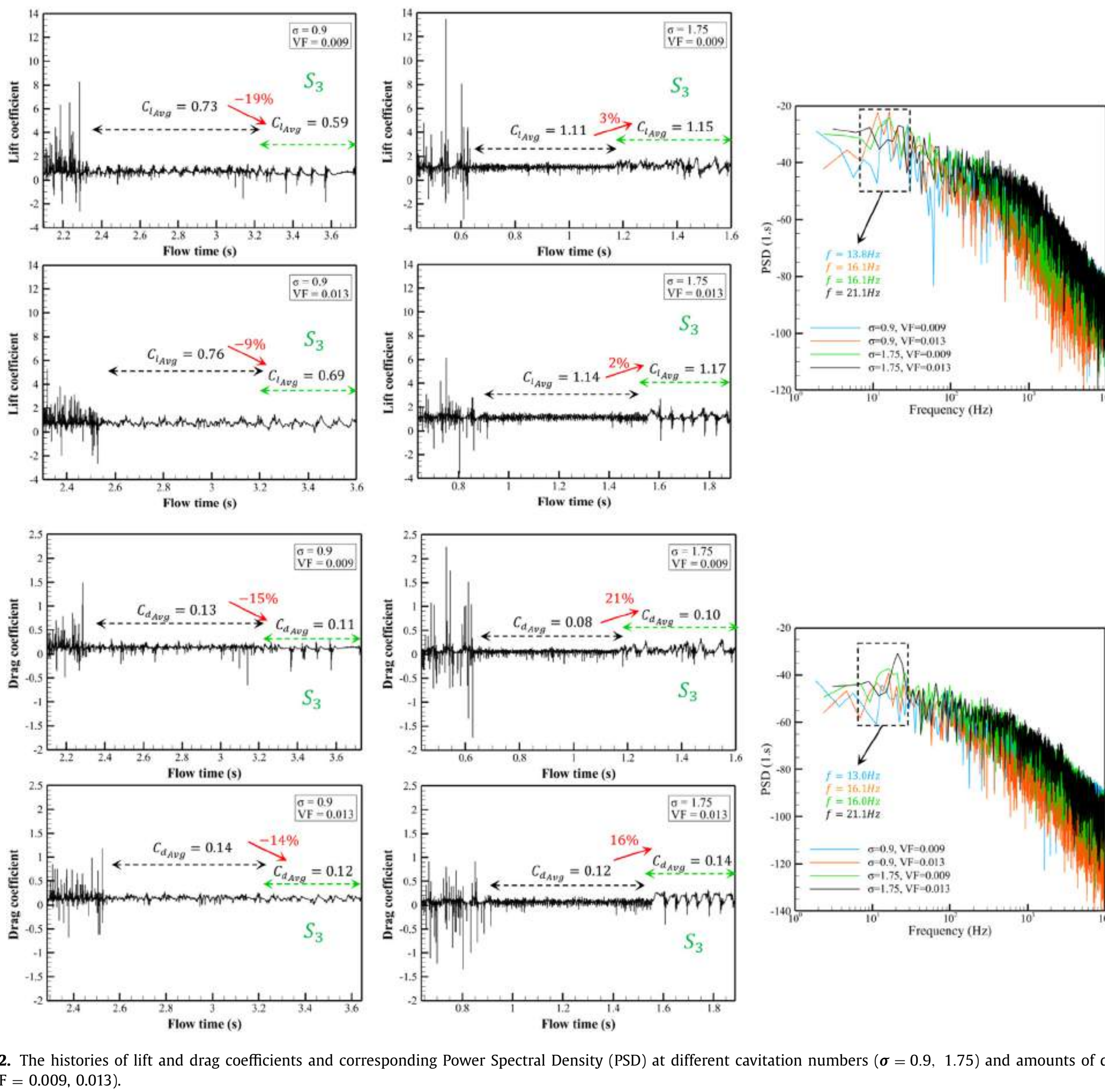

Fig. 12. The histories of lift and drag coefficients and corresponding Power Spectral Density (PSD) at different cavitation numbers ($\sigma = 0.9,\ 1.75$) and amounts of dissolved air (VF = 0.009, 0.013).

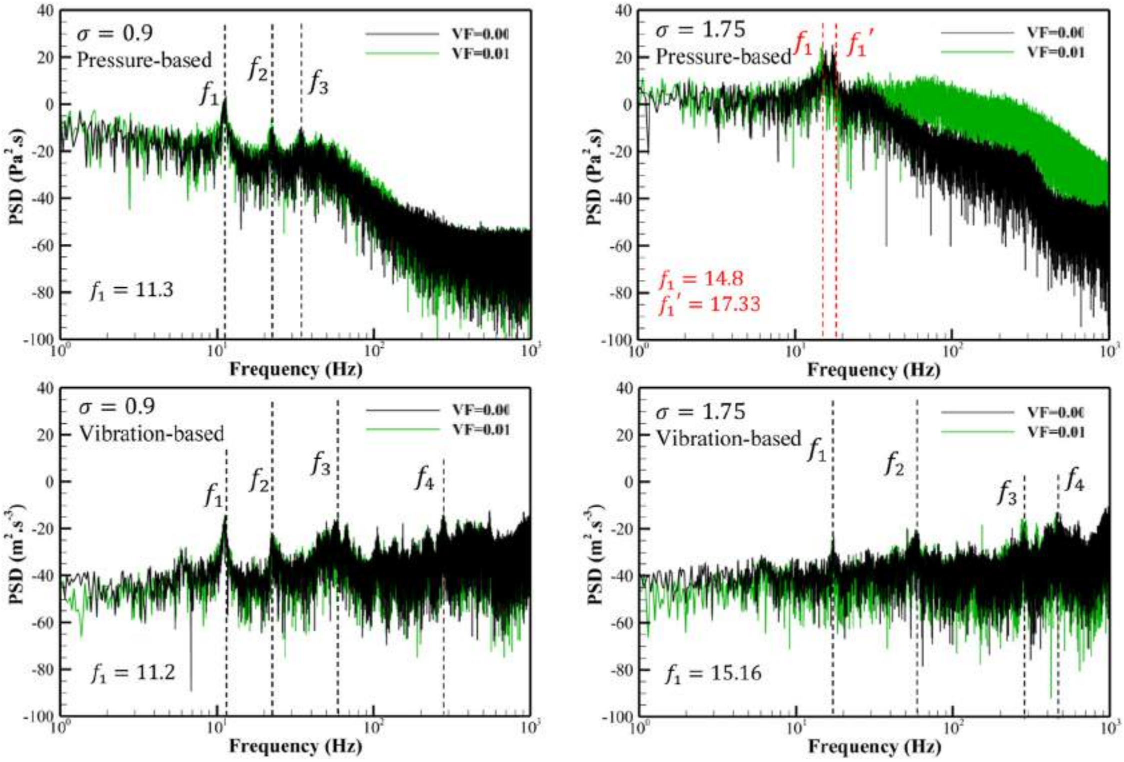

Fig. 13. Power spectral density of pressure fluctuation (top) and vibration (bottom) at P7.

Table 2
The shedding frequencies extracted from different sources.

	Exp. VF-based	Exp. Pressure-based	Num. VF-based	Num. C_L-based	Num. C_D-based
$\sigma = 0.9,\ VF = 0.009$	10 Hz	11.3 Hz	13.0 Hz	13.8 Hz	13.0 Hz
$\sigma = 0.9,\ VF = 0.013$	9.5 Hz	11.3 Hz	11.4 Hz	16.1 Hz	16.0 Hz
$\sigma = 1.75,\ VF = 0.009$	16.4 Hz	17.3 Hz	16.1 Hz	16.1 Hz	16.1 Hz
$\sigma = 1.75,\ VF = 0.013$	12.3 Hz	14.8 Hz	12.6 Hz	21.1 Hz	21.1 Hz

2.7. Validation and function analysis of modified RP

To validate the developed modified RP equation, the collapse process of a single bubble predicted by Eq. (46) compared with experimental data reported by Tinguely et al. [46] for the case with $p_v = 3460Pa$, $p = 80000Pa$, $\alpha_v = 1.0$ and $\alpha_{ng} = 0.0$ is shown in Fig. 4. The surface tension and dynamic viscosity are neglected. It is to notice that for those conditions the modified RP equation will transform to the standard one.

To show the influence of the merging process on the behavior of the bubble, it is applied to the Rayleigh-Plesset equation (Eq. (46)), and the radius of the bubble is calculated and compared with the corresponding radius given by the standard RP equation (Eq. (18)). Fig. 5 depicts the comparison of the bubble radius evolutions for different local driving pressures. In addition, the surface tension and dynamic viscosity are neglected. It is assumed that the operating condition in the cell, which contains the bubble, is $p_v = 3540Pa$, $\alpha_v = 0.8$ and $\alpha_{ng} = 0.009$, as well as; the initial radius of the bubble is equal to $10^{-6}m$. In addition, the surrounding pressure is in the range of 3000 to 6000 Pa. The result shows that the resistance of a bubble to collapse enhances when the bubble contains air. The inception can be substantially different as is observed for $p = 4000Pa$ when the bubble of pure vapor is collapsing (i.e. standard RP), while the mixture bubble is growing. One can conclude that the incipient cavitation will appear earlier by considering the merging process. By the extension of cavitation boundaries, larger cavities can be expected and resolved.

2.8. Numerical procedure, computational domain and meshing

The presented numerical modeling is carried out using Fluent software, and the modifications are applied using UDF coding. The unsteady Reynolds Averaged Navier-Stokes (uRANS) equations for the mixture phase are solved using the SIMPLEC algorithm.

The length and height of the computational domain and boundary conditions presented in Fig. 7 correspond to the real dimensions of the test chamber. The left and right walls are set to velocity inlet and pressure outlet, respectively. In addition, the top and bottom walls are assumed as stationary, no-slip surfaces. Also, the mesh distribution is presented in Fig. 6. The domain has 8 main blocks with the O-grid around the hydrofoil. The overall number of grid nodes on the hydrofoil's profile amounted to 368 and the edge normal to the foil had 101 nodes. The domain had an overall width of 0.09 mm discretized by 3 layers of 0.03 mm in thickness. The thin domain was selected to reduce the aspect ratio in the domain close to the hydrofoil in the O-grid region. The whole mesh consisted of 220 k hexahedra elements and the value y^+ on the hydrofoil was less than 1. Four different meshes were examined. Their parameters are summarized in Table 1.

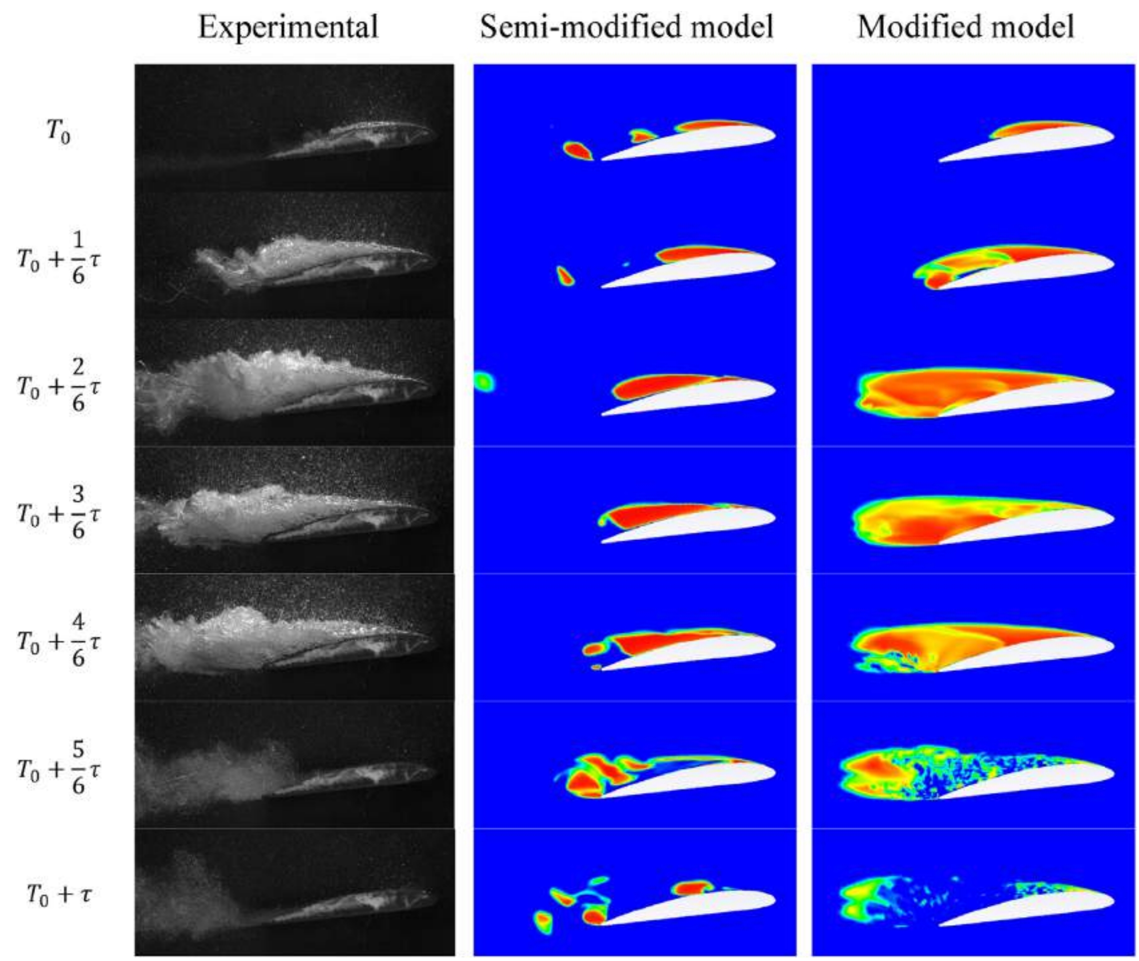

Fig. 14. The evolution of cavitating structure in a period at $\sigma = 0.9$ and VF = 0.013.

To check the performance of the mesh distributions, the pressure distribution along the hydrofoil is compared with the experimental data reported by Matsunari et al. [47] for the same hydrofoil. Based on the comparison, as shown in Fig. 7, the mesh distribution M4 is selected for further investigation since it gives the best results matching the experimental data.

3. Experimental setup and approach

The experiments were conducted in the hydraulic installation equipped with a test section designed to analyze the cavitating flow at the Department of Power Engineering and Turbomachinery, Silesian University of Technology. The structure of the closed-loop cavitation test setup along with the main elements are presented in Fig. 8. The operating fluid in the installation was water. The designed installation is capable to maintain a constant flow rate of 500 m^3/min with a corresponding 10.4 m/s flow velocity at the inlet and variable pressure level inside of the chamber in the range of 90 to 190 kPa. The main components of the installation are the test section, flow meter, tank, valve, elastic coupling and pump. The tank with 1.5 m^3 vol is equipped with an internal airbag that is capable to be inflated causing pressure change within the installation. Also, the temperature of the water was measured inside of the tank using the resistance thermometer APLISENS CT GN1 Pt100. The three pipeline compensators are mounted along the pipeline to reduce vibration propagation. The flow rate is measured which can be converted to flow velocity. The electric pump of 30 kW power runs the flow with a constant mass flow rate within the installation. The accuracy of the measuring devices; as well as, their working range was discussed in Ref. [36].

The test chamber along with other connected components are illustrated in Fig. 9. The test chamber has a rectangular cross-section with height (h), span (w) and length (L) of 189 mm, 70 mm and 700 mm, respectively. The chamber height to chord ratio equals $w/c = 2.7$. The water flow is straightened by the honeycomb. The invertors are applied to reduce the cross-section and convert the circular shape to a rectangular one. The test section has three transparent walls at the top, bottom and front sides. The tested hydrofoil was mounted on one side of the chamber at half of the chamber's height, 210 mm downstream from the chamber inlet.

In addition, the main measuring devices are a high-speed camera, lighting, data acquisition system, rig controller, image controller and trigger, which are discussed in Ref. [36].

In the present work, six levels of cavitation numbers were measured. The limit of the temperature difference during the test campaign was 3 °C. The temperature difference was neglected in the numerical simulations. The Reynolds number equals $Re = \frac{\rho_l u_{in} c}{\mu_l} \simeq 0.79 \times 10^6$, where ρ_l, u_{in}, c and μ_l represent the density of water, velocity of flow at the inlet, hydrofoil chord and dynamic viscosity of water, respectively. Each case is defined with a single cavitation number calculated as follows:

$$\sigma = (p_{in} - p_v)/\left(0.5\rho_l u_{in}^2\right) \quad (48)$$

where p_{in} and p_v denote the static pressure at inlet and water saturation pressure, respectively. Also, the value of inlet pressure is based on the average pressure calculated from instantaneous pres-

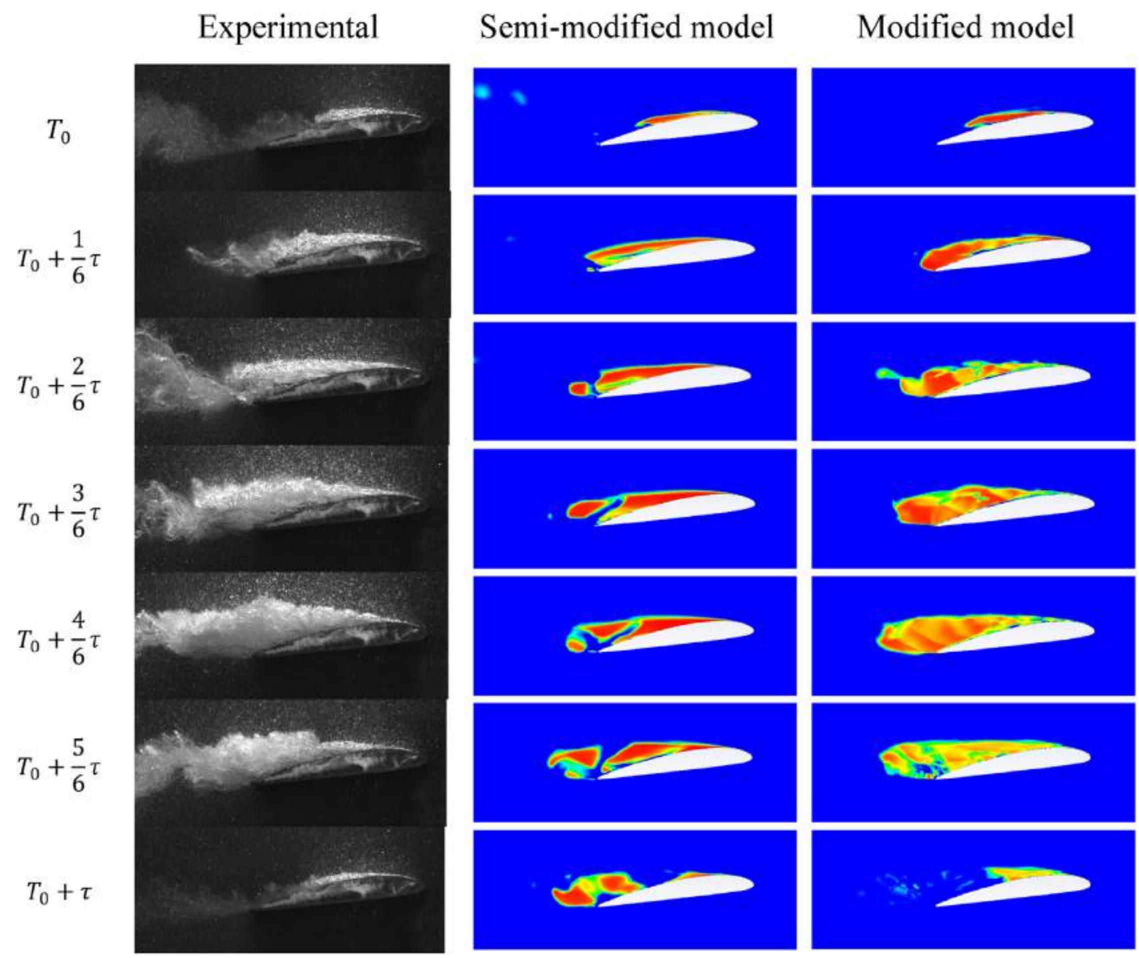

Fig. 15. The evolution of cavitating structure in a period at $\sigma = 0.9$ and VF = 0.009.

sure fluctuations detected during the round of the related experiment. Furthermore, the saturation pressure is calculated based on the average temperature calculated over the related experiment. Also, ρ_l shows the density of water calculated at the corresponding temperature and pressure in each case with a nominal cavitation number. Finally, u_{in} represents the velocity at the inlet, which is also based on the average value.

The experimental tests were conducted based on two specific levels of dissolved oxygen of 4.24 mg/l and 6.46 mg/l. Based on Henry's law, it corresponds to the air content of 10.84 mg/l and 16.52 mg/l, respectively. The multifunction meter CF-401 was employed to measure the oxygen levels before and after the experimental campaign in steady conditions. The average value of the oxygen is reported in this work. The ranges of oxygen levels for the first and second experimental campaigns were 4.3 - 4.18 mg/l and 6.77 - 6.15 mg/l, respectively.

4. Results and discussion

The three-phase cavitating flow is analyzed based on numerical and experimental approaches. To consider the effect of dissolved air on cavitation, the cavitation model is modified based on the merging theory. Based on this theory, the pressure of the nucleation bubbles is not only related to the vapor saturation pressure, but the air content influences the bubble pressure. In addition, three phases including water, vapor and air are considered compressible fluids. The $k-\varepsilon$ turbulence model is modified using Density-Corrected Based (DCM) to avoid the overestimation of turbulent kinetic energy. This work mainly focuses on the unsteady behavior of cavitating flow especially the shedding frequency and morphological analysis. To analyze the highly unsteady parameters, the Power Spectral Density (PSD) and Continues Wavelet Transform (CWT) methods are employed.

4.1. Unsteady characteristics

As shown in the previous section, by solving the Rayleigh-Plesset equation (Eq. (46)) it is confirmed that adding the dissolved air causes a longer collapsing time. Also, in some cases, it can avoid collapse. As such, one can expect different shedding frequencies when the merging theory is applied in the cavitation model. For this purpose, the Continuous Wavelet Transform (CWT) is used to calculate the corresponding shedding frequency during various stages of the simulation which are provided in Fig. 10 as the history of changes in both vapor volume fraction and lift coefficient. The simulations process is categorized into three different stages defined as follows:

- S_1 - the simulation with a Density Corrected-Based Model (DCM) without dissolved air.
- S_2 - the simulation with a Density Corrected-Based Model (DCM) and semi-modified cavitation model with dissolved air.
- S_3 - the simulation with a Density Corrected-Based Model (DCM) and modified cavitation model with dissolved air.

In the first stage (S_1) where the pure cavitation without air is simulated, it is observed that the fluctuation of the vapor volume fraction is smoother than in other sections. On the contrary, the lift coefficient demonstrates a highly dynamic behavior. Generally,

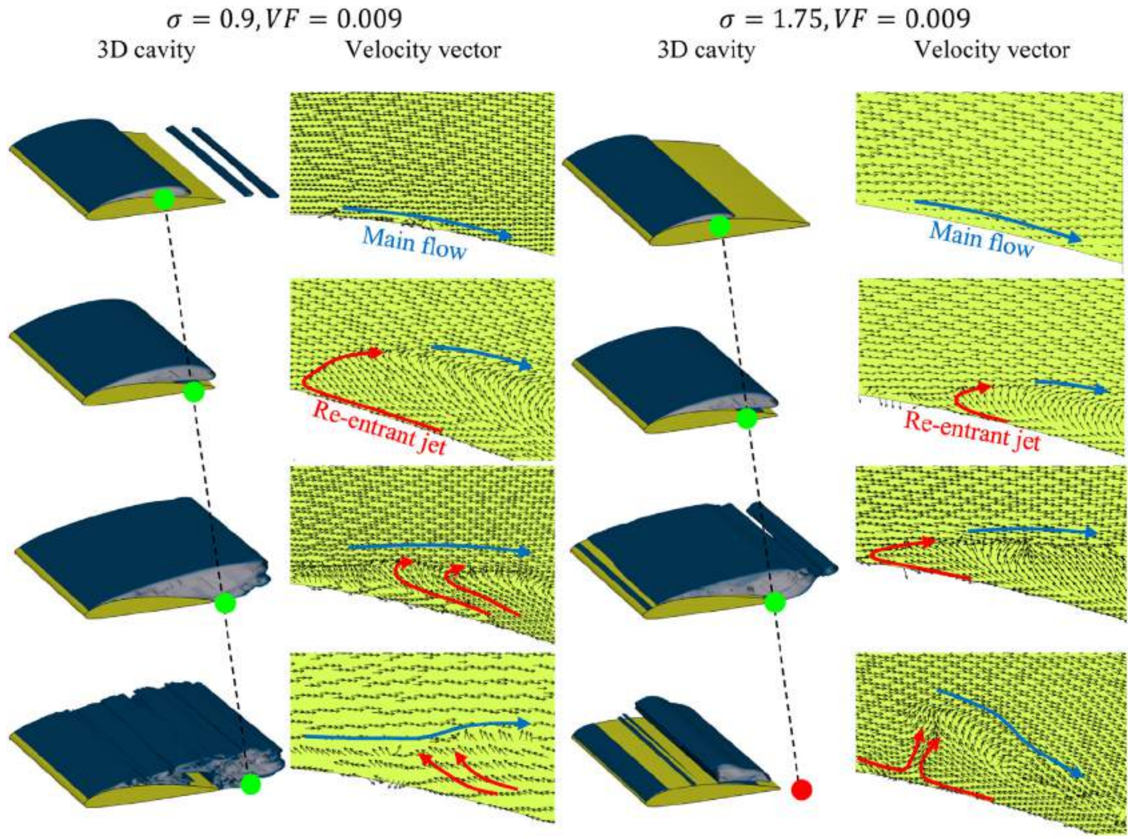

Fig. 16. 3D flow structure and velocity vector at $\sigma = 0.9,\ 1.75$ and VF = 0.009.

the fluctuations can be categorized into two types, the first type shows the period of cavitation and the second type demonstrates the secondary internal unsteadiness during each period. By adding the dissolved air into the simulation, the fluctuation of the vapor volume fraction during a period remained fairly the same, however; the internal fluctuation increased. Although the secondary unsteadiness is augmented in the volume of cavitation, the fluctuations of the lift coefficient are remarkably damped which means that a more uniform force acts on the hydrofoil during the time. By employing the merging theory and passing to S_3, the characteristics of the cavitating flow are changed in two ways. Firstly, the amplitudes of fluctuations considerably rose which shows the stronger and larger cavity around the hydrofoil. On the other hand, the reduction in shedding frequency is detected regardless of the amount of dissolved air.

Determination of the shedding frequency using experimental and numerical methods is a challenging task since not only different operating parameters can be highly influential on it but also the used approach to extract the frequency plays a vital role. Two numerical methods, including volume fraction-based and force-based and two experimental approaches, pressure-based and vibration-based, are presented and discussed in the following sections. To show the impact of merging theory on the cavity area and shedding frequency, the history of the vapor volume fraction and the corresponding PSD analysis at different cavitation numbers and volume fractions are presented in Fig. 11. A much stronger and larger cavity is generated around the hydrofoil which can be concluded by a larger amplitude of vapor volume fraction. Although the cavity area is remarkably enlarged in all of the cases, the percentage of enhancement is more obvious reflected in a higher cavitation number. It should be noted that the Power Spectral Density is applied for the last stage of simulation when the merging theory is taken into consideration. As such, the presented shedding frequency can be known as modified shedding frequency. Comparing the shedding frequency extracted by PSD, it is concluded that adding the dissolved air causes a lower shedding frequency which means that the cavitating flow is stabilized. As such, a larger cavity with lower dynamic behavior is expected to appear in the case with a higher amount of air content. Besides, in the same level of air content, the shedding frequency is augmented with increasing in cavitation number, although the average area of the cavity is lower compared with the case with a lower cavitation number. As a result, a smaller cavity with stronger unsteady nature is predicted.

The histories of lift and drag coefficients with the corresponding PSD analysis to extract the shedding frequency are presented in Fig. 12. As discussed in the above section, the lift and drag coefficients are considerably stabilized by adding the dissolved air regardless of the cavitation number and air volume fraction. In addition, the average value of the lift and drag coefficients are influenced by employing the merging theory; however, the percentage of differences are varied depending on the case. Although the average value of force coefficients are decreasing in the cases with a lower value of air content, the increment is observed for the case with a higher amount of air. The reason for the difference in the lift and drag coefficients is the change that appeared in the structure of the cavity. The pressure distribution around the hydrofoil is highly dependent on the type and length of the cavity. Furthermore, the PSD analysis is used to detect the shedding frequency. The order of the magnitude of frequency for different cases is similar to those provided for vapor volume fraction; however, the magnitudes are different. It is worth mentioning that the lift and drag coefficients as the components demonstrate a similar shedding frequency.

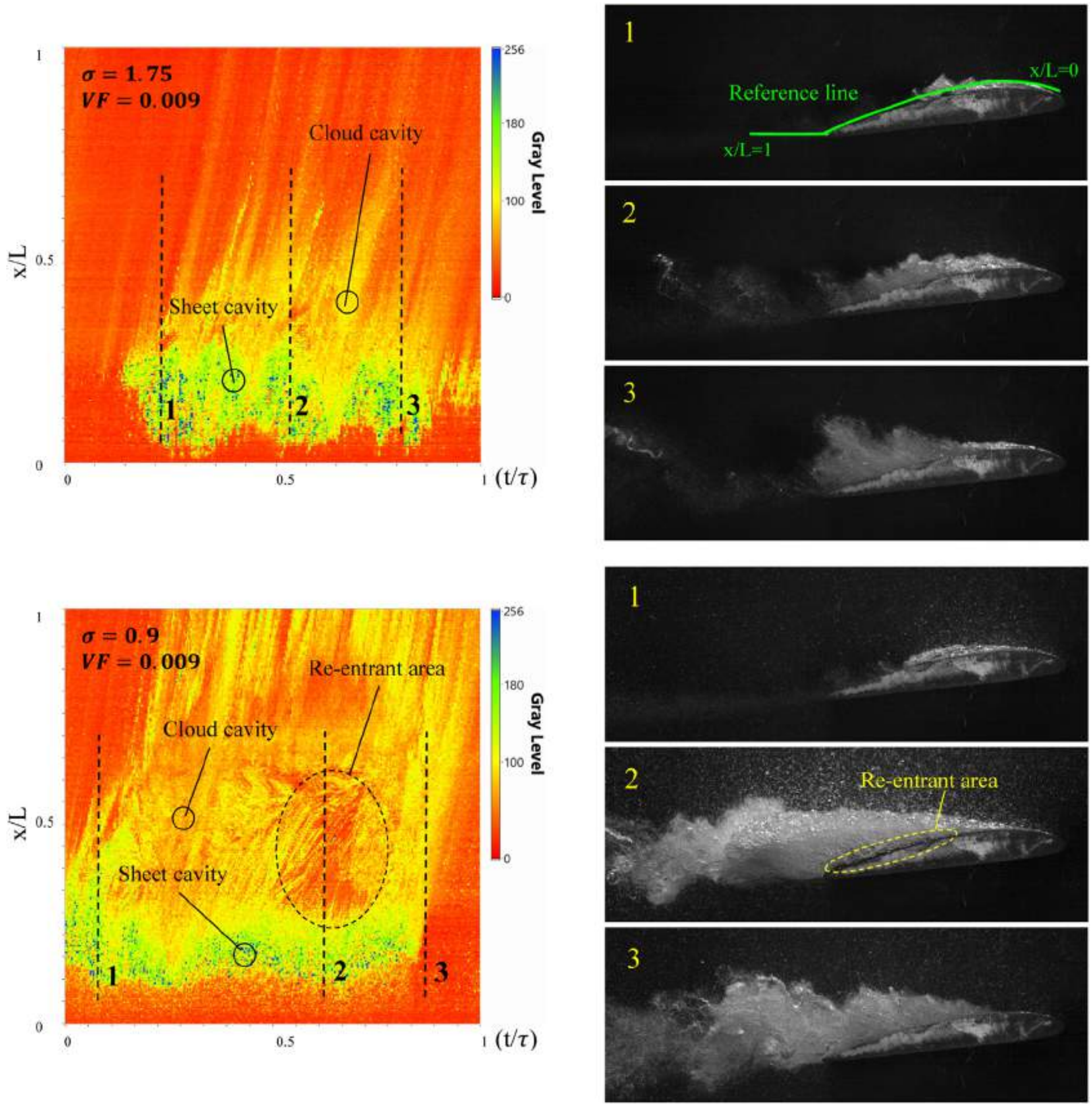

Fig. 17. Describing various regions of the cavity using a temporal-spatial distribution of gray level on the selected reference line at the suction side (one cycle at $\sigma = 0.9,\ 1.75$ and VF = 0.009).

After analysing and discussing the shedding frequency detected by the numerical approaches, it is necessary to investigate the experimental data and compare them with the numerical ones. For this purpose, the pressure-based and vibration-based shedding frequencies are provided in Fig. 13 which are extracted using Power Spectral Density (PSD). The pressure fluctuation measured at P7 is used which is equipped with a fast pressure sensor. Based on the PSD analysis, different peaks at the PSD distributions declare different modes of cavitating flow, and the first peak is known as the main shedding frequency. Moreover, the frequencies interestingly are matched together for the low cavitation number, and a slight difference is detected in the case with a high cavitation number. The shedding frequency for the low cavitation number is equal to 11.3 Hz for both air contents, and the values of 14.8 and 17.33 Hz go to VF = 0.009 and VF = 0.013, respectively in the case of high cavitation number. On the other hand, the PSD distribution of vibration demonstrates more peaks and modes. However, the first peak which is also known as the shedding frequency is common between PSD distribution of pressure and vibration. The latest observation denotes that the first peak (i.e. main frequency) is due to cavitating flow and other frequencies are due to the other external parameters.

After discussing the shedding frequency extracted by different methods, it is required to compare the magnitude of them to find the matched frequencies and the best approach. The magnitudes of shedding frequencies based on different approaches are summarized in Table 2. The magnitude of experimental VF-based and Pressure-based frequencies are comparable to the numerical VF-based ones. However, those extracted from the force coefficient variations are slightly different. It would be better to compare the shedding frequency extracted from the numerical force coefficient with the corresponding parameter from an experiment. The existed different sources for frequency extraction could be a reason for deviations. Although other reasons may exist which are difficult to detect. In fluid dynamics, vortex shedding is an oscillating flow that takes place when a fluid such as air or water flows past a bluff (as opposed to a streamlined) body at certain velocities, depending on the size and shape of the body. In this flow, vortices are created at the back of the body and detach periodically from either side of the body. Also, during the cavitating flow, the cavi-

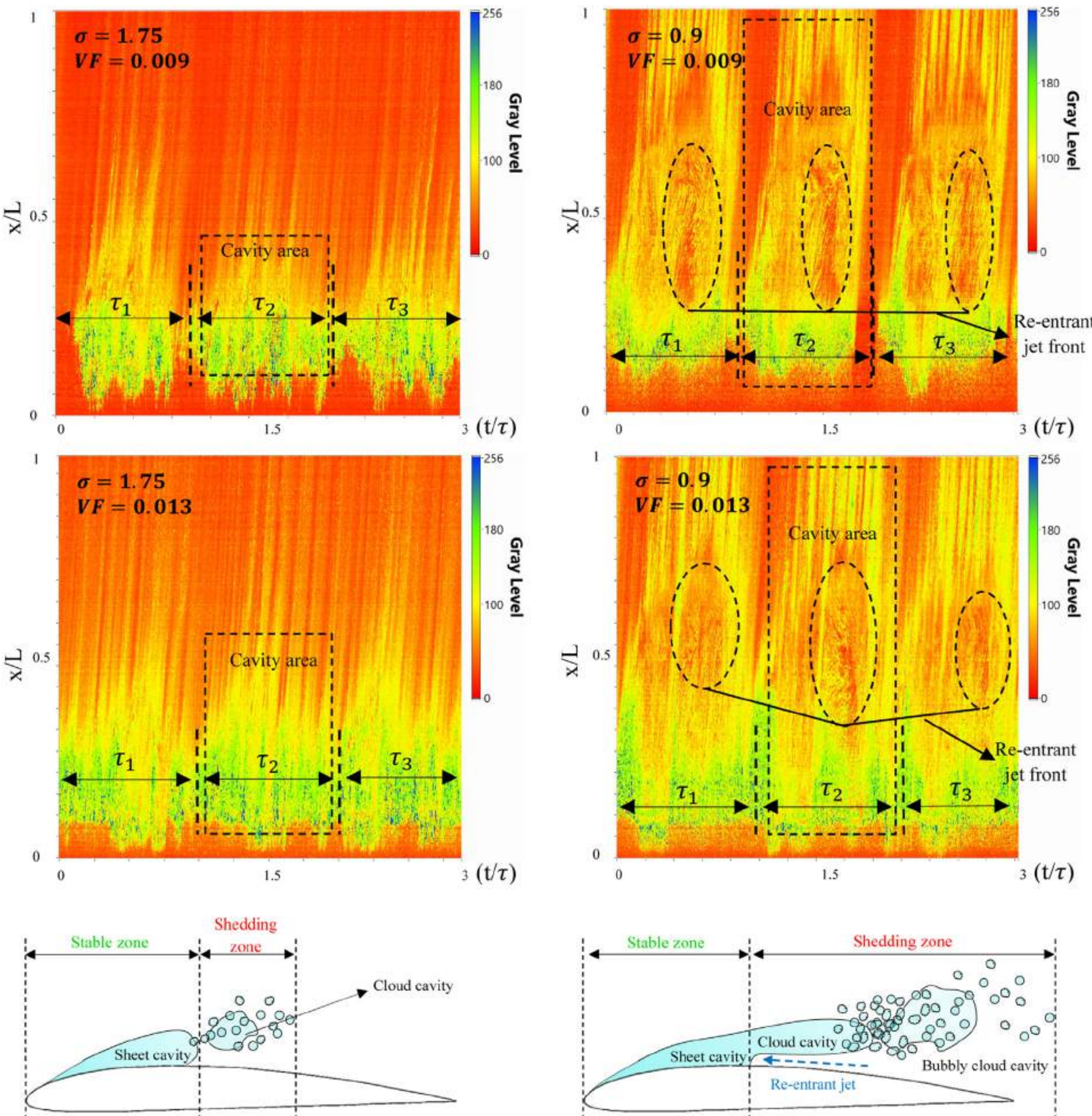

Fig. 18. Comparison of cavity length using a temporal-spatial distribution of gray level on the selected reference line at the suction side (three cycles at $\sigma = 0.9,\ 1.75$ and VF = 0.009, 0.013).

tation area emerges and then disappears passing downstream. As a result, based on the definition of shedding, the authors suggest the shedding frequency addresses the periodical cavitation generation and collapse. Also, the other frequencies apply to the hydrofoil, like the one extracted by force coefficient, may be considered as a product of the shedding process and have different magnitudes. So, talking about the main frequency, the source of it must be specified.

4.2. Morphological analysis

One of the important characteristics of the cavitating flow which is highly influenced by numerical methods is the structure of the cavity during the periods. The corrected turbulence model reduces the overestimation of turbulent viscosity and damping of the flow, especially inside the cavity region. In addition, the compressibility effect causes a better prediction of flow field parameters in the multiphase flow. Finally, the modified cavitation model coupled with merging theory considers the effect of dissolved air content. As such, gathering these modifications, the changes in the cavity structure are expected. The evolutions of the cavitation during a period at $\sigma = 0.9$ and VF = 0.013 based on the experimental observation, semi-modified and modified numerical approaches are illustrated in Fig. 14. Based on the experimental photos, it is observed that the cavitation starts from sheet cavity-type and extends with time. In the middle of the period, the largest cavity length so-called cloud cavity appears. Then, the cloud cavity is collapsed and shed downstream.

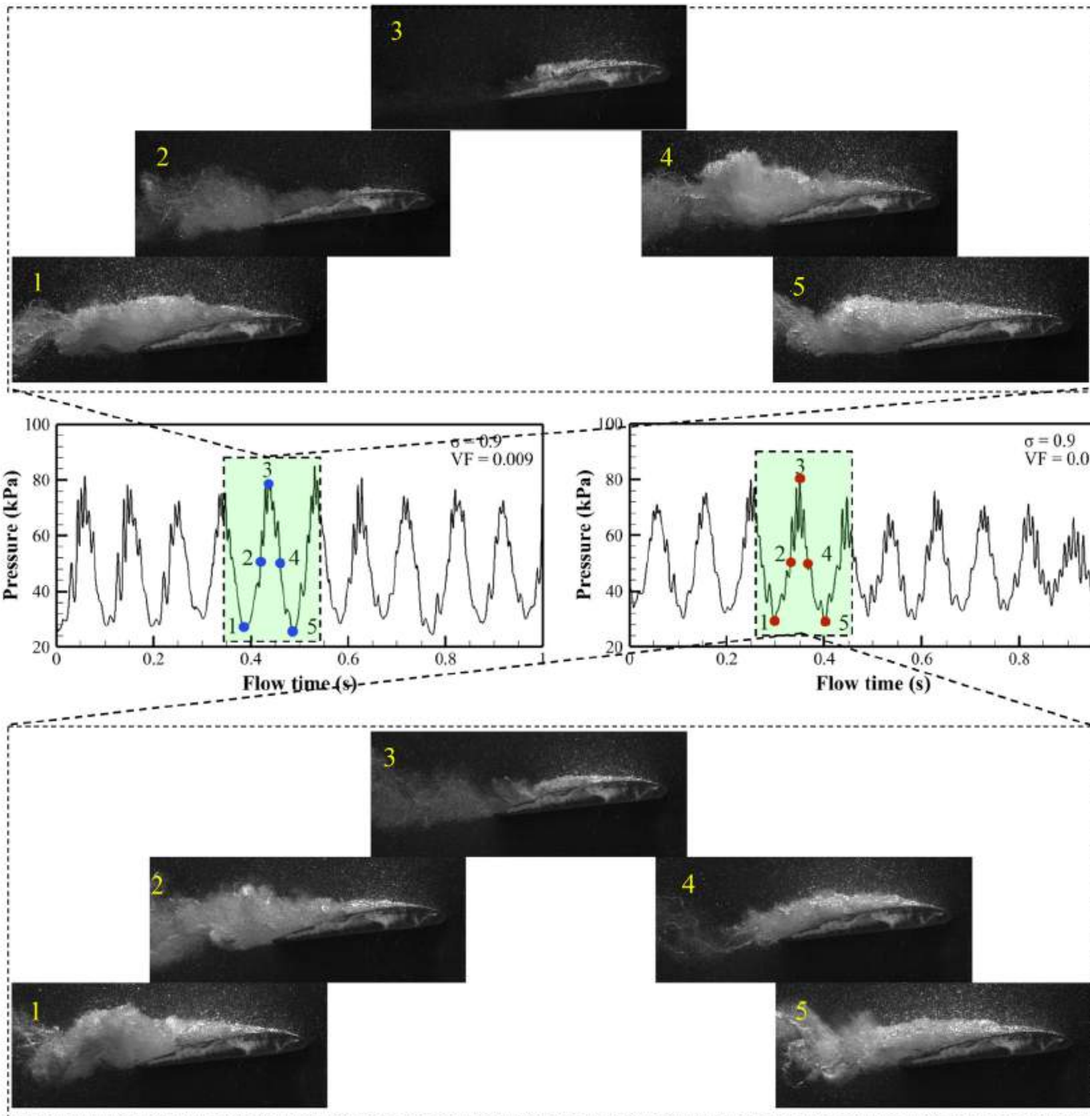

Fig. 19. Pressure fluctuation with corresponding selected cavity structure during one cycle at $\sigma = 0.9$ and VF = 0.009, 0.013.

Moreover, comparing the cavity structure predicted by the numerical model and the experimental observation, it is obvious that the semi-modified model predicted a smaller cavity. The modified model predicted a more extended cavity that is closer to the experimental observations. The evolutions of the cavitation during a period at $\sigma = 0.9$ and VF = 0.003 based on the experimental observation, semi-modified and modified numerical approaches are illustrated in Fig. 15. The procedure of the cavity evolution is similar to the case with a higher amount of air content. However, due to the lower amount of dissolved air content, the cavity length is smaller. Regardless of the dissolved air level, the contour of vapor volume fraction declares that the cavity contains almost pure vapor when the semi-modified model is employed. However, the content of the cavity is not uniform in the cases simulated using the modified model. The latest observation with a non-uniform vaporous cavity seems to be closer to reality.

One of the most important factors that initiate the collapsing process is the re-entrant jet. The re-entrant jet is known as a liquid sublayer adjacent to the suction side of the hydrofoil passing from the rear upwards to the leading edge. Despite the remarkable importance of the re-entrant jet, the mechanism by which it alters and converts sheet cavity to detached cloud cavity is complex. In addition, which parameters are effective on it, and how much the re-entrant jet is influential on the collapsing process need to be thoroughly analyzed. For this purpose, the quasi-3D cavity structure and the corresponding velocity vector are presented in Fig. 16, to show the details of the re-entrant configuration. It is worth mentioning that the effect of a cavitation number ($\sigma = 0.9$ and $\sigma = 1.75$) is studied in this section. It should be noted that the boundaries of the cavity are extended in width to have a better graphical presentation of the cavity structure. First, the numerical visualization declares that the cavity lasts longer at a lower cavitation number. It is due to the stronger cavity generated in this case. The effect of the re-entrant jet is also more dominant since the cloud cavity is not as dense as the sheet cavity; however, the re-entrant jet is not able to penetrate as much as it does in the case with a higher cavitation number. The latest observation will be also discussed in the following section captured by image processing using experimental observation. Furthermore, based on the velocity vector, we can see that the configuration of the re-entrant jet differs from the start point to the end point of a period. At the beginning of the period, no re-entrant jet can be detected, however; the re-entrant jet, which is moving in reverse direction compared to the main flow, is observed in the next step. The re-entrant jet has a curvy front which is changed to a sharp edge in a further step. On the other hand, no significant difference is detected in the configuration of the re-entrant jet comparing the cases with different cavitation numbers; however, the location of the re-entrant jet front is depending on the case.

Due to the highly dynamic nature of the cavitating flow, the analysis of experimental observation is a challenging task. To investigate the shedding path, collapse mechanism, and detection of re-entrant jet, the temporal-spatial distributions of a gray level using image processing are depicted. To detect the nature of the cavity at a different time over a period and re-entrant jet dynamics, the temporal-spatial distributions of gray level along the reference line in a period at $\sigma = 0.9,\ 1.75$ and VF $= 0.009$ are presented in Fig. 17. It is worth mentioning that the gray scale is in the range of 0 to 256 where the lowest and highest values illustrate the black and white pixels, respectively. Furthermore, the temporal-spatial distribution is carried out along the reference line x, as declared in Fig. 16. The reference line is started from the leading edge $(x/L = 0)$ and ended at a further distance from the trailing edge $(x/L = 1)$ to ensure catching the whole cavity region. Hence, the reference line is defined close to the surface of the hydrofoil to properly detect the re-entrant jet. The horizontal and vertical axes represent the non-dimensional time and location where τ and L are the period and length of the reference line. Three lines which are ordered from 1 to 3 represent the specific moments that correspond to the right-hand images which are tried to be selected in a way to show different modes of cavitation from generation to collapse. In the case with a higher cavitation number, the cavitation is started and ended with a sheet cavity. On the other hand, although the cavitation is started by a sheet cavity, it is ended with a detached cloud cavity at a lower cavitation number. Moreover, it is observed that the cavity region consists of a vaporous cavity region near the leading edge which is followed by the cloud cavity which is not homogeneous. As briefly discussed in the numerical section, the sheet cavity can be homogeneous with a dense vaporous medium; however, the tailed cloud cavity is more likely to contain scattered vapor bubbles. In addition, it is confirmed that no points or lines can be specified for the inception point of cavitation when no external factors such as roughness exist; however, it happens in a range of a region very close to the leading edge. In the case with a higher cavitation number, the re-entrant jet is not obviously near the surface of the hydrofoil. On the contrary, the re-entrant area is fully captured by the temporal-spatial distribution. It is declared that the re-entrant jet mostly contains water.

To have a comprehensive overview of the periodic characteristics of cavitating flow, cavity length, and spatial analysis of the re-entrant jet, the temporal-spatial distribution of gray level of experimental visualization of cavitating flow during three selected cycles at $\sigma = 0.9,\ 1.75$ and VF $= 0.009$, 0.013, are presented in Fig. 18. By adding the dissolved air, the cavity is remarkably elongated, which is more obvious in the case with a higher cavitation number. Moreover, the region where the cavity is detached, collapsed and shed downstream is significantly limited in the cases with a higher cavitation number compared to the elongated cloud cavity, which is longer than the hydrofoil chord, at a lower cavitation number. Besides, the cavity closure becomes continuous which makes it challenging to find the border between two interval cycles and the corresponding period τ. Furthermore, the spatial analysis of the re-entrant jet declares that the effective re-entrant jet is penetrated toward the leading edge more in the case with lower dissolved air. The reason for the latest observation is a larger sheet cavity, generated by adding dissolved air. It is worth mentioning that the front of the re-entrant jet usually collides with the sheet cavity and bans. Then, the generated re-circulation intensifies the detaching process.

The utilized visualization system is equipped with the trigger which makes it possible to match the captured frames with other measured unsteady parameters such as pressure and vibration. Using this technique one can make a relationship between the structure of the cavity and other characteristics. In this respect, one specific cycle is selected and the flow structure is matched with the pressure fluctuation in P7 in the corresponding moment. Fig. 19 presents the results for $\sigma = 0.9$ and VF $= 0.009$, 0.013. It is observed that there is a reverse relationship between the pressure level and volume of the cavity. Also, a similar observation is captured in both levels of dissolved air. The lowest value of local pressure occurs when the cavity is elongated since the pressure inside the cavity is considerably lower than the surrounding pressure. Also, it is declared that the flow structures in the middle of the half-cycle are not identical, denoting that the generation and collapsing processes have a different nature; however, the cycle is symmetric.

5. Conclusion

In the present work, it is tried to develop a numerical model which is compatible with the effect of dissolved anon-condensable gas. For this purpose, the Zwart-Gerber-Belamri cavitation model is modified based on the merging theory. Based on this theory, the pressure inside the vapor bubble is influenced by the surrounding dissolved air bubbles which are diffused inside. As a result, the pressure of inception is no longer equal to saturation vapor pressure, but it varies as a function of the local air volume fraction. On the other hand, the operating fluids (i.e. water, vapor and air) are assumed as compressible helping for better estimation of mixture density in case of high-pressure difference. The Density Corrected-Based Model (DCM) is employed to avoid the overestimation of turbulent viscosity usually calculated by the standard turbulence model. The experimental measurements and observations are obtained and used to validate the results. The following results can be illustrated:

- The shedding frequency is corrected and in good agreement with the experimental data.
- Adding dissolved air followed by stabilizing the cavitating flow which is concluded by lower shedding frequency.
- Employing the modified cavitation model leads to larger cavitation which is well-matched with the experimental observations.
- The difference in the cavity structure results in changing of force components such as lift and drag coefficients.
- Regardless of cavitation number and level of air content, the shedding frequencies extracted by the force coefficient are fairly similar to each other and slightly higher than those corresponding to the cavity evolution.
- Comparing the pressure-based and vibration-based PSD analyses, it is concluded that some first modes are identical, and the number of modes depends on the case, and the rest are due to other sources.
- A close agreement between the shedding frequencies based on the cavity evolution is detected by comparing the experimental and numerical data.
- Based on the temporal-spatial distribution of the gray level, it is concluded that the re-entrant jet is more observable and influential in the case with a larger cavity.
- Adding the dissolved air pushes back the front of the re-entrant jet toward the trailing edge.

Funding and conflicts of interests

The presented work was supported by the Polish National Science Centre funds within the project UMO-2016/21/B/ST8/01164 and the Silesian University of Technology in the form of a publication grant. Also, the authors certify that they have NO conflict of interest.

Declaration of Competing Interest

None.

CRediT authorship contribution statement

Emad Hasani Malekshah: Conceptualization, Methodology, Software, Investigation, Validation, Formal analysis, Data curation, Writing – original draft, Writing – review & editing. **Włodzimierz Wróblewski:** Conceptualization, Investigation, Writing – review & editing, Supervision.

Data Availability

The authors do not have permission to share data.

References

[1] R.E. Arndt, Cavitation in fluid machinery and hydraulic structures, Annu. Rev. Fluid Mech. 13 (1) (1981) 273–326.
[2] B. Ji, et al., Numerical simulation of cavitation surge and vortical flows in a diffuser with swirling flow, J. Mech. Sci. Technol. 30 (6) (2016) 2507–2514.
[3] E. Hasani Malekshah, W. Wróblewski, K. Bochon, M. Majkut, Evaluation of modified turbulent viscosity on shedding dynamic of three-phase cloud cavitation around hydrofoil–numerical/experimental analysis, Int. J. Numer. Methods Heat Fluid Flow (2022) Ahead-of-print, doi:10.1108/HFF-03-2022-0188.
[4] G. Chen, G. Wang, C. Hu, B. Huang, Y. Gao, M. Zhang, Combined experimental and computational investigation of cavitation evolution and excited pressure fluctuation in a convergent-divergent channel, Int. J. Multiph Flow 72 (2015) 133–140.
[5] R.T. Knapp, Recent investigations of the mechanics of cavitation and cavitation damage, Trans. ASME 77 (1955) 1045–1054.
[6] H. Ganesh, S.A. Mäkiharju, S.L. Ceccio, Bubbly shock propagation as a mechanism for sheet-to-cloud transition of partial cavities, J. Fluid Mech. 802 (2016) 37–78.
[7] C. Yuan, J. Song, L. Zhu, M. Liu, Numerical investigation on cavitating jet inside a poppet valve with special emphasis on cavitation-vortex interaction, Int. J. Heat Mass Transf. 141 (2019) 1009–1024.
[8] M. Sedlar, B. Ji, T. Kratky, T. Rebok, R. Huzlík, Numerical and experimental investigation of three-dimensional cavitating flow around the straight NACA2412 hydrofoil, Ocean Eng. 123 (2016) 357–382.
[9] G. Reisman, Y.C. Wang, C.E. Brennen, Observations of shock waves in cloud cavitation, J. Fluid Mech. 355 (1998) 255–283.
[10] Q. Le, J.P. Franc, and J.M. Michel, Partial cavities: global behavior and mean pressure distribution, 1993.
[11] M. Callenaere, J.P. Franc, J.M. Michel, M. Riondet, The cavitation instability induced by the development of a re-entrant jet, J. Fluid Mech. 444 (2001) 223–256.
[12] B. Ji, X. Luo, R.E. Arndt, Y. Wu, Numerical simulation of three-dimensional cavitation shedding dynamics with special emphasis on cavitation–vortex interaction, Ocean Eng. 87 (2014) 64–77.
[13] B. Ji, X. Luo, R.E. Arndt, X. Peng, Y. Wu, Large-eddy simulation and theoretical investigations of the transient cavitating vortical flow structure around a NACA66 hydrofoil, Int. J. Multiph. Flow 68 (2015) 121–134.
[14] A. Kolahan, E. Roohi, M.R. Pendar, Wavelet analysis and frequency spectrum of cloud cavitation around a sphere, Ocean Eng. 182 (2019) 235–247.
[15] E. Ghahramani, H. Ström, R. Bensow, Numerical simulation and analysis of multi-scale cavitating flows, J. Fluid Mech. 922 (2021).
[16] A. Peters, O. El Moctar, Numerical assessment of cavitation-induced erosion using a multi-scale Euler–Lagrange method, J. Fluid Mech. 894 (2020).
[17] O. Coutier-Delgosha, Numerical simulation of the unsteady behaviour of cavitating flows, Int. J. Numer. Methods Fluids 42 (5) (2003).
[18] E. Goncalves, R.F. Patella, Numerical simulation of cavitating flows with homogeneous models, Comput. Fluids 38 (9) (2009) 1682–1696.
[19] R.F. Kunz, et al., A preconditioned Navier–Stokes method for two-phase flows with application to cavitation prediction, Comput. Fluids 29 (8) (2000) 849–875.
[20] G.H. Schnerr, J. Sauer, Physical and numerical modeling of unsteady cavitation dynamics, in: Proceedings of the *4th International Conference on Multiphase Flow*, New Orleans, ICMF, 2001 vol. 1.
[21] P.J. Zwart, A.G. Gerber, T. Belamri, A two-phase flow model for predicting cavitation dynamics, in: Proceedings of the *5th international conference on multiphase flow*, 152, Yokohama, Japan, 2004.
[22] A.K. Singhal, M.M. Athavale, H. Li, Y. Jiang, Mathematical basis and validation of the full cavitation model, J. Fluids Eng. 124 (3) (2002) 617–624.
[23] S. Gopalan, J. Katz, Flow structure and modeling issues in the closure region of attached cavitation, Phys. Fluids 12 (4) (2000) 895–911.
[24] K. Laberteaux, S. Ceccio, Partial cavity flows. Part 1. Cavities forming on models without spanwise variation, J. Fluid Mech. 431 (2001) 1–41.
[25] H. Cheng, X. Long, B. Ji, X. Peng, M. Farhat, A new Euler-Lagrangian cavitation model for tip-vortex cavitation with the effect of non-condensable gas, Int. J. Multiph. Flow 134 (2021) 103441.
[26] O. Coutier-Delgosha, R. Fortes-Patella, J.L. Reboud, Evaluation of the turbulence model influence on the numerical simulations of unsteady cavitation, J. Fluids Eng. 125 (1) (2003) 38–45.
[27] H. Biao, W. Guo-Yu, Evaluation of a filter-based model for computations of cavitating flows, Chin. Phys. Lett. 28 (2) (2011) 026401.
[28] A. Yu, B. Ji, R. Huang, Y. Zhang, Y. Zhang, X. Luo, Cavitation shedding dynamics around a hydrofoil simulated using a filter-based density corrected model, Sci. China Technol. Sci. 58 (5) (2015) 864–869.
[29] G. Wang, B. Zhang, B. Huang, and M. Zhang, Unsteady dynamics of cloud cavitating flows around a hydrofoil, 2009.
[30] J. Holl, An effect of air content on the occurrence of cavitation, 1960.
[31] R. Taghavi, Cavitation Inception in Axisymmetric Turbulent Jets, University of Minnesota, 1985.
[32] R.E. Arndt, R. Taghavi, Cavitation in various types of shear flow, in: Water For Resource Development, ASCE, 1984, pp. 417–421.
[33] M.G. Mithun, P. Koukouvinis, I.K. Karathanassis, M. Gavaises, Numerical simulation of three-phase flow in an external gear pump using immersed boundary approach, Appl. Math. Model. 72 (2019) 682–699.
[34] E.S. Vasilakis, N. Kyriazis, P. Koukouvinis, M. Farhat, M. Gavaises, Cavitation induction by projectile impacting on a water jet, Int. J. Multiph. Flow 114 (2019) 128–139.
[35] C.P. Egerer, S. Hickel, S.J. Schmidt, N.A. Adams, Large-eddy simulation of turbulent cavitating flow in a micro channel, Phys. Fluids 26 (8) (2014) 085102.
[36] W. Wróblewski, K. Bochon, M. Majkut, E.H. Malekshah, K. Rusin, M. Strozik, An experimental/numerical assessment over the influence of the dissolved air on the instantaneous characteristics/shedding frequency of cavitating flow, Ocean Eng. 240 (2021) 109960.
[37] W. Wróblewski, K. Bochon, M. Majkut, K. Rusin, E.H. Malekshah, Numerical study of cavitating flow over hydrofoil in the presence of air, Int. J. Numer. Methods Heat Fluid Flow (2021).
[38] A.T.J. Hayward, Compressibility equations for liquids: a comparative study, Br. J. Appl. Phys. 18 (7) (1967) 965.
[39] M. Ivings, D. Causon, E. Toro, On Riemann solvers for compressible liquids, Int. J. Numer. Methods Fluids 28 (3) (1998) 395–418.
[40] V. Yakhot, S. Orszag, S. Thangam, T. Gatski, C. Speziale, Development of turbulence models for shear flows by a double expansion technique, Phys. Fluids A 4 (7) (1992) 1510–1520.
[41] C.E. Brennen, Cavitation and Bubble Dynamics, Cambridge University Press, 2014.
[42] A. Kubota, H. Kato, H. Yamaguchi, A new modelling of cavitating flows: a numerical study of unsteady cavitation on a hydrofoil section, J. Fluid Mech. 240 (1992) 59–96.
[43] J. Hinze, Turbulence, McGraw-Hill Publishing Co, New York, 1975 ed.
[44] E. Giannadakis, M. Gavaises, C. Arcoumanis, Modelling of cavitation in diesel injector nozzles, J. Fluid Mech. 616 (2008) 153–193.
[45] C.E. Brennen and C.E. Brennen, Fundamentals of multiphase flow, 2005.
[46] M. Tinguely, D. Obreschkow, P. Kobel, N. Dorsaz, A. De Bosset, M. Farhat, Energy partition at the collapse of spherical cavitation bubbles, Phys. Rev. E 86 (4) (2012) 046315.
[47] H. Matsunari, S. Watanabe, Y. Konishi, N. Suefuji, A. Furukawa, Experimental/numerical study on cavitating flow around Clark Y 11.7% hydrofoil, in: Proceedings of the 8th International Symposium on Cavitation, 2012, pp. 358–363.

Paper VIII:

Experimental analysis on dynamic/morphological quality of cavitation induced by different air injection rates and sites

Physics of Fluids ARTICLE scitation.org/journal/phf

Experimental analysis on dynamic/morphological quality of cavitation induced by different air injection rates and sites

Cite as: Phys. Fluids **35**, 013335 (2023); doi: 10.1063/5.0136521
Submitted: 26 November 2022 · Accepted: 28 December 2022 · Published Online: 23 January 2023

View Online Export Citation CrossMark

Emad H. Malekshah, Włodzimierz Wróblewski,[a)] Krzysztof Bochon, and Mirosław Majkut

AFFILIATIONS

Department of Power Engineering and Turbomachinery, Silesian University of Technology, 44-100 Gliwice, Poland

Note: This paper is part of the special topic, Cavitation.

[a)]**Author to whom correspondence should be addressed:** wlodzimierz.wroblewski@polsl.pl

ABSTRACT

Ventilated cavitating flow features resulting from the air injection at the hydrofoil surface are characterized based on experimental investigation. The experiments have been conducted in the cavitation tunnel at the Silesian University of Technology. The main focus of this work is to investigate how both the location of the injection hole at the surface of the hydrofoil (so-called injection site) and the injection rate have an impact on the cavitating flow in various flow conditions (i.e., different cavitation numbers). The Clark Y hydrofoil is fixed at an 8° angle of attack. In addition, three cavitation numbers, $\sigma = 1.1$, 1.25, and 1.6; five air injection rates, Q = 0, 0.25, 0.5, 0.75, and 1 l/min; and two injection sites at the surface of hydrofoil (Tap1-injection and Tap5-injection) are selected for the case studies. Furthermore, the level of dissolved air in water is kept constant at 11.7 mg/l. The unsteady measurements and high-speed imagining declare that, regardless of the injection rate, the injection site has a significant effect on the cavitation dynamic features and morphology. Moreover, it is shown that the effectiveness of air injection depends on the flow conditions.

I. INTRODUCTION

Cavitation is a well-known physical phenomenon due to its presence in various applications dealing with fluid flow. It occurs when the local pressure falls below the saturation vapor pressure and causes many problems such as noise and vibration,[1] erosion,[2,3] and changing the turbomachines' function.[4] Usually, the cavitation phenomenon is known for its negative effect on the proper functioning of hydraulic systems; however, in some particular cases, it leads to a positive effect. Air injection, which is a controlling approach to cavitation, has several technical advantages including erosion mitigation and drag reduction. In that sense, analyzing the ventilated cavitation dynamics around the hydrofoil leads to a better understanding of the physics behind this phenomenon.

The dynamics of the cavitating flow, including sheet and cloud cavities, has been widely investigated in the case of hydrofoil,[5–8] which shows the complexity of this phenomenon. The dynamical characteristics of the cavitating flow may be affected by various parameters, such as cavitation number,[9] quality of operating fluid,[10] and geometry.[11] The influence of each of these parameters needs to be investigated in an individual case study, which may be difficult to interpret, due to the interaction between them. For instance, Hasani Malekshah *et al.*[12] proved that the shedding frequency is reduced by about 21% and 38% at the cavitation numbers of 2.02 and 2.14, respectively, when the level of dissolved air content increases. The cavity first develops from the leading edge and then, from the trailing edge, a re-entrant jet arises, moves upstream on the wall, and finally cuts the developing vapor phase. As a result, the cloud cavity detaches and sheds downstream. It was first suggested by Furness and Hutton[13] that the principal reason for forming cloud cavitation is the re-entrant jet. This theory was confirmed by Le *et al.*,[14] Kubota *et al.*,[15] and Kawanami *et al.*[16] However, another theory introduced by Avellan *et al.*[17] noted that the principal mechanism generating the cloud cavitation is the laminar to turbulent transition within the boundary layer and instability growth on the surface of the cavity. Depart from the reason of cloud cavity generation, the behavior of cloud cavitation is inherently quite more aggressive than sheet cavitation, and it is capable of causing significant damage to solid surfaces. This is because when bubbles collapse, there are waves with incredibly high pressure. A controlling approach may lead to eliminating or reducing an unstable, destructive, and noisy regime. Air injection, which can be known as a controlling approach, has been widely studied for drag reduction and erosion mitigation purposes. Mäkiharju *et al.*[18] investigated how the gas layer that forms beneath a barge's surface reduces skin friction drag. They used a variety of injection orifice sizes, injection angles, and injection rates to inject gas. Through calculations and experiments, they examined the shape of the air pocket at different freestream velocities. Sanders *et al.*[19] quantified the skin friction reduction in a turbulent boundary layer of a flat plate caused by air injection using shear-stress measurements. They noticed that the skin frictional drag coefficient significantly reduces as the bubble number density increased close to the flat plate's surface. In another work, a remarkable reduction of the skin friction drag over a non-gradient pressure, laminar boundary layer on a flat plate is reported by Elbing *et al.*[20] when they increased the injection velocity to the square of the upstream velocity. Madavan *et al.*[21] experimentally proved a marked drag reduction over the tunnel wall during air bubble injection through 0.5 μm diameter holes into the water stream. The mitigation of cavitation erosion has been reported by Arndt *et al.*[22] They used instantaneous pressure measurement on the hydrofoil surface, hydrophone, and vibration measurements on the test section to show the impact of air injection on the cavitation. Not only does the air injection affect the drag and erosion reductions, but other dynamical characteristics, including shedding frequency, inception point, cavity length, etc., may be a matter of change. The experiments conducted by Wang *et al.*[23] demonstrated the changes in the shedding frequency of cloud cavitation around NACA hydrofoil as a result of water injection. Furthermore, Zhang *et al.*[24,25] used unsteady pressure measurement and high-speed visualization techniques and showed the important role of air injection in the significant reduction of the pressure peak around the hydrofoil and shedding frequency. In order to investigate the effects of bubble injection on cavitation in the presence of water and aviation jet fuel, Dunn *et al.*[26] conducted a series of experiments and injected a measured quantity of bubbles within a transparent Venturi nozzle. If a gas injection is to occur or not, they discovered that the location of cavitation inception may be spatially altered. Dong and Su[27] performed an experimental analysis of aeration-controlled cavitation. An analysis of the pressure waveforms both with and without aeration was done. The findings showed that the aeration process elevates the pressure level inside the cavitation zone considerably, and the associated pressure waves reflect a shock wave.

In the present study, the effects of air injection from the surface of the hydrofoil on cavitating flow are characterized experimentally. The working fluid is water with constant inlet velocity ($v_{\text{in}} = 10.4$ m/s), and the dissolved air level is kept constant (11.7 mg/l). This work aims to evaluate the dynamic features and morphology of the cavity of the cavitation depending on the air injection site on the suction surface of the hydrofoil (Tap1-injection and Tap5-injection), the air injection rate (Q = 0, 0.25, 0.5, 0.75, and 1 l/min), and cavitation number ($\sigma = 1.1$, 1.25, and 1.6).

II. EXPERIMENTAL SETUP

The experiments were conducted using hydraulic installation built and mounted at the laboratory of the Department of Power Engineering and Turbomachinery, The Silesian University of Technology. The schematic of the installation along with the main components is illustrated in Fig. 1. A replaceable test section (component no. 1) is a component of the closed-loop installation. Water serves as the circuit's working fluid, and a pump (component no. 2) powered by a 30 kW electric motor (component no. 11) propels it through the 200 mm pipes. This pump provides constant water flow in the circuit. A manual valve (component no. 3) is installed to control the water flow in an urgent situation as well as the electromagnetic flowmeter (component no. 4) to measure continuously the flow rate. To provide a uniform water flow inside the test chamber, a honeycomb (component no. 5) and a cross section inverter (component no. 6) are employed. Using these components, we can have a uniform flow at the chamber inlet. Then, the straightened water flow passes the test chamber which is equipped with ClarkY 11.7% hydrofoil. It is worth mentioning that the test chamber and studied object, which is the hydrofoil in this work, are replaceable. Then, the cross section is changed from rectangular to circular using a shaped diffuser. Afterward, the water flows back to the tank (component no. 7). The volume of the tank is 1.5 m^3 to preserve the required amount of water for the experiment. In addition, the tank is responsible for adjusting the pressure level inside the closed-loop circuit which is done using an elastic airbag (component no.8) mounted within the tank. With inflation and deflation of the airbag, the pressure level can be adjusted. Using this technique, the closed-loop circuit is operated with the same water flow and arbitrary pressure level. To monitor the temperature of the working fluid, a Pt100 thermocouple is installed inside the tank. In order to reduce vibrations caused by the operation of a high-power pump and cavitation, three elastic compensators (component no. 9), one before the tank, one after the pump and one between the tank, and the pump were inserted. To control the circuit, measurement, and visualization purposes, the monitoring unit (component no. 10) is used.

The test chamber is designed as horizontal with a rectangular cross section in which the hydrofoil is mounted. Three sides of the chamber, including the front, top and bottom, were made of polycarbonate which is transparent and enables cavitation observations. The backside of the chamber is made of metal and the hydrofoil and vibration sensors are mounted on it. Also, both the internal wall of the backside and the hydrofoil are painted with black color to reduce the light reflections and provide clear optical observation. The Clark Y hydrofoil's chord is $c = 70$ mm. Furthermore, the distance from the inlet to the hydrofoil leading edge is 3.2c where the length of the test chamber (i.e., the distance of the inlet to the outlet) is 10c. The chamber dimensions are large enough to observe the downstream shedding and are similar to the chambers reported in the literature. The height and width of the test chamber are fixed at 2.7c and 1c, respectively. As a result, the ratio of height to chord is fixed to 2.7, which is high enough to assume the confinement effect as minor on the performance of hydrodynamic cavitation. However, this ratio is taken even smaller, equal to 2.13 and 2.0 in the research carried out by Pernod *et al.*[28] and Watanabe *et al.*,[29] respectively. Furthermore, the hydrofoil's angle of attack is changeable; however, in the present case, it is fixed to 8°.

The effect of dissolved air on the dynamics and structure of the cavitation was investigated by Malekshah and Wróblewski.[30,31] The results declared that the configuration and unsteady characteristics of the cavitation are affected by the level of dissolved air in the working fluid. In that sense, it is necessary to inform about the level of dissolved air in the experiments. The experimental tests are conducted with one controlled level of dissolved oxygen which is equal to 4.6 mg/l. Based on Henry's law, it corresponds to the air content of 11.7 mg/l in

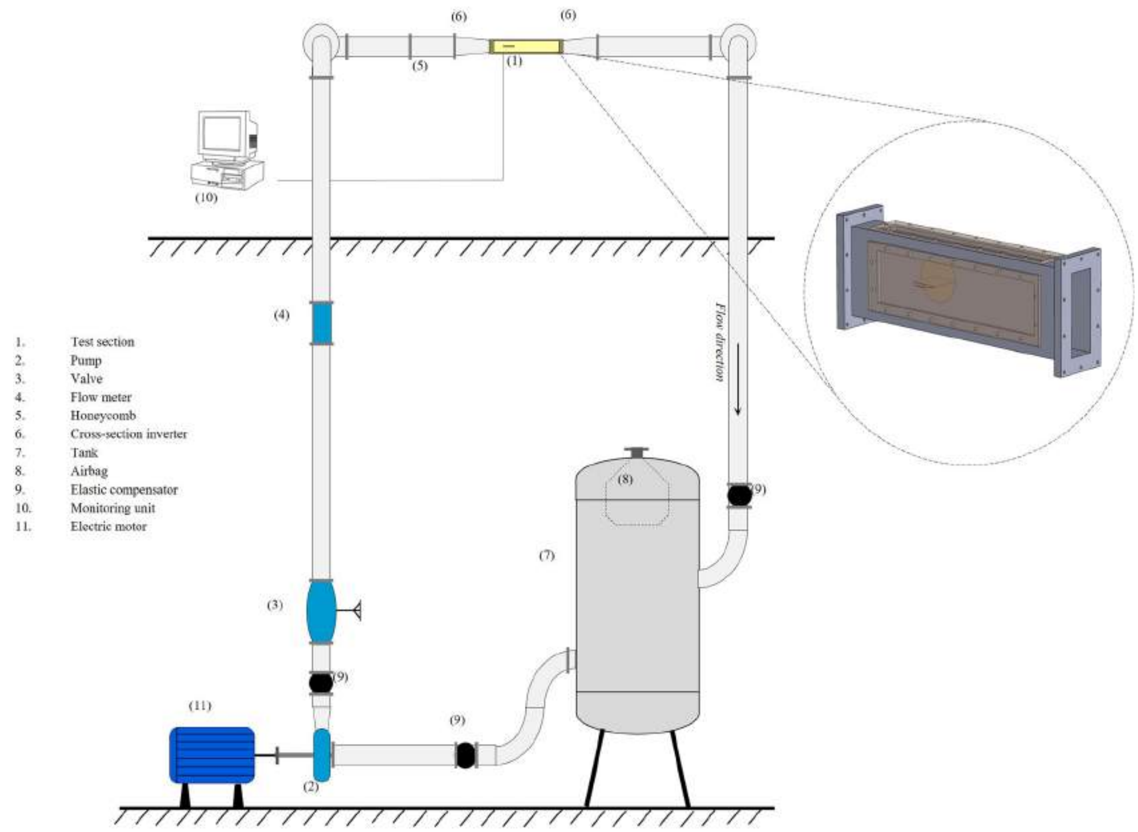

FIG. 1. Schematic of test rig along with the main components.

ambient pressure. The multifunction meter CF-401 is used to monitor the dissolved air level. This device can measure the dissolved air in liquid; as a result; the non-dissolved air bubbles were not taken into account. The measurements are carried out before and after each experimental campaign, and the average value is reported. In addition, the accumulated air within the tank due to the air injection is deployed after each experiment using exhaust valve installed at the top of the tank. Also, enough time internal, which is about 3–4 min, is given to make the quasi-steady state condition before starting new round of the experiment.

The schematic figure of the test chamber along with the hydrofoil, measuring, and visualization systems are presented in Fig. 2. The measuring unit consists of high- and low-frequency pressure sensors, pressure regulator, fast/ABS pressure transducers, vibration sensors, data acquisition, and computer. In addition, the visualization unit consists of a high-speed camera, MultiLED lighters, and a computer. The surface of the hydrofoil includes 10 holes, which are connected to the root of the fixing disk via internal channels created inside the hydrofoil. Then, these channels are followed by the impulse tubes and connected to the pressure transducers. Using these holes, channels, and tubes, the unsteady pressure at the surface of the hydrofoil is monitored. In addition, two other pressure sensors are installed at the inlet and outlet. Among the pressure sensors, two fast pressure sensors are employed to control the unsteady pressure at the tap P_8 and the outlet (P_{outlet}) and the remaining sensors are low-frequency ones. The models of high-frequency and low-frequency sensors are XP5 type with amplifier type ARD154 and APLISENS PC-28, respectively. The accuracy of the fast-frequency pressure sensor is 0.25% in 500 kPa full-scale. Moreover, the accuracy of the low-frequency sensor is 0.16% in 160 kPa full-scale. The temperature of the working fluid is monitored using resistance thermocouple type APLISENS CT-GN1 Pt100. The accuracy of the thermocouple in full-scale 0–100 °C is $\pm(0.15\,\mathrm{K} + 0.002|T|)$. The model of the employed electromagnetic flowmeter is UniEMP-05 DN200, which is capable to measure the flow rate up to 1080 m^3/h with an accuracy of $\pm$0.25%. Two piezoelectric accelerometers are mounted on the backside of the test chamber. These accelerometers measure the vibration caused by the cavitating flow. The accelerometers are connected with the 0028 (RFT) type charge amplifier connected with the fast analogue-to-digital converter AC 16 bit, 250 kS/s. The system is calibrated before the experiments using the electrodynamic vibration calibrator EET101 (RFT) type. The maximum error of this type of accelerometer is less than 5%.

The measurement system was set based on the National Instruments module NI USB 6216. Furthermore, the pressure measuring cluster cooperates with the NI/PXI-6255 module. The data acquisition process and the executive elements are controlled using a LabView program. The high-speed video camera Phantom Miro C110 with a recording speed of 3200 f/s and spatial resolution of 960 $\times$ 280 pixels,

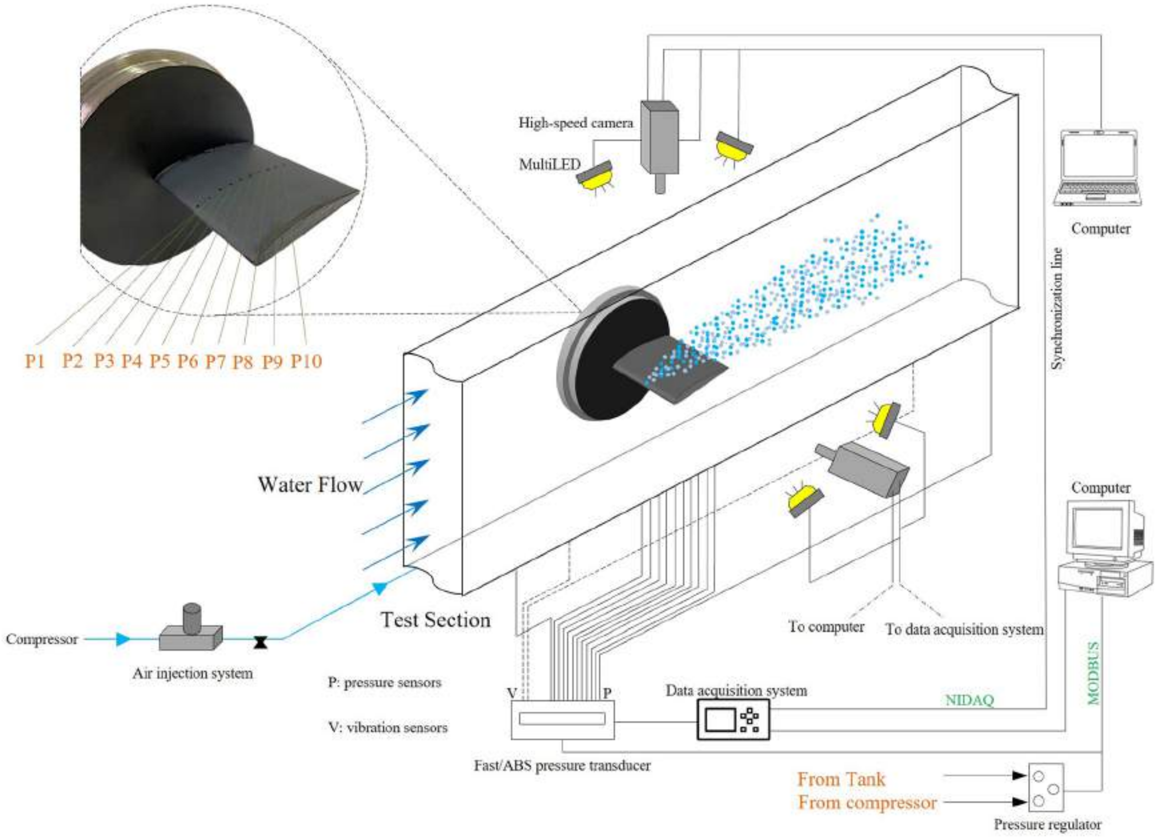

FIG. 2. Schematic of experimental setup including measuring and visualization systems.

is used. The interested zone is lightened using the MULTILED L48-XF. For the air injection, Brooks Model SLA5850S Mass Flow Controller is used with accuracy up to 1200 lpm: $\pm 1.0\%$ of rate (20%–100% FS).

In the majority of investigations, a data reduction equation (DRE) is used to integrate the measured values of several variables to get the intended result. One of the most important parameters of the experimental facility is uncertainty, which needs to be considered in the evaluation process. It is determined based on the definition of the cavitation number. The cavitation number, which describes the flow condition, is defined as follows:

$$\sigma = \frac{p_{in} - p_v}{\frac{1}{2}\rho {v_{in}}^2}, \tag{1}$$

where p_{in}, p_v, ρ, and v_{in} define the inlet pressure, vapor pressure, density, and flow velocity at the test chamber inlet, respectively.

In addition, the inlet velocity is calculated as follows:

$$v_{\mathrm{in}} = \frac{Q}{A} = \frac{Q}{h.w}, \tag{2}$$

where Q, A, h, and w show the volume flow rate, cross section area, height, and width of the test chamber, respectively.

Based on the approach introduced by Coleman and Steele,[32] the uncertainty of the flow velocity can be easily calculated as follows:

$$U_{v_{\mathrm{in}}}{}^2 = \left(\frac{\partial v_{\mathrm{in}}}{\partial Q}\right)^2 U_Q^2 + \left(\frac{\partial v_{\mathrm{in}}}{\partial h}\right)^2 U_h^2 + \left(\frac{\partial v_{\mathrm{in}}}{\partial w}\right)^2 U_w^2. \tag{3}$$

Then, the relative uncertainty of flow velocity is calculated as follows:

$$\left(\frac{U_{v_{\mathrm{in}}}}{v_{\mathrm{in}}}\right)^2 = \left(\frac{U_Q}{Q}\right)^2 + \left(\frac{U_h}{h}\right)^2 + \left(\frac{U_w}{w}\right)^2. \tag{4}$$

Furthermore, the uncertainty of the cavitation number is calculated as follows:

$$U_\sigma{}^2 = \left(\frac{\partial \sigma}{\partial P_{\mathrm{in}}}\right)^2 U_{P_{\mathrm{in}}}^2 + \left(\frac{\partial \sigma}{\partial P_v}\right)^2 U_{P_v}^2 + \left(\frac{\partial \sigma}{\partial \rho}\right)^2 U_\rho^2 + \left(\frac{\partial \sigma}{\partial v_{\mathrm{in}}}\right)^2 U_{v_{\mathrm{in}}}^2. \tag{5}$$

The relative uncertainty is calculated as follows:

$$\frac{U_\sigma}{\sigma} = \sqrt{\begin{aligned} &\left(\frac{P_{\mathrm{in}}}{P_{\mathrm{in}} - P_v}\right)^2 \left(\frac{U_{P_{\mathrm{in}}}}{P_{\mathrm{in}}}\right)^2 + \left(\frac{P_v}{P_{\mathrm{in}} - P_v}\right)^2 \left(\frac{U_{P_v}}{P_v}\right)^2 \\ &+ \left(\frac{U_\rho}{\rho}\right)^2 + 4\left(\frac{U_{v_{\mathrm{in}}}}{v_{\mathrm{in}}}\right)^2. \end{aligned}} \tag{6}$$

Based on the experimental condition during the present sets of the experiment, the relative uncertainties of inlet pressure, vapor saturation pressure, density, and mean inlet velocity are 0.0016, 0.0117, 4×10^{-5}, and 0.0026, respectively. Then, the impact of each physical

TABLE I. The influence of every single parameter on the uncertainty of $\boldsymbol{\sigma}$.

X_i	Range of X_i	$U(X_i)/X_i$	Maximum contribution to $(U_\sigma/\sigma)^2$
P_{in}	60–90 kPa	0.0016	2.7×10^{-6}
P_v	2.728 kPa	0.0117	1.3×10^{-7}
ρ	997.65 kg m^{-3}	4×10^{-5}	8×10^{-10}
ν	10.4 m s^{-1}	0.0026	2.7×10^{-5}
Total	...	...	2.9×10^{-5}

value on the uncertainty of the cavitation number (σ) can be given in Table I. Therefore, the uncertainty U_σ/σ of cavitation number amounts to 0.54%.

III. DESCRIPTION OF PROBLEM

The present research is a part of an investigation which aims to analyze the effect of the presence of air on cavitation. In contrast to the previous studies that investigated the impact of the dissolved air, it focuses on ventilated cavitation. Despite the air injection being considered, the experiments have been conducted on a controlled level of dissolved air. Although many efforts have already been taken on studying ventilated cavitation, the purpose of the present investigation is to assess how the air injection site (i.e., air injector location) on the surface of a hydrofoil and air injection rate affects the cavitation structure. This is done at different cavitation numbers to understand how the possible effects may be varied.

As explained priorly, ten holes at the surface of the hydrofoil distributed at the mid-span may be used to measure the pressure or to inject air. To study the injection site effect, the air is injected from the first or fifth hole, called Tap1-injection and Tap5-injection, respectively. The injection rates are at controlled levels of Q = 0, 0.25, 0.5, 0.75, and 1 l/min. In addition, all of these test cases are conducted in three cavitation numbers of $\sigma = 1.1$, 1.25, and 1.6.

From a scientific point of view, the paper is organized to first determine which injection site is more efficient in controlling the cavitation's non-morphological features, and second, to deeper understand the efficient case.

A schematic of cavitating flow with air injection from the fifth hole (i.e., Tap5-Injection) is presented in Fig. 3. The schematic is to show the general nature of the ventilated cavitation but not a specific case, to depict details of this phenomenon. In the non-cavitation case, the bubbly mixture of air and water gets advected downstream from where the air is injected toward the direction of the stream in the cloudy puff state. Increasing the cavitation number leads to emerging of cavitating flow from cavitation sites at the leading edge. Depending on the cavitation number, the cavitating flow may cover the air jet in the lower cavitation number. When the cavitating flow approaches the air jet, it is pushed aside resulting in forming a gap, which is shown by red arrows. By moving further downstream, the cavitating flow and air cloud merge and form a uniform cloud. Moreover, the air jet spreads downstream with an angle depending on the stream velocity, although it is not the case study in the present work. The injected air jet can be categorized into three types based on its shape: 1. Bubbly Puff which consists of numerous small bubbles; 2. cloud cavity, a two-phase flow

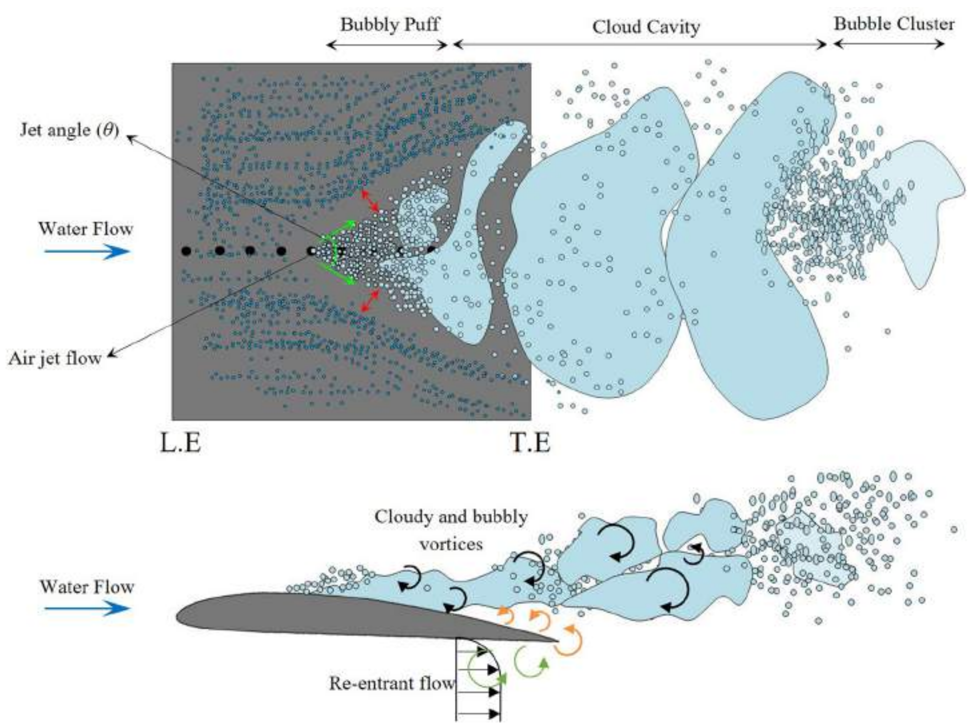

FIG. 3. Schematic of air injection through the cavitating flow from top-view (above) and side-view (bottom).

composed of vapor bubbles, air bubbles, vapor-air bubbles, and water; and 3. bubble cluster resulted from collapsed cloud cavity. The ventilated cavitating flow contains strong vortices throughout the domain causing highly turbulent and chaotic flow. One of the main parameters leading to detaching the cloud cavity from the surface of the hydrofoil is the adverse pressure gradient due to the re-entrant jet. The re-entrant jet is initiated close to the trailing edge at the pressure side and flows along the suction side toward the leading edge.

IV. RESULTS AND DISCUSSION

The ventilated cavitating flow around a hydrofoil is characterized experimentally. The experiments are conducted in a water tunnel considering the effect of the air injection site (i.e., location of the injector) on the surface of the hydrofoil (Tap1-injection and Tap5-injection), the air injection rate (Q = 0, 0.25, 0.5, 0.75, and 1 l/min), and cavitation number ($\sigma = 1.1$, 1.25, and 1.6). The working fluid is water, and the amount of dissolved air is constant (11.7 mg/l) during all experimental campaigns. The unsteady characteristics study and morphological analysis have been performed to understand the physics of this phenomenon.

A. Averaging of pressure coefficient

The risk of cavitation is high in the turbomachines in conjunction with the strong dynamic pressure, which depends on flow velocity. Due to the effect of cavitation on the pressure distributions formed around the hydrofoil and depending on its nature and intensity, it may either change the lifting capabilities of the hydrofoils. In this regard, analyzing the averaged pressure distribution is an approach to finding out the capability of hydrofoil under different cavitating flow conditions. To improve the reliability of the experimental data, all of the test cases were repeated three times. It is not expected to provide similar runs due to marginal experimental errors, however, it is important to have close results in each round of tests. The distribution of averaged pressure coefficient around the hydrofoil along with the error bars as a function of cavitation number and injection rate for both injection sites are presented in Fig. 4. The pressure coefficient is defined as follows:

$$C_p = \frac{p - p_\infty}{\frac{1}{2}\rho {v_{in}}^2}, \tag{7}$$

where p, p_∞, ρ, and v_{in} define the local pressure, ambient pressure, density, and flow velocity at the test chamber inlet, respectively.

The results of averaging declare that the maximum difference between the upper and lower value of pressure in one point is 9.6%. By this, the reliability of averaged values is verified.

B. Air injection rate effect on pressure coefficient

To study the impact of air injection rate on the pressure on the surface of hydrofoil, the distributions of pressure coefficient on three injection rates (Q = 0 l/min non-injected, 0.5 l/min medium, and 1 l/min maximum) and two cavitation numbers are presented in Fig. 4. Overall, the results declare a significant effect of air injection rate on the pressure coefficient. In all cases, the changes over the sheet cavity (i.e., the part before the sudden drop of pressure coefficient) are more sensitive than other parts. Moreover, the reduction of the pressure coefficient at the first hole is almost the same when the cavitation number is changed. As such, in this sense, the changes in pressure affected by air injection are independent of the cavitation number. By increasing the air injection rate, the sheet cavity is elongated, which can be concluded from a long flat area of the pressure coefficient distribution. The latest observation proves that air injection leads to less

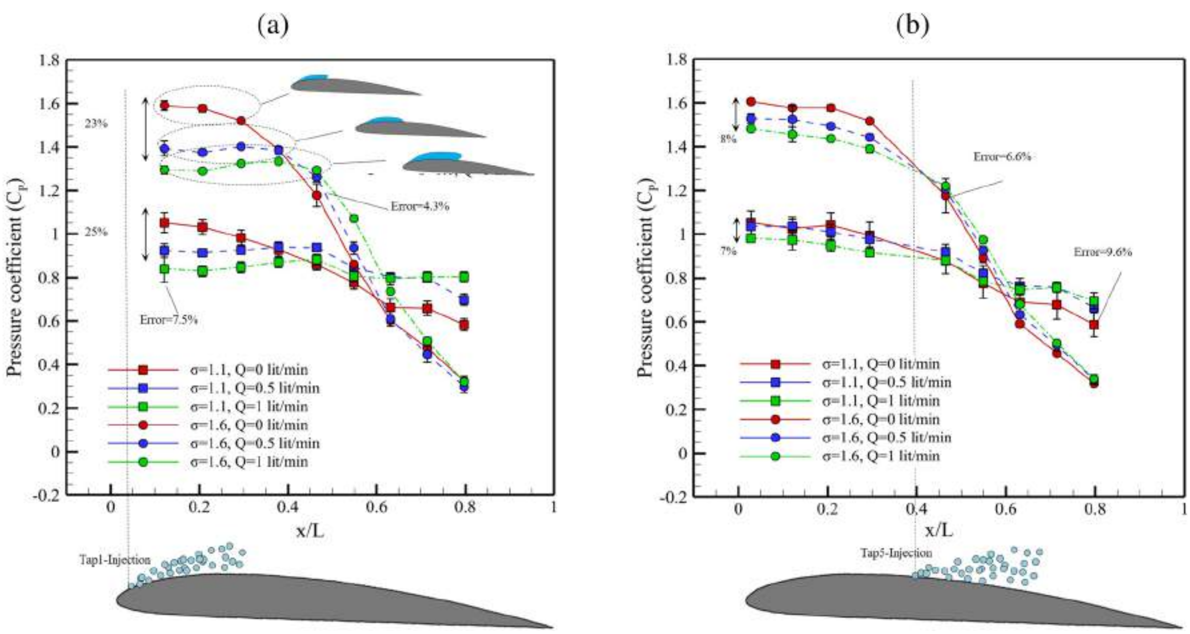

FIG. 4. Averaging of pressure coefficient and effect of air injection rate at various cavitation numbers, air injection rates, and sites: (a) Tap1-injection and (b) Tap5-injection.

chaotic cavitating flow since the sheet cavity always is characterized by less shedding frequency and destructive features and a more uniform structure.

C. Air injection site effect on pressure coefficient

The effect of the air injection site on the distribution of pressure coefficient for different injection sites (Tap1-injection and Tap5-injection) and cavitation numbers ($\sigma = 1.25$ and 1.6), is shown in Fig. 5. The red and blue highlights represent the margin between Tap1-injection and Tap5-injection with non-injection case, respectively. In the sheet cavity region (i.e., the region where the pressure coefficient is almost flat), it is observed that the reduction of the pressure coefficient almost doubled when the air is injected from Tap1. It is because air is directly injected into the sheet cavity earlier spatially when the Tap1 is operating. In addition, the profiles declare that when Tap5 is operating, the pressure coefficient drops in the upstream region, where no air is injected. The pressure coefficient drop at the upstream region may be resulted from changing the velocity field due to the air jet. On the other hand, the results demonstrate that the Tap1-injection is more effective even outside of the sheet cavity. For both cavitation numbers, it is observed that the red highlight, which is a margin between Tap1-injection and non-injection case, is remarkably bigger. As such, it can be concluded that Tap1-injection is more effective in sense of changing the pressure distribution around the hydrofoil.

D. Air injection effect on shedding frequency

The shedding frequency is one of the essential parameters which needs to be analyzed in the cavitation phenomenon since it plays an important role in some physical disadvantageous such as vibrations and noise due to periodic bubbles collapse and vortex shedding induced forces. The shedding frequencies vs injection rate for different cavitation numbers and injection sites are shown in Fig. 6. The shedding frequency is calculated based on the fast Fourier transform (FFT) analysis of pressure fluctuation at Tap8. The results show that the

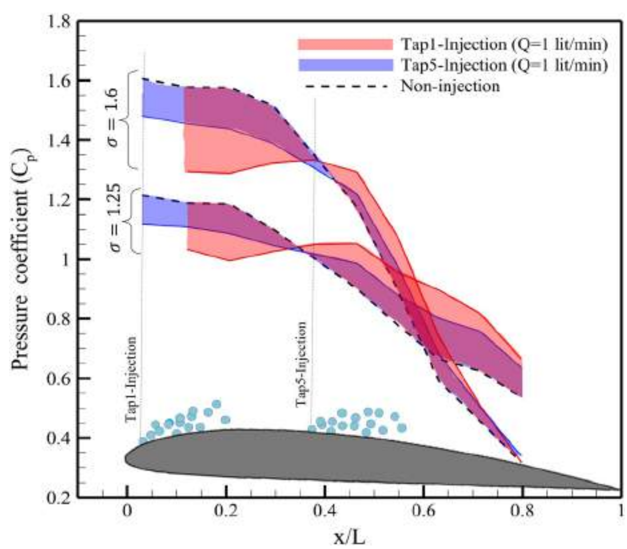

FIG. 5. Effect of air injection site on the distribution of pressure coefficient.

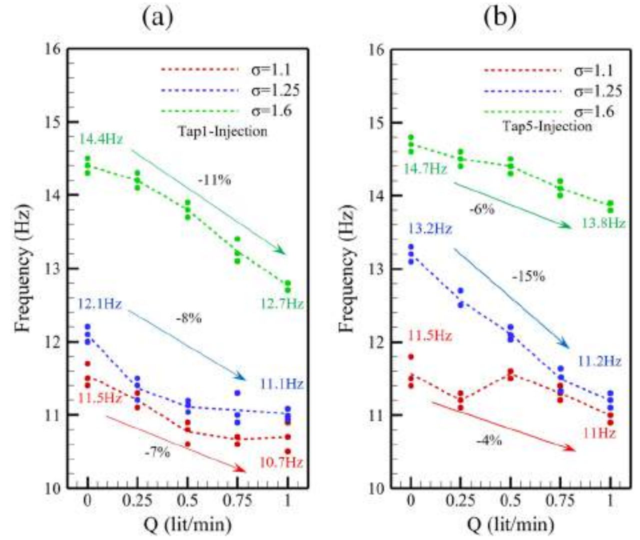

FIG. 6. Shedding frequency vs air injection rate as a function of cavitation number: (a) Tap1-injection and (b) Tap5-injection.

shedding frequency reduces when the air injection rate increases. As such, it means that the ventilated cavitation is less fluctuating than the pure vapor cavitation. On the other hand, for higher cavitation numbers, the air injection leads to a stronger reduction of shedding frequency. It is due to strong cavitation in low cavitation numbers which covers the air jet. Comparing the effect of the injection site on the shedding frequency, it is noticed that the shedding frequency tends to reduce more in Tap1-injection except in $\sigma = 1.25$ case.

E. Air injection effect on vibrations

Vibrations usually appear during the cavitating flow which results from the induced periodic force imposed on the object. Due to this fact, finding approaches to reduce the vibration is desirable. The vibration of the test chamber and the corresponding power spectra density (PSD) for different injection sites and rates at $\sigma = 1.1$ are presented in Fig. 7. It is revealed that the main frequency of vibration changes slightly. However, the frequency of cases with Tap1-injection tends to be reduced when the injection rate increases. Despite slight changes in the main frequency, the amplitude of the vibration decreases significantly. It is found that the amplitude of vibration for Tap1-injection and Tap5-injection cases drop 100% and 57%, respectively. The latest observation declares a promising outcome of air injection into a cavitating flow. On the other hand, it is proved that not only injection from Tap1 is more effective in the reduction of vibration frequency, but also almost double vibration mitigation is recorded compared to Tap5-injection.

Comparing the pressure coefficient distribution, shedding frequency and vibration of the cases with Tap1-injection and Tap5-injection, it is proved that the injection from Tap1 is more effective in sense of making a bigger difference in the studied characteristics. As a result, it can be concluded that the more effective injection site is the one which is closer to the inception point. In Secs. IV F–I, the

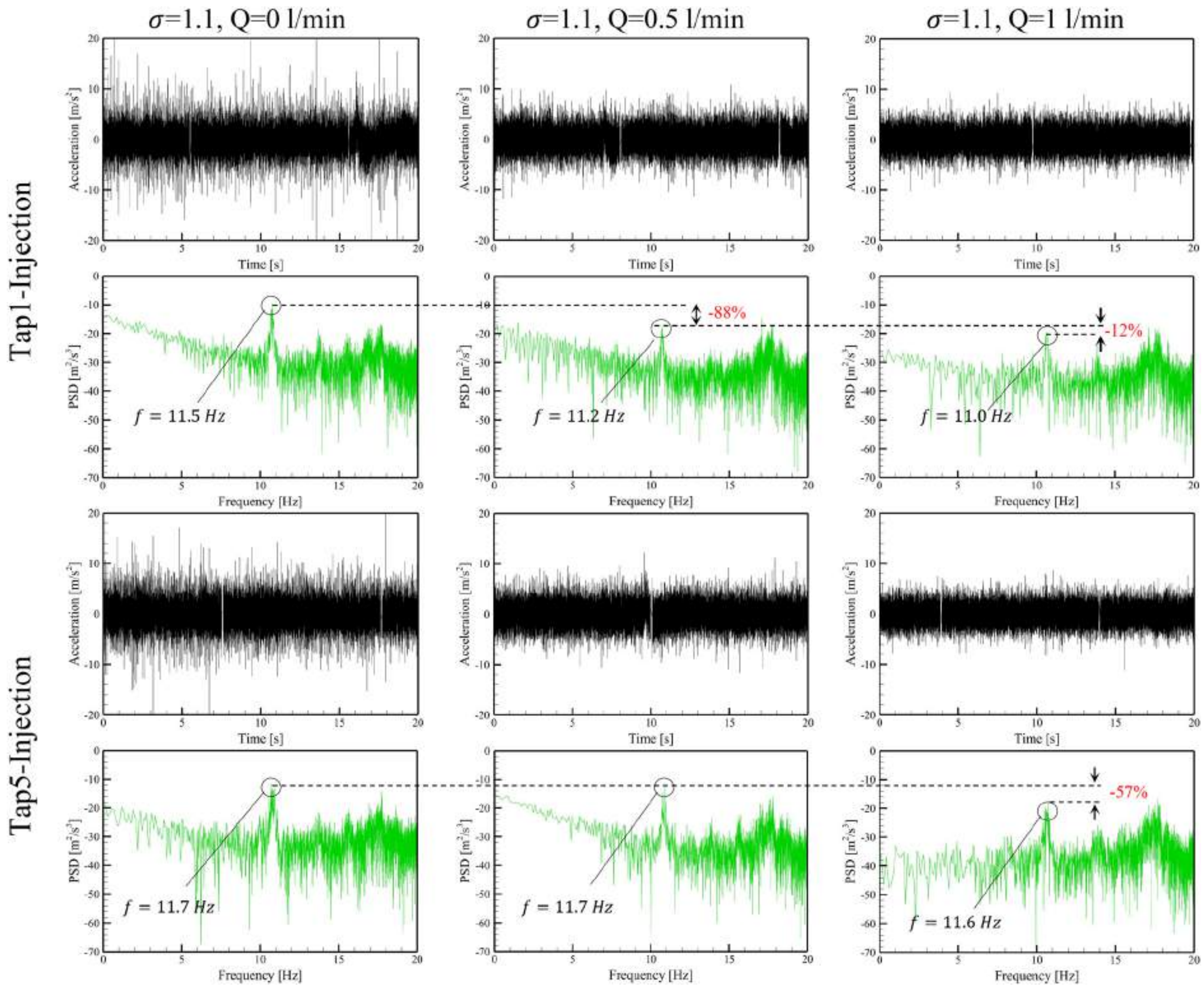

FIG. 7. Power Spectral Density (PSD) of vibration at various air injection rates and sites.

morphological features of the ventilated cavitation for the cases with Tap1-injection will be analyzed and discussed.

F. Flow visualization

The cavitating flow visualization is carried out using a high-speed camera. This technique makes it possible to track the cavity evolution from inception to detaching and shedding. In this respect, the cavity evolution of the Tap1-injection case is visualized during a period for different cavitation numbers and injection rates, as shown in Fig. 8. Basically, a period starts from emerging a sheet cavity at the leading edge where the local pressure drops below the saturation pressure. The sheet cavity grows gradually in time. Usually, the sheet cavity grows up to $^{3}/_{4}$ or full chord depending on the cavitation number. Then, the sheet cavity starts to detach from the surface of the hydrofoil due to the re-entrant jet and an upward buoyant force. Upon detaching the cavity, a cloud of bubbles forms the so-called cloud cavity. Usually, the cloud cavity is significantly larger and contains strong vortices. The visualization results demonstrate that the larger cavity appears in the case of a higher cavitation number which was also observed inside the Venturi nozzle by Malekshah *et al.*[33] Although the cavity shrinks in the last steps of a period in the non-injection case, the air injection causes continuous cavitation during a period. It is observed that the cavity is extended and existed during a period when the air is injected.

G. Morphological effect of air injection

The mean value of the gray level, as shown in Fig. 9, is calculated based on five periods of cavity evolution for cavitation numbers $\sigma = 1.1$, 1.25, and 1.6 and injection rates Q = 0, 0.25, 0.5, and 0.75 1 l/min. The mean cavitation plots show the general shape of cavitation with dynamic features eliminated. It is shown that the cavity enlarges with decreasing the cavitation number. This is also observed in the cavity evolution visualization. Similarly, the cavity is expanded when the air is injected. In other words, the size of the cavity has a direct relation with the air injection rate. Not only the cavity is

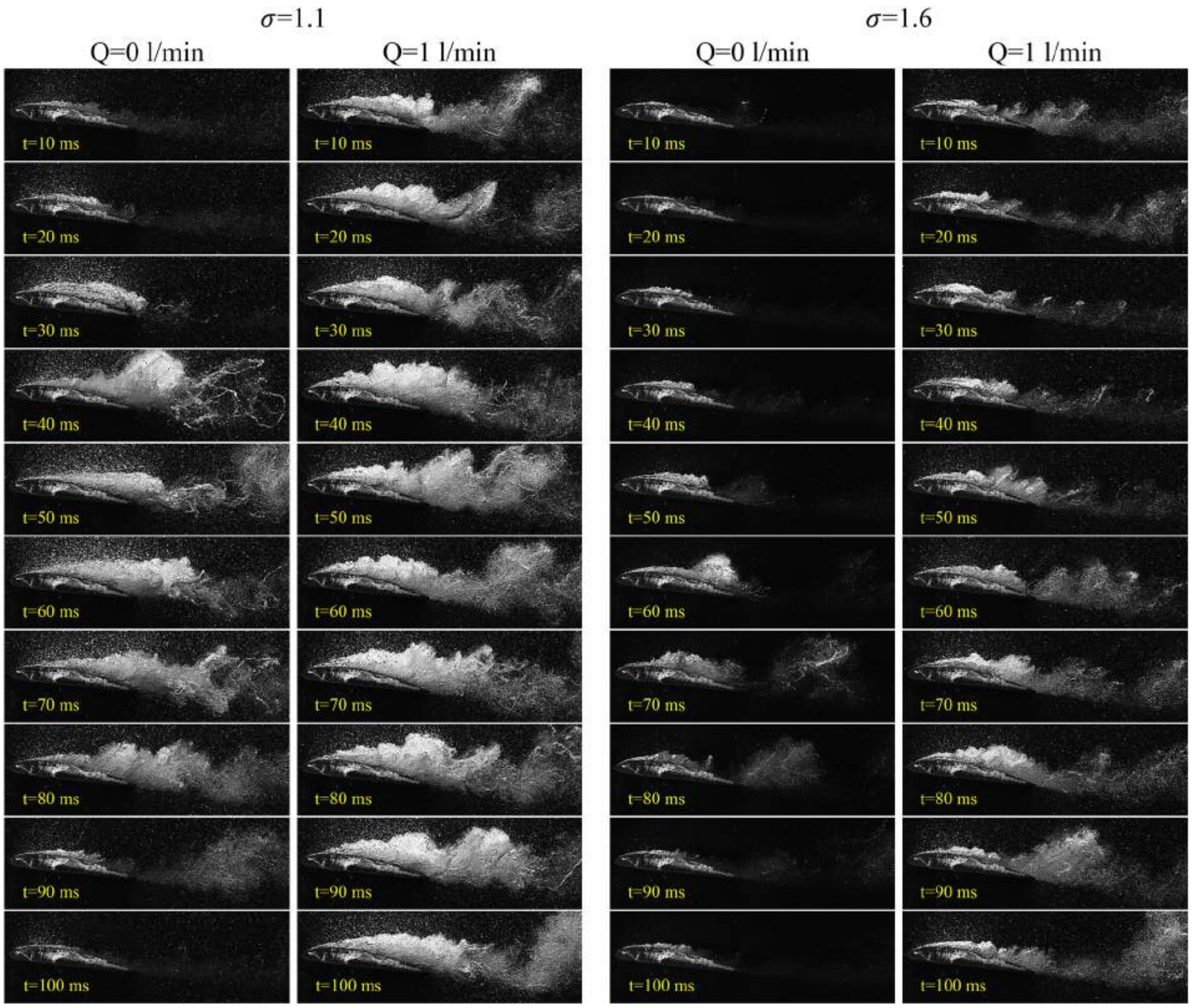

FIG. 8. Cavity evolution in one period at various cavitation numbers and air injection rates (Tap1-injection).

expanded as a result of air injection, but the intensity of the cloud cavity also rises which is exposed by brighter cavity regions in the cases with higher injection rates. Also, to provide the schematic boundary of cavity the gray scale value of 180 is used; however, some modifications are applied to have smooth boundary.

H. Morphology of jet domain

Depending on the operating cavitation number σ and air injection rate Q, some possible configurations of the jet domain are observed such as invisible jet and unstable cloudy jet. High-speed imaging of the ventilated cavitating flow through Tap1 on the hydrofoil surface resulted in instantaneous flow patterns and the temporal-spatial gray level distribution is shown in Fig. 10. The gray level distribution is calculated on the reference line (x/l = 0.2). Obviously, the lower cavitation number results in stronger cavitation. For the lower cavitation numbers, $\sigma = 1.1$ and 1.25, the injection jet is not visible since the strong cavitation cloud covers the jet puff, as shown in the instantaneous flow pattern. However, for a higher cavitation number of $\sigma = 1.6$ where the cloud cavity is weaker, the triangular shape of the injection jet is easily observed. The gray level distribution represents the clearer appearance of the injection jet, which is highlighted with a blue box, for the higher cavitation number. The latest observation does not imply the higher effectiveness of the injection jet for a higher cavitation number, however, it demonstrates the effect of cavitation number on the configuration of the air jet. Regardless of the cavitation number and configuration of the jet domain, it is found that a gap is formed. It is observed in both instantaneous flow imaging and gray level which are highlighted with green arrow and green box, respectively. The air jet, which is shown by blue arrows, pushes back

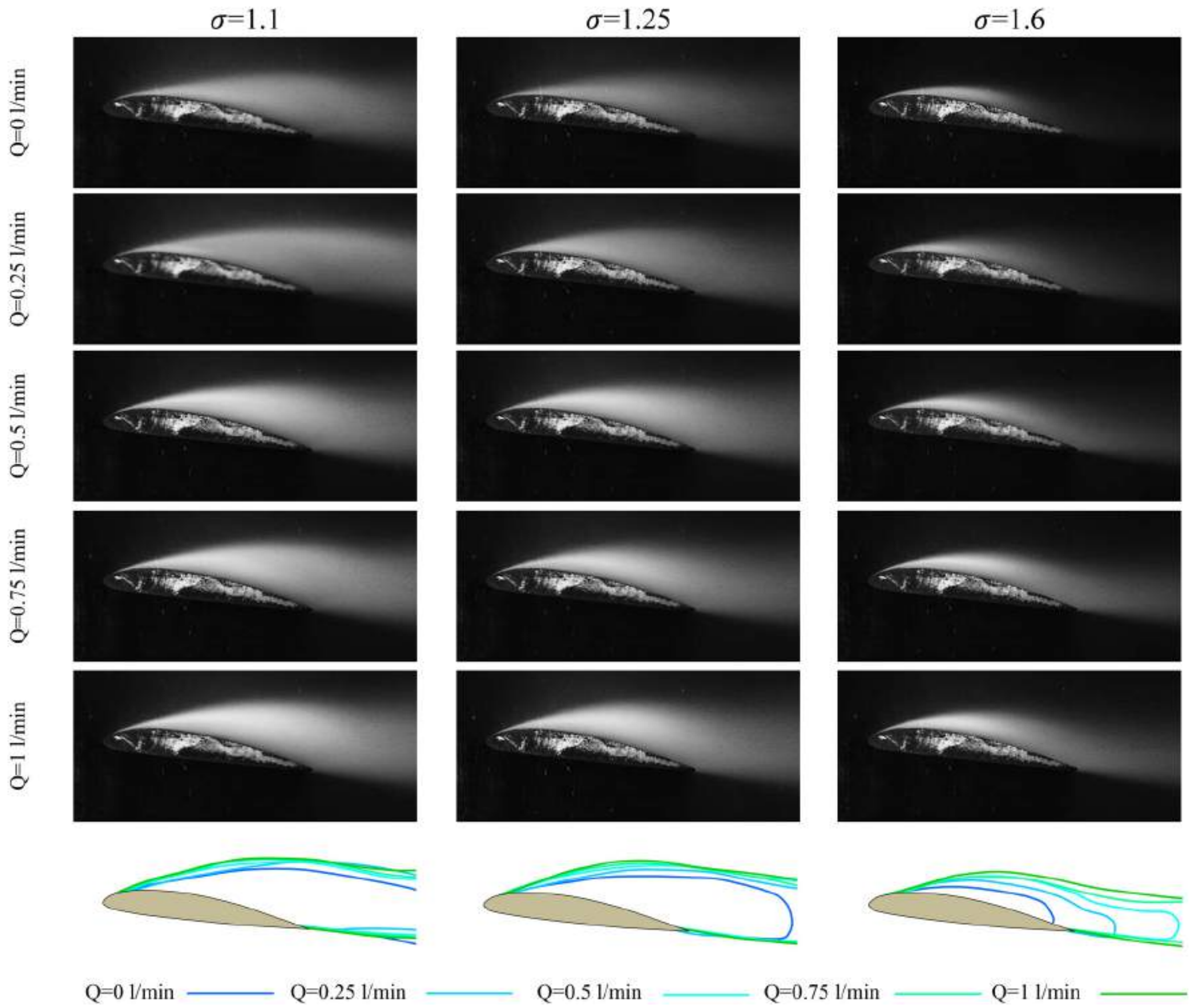

FIG. 9. Mean value of gray level (above) and schematic drawing of cavity borders at various cavitation numbers and air injection rates (Tap1-injection).

the cavitating flow shown by red arrows. As a result, a gap is created, which is shown by a green arrow, in all cases. It may be due to a significant momentum transfer by the air jet.

I. Temporal-spatial gray-level distributions

The temporal-spatial gray scale distributions at various cavitation numbers and air injection rate ventilated cavitating flow through the Tap1 hole are presented in Fig. 11. The gray level distribution is calculated along the reference line ($z = 0$). Using this technique is aimed to detect the global configuration of the cavity along the length of the test chamber under the impact of cavitation number and injection rate. The image processing of position-time diagram is discussed in previous research done by Xu *et al.*,[34] Jahangir *et al.*,[35] and Budich *et al.*[36]

A lower cavitation number leads to an elongated cavity. It is due to stronger cavitation for lower cavitation numbers. On the other hand, the periodicity of the cavitating flow is more obvious for higher cavitation numbers where the length of the cavity fluctuates strongly. However, in the case of lower cavitation numbers, the cavity covers the whole of the test chamber. The cavity significantly grows when the air is injected through the hole. Air injection results in continuity of the cavitation during the time. Not only the air injection led to almost temporally permanent cavitation, but also a spatially longer cavity region appeared.

V. CONCLUSION

An experimental investigation is conducted to study the cavitating flow with air injection from the surface of ClarkY 11.7% hydrofoil. These experiments aim to find the effect of air injection site (i.e., location of injection hole at the surface of hydrofoil), air injection rate ($Q = 0$, 0.25, 0.5, 0.75, and 1 l/min) on various cavitation numbers ($\sigma = 1.1$, 1.25, and 1.6). The dynamical and morphological effects of these parameters on the cavitation process are analyzed using unsteady measurements of pressure and vibration and high-speed imaging. The

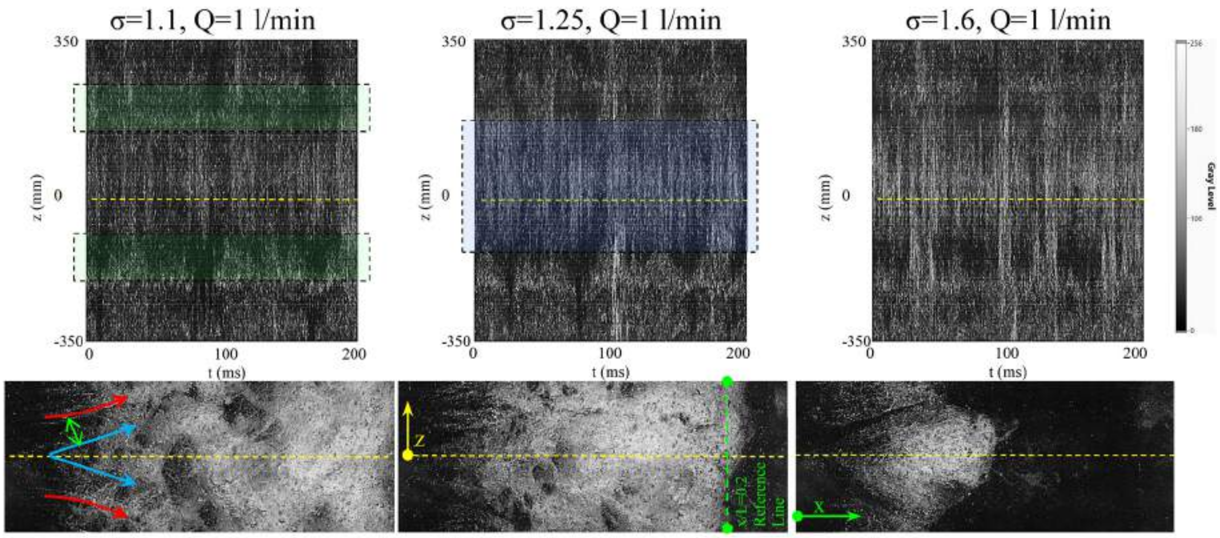

FIG. 10. Observation of air jet structure using instantaneous top-view snapshot and gray level distribution at various cavitation numbers and air injection rates (Tap1-injection).

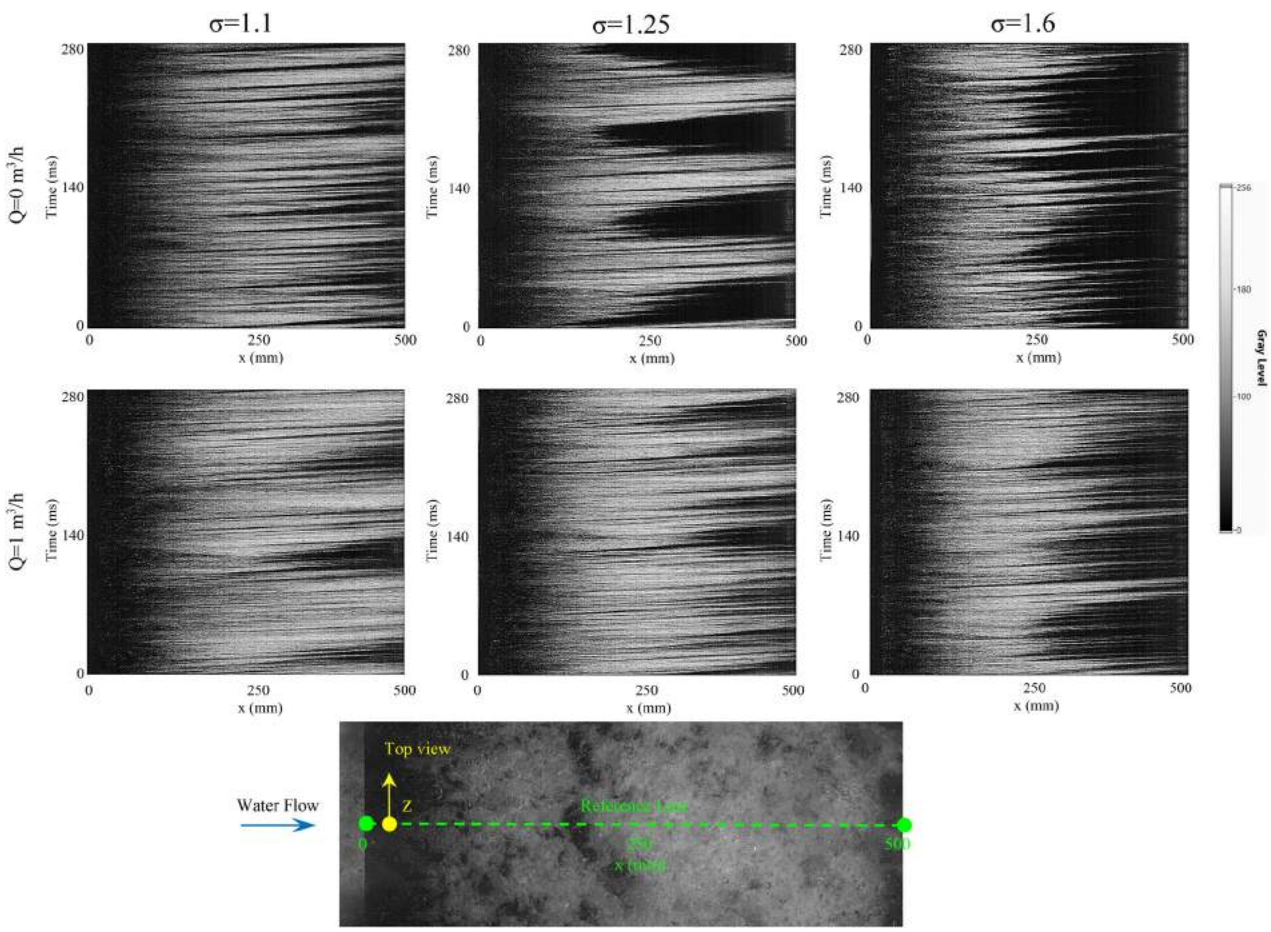

FIG. 11. Temporal-spatial gray level distributions at various cavitation numbers and air injection rates (Tap1-injection).

results showed that the pressure coefficient distribution changes in both sheet and cloud cavity regions as a consequence of air injection. Increasing air injection from 0 to 1 dm^3/min leads to pressure coefficient change in the range of 7%–23% depending on cavitation number. Moreover, changes in the pressure coefficient are significantly higher in the case of Tap1-injection. Furthermore, the shedding frequency reduces in the range of 4%–11% when the injection rate increases from 0 to 1 dm^3/min depending on the cavitation number and injection site. The vibration frequency of the test chamber is mitigated by 100% and 57% in cases of Tap1-injection and Tap5-injection, respectively. Overall, it is proved that the effectiveness of air injection on the cavitation characteristics remarkably depends on the air injection site. In addition, the effectiveness of air injection as a controlling approach also depends on flow conditions (i.e., cavitation number). Specifically, in the present case study, it is concluded that the Tap1-injection seems to be more efficient in the sense of a stronger difference in unsteady features; however, from a general point of view, injecting air from close to the inception point leads to a bigger difference on unsteady features of cavitation. The mean value of gray level demonstrates that the cavity is expanded with increasing air injection regardless of cavitation number. Hence, the triangular shape of the air jet is covered with a cloud cavity for low cavitation numbers; however, the injection effects on unsteady features are diminished.

ACKNOWLEDGMENTS

This project was supported by the Polish National Science Centre, Poland, funds within the Project No. UMO-2016/21/B/ST8/01164. Moreover, the project was additionally supported by the Department of Power Engineering and Turbomachinery, The Silesian University of Technology within the Grant No. BKM-586/RIE5/2022 (08/050/BKM_22/274).

AUTHOR DECLARATIONS

Conflict of Interest

The authors have no conflicts to disclose.

Author Contributions

Emad Hasani Malekshah: Conceptualization (equal); Data curation (equal); Formal analysis (equal); Investigation (equal); Methodology (equal); Software (equal); Validation (equal); Visualization (equal); Writing – original draft (equal). **Włodzimierz Wróblewski:** Conceptualization (equal); Formal analysis (equal); Investigation (equal); Project administration (equal); Resources (equal); Supervision (equal); Writing – original draft (equal). **Krzysztof Bochon:** Data curation (equal); Investigation (equal). **Mirosław Majkut:** Data curation (equal); Investigation (equal); Visualization (equal).

DATA AVAILABILITY

The data that support the findings of this study are available from the corresponding author upon reasonable request.

REFERENCES

[1]Y. Tsujimoto, K. Kamijo, and C. E. Brennen, "Unified treatment of flow instabilities of turbomachines," J. Propul. Power **17**(3), 636–643 (2001).
[2]R. Fortes Patella and J.-L. Reboud, "A new approach to evaluate the cavitation erosion power," J. Fluids Eng. **120**(2), 335–344 (1998).
[3]R. F. Patella, J.-L. Reboud, and A. Archer, "Cavitation damage measurement by 3D laser profilometry," Wear **246**(1–2), 59–67 (2000).
[4]B. Pouffary *et al.*, "Numerical simulation of 3D cavitating flows: Analysis of cavitation head drop in turbomachinery," J. Fluids Eng. **130**(6), 061301 (2008).
[5]M. Dular *et al.*, "Scale effect on unsteady cloud cavitation," Exp. Fluids **53**(5), 1233–1250 (2012).
[6]W. Wróblewski *et al.*, "Numerical study of cavitating flow over hydrofoil in the presence of air," Int. J. Numer. Methods Heat Fluid Flow **32**, 1440 (2022).
[7]W. Wróblewski *et al.*, "An experimental/numerical assessment over the influence of the dissolved air on the instantaneous characteristics/shedding frequency of cavitating flow," Ocean Eng. **240**, 109960 (2021).
[8]E. H. Malekshah *et al.*, "Evaluation of modified turbulent viscosity on shedding dynamic of three-phase cloud cavitation around hydrofoil–numerical/experimental analysis," Int. J. Numer. Methods Heat Fluid Flow **32**(12), 3863–3880 (2022).
[9]H. Soyama, "Luminescence intensity of vortex cavitation in a venturi tube changing with cavitation number," Ultrason. Sonochem. **71**, 105389 (2021).
[10]S. A. Mäkiharju, H. Ganesh, and S. L. Ceccio, "The dynamics of partial cavity formation, shedding and the influence of dissolved and injected non-condensable gas," J. Fluid Mech. **829**, 420–458 (2017).
[11]Y. Liu *et al.*, "Experimental investigation of the dynamic cavitation behavior and wall static pressure characteristics through convergence-divergence venturis with various divergence angles," Sci. Rep. **10**(1), 14172 (2020).
[12]E. Hasani Malekshah, W. Wróblewski, and M. Majkut, "Dissolved air effects on three-phase hydrodynamic cavitation in large scale Venturi—Experimental/numerical analysis," Ultrason. Sonochem. **90**, 106199 (2022).
[13]R. Furness and S. Hutton, "Experimental and theoretical studies of two-dimensional fixed-type cavities," J. Fluids Eng. **97**(4), 515–521 (1975).
[14]Q. Le, J.-P. Franc, and J.-M. Michel, "Partial cavities: Global behavior and mean pressure distribution," J. Fluids Eng. **115**(2), 243–248 (1993).
[15]A. Kubota *et al.*, Unsteady structure measurement of cloud cavitation on a foil section using conditional sampling technique. J. Fluids Eng. **111**(2), 204–210 (1989).
[16]Y. Kawanami *et al.*, "Mechanism and control of cloud cavitation," J. Fluids Eng. **119**(4), 788–794 (1997).
[17]F. Avellan, "Generation mechanism and dynamics of cavitation vortices down stream of a fixed leading edge cavity," *Proceedings of the 17th ONR Symposium on Naval Hydrodynamics, Netherlands* (TUDelft, 1988), p. 317.
[18]S. A. Mäkiharju *et al.*, "The topology of gas jets injected beneath a surface and subject to liquid cross-flow," J. Fluid Mech. **818**, 141–183 (2017).
[19]W. C. Sanders *et al.*, "Bubble friction drag reduction in a high-Reynolds-number flat-plate turbulent boundary layer," J. Fluid Mech. **552**, 353–380 (2006).
[20]B. R. Elbing *et al.*, "Bubble-induced skin-friction drag reduction and the abrupt transition to air-layer drag reduction," J. Fluid Mech. **612**, 201–236 (2008).
[21]N. Madavan, S. Deutsch, and C. Merkle, "Reduction of turbulent skin friction by microbubbles," Phys. Fluids **27**(2), 356–363 (1984).
[22]R. E. Arndt, C. Ellis, and S. Paul, "Preliminary investigation of the use of air injection to mitigate cavitation erosion," J. Fluids Eng. **117**(3), 498–504 (1995).
[23]W. Wang *et al.*, "Effect of water injection on the cavitation control: Experiments on a NACA66 (MOD) hydrofoil," Acta Mech. Sin. **36**(5), 999–1017 (2020).
[24]N. Zhang *et al.*, "Experimental study on the influence of air injection on unsteady cloud cavitating flow dynamics," Adv. Mech. Eng. **8**(11), 168781401667667 (2016).
[25]Y. Zhang *et al.*, *Fundamentals of Cavitation and Bubble Dynamics with Engineering Applications* (SAGE Publications, Sage, UK/London, England, 2017).
[26]P. F. Dunn *et al.*, "Experimental characterization of aviation-fuel cavitation," Phys. Fluids **22**(11), 117102 (2010).
[27]Z.-Y. Dong and P.-L. Su, "Cavitation control by aeration and its compressible characteristics," J. Hydrodyn. **18**(4), 499–504 (2006).
[28]L. Pernod *et al.*, "Experimental and numerical investigation of the fluid-structure interaction on a flexible composite hydrofoil under viscous flows," Ocean Eng. **194**, 106647 (2019).

[29] S. Watanabe, W. Yamaoka, and A. Furukawa, "Unsteady lift and drag characteristics of cavitating Clark Y-11.7% hydrofoil," in *IOP Conference Series: Earth and Environmental Science* (IOP Publishing, 2014).

[30] E. H. Malekshah and W. Wróblewski, "Effect of turbulence modelling and non-condensable gas on cloud cavity dynamics," Int. J. Heat Fluid Flow **98**, 109070 (2022).

[31] E. H. Malekshah and W. Wróblewski, "Merging theory-based cavitation model adaptable with non-condensable gas effects in prediction of compressible three-phase cavitating flow," Int. J. Heat Mass Transfer **196**, 123279 (2022).

[32] H. W. Coleman and W. G. Steele, *Experimentation, Validation, and Uncertainty Analysis for Engineers* (John Wiley & Sons, 2018).

[33] E. H. Malekshah *et al.*, "Experimental analysis on unsteady characteristics of sheet/cloud cavitating Venturi flow under the effect of dissolved air," Arch. Thermodyn. **43**, 63–84 (2022).

[34] S. Xu *et al.*, "Experimental study of the cavitation noise and vibration induced by the choked flow in a Venturi reactor," Ultrason. Sonochem. **67**, 105183 (2020).

[35] S. Jahangir, W. Hogendoorn, and C. Poelma, "Dynamics of partial cavitation in an axisymmetric converging-diverging nozzle," Int. J. Multiphase Flow **106**, 34–45 (2018).

[36] B. Budich, S. Schmidt, and N. A. Adams, "Numerical simulation and analysis of condensation shocks in cavitating flow," J. Fluid Mech. **838**, 759–813 (2018).

Paper IX:

Investigation on natural to ventilated cavitation considering the air-vapor interactions by Merging theory with insight on air jet location/rate effect

International Journal of Heat and Mass Transfer 220 (2024) 124968

Contents lists available at ScienceDirect

International Journal of Heat and Mass Transfer

journal homepage: www.elsevier.com/locate/ijhmt

Investigation on natural to ventilated cavitation considering the air-vapor interactions by Merging theory with insight on air jet location/rate effect

Emad Hasani Malekshah *, Włodzimierz Wróblewski, Mirosław Majkut

Department of Power Engineering and Turbomachinery, Silesian University of Technology, 44-100, Gliwice, Poland

A R T I C L E I N F O

Keywords:
Ventilated cavity
Three-phase cavitation
Dissolved air
Cavitation model
Merging theory

A B S T R A C T

Cavitation is of significant practical importance since unstable flow characteristics can have noticeable consequences on objects nearby. An essential approach for controlling the cavitation flow field's instability is air injection. This work aims to conduct a numerical and experimental investigation on the natural to ventilated cavitation around a Clark Y hydrofoil. Having three phases: water, vapor, and air, the cavitation model is adjusted based on the Merging theory to consider the impact of dissolved air on cavitation. Furthermore, the Density Corrected-based Method (DCM) is used to alter the turbulence model. The experimental tests are carried out in the water tunnel, which can maintain the constant water flow rate (Q_{water}=490 m^3/h) and regulate the pressure level (105–180 kPa). The Clark Y hydrofoil is fixed at an angle of attack of 8° and includes injection and pressure taps. Two holes, called Tap1-injection and Tap5-injection, are alternatively used for air injection purposes.

Two cavitation numbers (σ=1.1, 1.6) and three air injection rates ($Q = 0$, 0.5, 1 l/min) are considered current case studies. The results demonstrate the meaningful impact of location and rate of aeration on the dynamic/average characteristics of cavitation. Increasing the air injection rate results in an increase in the pressure coefficient values, a decrease in the shedding frequency, and an elongation of the cavity with an M-shaped structure. Also, during a cycle of cavity development, air injection may take place in the reversed jet, perpendicular jet, or direct jet configurations. In addition, a close agreement between numerical and experimental results is recorded.

1. Introduction

Cavities are formed when the local pressure falls below the saturated vapor pressure within a liquid. The term for this phenomenon is cavitation [1]. Cavitation flow, which includes phase transitions, unsteady characteristics, and turbulence, is a complicated multiscale cavity flow that occurs in a variety of fluidic devices, including water turbines, marine propellers, hydrofoils, and underwater vehicles [2,3]. In fluid machinery, cavitation can lead to significant challenges, such as significant reduction in efficiency, vibration, noise, and even erosion. Since cavitation is quite hard to eliminate, research on understanding this phenomenon is still ongoing. Therefore, looking to efficient strategies for better control cavitation remains a critical scientific problem. [4]. To effectively control the dynamics of cavitation, especially its unsteady flow characteristics, we must first gain a deep understanding of this phenomenon and then implement strategies and methods [5]. Knapp [6] identified and examined the mechanics of cavitation, pointing out that the cavity broke off when the re-entrant flow started to move toward it in a reverse direction than the main flow. Also, it should be noted that breaking off may be affected by other factors such as operating fluid quality and ventilation of non-condensable gas.

Cavitation can be controlled using passive or active flow control approaches. Whether additional energy is added or not distinguishes the two methods [7]. To control cavitating flow in the passive approach, hydrofoil surface characteristics are often changed. Che et al. [8] fitted a barrier on the trailing edge of a hydrofoil. The results showed that while it can suppress sheet cavity and prevent re-entrant jet, it has a modest effect on cavitation control under the transitional cavity oscillation state. Zhang et al. [9] placed obstacles on the hydrofoil to reduce cloud cavitation shedding and increase low pressure distribution. Kadivar et al. [10,11] used cylindrical cavitating-bubble generators (CCGs) on the hydrofoil suction side and declared that CCGs may efficiently suppress cavitation and reduce cavitation-induced vibration. The passive control method has many benefits, such as it does not require external energy and is simple to implement; however, in practice, the operating

* Corresponding author.
E-mail address: emad.hasani@polsl.pl (E. Hasani Malekshah).

https://doi.org/10.1016/j.ijheatmasstransfer.2023.124968
Received 26 June 2023; Received in revised form 4 November 2023; Accepted 14 November 2023

Nomenclature

u	time-averaged mixture velocity (m.s^{-1})
P	time-averaged pressure (Pa)
g	gravity acceleration (m.s^{-2})
R	source term
k	turbulent kinetic energy (m^2.s^{-2})
ε	turbulent energy dissipation rate (m^2.s^{-3})
μ_t	dynamic turbulent viscosity (kg.m^{-1}.s^{-1})
G_k	production of turbulent energy term (kg.m^{-1}.s^{-2})
r_B	radius of a sphere-shaped bubble (m)
S	surface tension (Pa)
p	local fluid pressure (Pa)
p_B	pressure of mixture bubble (Pa)
p_{G0}	partial pressure of reference bubble (Pa)
r_0	reference radius (m)
ρ	density (kg.m^{-3})
μ	viscosity (Pa.s)
α	volume fraction
μ_t	turbulent viscosity
γ	heat capacity ratio

Subscripts

v	vapor
l	liquid
ng	non-condensable gas
nuc	nucleation
vap	vaporization
$cond$	condensation
e	evaporation
c	condensation

conditions of hydraulic machinery do not always remain the same [12], making it challenging for passive methods to perform precise adjustment while the operating conditions of hydraulic machinery change [13].

Active control approaches are different from passive control approaches, which typically involve injecting water or gas into the flow field. Injecting a non-condensable gas through the cavity will alter the pressure level when cavitation is growing, considering that it decreases the cavitation collapse rate, increases the least volume of the cavity, and drastically increases the cavity's void ratio [14]. According to Maltsev et al. [15], the active approach efficiently prevents the flow separation of hydrofoils with a high angle of attack. De Giorgie et al. [16] used a single synthetic jet actuator in the NACA0015 hydrofoil resulted in a certain level of cloud cavitation control. Using an air injection experiment, Arndt et al. [17] discovered that air injection would be efficient in reducing cavitation erosion. Reisman et al. [18] examined the effects of pulsed and continuous air injection on oscillating foil under sheet-cloud cavitation conditions. They concluded that air injection could minimize cavitation noise, while pulsed air injection, with a similar volumetric flow rate, could decrease cavitation noise significantly more than continuous air injection. When Pham et al. [19] investigated the mechanisms of unstable sheet cavitation and cloud cavitation; they observed that the cavitation flow is blocked over a specific range of ventilation-gas flow rates. Using the wedge model, Mäkiharju et al. [20] investigated how non-condensable gasses impact the growth of cloud cavitation and revealed that gas injection suppresses cavitation and periodic oscillations. To understand how gas entrainment and the Froude number impact the structure of cavitation flow, Liu et al. [21] evaluated the four most stable states of ventilated cavitation. To model both ventilated cavitation and natural cavitation, Ji and Luo [22] introduced a three-element cavitation model derived from Reynolds-averaged Navier-Stokes (RANS) equations. They showed that as the gas injection rate is increased, the expansion of the vapor cavity is noticeably reduced. Unstable ventilated cavitation around a NACA66 hydrofoil was investigated by Sun et al. [23]. They showed that ventilated cloud cavity sheds at a rate that is quicker than natural cavitation and that ventilation causes powerful, large-scale, pulsing eddy flows to spin into smaller-scale eddies. Malekshah et al. [24] conducted an experimental study on the impact of air injection through the hydrofoil surface on cavitating flow. Water is used as operating fluid, and the amount of dissolved air is maintained at a constant level (11.7 mg/l) with a steady inflow velocity of 10.4 m/s. This study aims to assess the dynamic characteristics and morphological characteristics of the cavity in relation to the air injection locations on the suction surface of the hydrofoil, the air injection rates, and the cavitation number.

Water usually includes a certain amount of dissolvable gas, which is difficult to remove. Cavitation phenomena typically initiate from nuclei, which are small gas or vapor bubbles or particles present in the liquid. These nuclei can preexist in the liquid or form due to several factors, such as turbulence or contamination. When the dissolved gas is taken into consideration, the partial pressure of the vapor-filled nucleus is made up of the partial pressure of the dissolved gas plus the partial pressure of the vapor. The incipient cavitation, known as an initial point of an emerging large-scale cavity, is significantly affected by changes in the partial pressure of the nuclei. According to Holl [25], during a single run of an experiment, vaporous and gaseous cavitation could take place simultaneously. In this research, "gaseous cavitation" refers to the situation where dissolved air is present in the working fluid and interacts with vapor cavities. Although the two forms of cavitation are fundamentally distinct from each other, it can be difficult to distinguish them. However, the cavitation process is significantly influenced in situations where there is a large amount of dissolved gas. It is vital to consider the impact of dissolved gas to make considerable progress in predicting the cavitating flow that closely matches the experimental data. By taking into account the influence of non-condensable gas, Vasilakis et al. [26] and Mithun et al. [27] suggest a three-phase cavitation model. Egerer et al. [28] also performed an implicit analysis of water quality. Even though the impact of non-condensable gas has been considered, the assumption that the gas concentration is equally distributed over the entire region is regarded as a weakness in this suggested model. Based on numerical models and experimental measurements, Wróblewski et al. [29,30] examined the impact of dissolved air on cavitation around the Clark Y hydrofoil, the associated unsteady features, and the shedding frequencies. They considered liquid, vapor, and air as the three governing phases using the 3phases model. Based on computational and experimental techniques, Malekshah et al. [31] examined the impact of dissolved air on cavitation within the Venturi flow. The test campaigns were conducted in a closed-circuit water tunnel that included a Venturi test section. The findings support the significant impact of dissolved air on the structure, evolution, and transient/averaged characteristics of the cavity. It has been noted that there are changes to the incipient point along with the sizes of the sheet cavity and cloud cavity. To model cavitating turbulent flow around a Clark-Y hydrofoil and examine the bubble dynamics, Wang et al. [32] developed a multiscale Eulerian-Lagrangian technique. To accurately represent the massive vapor volumes through Eulerian analysis, the LES was combined with the VOF approach. The Rayleigh-Plesset equation along with a bubble motion equation was then solved considering the compressibility effect to monitor micro-scale Lagrangian bubbles. The oscillations in bubble size, bubble motion, and cavity shedding features are satisfactorily predicted by the models and are in good agreement with the experimental data. Ghahramani et al. [33] investigate a multiscale cavitating flow around a sharp-edged bluff body. A type of hybrid cavitation model is suggested for numerical analysis by combining a mixture model and a Lagrangian bubble model. The Lagrangian model uses a four-way coupling technique and novel submodels to consider a variety of small-scale cavitation dynamics events. The findings demonstrate that small-scale cavities play a role not only in the formation and collapse of large-scale structures but also in their growth. Malekshah and Wróblewski [34] aimed to investigate the cavitating flow generated around a hydrofoil when there is dissolved air present in the water (that is, operating fluid). The k-ε RNG turbulence model is being improved by implementing DCM and FBM to achieve precise numerical estimations. For situations with and without dissolved air (that is, air content of 0 and 2.1 ppm), numerical simulations of the cavitating flow are carried out, with the selected cavitation numbers within the range of σ=0.9 to 2.5.

The addition of dissolved air to the water makes the nature of cavitation different. Turbulence and cavitation models, which are crucial in predicting the result of the cavitating flow, must be modified to obtain more accurate findings to avoid damping effects. The Schnerr-Sauer cavitation model was modified by Cheng et al. [35] to better account for the existence of non-condensable gas. In this sense, they linked the local concentration of gasses to the cavitation model by developing an updated mass transfer source term. It has been established that the formation of the cavitation shape downstream of the hydrofoil is remarkably affected by the gas content. Malekshah and Wróblewski [36] focused on developing a numerical model that can account for the impact of dissolving non-condensable gas. The ZGB cavitation model has been modified according to the Merging Theory. According to this concept, the surrounding dissolved air bubbles that are dispersed within have an impact on the pressure of the vapor bubble. In the current study, the significant impact of gas content on cavitating flow is declared and the effectiveness of the suggested numerical model in predicting three-phase cavitating flow is evaluated.

This work focuses on natural and ventilated cavitation, with a special emphasis on the location and rate of air injection. To take into account the impact of dissolved air, the Merging theory is proposed which is compatible with the effect of dissolved non-condensable gas as developed by Malekshah and Wróblewski [36]. The cavitation behavior is analyzed under the effect of the cavitation number (σ=1.1, 1.6), location (Tap1-injection and Tap5-injection) and the rate ($Q = 0$, 0.5, 1 l/min) of air injections.

2. Numerical method

2.1. Multiphase model

Homogeneous mixture theory is used to deal with multiphase flow. The liquid-vapor-gas flow (i.e., three phases in this case) is treated as a single homogeneous fluid that has an identical velocity vector for every phase $\boldsymbol{u}$, which neglects the slip between the phases. As a result, there are fewer governing equations in general. Hence, the temperature is assumed to be constant throughout the domain, resulting in the removal of the energy conservation law. Mass, together with momentum and energy conservation laws, serves as the governing equations (Eqs. (1)–(2)):

$$\frac{\partial \rho}{\partial t} + \nabla\cdot(\rho \boldsymbol{u}) = 0, \tag{1}$$

$$\frac{\partial}{\partial t}(\rho \boldsymbol{u}) + \nabla\cdot(\rho \boldsymbol{u}\boldsymbol{u}) = -\nabla P + \nabla\cdot\left[\mu\left(\nabla \boldsymbol{u} + \nabla \boldsymbol{u}^T\right)\right] + \rho g, \tag{2}$$

$$\begin{cases} \rho = \rho_v\alpha_v + \rho_l(1-\alpha_v) + \rho_{ng}\alpha_{ng} \\ \mu = \mu_v\alpha_v + \mu_l(1-\alpha_v) + \mu_{ng}\alpha_{ng} \end{cases}, \tag{3}$$

Due to its minimal impact on the present problem, the last term in the RHS of Eq. (2), which describes the body force, is ignored in the numerical method. Because the computational model accounts for the existence of air, a third term reflecting the proportion of non-condensable gas (in this case, air) is included in the density ρ and viscosity μ of a working fluid in Eq. (3). The continuity equations related to the vapor volume fraction (α_v) as well as the air volume fraction (α_{ng}) are solved using the mixture model that incorporates three phases: liquid, vapor, and air (3phases model). Modeling is done between species to simulate the mass transfer among a liquid and a combination of gaseous phases:

$$\frac{\partial \rho_v\alpha_v}{\partial t} + \nabla\cdot(\rho_v\alpha_v\boldsymbol{u}) = R, \tag{4}$$

$$\frac{\partial \rho_{ng}\alpha_{ng}}{\partial t} + \nabla\cdot(\rho_{ng}\alpha_{ng}\boldsymbol{u}) = 0, \tag{5}$$

$$\alpha_l + \alpha_v + \alpha_{ng} = 1. \tag{6}$$

The source term R in Eq. (4), which denotes the mass transfer per volume unit among the liquid and vapor phases during evaporation and condensation, respectively; regulates the phase transition.

2.2. Standard and modified $k-\varepsilon$ RNG turbulence model

The following equations define the standard k-ε RNG turbulence model:

$$\frac{\partial(\rho k)}{\partial t} + \nabla\cdot(\rho\boldsymbol{u}k) = \nabla\cdot\left[\left(\mu + \frac{\mu_t}{\sigma_k}\right)\nabla k\right] + G_k - \rho\varepsilon, \tag{7}$$

$$\frac{\partial(\rho\varepsilon)}{\partial t} + \nabla\cdot(\rho\boldsymbol{u}\varepsilon) = \nabla\cdot\left[\left(\mu + \frac{\mu_t}{\sigma_\varepsilon}\right)\nabla\varepsilon\right] + \frac{c_1\varepsilon}{k}G_k - c_2\rho\frac{\varepsilon^2}{k}. \tag{8}$$

The turbulent viscosity is denoted by $\mu_t = \rho C_\mu k^2/\varepsilon$, and the constant C_μ is considered to be equal to 0.084 [37]. Furthermore, k and ε stand for the turbulent kinetic energy and turbulent energy dissipation rate, respectively. Additionally, G_k indicates the turbulent energy production term.

A density correction-based model (DCM) introduced by Coutier-Delgosha et al. [38] is the basis for the modification of the k-ε RNG turbulence model, which decreases the turbulent viscosity of the mixture and prevents its overestimation. The following is a description of the modified turbulent viscosity.

$$\mu_t = f(\rho)C_\mu k^2/\varepsilon, \tag{9}$$

where

$$f(\rho) = \rho_v + \left(\frac{\rho_v - \rho}{\rho_v - \rho_l}\right)^n(\rho_l - \rho_v). \tag{10}$$

Here, n is equal to 10, as proposed by Coutier-Delgosha et al. [38].

2.3. Zwart-Gerber-Belamri (ZGB) cavitation model

The Rayleigh-Plesset equation (RP), which describes the growth of a vapor bubble in a liquid, served as the basis for the current cavitation model [39]:

$$r_m\frac{d^2r_m}{dt^2} + \frac{3}{2}\left(\frac{dr_m}{dt}\right)^2 + \frac{2S}{r_m} = \frac{p_v - p}{\rho_l}, \tag{11}$$

where r_m stands for the radius of a sphere-shaped bubble, p is the local fluid pressure, p_v is the saturation pressure, and S indicates the surface tension.

The ZGB mode is based on a simplified version of the Rayleigh-Plesset equation, as described in Eq. (12), for the formation of vapor bubbles in the fluid using the concept of bubble mass transfer rate [36].

$$R = \frac{3\alpha_v\rho_v}{r_B}\sqrt{\frac{2}{3}\frac{p_v - p}{\rho_l}}, \tag{12}$$

The following formulations provide the source term R used to explain condensation ($R = R_c$) and evaporation ($R = R_e$) [40].

$$\begin{cases} R_e = F_{vap}\dfrac{3\alpha_{nuc}(1-\alpha_v)\rho_v}{r_B}\sqrt{\dfrac{2}{3}\dfrac{p_v - p}{\rho_l}}, \ p_v > p \\ R_c = -F_{cond}\dfrac{3\alpha_v\rho_v}{r_B}\sqrt{\dfrac{2}{3}\dfrac{p - p_v}{\rho_l}}, \ p_v < p \end{cases}. \tag{13}$$

where $F_{vap} = 50$, $F_{cond} = 0.1$, $\alpha_{nuc} = 5 \times 10^{-4}$ and $r_B = 1 \times 10^{-6}$m.

2.4. Modified cavitation model

2.4.1. Growth of a gas-containing bubble [3]

Essentially, the working liquid may contain a certain amount of dissolved gas and non-dissolvable gas bubbles. The dissolved gas and vapor may constitute a mixture phase; however, the non-dissolvable gas bubbles remain undissolved. Therefore, the non-dissolved gas bubbles are ignored in the current modification of the cavitation model, which only takes the effect of dissolved air into account.

The bubble contents must be considered to make progress with the prediction of three-phase cavitating flows because of their major influence on cavitation's onset. To provide a broad insight, it is proposed that the bubble includes a vapor as well as a certain amount of non-condensable gas, having a reference radius of r_0 with a partial pressure that is equal to p_{G0}. Additionally, the thermal impact is ignored, and air serves as the non-condensable gas in the current study. The pressure of a mixture bubble p_m, in the scenario where gas diffuses to the vapor phase, is then determined from Eq. (14) [39], assuming the diffusive mass transfer between the air and vapor phase as well as; negligible mass transfer between air and liquid phases.

$$p_m = p_V + p_{G0}\left(\frac{r_0}{r}\right)^{3\gamma}, \tag{14}$$

where $\gamma = 1.4$ is the heat capacity ratio of air. Also, r_0 and r shows reference radius and radius in the new equilibrium condition, respectively.

As a result, the Rayleigh-Plesset equation, when the gas concentration is not negligible, is described as follows:

$$r_m\frac{d^2r_m}{dt^2} + \frac{3}{2}\left(\frac{dr_m}{dt}\right)^2 + \frac{2S}{r_m} = \frac{p_v - p}{\rho_l} + \frac{p_{G0}}{\rho_l}\left(\frac{r_0}{r}\right)^{3\gamma}, \tag{15}$$

The modified cavitation source terms are obtained using the same method as for the ZGB cavitation source term, by ignoring the impacts of the second-order terms and surface tension:

$$\begin{cases} R_e = F_{vap}\dfrac{3\alpha_{nuc}(1-\alpha_v)\rho_v}{r_B}\sqrt{\dfrac{2}{3}\dfrac{p_m - p}{\rho_l}}, \ p_m > p \\ R_c = -F_{cond}\dfrac{3\alpha_v\rho_v}{r_B}\sqrt{\dfrac{2}{3}\dfrac{p - p_m}{\rho_l}}, \ p_m < p \end{cases}. \tag{16}$$

p_m is computed utilizing the established model known as the Merging theory [36], discussed in the following section.

2.4.2. Merging process of vapor and gas phases [36]

The current approach suggests including the non-condensable gas, in this example air, into the cavitation model. This method contributes to the formation, expansion, and collapse of a mixture bubble, which can help the prediction to get closer to experimental data.

Although some variables, such as α_{nuc} and R_B, are impacted due to the presence of non-condensable gas, the most significant alteration is found in the estimation of pressure p_B. Under the assumption of the polytropic behavior of a bubble, the mixture pressure p_m is computed as the sum of partial pressures of gas and vapor (p_v and $p_{G0}\left(\frac{r_0}{r}\right)^{3\gamma}$). The merging process concept is used for this purpose relying upon the Eulerian point of view, and Fig. 1 illustrates the process, helping to schematically explain the concept. Furthermore, the concept of merging processes is discussed below.

If gas bubbles have an initial radius of r_B and are in equilibrium, the partial pressure of the bubble must meet the following equation (Eq. (17)) assuming that the surface tension and viscosity are ignored.

$$p_\infty = p_v + p_{g0}, \tag{17}$$

where the initial ambient pressure, vapor pressure, and partial pressure of the non-condensable gas within the bubble are denoted by p_∞, p_v and p_{g0}, respectively. At the initial condition, the partial vapor pressure is lower than the partial pressure of non-condensable gas. The initial ambient pressure for the current study was adjusted to be equal to the inlet pressure p_{in} in equilibrium. Consequently, the vapor pressure can also be ignored. Thus, Eq. (17) is provided:

$$p_{g0} = p_\infty = p_{in}, \tag{18}$$

The total number of gas microbubbles of gas in each computational cell is computed as follows, knowing that the gas volume fraction equals α_{ng}:

$$V_{g0} = \alpha_{ng}.V_{cell}, \tag{19}$$

$$n_0 = \frac{3}{4}\frac{V_{g0}}{\pi r_B^3}, \tag{20}$$

where n_0 is the number of small gas bubbles that exist in each cell's initial equilibrium under the initial condition, and V_{cell} and V_{g0} stand for the cell volume and the gas volume, respectively.

A sudden pressure drop occurs whilst the bubble travels through the far-field into the cavitation zone, and as a result, the radius increases. Consequently, the following equations (Eqs. (21)–(22)) arise from the new equilibrium condition.

$$p_{g1} = p, \tag{21}$$

$$r_{g1} = R_B\sqrt[3\gamma]{p_{g0}/p_{g1}}, \tag{22}$$

where p is the local pressure. Also, r_{g1} denotes the new radius.

Under the new equilibrium condition, the total volume of non-condensable gas is then determined as follows:

$$V_{g1} = \sum_{i=1}^{n_0}\frac{4}{3}\pi r_{g1}^3. \tag{23}$$

Additionally, it is assumed that the gas bubbles combine to form a single gas bubble, so its pressure and radius are given as:

$$p_{g2} = p, \tag{24}$$

$$r_{g2} = \sqrt[3]{n}r_{g1}, \tag{25}$$

when the local pressure and the pressure of a single gas bubble are equal.

The radius of the vapor bubble r_v is calculated using the following formula:

$$V_v = \alpha_v V_{cell}, \tag{26}$$

$$r_v = \sqrt[3]{\frac{3}{4}\frac{V_v}{\pi}}. \tag{27}$$

Whenever the total volume of vapor and gas bubbles ($V_T = V_v + V_{g1}$) is sufficiently larger than the cell volume, these two bubbles will merge. Otherwise, a fusion of vapor and gas bubbles is difficult to happen. Therefore, in the current paper, only when the total amount of vapor and

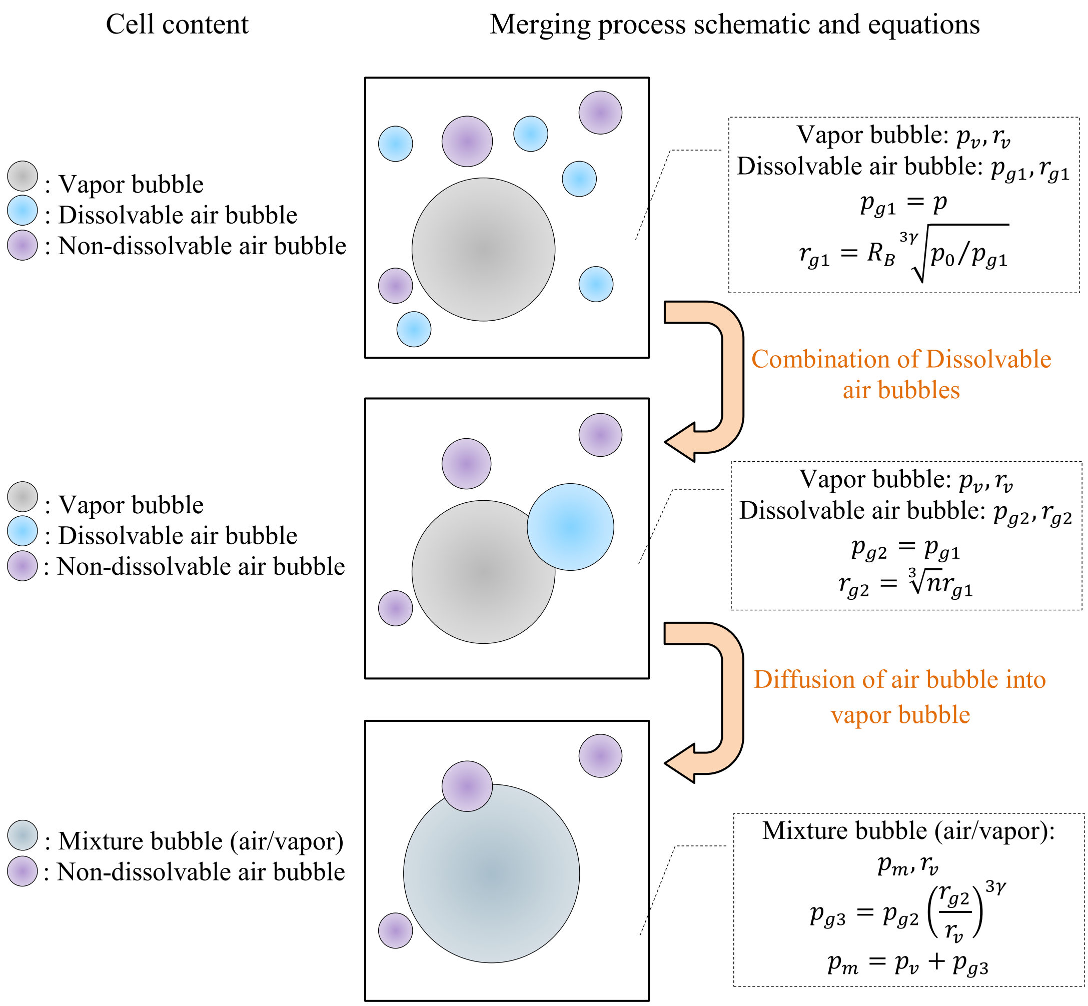

Fig. 1. Merging process of vapor and gas bubbles (if $r_v > r_{g2}$).

gas equals $\frac{1}{100}$ of a cell ($V_C = \frac{1}{100} V_{cell}$), the merging process will begin.

Under such conditions, two possibilities for the merging of vapor and gas bubbles may be taken into consideration:

$$\begin{cases} p_m = p_v + p_{g2}\left(\frac{r_{g2}}{r_v}\right)^{3\gamma}, & r_v > r_{g2} \\ p_m = p_v, & r_v \le r_{g2} \end{cases}. \tag{28}$$

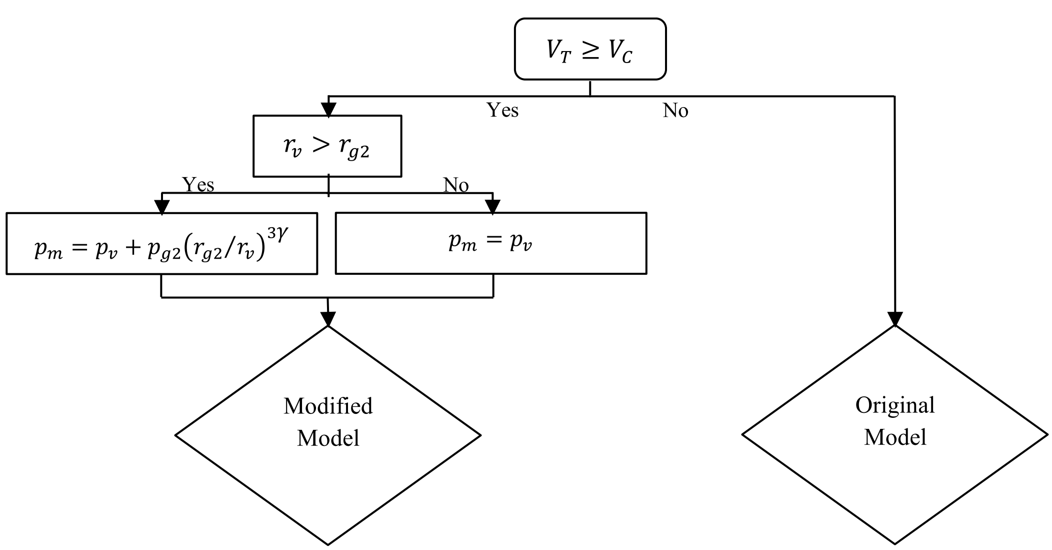

Fig. 2. Switching process between the original and modified cavitation models.

It should be noted that the original cavitation model (that is, ZGB) must be retrieved and that the modified cavitation model will only activate once the critical volume ratio is satisfied. Fig. 2 shows the switch process between the original and modified cavitation models.

The following is a revised version of Eq. (16) that uses the Merging theory:

$$r_m\frac{d^2r_m}{dt^2}+\frac{3}{2}\left(\frac{dr_m}{dt}\right)^2+\frac{4\mu_l}{\rho_l r_m}\left(\frac{dr_m}{dt}\right)+\frac{2S}{\rho_l r_m}=\frac{\left(p_v+p_{g2}\left(r_{g2}/r_v\right)^{3\gamma}\right)-p}{\rho_l}. \quad (29)$$

3. Computational and domain and meshing

In this study, a Clark Y hydrofoil is used that has a chord length of $c = 0.07$ m. The span is also 0.07 m, and the angle of attack is 8°. The computational domain and the hydrofoil geometry model are compatible with the experimental setup described above. The computational domain, boundaries, and dimensions are depicted in Fig. 3; the inlet is 3.2c from the hydrofoil's leading edge, the outlet is located 5.8c from the hydrofoil's trailing edge, and the top wall extends 2.5c above the lower wall. A small hole with a diameter of 0.5 mm is made at locations P1 to P11 to deal with ventilation and pressure measurement. The locations of taps from the leading edge are summarized in Table 1.

The inlet velocity, with a constant velocity of v_{in}=10.45 m/s, defines the inlet boundary. The pressure is set at the outlet boundary, allowing regulation of the flow-field cavitation.

The flow field temperature is set at 25 °C. The upper and lower walls, as well as the hydrofoil surface, are addressed as non-slip walls. To simplify the simulation, the side walls are set as symmetry. Air is injected through the first or fifth holes, called Tap1-injection and Tap5-injection, respectively, to examine the effect of the injection location. In addition, the regulated injection rates are $Q = 0$, 0.5, and 1 l/min. Furthermore, each of these testing scenarios is also run in two different cavitation numbers: σ=1.1 and 1.6, where it is calculated as follows:

$$\sigma=\frac{p_{in}-p_v}{\frac{1}{2}\rho v_{in}^2},\quad v_{in}=\frac{Q}{A}=\frac{Q}{hw}. \quad (30)$$

where Q is the volume flow rate, $A = hw$ is the cross-section area of the test chamber. The height (h) and span (w) of the chamber are equal to 0.189 m and 0.07 m, respectively. The inlet pressure, vapor pressure, and inlet velocity are described, respectively, by the variables p_{in}, p_v, and v_{in}.

The three grid layouts listed in Table 2, are compared and examined in this investigation to find the best possible balance between computation accuracy and the use of resources. At the adjacent foil surface, the computational domain utilizing a C-Grid is refined to be sufficiently precise. Fig. 4 depicts a typical three-dimensional hydrofoil surface mesh that includes 80 nodes along the spanwise axis.

Fig. 5 presents the time-averaged lift coefficient (C_L) and drag coefficient (C_D). Once mesh 2 is refined further into mesh 3, the estimated time-averaged results are rather close, indicating that mesh 2 might be approaching convergence and is deemed suitable to conduct the mean and unsteady features of cavitation in this research.

4. Experimental setup

The tests were carried out utilizing hydraulic equipment in the laboratory of the Department of Power Engineering and Turbomachinery at the Silesian University of Technology. Fig. 6-a shows the schematic of the installation. The main components of the water tunnels are the test section, tank, pump, valve, flowmeter, membrane, and pipes. The water tunnel is operated using an electric pump which is able to maintain a constant water flow rate (Q_{water}=490 m^3/h), and the membrane regulates the pressure inside the tank in the range of 105–180 kPa. Furthermore, the test section can be replaced, which makes it possible to change the object studied.

The controlled concentration of dissolved oxygen used for the experimental testing is 4.6 mg/l. According to Henry's law, it corresponds to an air content of 11.7 mg/l at atmospheric pressure. Before and after each experimental campaign, the dissolved air is measured, and the mean amount is presented. The CF-401 multifunction meter with COG-1 oxygen sensor and precision of ±0.01 mg/l, is used to monitor the dissolved oxygen concentration.

Fig. 6-b shows a schematic representation of the test chamber together with the hydrofoil, measurement, and visualization equipment. The Clark Y hydrofoil with 11 holes on the suction side is mounted in the test section. These holes can be used for pressure measurement and air injection, whereas in the present work, the first and fifth holes (i.e. Tap1 and Tap5), are selected for air injection purposes. These two injection holes have been intentionally chosen to be placed proximately to the cavitation's initial point of the cavitation and its internal region. However, future investigations may analyze additional locations in forthcoming research.

The holes are connected to the root of the fixing disk through internal channels in the hydrofoil. These channels are followed by the impulse tubes and connected to the pressure transducers and one selected, to the

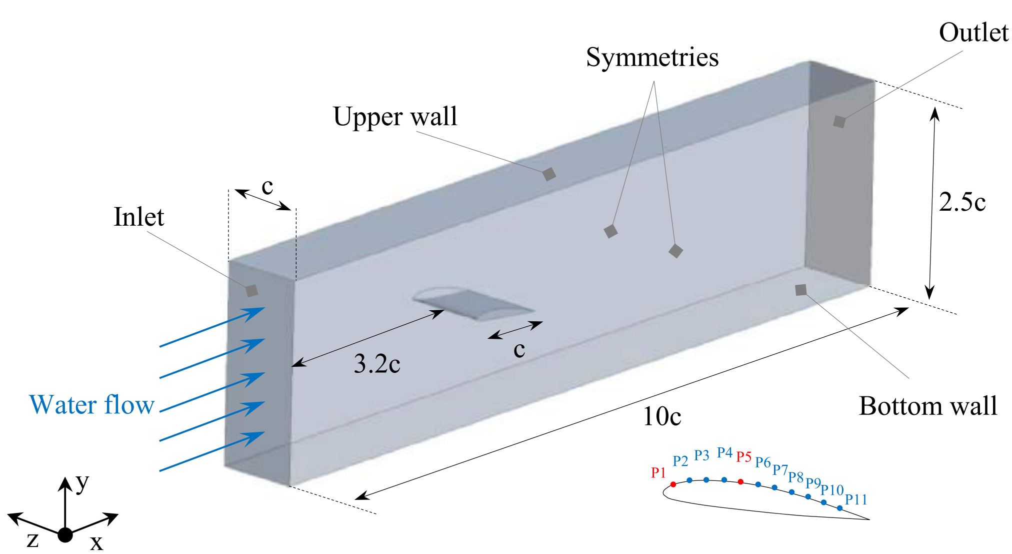

Fig. 3. Schematic of the computational domain, dimensions, and boundary conditions.

Table 1
The locations of taps from the leading edge.

Tap No.	P1	P2	P3	P4	P5	P6	P7	P8	P9	P10	P11
Location (mm)	2.8	8.4	14.1	19.8	25.4	31.1	36.8	42.4	48.1	53.8	59.5

Table 2
Details of grid layouts.

Mesh No.	Total nodes (million)	Nodes around hydrofoil	Nodes of spanwise
Mesh 1	1.28	115 × 82	60
Mesh 2	1.59	130 × 92	60
Mesh 3	1.84	140 × 102	70

air injector. The XP5 type with amplifier type ARD154 and APLISENS PC-28 are the models of high-frequency and low-frequency sensors, respectively. The fast-frequency pressure sensor has a full-scale accuracy of 0.25% at 500 kPa. Additionally, the low-frequency sensor's accuracy at full-scale 160 kPa is 0.16%. The Brooks model SLA5850S Mass Flow Controller, with precision up to 1200 lpm: 1.0% of the rate (20%−100% FS), is utilized for air injection. The National Instruments USB 6216 module served as the basis for the measuring system. Furthermore, the NI/PXI-6255 module works in conjunction with the pressure measurement cluster. A LabView program is used to manage the executive components and the data collection process.

Additionally, the cavitation flow is recorded using a high-speed camera. The Phantom Miro C110 high-speed video camera Phantom Miro C110 is used with a recording speed of 3200 f/s and a spatial resolution of 960 × 280 pixels. Furthermore, MultiLED lighters are used for lightening.

The detailed characteristics of the water tunnel, test section, measurement and visualization systems are discussed in Ref. [24].

Uncertainty analysis is one of the most crucial factors that must be considered during experimental assessment. Having the definition of cavitation number in Eq. (30), the relative uncertainty is also computed

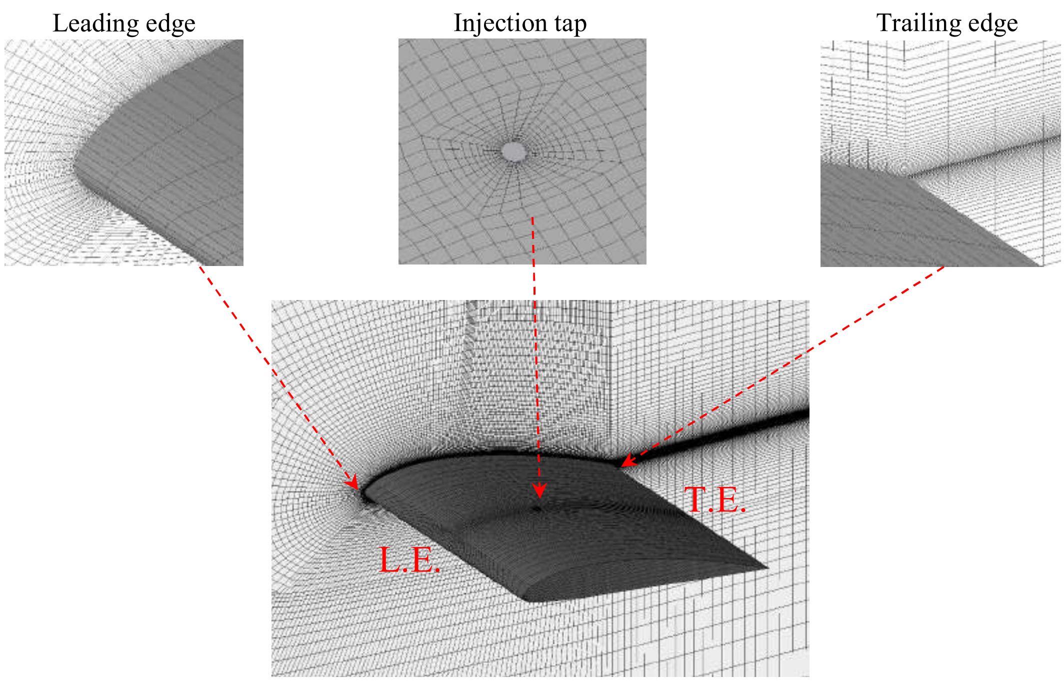

Fig. 4. The surface meshing of the 3-D hydrofoil domain.

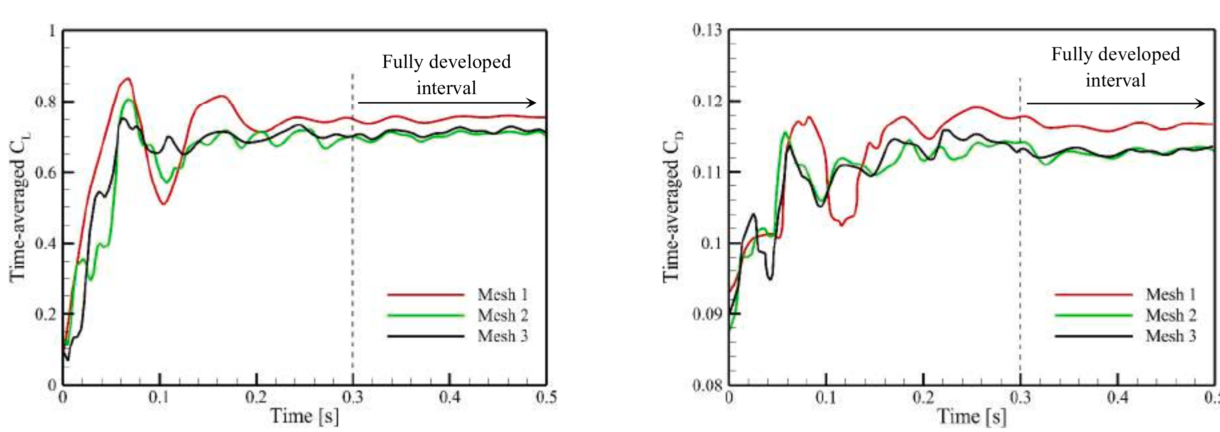

Fig. 5. Time-averaged lift and drag coefficients computed using various mesh resolutions (Q = 0 l/min, σ=1.1).

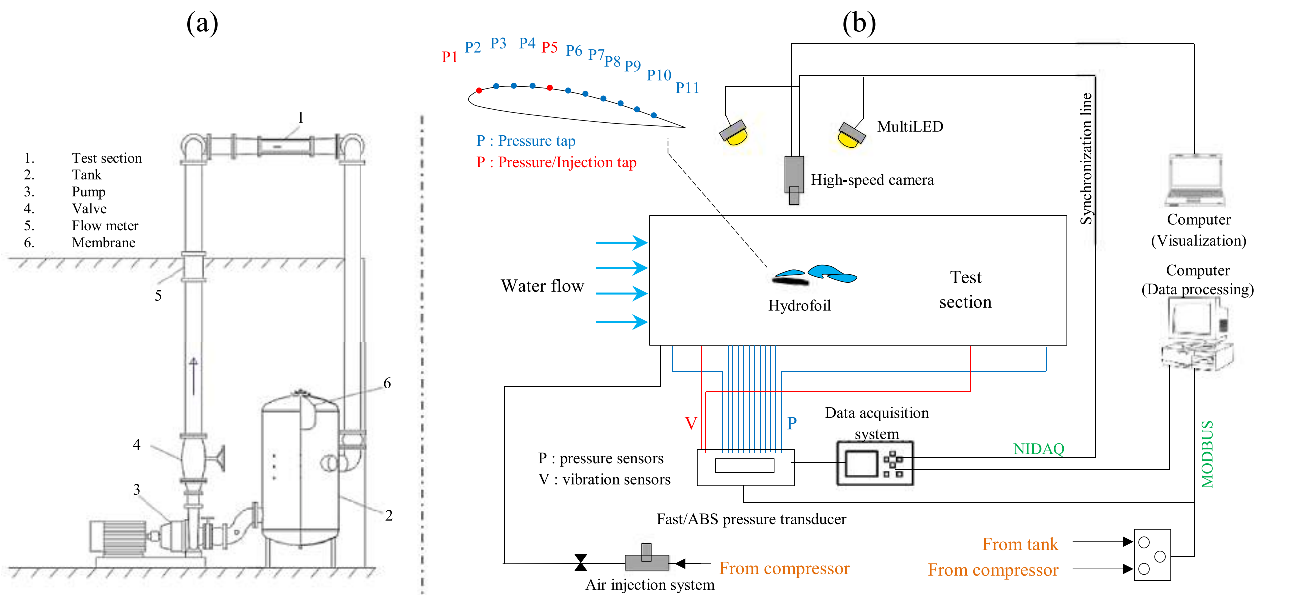

Fig. 6. (a) Schematic of the water tunnel including main components; (b) Schematic of the test section including measurement, air injection, and visualization systems.

using the formula below [31]:

$$\frac{U_\sigma}{\sigma}=\sqrt{\left(\frac{p_{in}}{p_{in}-p_v}\right)^2\left(\frac{U_{p_{in}}}{p_{in}}\right)^2+\left(\frac{p_v}{p_{in}-p_v}\right)^2\left(\frac{U_{p_v}}{p_v}\right)^2+\left(\frac{U_\rho}{\rho}\right)^2+4\left(\frac{U_{v_{in}}}{v_{in}}\right)^2}. \tag{31}$$

Table 3 shows the effects of each physical parameter on the uncertainty of the cavitation number. Thus, the uncertainty of the cavitation number U_σ/σ equals 0.54%.

The detailed procedures for conducting an uncertainty analysis can be found in Ref. [24].

5. Results and discussion

This work focuses on a numerical and experimental analysis of natural and ventilated cavitation around a Clark Y hydrofoil. Having water and vapor as two main phases, the third phase, which is air, is considered, while dissolved air and ventilation air jet play a role in the current problem.

The cavitation model is adjusted based on the Merging theory to consider the impact of dissolved air on the cavitation. According to this concept, the air content affects the pressure of the nucleation bubble, which is connected to the vapor saturation pressure. To avoid overestimation of turbulent viscosity, we use the Density Corrected-based Method (DCM) to modify the turbulence model. A three-dimensional model of the test section with real scale is prepared, which also includes the 3D hydrofoil. The hydrofoil is equipped with 11 holes, which can be used alternatively as a pressure or injection tap. However, in this study, the first and fifth taps, called Tap1-injection, and Tap5-injection, are used for injection only. In the current case studies, two cavitation numbers (σ=1.1, 1.6) and three air injection rates ($Q = 0$, 0.5, 1 l/min) are considered.

Table 3
The impact of each parameter on the uncertainty of **σ**.

	Range of X_i	$U(X_i)/X_i$	Maximum contribution to $(U_\sigma/\sigma)^2$
p_{in}	60-90 kPa	0.0016	2.7×10^{-6}
p_v	2.728 kPa	0.0117	1.3×10^{-7}
ρ	997.65 kg.m^{-3}	4×10^{-5}	8×10^{-10}
v	10.4 m.s^{-1}	0.0026	2.7×10^{-5}
Total	–	–	2.9×10^{-5}

The estimated and measured pressure coefficients based on numerical simulation and experimental data, respectively; are shown in Fig. 7 (σ=1.1 and 1.6, $Q = 0$ and 1 l/min) to examine the effect of air injection rate on the pressure distribution on the surface of the hydrofoil.

The pressure coefficient is defined as follows:

$$C_p=\frac{p-p_\infty}{\frac{1}{2}\rho v_{in}^2}. \tag{32}$$

where p, p_∞, ρ and v_{in} define the pressure, ambient pressure, density, and flow velocity at the test chamber inlet, respectively.

The present graphs are useful for comparing numerical predictions with experimental measurements, but they may also perfectly illustrate how the injection rate affects the behavior of a mean characteristic, in this example the pressure coefficient of ventilated cavitation around the hydrofoil. Also, the range of error for the experimental data points is 1% to 4%. The numerical and experimental results are compared, and it is determined that there is a convincing consistency between them. However, computational calculations forecast a delayed drop in the pressure coefficient. This indicates that the predicted sheet cavity is longer than that in the experiments. However, in all cases and with an alteration of the injection rate, the changes that occur in the sheet cavity, that is, the area before a sharp drop in the pressure coefficient, are more apparent than those in other areas. According to a prolonged flat region of Cp, the sheet cavity is lengthened by increasing the air injection rate.

According to Fig. 8, at least five evolution cycles of the vapor cavity are chosen to calculate the shedding in the fully developed ventilated stage. It is done because the transitional interval might substantially intensify the statistical uncertainties triggered by the ventilation start-up moment. It is noted that the fluctuation of vapor volume is more noticeable in the initial step when there is pure vapor cavitation without air than in other parts. Also, by including the dissolved air, more stable periodic fluctuations emerged.

Dynamic cavitating flow generates a large fluctuation in hydrofoil surface pressure as it passes through the cavity-shedding process. Therefore, it is challenging to predict the dynamic pressure. The results of the experimental observations are presented along with the numerical predictions to provide the pressure spectral distribution (i.e., the power spectral density) at point P8 (Tap8) in Fig. 9. The diagrams show how to

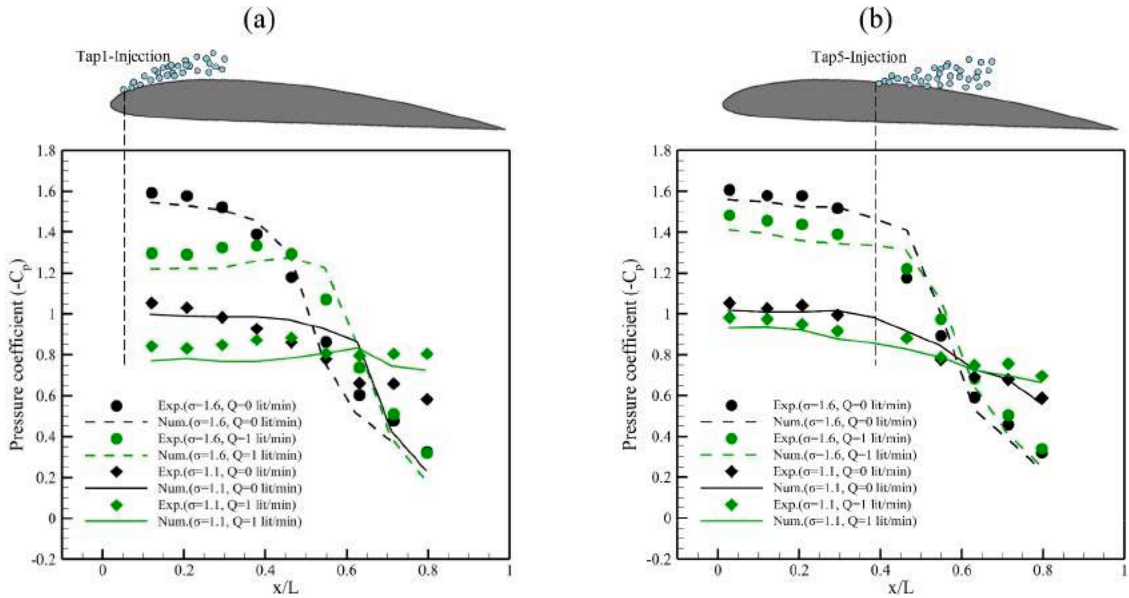

Fig. 7. Pressure coefficient (-C_p) as a function of the cavitation number (σ) and injection rate (Q) for (a) Tap1-injection and (b) Tap5-injection.

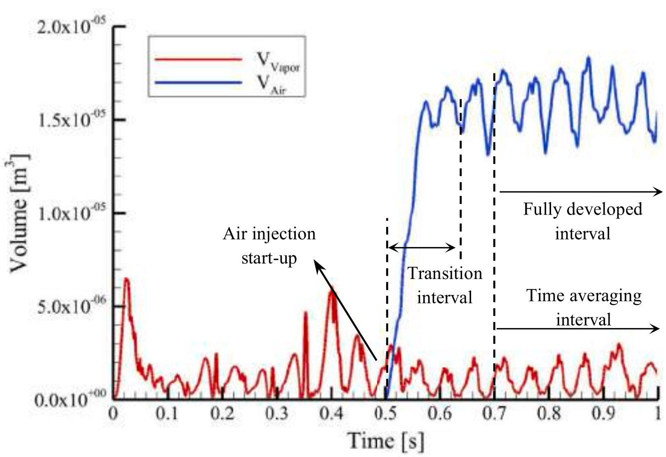

Fig. 8. The time evolution of the volume cavity and the time averaging scheme (Q = 0.5 l/min, σ=1.6, Tap1-injection).

calculate the shedding frequency, and the following part provides a detailed comparison. In the case of $Q = 1$ l/min, σ=1.6, Tap1-injection, while the primary frequency of cavitation shedding as found experimentally is $f = 10.7$ Hz, the main shedding frequency estimated using numerical modeling is $f = 13.0$ Hz. Therefore, the simulation error is equal to 21% and, given the complex nature of the cavitating flow, this level of accuracy is promising. Thus, the periodicity of the cavitation flow has been effectively captured, indicating that the cavitation dynamics can be reliably predicted by the numerical method that has been suggested.

Since periodic forces caused by vortex shedding play an essential role in several physical disadvantages, especially vibrations and noise, the shedding frequency corresponds to one of the crucial characteristics that must be examined in the cavitation phenomenon. Fig. 10 depicts the shedding frequencies against the injection rate for $Q = 0$, 0.5, 1 l/min, σ=1.1, 1.6. Based on the power spectral density (PSD) examination of the pressure fluctuation at P8, the shedding frequency is determined. It should be noted that the range of error for the experimental and numerical data points are 3% to 7% and 5% to 9%, respectively. The findings indicate that, while the air injection rate increases, the frequency of shedding decreases. Therefore, it indicates that, compared to natural cavitation, ventilated cavitation has a lower periodicity. In addition, air injection tends to produce a much higher decrease in shedding frequency in cases of higher cavitation numbers. Generally, numerical modeling predicts higher shedding frequencies compared to measured ones, whereas the error between the numerical and experimental cases is in the range of 13% to 32%.

The transient cavity evolution according to the computational and experimental results is compared in Fig. 11. There are four distinct stages in the cavity structure evolution: (1) The sheet cavity steadily expands to produce a uniform cloud cavity between t_0*+0 ms* and t_0*+24 ms*. The secondary flow runs upstream slowly adjacent to the surface, the sheet cavity reaches its maximum size, and then the re-entrant jet is formed beneath the cavity closure at t_0*+24 ms*. (2) The re-entrant jet develops upstream of the hydrofoil from t_0*+24 ms* to t_0*+36 ms*, finally leading the sheet cavity to break down into a U shape. (3) The sheet cavity completely disappeared and transformed into a large-scale cloud cavity at t_0*+48 ms*. The cavity of the cloud sheds and propagates downstream, whereas a new sheet cavity develops throughout the low-pressure area close to the hydrofoil's leading edge. (4) As the cavity cloud moves downstream toward the high-pressure zone between t_0*+48 ms* and t_0*+60 ms*, it starts to collapse. The resolution of these evolution stages declares the ability of the numerical method to capture unsteady cavitation.

Given the five cycles of cavity evolution for $Q = 0$, 0.5, 1 l/min, σ=1.1 and 1.6, Tap5-injection, schematic interpretation of the cavity boundary the mean value of the gray level, is computed and shown in Fig. 12. By averaging the gray level of each pixel of the captured image over a specific period, the mean value of the gray level is a sort of image processing that shows the mean cavity length. By averaging the gray level of each pixel of the captured image over a specific period, the mean value of the gray level is a sort of image processing that shows the mean cavity length. Although extending the period can help provide more accurate average results, five cycles are assumed to be sufficient in this case. Ref. [41]. has further information about the mean value of the gray level. Additionally, as shown in Fig. 12, the boundary of the mean value of the gray level is manually marked for every case to have simpler and better comparisons between the cavity lengths. Also, it is not intended to evaluate the exact dimensions of cavity but providing a comparison between numerical predictions and experimental measurements, is aimed. It should be noted that since the cases of $Q = 1$ l/min, σ=1.1 and $Q = 0.5$ l/min, σ=1.1 have almost similar cavity lengths, the case with Q

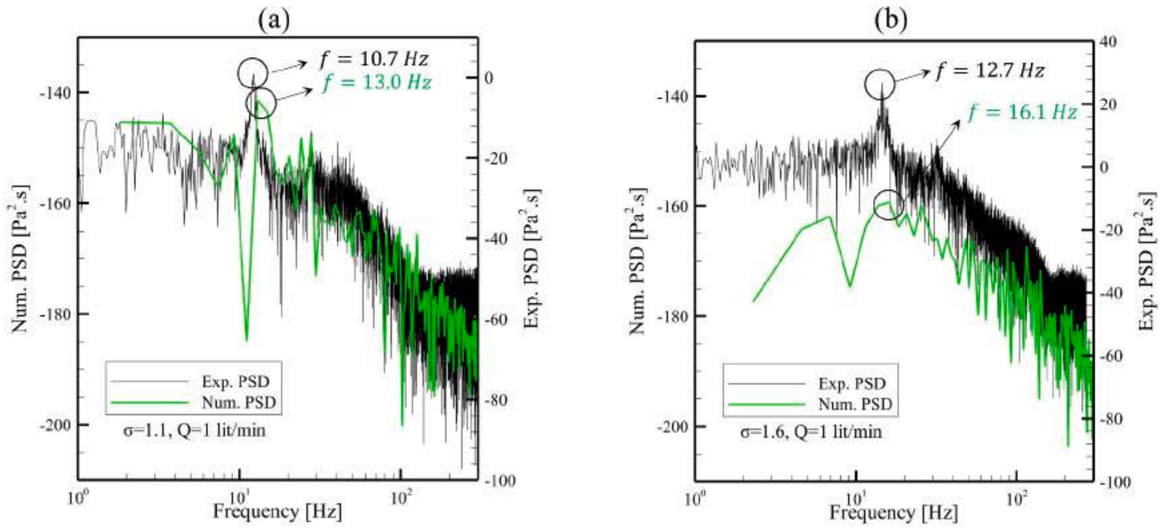

Fig. 9. Power spectral density (PSD) of vapor volume evolution ((a) $Q = 1$ l/min, σ=1.1 and (b) 1.6, Tap1-injection).

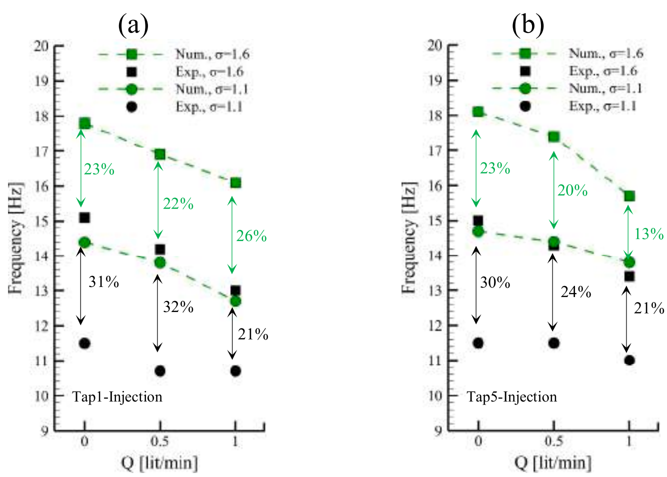

Fig. 10. Shedding frequency under the effect of injection rate (Q) and cavitation number (σ) for (a) Tap1-injection and (b) Tap5-injection (right).

= 0.5 l/min is neglected. It is shown that when the cavitation number decreases, the cavity grows larger. Similarly, when air is added, the cavity grows. In this sense, the air injection rate and the size of the cavity are directly related.

The Q distribution for natural and ventilated cavitation, which is colored by vorticity magnitude, is shown in Fig. 13. Overall, the development of vortices during ventilated cavitation and natural cavitation are comparable, however, more complications in ventilated cavitation are seen. The vorticity near the leading edge is low for natural cavitation during the initial stage (t_0+*12 ms* to t_0+*24 ms*), but it is much farther downstream of the sheet cavity. This finding suggests that in the rear part of the sheet cavity, the rotation effect is dominant. The Q distribution along the trailing edge becomes complex between t_0+*36 ms* and t_0+*60 ms*. The dominating zone of rotation occurs in the inner region of the shedding cavity, which causes the cavitating flow to become extremely unstable. Furthermore, Fig. 13 provides a schematic illustration of the structure of the generated cavity for ventilation cavitation. It is observed that injection will affect the structure of the cavity. From the top, it can be identified that the injection squeezes the cavity, forming an M-shape. Therefore, the same effect is happening from the front, where the cavity's mid-section has been dragged inward.

The jet structure of the injected air during an evolution period is illustrated in Fig. 14. From growing the sheet cavity (t_0), the jet is sucked toward the inlet which is named 'Reversed Jet'. It is due to the low-pressure zone when the cavity emerges. However, looking at the sheet cavity (t_0+*6 ms*), it is observed that the jet is significantly shed downstream, which is due to the strong downward cavity flow. This type of jet is named 'Shed Jet' because it sheds in the direction of downstream flow. When the cavity cloud is expanded (t_0+*24 ms*), the air jet is pulled toward the cavity region. Also, this type of jet is named 'Cavitation-Pulled Jet' because it is drawn inside the cavity region, which is identified as a low-pressure area. Furthermore, the narrow beam of the air jet that has less volume than in the previous step, which is the isosurface of $\alpha_a = 0.9$, indicates that much of the injected air is dispersed through the cloud. Finally, the air jet is sucked toward the leading edge once again and generates the Reversed Jet when the new sheet cavity emerges (t_0+*36 ms*).

6. Conclusions

The natural/ventilated cavitation around a Clark Y hydrofoil is studied using numerical simulation and experimental measurements. To take the dissolved air into account, multiphase (i.e., water, vapor, and air) modeling is employed where the ZGB cavitation model is modified based on the Merging theory, which considers the vapor-air interaction. Additionally, the k-ε turbulence model is modified using the Density Corrected-Based Model (DCM). The impact of air injection location and rate on the behavior of cavitation is emphasized. The following findings can be outlined:

- Air injection rate not only increases the $-C_p$ value, but also alters the pressure distribution.
- Increasing the air injection leads to a decrease in the shedding frequency at every injection location.
- Numerical simulations predict higher shedding frequencies compared to the measured ones.
- The higher shedding frequency of numerical modeling may be justified by a smaller predicted cavity. It must be underlined that the smaller cavity can easily have strong dynamic behavior.
- Increasing the air injection rate leads to an extended cavity with an M-shaped structure.
- Three different configurations for air injection may occur during a cycle of cavity evolution, including Reversed jet, Cavitation-Pulled jet, and Shed jet.

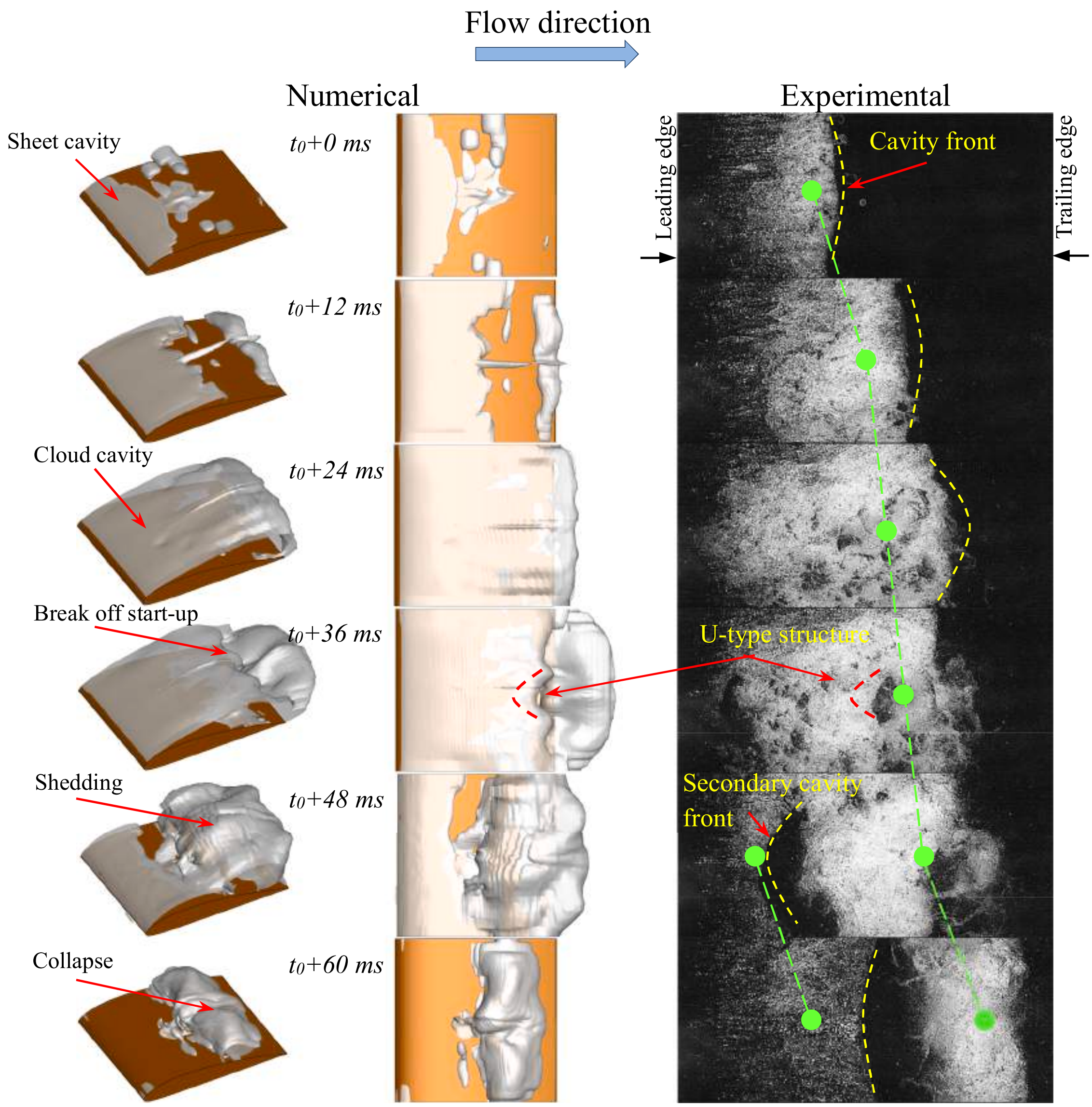

Fig. 11. Comparison of cavity evolution in a cycle between numerical prediction and experimental observation (Q = 1 l/min, σ=1.1, Tap5-injection).

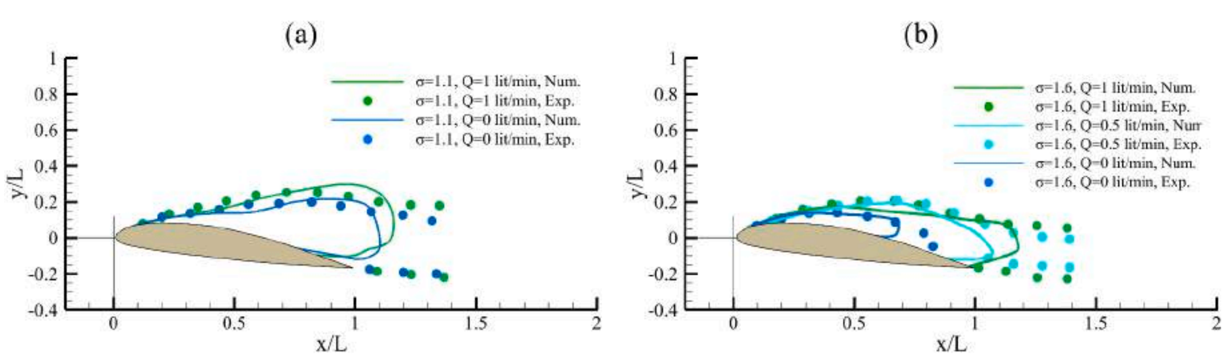

Fig. 12. Schematic interpretation of the cavity boundary using a mean gray level value (Tap5-injection, (a) σ=1.1 and (b) σ=1.6).

CRediT authorship contribution statement

Emad Hasani Malekshah: Conceptualization, Methodology, Software, Investigation, Validation, Formal analysis, Writing – original draft, Writing – review & editing. **Włodzimierz Wróblewski:** Conceptualization, Writing – review & editing, Supervision, Funding acquisition. **Mirosław Majkut:** Software, Investigation.

Declaration of Competing Interest

The authors certify that they have NO affiliations with or involvement in any organization or entity with any financial interest (such as

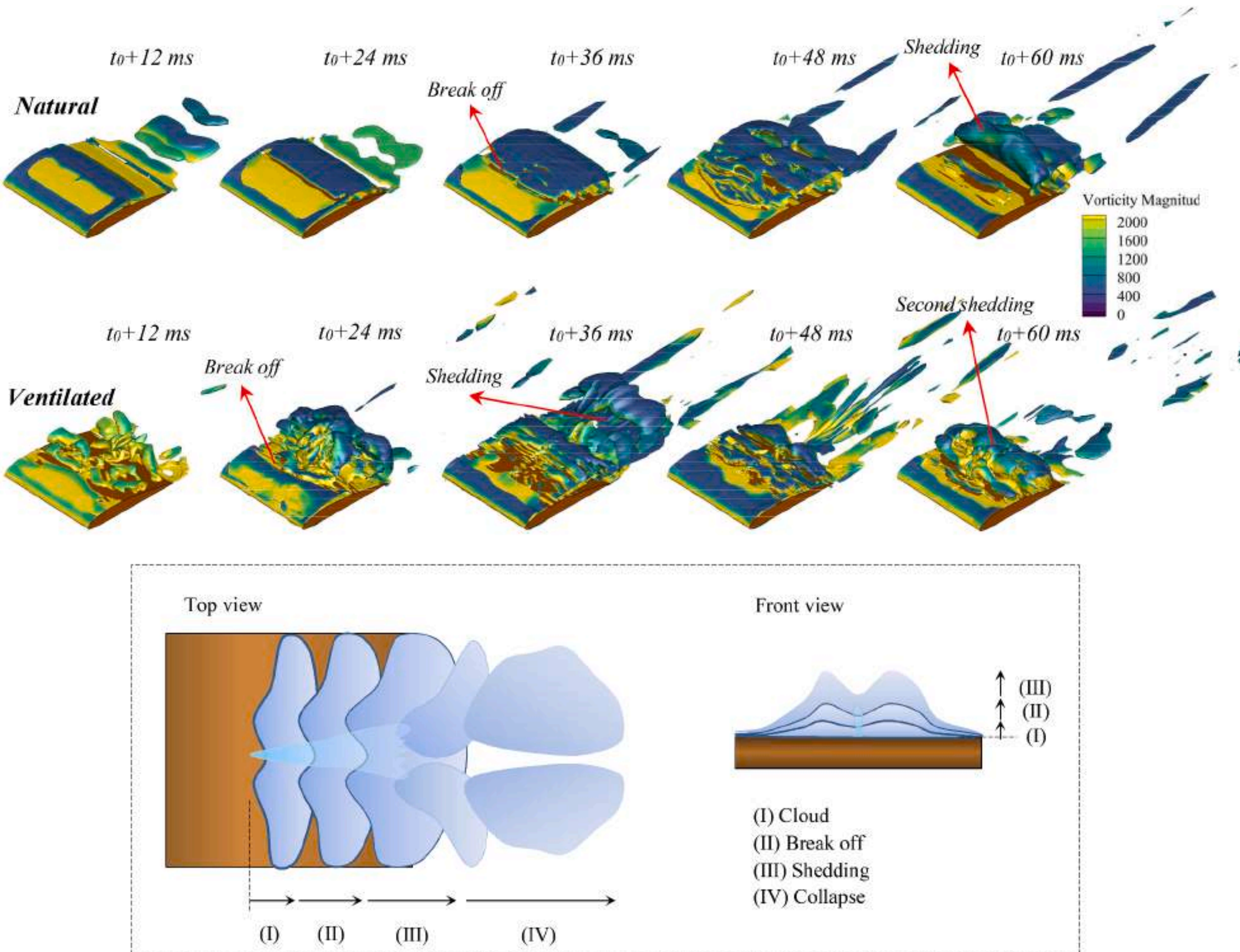

Fig. 13. (Above) The structures of the vortex based on the Q criterion ($Q_{criterion} = 40,000\ s^{-2}$) colored by the vorticity magnitude for natural and ventilated cavitation ($Q = 0$, 1 l/min, $\sigma = 1.1$, Tap5-injection) (Bottom) Schematic of the cavity structure under the effect of ventilation.

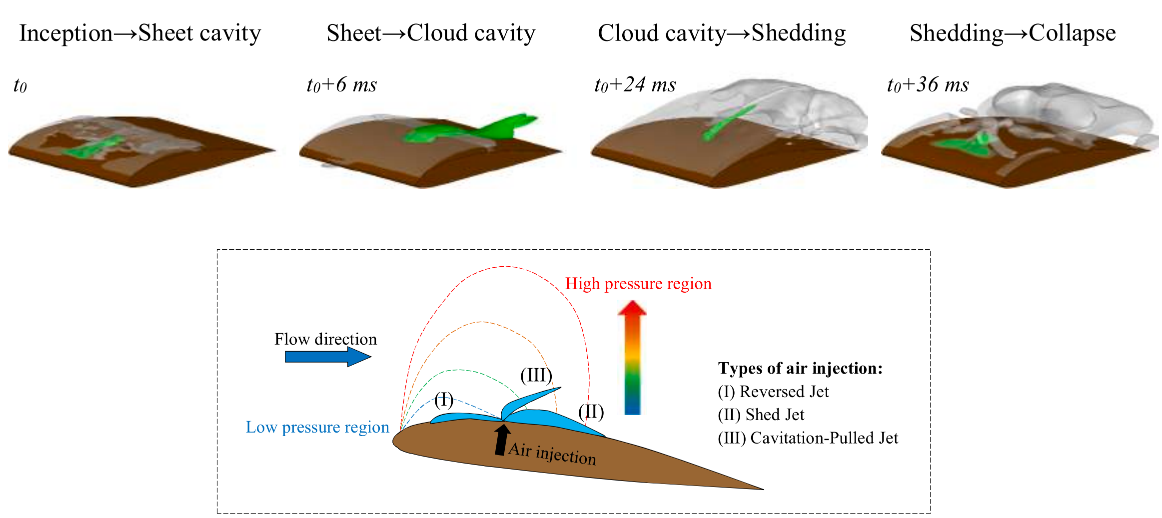

Fig. 14. (Above) Structure of the air injection jet presented by isosurfaces of vapor and air volume ($\alpha_v = 0.2$, $\alpha_a = 0.9$). (Bottom) Schematic of different types of air injection jet structure during cavity evolution ($Q = 1$ l/min, σ=1.1, Tap5-injection).

honoraria; educational grants; participation in speakers' bureaus; membership, employment, consultancies, stock ownership, or other equity interest; and expert testimony or patent-licensing arrangements), or non-financial interest (such as personal or professional relationships, affiliations, knowledge or beliefs) in the subject matter or materials discussed in this manuscript.

Data availability

Data will be made available on request.

Acknowledgments

This project is supported by the Polish National Science centre, Poland funds within the project UMO-2016/21/B/ST8/01164. The authors thank the Department of Power Engineering and Turbomachinery, The Silesian University of Technology, for funding this work under the statutory research funds (for young scientists). In addition, the project was supported by the Foundation for Polish Science (FNP).

References

[1] C. Peng, S. Tian, G. Li, M.C. Sukop, Simulation of multiple cavitation bubbles interaction with single-component multiphase Lattice Boltzmann method, Int. J. Heat Mass Transf. 137 (2019) 301–317.
[2] T. Sun, Y. Wei, L. Zou, Y. Jiang, C. Xu, Z. Zong, Numerical investigation on the unsteady cavitation shedding dynamics over a hydrofoil in thermo-sensitive fluid, Int. J. Multiphase Flow 111 (2019) 82–100.
[3] C.E. Brennen, "Fundamentals of multiphase flow," 2005.
[4] E. Hasani Malekshah, W. Wróblewski, K. Bochon, M. Majkut, Evaluation of modified turbulent viscosity on shedding dynamic of three-phase cloud cavitation around hydrofoil – numerical/experimental analysis, Int. J. Numeric. Method. Heat Fluid Flow 32 (12) (2022) 3863–3880, https://doi.org/10.1108/HFF-03-2022-0188.
[5] T. Sun, X. Ma, Y. Wei, C. Wang, Computational modeling of cavitating flows in liquid nitrogen by an extended transport-based cavitation model, Sci. China: Technol. Sci. 59 (2016) 337–346.
[6] R.T. Knapp, Recent investigations of the mechanics of cavitation and cavitation damage, Trans. Am. Soc. Mech. Eng. 77 (7) (1955) 1045–1054.
[7] M.V. Timoshevskiy, I.I. Zapryagaev, K.S. Pervunin, L.I. Maltsev, D.M. Markovich, K. Hanjalić, Manipulating cavitation by a wall jet: experiments on a 2D hydrofoil, Int. J. Multiphase Flow 99 (2018) 312–328.
[8] B. Che, L. Cao, N. Chu, D. Likhachev, D. Wu, Effect of obstacle position on attached cavitation control through response surface methodology, J. Mech. Sci. Technol. 33 (2019) 4265–4279.
[9] L. Zhang, M. Chen, X. Shao, Inhibition of cloud cavitation on a flat hydrofoil through the placement of an obstacle, Ocean Eng. 155 (2018) 1–9.
[10] E. Kadivar, M.V. Timoshevskiy, K.S. Pervunin, O. el Moctar, Cavitation control using cylindrical cavitating-bubble generators (CCGs): experiments on a benchmark CAV2003 hydrofoil, Int. J. Multiphase Flow 125 (2020), 103186.
[11] E. Kadivar, O. el Moctar, K. Javadi, Stabilization of cloud cavitation instabilities using cylindrical cavitating-bubble generators (CCGs), Int. J. Multiphase Flow 115 (2019) 108–125.
[12] W. Wang, Z. Li, M. Liu, X. Ji, Influence of water injection on broadband noise and hydrodynamic performance for a NACA66 (MOD) hydrofoil under cloud cavitation condition, Appl. Ocean Res. 115 (2021), 102858.
[13] C. Wang, Cavity Flow Mechanism Analysis and Passive Flow Control Technology Research, Dalian University of Technology, Dalian, China, 2013.
[14] S. Shao, Y. Wu, J. Haynes, R.E. Arndt, J. Hong, Investigation into the behaviors of ventilated supercavities in unsteady flow, Phys. Fluids 30 (5) (2018), 052102.
[15] L. Maltsev, V. Dimitrov, E. Milanov, I. Zapryagaev, M. Timoshevskiy, K. Pervunin, Jet control of flow separation on hydrofoils: performance evaluation based on force and torque measurements, J. Eng. Thermophys. 29 (3) (2020) 424–442.
[16] M.G. De Giorgi, A. Ficarella, D. Fontanarosa, Active control of unsteady cavitating flows in turbomachinery, in: Turbo Expo: Power for Land, Sea, and Air, 58554, American Society of Mechanical Engineers, 2019 p. V02AT45A027.
[17] R.E. Arndt, C. Ellis, and S. Paul, "Preliminary investigation of the use of air injection to mitigate cavitation erosion," 1995.
[18] G. Reisman, M. Duttweiler, and C. Brennen, "Effect of air injection on the cloud cavitation of a hydrofoil," 1997.
[19] T. Pham, F. Larrarte, and D.H. Fruman, "Investigation of unsteady sheet cavitation and cloud cavitation mechanisms," 1999.
[20] S.A. Mäkiharju, H. Ganesh, S.L. Ceccio, The dynamics of partial cavity formation, shedding and the influence of dissolved and injected non-condensable gas, J. Fluid Mech. 829 (2017) 420–458.
[21] T. Liu, B. Huang, G. Wang, M. Zhang, D. Gao, Experimental investigation of the flow pattern for ventilated partial cavitating flows with effect of Froude number and gas entrainment, Ocean Eng. 129 (2017) 343–351.
[22] J. Bin, X.-w. Luo, X.-x. Peng, Y. Zhang, Y.-l. Wu, H.-y. Xu, Numerical investigation of the ventilated cavitating flow around an under-water vehicle based on a three-component cavitation model, J. Hydrodyn., Ser. B 22 (6) (2010) 753–759.
[23] T. Sun, Z. Wang, L. Zou, H. Wang, Numerical investigation of positive effects of ventilated cavitation around a NACA66 hydrofoil, Ocean Eng. 197 (2020), 106831.
[24] E.H. Malekshah, W. Wróblewski, K. Bochon, M. Majkut, Experimental analysis on dynamic/morphological quality of cavitation induced by different air injection rates and sites, Phys. Fluids 35 (1) (2023), https://doi.org/10.1063/5.0136521.
[25] J. Holl, "An effect of air content on the occurrence of cavitation," 1960.
[26] E.S. Vasilakis, N. Kyriazis, P. Koukouvinis, M. Farhat, M. Gavaises, Cavitation induction by projectile impacting on a water jet, Int. J. Multiphase Flow 114 (2019) 128–139.
[27] M.-G. Mithun, P. Koukouvinis, I.K. Karathanassis, M. Gavaises, Numerical simulation of three-phase flow in an external gear pump using immersed boundary approach, Appl. Math. Model. 72 (2019) 682–699.
[28] C.P. Egerer, S. Hickel, S.J. Schmidt, N.A. Adams, Large-eddy simulation of turbulent cavitating flow in a micro channel, Phys. Fluids 26 (8) (2014), 085102.
[29] W. Wróblewski, K. Bochon, M. Majkut, E.H. Malekshah, K. Rusin, M. Strozik, An experimental/numerical assessment over the influence of the dissolved air on the instantaneous characteristics/shedding frequency of cavitating flow, Ocean Eng. 240 (2021), 109960, https://doi.org/10.1016/j.oceaneng.2021.109960, 2021/11/15/.
[30] W. Wróblewski, K. Bochon, M. Majkut, K. Rusin, E. Hasani Malekshah, Numerical study of cavitating flow over hydrofoil in the presence of air, Int. J. Numeric. Method. Heat Fluid Flow 32 (5) (2022) 1440–1462, https://doi.org/10.1108/HFF-03-2021-0204.
[31] E. Hasani Malekshah, W. Wróblewski, M. Majkut, Dissolved air effects on three-phase hydrodynamic cavitation in large scale Venturi- Experimental/numerical analysis, Ultrason. Sonochem. 90 (2022), 106199, https://doi.org/10.1016/j.ultsonch.2022.106199, 2022/11/01/.
[32] Z. Wang, H. Cheng, B. Ji, Euler–Lagrange study of cavitating turbulent flow around a hydrofoil, Phys. Fluids 33 (11) (2021), https://doi.org/10.1063/5.0070312.
[33] E. Ghahramani, H. Ström, R.E. Bensow, Numerical simulation and analysis of multi-scale cavitating flows, J. Fluid Mech. 922 (2021) A22, https://doi.org/10.1017/jfm.2021.424. Art no. A22.
[34] E. Hasani Malekshah, W. Wróblewski, Effect of turbulence modelling and non-condensable gas on cloud cavity dynamics, Int. J. Heat Fluid Flow 98 (2022), 109070, https://doi.org/10.1016/j.ijheatfluidflow.2022.109070, 2022/12/01/.
[35] H. Cheng, X. Long, B. Ji, X. Peng, M. Farhat, A new Euler-Lagrangian cavitation model for tip-vortex cavitation with the effect of non-condensable gas, Int. J. Multiphase Flow 134 (2021), 103441.
[36] E. Hasani Malekshah, W. Wróblewski, Merging theory-based cavitation model adaptable with non-condensable gas effects in prediction of compressible three-phase cavitating flow, Int. J. Heat Mass Transf. 196 (2022), 123279, https://doi.org/10.1016/j.ijheatmasstransfer.2022.123279, 2022/11/01/.
[37] V. Yakhot, S. Orszag, S. Thangam, T. Gatski, C. Speziale, Development of turbulence models for shear flows by a double expansion technique, Phys. Fluids A 4 (7) (1992) 1510–1520.
[38] O. Coutier-Delgosha, R. Fortes-Patella, J.-L. Reboud, Evaluation of the turbulence model influence on the numerical simulations of unsteady cavitation, J. Fluids Eng. 125 (1) (2003) 38–45.
[39] C.E. Brennen, Cavitation and Bubble Dynamics, Cambridge University Press, 2014.
[40] P.J. Zwart, A.G. Gerber, T. Belamri, A two-phase flow model for predicting cavitation dynamics, in: Fifth international conference on multiphase flow, Yokohama, Japan 152, 2004.
[41] X. Long, J. Zhang, J. Wang, M. Xu, Q. Lyu, B. Ji, Experimental investigation of the global cavitation dynamic behavior in a venturi tube with special emphasis on the cavity length variation, Int. J. Multiphase Flow 89 (2017) 290–298, https://doi.org/10.1016/j.ijmultiphaseflow.2016.11.004, 2017/03/01/.